NORTH ATLANTIC TREATY ORGANIZATION

SCIENCE AND TECHNOLOGY ORGANIZATION

AC/323(AVT-240)TP/902

www.sto.nato.int

STO TECHNICAL REPORT **TR-AVT-240**

Hypersonic Boundary-Layer Transition Prediction

(Prédiction de la transition de la couche limite hypersonique)

Summary Report of the NATO STO AVT-240 Task Group.

Published August 2020

NORTH ATLANTIC TREATY ORGANIZATION

SCIENCE AND TECHNOLOGY ORGANIZATION

AC/323(AVT-240)TP/902

www.sto.nato.int

STO TECHNICAL REPORT **TR-AVT-240**

Hypersonic Boundary-Layer Transition Prediction

(Prédiction de la transition de la couche limite hypersonique)

Summary Report of the NATO STO AVT-240 Task Group.

The NATO Science and Technology Organization

Science & Technology (S&T) in the NATO context is defined as the selective and rigorous generation and application of state-of-the-art, validated knowledge for defence and security purposes. S&T activities embrace scientific research, technology development, transition, application and field-testing, experimentation and a range of related scientific activities that include systems engineering, operational research and analysis, synthesis, integration and validation of knowledge derived through the scientific method.

In NATO, S&T is addressed using different business models, namely a collaborative business model where NATO provides a forum where NATO Nations and partner Nations elect to use their national resources to define, conduct and promote cooperative research and information exchange, and secondly an in-house delivery business model where S&T activities are conducted in a NATO dedicated executive body, having its own personnel, capabilities and infrastructure.

The mission of the NATO Science & Technology Organization (STO) is to help position the Nations' and NATO's S&T investments as a strategic enabler of the knowledge and technology advantage for the defence and security posture of NATO Nations and partner Nations, by conducting and promoting S&T activities that augment and leverage the capabilities and programmes of the Alliance, of the NATO Nations and the partner Nations, in support of NATO's objectives, and contributing to NATO's ability to enable and influence security and defence related capability development and threat mitigation in NATO Nations and partner Nations, in accordance with NATO policies.

The total spectrum of this collaborative effort is addressed by six Technical Panels who manage a wide range of scientific research activities, a Group specialising in modelling and simulation, plus a Committee dedicated to supporting the information management needs of the organization.

- AVT Applied Vehicle Technology Panel
- HFM Human Factors and Medicine Panel
- IST Information Systems Technology Panel
- NMSG NATO Modelling and Simulation Group
- SAS System Analysis and Studies Panel
- SCI Systems Concepts and Integration Panel
- SET Sensors and Electronics Technology Panel

These Panels and Group are the power-house of the collaborative model and are made up of national representatives as well as recognised world-class scientists, engineers and information specialists. In addition to providing critical technical oversight, they also provide a communication link to military users and other NATO bodies.

The scientific and technological work is carried out by Technical Teams, created under one or more of these eight bodies, for specific research activities which have a defined duration. These research activities can take a variety of forms, including Task Groups, Workshops, Symposia, Specialists' Meetings, Lecture Series and Technical Courses.

The content of this publication has been reproduced directly from material supplied by STO or the authors.

Published August 2020

ISBN 978-92-837-2227-4

Table of Contents

List of Figures

List of Tables

List of Acronyms

ACE	Actively Controlled Expansion
AEDC	Arnold Engineering Development Center
AFRL	Air Force Research Laboratory (USA)
AGARD	Advisory Group for Aerospace Research and Development (predecessor to STO)
AIAA	American Institute of Aeronautics and Astronautics
AVT	Applied Vehicle Technology Panel
CUBRC	Calspan-University at Buffalo Research Center
DLR	Deutsches Zentrum für Luft- und Raumfahrt (German Aerospace Center)
DNS	Direct Numerical Simulation
HIFiRE	Hypersonic International Flight Research Experimentation
JAXA	Japan Aerospace Exploration Agency
NASA	National Aeronautics and Space Administration
RTO	Research and Technology Organization (predecessor to STO)
RWTH	Aachen Rheinisch Westfälische Technische Hochschule Aachen
TU	Technical University
USAFA	US Air Force Academy
VKI	von Karman Institute for Fluid Dynamics

AVT-240 Membership List

CO-CHAIRS

Rolf RADESPIEL*
Technical University Braunschweig
GERMANY
Email: r.radespiel@tu-bs.de

Steven SCHNEIDER*
Purdue University
UNITED STATES
Email: steves@ecn.purdue.edu

MEMBERS

David ADAMCZAK*
Airforce Defense Laboratory (AFRL)
UNITED STATES
Email: david.adamczak@us.af.mil

Syed ALI*
Technische Universitaet Braunschweig
GERMANY
Email: s.ali@tu-braunschweig.de

Thierry ANDRE*
MBDA
FRANCE
Email: thierry.andre@mbda-systems.com

Alexander Arndt*
University of Notre Dame
UNITED STATES
Email: Alexander.J.Arndt.13@nd.edu

Armani BATISTA
University of Delaware
UNITED STATES
Email: abatista@udel.edu

Karen T. BERGER*
NASA Langley Research Center
UNITED STATES
Email : karen.t.berger@nasa.gov

Matthew BORG*
Air Force Research Laboratory
UNITED STATES
Email: matthew.borg.3@us.af.mil

Rodney BOWERSOX*
Texas A&M University
UNITED STATES
Email: bowersox@tamu.edu

Graham CANDLER*
University of Minnesota
UNITED STATES
Email: candler@aem.umn.edu

Gennaro CARDONE*
Università degli Studi di Napoli "Federico II"
ITALY
Email: gcardone@unina.it

Katya CASPER*
SNL
UNITED STATES
Email: kmcaspe@sandia.gov

Bayram CELIK
Istanbul Technical University
TURKEY
Email: celikbay@itu.edu.tr

Salvatore CERASOULO*
University of Naples "Federico II"
ITALY
Email : cerasuolo.salvatore@libero.it

Adriano CERMINARA*
University of Southampton
ITALY
Email: a.cerminara@soton.ac.uk

*** Contributing author**

Ross CHAUDRY*
University of Minnesota
UNITED STATES
Email: chaudhry.ross@gmail.com

Meelan. M CHOUDHARI*
NASA Langley Research Center
UNITED STATES
Email: meelan.m.choudhari@nasa.gov

Amanda CHOU*
NASA Langley Research Center
UNITED STATES
Email: amanda.chou@nasa.gov

Brandon CHYNOWETH*
Purdue University
UNITED STATES
Email: bchynowe@purdue.edu

Thomas CORKE*
University of Notre Dame
UNITED STATES
Email: tcorke@nd.edu

Alex CRAIG*
University of Arizona
UNITED STATES
Email: sacraig@email.arizona.edu

Russell CUMMINGS
US Air Force
UNITED STATES
Email: russ.cummings@usafa.edu

Antonio DI GIOVANNI*
Technische Universitaet Munich
ITALY
Email: Antonio.DiGiovanni@aer.mw.tum.de

Lian DUAN*
Missouri University of Science & Technology
UNITED STATES
Email: duanl@mst.edu

Antoin DURANT*
MBDA
FRANCE
Email: antoine.durant@mbda-systems.com

Joshua EDELMAN*
Purdue University
UNITED STATES
Email: jedelma@purdue.edu

Hermann FASEL*
University of Arizona
UNITED STATES
Email: faselh@email.arizona.edu

Kathryn GRAY*
Purdue University
UNITED STATES
Email: gray144@purdue.edu

Guillame GROSSIR*
von Karman Institute for Fluid Dynamics (VKI)
BELGIUM
Email: grossir@vki.ac.be

Christoph HADER*
University of Arizona
UNITED STATES
Email: christoph.hader@gmail.com

Stefan HEIN*
Deutsches Zentrum für Luft und Raumfahrt (DLR)
GERMANY
Email: stefan.hein@dlr.de

Joseph JEWELL*
US Air Force Research Laboratory
Email: jjewell@gmail.com
UNITED STATES

Heath JOHNSON*
Virtus
UNITED STATES
Email: hjohnson@aem.umn.edu

Thomas JULIANO*
University of Notre Dame
UNITED STATES
Email: tjuliano@nd.edu

Roger KIMMEL*
US Air Force
UNITED STATES
Email: roger.kimmel@us.af.mil

***Contributing author**

Rudolph KING
NASA Langley Research Center
UNITED STATES
Email: rudolph.a.king@nasa.gov

Lindsay KIRK*
NASA Johnson Space Center
UNITED STATES
Email: Lindsay.C.Kirk@nasa.gov

Travis KOCIAN*
Texas A&M University
UNITED STATES
Email : tskocian@gmail.com

Joseph KUEHL*
Baylor University
UNITED STATES
Email: Joe_Kuehl@Baylor.edu

Andrew LEIDY*
Texas A&M University
UNITED STATES
Email: Andrew.leidy@nasa.gov

Madlen LEINEMANN*
Technische Universitaet Braunschweig
GERMANY
Email: m.leinemann@tu-braunschweig.de

Fei LI*
NASA Langley Research Center
UNITED STATES
Email: fei.li@nasa.gov

Eric MARINEAU*
American Economic Development Council (AEDC)
UNITED STATES
Email: eric.marineau@navy.mil

Eric MATLIS*
University of Notre Dame
UNITED STATES
Email: Eric.H.Matlis.1@nd.edu

Matthew MCGILVRAY
University of Oxford
AUSTRALIA
Email: matthew.mcgilvray@eng.ox.ac.uk

Fernando MIRO MIRO*
von Karman Institute for Fluid Dynamics (VKI)
BELGIUM
Email: fernando.miro.miro@vki.ac.be

Alexander MOYES
Texas A&M University
UNITED STATES
Email: alexandermoyes7@gmail.com

Christian MUNDT
University of the Bundeswehr
GERMANY
Email: Christian.mundt@unibw.de

Federico MUNOZ*
Technische Universitaet Braunschweig
GERMANY
Email: f.munoz@tu-braunschweig.de

Ian T. NEEL*
NASA Langley Research Center
UNITED STATES
Email: ian.t.neel@nasa.gov

Pedro Parades PAREDES GONZALES*
NASA Langley Research Center
SPAIN
Email: pedro.paredes@nasa.gov

Fabio PINNA*
von Karman Institute for Fluid Dynamics (VKI)
BELGIUM
Email: fabio.pinna@vki.ac.be

Helen L. REED*
Aerospace Engineering
UNITED STATES
Email: helen.reed@tamu.edu

Eli RESHOTKO*
Case Western Reserve University
UNITED STATES
Email: exr3@case.edu

Neil D. SANDHAM*
University of Southampton
UNITED KINGDOM
Email: n.sandham@soton.ac.uk

*** Contributing author**

Bill SARIC*
Texas A&M University
UNITED STATES
Email: saric@tamu.edu

Dr. Carlo SCALO*
Purdue University
ITALY
Email: scalo@purdue.edu

Thomas SCHILDEN*
RWTH Aachen
GERMANY
Email: t.schilden@aia.rwth-aachen.de

Wolfgang SCHROEDER*
RWTH Aachen
GERMANY
Email: office@aia.rwth-aachen.de

Michael SEMPER
US Air Force Academy
UNITED STATES
Email: Michael.Semper.ctr@usafa.edu

Scott STANFIELD*
ISSI
UNITED STATES
Email: Scott.Stanfield.ctr@wpafb.af.mil

Christian STEMMER*
Technische Universität München
GERMANY
Email: Christian.Stemmer@aer.mw.tum.de

Hideyuki TANNO*
JAXA
JAPAN
Email: tanno@spaceships.isas.jaxa.jp

Nigel TAYLOR*
MBDA
UNITED KINGDOM
Email: nigel.j.taylor@mbda-systems.com

Alexander THEISS*
Deutsches Zentrum für Luft- und Raumfahrt (DLR)
GERMANY
Email: alexander.theiss@dlr.de

Vassilis THEOFILIS
University of Liverpool
SPAIN
Email: v.theofilis@liverpool.ac.uk

Onur TUNCER
Istanbul Technical University
TURKEY
Email: tuncero@itu.edu.tr

Tim WADHAMS
CUBRC
UNITED STATES
Email: wadhams@cubrc.org

Alexander WAGNER*
Deutsches Zentrum für Luft- und Raumfahrt (DLR)
GERMANY
Email: alexander.wagner@dlr.de

Ross Martin WAGNILD*
SNL
UNITED STATES
Email: rmwagni@sandia.gov

Viola WARTEMANN*
DLR – German Aerospace Centre
GERMANY
Email: viola.wartemann@dlr.de

Bradley WHEATON*
Johns Hopkins University
UNITED STATES
Email: Bradley.Wheaton@jhuapl.edu

Sebastian WILLEMS
German Aerospace Center
GERMANY
Email: sebastian.willems@dlr.de

Kemal Bulent YUCEIL
Istanbul Technical University
TURKEY
Email: yuceil@itu.edu.tr

Mirko ZACCARA*
University of Naples “Federico II”
ITALY
Email: mirko.zaccara@outlook.com

*** Contributing author**

PANEL/GROUP MENTOR

Prof. Dr. Cord ROSSOW
Deutsches Zentrum für Luft und Raumfahrt (DLR)
GERMANY
Email: cord.rossow@dlr.de

Hypersonic Boundary-Layer Transition Prediction
(STO-TR-AVT-240)

Executive Summary

Hypersonic boundary-layer transition can have dramatic effects on aeroheating and control authority, yet it remains very difficult to predict, even after half a century of research. Applications include missiles for time-critical strike, hypersonic cruise vehicles, reusable launch and re-entry vehicles, and missile-defence interceptors. Although researchers have been working toward mechanism-based prediction methods for several decades, designers are still using empirical methods, and there is a need to narrow the gap between the two groups. Recently, quiet hypersonic wind tunnels have become available to the research community, high enthalpy facilities have been used to obtain useful data related to instability and transition, and some high-quality flight data were accumulated. Moreover, new instrumentation has been developed for identification and analysis of the instability mechanisms that lead to transition. Also, sophisticated new computational capabilities have shown progress to the point where computations of the Parabolized Stability Equations are becoming a state-of-the-art engineering method, at least for perfect-gas flows, and Direct Numerical Simulation (DNS) of the transition processes is now feasible. DNS even allows taking into account the freestream disturbance environment, when known. It appears that definitive progress on the difficult problem of hypersonic boundary layer transition is possible by coordinating the various international research efforts.

Hypersonic transition can be caused by several different mechanisms, is affected by various freestream and surface perturbations, and can occur under a variety of flow conditions. In order to develop mechanism-based methods for prediction and control, generic geometries need to be investigated in order to understand the various instabilities that may occur in each case, how they cause transition, and their sensitivity to the flow parameters. Accordingly, the activities of the AVT-240 Task Group were divided into multiple Subtasks. Each Subtask represented an important building block in the overall problem of hypersonic transition, wherein several experts from various NATO nations embarked in cooperative research, each with their own financial support. A number of researchers worked on multiple Subtasks, using similar facilities, instrumentation, and computer codes, yielding a significant overlap as well as synergy between the different Subtask Teams. These subtasks covered:

- Second-mode transition on slender geometries in quiet and conventional ground based facilities;
- Cross-flow transition on conical geometries at wind tunnel flow conditions;
- Mechanism of windside forward transition on sharp and blunted cones at angle of attack; and
- Mechanism of boundary layer transition on nonablating capsules and its sensitivities.

As described in this document, substantial progress was achieved in addressing these major problems in hypersonic transition.

Prédiction de la transition de la couche limite hypersonique

(STO-TR-AVT-240)

Synthèse

La transition de la couche limite hypersonique peut avoir des effets spectaculaires sur l'échauffement aérodynamique et l'action sur les commandes de vol, mais elle reste très difficile à prédire, même après un demi-siècle de recherches. Les applications concernent notamment les missiles pour les frappes critiques, les véhicules de croisière hypersoniques, les véhicules réutilisables de lancement et de rentrée, ainsi que les intercepteurs antimissiles. Bien que les chercheurs travaillent depuis plusieurs décennies à des méthodes de prédiction basées sur des mécanismes, les concepteurs utilisent toujours des méthodes empiriques et il est nécessaire de combler le fossé entre ces deux groupes d'acteurs. Depuis peu, la communauté de la recherche a accès à des souffleries hypersoniques à faibles turbulences, elle utilise des installations à haute enthalpie pour obtenir des données utiles liées à l'instabilité et la transition, et elle a accumulé des données de vol de grande qualité. Par ailleurs, une nouvelle instrumentation a été développée pour l'identification et l'analyse des mécanismes d'instabilité qui mènent à la transition. En outre, les nouvelles capacités de calcul sophistiquées ont progressé au point que le calcul des équations de stabilité paraboliséees devient une méthode d'ingénierie de pointe, au moins pour les écoulements de gaz parfait, et que la simulation numérique directe (DNS) des processus de transition est désormais faisable. La DNS permet même de tenir compte de l'environnement de turbulence en écoulement libre, lorsque celui-ci est connu. Il semble que des progrès définitifs soient possibles sur l'épineux problème de la transition de la couche limite hypersonique, grâce à la coordination des divers travaux de recherche internationaux.

La transition hypersonique peut être provoquée par plusieurs mécanismes différents, subit l'influence de divers écoulements libres et perturbations de surface, et peut se produire dans diverses conditions d'écoulement. Le développement de méthodes de prédiction et de contrôle basées sur des mécanismes passe par l'étude des géométries générales, qui permettent de comprendre les diverses instabilités susceptibles de survenir dans chaque cas, la façon dont elles provoquent la transition, ainsi que leur sensibilité aux paramètres d'écoulement. En conséquence, les activités du groupe de travail AVT-240 ont été divisées en multiples tâches secondaires. Chaque tâche secondaire représentait un module important du problème global de la transition hypersonique, pour lequel plusieurs experts de divers pays de l'OTAN se sont engagés dans des recherches en coopération, chacun avec leur propre soutien financier. Un certain nombre de chercheurs ont travaillé à de multiples tâches secondaires, en utilisant des installations, une instrumentation et des codes informatiques similaires, ce qui a produit un chevauchement important des travaux et une synergie entre les différentes équipes. Les tâches secondaires étaient les suivantes :

- La transition de second mode sur les géométries plus effilées dans les installations terrestres conventionnelles et à faibles turbulences ;
- La transition transversale sur les géométries coniques en conditions d'écoulement des souffleries ;
- Le mécanisme de transition vers l'avant sur l'intrados sur les cônes effilés et émoussés à l'angle d'attaque ; et
- Le mécanisme de transition de la couche limite sur des capsules non érodables et ses sensibilités.

Ainsi que ce document le décrit, des progrès sensibles ont été réalisés dans le traitement de ces problèmes majeurs de la transition hypersonique.

Chapter 1 - GENERAL INTRODUCTION

Rolf Radespiel
Technische Universität Braunschweig
GERMANY

Steven Schneider
Purdue University
UNITED STATES

1.0 NOMENCLATURE

AGARD	Advisory Group for Aerospace Research and Development (predecessor to STO)
AIAA	American Institute of Aeronautics and Astronautics
AEDC	Arnold Engineering Development Center
AFRL	Air Force Research Laboratory (USA)
AVT	Applied Vehicle Technology Panel
CUBRC	Calspan University at Buffalo Research Center
DLR	Deutsches Zentrum für Luft und Raumfahrt (German Aerospace Center)
DNS	Direct Numerical Simulation
HIFiRE	Hypersonic International Flight Research Experimentation
JAXA	Japan Aerospace Exploration Agency
NASA	National Aeronautics and Space Administration
RTO	Research and Technology Organization (predecessor to STO)
RWTH	Rheinisch Westfälische Technische Hochschule Aachen
TU	Technical University
USAFA	US Air Force Academy
VKI	Von Karman Institute for Fluid Dynamics

1.1 BACKGROUND

Hypersonic boundary layer transition has been studied for more than half a century. Over the years, AGARD and RTO/AVT has organized several symposia on this topic, including the recent Specialists' Meeting on Hypersonic Boundary-Layer Transition (AVT-200). Aeroheating and the effect of transition on aerodynamic forces and moments are the principal design drivers for hypersonic vehicles such as missiles for time-critical strike, hypersonic cruise vehicles, reusable launch and re-entry vehicles, and ballistic-missile interceptors. Therefore, the simulation and control of transition represents a fundamental and critical issue for these vehicle configurations. Although researchers have been working toward mechanism-based prediction methods for a number of decades, designers are still using empirical methods, and there is a need to narrow the gap between the two groups. Recently, quiet hypersonic wind tunnels have become available to the research community, high enthalpy facilities have been used to obtain useful data related to instability and transition, and some high-quality flight data were accumulated. Moreover, new instrumentation has been developed for identification and analysis of the instability mechanisms that lead to transition. Also, sophisticated new computational capabilities have shown progress to the point where computations of the Parabolized Stability Equations are becoming a state-of-the-art engineering method, at least for perfect-gas flows, and Direct Numerical Simulation (DNS) of the transition processes is now feasible. DNS even allows taking into account the freestream disturbance environment. It appears that definitive progress on the difficult problem of hypersonic boundary layer transition is possible by coordinating the various international research efforts.

1.2 OBJECTIVES OF TASK GROUP AVT-240

Although hypersonic transition is sometimes viewed as a narrow technical area, the related flow phenomena are rooted in a broad range of flow instabilities, and furthermore, transition is affected by various freestream and surface perturbations, and it occurs under a variety of flow conditions. In order to develop mechanism-based methods for prediction and control, various generic geometries need to be investigated in order to understand the various instabilities that may occur in each case, how they cause transition, and their sensitivity to the flow parameters. Accordingly, the activities of the AVT-240 Task Group were divided into multiple Subtasks. Each Subtask represents an important building block in the overall problem of hypersonic transition, wherein several experts from various NATO nations embarked in cooperative research, each with their own financial support. A number of researchers worked on multiple Subtasks, using similar facilities, instrumentation, and computer codes, yielding a significant overlap as well as synergy between the different Subtask Teams.

The primary objective of the Task Group AVT-240 was to establish the scientific foundations that would aid the characterization and physics based prediction of hypersonic boundary layer transition in the following specific areas:

- Ability to predict second mode transition on slender geometries in quiet and conventional ground based facilities;
- Ability to predict cross-flow transition on conical geometries at wind tunnel flow conditions;
- Mechanism of wind-side forward transition on sharp and blunted cones at angle of attack; and
- Mechanism of boundary layer transition on non-ablating capsules and its sensitivities.

As described in this document, a substantial progress was achieved in addressing these major problems in hypersonic transition. However, it does not mean that the problem of predicting hypersonic boundary layer transition is generally solved. Rather, the present cooperative approach has paved the way to moving forward in an area where the limitations of individual research groups would have allowed a rather small chance of success in the absence of such collaboration.

1.3 APPROACH AND RESULTS OF TASK GROUP AVT-240

The Subtasks comprising the overall effort address important transition phenomena that were not sufficiently well understood at the onset of the Task Group's work. The task teams combined theoretical results, advanced flow simulations, and wind tunnel experiments to advance the scientific knowledge base on each of the relevant subtopics. The work of the Task Group was carried out during the years 2015 – 2018, involving frequent contacts via telephone and email communications, and semi-annual meetings. The fall meeting was held as part of the business week meeting of the AVT Panel, whereas the spring meeting rotated between the various research groups within AVT-240. As described in Section 1.4, a large portion of the research conducted under AVT-240 has already been published in conference papers and archival publications. Rather than providing a comprehensive account of the entire set of activities, this report provides a summary of the main body of results based on the AVT-240 effort.

1.3.1 Second Mode Instability

At hypersonic Mach numbers, the transition to turbulence in essentially 2-D or axisymmetric boundary layers is primarily governed by the second mode instability. For adiabatic flows, the second mode instability is relevant to both slender cones at zero angle of attack and wedge-like geometries such as the research vehicle X-43, at freestream Mach numbers of greater than four to seven, depending on the nose radius. Physically, the second mode disturbance is similar to a trapped acoustic wave near the wall. These disturbances have been found in experiments and validated by theory and computations. For cooled surfaces, the second mode is further destabilized, and hence, can dominate at even lower Mach numbers. Particular attention must be given to the thermal boundary layer and other effects (air chemistry, surface catalysis, wall temperature, etc.) that modify it. Promising techniques for transition delay include ultrasonically absorptive surface coatings to damp the second mode waves, and high enthalpy CO_2 and air/CO_2 mixtures to suppress the second mode through the absorption of acoustic disturbance energy via vibrational relaxation.

For edge Mach numbers greater than about 4, the second mode will likely be a dominant transition mechanism on smooth axisymmetric vehicles flying ballistic trajectories at zero (or low) angle of attack. This mechanism will also occur on 3D geometries, on sections of the body where the surface streamlines are relatively straight, although in 3D flows it will coexist with the cross-flow instability. Careful shaping of the surface might minimize the cross-flow instability, leaving the second mode modes as the dominant primary instability.

Experimental and computational groups closely collaborated in both discovery and validation activities that were focused on common geometries that included the near-sharp, 7° half-angle, right-circular cone, a near-sharp elliptic cone, and a flared cone. The flared cone was primarily used in the quiet tunnels to achieve the larger growth in second mode instability that is required in a low disturbance environment, given the limited quiet Reynolds numbers that are presently available.

Most facilities are “conventional” and not designed as “quiet”, and it is important to assess and relate the observations from these facilities to in-flight transition. Therefore, the effects of the freestream disturbances on second mode evolution were evaluated experimentally and computationally at different Mach numbers, and in low and high enthalpy environments, by groups at AEDC, Sandia National Laboratories, CUBRC, AFRL, NASA, DLR, JAXA, Purdue University, TU Braunschweig, Texas A&M University, and Minnesota University. Those results are presented in Chapter 2 of this report. They indicate the feasibility of predicting transition due to second mode instabilities in conventional tunnels by employing the so-called amplitude methods.

The transition processes extending into the nonlinear stages were also studied by the AVT-240 Group, including the factors related to the experimental observations of streaks and overshoot in skin-friction and heat transfer. Nonlinear interaction could be assessed for the first time in cold flow quiet tunnels, while the analysis took advantage of numerous simulations performed within the Group. The groups at Purdue, Texas A&M, University of Arizona, Minnesota, NASA carried out this work. The results are presented in Chapter 4 of this report. High enthalpy effects on second mode transition were evaluated by groups at DLR, Sandia, VKI, and JAXA, as reported in Chapter 5.

Passive porous walls appear very promising for suppressing the second mode. Recent research involved multidisciplinary investigations of material and fluid physics sciences. A range of designs and analysis methods were investigated by the groups at DLR and Purdue University, as presented in Chapter 3 of this report.

1.3.2 Characterization of Wind Tunnel Freestream Disturbances

Freestream disturbances in hypersonic wind tunnels are usually composed of acoustic disturbances, vorticity disturbances, and fluctuations of flow entropy. The acoustic disturbances are generated by high-speed turbulent boundary layers along the nozzle walls that radiate noise into the wind tunnel test section. These disturbances increase rapidly with flow speed, at least up to Mach 6, and hence, they appear to strongly influence the transition processes in hypersonic wind tunnels with turbulent nozzles. Five hypersonic wind tunnels with laminar nozzle boundary layers exist worldwide. These are operated by the universities at Purdue, Texas A&M, Beijing University (which has 2 such facilities), and the National Defence University of China, and these tunnels are effective in reducing the acoustic disturbances by at least one order of magnitude. However, the facilities are limited in Reynolds number so that only selected hypersonic transition processes can be investigated in them, whereas the duplication of flight Reynolds number and Mach number is generally not possible. Fluctuations of freestream vorticity and entropy originate from the tunnel settling chamber and the subsequent changes imposed by the wind tunnel nozzle. The role that the individual disturbances play in the typically observed transition scenarios is mostly unknown. Unfortunately, existing measurements mostly provide data in terms of the rms amplitudes, without any evaluation of the disturbance spectra up to the very high frequencies corresponding to second mode instabilities in transitional hypersonic boundary layers. It is believed that new probes and new instrumentation will greatly help the physical characterization of freestream disturbance levels and make the numerical rebuilding of transition experiments possible.

The research partners undertook coordinated experimental and numerical work to yield freestream data that are physically relevant to the transition processes in hypersonic flows. The new experimental data now available covers a spectral range of disturbances that was previously not achieved by using hot-wire probes. The groups from NASA, AEDC, Braunschweig, Sandia, and Purdue tested a range of freestream probes and sensors. Numerical simulations addressed the problem of disturbance generation, i.e., at the nozzle walls. For the first time, the acoustic noise level in hypersonic wind tunnels was computed from direct simulations provided by Missouri University of Science and Technology and NASA. Also, numerical simulations of RWTH Aachen and Minnesota provided the transfer of disturbances to the detailed location of the flow sensor as mounted on the probe. Chapter 6 presents the results of this collaborative research effort.

1.3.3 Blunt Shapes

While many transition measurements have been performed in the past on blunt hypersonic geometries, little was known about the detailed transition mechanisms at the start of the Task Group. On the windward side of very blunt re-entry shapes, transition had been previously observed for nominally smooth surfaces and even for cases where linear stability analysis indicated a stable boundary layer. Instability experiments on blunt shapes have not been feasible in quiet wind tunnels, as the accessible Reynolds number is too small in these facilities. The use of large nose bluntness on slender cone models in conventional facilities had revealed the so-called transition reversal, where an unknown mechanism resulted in significantly earlier transition than that on models with smaller nose radii. Theoretical considerations had therefore led to the hypothesis that roughness effects create disturbances that undergo transient growth, leading to amplitudes that are large enough for transition to occur. However, in wind tunnels with significant freestream disturbances, there could be also combined effects of freestream disturbances and small surface roughness, creating an alternate path to transition.

The research partners selected two common generic shapes to investigate the receptivity processes and disturbance evolution on blunt shapes, namely, the generic Apollo capsule shape and the blunted cone. While

increasing the nose bluntness of slender cones usually increases the measured transition length on wind tunnel models, this trend is reversed at sufficiently large values of the nosetip Reynolds number, so that the transition onset location eventually moves upstream with a further increase in nosetip bluntness. This transition reversal phenomenon, which cannot be explained on the basis of the usual linear stability theory, was the focus of collaborative investigations in the wind tunnels of AEDC, AFRL, and VKI, while NASA provided numerical estimates of optimal disturbance growth. Chapter 7 reports that the transient growth analysis is in qualitative agreement with the experimental observations, albeit a definitive link between transient growth and transition onset has not yet been established.

The Apollo shape at angles of attack was selected to investigate transition on the windward side of the blunt geometry. Apollo was chosen because significant and valuable wind tunnel data already exist for that shape and the windward side boundary layer is not affected by cross-flow instabilities. Fundamental knowledge on the transition mechanisms of the blunt Apollo shape was obtained by performing wind tunnel tests using well instrumented models with smooth surfaces, as well as isolated and distributed roughness in cold flow by Texas A&M, Braunschweig, and for higher freestream enthalpies by JAXA. The results indicate that theory-based correlations provide reasonable correlation with roughness induced transition measured in conventional, cold, hypersonic wind tunnels as detailed in Chapter 9, while the accuracy of these correlations at higher enthalpies and for strongly cooled walls remains to be seen. DLR, NASA, Aachen, and TU Munich contributed to the rebuilding of these experiments by employing optimal growth analyses and DNS, resulting in new knowledge on the sensitivities of roughness induced transition mechanisms, as detailed in Chapter 8.

1.3.4 Cross-Flow Dominated Transition

Transition on hypersonic lifting bodies is likely to be influenced by the mean cross-flow velocity component that is subject to a cross-flow instability. Much is known about cross-flow dominated transition at subsonic and supersonic Mach numbers. In those Mach number regimes, validated flow simulation codes can predict the modal characteristics of cross-flow instability and the resulting transition location with reasonable accuracy. The understanding gained through a combination of experiments and simulations has led to the development of successful methods for cross-flow transition control that have been validated up to supersonic Mach numbers.

The Task Group therefore undertook an analogous, coordinated effort on the prediction and control of cross-flow transition for the higher, i.e., hypersonic Mach numbers that are expected on both future air vehicles and airbreathing launch systems. The objective was to utilize the assets of multilateral experimental facilities, flight tests, and expertise in computational flow simulation. The research partners selected two common generic shapes: a 7 deg. half-angle right-circular cone at angles of attack from 4 deg. to 6 deg., and a 2:1 elliptic cone at 0 deg. angle of attack. In both geometries, a mean cross-flow velocity component is present, and the dominant transition mechanisms are through the cross-flow instability.

The groups have obtained new fundamental knowledge of the linear and nonlinear cross-flow transition mechanisms on the two model shapes, by performing wind tunnel tests using well instrumented models with smooth surfaces in cold hypersonic flow by Purdue, Texas A&M, University of Notre Dame, and AFRL, while flight test data from HIFiRE flights provided important insight on ground-to-flight extrapolation. Companion numerical simulations of these experiments were performed by Texas A&M, NASA, and Minnesota. The results presented in Chapters 10 and 11 of this report provide a significant basis of new knowledge about the relevant paths to transition in cross-flow dominated flows, including high-frequency, strongly amplified secondary instability modes. Advanced experimental techniques took

advantage of the international know-how and exchange, for example, the use of infrared techniques for global measurements of surface heat-transfer (Chapter 13).

The stationary cross-flow instability mode is known to be highly sensitive to surface roughness. This characteristic is the basis for the patterned Discrete Roughness Elements (DREs) used for cross-flow transition control. Hence, the effect of surface roughness on hypersonic cross-flow transition experiments was a particular focus. Wind tunnel experiments conducted by Notre Dame at USAFA and by Texas A&M on the 7 deg. half-angle right-circular cone at an angle of attack, and on a 2:1 elliptic cone at zero angle are reported on Chapter 12. The results reveal prediction and control of turbulent transition in these cases, as well as the sensitivity to initial conditions including surface roughness, and freestream acoustic disturbance levels.

The complex receptivity process of the fully 3D flow over a generic forebody was studied by wind tunnel experiments and by Direct Numerical Simulations. Chapter 14 shows that cross-flow instabilities have different receptivity characteristics relative to the boundary layer close to the forebody plane of symmetry.

1.4 DISSEMINATION OF RESULTS

The scientific work of the AVT-240 Task Group has resulted in numerous conference and journal publications by its members over the last 4 years. The number of publications is so large that collecting and documenting them all is beyond the scope of the present final report. Most of these publications are cited in the references of the individual chapters of the present final report.

The team of AVT-240 organized two Technical Sessions devoted to its joint research at the AIAA SciTech Forum in January 2018. The presentations composing these sessions described the most important joint results of the team and highlighted the collaborative approach of AVT-240. The papers written from these presentations appeared in a Special Issue of the *Journal of Spacecraft and Rockets,* Volume 56, Number 2, March-April, 2019.

1.5 CONCLUSIONS

The Task Group AVT-240 was formed to establish and/or strengthen the scientific foundations of hypersonic boundary layer transition in areas where previous knowledge was not sufficient to establish a sound prediction methodology. A strong collaboration between researchers performing advanced flow experiments, specialists in numerical flow simulations, and theoreticians has allowed the Task Group to substantially accelerate the scientific progress in its field.

For boundary layer edge Mach numbers of greater than about 4, the second mode will likely be a dominant transition mechanism over large surface areas of slender vehicles at moderate angles of attack. The results of AVT-240 indicate the feasibility to predict transition due to second modes in conventional tunnels using so-called amplitude methods. These amplitude methods might later be extrapolated to freestream conditions with low disturbance levels, as in flight. The Task Group has demonstrated the feasibility of numerically rebuilding the acoustic disturbance environment in the test section of a conventional cold hypersonic wind tunnel, as well as the response of flow probes to these disturbances, for the first time. The Group has also identified a range of transition paths for cross-flow dominated transition in hypersonic flow environments, and has also studied approaches for controlling these instabilities. This knowledge should serve as a basis for building accurate

prediction methods to be used within vehicle design cycles. The Group has also studied theoretical concepts based on the transient growth paradigm for transition in cases where the boundary layer is linearly stable. This is a typical situation encountered for blunt aerodynamic shapes including blunt cones and re-entry capsules. Advanced analysis, DNS, and experiments of such cases are generally consistent with the theoretical hypotheses. However, a direct proof of transient growth as the dominant transition mechanism is still pending.

Our progress in substantially augmenting the knowledge base related to several major problems in hypersonic transition does not mean that the problem of predicting and controlling hypersonic boundary layer transition is generally solved. Open questions include transition phenomena in shock-boundary layer interactions, the effects of strongly cooled walls, high flow enthalpy, and surface ablation, the ability to predict flow fields that exhibit multiple primary instabilities, robust control of flow instabilities that are responsible for transition, the establishment of computationally more efficient transition prediction approaches compared to DNS, and the need for flow experiments in low disturbance environments with higher Reynolds numbers than presently accessible. Nevertheless, the present cooperative approach has demonstrated an effective path to continue moving forward in an area wherein the limitations within individual research groups would allow only small chances of success otherwise.

Chapter 2 - COMPILATION AND ANALYSIS OF SECOND-MODE AMPLITUDES ON SHARP CONES IN HYPERSONIC WIND TUNNELS

Eric C. Marineau
Arnold Engineering Development Complex
UNITED STATES

Guillaume Grossir
von Karman Institute for Fluid Dynamics
BELGIUM

Alexander Wagner
German Aerospace Center (DLR)
GERMANY

Madlen Leinemann and Rolf Radespiel
Technische Universität Braunschweig
GERMANY

Hideyuki Tanno
Japan Aerospace Exploration Agency (JAXA)
JAPAN

Tim P. Wadhams
CUBRC
UNITED STATES

Brandon C. Chynoweth and Steven P. Schneider
Purdue University
UNITED STATES

Ross M. Wagnild and Katya M. Casper
Sandia National Laboratories
UNITED STATES

2.0 NOMENCLATURE

A	pressure fluctuation RMS normalized by the mean edge pressure
a	pressure spectral amplitude on cone surface normalized by mean edge pressure, 1/Hz$^{0.5}$
A_0	initial amplitudes of the second-mode normalized by the mean edge pressure
A_{max}	maximum pressure fluctuation RMS of the second-mode normalized by the mean edge pressure
C_R	receptivity coefficient
d_n	nozzle diameter at the exit plane, m
F	dimensionless frequency
f	frequency, Hz
h_n	nozzle height at the exit plane, m
l	constant for freestream noise fit

L_c	cone length, m
L_n	nozzle length, m
M	Mach number
m	slope of the freestream noise power spectral density
N	N factor
p	mean pressure, Pa
R	stability Reynolds number defined as square root of Reynolds number based on freestream quantities and surface coordinate
R_n	nose radius, mm
R_T	stability Reynolds number at start of transition, m
Re/m	freestream unit Reynolds number, 1/m
Re_x	Reynolds number based on freestream condition and surface coordinates
S_T	surface coordinate at start of transition, m
u	velocity, m/s
w	constant for second-mode bandwidth
w_n	nozzle width at the exit plane, m
α	dimensionless second-mode growth rate
δ_n	nozzle wall boundary-layer thickness, m
Γ_0	normalized freestream noise amplitude integrated over the second-mode bandwidth
γ_0	normalized pitot noise spectral amplitude, 1/Hz
Δf	second-mode bandwidth, Hz
ϕ	freestream noise power spectral amplitude, Pa^2/Hz
θ_c	cone half-angle, deg
ρ	density, kg/m^3
$Subscripts$	
e	boundary layer edge conditions
ET	end of transition
T or ST	at start of transition
w	wall conditions
0	stagnation conditions or at neutral point
os	outer scaling
∞	freestream conditions

2.1 INTRODUCTION

Over the last 10 years, second-mode amplitude measurements have been performed in several hypersonic wind tunnels worldwide using fast-response piezoelectric pressure sensors (PCB-132) [1–10]. These measurements can provide quantitative growth rates and breakdown amplitudes of the second-mode instability which dominates the boundary layer transition (BLT) process for hypersonic flows over slender bodies at moderate angles of attack. The same pressure sensors enabled fast pitot-pressure measurements to quantify the freestream noise content at frequencies up to approximately 750 kHz [11–13]. Such high frequency measurements are required to characterize the spectral amplitudes of the freestream noise over the range of unstable second-mode frequencies.

Over the same time period, the development of robust and user-friendly linear stability theory (LST) and parabolized stability equation (PSE) solvers such as STABL and STABL-3D [14] have democratized the access to LST and PSE predictions. Such tools have facilitated fully integrated experimental and computational studies of second-mode dominated hypersonic BLT [5, 10]. These studies have contributed to the development of a new wind-tunnel prediction methodology [15] based on Mack's amplitude method [16]. The method uses linear stability computations, tunnel noise measurement, and experimentally determined correlations for the second-mode breakdown amplitudes and receptivity coefficients to predict the start of BLT. The new methodology allows a more efficient use of conventional (noisy) wind tunnels to characterize BLT on hypersonic vehicles. This is key, as current quiet wind tunnels only operate at Mach 6, moderate Reynolds numbers, and low enthalpies. These limitations mean that conventional wind tunnels must be used for the test and evaluation of hypersonic vehicles.

The main objectives of this current international research effort undertaken by the North Atlantic Treaty Organization (NATO) Science and Technology Organization (STO) Applied Vehicle Technology (AVT)-240 specialists' group was to compile and analyze second-mode amplitudes measured on sharp slender cones at 0 deg angle of attack (AOA). For the most part, the study involves the reanalysis and interpretation of existing data sets from 11 hypersonic wind tunnels from 3 NATO countries (Belgium, Germany, and USA) and Japan that provide second-mode amplitudes at Mach numbers M between 5 and 14, unit Reynolds numbers Re/m between 1.5 and 16×10^6/m per meter, and wall-to-total temperature ratios T_w/T_0 between 0.1 and 0.8. This wide range of key parameters and tunnel sizes makes it possible to evaluate their effect on the second-mode growth rates, initial amplitudes (A_0) and maximum amplitudes (A_{max}) near the onset of BLT.

This chapter is organized as follows. Section 2.2 describes the experimental facilities, test conditions, test articles, and pressure instrumentation. Section 2.3 presents the computational methodology and discusses the scaling of sharp cone stability and the effect of the Mach number and wall temperature ratio. Section 2.4 compiles the second-mode amplitude measurements and introduces the methodology used to compare the measurements to PSE. Section 2.5 explores the effect of Re/m on the initial amplitudes and correlate the amplitudes. The chapter concludes by summarizing the main findings and providing an overview of future research.

2.2 EXPERIMENTAL METHOD

2.2.1 Experimental Facilities and Test Conditions

The current study uses BLT data collected in 11 ground test facilities operated by 9 organizations located in 4 countries. The facilities are the Sandia National Laboratories (SNL) Hypersonic Wind Tunnel [17] with its interchangeable Mach 5, 8, and 14 nozzles (HWT-5, HWT-8 and HWT-14); the Purdue University Boeing/AFOSR Mach-6 Quiet Tunnel (BAM6QT) [18]; the NASA Langley Research Center 15-Inch Mach 6 Wind Tunnel (15inM6), 20-Inch Mach 6 Wind Tunnel (20inM6), and 31-Inch Mach 10 Wind Tunnel (31inM10) [19]; the Technical University Braunschweig (TUB) Mach 6 Hypersonic Ludwieg Tube Braunschweig (HLB) [20]; the German Aerospace Center (DLR) High Enthalpy Shock-tunnel Göttingen (HEG) [21] with its Mach 8 nozzle; the Japan Aerospace Exploration Agency (JAXA) High Enthalpy Shock Tunnel (HIEST) [22] with its Mach 8 nozzle; The von Karman Institute for Fluid Dynamics (VKI) Longshot hypersonic wind-tunnel [23] with its Mach 10 nozzle, the CUBRC Large Energy National Shock Tunnel I (LENS I) [24, 25] with its Mach 10 nozzle; and the Arnold Engineering Development Complex (AEDC) Hypervelocity Wind Tunnel 9 (T9) [26, 27] with

its interchangeable Mach 10 and 14 nozzles. The CUBRC data were not included in this chapter since they were being collected and processed at the time of writing. These data will be included in a future publication.

The facility characteristics and dimensions are listed in Table 2-1. The list includes eight blowdown tunnels, three shock tunnels, two Ludwieg tubes, and one gun tunnel. The overall range of Mach numbers and unit Reynolds numbers are between 5-14 and 1.5-16$\times 10^6$/m, respectively. It is important to note that the unit Reynolds numbers and Mach numbers listed in Table 2-1 do not represent the entire operational envelope of each facility, but strictly covers the range of conditions pertaining to the BLT data analyzed in this chapter. The flow is expanded through contoured axisymmetric nozzles with the exception of the NASA 20inM6 and 31inM10 with two-dimensional nozzles. The nozzle exit diameters vary from 0.24 m for the Purdue BAM6QT to 1.52 m for AEDC T9. The relative scales of the nozzles are shown in Figure 2-1 where the facilities are arranged by increasing Mach numbers and nozzle exit dimensions. All the facilities have conventional (noisy) freestreams with the exception of the BAM6QT that generates a quiet freestream by maintaining a laminar boundary-layer on its highly polished nozzle wall. The BAM6QT can also produce a noisy freestream by closing the bleed-valve located upstream of the nozzle throat [18].

Table 2-1: Description Of Ground Test Facilities, Geometries, And Cone Test Articles.

Name	Organization	Operation	Geometry	M_∞	Re/m [/m x 10^{-6}]	d_n [m] or h_n x w_n [m]	Θ_c [deg]	R_n [mm]	L_e [m]
HWT-5	SNL	Blowdown	Axisymmetric	5	10 - 12.8	0.46	7	0.03	0.52
BAM6QT	Purdue	Ludwieg Tube	Axisymmetric	6	6.4 - 12	0.24	2.5, 3, 7 & flared	0.03	0.52
15inM6	NASA	Blowdown	Axisymmetric	6	6.7	0.38	7	0.03	0.52
HLB	TUB	Ludwieg Tube	Axisymmetric	6	5.0 - 16	0.50	7	0.09	0.50
20inM6	NASA	Blowdown	2D	6	6.8 - 13	0.51 x 0.51	7	0.03	0.51
HWT-8	SNL	Blowdown	Axisymmetric	8	4.1 - 13	0.36	7	0.03	0.52
HEG	DLR	Shock Tunnel	Axisymmetric	8	1.5 - 2.4	0.59	7	2.5	1.10
HIEST	JAXA	Shock Tunnel	Axisymmetric	8	3.3 - 4.8	0.80	7	2.5	1.00
Longshot	VKI	Gun Tunnel	Axisymmetric	10	3.3 - 12	0.43	7	0.2	0.80
31inM10	NASA	Blowdown	2D	10	1.7 - 6.6	0.79 x 0.79	7	0.03	0.52
LENS I	CUBRC	Shock Tunnel	Axisymmetric	10	2.0 - 15	1.22	7	0.15	2.44
Tunnel 9	AEDC	Blowdown	Axisymmetric	10	2.0 - 15	1.52	7	0.15	1.55
HWT-14	SNL	Blowdown	Axisymmetric	14	3.3	0.46	7	0.03	0.52
Tunnel 9	AEDC	Blowdown	Axisymmetric	14	1.7 - 12	1.52	7	0.15	1.55

2.2.2 Test Articles and Instrumentation

BLT measurements have been performed on 7-deg half-angle cones in each of the tunnels listed in the previous section. To promote transition under quiet flow, the BAM6QT experiments were also performed on a flared cone to destabilize the second-mode as well as on 2.5 and 3-deg cones. The shallower cones enable longer running lengths compared to 7-deg cones with similar base diameters and tunnel blockage. The characteristics of the test articles are found in the last three columns of Table 2-1. With the exception of the HEG and HIEST experiments with a 2.5 mm nosetip radius, the cones can be considered sharp as the nosetips radii (from 0.03 to 0.2 mm) should be small enough to avoid any significant influence of bluntness on the second-mode growth and receptivity. Recent DNS studies by Balakumar and Chou [28] of the Tunnel 9 Mach 10 sharp cone transition experiments [5] showed that the receptivity coefficients increase only slightly with increasing nosetip Reynolds numbers. For all the experiments, the amplitude of the pressure fluctuations on the surface of the cone were measured with flush-mounted PCB-132 piezoelectric pressure transducers. These sensors have a resonant frequency above 1 MHz, and a flat frequency response to at least several hundred kilohertz. The number of sensors, sensor

locations, and number of instrumented rays varied among the experiments. However, in most cases, the number of sensors and sensor spacing were sufficient to characterize the growth rates and breakdown amplitudes. More details about the test articles, instrumentation, and data acquisition can be found in Casper et al. [9, 29] for the SNL experiments, Berridge et al. [2] and Rufer and Berridge [3] for NASA experiments, Wagner et al. [7] for the HEG experiments, Tanno et al. [8] for the HIEST experiments, Grossir et al. [4] for the VKI experiments, and Marineau et al. [5, 10] for the AEDC experiments.

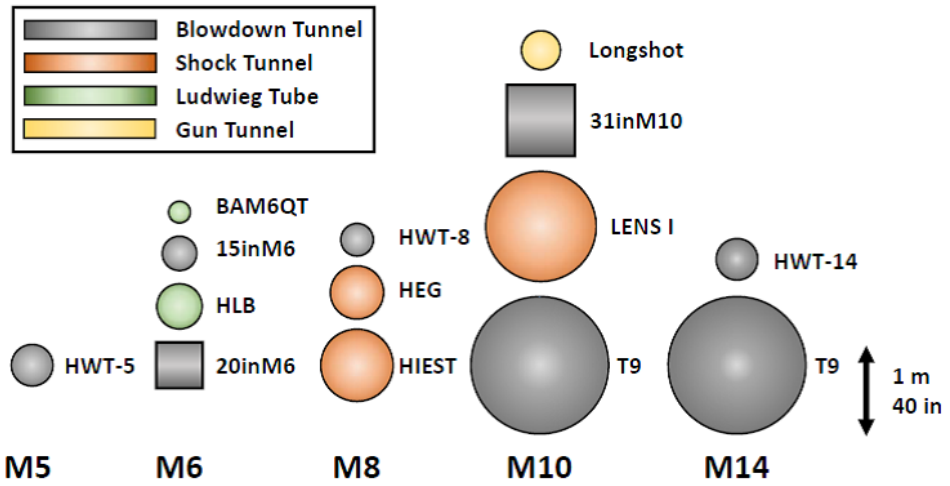

Figure 2-1: Depiction Of Ground Test Facilities Geometries And Dimensions Of The Nozzle Exit Plane.

2.3 COMPUTATIONAL METHOD

2.3.1 Linear Stability Computations

The mean flow for the stability analysis is calculated using a structured, axisymmetric computational fluid dynamic (CFD) solver which is part of the STABL software from Johnson and Candler [14] and solves the reacting Navier-Stokes equations. This flow solver is based on the finite-volume formulation. The inviscid fluxes are based on the modified Steger-Warming flux vector splitting method and are second-order accurate with a monotonic upstream-centered scheme for conservation laws (MUSCL) limiter as the total variation diminishing (TVD) scheme. The viscous fluxes are second-order accurate. The time integration method is the implicit, first-order data parallel line relaxation (DPLR) method. Sutherland's law is used for the viscosity, and the heat conductivity is calculated using Eucken's relation. The mean flow for each case is computed on a single-block, structured grid. Each grid is clustered near the wall and the nose of the test geometry in order to capture the fluid gradients at these locations. The stability analyses are performed using the PSE-Chem solver [14], which is also part of the STABL software suite. PSE-Chem solves the reacting, two-dimensional, axisymmetric, linear parabolized stability equations (PSE) to predict the amplification of disturbances as they interact with the boundary-layer. The PSE-Chem solver includes finite-rate chemistry and translational-vibrational energy exchange.

2.3.2 Scaling of Sharp Cone Stability

The scaling from Stetson et al. [30] was used by Marineau et al. [5] to compare sharp cone stability measurements at different unit Reynolds numbers. For convenience, the dimensionless frequency F is defined using the freestream conditions as

$$F = \frac{2\pi f}{u_\infty Re/m}, \tag{2-1}$$

where u_∞ is the freestream velocity. For sharp cone data, Marineau [15] has shown that the maximum N factor envelope, computed with PSE, can be expressed as

$$N = \alpha R + b, \tag{2-2}$$

where α and b are constants and R is the the stability Reynolds number defined as

$$R = \sqrt{Re_x}. \tag{2-3}$$

The stability Reynolds number at the neutral point is obtained by solving Equation 2-2 for R with N=0 which leads to

$$R_0 = \frac{-b}{\alpha}. \tag{2-4}$$

In addition, the most unstable second-mode frequency, which corresponds to the frequency of the maximum N factors can be expressed as

$$F = \frac{g}{R^h}, \tag{2-5}$$

where g and h are constants. In practice $h \approx 1$, such that F approximately scales as $1/R$. In cold hypersonic wind tunnels, the variation of the wall-to-total temperature ratio T_w/T_0 at a given nominal Mach number is small, such that the same set of constants (α,b,g and h) can be used to parametrize the PSE solutions. Generally, the total temperature is kept as low as possible to maximize the unit Reynolds number for a given stagnation pressure while avoiding flow condensation. This means that cold flow wind tunnels operating at the same nominal Mach number generally operate at similar T_w/T_0. Scaled PSE solutions for a sharp 7-deg cone in HWT-8 at 3 unit Reynolds number and wall temperature ratios are shown in Figure 2-2 along with the curve-fits based on Equations 2-2 and 2-5. The unit Reynolds numbers and T_w/T_0 are 3.6, 7.4, and 10×10^6/m and 0.35, 0.48, and 0.48, respectively. The variation in T_w/T_0 among the 3 solutions has a minor effect on the quality of the fit. The only discernible difference is the minor increase of F at the lowest unit Reynolds number solution which is most likely due to the thinner boundary layer at the lower T_w/T_0 compared to the two other solutions.

2.3.3 Effect of Mach Number and Wall Temperature Ratio on Sharp Cone Stability

Linear fits of the PSE solutions for freestream Mach numbers of 5, 6, 8, 10, and 14 are shown in Figure 2-3. In order to prevent flow condensation, the stagnation temperature has to increase with Mach number. This leads to a decrease of T_w/T_0 from 0.7 at Mach 5 to 0.2 at Mach 14. These conditions are representative of the cold-flow tunnels presented in Section 2.2. The curves at Mach 14 correspond to the Tunnel 9 and HWT-14 which operate at different wall-to-total temperature ratios of 0.2 and 0.3 respectively. The Mach number has a strong effect on the growth rate as shown in Figure 2-4a. A strong increase occurs between Mach 5 and Mach 6 followed with a monotonic decrease. These trends are consistent with previous studies from the literature [31, 32]. The

variation of the neutral point with Mach number is presented in Figure 2-4b. R_0 decreases from Mach 5 to 10 and increases from Mach 10 to 14. The PSE solutions presented in this section are used to scale the measured amplitude as N factors and to estimate the initial amplitudes in Section 2.4 and 2.5, respectively.

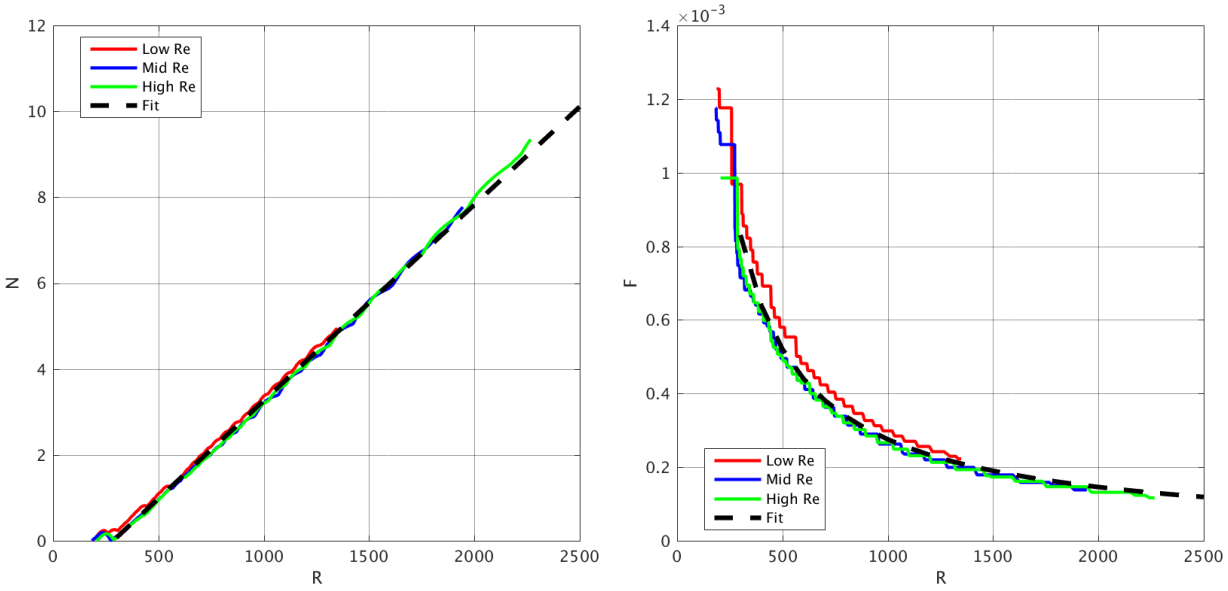

(a) N vs. R (b) F vs. R

Figure 2-2: N vs. R and F vs. R for 3 Re/m and T_0 Conditions in HWT-8.

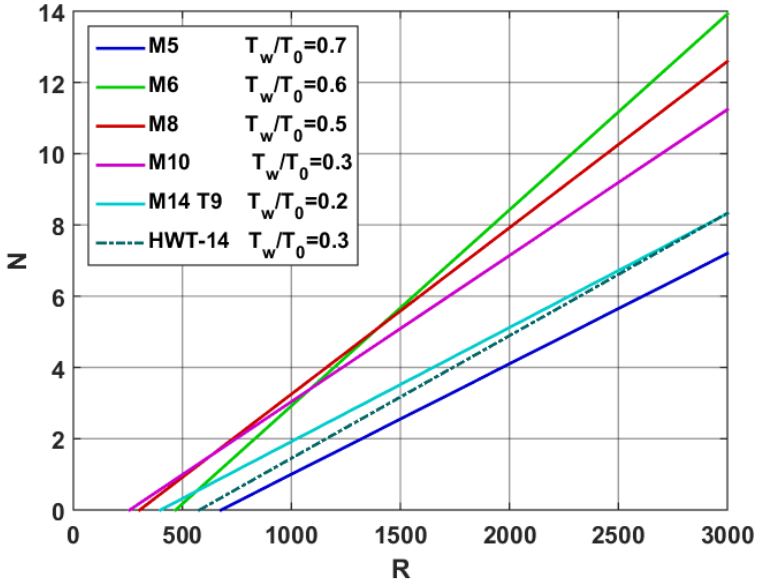

Figure 2-3: N vs. R for Cold-Flow PSE Solution With Mach Numbers Between 5 And 14.

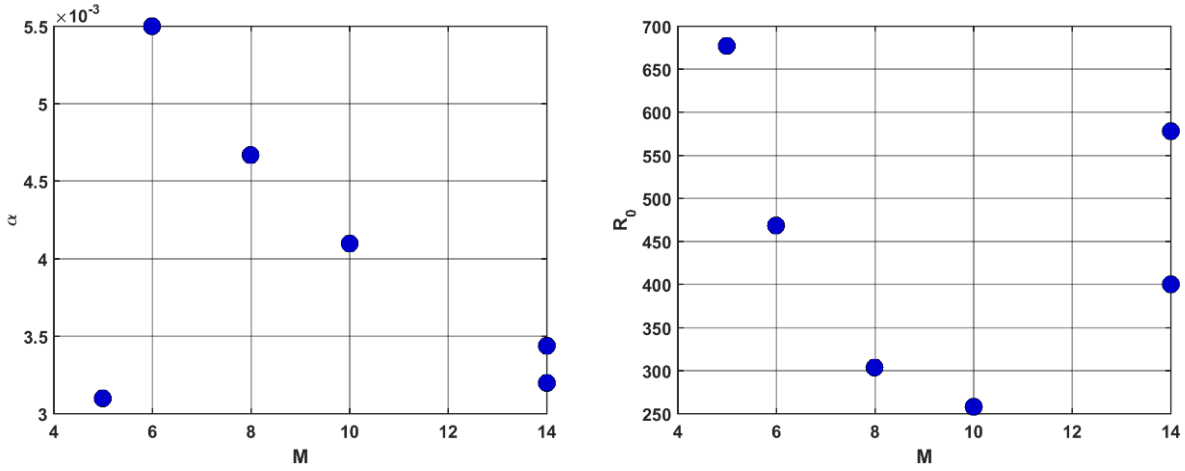

(a) Growth rate $\alpha(dN/dR)$ as a function of the Mach number

(b) Stability Reynolds number at neutral point

Figure 2-4: Effect M_∞ on α and R_0 for Cold-Flow PSE solutions at M = 5, 6, 8, 10 and 14.

2.4 COMPILATION AND ANALYSIS OF SECOND-MODE AMPLITUDES

2.4.1 Methodology

This section compiles and analyzes second-mode amplitudes obtained from surface pressure fluctuation measurements from PCB-132 pressure sensors. The second-mode amplitudes at each PCB sensor location are computed by integrating the power spectral density (PSD) over the second-mode peak. The steepness of the PSD near the second-mode peak implies that the most of the energy is located near the peak and that variations in bounds of integration have a small effect on the computed amplitudes. The PSD are calculated using Welch's method using Hanning windows with 50 percent overlap and a fast Fourier transform (FFT) length of 4,096 points. To compare the amplitudes at different unit Reynolds numbers (and freestream pressures), the amplitudes are normalized by the static pressure at the cone surface. In this study, the cone pressures are obtained by using the Taylor-Maccoll conical-flow solution.

The analysis of the second-mode amplitudes follows the methodology from Marineau et al. [10]. As previously mentioned, the sharp cone N factors from PSE can be expressed as a linear function of R. Prior to the start of transition (in the linear regime), the second mode amplitude A exhibits an exponential growth such that

$$A = ce^{dR}, \tag{2-6}$$

where c and d are constants. Fitting the measured amplitudes using Equation 2-6 reveals that $d \approx \alpha$ which is not surprising because

1) Both constants correspond to the growth rate.

2) The measured and computed growth rates agree well.

In Figure 2-5, the exponential fit of the measured amplitude using Equation 2-6 with $d = \alpha$ (red line) shows good agreement with the circumferentially averaged measurements (black line) for conditions C1, C2, C3, C4, and C5 corresponding to Re/m of 11.9, 7.1, 3.5, 2.1, and 1.7×10^6/m. In addition, since

$$A = A_0 e^N = A_0 e^{\alpha R+b}, \tag{2-7}$$

the initial amplitude can be estimated by combining Equations 2-6 and 2-7 as

$$A_0 = ce^{-b}. \tag{2-8}$$

Here, A_0 can be interpreted as a mean initial amplitude for the unstable frequencies over the range of fitted amplitudes. This is an approximation as the initial amplitudes are expected to vary as a function of frequency. However, as seen by the quality of the fits in Figure 2-5 and the results to be presented in Section 2.4.2, Equation 2-6 provides a good model for the second-mode growth. Finally, Equations 2-7 and 2-8 estimate the experimentally measured N factors as

$$N(s) = ln(A(s)e^b/c). \tag{2-9}$$

The N factors determined experimentally with Equation 2-9 and computed with PSE are compared in Section 2.4.4.

2.4.2 Effect of Unit Reynolds Number, Mach Number, and Tunnel Geometry

The measured amplitudes as a function of the stability Reynolds number are plotted in Figure 2-6. The arrows indicate the start of transition in Tunnel 9 based on heat transfer measurements. The solid lines are exponential fits of the amplitude using the growth rate from the PSE solutions as described in Section 2.4.1. Figure 2-6a presents the Tunnel 9 Mach 14 data for 5 conditions corresponding to Re/m equal to 11.9, 7.1, 3.5, 2.1, and 1.7×10^6/m. The HWT-14 amplitudes at 3.3×10^6/m are also included for comparison. The Tunnel 9 data consist of circumferentially averaged amplitudes from 3 rays [10] (shown in Figure 2-5). Several important observations can be made from Figure 2-6a.

1) The second-mode saturation (maximum) amplitudes A_{max} do not vary significantly with Re/m.

2) The R location of A_{max} occurs slightly downstream of R_T.

3) The measured growth rate $\frac{dA}{dR}$ does not significantly change with Re/m.

4) The measured $\frac{dA}{dR}$ agrees with the computed growth rate α as shown by the overall quality of the curve-fits.

5) At a fixed R value, the amplitudes decrease with Re/m which combined with observations 1, 2 and 3 implies that the R_T increase with Re/m.

6) At comparable Re/m (3.3 and 3.5×10^6) the smaller HWT-14 produces amplitudes 3 to 5 times greater than the larger Tunnel 9.

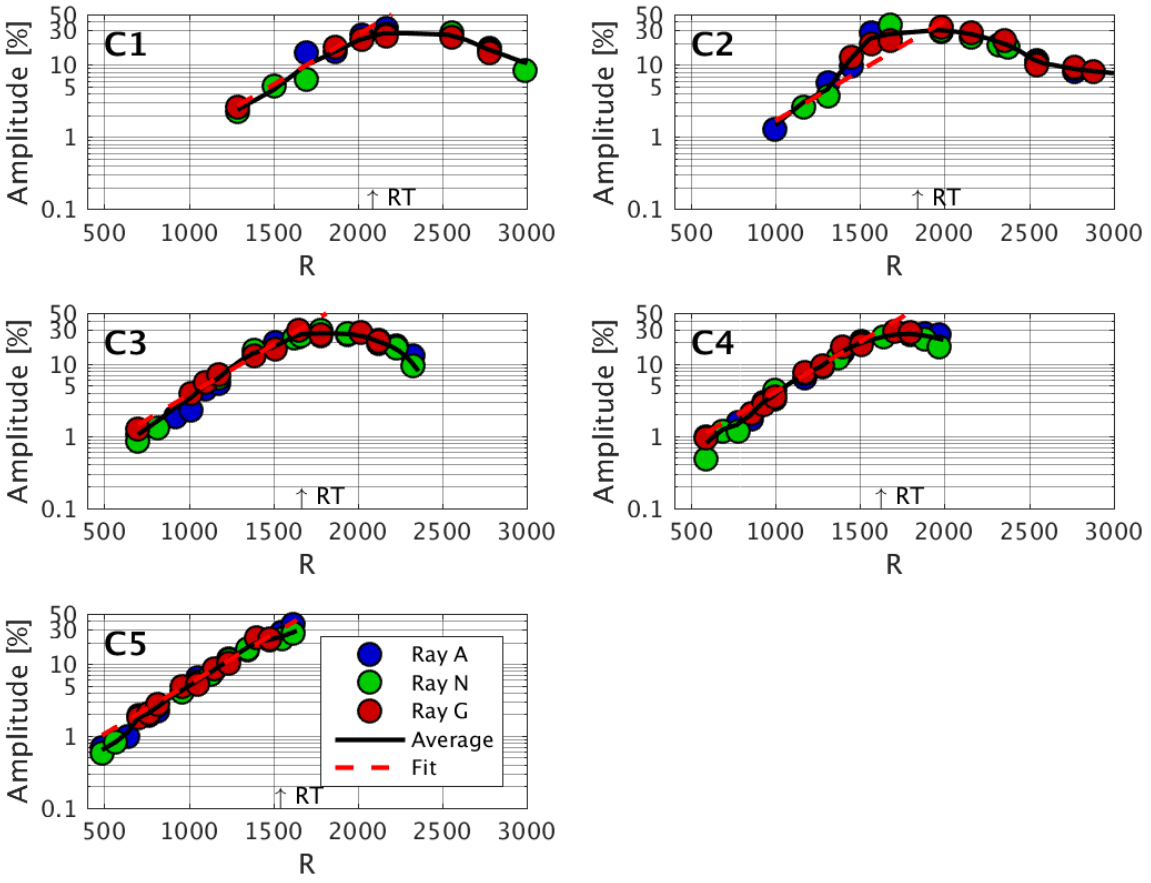

Figure 2-5: A vs. R At M = 14 In T9 For Re/m = 11.9, 7.1, 3.5, 2.5, And 1.7×10^6/m (C1 to C5), Where ↑ RT ≡ R$_T$.

Observations 3 and 4 indicate that the growth rate computed with PSE can predict the measured growth rate. Observation 5 implies that the initial amplitudes of the waves decrease with the unit Reynolds number. This is investigated further in Section 2.5. Figure 2-6b presents similar results for the Tunnel 9 data at Mach 10. VKI measurements at 6.2, 4.7 and 3.8×10^6/m are also included for comparison. As for Mach 14, the predicted growth rate matches the measurements quite well. The amplitudes measured in VKI are approximately 5 times larger than that in Tunnel 9 at similar Re/m. In addition, the saturation amplitudes measured in Tunnel 9 and VKI are similar. The maximum amplitudes A_{max} decrease with increasing Re/m. The reason for this behavior is not clear, but could be sensor related since the wavelength of the second-mode decreases with unit Re/m due to the thinner boundary-layer. This makes the measurements more susceptible to spatial averaging over the sensing element area. In addition, the frequencies increase with Re/m which makes the measurements more uncertain as the upper limit of the PCB-132 bandwidth is not precisely known and could vary among the sensors. As for Mach 14, the second-mode saturation occurs slightly downstream of the start of transition S_T. The saturation amplitudes at Mach 10 and 14 are comparable.

Figure 2-6c present amplitude measurements for the NASA 31inM10. The quality of the fit is difficult to assess due to the low number of sensors and large sensor spacing. The saturation amplitudes are comparable to that of Tunnel 9 at the same nominal Mach number. The amplitudes measured in HWT-8 are shown in Figure 2-6d. The measurements are consistent with the Mach 10 and Mach 14 measurement regarding the effect of Re/m on the amplitude of the waves and the saturation location. The saturation amplitudes, varying from 20% to 30%, are similar to the measurements at Mach 10 and 14. Therefore, it appears that the Mach number has a weak effect on the saturation amplitudes at Mach numbers between 8 and 14.

The plots in Figure 2-6e and 2-6f present Mach 6 measurements from the 20inM6 and HLB. In the HLB, the test article is positioned above the nozzle centerline to avoid the turbulence and the velocity deficit downstream of the center-body valve. The saturation amplitudes in both Mach 6 tunnels are similar at approximately 10% which is significantly lower than at the higher Mach numbers. The data at the two lowest Re/m in the 20inM6 shows good agreement with the fit. The agreement is harder to evaluate at the higher Re/m because of the low number of sensors in the region of exponential growth. For most Re/m, the amplitudes measured by the most upstream sensor are significantly lower than the fit. This might be due to the lower noise content at higher frequency, as the fit essentially assumes a constant initial amplitude. The large number of sensors and the wide range of Re/m in the HLB experiments make it possible to assess the quality of the curve-fits and the effect of Re/m on the saturation location. In general, the growth rate is well predicted by PSE. In addition, the effect of Re/m is consistent with the data at higher Mach numbers as the amplitudes decrease with Re/m at a fixed R.

The second-mode amplitudes for Re/m near 6.5×10^6/m in four Mach 6 wind tunnels are shown in Figure 2-7. Data from the 20inM6, 15inM6, HLB and BAM6QT (Noisy and Quiet) are included. The dashed lines are exponential fits from Equation 2-7 using the growth rate from PSE. The measured growth rates are similar in the 20inM6, 15inM6, and HLB. Since BAM6QT has only one measurement location, it is not possible to evaluate the quality of the fit for that tunnel. The amplitudes in the HLB, 15inM6, and BAM6QT (noisy) are within $\approx$ 25%, but 2 to 3 times larger than in the 20inM6. The differences could be due to the lower freestream noise content in the 20inM6 as indicated by pitot noise measurements compiled by Duan et al. [33]. This should be explored further by systematically comparing the freestream noise PSD in the different facilities. The amplitudes in BAM6QT under quiet flow are approximately 450 times smaller than under noisy flow [1].

The second-mode amplitudes in the HEG and HIEST shock tunnels are presented in Figure 2-8 for 7-deg cones with a 2.5 mm nosetip radius. The freestream Mach number and stagnation enthalpy are approximately constant at 8 and 3 MJ/kg respectively. The unit Reynolds number varying from 2.5×10^6 to 4.8×10^6/m are specified in the legend. The maximum second-mode amplitudes are between 20% and 30%, which is comparable to the values achieved for cold flow in the HWT-8. At each condition, the growth rate dA/dR appears fairly constant prior to saturation. However, the growth rates vary among the conditions. For instance, the HIEST run at Re/m = 3.3×10^6 has a much steeper slope compared to the other conditions. These variations in growth rate could be due to the effect of the nosetip bluntness. Future comparisons with PSE solutions could help better understand these variations.

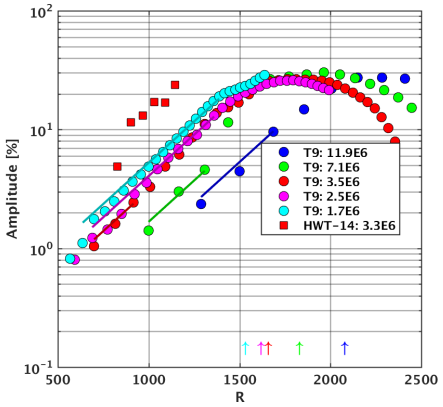

(a) Mach 14: T9 and HWT-14

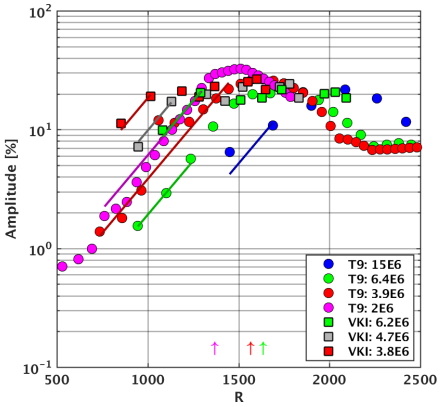

(b) Mach 10: T9 and VKI

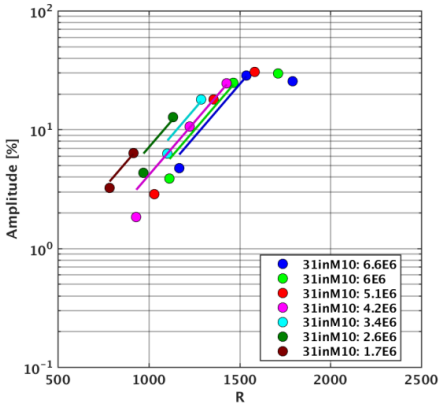

(c) Mach 10: 31inM10

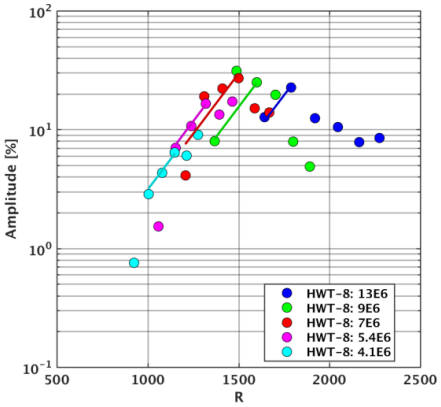

(d) Mach 8: HWT-8

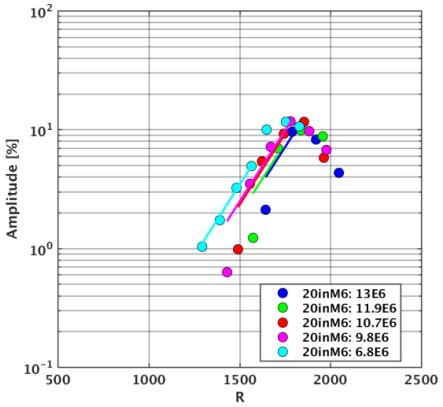

(e) Mach 6: 20inM6

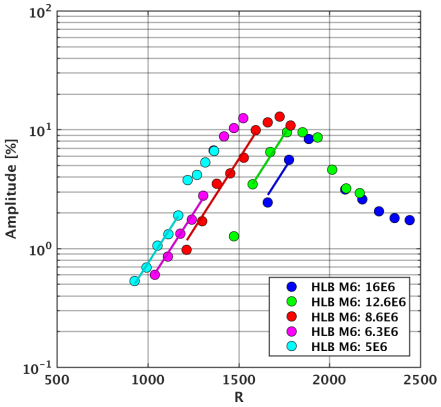

(f) Mach 6: HLB

Figure 2-6: A vs. R At M = 6, 8, 10, and 14 For Cold Flow Tunnels.

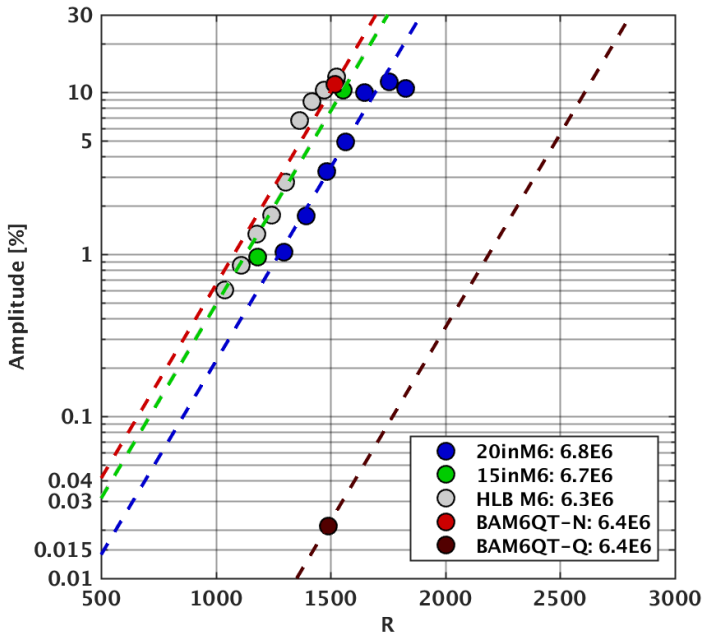

Figure 2-7: A vs. R at M = 6 For Re/m $\approx 6.5\times10^{6}$/m.

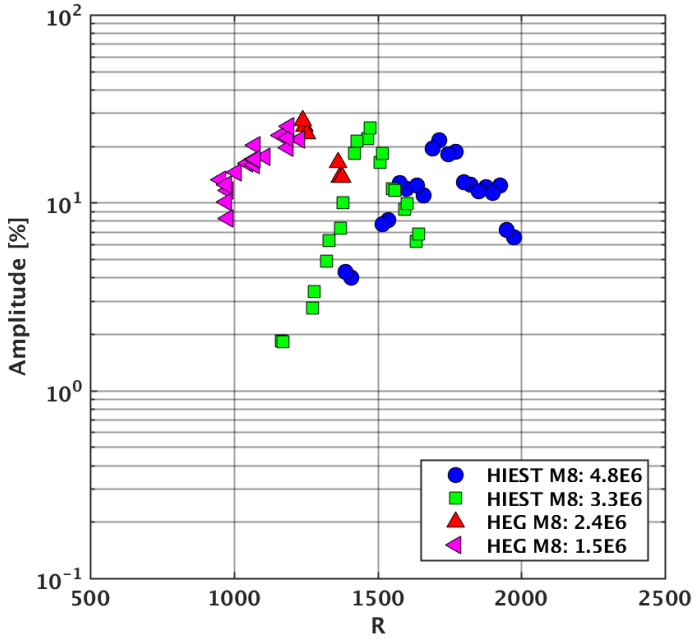

Figure 2-8: A vs. R at M = 8 in HIEST and HEG for $h_0 \approx 3$ MJ/kg.

2.4.3 Maximum Second-Mode Amplitudes

Marineau [15] presented a correlation for the maximum amplitudes for blunt and sharp cones at a nominal freestream Mach number of 10. The correlation included sharp cones data at nonzero AOA as well as blunt cone data with small nosetip radii at 0 deg AOA where transition still appeared to be second-mode dominated, but where the edge Mach number and breakdown amplitudes were much lower. The results from Marineau [15] were consistent with sharp cone measurements in several hypersonic wind tunnels that revealed increasing maximum amplitudes with increasing edge Mach numbers [9]. Fedorov and Kozlov [34] compiled these measurements to show a linear relationship between the edge Mach number and the maximum pressure amplitudes. The pressure amplitudes normalized by the boundary-layer edge pressure are approximately 6% at $M_e \approx 4.6$ and 24% at $M_e \approx 6.8$ which are similar to the values measured in Tunnel 9.

The maximum second-mode amplitudes compiled in this study for sharp cones at 0 deg AOA are plotted as a function of the edge Mach number in Figure 2-9. The data all are for 7-deg cones with the exception of the BAM6QT-Q (quiet) data on a flared cone ($M_e \approx 5$), and a 3-deg cone ($M_e \approx 5.8$) and the BAM6QT-N (noisy) data on a 2.5-deg cone ($M_e \approx 5.8$). For the sharp cones, M_e is obtained from the Taylor-Maccoll conical-flow solution. For the flared cone, M_e is from the mean flow CFD solution (return from enthalpy overshoot to 100.3% of the freestream total enthalpy). The data from Figure 2-9 shows a weak variation of A_{max} with M_e at $M_e >\approx$ 5.8. At $M_e \approx 10$, the mean value of A_{max} ($\pm$ one standard deviation) are 27.8% $\pm$ 1.8%, compared to 26.3% $\pm$ 4.1% at $M_e \approx 8$ and 23.6% $\pm$ 4.5% for M_e between 6 and 7. The sharp decrease of A_{max} for M_e less than 5.8 is consistent with the results presented by Marineau [15] on blunt cones at a nominal freestream Mach number of 10. The values of A_{max} from HLB and 20inM6 are consistent. The mean value of A_{max} at $M_e \approx 5.3$ is 11% $\pm$ 1.8%. The values obtained in the BAM6QT under quiet flow are higher than the values under noisy flow at a similar edge Mach number. This seems to indicate that the tunnel noise decreases the maximum second-mode amplitudes. The effect of tunnel noise on A_{max} warrants further investigation.

2.4.4 Scaling of the Second-Mode Amplitudes and Comparison with Linear Stability

The measured amplitudes are normalized using the methodology presented in Section 2.4.1. Using Equation 2-9, the measured amplitude can be expressed as N factors. The measured and computed N factors are compared in Figure 2-10. The arrows indicate the start of transition in Tunnel 9 based on heat transfer measurements. Figure 2-10a presents the Tunnel 9 Mach 14 data for 5 conditions with Re/m equal to 11.9, 7.1, 3.5, 2.1, and 1.7×10^6/m. The HWT-14 data at 3.3×10^6/m are also included. Good agreement with PSE and low experimental scatter are found. Over all the conditions, the computed and measured N factors are within $\pm$0.5 with the exception of the 7.1×10^6/m condition near the start of transition (within $\pm$1). An inspection of the PSD for this condition revealed an anomaly near 300 kHz where the amplitudes appear to be artificially amplified [10]. The experimental N factors at Mach 10 for Tunnel 9, VKI and 31inM10 shown in Figure 2-10b and 2-10c also agree with PSE. The wide range of Re/m between 2.0 and 15×10^6/m makes apparent the increase of N_T (experimental and computed) with Re/m. This behavior is consistent with Marineau [15]. The smaller VKI tunnel produces lower N_T compared to Tunnel 9. The increase of N_T with Re/m is also visible at Mach 8 in Figure 2-10d and Mach 6 in Figure 2-10e and 2-10f. In addition, the decreased growth rates with increasing freestream Mach numbers are correctly predicted with PSE as supported by the slope dN/dR for each Mach number.

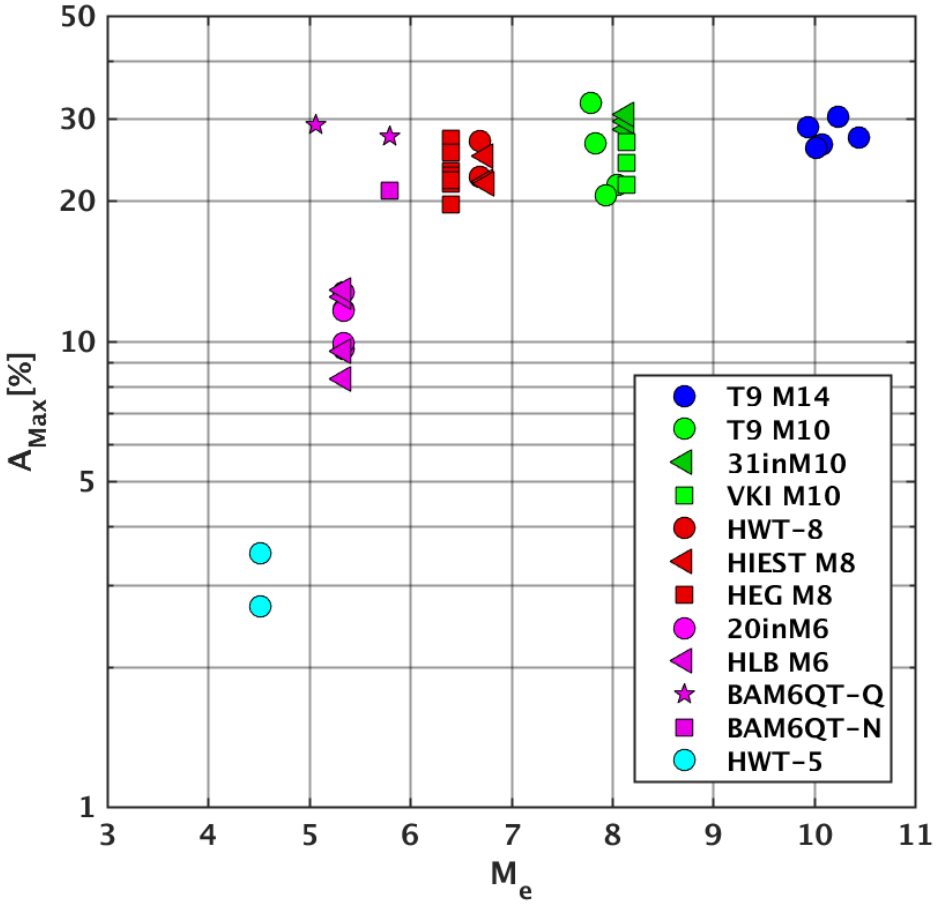

Figure 2-9: A_{max} vs. M_e.

2.5 SCALING OF INITIAL AMPLITUDES AND AMPLITUDE CORRELATION

2.5.1 Scaling of Initial Amplitudes with Unit Reynolds Number

This section explores the effect of Re/m on A_0. The objective is to provide a simple scaling for the variation of A_0 with Re/m for a fixed tunnel geometry and fixed Mach number. The analysis takes into account the variation of the freestream noise content with Re/m and the effect of Re/m on the unstable second-mode frequencies. We assume that the PSD of the freestream noise ϕ has a constant negative spectral slope equal to $-m$ (where m is positive) over the frequency range of interest. This assumption is reasonable based on fluctuating pitot-pressure measurements from multiple facilities [33]. Using the outer scaling [35] to account for the effect of Re/m on the PSD, we get

$$\phi_{os} = l f_{os}^{-m}, \tag{2-10}$$

where

$$\phi_{os} = \frac{\phi u_\infty}{p_\infty^2 \delta_n}, \tag{2-11}$$

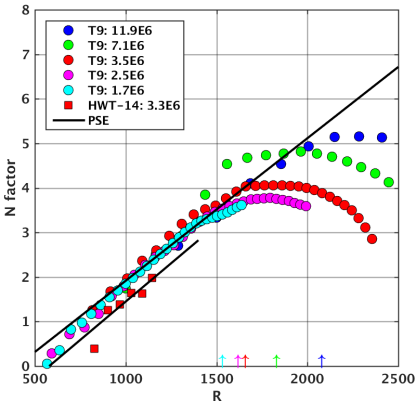

(a) Mach 14: T9 and HWT-14

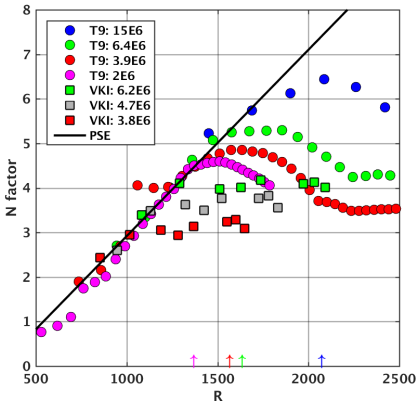

(b) Mach 10: T9 and VKI

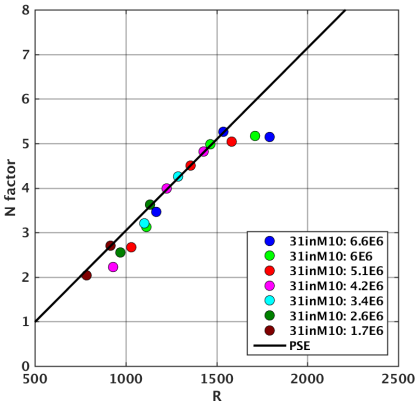

(c) Mach 10: 31inM10

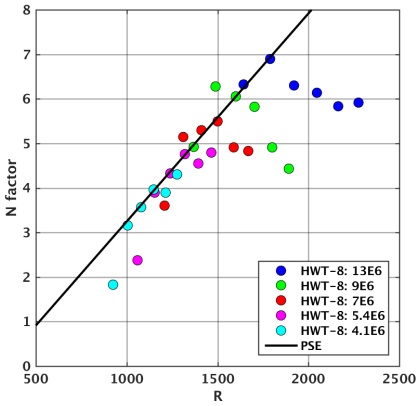

(d) Mach 8: HWT-8

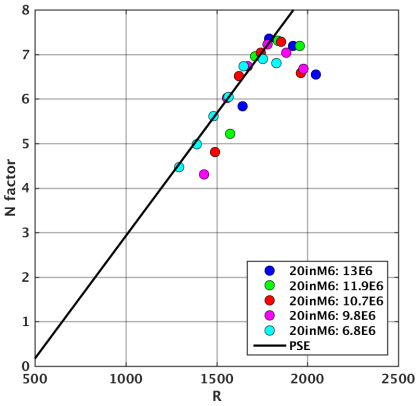

(e) Mach 6: 20inM6

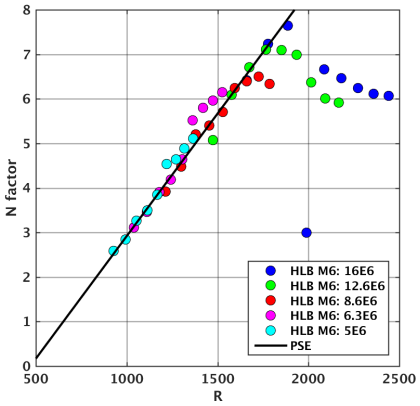

(f) Mach 6: HLB

Figure 2-10: N vs. R At M = 6, 8, 10, and 14 For Cold-Flow Tunnels.

and

$$f_{os} = \frac{f\delta_n}{u_\infty}. \tag{2-12}$$

Next, we define the freestream noise amplitude integrated over the second-mode bandwidth as

$$\Gamma_0 = \gamma_0\sqrt{\Delta f}, \tag{2-13}$$

where spectral amplitudes are

$$\gamma_0 = \sqrt{\frac{\phi_0}{p_\infty^2}}. \tag{2-14}$$

The second-mode bandwidth is assumed proportional to the frequency as in [15] such that

$$\Delta f = w f_0, \tag{2-15}$$

where w is a constant. The initial amplitude can be related to the freestream noise content using the receptivity coefficient as

$$A_0 = C_R\Gamma_0. \tag{2-16}$$

Substituting Equations 2-10 to 2-15 into Equation 2-16 yields

$$A_0 = C_R\sqrt{wl}\left(\frac{f_0\delta_n}{u_\infty}\right)^{\frac{1-m}{2}}, \tag{2-17}$$

where f_0 is the unstable second-mode frequency corresponding initial amplitude. Because the spectral amplitudes of freestream noise decrease with frequency, A_0 decreases when f_0 increases. In Section 2.4.1, A_0 obtained in the curve-fit was interpreted as a mean initial amplitude over a range of unstable frequencies upstream of the transition location. These unstable frequencies will increase with unit Reynolds number due to the thinner boundary-layer. This effect can be accounted for by substituting the dimensionless frequency F_0 (see Equation 2-1) into Equation 2-17. This substitution yields

$$A_0 = C_R\sqrt{wl}\left(\frac{F_0\delta_n Re/m}{2\pi}\right)^{\frac{1-m}{2}}. \tag{2-18}$$

The frequency F_0 can be evaluated at the neutral point R_0 by substituting Equation 2-4 into 2-5. Substituting the result into Equation 2-18 yields

$$A_0 = C_R\sqrt{wl}\left(\frac{g\alpha^h\delta_n Re/m}{-2\pi b^h}\right)^{\frac{1-m}{2}}. \tag{2-19}$$

For a fixed Mach number and tunnel geometry, all the parameters in Equation 2-19 are constant with the exception of δ_n and Re/m. This also assumes that the receptivity coefficient is not a function of Re/m. This assumption is reasonable based on recent DNS studies by Balakumar and Chou [28]. Since the boundary-layer on the nozzle wall is turbulent, we can use the usual scaling for turbulent boundary layers [36] to account for the effect of Re/m on δ_n. This scaling takes the form

$$\frac{\delta_n}{L_n} \sim (Re/mL_n)^{-1/5}, \tag{2-20}$$

where L_n is the nozzle length. Substitution of Equation 2-20 into Equation 2-19 gives

$$A_0 \sim (Re/mL_n)^{\frac{4}{5}(\frac{1-m}{2})}. \tag{2-21}$$

Pitot noise measurements in multiple facilities [33] have shown that m =3.5 is a reasonable approximation for the spectral slope. Substituting this value into Equation 2-21 yields

$$A_0 \sim (Re/mL_n)^{-1}. \tag{2-22}$$

Equation 2-22 provides a simple relationship between A_0 and Re/m for fixed tunnel dimensions and Mach number. The validity of this expression will be evaluated in the next section.

2.5.2 Compilation of Initial Amplitudes

The initial amplitudes can be estimated from the measured amplitudes and PSE using Equation 2-8. Figure 2-11 presents A_0 as a function of Re/m for Tunnel 9 at Mach 10 and 14, 31inM10, 20inM6, and HLB. Curve-fits based on Equation 2-22 are also shown. Larger initial amplitudes are found in Tunnel 9 at Mach 14 compared to Mach 10. The larger initial amplitudes at Mach 14 are most likely due to the stronger tunnel noise at the higher Mach number. The initial amplitudes in the smaller 31inM10 tunnel are slightly larger than in Tunnel 9. This is consistent with the analysis of Marineau [15] based on linear stability theory and Pate's correlation [37]. Both Mach 6 tunnels have much lower amplitudes than the higher Mach number tunnels despite their smaller dimensions. This is consistent with a decrease in tunnel noise with decreasing Mach number. A decrease of the receptivity coefficient C_R with Mach number could also contribute. For unit Reynolds numbers smaller than approximately 10×10^6/m, the initial amplitude in HLB are approximately twice as large as in 20inM6. These results are consistent with the Pitot noise measurements compiled in Duan et al. [33] which showed lower tunnel noise levels in 20inM6. The curve-fits agree well with the Mach 6 data with the exception of the two HLB data points at $Re/m > 10\times10^6$/m. It would be useful to investigate if this behavior is related to an unexpected decrease in tunnel noise in HLB at $Re/m > 10\times10^6$/m.

2.5.3 Correlation of Second-Mode Amplitudes

In this section, the second-mode amplitudes are estimated using the N factors computed with PSE and the curve-fits for the initial amplitudes obtained in Section 2.5.2. This allows the computation of the second-mode amplitudes using Equation 2-8. Figure 2-12 compares the measured amplitudes with the amplitude computed using Equation 2-8. Reasonable agreement is obtained between the measured and estimated amplitudes. This implies that PSE can predict the growth of the waves and that the initial amplitudes can be estimate using curve-fits based on Equation 2-22. For amplitudes greater than 4% and below the saturation, the standard error between the measurements and correlation is approximately 25%. This is reasonably good considering the simple relationship ($A_0 \sim Re/m^{-1}$) between the initial amplitudes and the unit Reynolds number. Considering that the amplitudes grow exponentially, much smaller errors $\sim$10% are to be expected when using this methodology to estimate N_T or S_T. In addition, it is likely that improvements could be made by relating the initial amplitude to the measured freestream noise content in each facility as in [15].

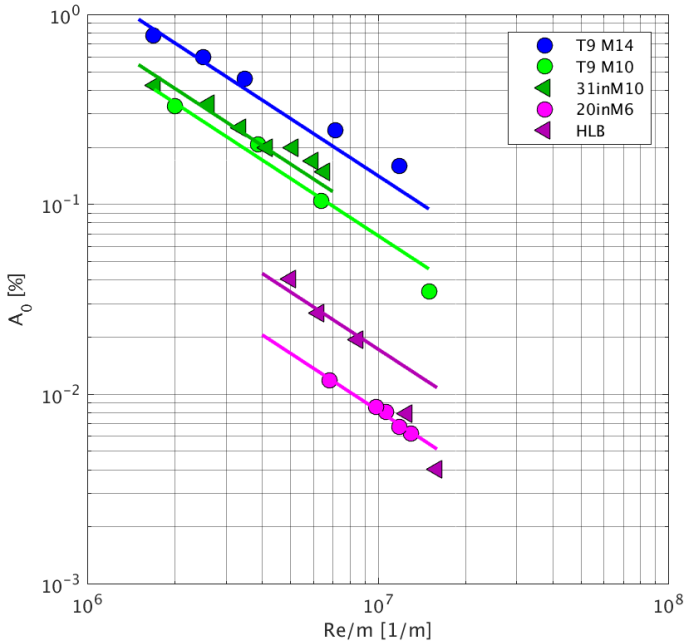

Figure 2-11: A_0 vs. Re/m. Solid Lines Are Fit For Equation 2-22, $A_0 \sim$ Re/m$^{-1.}$

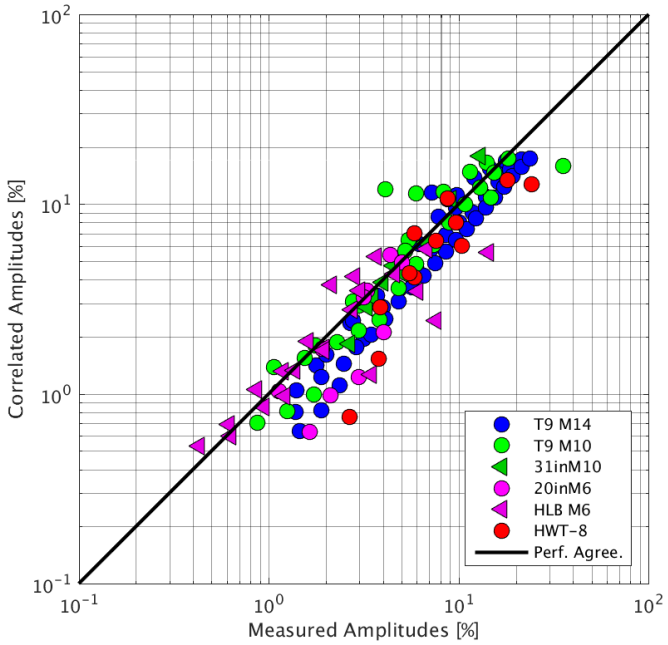

Figure 2-12: Comparison Between The Measurements And The Amplitudes Computed Using Equation 2-8.

2.6 CONCLUSIONS AND FUTURE WORK

The main objectives of this international research effort coordinated by the NATO STO AVT-240 specialists' group were to compile and analyze second-mode amplitudes measured on sharp slender cones. The data were from 11 hypersonic wind tunnels from 9 organizations located in 3 NATO countries (Belgium, Germany, and USA) and Japan. These tunnels provided second-mode amplitude measurements at Mach numbers between 5 and 14, unit Reynolds numbers Re/m between 1.5 and 16×10^6/m, and wall-to-total temperature ratios T_w/T_0 between 0.1 and 0.8. The study showed that the measured second-mode growth rates can be predicted with PSE over a wide range of hypersonic conditions. PSE and measurements both showed decreasing growth rates with increasing Mach numbers greater than 6. The maximum second-mode amplitudes were found to vary weakly (from $\sim$20 to 30%) for M_e greater than approximately 5.8, but to significantly decrease at lower M_e. The maximum N factor envelope from PSE and the measured amplitudes were used to estimate the initial amplitudes A_0. At each Mach number, A_0 approximately scales as Re/m^{-1}. This leads to an increase in the transition N factors with Re/m which is consistent with the findings from Marineau [15]. As Re/m increases, the unstable second-mode frequencies also increase such that the tunnel noise spectral amplitudes are lower over that range of unstable frequencies. This explains the decrease of A_0 with Re/m.

The effect of tunnel size was explored by plotting the second-mode amplitudes from multiple facilities producing the same nominal freestream Mach number. Data from multiple cold flow wind tunnels were available at Mach 14 (HWT-14 and T9), Mach 10 (VKI, 31inM10, and T9), and Mach 6 (BAM6QT, 15inM6, HLB and 20inM6). The analysis showed that the second-mode amplitudes at similar Re/m and R decrease with increasing tunnel dimensions. This is likely because the smaller tunnels have a thinner boundary layer that produces more acoustic noise over the range of unstable second-mode frequencies. Overall, the results indicate that amplitude-based methods for hypersonic BLT predictions [15, 28] should be applicable across a wide range of hypersonic conditions, as clear and potentially universal trends were found for the effect of Re/m and tunnel sizes across the wide range of conditions. Such physics based methods are preferable to purely empirical methods such as Pate's correlation [37], as they are applicable to arbitrary geometries and are likely to provide a viable path in using ground-test data for flight prediction.

Future research will include a comparison of Mach 10 data from T9, 31inM10, and VKI with new data from LENS I at the same nominal Mach number. The LENS I study will involve similar instrumentation density and test conditions as the Tunnel 9 experiments. The effect of tunnel size and nozzle geometry (2D vs. axisymmetric) on the second-mode amplitudes also needs to be investigated in more detail.

2.6.1 Acknowledgments

Eric Marineau would like to acknowledge the Test Resource Management Center T&E / S&T HSST program for their funding as part of the Center of Testing Excellence. The authors would like to acknowledge Shann Rufer and Dennis Berridge for helping interpreting previously published data from the NASA Langley hypersonic wind tunnels. Sandia National Laboratories is a multi-mission laboratory managed and operated by National Technology and Engineering Solutions of Sandia, LLC., a wholly owned subsidiary of Honeywell International, Inc., for the U.S. Department of Energy's National Nuclear Security Administration under contract DE-NA0003525.

2.7 REFERENCES

[1] Estorf, E., Radespiel, R., Schneider, S., Johnson, H., and Hein, S., "Surface-Pressure Measurements of Second-Mode Instability in Quiet Hypersonic Flow," *AIAA Paper 2008-1153*, January 2008.

[2] Berridge, D., Casper, K., Rufer, S., Alba, C., Lewis, D., Beresh, S., and Schneider, S., "Measurements and Computations of Second-Mode Instability Waves in Several Hypersonic Wind Tunnels," *AIAA Paper 2010-5002*, June-July 2010.

[3] Rufer, S. and Berridge, D., "Experimental Study of Second-Mode Instabilities on a 7-Degree Cone at Mach 6," *AIAA Paper 2011-3877*, June 2011.

[4] Grossir, G., Pinna, F., Bonucci, G., Regert, T., Rambaud, P., and Chazot, O., "Hypersonic Boundary Layer Transition on a 7 Degree Half-Angle Cone at Mach 10," *AIAA Paper 2014-2779*, June 2014.

[5] Marineau, E., Moraru, C., Lewis, D., Norris, J., Lafferty, J., Wagnild, R., and Smith, J., "Mach 10 Boundary-Layer Transition Experiments on Sharp and Blunted Cones," *AIAA Paper 2014-3108*, June 2014.

[6] Marineau, E., Moraru, C., Lewis, D., Norris, J., Lafferty, J., and Johnson, H., "Investigation of Mach 10 Boundary Layer Stability of Sharp Cones at Angle-of-Attack, Part 1: Experiments," *AIAA Paper 2015-1737*, January 2015.

[7] Wagner, A., Kuhn, M., Schramm, J.M., and Hannemann, K., "Experiments on Passive Hypersonic Boundary Layer Control Using Ultrasonically Absorptive Carbon-Carbon Material with Random Microstructure," *Experiments in Fluidsl*, Vol. 54, No. 10, October 2013, pp. 1–10.

[8] Tanno, H., Komuro, T., Sato, K., Itoh, K., Takahashi, M., and Fujii, K., "Measurement of Hypersonic High-Enthalpy Boundary Layer Transition on a 7° Cone Model," *AIAA Paper 2010-0310*, January 2010.

[9] Casper, K., Beresh, S., Henfling, J., Spillers, R., Pruett, B., and Schneider, S., "Hypersonic Wind-Tunnel Measurements of Boundary-Layer Transition on a Slender Cone," *AIAA Journal*, Vol. 54, No. 4, January 2016, pp. 1250–1263.

[10] Marineau, E., Moraru, C., and Daniel, D., "Sharp Cone Boundary-Layer Transition and Stability at Mach 14," *AIAA Paper 2017-0766*, January 2017.

[11] Bounitch, A., Lewis, D., and Lafferty, J., "Improved Measurements of "Tunnel Noise" Pressure Fluctuations in the AEDC Hypervelocity Wind Tunnel No 9," *AIAA Paper 2011-1200*, January 2011.

[12] Rufer, S. and Berridge, D., "Pressure Fluctuation Measurements in the NASA Langley 20-Inch Mach 6 Wind Tunnel," *AIAA Paper 2012-3262*, June 2012.

[13] Schilden, T., Schröder, W., Ali, S., Schreyer, A., Wu, J., and Rodespiel, R., "Analysis of Acoustic and Entropy Disturbances in a Hypersonic Wind Tunnel," *Physics of Fluids*, Vol. 28, No. 5, May 2016, pp. 056104.

[14] Johnson, H. and Candler, G., "Hypersonic Boundary Layer Stability Analysis Using PSE-Chem," *AIAA Paper 2005-5023*, June 2005.

[15] Marineau, E., "Prediction Methodology for Second-Mode-Dominated Boundary-Layer Transition in Wind Tunnels," *AIAA Journal*, Vol. 55, No. 2, 2017, pp. 484–499.

[16] Mack, L., "Transition and Laminar Instability," *NASA-CP-153203, Jet Propulsion Lab, Pasadena, California*, 1977.

[17] Beresh, S., Casper, K., Wagner, J., Henfling, J., Spillers, R., and Pruett, B., "Modernization of Sandia's Hypersonic Wind Tunnel," *AIAA Paper 2015-1338*, January 2015.

[18] Schneider, S., "Fabrication and Testing of the Purdue Mach-6 Quiet-Flow Ludwieg Tube," *AIAA Paper 2000-0295*, January 2000.

[19] Berger, K., Rufer, S., Hollingsworth, K., and Wright, S., "NASA Langley Aerothermodynamics Laboratory: Hypersonic Testing Capabilities," *AIAA Paper 2015-1337*, January 2015.

[20] Estorf, M., Wolf, T., and Radespiel, R., "Experimental and Numerical Investigations on the Operation of the Hypersonic Ludwieg Tube Braunschweig," *In Proceedings 5th European Symposium on Aerothermodynamics for Space Vehicles, ESA SP-563*, 2005.

[21] Hannemann, K., Schramm, J.M., and Karl, S., "Recent Extensions to the High Enthalpy Shock Tunnel Göttingen (HEG)," *2nd International ARA Days, Arcachon, France*, 2008.

[22] Itoh, K., *Advanced Hypersonic Test Facilities*, chap. Characteristics of the HIEST and its Applicability for Hypersonic Aerothermodynamic and Scramjet Research, American Institute of Aeronautics and Astronautics, 2002, pp. 239–253.

[23] Grossir, G., Masutti, D., and Chazot, O., "FLow Characterization and Boundary Layer Transition Studies in VKI Hypersonic Facilities," *AIAA Paper 2015-0578*, January 2015.

[24] Holden, M., "Recent Advances in Hypersonic Test Facilities and Experimental Research," *AIAA Paper 1993-5005*, November-December 1993.

[25] Holden, M., Wadhams, T., Maclean, M., Dufrene, A., Mundy, E., and Marineau, E., "Review of Basic Research and Development Programs Conducted in the LENS Facilities in Hypersonic Flows," *AIAA Paper 2012-0469*, January 2012.

[26] Lafferty, J., Coblish, J., Marineau, E., Norris, J., Kurits, I., Lewis, D.R., Smith, M., and Marana, M., "The Hypervelocity Wind Tunnel No. 9; Continued Excellence Through Improvement and Modernization," *AIAA Paper 2015-1340*, January 2015.

[27] Marren, D. and Lafferty, J., *Advanced Hypersonic Test Facilities*, chap. The AEDC Hypervelocity Wind Tunnel 9, American Institute of Aeronautics and Astronautics, 2002, pp. 467–477.

[28] Balakumar, P. and Chou, A., "Transition Prediction in Hypersonic Boundary Layers Using Receptivity and Freestream Spectra," *AIAA Journal*, Vol. 56, No. 1, September 2017, pp. 193–208.

[29] Casper, K., Beresh, S., Henfling, J., Spillers, R., Pruett, B., and Schneider, S., "Hypersonic Wind-Tunnel Measurements of Boundary-Layer Pressure Fluctuations," *AIAA Paper 2009-4054*, June 2009.

[30] Stetson, K., Thompson, E., Donaldson, J., and Siler, L., "Laminar Boundary Layer Stability Experiments on a Cone at Mach 8, Part 1: Sharp Cone," *AIAA Paper 1983-1761*, July 1983.

[31] Bitter, N. and Shepherd, J., "Stability of Highly Cooled Hypervelocity Boundary Layers," *Journal of Fluid Mechanics*, Vol. 778, September 2015, pp. 586–620.

[32] Mack, L., "Boundary-Layer Linear Stability Theory," *AGARD Report No. 709*, North Atlantic Treaty Organization 1984.

[33] Duan, L., Choudhari, M., Chou, A., Munoz, F., Ali, S., Radespiel, R., Schilden, T., Schröder, W., Marineau, E., Casper, K., Chaudhry, R., Candler, G., Gray, K., Sweeney, C., and Schneider, S., "Characterization of Freestream Disturbances in Conventional Hypersonic Wind Tunnels," *AIAA Paper 2018-0347*, January 2018.

[34] Federov, A. and Kozlov, K., "Receptivity of High-Speed Boundary Layer to Solid Particulates," *AIAA Paper 2011-3925*, June 2011.

[35] Beresh, S., Henfling, J., Spillers, R., and Pruett, B., "Fluctuating Wall Pressures Measured Beneath a Supersonic Turbulent Boundary Layer," *Physics of Fluids*, Vol. 23, No. 7, July 2011, pp. 075–110.

[36] Smits, A. and Dussauge, J.P., *Turbulent Shear Layers in Supersonic Flow*, Springer, 2nd ed., 2006, p. 213.

[37] Pate, S., "Dominance of Radiated Aerodynamic Noise on Boundary-Layer Transition in Supersonic/Hypersonic Wind Tunnels," *AEDC-TR-77-107*, 1978.

Chapter 3 - NUMERICAL INVESTIGATION OF SECOND MODE ATTENUATION OVER CARBON/CARBON POROUS SURFACES

Carlo Scalo
Purdue University
UNITED STATES OF AMERICA

Viola Wartemann and Alexander Wagner
Deustches Luft-und-Raumfahrt Zentrum
GERMANY

3.1 INTRODUCTION

The design of hypersonic vehicles is constrained by the considerable heat transfer and shear stress loads imparted on the vehicles surface by the boundary layer. While being already critical in the laminar regime, such loads are significantly enhanced by the transition to turbulence. Reed *et al.* [1] highlighted the differences in fully turbulent and fully laminar trajectories for a hypersonic flight vehicle, reporting that the vehicle would experience a heat flux approximately 5 times higher under turbulent conditions and, therefore, would require at least twice the weight in thermal protection systems (TPS). Recent studies in the framework of the national Aerospace Plane Project led by the Defense Science Board committee [2] quantify the drop in performance of high-speed vehicles due to transition, reporting that the payload-to-weight ratio for fully laminar conditions is three times larger than for fully turbulent. These studies emphasize the importance of laminar-to-turbulent transition delay for sustainability of high-speed flight, and the need for any realizable technology for boundary layer control to be symbiotic with TPS.

Hypersonic vehicles that fly at small angles of attack and with high lift-to-drag ratios tend to have predominantly symmetric geometries and slender shapes. Under these conditions, second-mode waves become the main mechanism driving transition to turbulence [3]. The second mode was discovered by Mack [4] and consists of traveling ultrasonic acoustic waves trapped within the boundary layer; they are found to be amplified by wall-cooling conditions, that is when the wall temperature is below adiabatic temperatures, $T_w < T_{ad}$, which is commonly the case. Mack's studies on the evolution of these and higher modes [5] stressed the importance of second-mode attenuation in any attempt to increase the transitional Reynolds number in high speed flows.

Malmuth *et al.* [6] proved through Linear Stability Theory (LST) the capability of ultrasonically absorbing coatings (UACs) to mitigate the second mode, confirmed by experiments that followed. The first experimental validation of this principle is due to Fedorov *et al.*[7], who constructed a cone with a half angle of 5 degrees with two different surfaces: one smooth and impermeable, and the other perforated with regularly space micro holes. They reported that the porous surface was capable of doubling the transitional Reynolds number in comparison with the smooth surface in experiments at Mach 5 at the T-5 hypersonic wind tunnel located at Caltech.

The development of UACs continued, with the goal of combining the acoustic absorption and TPS characteristics into one solution. Knowing that an irregular porous structure is naturally found in TPS materials used for hypersonic vehicles, Fedorov *et al.* [8, 9] conducted experiments in the Mach 6 wind tunnel T-326 at the

Institute of Theoretical and Applied Mechanics (ITAM) in Novosibirsk, Russia over a felt-metal surface with an irregular porous structure (as well as another surface with regular microstructure). These experiments were the first to produce data capable of quantitatively demonstrating the attenuation of the second-mode waves via UACs, confirmed by stability analysis, but also showed a small destabilization of the first mode.

Chokani *et al.* [10] performed a bispectral analysis on this same data with the goal of identifying nonlinear mechanisms that could be triggered by the use of porous coatings; this was motivated by the observation of a weak enhancement of first-mode waves. The experiments revealed the occurrence of nonlinear phase locking, which is the most efficient method for a mode to feed itself or to transfer energy between modes, involving only the first mode, in the presence of porous walls and not over an impermeable surface. This effect was also shown to be small, not impacting the overall stabilizing role of the porous coating. More recently, Lukashevich *et al.* [11], performed new experiments in ITAM's tunnel, where it was shown that placing the porous insert in the region where the second mode is stable leads to an increase in the disturbance signal amplitude; the opposite is observed when the insert is placed in regions of second-mode growth.

Inspired by some of these results, Wagner *et al.* [12–14] pioneered the use of carbon-carbon (C/C), an intermediate state of C/C Silicon Carbide (C/C-SiC) already employed on hypersonic vehicles [15, 16], to control second-mode waves. Experiments at Mach 7.5 have been conducted in the DLR High Enthalpy Shock Tunnel Göttingen (HEG), and the stabilization of the second mode as well as an increase in the laminar portion of the boundary layer over the porous surface have been observed. For these flow conditions, Wartemann *et al.* [17] has performed an analysis based on the parabolized stability equations, confirming the effectiveness of porous surfaces based on C/C in achieving transition delay. The present paper is the first step towards performing a full direct numerical simulation of a spatially developing boundary layer over a conical surface with assigned complex broadband wall-impedance representative of the distributed random porosity of C/C surfaces.

Most of previous high-fidelity numerical studies of attenuating, canceling, or reinforcing second-mode instabilities in high-speed flow over porous walls have focused on uniformly spaced and/or geometrically regular porosity in temporally developing boundary layers [18–22]. More recently, Wang & Zhong [23] have performed direct numerical simulations of a hypersonic boundary layer over a flat plate modeling the effects of the irregular felt-metal surface used in the experiments conducted by Fedorov [9]. Their studies concluded that the modeled felt-metal porous surface destabilized the first mode and attenuated the second, consistent with the experiments.

The current manuscript will focus on axi-symmetric flow over a sharp 7°-half-angle cone, analyzing the three lowest Reynolds numbers investigated in the experiments by Wagner [12, 13] (see Table 3-1). The novelty of the adopted computational approach lies in the time-domain impedance boundary conditions (TDIBC) technique, as implemented by Scalo *et al.* [24] in the context of subsonic compressible near-wall turbulence, allowing the exact application of any complex impedance boundary conditions in direct numerical simulations.

3.2 PHYSICAL MODEL AND COMPUTATIONAL APPROACH

The numerical study performed in this work is based on tests conducted by Wagner *et al.* [13] in the DLR High Enthalpy Shock Tunnel Göttingen (HEG). In the present study, test conditions of $Re_m = 1.46 \cdot 10^6$ m $^{-1}$, $Re_m = 2.43 \cdot 10^6$ m $^{-1}$ and $Re_m = 4.06 \cdot 10^6$ m $^{-1}$ are chosen; all free stream conditions and the parameters of these runs are reported in Table 3-1. Simulations of spatially developing boundary layer are carried out over a

Table 3-1: Selected Flow Parameters from Wagner's Experiments [13]

Re_m [1/m]	M_∞ [−]	p_∞ [Pa]	T_∞ [K]	ρ_∞ [kg/m^3]	u_∞ [m/s]	p_e [Pa]	T_e [K]	ρ_e [kg/m^3]	u_e [m/s]
$1.46 \cdot 10^6$	7.3	789	267	0.0102	2409	1944	345	0.0187	2376
$2.43 \cdot 10^6$	7.4	1453	285	0.0177	2480	3443	368	0.0324	2446
$4.06 \cdot 10^6$	7.4	2129	268	0.0276	2422	5076	347	0.0508	2388

0.95 m length cone, starting at 0.05m from the tip. A sharp cone with a half angle of 7 degrees is the geometry of choice, being an idealization of Wagner's 2.5mm-round-tip cone model actually employed for the transition delay experiments over C/C.

High-order structured compact-finite-difference simulations are carried out with the CFDSU solver (more details are given in Section III.A) with the objective of capturing the perturbation evolution with minimum numerical dissipation and high resolving power for a given amount of points per wavelength. Simulations are performed with inlet flow conditions to the high-order simulations starting at $x = 0.05$m from the tip (Figure 3-1), and informed by combining the Taylor-Maccoll [25] inviscid solution with a viscous solution for the boundary layer. The latter is derived by applying the Mangler [26] transformation for bodies of rotation to the compressible boundary layer similarity solution for a perfect gas over a flat plate [27], as done by Lees [28] for the flow over a cone.

Using this transformation one can describe the spatial evolution of a boundary layer through the use of the following similarity variables

$$\xi = \int_0^x \rho_e U_e \mu_e r_\perp^2 dx \tag{1}$$

$$\eta = \frac{U_e r_\perp}{\sqrt{2\xi}} \int_0^y \rho dy \tag{2}$$

where x is the streamwise direction (tangential to the wall), y the one normal to the wall, and $r_\perp(x)$ is the cone radius as measured perpendicularly to its axis of rotational symmetry.

Noting that for a cone of half angle ψ_c the radius of cross section of a body of revolution can be written as $r\perp = x \sin \psi_c$ and also that the flow properties after a conical shock are constant along straight lines originating from the tip of the cone, it is assumed that the properties at the boundary layer edge are independent of x, and hence the similarity variables 1 and 2 can be simplified to

$$\xi = \frac{\rho_e U_e \mu_e x^3 \sin^2 \psi}{3} \tag{3}$$

$$\eta = \sqrt{\frac{3U_e}{2x\rho_e\mu_e}} \int_0^y \rho dy \tag{4}$$

This allows to numerically solve the boundary layer equations as a nonlinear ordinary differential equation (ODE) with η as the only dimensionless coordinate over which to perform the integration. In practice, the solution is generated on a very fine grid in the η-space and then mapped back to the (x, y)-space and interpolated

bilinearly on the grid used to perform the Navier-Stokes calculations. As shown later in Figure 3-3 excellent matching is observed between the thus-obtained semi-analytical flow and steady Navier-Stokes calculations.

Simulations are first carried out under quiet conditions (no perturbations), allowing the mean flow to be fully established and all residual perturbations (artifacts of the flow initialization, retained by the low-dissipation numerics) to be convected out of the domain. The solution was allowed to relax on the Navier-Stokes grid for approximately 4 flow-through cycles, based on the free-stream velocity and the domain extent, before perturbations were applied.

The grid used to discretize the conical domain is a structured spherical grid with the origin at the tip of the cone. The version of CFDSU under development at purdue is able to perform a trivariate coordinate system transformation, mapping a general curvilinear coordinate system onto a uniform and orthogonal spatial domain. The choice of spherical coordinates guarantees perfect orthogonality (reduced numerical errors in the grid transformation step) between gridlines and is advantageous since it can be described very trivially analytically. The disadvantage of this grid is that the resolution in the wall normal direction (y) decreases as we move away from the origin; this issue is mitigated by the streamwise boundary layer growth. The spherical grid is stretched in the wall-normal (angular) direction with a half-tangent hyperbolic law to resolve not only the boundary layer of the mean flow, but also the acoustic-wave-induced Stokes boundary layer thickness.

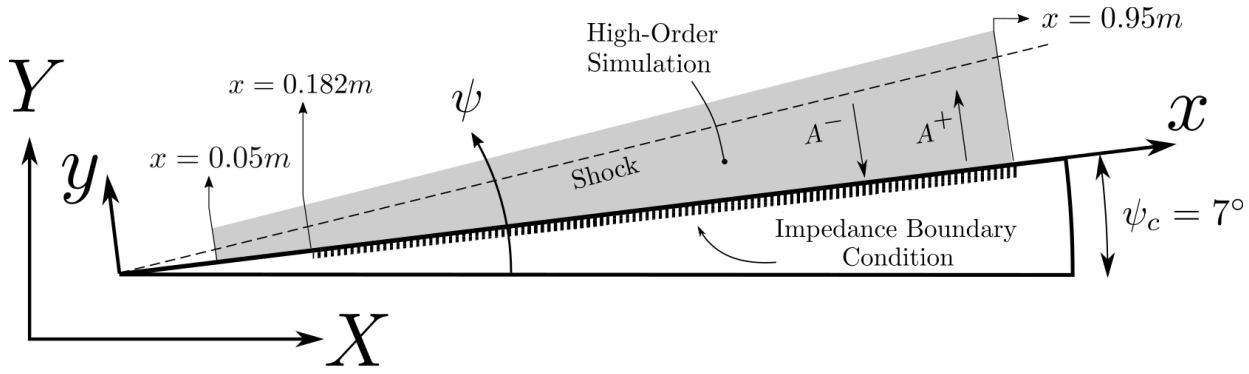

Figure 3-1: Computational Setup of DNS of Second-mode Waves Over Complex Impedance Boundary Conditions.

The inflow plane of the high-order Navier-Stokes simulations is located under the shock, at a streamwise distance of $x = 0.05$ m from the tip (Figure 3-1). Here, hardly imposed Dirichlet boundary conditions are used, informed from the pre-calculated semi-analytical steady laminar viscous solution described above. Outlet conditions are homogeneous Neumann for all flow quantities. At the wall, no-slip, no penetration and, when and where active, suction and blowing conditions are imposed. At the top boundary (above the shock) steady freestream conditions are imposed.

Inlet and outlet sponge layers of approximately 0.045 m in thickness are used to control spurious oscillations due to the introduction of the shock in the domain at the inlet and to prevent the formation of upstream traveling disturbances near the outlet, in both cases arising in the subsonic portion of the boundary layer. These layers relax the instantaneous flow to the aforementioned semi-analytical steady laminar solution.

A shock capturing scheme based on implementations by Cook [29] and Kawai [30] was used to thicken the shock and make it resolvable on the computational grid. This is done by applying artificial viscosity and conductivity in the regions where the shock is detected. To ensure that no artificial dissipation is introduced inside the boundary

layer, the shock capturing scheme is deactivated in the region $\psi - \psi_c < 1^\circ$.

Due to the short duration of the test run, the surface of the model does not have time to heat up and thus can be assumed to be isothermal with a temperature of 300 K. For runs modeling the porous carbon/carbon surfaces, impedance boundary conditions (see Eqn. 8) were applied, controlling the transpiration velocity as a function of the wall pressure fluctuations. The value of the impedance is extracted from a pore-scale acoustic analysis called the inverse Helmholtz solver, (Section §3.3.2) and compared to low-order algebraic models (Section §3.5.2). This approach allows to model the acoustic response of the porous surface without the need to resolve its complex geometrical structure. This strategy allows to retain high resolution on the flow side by removing the grid resolution requirements that would be needed to capture the acoustic wave propagation in the pores.

3.3 COMPUTATIONAL TOOLS

3.3.1 High-Order Structured Compact-Finite-Difference Solver in Curvilinear Coordinates: CFDSU

CFDSU solves the fully-compressible Navier-Stokes equations on a structured curvilinear grid using a sixth-order compact and staggered finite difference scheme [31]. Compact methods outperform conventional finite difference schemes based on spatially local discretization at high wavenumbers without restricting the geometry and boundary conditions of the problem demanded by a spectral method [32, 33].

The governing flow equations are solved in a curvilinear coordinate system for the contravariant components of velocity. The full set of transformed equations can be found in Nagarajan *et al.* [34]. Recent developments of the code at Purdue University have enabled the use of fully three-dimensional, non-orthogonal grid transformations in the code.

CFDSU has also been equipped with Time-Domain Impedance Boundary Conditions (TDIBC) based on the formalism of Fung and Yu [35] and the implementation in fully compressible Navier-Stokes codes by Scalo *et al.* [24]. The TDIBC formulation belongs to the class of characteristic boundary conditions [36] and is implemented based on the complex wall softness coefficient, $\hat{S}(\omega)$, which is related to the reflection coefficient, $\hat{R}(\omega)$, via

$$\hat{S}(\omega) = \hat{R}(\omega) + 1, \tag{5}$$

and is evaluated using the complex poles and residues that describe the IBC (see Equation (12)) being ultimately imposed in the time-domain in the Navier-Stokes calculations. Following, $\hat{R}(\omega)$ relates the incident, $\hat{A}^-$, and reflected, $\hat{A}^+$, waves (Figure 3-1) in the frequency domain via

$$\hat{R} = \frac{\hat{A}^+}{\hat{A}^-} \tag{6}$$

where the time-domain definition of the incident and reflected waves is,

$$\begin{cases} A^-(t) = v'(t) + \dfrac{p'(t)}{\rho_0 a_0} \\ A^+(t) = v'(t) - \dfrac{p'(t)}{\rho_0 a_0} \end{cases} \quad \text{and} \quad \begin{cases} \hat{A}^-(\omega) = \hat{v}(\omega) + \dfrac{\hat{p}(\omega)}{\rho_0 a_0} \\ \hat{A}^+(\omega) = \hat{v}(\omega) - \dfrac{\hat{p}(\omega)}{\rho_0 a_0} \end{cases} \tag{7}$$

where v' and p' are the fluctuating values of wall normal velocity and pressure respectively, and ρ_0 and a_0 are the base density and speed of sound of the fluid.

Adopting a harmonic convention to transform the variables to frequency domain, the specific acoustic impedance $Z_*(\omega)$ (made dimensionless via the base impedance $\rho_0\, a_0$) is defined as a function of the perturbed pressure $p'(t)$ and its induced normal velocity component $v'(t)$ into a porous surface, satisfying the relation:

$$\hat{p}(\omega) = \rho_0 a_0 Z_*(\omega)\hat{v}(\omega). \tag{8}$$

Fung and Yu [35] demonstrated that it is possible to evaluate the outgoing wave by a causal convolution of the incident wave. The wall normal velocity can then be recovered and imposed as a Dirichlet Boundary condition at each time step,

$$v' = \frac{1}{2}\left[A \quad + A^{+}\right]. \tag{9}$$

The staggered variable arrangement does not place pressure nodes at the boundary and, as such, only requires condition 9 to be imposed to continue the calculations.

3.3.2 Pore-Cavity Inverse Ultrasonic Solver: IHS

The inverse Helmholtz solver (iHS) is a novel computational methodology that allows the evaluation of the spatial distribution of acoustic impedance at the open surface of an arbitrarily shaped cavity for a given frequency. This technique spatially integrates the linearized Navier-Stokes equations transformed into the frequency domain

$$j\omega\frac{\rho_0}{p_0}\hat{p} \quad j\omega\frac{\rho_0}{T_0}\hat{T} + \rho_0\frac{\partial\hat{u}_k}{\partial x_k} = 0, \tag{10a}$$

$$j\omega\rho_0\hat{u} + \frac{\partial\hat{p}}{\partial x} \quad \mu\frac{\partial}{\partial x_k}\left(\frac{\partial}{\partial x_k}\hat{u}\right) = 0, \tag{10b}$$

$$j\omega\rho_0\hat{v} + \frac{\partial\hat{p}}{\partial y} \quad \mu\frac{\partial}{\partial x_k}\left(\frac{\partial}{\partial x_k}\hat{v}\right) = 0, \tag{10c}$$

$$j\omega\rho_0 c_v\hat{T} + p_0\frac{\partial\hat{u}_k}{\partial x_k} = \kappa\frac{\partial}{\partial x_k}\left(\frac{\partial}{\partial x_k}\hat{T}\right), \tag{10d}$$

on an unstructured grid for a broad range of frequency values (where ω is a real-valued input to the solver), from the cavity walls (with assigned no-slip, isothermal conditions) up to the open surface, where the local value of impedance for each frequency is retrieved as a result of the calculation (see Patel *et al.* [37–39] for more details).

Multiple instances of the iHS can be concurrently executed to reconstruct the full, broadband acoustic impedance at the open surface of any given geometry. Such an impedance can then be implemented as a time-domain impedance boundary condition (IBC) in flow-side-only simulations as discussed in the previous Section (§3.3.1).

In order to apply this technique to a material composed of arbitrarily distributed geometrically complex cavities, such as a C/C block, high resolution images are needed. The descriptive images, such as the ones shown in figure 3-9, are read as two dimensional arrays containing greyscale values of each pixel using an image processing code

written in `Python`. A filter is then applied wherein each pixel with a greyscale value under a given threshold is considered to be part of a pore. The images are then scanned for connected regions that represent each pore, and an automatic approximation to a rectangular slot or a cylindrical hole is made based on the pore's extent in each direction. Finally, pixels are converted to micrometers and used to recover the significant dimensions of each pore, which can be used to determine the porosity and eventually the impedance of the C/C surface.

Once the surface porosity and significant dimensions of each surface pore are known, the inverse Helmholtz solver (iHS) [40] is used to evaluate the broadband surface averaged specific acoustic impedance of each pore. These impedances are then combined, assuming that the hard walled portion of the surface has zero admittance, such that the total surface averaged impedance of the sample is given by,

$$Z_*(\omega) = \left(\sum_{i=1}^{N_{\text{pores}}} \frac{1}{Z_{i,*}(\omega)} \frac{A_i}{A_{\text{total}}} \right)^{-1}, \tag{11}$$

where Z_i is the specific acoustic impedance of the ith pore, and A_i its surface area.

Time domain impedance boundary condition (TDIBC) application requires that the acoustic impedance be specified as a set of complex poles and residues representing a superposition of causal second-order oscillators. These poles and residues are obtained by fitting the wall softness coefficient corresponding to the evaluated broadband acoustic impedance from the iHS,

$$\widehat{S}(\omega) = \frac{2}{1 + Z_*(\omega)} \approx \sum_{k=1}^{n_o} \left[\frac{\mu_k}{s - p_k} + \frac{\tilde{\mu}_k}{s - \tilde{p}_k} \right], \tag{12}$$

where, $\widehat{S}$ is the wall softness coefficient, n_o the number of oscillators, μ_k the residues, p_k the poles, and $s = j\omega$. In Equation (12), the superscript ($\tilde{}$) denotes complex conjugate.

The fit is performed following the procedure described in Lin *et al.* (2016) [41], where the values and quantity of poles and residues are varied iteratively while minimizing the difference between the wall softness evaluated using the impedance obtained from the iHS for a discrete set of frequencies, and the one evaluated using the poles and residues obtained in the previous iteration.

3.4 ANALYTICAL IMPEDANCE MODELS FOR POROUS MATERIALS

3.4.1 Homogeneous Absorber Theory

The Homogeneous Absorber Theory (HAT)[42] models the *normal* impedance of a porous absorber as,

$$Z_{\text{HAT}} = Z_\infty \frac{1 + e^{-j2k_a H}}{1 - e^{-j2k_a H}} \tag{13}$$

which corresponds to the effective impedance of the absorber when the wave propagates normal to its surface (see discussion in Subsection C). The other parameters in 13 are

$$k_a = k\sqrt{\kappa}\sqrt{1 - j\frac{\omega_k}{\omega}}, \quad Z_\infty = Z_0 \frac{\sqrt{\kappa}}{\phi}\sqrt{1 - j\frac{\omega_k}{\omega}}$$

and ω_k, the breaking frequency, is given by

$$\omega_k = \frac{\Xi\phi}{\rho_0\kappa} \tag{14}$$

where, κ is the structure factor, Ξ the flow specific resistivity, ϕ the volume porosity, k and $\omega = 2\pi f$ are the wave number and angular frequency of incident wave, H the total depth of the absorber, and $Z_0 = \rho_0 a_0$ the base impedance. The breaking frequency of the absorber can be interpreted as the (approximate) demarcation between two distinct behaviors of wave propagation inside the porous media: for $\omega \ll \omega_k$, the propagation is dispersive; for $\omega \gg \omega_k$ there is no frequency dependency on the propagation speed of the waves.

3.4.2 Fedorov's Model for Porous Absorber Impedance

Fedorov and Malmuth [43] used the following expression to estimate the impedance due to wave propagation through a regular porous media composed of cylindrical holes with axes oriented normal to the surface (and aligned with the wave propagation direction)

$$Z_{\text{fedorov}} = Z_0 \left(\frac{\phi}{Z_{\infty,*}} \tanh(\Lambda H) \right)^{1}, \tag{15}$$

where Λ is the propagation constant, whose dimensions are the inverse of a length. Fedorov *et al.* [8] extended the model to porous media with random porous structure through the use of the non-dimensional dynamic density (ρ^*_{dyn}) and the non-dimensional dynamic compressibility (C^*_{dyn}) based on previous theoretical work performed by Johnson *et al.* [44] and Allard & Champoux [45]. In his 2003 publication [8], Fedorov non-dimensionalized the resulting expression for the impedance of the metal felts in a manner consistent with his LST framework. Since we are interested in comparing his model with the current iHS and HAT predictions, we recast some of equations and parameters of his model in the following form,

$$Z_{\infty,*}(\omega) = \sqrt{\rho^*_{\text{dyn}}(\omega)/C^*_{\text{dyn}}(\omega)}, \quad \Lambda(\omega) = j\omega\sqrt{\rho_{\text{dyn}}(\omega)/K_{\text{dyn}}(\omega)}, \quad \rho^*_{\text{dyn}}(\omega) = \kappa\left[1 + \frac{g^*(\lambda_1^*)}{\lambda_1^*}\right],$$
$$C^*_{\text{dyn}}(\omega) = \gamma \quad \frac{\gamma \quad 1}{1 + g^*(\lambda_2^*)/\lambda_2^*}, \quad \rho^*_{\text{dyn}} = \rho_{\text{dyn}}(\omega)/\rho_w, \quad C^*_{\text{dyn}}(\omega) = \gamma P_w/K_{\text{dyn}}(\omega),$$
$$g^*(\lambda) = \sqrt{1 + \frac{4\kappa\mu\lambda^*}{\Xi\phi r_p^2}}, \quad \lambda_1^* = \frac{j\kappa\rho_w\omega}{\phi\Xi}, \quad \lambda_2^* = 4\,Pr\,\lambda_1^*, \quad \text{and} \quad r_p = s_h\sqrt{\frac{8\mu\kappa}{\Xi\phi}}.$$

where the superscript (*) or subscript ($_*$) refers to non-dimensional quantities (and not to the complex conjugate). All of the parameters present in these equations variables have been previously defined except for: $K_{\text{dyn}}(\omega)$, which is the dynamic bulk modulus relating the divergence of the average molecular displacement of the gas to the average pressure variation; r_p, the characteristic size of the pores; s_h, a shape factor that accounts for the anisotropy of the pores. As a way of estimating the shape factor for the current C/C samples, and consistently with Fedorov [8], we treat r_p as a hydraulic radius, i.e. the ratio of the doubled pore area to the pore perimeter at the surface. With this assumption, we use Figure 3-9 to visually estimate the shape factor for the classical C/C sample obtaining $s_h \approx 1.26$. The Prandtl number, Pr is taken to be 0.704.

In Fedorov [8] the propagation constant multiplied by the depth, ΛH, (made dimensional here) was expressed as proportional to $j\omega H\sqrt{\rho_{\text{dyn}}(\omega)K_{\text{dyn}}(\omega)}$, while in Allard & Champoux [45] it was expressed as $\Lambda H =$

$j\omega H\sqrt{\rho_{\text{dyn}}(\omega)/K_{\text{dyn}}(\omega)}$. The latter is the expression adopted herein as we believe that what reported in Fedorov [8] is a mere typographical error. For porous absorbers with high flow resistivity, Ξ, coincidentally both expressions yield similar overall impedances due to the asymptotic nature of the hyperbolic tangent function.

3.4.3 Wave Angle Effects on Acoustic Absorption

The wave angle is an important factor significantly affecting the overall acoustic performance of the absorber. This is typically taken into account, with the assumption of a locally reacting surface, as a correction to the value of the normal impedance, yielding the *effective* impedance

$$Z_{eff}(\omega) = Z(\omega)\cos(\theta_i) \tag{16}$$

ultimately used in linear acoustic relations to predict the absorption coefficient β, given by

$$\beta(\omega) = 1 - \left(\frac{|\hat{A}^+|}{|\hat{A}^-|}\right)^2 = 1 - \left|\frac{1 - Z_{eff,*}(\omega)}{1 + Z_{eff,*}(\omega)}\right|^2, \tag{17}$$

which is evaluated by comparing the amplitude of the incident wave $|\hat{A}^-|$ to the reflected wave $|\hat{A}^+|$, representing a figure of merit of the absorber.

The cosine term in (16) accounts for the wave incidence angle θ_i, intended as zero when the direction of wave propagation is normal to the surface of the absorber; $Z(\omega)$ is hence intended as the normal impedance and is the only one that should be imposed in Navier-Stokes calculations with time-domain impedance boundary conditions (TDIBC). To verify this, we have performed two-dimensional Navier-Stokes calculations, mimicking Wagner's benchtest experiments [39], where a quasi-planar acoustic wave was introduced through a source term controlling the main propagation direction angle. Although the experimental setup was constructed to measure waves with angle of incidence of $\theta_i = 30^o$, we also performed a simulation of a wave normal reflection.

Figure 3-2 shows a comparison between the absorption coefficient predicted via the cosine correction (see Eqn (17)), that is using the effective value of impedance (16) and the Navier-Stokes calculations, showing very good agreement. It is important to stress that the IBCs imposed in the Navier-Stokes calculations: (1) only affect the inviscid wall-normal flux; (2) only impose the normal impedance, i.e. values of impedance as predicted by Eqs (13) or (15) and *not* the effective value, that is Eq (16).

3.5 RESULTS

The goal of this section is to reproduce and analyze the disturbance amplification mechanism in a hypersonic flow over a sharp cone with impermeable smooth walls through the excitation of the boundary layer with a broadband frequency pulse. Then, we model the acoustic response of real C/C materials through the iHS technique (section §3.3.2), compare it against impedance estimates from low-order acoustic models as well as benchtest ultrasonic acoustic characterization experimental results by Wagner *et al.*[39] and, ultimately, test its attenuation capability by assigning the predicted impedance as a boundary condition to Navier-Stokes calculations, which allows a comparison with the tests conducted in HEG with a C/C porous insert.

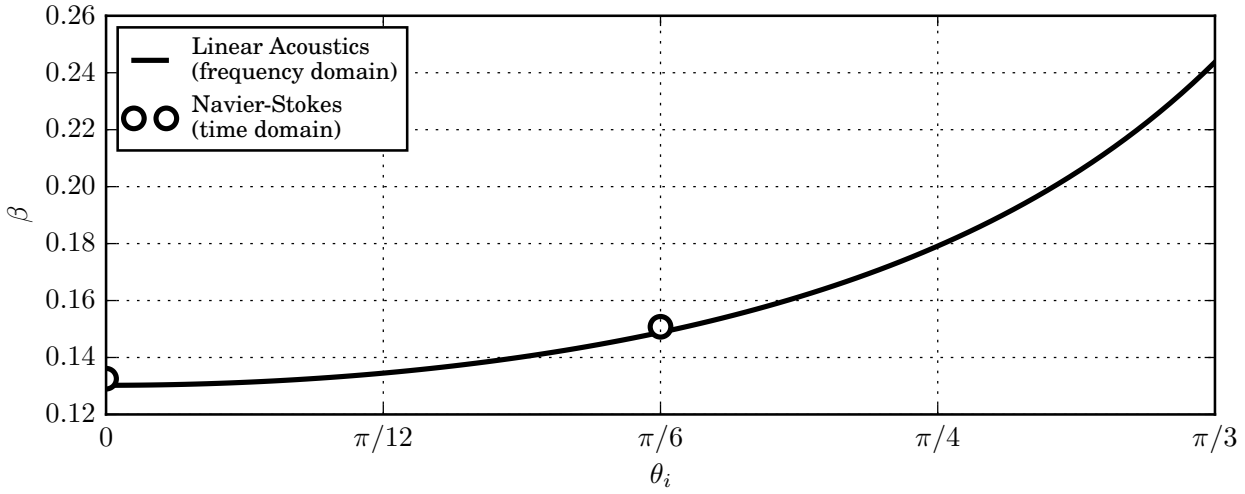

Figure 3-2: Absorption Coefficient (β) Versus Incidence Angle (θ_i) for $f = 300\text{kHz}$, $p_0 = 10\text{kPa}$ and $T_0 = 300\text{K}$.

Table 3-2: Grid Resolution Metrics for the Three Reynolds Numbers Chosen in this Paper.

Re_m	$1.46 \cdot 10^6$ [1/m]			$2.43 \cdot 10^6$ [1/m]			$4.06 \cdot 10^6$ [1/m]		
n_x	4608	6912	9216	4608	6912	9216	4608	6912	9216
n_y	128	256	384	128	256	384	128	256	384
$(\Delta x/\delta)_{0.14m}$	0.1560	0.1080	0.0809	0.2354	0.1637	0.1225	0.2746	0.1814	0.1383
$(\Delta x/\delta)_{0.95m}$	0.0591	0.0403	0.0304	0.0922	0.0605	0.0451	0.1006	0.0689	0.0506
$(\Delta y_{min}/\delta)_{0.14m}$	0.0137	0.0070	0.0046	0.0207	0.0106	0.0070	0.0242	0.0117	0.0079
$(\Delta y_{min}/\delta)_{0.95m}$	0.0363	0.0182	0.0121	0.0566	0.0273	0.0180	0.0618	0.0311	0.0202

An approximate steady laminar solution obtained by blending of the compressible Blasius boundary layer solution applied to a supersonic sharp cone [26, 28] with the inviscid Taylor-Maccoll [25] flow is introduced in the Navier-Stokes calculation both as an inlet and initial condition. After initialization, the inputted solution needs to adapt to the discretized full Navier-Stokes equations. The boundary layer profiles at various locations after this (merely numerical) transient adjustment are shown in Figure 3-3 for $Re_m = 4.06 \cdot 10^6$ m ^{1}; excellent matching between the approximate solution and the steady Navier-Stokes calculations are observed. The same degree of agreement was also achieved for the lower Reynolds numbers cases (not shown). As shown in Table 3-2, the highest Reynolds number is the most stringent case in terms of grid requirements. Given the long streamwise extent of the computational domain, the accuracy of the boundary layer profiles towards the end of the cone is very sensitive to the degree of numerical dissipation. In fact, preliminary runs with more dissipative settings of numerical filtering have shown to overpredict the boundary layer thickness for large values of x.

3.5.1 Broadband Pulse Disturbance Amplification Over Smooth/Impermeable Wall

After the establishment of an unperturbed steady base state, controlled velocity disturbances with an amplitude of $1\ \text{m/s}$ are imposed via suction and blowing at the wall for a finite amount of time ($1.67\ \mu s$) and in a finite-length

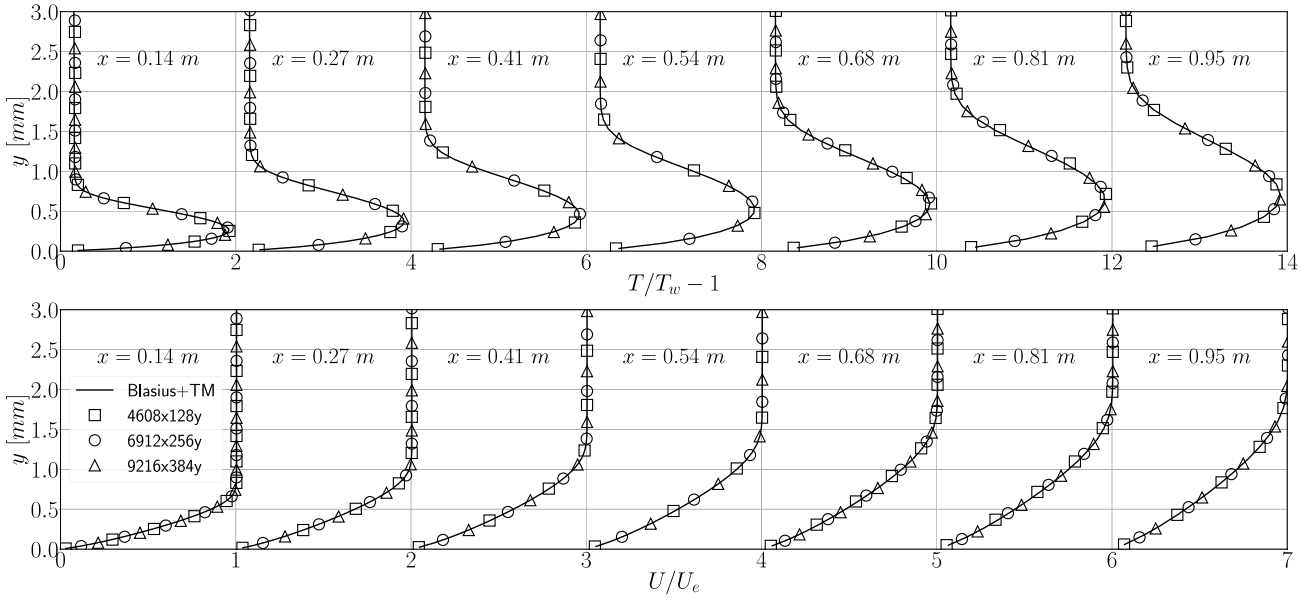

Figure 3-3: Temperature and Streamwise Velocity Profiles from the Unperturbed DNS (symbols); Analytical Approximation Combining Mangler-Transformed Blasius and Taylor-Maccoll Solutions (lines).

interval ($x = 0.14 \pm 0.0036$ m) following the expression (in m/s):

$$v(x, y = 0, t) = \cos(\pi\xi)^3 \sin(2\pi f t), \quad \text{for } 0 \leq t \leq 1/f \tag{18}$$

where ξ is a variable with values ranging in $[\ \ 1, 1]$ which is mapped to the actual spatial interval of application of the pulse, and $f = 600$kHz is the frequency around the which the pulse spectrum is centered. This perturbation aims at mimicking a natural transition scenario, as well as helping identifying the most amplified frequency inside the boundary layer as a function of the streamwise position on the surface of the cone. It was first used by Gaster and Grant [46] in incompressible boundary layer transition simulations and by Sivasubramanian *et al.* [47] in hypersonics.

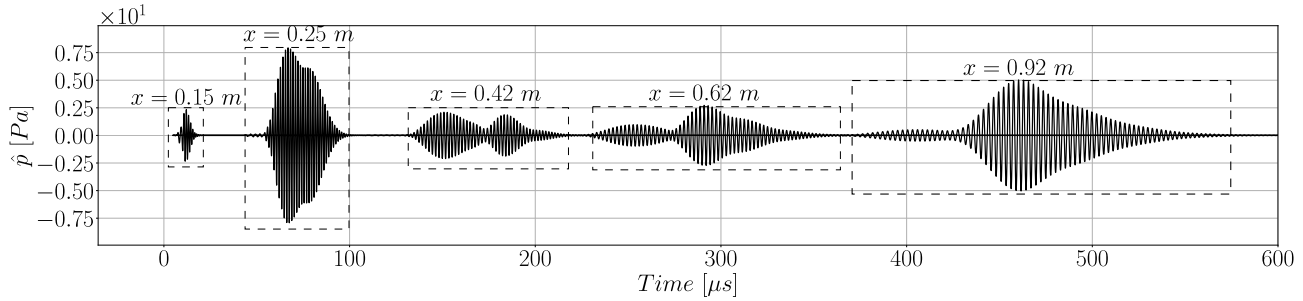

Figure 3-4: Time Series of the Pressure Perturbation at Different Streamwise Locations for $Re_m = 4.06 \times 10^6$ [1/m] with $n_x = 9216$ And $n_y = 384$.

Figure 3-4 shows the pressure time series at the wall for different streamwise locations. A rapid amplification of the overall pressure signal is observed initially, from x=0.15 m up to approximately x=0.25 m, followed by a later gentler growth. However, the total disturbance amplitude contains energy at various frequencies, and, although

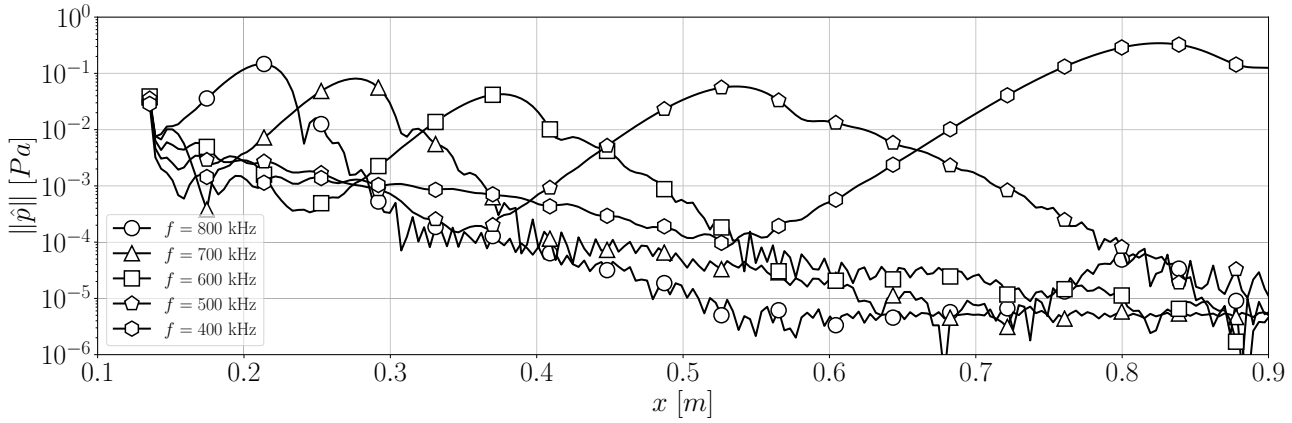

Figure 3-5: Amplitude of Pressure Disturbance at the Wall for Different Frequency Components with $n_x = 6912$, $n_y = 256$ and $Re_m = 4.0 \times 10^6$ m [1].

the pulse excitation inputs a similar amount of energy in all the frequencies range relevant to the boundary layer instability, some of the components experience a long region of decay before reaching their unstable region (Figure 3-5). In the end, the overall amplitude of the signal depends on the balance between the attenuation in the stable region and the overall integrated growth in the unstable region of each frequency component. In fact, consistently with amplification dynamics of instability waves in (canonical) hypersonic boundary layers, higher frequency modes experience growth earlier, i.e. where the boundary layer is thinner and, simultaneously, the remaining frequency components are attenuated.

The early rapid overall pressure signal amplitude increase is hence due to the high-frequency component, in the range of 800 kHz for $Re_m = 4.0 \times 10^6$, of the inputted broadband disturbance pulse. After this initial phase, a rapid decay is also observed due to the fast evolution of the boundary layer thickness in its early stages, what changes the quickly unstable frequency band. At last, the later gentler growth shown in Figure 3-4 happens because, as the signal moves downstream, the boundary layer thickness evolution becomes slower and the overall integrated growth becomes steadily bigger than the initial attenuation.

A Fourier analysis of such times series is shown in Figure 3-6, demonstrating that, for all Reynolds numbers considered, the initial broadband characteristic of the signal is very rapidly lost and the power spectrum concentrates in a narrow band of ultrasonic frequencies, consistent with second-mode amplification mechanisms for each flow conditions considered. Experimental studies conducted by Stetson [48] confirmed the validity of the following estimation for the second-mode frequency

$$f = \frac{U_e}{2\delta}, \tag{19}$$

where U_e is the boundary layer edge velocity and δ is the boundary layer thickness, defined as the wall normal distance where $u \simeq 0.999 U_e$. Predictions based on (19) are plotted in Figure 3-6 showing good agreement with the DNS results. A detailed phase speed analysis reveals that both slow and fast modes [49] are observed in the current DNS; however, most of the disturbance energy and growth are carried by the slow mode (not shown), corresponding to Mack's second mode after the phase speed synchronization point (see discussion on terminology of instability modes in Egorov [21]).

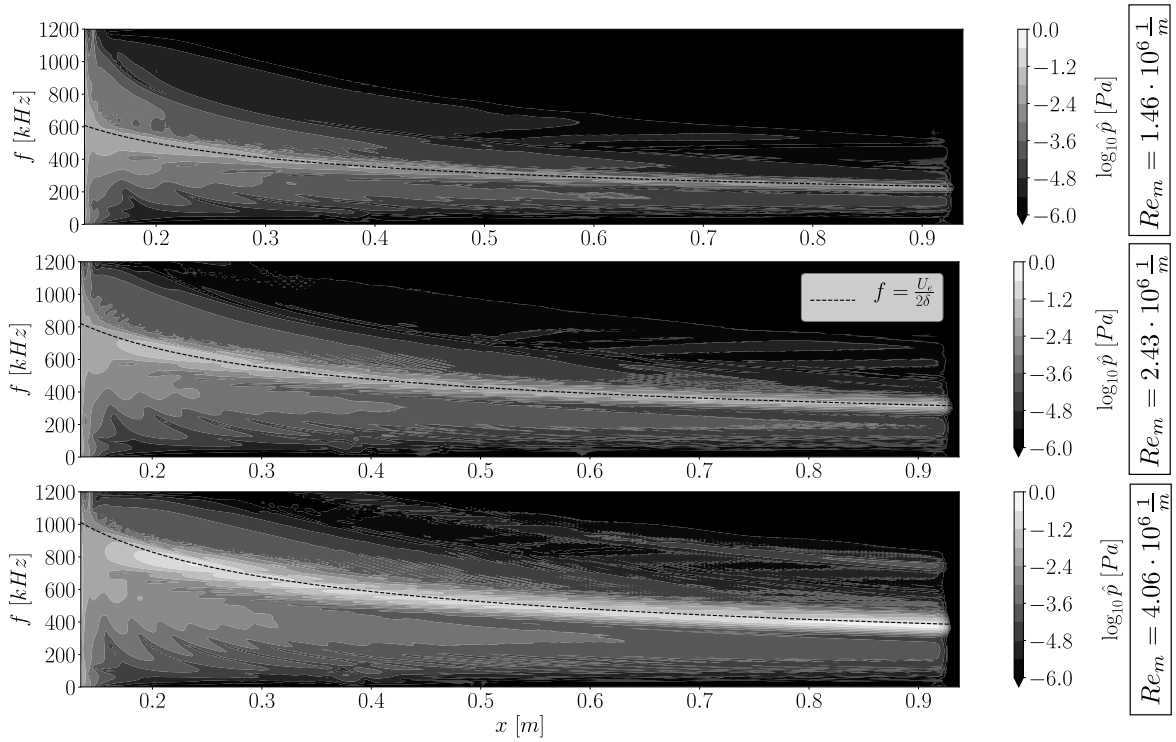

Figure 3-6: Contours of Fourier-Mode Amplitude as a Function of Frequency and Space for the Three Reynolds Numbers Considered and $n_x = 6912$ and $n_y = 256$.

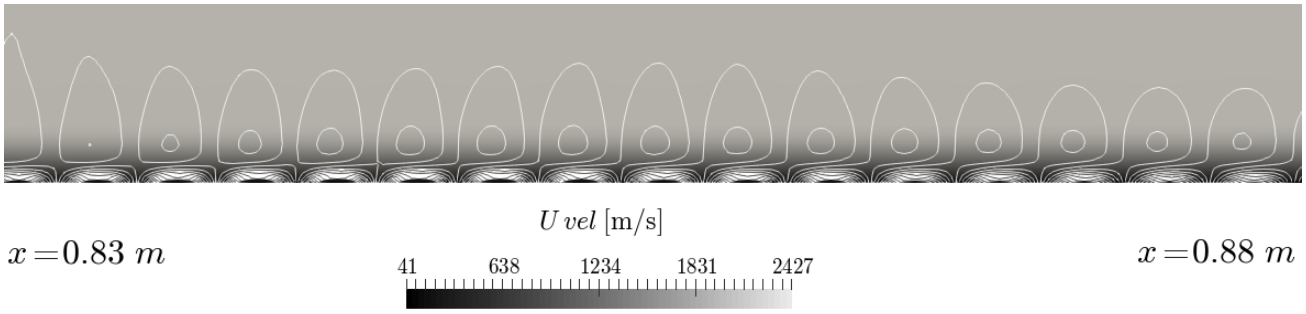

Figure 3-7: Pressure Oscillation Isosurfaces in the Boundary Layer Region for $n_x = 4608$, $n_y = 128$ And $Re_m = 4.0 \times 10^6$ m ^{1}.

The broadband pulse excitation is able to capture the correlation between the most amplified frequencies in the boundary layer and its thickness revealing information similar to stability analysis. It is observed that the second-mode frequency follows closely the boundary layer thickness: the higher the Reynolds number, the thinner the boundary layer and the higher the excited frequencies. Figure 3-7 shows pressure isosurfaces near the surface of the cone, reminiscent of acoustically channeled waves with some power transmitted (or lost) outwards through the sonic line, characteristic of the second mode (Egorov [21]).

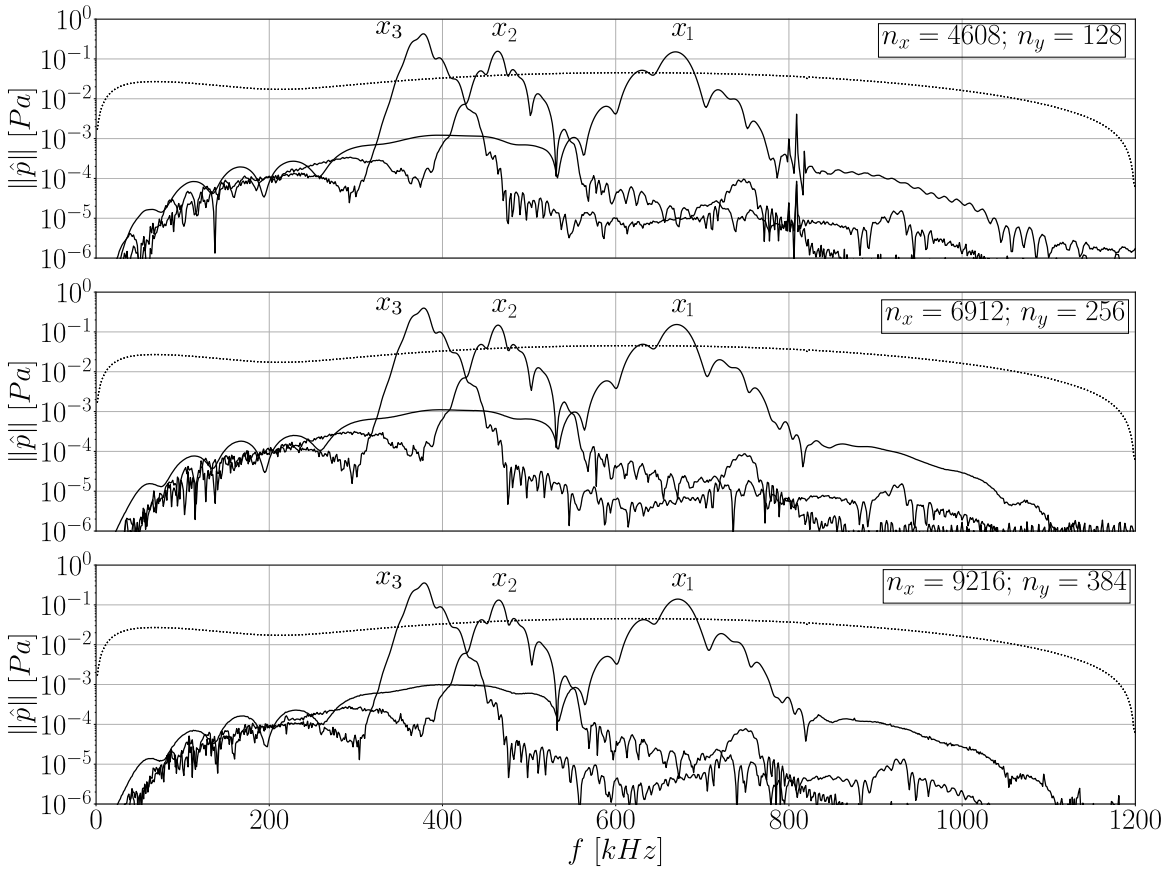

Figure 3-8: Grid Convergence Analysis for the Perturbation Spectrum at $x_1 = 0.3$ m, $x_2 = 0.6$ m and $x_3 = 0.9$ m in an Axisymmetric Simulation of Broadband Pulse Propagation at $Re_m = 4.06 \times 10^6$ m [1].

Another phenomenon that occurs as the imposed pulse advects downstream, is that its magnitude becomes large enough to excite higher harmonics. For the high Re_m case, specifically, the appearance of the first first harmonic of the second mode is visible after x = 0.7m, shown in Figure 3-13. At the very end of the computational domain, a sponge layer, starting around $x = 0.94$ m, damps the imposed disturbances before they reach the outflow boundary condition. No sign of spurious upstream disturbances has been identified in the subsonic part of the boundary layer near the outflow.

The spatial resolution and the numerical discretization strategy play a crucial role in the quality of the prediction of the evolution dynamics of high frequency perturbations, such as second-mode waves. The grid convergence study in Figure 3-8 demonstrates adequate spectral resolution on the intermediate grid adopted ($n_x = 6912$,$n_y =$

256); results on the coarser grid ($n_x = 4608$,$n_y = 128$) are also adequate, with the exception of spurious energy accumulation at $f = 800$kHz. The latter is actually due to a numerical disturbance originating from the interaction of the inflow sponge layer and the coarse grid, and insufficient resolution of the propagating waves. This spurious wave source propagates into the domain and it not damped due to the low artificial diffusion of the scheme. While the dynamics of the disturbance evolution inside the conical hypersonic boundary layer are not altered by this spurious perturbation, only intermediate or high resolutions ($n_x \geq 6912$,$n_y \geq 256$) of such full cone axisymmetric computations, will be considered.

The finest grid resolution available ($n_x = 9216$,$n_y = 384$) is capable of adequately resolving wave lengths of 0.8 mm, assuming a minimum requirement of 8 points per wavelength for compact finite difference schemes. Being the boundary layer thickness towards the end of the cone of the order of 2 mm, this resolution is not adequate to capture the nonlinear breakdown to turbulence. The effects of porous walls on the latter will be investigated in future computations focused on (inevitably) shorter sections of the cone.

3.5.2 Impedance Characterization of Carbon-Fiber-Reinforced Carbon Ceramics (C/C)

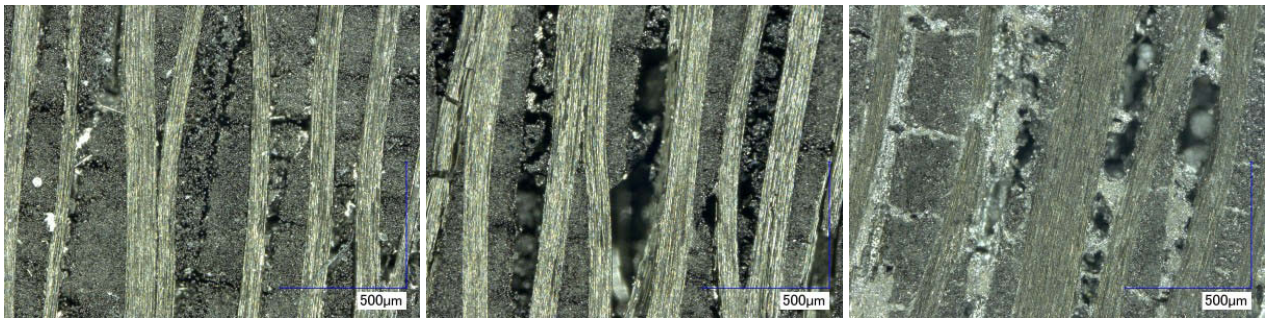

Figure 3-9: Reflected-Light Microscopy Generated Images of Classic (Untreated) C/C (left), Optimized C/C (middle), and Optimized C/C-SiC (right) [50].

Carbon/carbon Silicon Carbide (C/C-SiC) is a material that has already been used as a Thermal Protection System (TPS) in hypersonic flight [15, 16]. C/C represents an intermediate state of its manufacturing process. The porosity of C/C materials is a result of thermal stresses that appear in the cool down process of the material after pyrolyzation of the matrix. This material offers excellent thermal resistance, low expansion and specific weight as well as high temperature stability in non oxidizing atmospheres. However, C/C cannot be used when the oxidizing effects are important in the flow without a protective treatment. Resistance against oxidation is acquired by the infiltration of a liquid phase of silicon into the porous carbon, followed by a reaction to SiC. If this infiltration is done in the untreated C/C, its microstructural gaps will be filled and the acoustic absorption properties of the material lost.

To solve this problem, DLR Stuttgart developed a technique that is able to selectively insert cavities into the C/C structure by replacing carbon fibers with a non-stable material that will degrade after the pyrolyzation step in the desired locations, that allowed to nearly double the porosity [51]. The existence of larger gaps in this optimized C/C (Figure 3-9) allows it to retain a certain porosity degree after the SiC reaction. This results in the optimized C/C-SiC, which combines the properties of oxidation resistance with acoustic absorption and, therefore, it could be a suitable material for in flight transition delay.

The complex acoustic impedance of the classic C/C sample shown in Figure 3-9 was estimated via various methodologies with results shown in Figure 3-10. The acoustic analysis of the optimized C/C and C/C-SiC are deferred to future work.

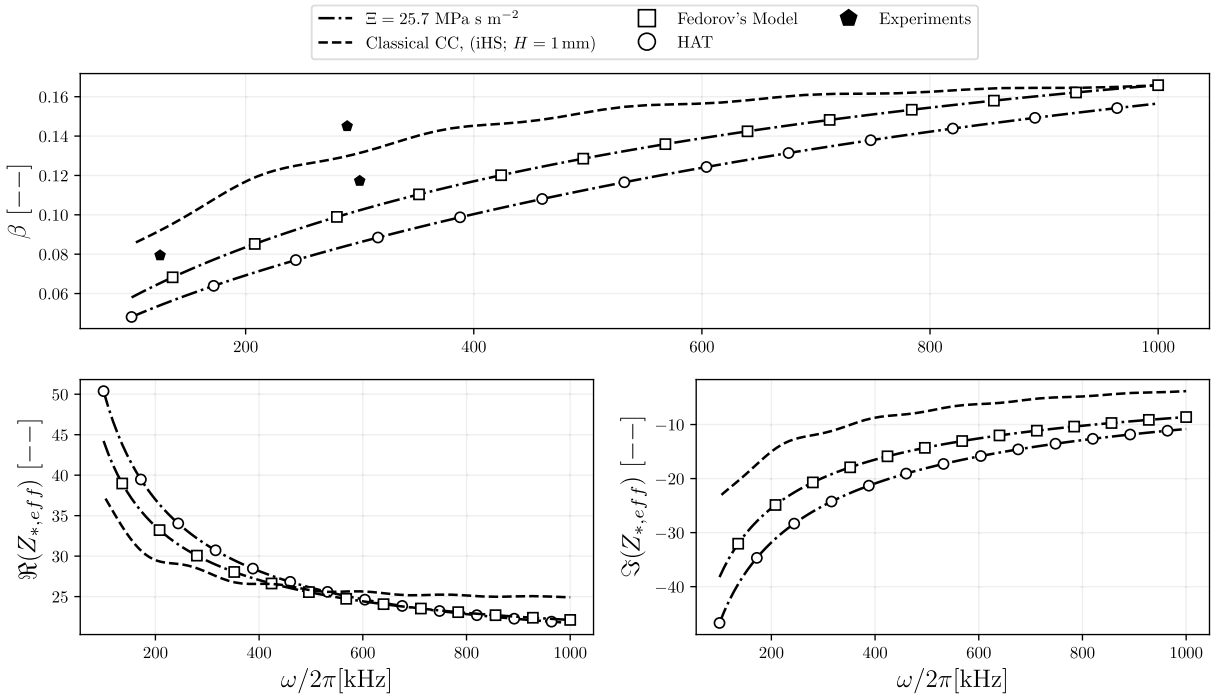

Figure 3-10: Comparison of Real $\Re(Z_{*,eff})$ and Imaginary $\Im(Z_{*,eff})$ Parts of the Specific Impedance $Z_{*,eff}(\omega)$, and Absorption Coefficient β, Obtained from Various Models at $\theta_i = 30°$ and Wall Conditions Corresponding to $Re_m = 4.06 \times 10^6$ m [1].

Experimentally determined and theoretically predicted values of β Eq (17) are plotted in Figure 3-11. The experimentally determined absorption coefficient by Wagner [39] was obtained by comparing the amplitude of a wave reflected off an acoustically absorptive surface to the same wave reflecting off a purely reflective (impermeable) boundary. This absorption process is not only a function of the porous absorber, but also of the flow properties themselves, for example, it will depend on the angle of incidence, which will change the *effective* impedance, $Z_{eff,*}(\omega)$, which should be used to evaluate β. In order to enable comparison between the experiments performed by Wagner [39] all the results presented in Figure 3-10 and Figure 3-11 consider an angle of incidence of $\theta_i = 30^o$.

The predictions of acoustic impedance evaluated using the inverse Helmholtz solver (iHS) are compared with experimental results of benchtest acoustic characterization of ultrasonically absorptive porous samples [39] and two different theoretical models: (1) the homogeneous absorber theory (HAT) detailed in Moser [42] and utilized by Wagner [13], and (2) the model for acoustic impedance of a porous surface with random porosity used by Fedorov [8] in his LST calculations of second-mode attenuation over a felt metal coatings. Both these models have been briefly summarized above in section 3.4.

The use of these models relies on the determination of physical parameters that describe some characteristics of the flow through the porous medium such as: the porosity (ϕ), which is the ratio of the pore volume to the total volume; the flow resistivity (Ξ), that represents the resistance (pressure difference) to the flow of air through the medium; and the structure factor (κ), that accounts for the presence of some "blind" and tortuous paths in the absorber. Wagner [13] in 2014 reports for the first time the values that characterize the classical C/C material, which are summarized in Table 3-3. Although ϕ and Ξ can be experimentally obtained [52], κ cannot be measured or calculated directly for randomly structured porous materials and it was inferred from the experimentally measured reflection coefficient. In 2018 DLR has remeasured the flow resistivity Ξ of the classical C/C sample, reporting an almost doubled value than what was previously published. The reason for the difference in the measured Ξ was attributed to the better sealing of the samples – the edge of the samples was galvanized with copper to avoid leakage – in the more recent experiments. Results from these new measurements are also reported in Table 3-3 and will be the one used in the present analysis to inform the choice of parameters in the HAT and Fedorov's model.

The acoustic characterization experiments by Wagner [39] provide wave absorption data for a discrete set of frequencies since a different transducer receiver pair is needed for testing different frequencies. However, in order to execute the implementation of TDIBC a continuous reconstruction of the complex impedance in the frequency domain is required. Wagner's data is hereby compared against various acoustic absorption models to assess their predictive capability both in the form of complex impedance versus frequency at one pressure corresponding to flow conditions of $Re_m = 4.06 \times 10^6 \mathrm{m}^{-1}$(Figure 3-10) and in the form of absorption coefficient β at various frequencies versus pressure (Figure 3-11).

For the predictions carried out numerically by the iHS methodology, a blind-hole porosity assumption was used. A surface (and hence also volume) porosity of 0.078 is used, as obtained from the processing of the high-resolution C/C surface images. A nominal depth of $H = 1\,\mathrm{mm}$, common to all pores, has been assumed based on visual inspection of depth-wise slices of a C/C sample provided by DLR Stuttgart [40].

For the chosen value of flow resistivity, $\Xi = 25.7$ MPa s m^{-2}, both the HAT and Fedorov's model underestimate the absorption coefficient at low base pressures and relative to the iHS predictions. As the pressure increases, the absorption coefficient prediction based on the iHS starts to deviate from the experimental data, and both low-order models provide better (but still not satisfying) predictions. An overall under-prediction of the magnitude of the absorption coefficient is observed by all models.

The discrepancy of iHS results is attributed to the underestimated volume porosity given that only a limited selection of the largest visible pores in Figure 3-9 (left) were used for the direct impedance estimate. This leads us to conclude that the smaller pores, which were ignored in the selection surface porosity estimate step (section §3.3.2), play an important role in the absorption. The latter contribution is, on the other hand, captured by low-order models for porous acoustic absorbers, especially at higher pressures. In the end, since the experiments performed in the HEG at DLR go up to a maximum pressure of 0.1×10^5 Pa, the iHS is a better predictive

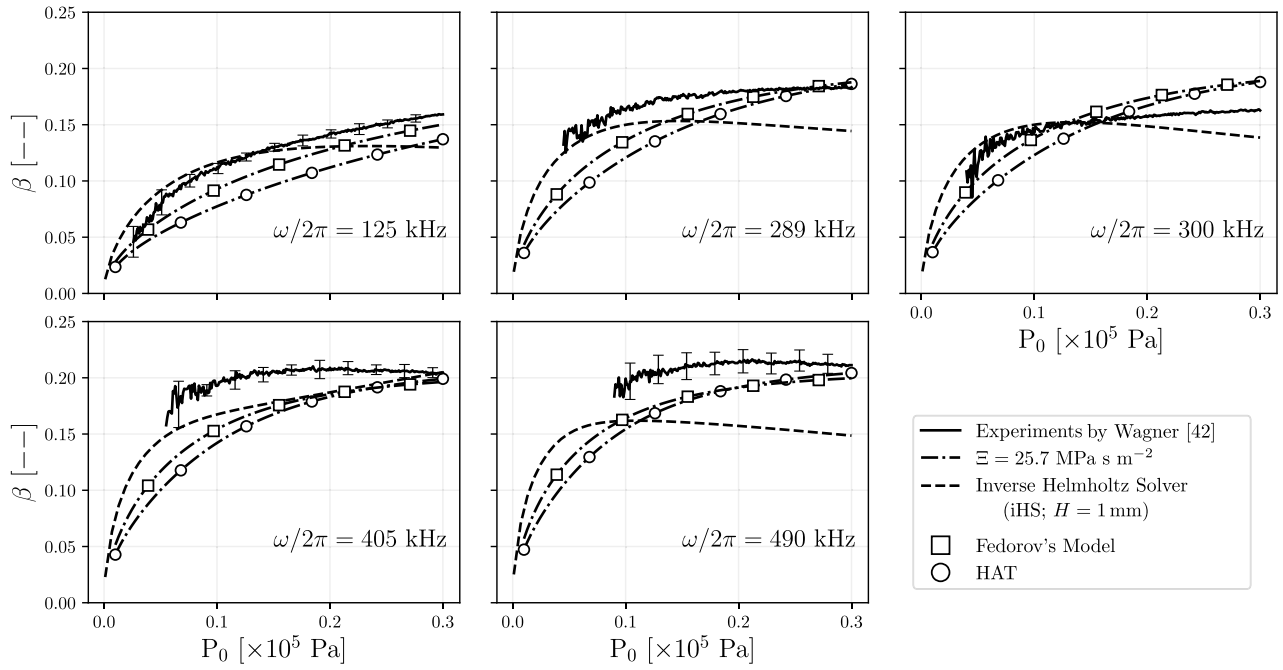

Figure 3-11: Comparison of Measured and Predicted Absorption Coefficient β for the Classical C/C Versus Base Pressure.

tool than the theoretical models limited to the range of pressures reproduced by the DNS results in the present manuscript.

It is also worth noting that although the acoustic impedance estimate by the use of the theoretical models presented by Fedorov and the HAT explicitly accounts for the influence of the thickness of the absorber, the high magnitude of flow resistivity (Ξ) of this material, in the order of 10 [MPa s m ^{2}], results in unchanged absorption characteristics for $H \geq 1\,\mathrm{mm}$, i.e. the absolute thickness of the absorber for such high values of Ξ becomes irrelevant for thicknesses larger than 1 mm. This also implies that the absorbed wave is evanescent with respect to the depth of the absorber (infinitely thick absorber model), and wave-reflection from the impermeable backing of the absorber is not important. Another observation is that the use of a lower flow resistivity (Ξ) value, such as the (now obsolete) value measured by Wagner [13] in 2014, would lead to a higher absorption coefficient and hence an unexpected better agreement with the measured absorption coefficient than the more recently obtained value.

Figure 3-10 compares complex impedance prediction of various models versus frequency at one given base pressure $p_0 = 5076$ Pa. Because of the difficulty of measuring the propagation and reflection of an ultrasonic wave at low pressures and because of the need for a separate transducer/receiver pair for each frequency, only a few experimental data points could be included in these plots. These points are not sufficient to make a statement on which is the best way of predicting the complex impedance trend versus frequency but they reiterate the previous observations that the iHS is more accurate in this low pressure regime than the other low-order models, and that a lower flow resistivity (Ξ) value would lead to a better agreement of the low-order acoustic models with the experimental data.

Table 3-3: Properties of the Porous Absorber Investigated

Experiment	ϕ [–]	κ [–]	Ξ [MPa s m^{-2}]	Depth, H [m]
Wagner (2014) [13]	0.15	8.0	13.3	5.0×10^{-3}
DLR (2018)	0.15	8.0	25.7	5.0×10^{-3}

A word of caution regarding the adoption of the various models analyzed herein is that none of them take into account impedance changes due to grazing flow effects; the latter, however, are expected to be negligible due to the small size of the pores. Minimal-unit pore-resolved simulations are currently ongoing to assess this effect. It is also important to note that the evaluated specific impedance Z_*, despite being dimensionless, is a function of the thermodynamic base state. The impedance estimates presented here were obtained for the pressure conditions at the surface of the cone model, i.e. the conditions after the conical shock, at the wall as predicted by the inviscid Taylor-Maccoll solution, and depend on the Reynolds numbers as seen in Table 3-1 (see p_e value, which corresponds to the pressure at the wall, and hence within the C/C pores). In conclusion, the effective impedance of the C/C surface is a function of the thermodynamic state of the gas that fills the C/C pore space and hence directly relatable to the external flow conditions.

3.5.3 Porous Walls and Second-Mode Attenuation

Once we have modeled the acoustic energy absorption at the wall for the different C/C samples, we are able to input this information in the DNS as a complex impedance boundary condition. Only the impedance estimates from the iHS methodology are taken into considerations for the current sets of runs. Simulations with IBCs are run quiescent first and then, after spurious transient waves due to initialization errors are convected out of the domain, a broadband pulse is applied via suction and blowing at the wall (Eqn. 18), with results shown in Figure 3-12.

The effects of frequency and Reynolds numbers on the evolution of the Fourier mode of pressure are analyzed. It is noted that, for all cases considered, the disturbance energy for the impermeable wall case and for the porous case start at the same level and keep the same amplitude relative to each other before the impedance strip starts (denoted by the vertical dotted line). Once the pulse is advecting over the impedance boundary, acoustic energy is being extracted from the signal and its amplitude falls below the impermeable-wall baseline until the end of the domain. It is observed that the second mode experiences higher attenuation rates due to the C/C in the regions where the mode is already stable and lower growth rates in the regions of instability for the advection over the porous walls in comparison with the run over solid walls. The combination of these phenomena lead to the decrease in the maximum power content for each frequency throughout the domain and depicts the capability of ultrasonic absorbing coating to dampen the second-mode instability in a hypersonic boundary layer. Another noticeable behavior is that the location of the maximum pressure amplitude moves upstream due to the porous walls.

Low-amplitude short-wavelength oscillations are observable at high Reynolds numbers at the later stages of the second-mode evolution (in Figure 3-12). Such spatial variations in the amplitude of the Fourier modes of pressure at the wall, $||\hat{p}||$, may indicate the presence of a short-wave-length standing wave or spatial modulation of that particular temporal frequency, or nonlinear spectral broadening. These oscillations cannot be attributed to lack of grid resolution (see Figure 3-8) and their origin will be scrutinized in more detail in future work.

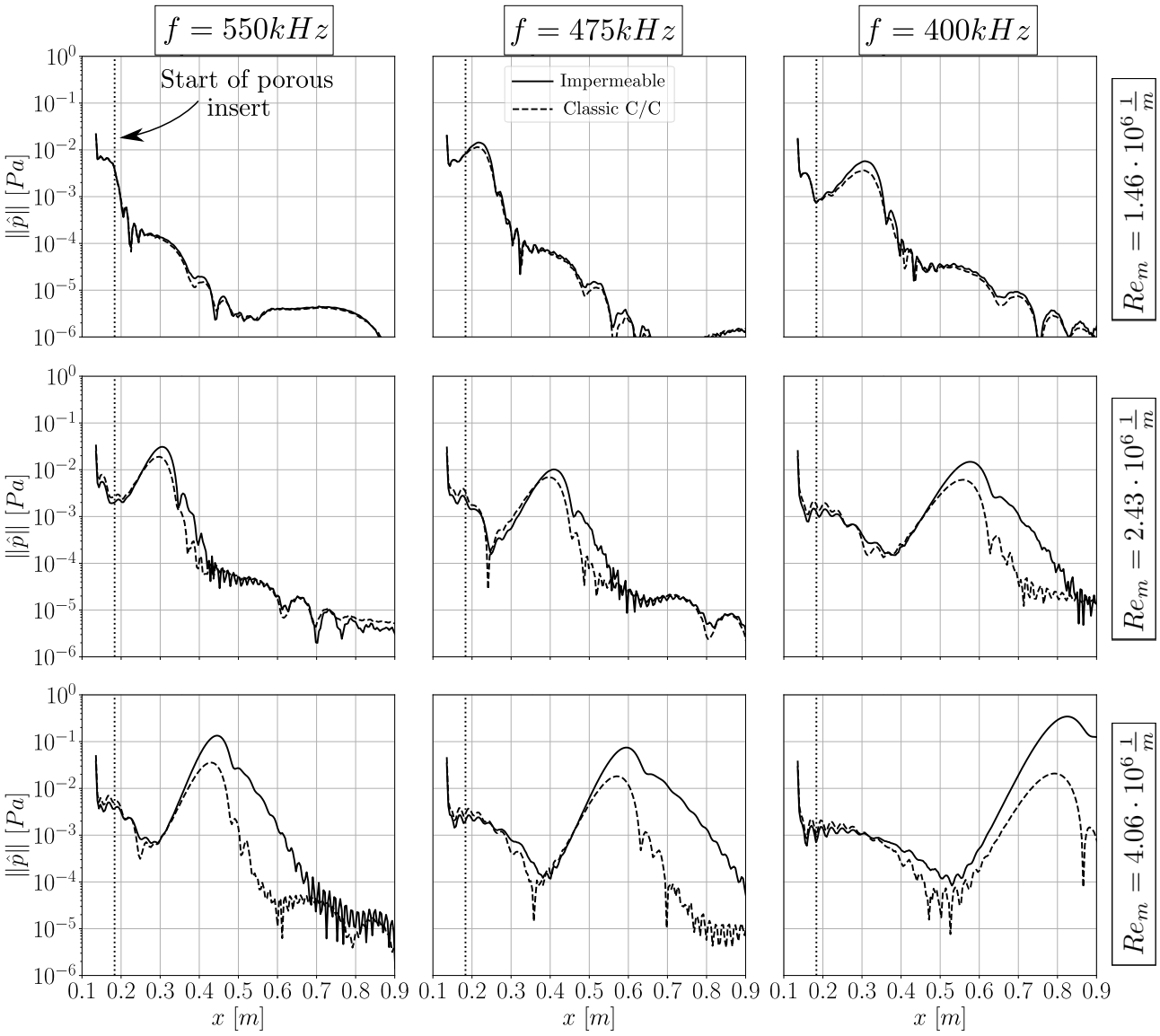

Figure 3-12: Spatial Distribution of the Fourier Transform of Pressure Fluctuations at the Wall for Different Frequencies in the Broadband-Pulsed Simulations over Porous and Impermeable Walls.

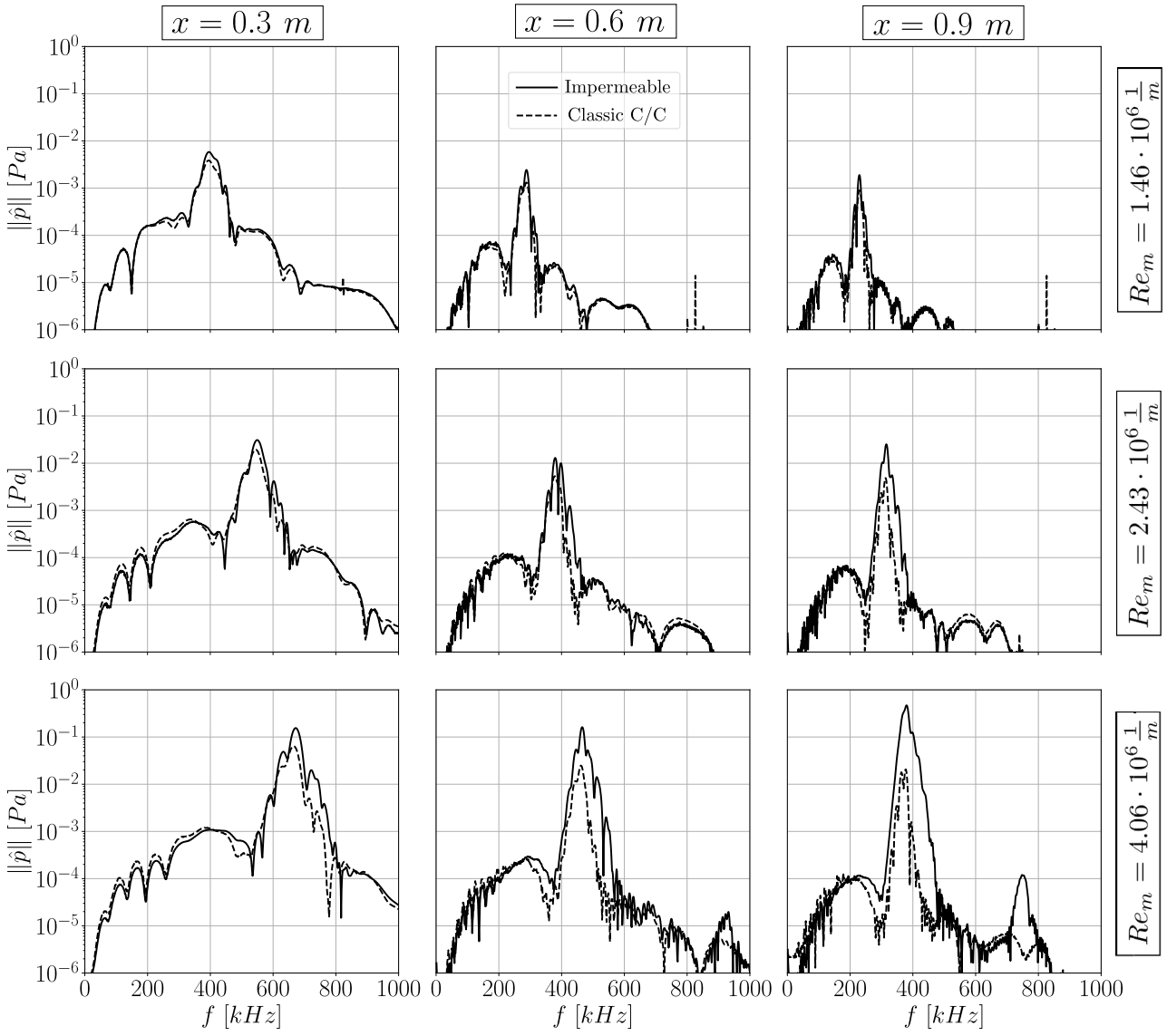

Figure 3-13: Frequency Domain Distribution of the Power Spectrum at the Wall for Different Streamwise Locations in the Advection of a Broadband Pulse Simulations Over Porous and Impermeable Walls.

Figure 3-13 shows the power spectrum at a given streamwise location on the surface of the cone to see how it is distributed over the frequency domain, for all the Reynolds numbers considered in this study. In this plot we observe that the effectiveness of the porous walls in absorbing energy starts to become relevant for frequencies above 200 kHz and that the maximum amplitude of the power spectrum attenuated at the three different probed locations for all Reynolds numbers occurs beyond this frequency. The effectiveness of the attenuation of the spectrum induced by the porous surfaces increases with Reynolds numbers. The reason for this interesting behavior is believed to be because of the shift of the spectrum to higher frequencies and, since all acoustic models presented predicts that the absorption coefficient of the C/C based materials increase with frequency, the UAC becomes more effective.

Wagner [13] reported a similar behavior in his transition delay experiments in the HEG tunnel at DLR Göttingen but for a different range of Re_m. He observed that, as the Reynolds numbers increased from $4.0 \cdot 10^6$ m ^{1} to $9.8 \cdot 10^6$ m ^{1} the relative transition delay on the porous surface increased from 0.15 to 0.29. With the same reasoning, we speculate that the reason why the experiments conducted by Willems *et al.* [53] weren't able to measure any attenuation of the second-mode waves with the same C/C sample from DLR is that the frequency of the second-mode waves were approximately 100 kHz at the flow conditions chosen for that study. Another factor that could have influenced the results are the very low pressures (from 0.003×10^5 to 0.008×10^5 Pa) at which the tests by Willems *et al.* were carried. These pressure levels lead to low absorption coefficients (shown in Figure 3-11).

Another evidence of the hypersonic boundary layer transition delay capability of acoustic energy absorption can be found the furthest downstream probed location of the highest Reynolds number. At this position, the advection of the broadband pulse over impermeable walls was amplified to the point that started to excite the first overtone (or harmonic) of the second-mode waves. However, the presence of porous walls dampens such high frequency modes more effectively than the second mode itself (which cascades energy onto the higher modes due to nonlinear effects, when present). This means that the disturbance with the same initial amplitude would need to propagate further downstream to reach the necessary strength to trigger transition into turbulence effectively delaying transition.

3.6 CONCLUSION

The effect of realistic acoustically absorptive surfaces on the second mode in a hypersonic boundary layer over a sharp slender cone was numerically studied in the present work. High order simulations informed by the analytical relations of that describing the supersonic viscous flow of a perfect gas over a sharp cone were performed and the high order simulations were capable of holding the solution and matching accurately the shape and growth of the boundary layer profiles as they moved downstream of the cone. In addition, a novel technique (iHS) was used to solve the acoustic response at the mouth of the cavities present in porous materials and to model their collective influence through a surface averaging. The complex impedance obtained as a result was used to model the impact of the ultrasonically absorptive surface in a spatially developing boundary layer simulation without having to resolve the intricate porous structure. The result of this simulation was then compared with previously published theoretical models and a better agreement with experimental data for the low pressure domain is achieved.

Artificial disturbances were introduced in the boundary layer and their evolution with downstream advection

was observed. With the introduction of a broadband pulse and its advection over a solid surface we were able to identify the second-mode dynamics over an impermeable wall, used as a baseline, and over materials currently being developed to be used in hypersonic transition control such as the 'classical' C/C. In conclusion, for the frequencies and flow condition tested the C/C was found capable of attenuating the second-mode and delaying boundary layer transition into turbulence.

All results shown in the present contribution are for a sharp-tip cone. The presence of a non-negligible tip bluntness increases the boundary layer thickness (for the same free-stream conditions) and hence lowers growth rates and the frequency of second-mode waves. Although this will lower the effectiveness of the acoustic absorption properties of the porous walls, resulting in a less effective attenuation of second-mode waves, we would be still in a suitable region for the tested C/C porous material.

3.7 ACKNOWLEDGMENTS

We acknowledge the support of the Rosen Center for Advanced Computing (RCAC) at Purdue, the Air Force Office of Scientific Research (AFOSR) grants, FA9550-16-1-0456, FA9550-16-1-0209, the AFOSR YIP 2018 (FA9550-18-1-0292) and the NSF (Fluid Dynamics Program) Award No. 00068647. We acknowledge the very fruitful discussions with Dr. Ivett Leyva (AFOSR), Dr. Eric Marineau (ONR), Prof. Schneider and all of the members of the NATO AVT-240 Task Force on Hypersonic Transition. Victor Sousa also acknowledges the support of the prestigious Lynn Fellowship administered by the interdisciplinary Computational Science and Engineering (CS&E) graduate program at Purdue University.

The content of this chapter is taken from the manuscript: Sousa, Patel, Chapelier, Wartemann, Wagner and Scalo "Numerical Investigation of Second Mode Attenuation over Carbon/Carbon Porous Surfaces", published in *Journal of Spacecraft and Rockets* in 2019 [54].

3.8 REFERENCES

[1] Reed, H.L., Kimmel, R., Schneider, S., Arnal, D., and Saric, W., "Drag prediction and transition in hypersonic flow," *AGARD Conference Proceedings*, Vol. 3, AGARD, 1997, pp. C15–C15.

[2] Force, N., "Report of the defense science board task force on the national aerospace plane (NASP)," Tech. rep., Technical report, Defense Science Board, Office of the Secretary of Defense, Washington, DC 20301-3140, 1992.

[3] Mack, L., "Boundary-Layer Stability Theory," Document 900-277, Rev. A," *Jet Propulsion Lab., Pasadena, CA*, 1969.

[4] Mack, L., "Computation of the stability of the laminar boundary layer," *Methods in Computational Physics*, Vol. 4, 1965, pp. 247–299.

[5] Mack, L.M., "On the inviscid acoustic-mode instability of supersonic shear flows," *Theoretical and Computational Fluid Dynamics*, Vol. 2, No. 2, 1990, pp. 97–123.

[6] Malmuth, N., Fedorov, A., Shalaev, V., Cole, J., Hites, M., Williams, D., and Khokhlov, A., "Problems in high speed flow prediction relevant to control," *2nd AIAA, Theoretical Fluid Mechanics Meeting*, 1998, p. 2695, (AIAA-1998-2695).

[7] Fedorov, A.V., Malmuth, N.D., Rasheed, A., and Hornung, H.G., "Stabilization of hypersonic boundary layers by porous coatings," *AIAA journal*, Vol. 39, No. 4, 2001, pp. 605–610.

[8] Fedorov, A., Shiplyuk, A., Maslov, A., Burov, E., and Malmuth, N., "Stabilization of a hypersonic boundary layer using an ultrasonically absorptive coating," *Journal of Fluid Mechanics*, Vol. 479, 2003, pp. 99–124.

[9] Fedorov, A.V., Kozlov, V.F., Shiplyuk, A.N., Maslov, A.A., and Malmuth, N.D., "Stability of hypersonic boundary layer on porous wall with regular microstructure," *AIAA journal*, Vol. 44, No. 8, 2006, pp. 1866–1871.

[10] Chokani, N., Bountin, D.A., Shiplyuk, A.N., and Maslov, A.A., "Nonlinear aspects of hypersonic boundary-layer stability on a porous surface," *AIAA journal*, Vol. 43, No. 1, 2005, pp. 149–155.

[11] Lukashevich, S., Morozov, S., and Shiplyuk, A., "Experimental study of the effect of a passive porous coating on disturbances in a hypersonic boundary layer 2. Effect of the porous coating location," *Journal of Applied Mechanics and Technical Physics*, Vol. 57, No. 5, 2016, pp. 873–878.

[12] Wagner, A., Kuhn, M., Schramm, J.M., and Hannemann, K., "Experiments on passive hypersonic boundary layer control using ultrasonically absorptive carbon–carbon material with random microstructure," *Experiments in fluids*, Vol. 54, No. 10, 2013, pp. 1606.

[13] Wagner, A., *Passive Hypersonic Boundary Layer Transition Control Using Ultrasonically Absorptive Carbon-Carbon Ceramic with Random Microstructure*, Ph.D. thesis, Katholieke Universiteit, Leuven, 2014.

[14] Wagner, A., Hannemann, K., and Kuhn, M., "Ultrasonic absorption characteristics of porous carbon–carbon ceramics with random microstructure for passive hypersonic boundary layer transition control," *Experiments in Fluids*, Vol. 55, No. 6, 2014, pp. 1750.

[15] Turner, J., Hoerschgen, M., Jung, W., Stamminger, A., and Turner, P., "SHEFEX - Hypersonic Re-entry Flight Experiment Vehicle and Subsystem Design, Flight Performance and Prospects," *14th AIAA/AHI Space Planes and Hypersonic Systems and Technologies Conference*, 2006, p. 8115, AIAA-2006-8115.

[16] Weihs, H., Longo, J., and Turner, J., "The sharp edge flight experiment SHEFEX II, a mission overview and status," *15th AIAA International Space Planes and Hypersonic Systems and Technologies Conference*, 2008, p. 2542.

[17] Wartemann, V., Wagner, A., Kuhn, M., Eggers, T., and Hannemann, K., "Passive hypersonic boundary layer transition control using an ultrasonically absorptive coating with random microstructure: Computational analysis based on the ultrasonic absorption properties of carbon-carbon," *Procedia IUTAM*, Vol. 14, 2015, pp. 413–422.

[18] Brès, G., Colonius, T., and Fedorov, A., "Stability of temporally evolving supersonic boundary layers over micro-cavities for ultrasonic absorptive coatings," *5th AIAA Theoretical Fluid Mechanics Conference*, 2008, p. 4337.

[19] Fedorov, A., Brès, G., Inkman, M., and Colonius, T., "Instability of hypersonic boundary layer on a wall with resonating micro-cavities," *49th AIAA Aerospace Sciences Meeting including the New Horizons Forum and Aerospace Exposition*, 2011, p. 373.

[20] Brès, G.A., Inkman, M., Colonius, T., and Fedorov, A.V., "Second-mode attenuation and cancellation by porous coatings in a high-speed boundary layer," *Journal of Fluid Mechanics*, Vol. 726, 2013, pp. 312–337.

[21] Egorov, I.V., Fedorov, A.V., and Soudakov, V.G., "Receptivity of a hypersonic boundary layer over a flat plate with a porous coating," *J. Fluid Mech.*, Vol. 601, 4 2008, pp. 165–187.

[22] De Tullio, N. and Sandham, N.D., "Direct numerical simulation of breakdown to turbulence in a Mach 6 boundary layer over a porous surface," *Phys. Fluids*, Vol. 22, 2010, pp. 094105.

[23] Wang, X. and Zhong, X., "Effect of porous coating on boundary-layer instability," *48th AIAA Aerospace Sciences Meeting*, AIAA, 2010, p. 1243, AIAA-2010-1243.

[24] Scalo, C., Bodart, J., and Lele, S.K., "Compressible turbulent channel flow with impedance boundary conditions," *Phys. Fluids*, Vol. 27, No. 035107, 2015.

[25] Taylor, G.I. and Maccoll, J., "The air pressure on a cone moving at high speeds.—I," *Proc. R. Soc. Lond. A*, Vol. 139, No. 838, 1933, pp. 278–297.

[26] Mangler, W., "Zusammenhang zwischen ebenen und rotationssymmetrischen Grenzschichten in kompressiblen Flüssigkeiten," *ZAMM-Journal of Applied Mathematics and Mechanics/Zeitschrift für Angewandte Mathematik und Mechanik*, Vol. 28, No. 4, 1948, pp. 97–103.

[27] Illingworth, C., "Steady flow in the laminar boundary layer of a gas," *Proc. R. Soc. Lond. A*, Vol. 199, The Royal Society, 1949, pp. 533–558.

[28] Lees, L., "Laminar heat transfer over blunt-nosed bodies at hypersonic flight speeds," *Journal of Jet Propulsion*, Vol. 26, No. 4, 1956, pp. 259–269.

[29] Cook, A.W., "Artificial fluid properties for large-eddy simulation of compressible turbulent mixing," *Physics of fluids*, Vol. 19, No. 5, 2007, pp. 055103.

[30] Kawai, S. and Lele, S.K., "Localized artificial diffusivity scheme for discontinuity capturing on curvilinear meshes," *Journal of Computational Physics*, Vol. 227, No. 22, 2008, pp. 9498–9526.

[31] Lele, S.K., "Compact finite difference schemes with spectral-like resolution," *Journal of Computational Physics*, Vol. 103, No. 1, 1992, pp. 16–42.

[32] Jiang, X. and Lai, C.H., *Numerical techniques for direct and large-eddy simulations*, CRC Press, 2009.

[33] Nagarajan, S., Lele, S.K., and Ferziger, J.H., "A robust high-order compact method for large eddy simulation," *Journal of Computational Physics*, Vol. 191, No. 2, 2003, pp. 392–419.

[34] Nagarajan, S., Lele, S., and Ferziger, J., "Leading-edge effects in bypass transition," *J. Fluid Mech.*, Vol. 572, 2007, pp. 471–504.

[35] Fung, K.Y. and Ju, H., "Time-domain impedance boundary conditions for computational acoustics and aeroacoustics," *Int. J. Comput. Fluid D.*, Vol. 18, No. 6, 2004, pp. 503–511.

[36] Poinsot, T.J. and Lele, S.K., "Boundary conditions for direct simulations of compressible viscous flows," *Journal of Computational Physics*, Vol. 101, 1992, pp. 16–42.

[37] Patel, D., Gupta, P., and Scalo, C., "Surface Impedance Determination via Numerical Resolution of the Inverse Helmholtz Problem," *23rd AIAA/CEAS Aeroacoustics Conference*, June 2017, p. 3695, (AIAA-2017-3695).

[38] Patel, D., Gupta, P., and Scalo, C., "Acoustic Impedance Calculation via Numerical Solution of the Inverse Helmholtz Problem," *arXiv preprint arXiv:1708.02069*, 2017.

[39] Wagner, A., Martinez Schramm, J., Dittert, C., Sousa, V., Patel, D.I., and Scalo, C., "Experimental and numerical acoustic characterization of ultrasonically absorptive porous materials," *2018 Joint Thermophysics and Heat Transfer Conference*, 2018, p. 2948.

[40] Patel, D., Gupta, P., Scalo, C., Rothermel, T., and Kuhn, M., "Towards Impedance Characterization of Carbon-Carbon Ultrasonically Absorptive Coatings via the Inverse Helmholtz Problem," *55th AIAA Aerospace Sciences Meeting*, January 2017, p. 0460, (AIAA-2017-0460).

[41] Lin, J., Scalo, C., and Hesselink, L., "High-fidelity simulation of a standing-wave thermoacoustic–piezoelectric engine," *J. Fluid Mech.*, Vol. 808, Dec 2016, pp. 19–60.

[42] Möser, M., *Engineering acoustics: an introduction to noise control*, Springer Science & Business Media, 2009.

[43] Fedorov, A.V., Malmuth, N.D., Rasheed, A., and Hornung, H.G., "Stabilization of Hypersonic Boundary Layers by Porous Coatings," *AIAA Journal*, Vol. 39, No. 4, 2001, pp. 605–610.

[44] Johnson, D.L., Koplik, J., and Dashen, R., "Theory of dynamic permeability and tortuosity in fluid-saturated porous media," *Journal of fluid mechanics*, Vol. 176, 1987, pp. 379–402.

[45] Allard, J.F. and Champoux, Y., "New empirical equations for sound propagation in rigid frame fibrous materials," *The Journal of the Acoustical Society of America*, Vol. 91, No. 6, 1992, pp. 3346–3353.

[46] Gaster, M. and Grant, I., "An experimental investigation of the formation and development of a wave packet in a laminar boundary layer," *Proceedings of the Royal Society of London A: Mathematical, Physical and Engineering Sciences*, Vol. 347, The Royal Society, 1975, pp. 253–269.

[47] Sivasubramanian, J. and Fasel, H.F., "Numerical investigation of the development of three-dimensional wavepackets in a sharp cone boundary layer at Mach 6," *J. Fluid Mech.*, Vol. 756, 10 2014, pp. 600–649.

[48] Stetson, K.F., "Comments on hypersonic boundary-layer transition," Tech. rep., Wright Research and Development Center, 1990.

[49] Fedorov, A.V., "Receptivity of a high-speed boundary layer to acoustic disturbances," *Journal of Fluid Mechanics*, Vol. 491, 2003, pp. 101–129.

[50] Wagner, A., Wartemann, V., Kuhn, M., Dittert, C., and Hannemann, K., "The potential of ultrasonically absorptive TPS materials for hypersonic vehicles," *20th AIAA International Space Planes and Hypersonic Systems and Technologies Conference*, 2015, p. 3576.

[51] Dittert, C. and Kütemeyer, M., "Octra-optimized Ceramic for Hypersonic Application with Transpiration Cooling," *Advances in High Temperature Ceramic Matrix Composites and Materials for Sustainable Development*, Vol. 263, 2017, pp. 389.

[52] Fellah, Z.E.A., Berger, S., Lauriks, W., Depollier, C., Aristegui, C., and Chapelon, J.Y., "Measuring the porosity and the tortuosity of porous materials via reflected waves at oblique incidence," *The Journal of the Acoustical Society of America*, Vol. 113, No. 5, 2003, pp. 2424–2433.

[53] Willems, S., Gülhan, A., Ward, C.A., and Schneider, S.P., "Free transition on a slender cone in a quiet and a conventional wind tunnel and the effect of ultrasonically absorptive materials," *Progress in Flight Physics–Volume 9*, Vol. 9, 2017, pp. 497–516.

[54] Sousa, V.C.B., Patel, D., Chapelier, J.B., Wartemann, V., Wagner, A., and Scalo, C., "Numerical Investigation of Second-Mode Attenuation over Carbon/Carbon Porous Surfaces," *Journal of Spacecraft and Rockets*, Vol. 56, No. 2, 2019, pp. 319–332.

Chapter 4 – A HISTORY AND PROGRESS OF RESEARCH ON BOUNDARY-LAYER TRANSITION ON A MACH 6 FLARED CONE

Brandon Chynoweth and Steven Schneider
Purdue University
UNITED STATES

Christoph Hader and Hermann Fasel
University of Arizona
UNITED STATES

Armani Batista and Joseph Kuehl
University of Delaware
UNITED STATES

Thomas Juliano
University of Notre Dame
UNITED STATES

Bradley Wheaton
Johns Hopkins University Applied Physics Laboratory
UNITED STATES

4.1 INITIAL DEVELOPMENT AND TESTING OF THE FLARED CONE GEOMETRY

It is important to develop accurate boundary-layer transition prediction methods to aid in the design of hypersonic vehicles since transition can have significant impacts on surface heating, skin friction, drag, moments, and other properties. In low-disturbance environments, such as flight, boundary-layer transition generally occurs through the linear and non-linear growth of instabilities [1]. One such disturbance that can cause transition on axisymmetric geometries near 0° angle-of-attack for hypersonic vehicles is the second-mode instability. This instability is similar to an acoustic wave trapped between a surface and the sonic line within the boundary layer; the range of frequencies amplified depends strongly on the local boundary-layer thickness [2]. As an instability packet convects in the downstream direction, linear and non-linear growth occurs until the pressure fluctuations reach a sufficient magnitude to cause breakdown and transition begins. The integrated growth of the instability can be expressed via the e^N method, where the N -factor is the ratio of the instability amplitude at a given location to the initial disturbance amplitude.

Improved understanding of the physics underlying the second-mode transition process can be obtained by complementary experimental and computational investigations. The nonlinear growth and breakdown of the second-mode instability can be measured under low-noise conditions in a “quiet” wind tunnel, with freestream noise levels similar to those in flight [3]. Computational analysis of the flow identifies the modes responsible for boundary-layer instability and their interactions. Continuing experimental and computational efforts will lead to the development of mechanism-based methods for better estimation of hypersonic boundary-layer transition [4].

Mack [5] demonstrated that the second-mode instability is more amplified than the first mode in adiabatic, flat plate boundary layers for edge Mach numbers greater than about 4. For this reason, second-mode-induced boundary-layer transition is frequently studied in the Boeing/AFOSR Mach-6 Quiet Tunnel (BAM6QT), a hypersonic quiet tunnel [6]. The first such investigation in the BAM6QT, with hot-wire anemometry on a 7°-half-angle cone at 0° angle of attack by Rufer [7, 8], only observed transition under noisy flow conditions. Surface-pressure measurements of the second-mode instability under both quiet and noisy flow in the BAM6QT were later obtained by Casper et al. [9] using a 0.517-m-long, 7°-half-angle cone with a sharp nosetip. Under noisy flow conditions, the second-mode waves grew in the laminar boundary layer, saturated, and broke down resulting in a turbulent boundary layer. When the same model was tested under quiet conditions, the second-mode instability was only measured at the farthest downstream sensor on the model. Casper's measurements were made at the maximum unit Reynolds number (Re_∞) at which the BAM6QT was capable of maintaining a laminar boundary layer on the nozzle wall, and thus quiet flow. At the time of the measurements, the BAM6QT maximum quiet Re_∞ was 10.3×10^6/m; for this model, the Reynolds number based on model length (Re_L) was 4.3×10^6. Because the BAM6QT could not achieve a higher Reynolds number under quiet flow, the growth and breakdown of the second-mode instability under quiet conditions could not be observed and studied. In order to study transition due to the second-mode instability under quiet flow, a different geometry was needed that wouldperhaps be more unstable to the second-mode instability.

Large wave amplitudes, presumably transitioning to turbulence, could be observed experimentally at smaller Re_L if a constant band of frequencies is amplified for a large spatial extent by maintaining a nearly constant boundary-layer thickness. Johnson et al. [10] demonstrated an optimization process capable of designing geometries with high second-mode N-factors. The N-factor is They combined full Navier-Stokes CFD calculations, stability analysis, and design optimization to create geometries exploiting this tuning of the second-mode frequency to the boundary-layer thickness. Their stability analyses employed the Stability and Transition Analysis for hypersonic Boundary Layers (STABL) software suite [11]. Axisymmetric and three-dimensional geometries were optimized for a given set of freestream conditions to find the most stable (smallest N-factor) and the least stable (highest N-factor) configurations. Among the axisymmetric geometries, it was found that a flared cone created an adverse pressure gradient that resulted in a nearly constant boundary-layer thickness, and thus the highest N-factor by the end of the vehicle.

The work of Johnson et al. suggested a way to obtain natural transition at low Re_L, but their designs were optimized for flow conditions typical for CUBRC LENS I. It was not clear if the same results would be achieved on scaled-down models at low enthalpy in the BAM6QT. Therefore, Juliano [12] and Wheaton [13] performed a small computational study using the same STABL suite to attempt to find an axisymmetric geometry with high second-mode N-factors at BAM6QT flow conditions. The geometries simulated by Juliano were based on a family of parabolic arcs and those investigated by Wheaton were based on a family of circular arcs. Both authors used fixed nosetip radii of 1 mm and base diameters of 10 cm. The base diameter was selected because it is near the maximum size of a slender model that can be started reliably in the BAM6QT. The relatively blunt 1 mm nosetip radius was initially selected for ease of grid generation. Computations were performed at conditions representative of the maximum quiet pressure in the BAM6QT at the time: the stagnation pressure and temperature were 965 kPa and 433 K, respectively, and the wall boundary condition was isothermal with a 300 K temperature.

Figure 4-1 compares the boundary-layer thickness of the circular arc and the parabolic arc geometries that resulted in the largest N-factors in the limited study. For both geometries, the boundary layer thickness is nearly constant for distances greater than 10 cm from the nosetip. In both cases, the maximum calculated N-factors

for both geometries were much larger than the ≈ 8–11 often observed at transition in low-noise flows [14]. The largest N-factor of any disturbance frequency for BAM6QT flow conditions was 16.4 for the circular arc geometry with a 3-meter radius of curvature and a 1-mm radius nosetip. This N-factor was initially thought to be more than sufficient to induce natural transition under quiet flow, and the 3-meter circular arc geometry was selected for experimental testing. Note that N-factor results published prior Wheaton et al. [15] were artificially high due to a numerical error in the Parabolized Stability Equation (PSE) marching procedure.

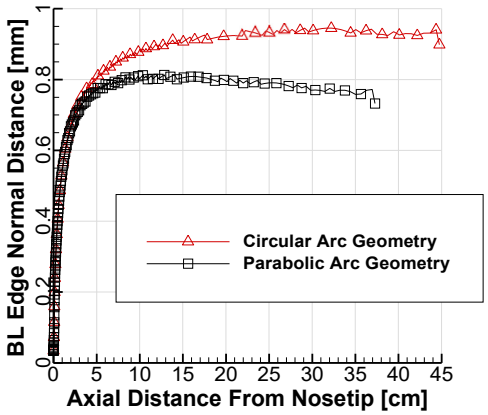

Figure 4-1: Boundary-layer Thickness for the Circular Arc and Parabolic Arc Geometries with the Largest Computed N-Factors.

Berridge and Chou [15] performed the first experiments with the flared cone model in the BAM6QT using only PCB132A31 pressure sensors capable of measuring instabilities up to 1 MHz as the primary instrumentation. With a blunt 1-mm nose radius, large second-mode waves and their harmonics were measured indicating that the instability was experiencing non-linear growth. Experimental frequencies were within 5% of the frequency computed using STABL. At the farthest downstream location, computations indicated an N-factor of 13 but transition had not yet occurred.

A direct numerical simulation (DNS) was performed by Balakumar [16] to compare with the experimental results. Good agreement was found between the computations and the flared cone experiments with a 1-mm nose radius. In addition, Balakumar [17, 18] performed DNS on the straight-flare cone tested in the NASA Langley Mach 6 Quiet Tunnel. He found that decreasing the nosetip radius resulted in increased receptivity, larger initial disturbance amplitudes, and larger N-factors. It was decided to fabricate a much sharper nosetip for the circular-arc model at Purdue University to generate second-mode instabilities with higher amplitudes that might lead to transition.

A "sharp" nosetip with a radius of 0.16 mm and initial opening half-angle of 1.5° was fabricated and tested under quiet tunnel conditions by Chou [19, 20]. Temperature-sensitive paint (TSP) results showed an unexpected heating pattern under quiet flow conditions. At a Re_∞ of approximately 12×10^6/m streaks of heating formed around the circumference of the model at a distance of 37.5 cm from the nosetip. A PCB sensor near these streaks measured a large second-mode wave as well as harmonics that suggested non-linear growth was occurring. Moving in the downstream direction, the streaks disappeared and heating returned to near baseline laminar levels at an axial position of approximately 40 cm. Near the aft end of the model, streaks of heating occurred again and pressure fluctuation measurements indicated a transitional boundary layer.

4.2 EXPERIMENTS WITH A SHARP NOSETIP

4.2.1 Results with a Smooth Wall

After the unique hot-cold-hot heating pattern was observed with the sharp nosetip, experiments initially focused on characterizing the transition process caused by the second-mode instability on the flared cone. Previous experiments in the NASA Mach-6 Quiet Tunnel now located at Texas A&M University had shown that noise from a turbulent boundary layer near the end of the nozzle radiated noise onto the test article. Although Casper [21] showed that the boundary layer on the BAM6QT nozzle wall was laminar past the nozzle exit, there was a small risk that placing a model in the tunnel might cause this to change. At a Re_∞ = 12 × 10^6/m , two experiments were performed with the flared cone nosetip positioned 1.8 and 2.0 m from the throat. No significant changes in either the temperature-sensitive paint (TSP) or pressure fluctuation data occurred, verifying that the results on the flared cone were not influenced by noise radiating onto the surface of the model.

A flared cone with a larger base diameter was fabricated at Purdue University in order to increase Re_L and to observe more of the transition process at a lower stagnation pressure, allowing a larger 7-inch by 14-inch plexiglass window to be used [22]. In Figure 4-2 it can be seen that the larger window provides a field of view which facilitates simultaneous comparisons between TSP and pressure fluctuation measurements to correlate second-mode amplitudes with heating structures that form on the surface. During this set of experiments, the model was rolled 30˚ between runs. The streamwise streaks of heating rolled by the same angle, showing that the vortices were body fixed.

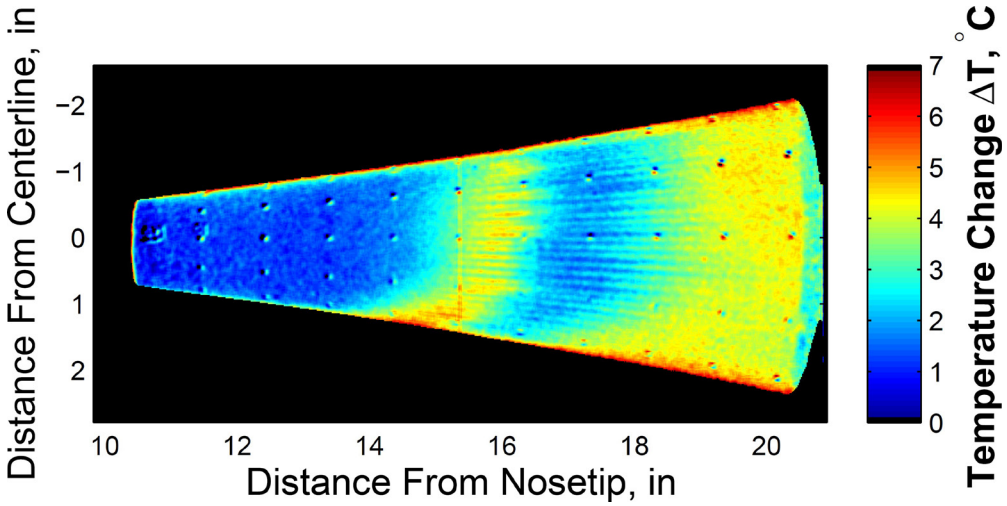

Figure 4-2: TSP Image of the Larger Base Diameter Flared Cone Model with the 7-inch by 14-inch Plexiglass Window at a Re_∞ ≈ 10 × 10^6/m from Reference [22].

Many of the early experiments with the flared cone resulted in non-axisymmetric formation of the streaks of heating. Willems [23] showed that a small angle of attack (AoA) could lead to similar non-uniform transition due to the second-mode instability on a 3˚ half-angle cone. He used a specialized angle-of-attack adapter capable of making micro-adjustments to position the model at an AoA = 0.0˚. A similar adapter capable of minor pitch and yaw adjustments on the flared cone model was fabricated at Purdue University. Figure 4-3a is a TSP image

of the flared cone prior to adjustment at a Re_∞ of 9.7 × 10^6/m from Chynoweth [24]. The streamwise streaks begin almost 5 cm further on the bottom than on the top. Figure 4-3b shows the TSP measurements after pitching the model downward by about 0.1˚ and yawing the model less than 0.1˚ towards the camera. The streaks begin uniformly around the circumference starting near 39 cm from the nosetip. With the model at 0.0˚ AoA, the study of the second-mode wave is not influenced by other instabilities such as cross-flow which can be caused by a small angle-of-attack.

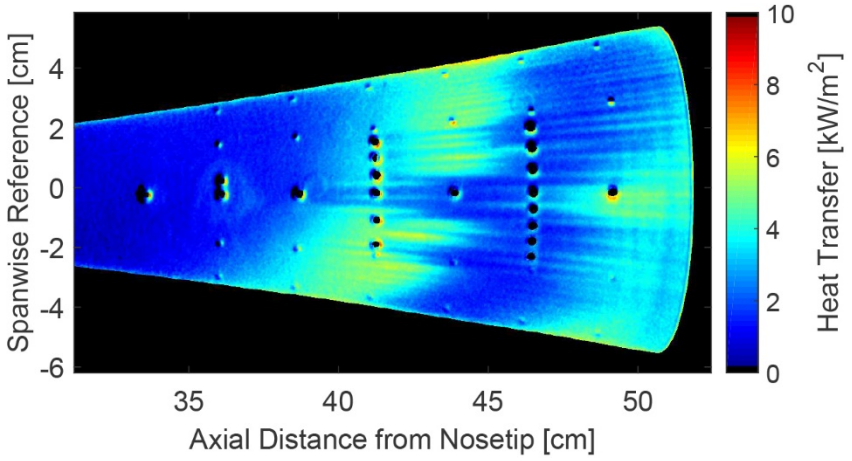

(a) Prior to AoA Adjustment

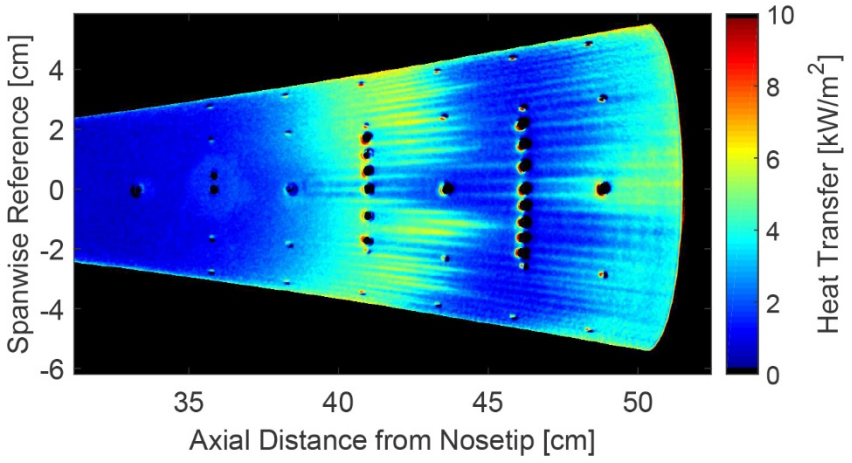

(b) After AoA Adjustments

Figure 4-3: TSP Images Showing the Effect of Adjusting the Angle of Attack on the Axisymmetric Formation of the Streamwise Streaks of Heating from Reference [24].

Studies of the flared cone with a smooth wall were performed over the course of five years by Chynoweth [24, 25]. A wide range of Re_∞ between 7.3 × 10^6/m and 12 × 10^6/m were tested. For all experiments with a smooth wall, a second-mode wave was measured growing in the streamwise direction. Increasing Re_∞ caused the heating pattern and transition location to move upstream on the surface of the model. Additionally, as Re_∞ increased the frequency of the second-mode instability also increased as the boundary-layer thinned, but the main features of the growth and breakdown of the second-mode instability remained similar.

The following is a discussion of experimental results on the flared cone at a $Re_\infty \approx 11 \times 10^6$/m. These experimental results are directly compared to DNS in Section 4.5. Figure 4-4 shows the heat transfer rates to the surface of the flared cone. Streamwise streaks begin to form around the circumference of the model near 38 cm from the nosetip. At 42 cm the heating rates decrease to near laminar baseline levels. DNS simulations indicate that the cooler region is associated with the vortices which cause the hot streaks lifting off the surface of the model. The vortices move back towards the surface at 47 cm causing a second increase in heating rates.

Figure 4-5 shows the power spectral density (PSD) for five sensors. A second-mode instability with a frequency near 300 kHz is measured. The harmonics at 600 kHz indicate that non-linear growth is occurring. The instability fluctuation magnitude reaches nearly 30% of the mean surface pressure at 39 cm from the nosetip. Downstream of the maximum fluctuation magnitude, the instability begins to break down. Pressure fluctuations drop to less than 10% of the mean surface pressure through the aft end of the model. During this process, a broadening of the second-mode bandwidth occurs. Computations by Kuehl in Section 4.3 focus on explaining the underlying physics that may be responsible for this broadening.

Figure 4-6 compares the location of important second-mode pressure features with an average heat-transfer profile extracted along streamlines through the streaks of heating in Figure 4-4. The location of the maximum pressure fluctuation magnitude and maximum heat transfer rate both occur with a laminar boundary layer. Once breakdown begins and heating rates decrease, the first increase in intermittency occurs indicating that transition has begun. Approximately 5 cm downstream from where the first increase in intermittency occurs, an almost fully turbulent boundary layer is measured and heating rates have increased to similar values as the upstream set of streaks.

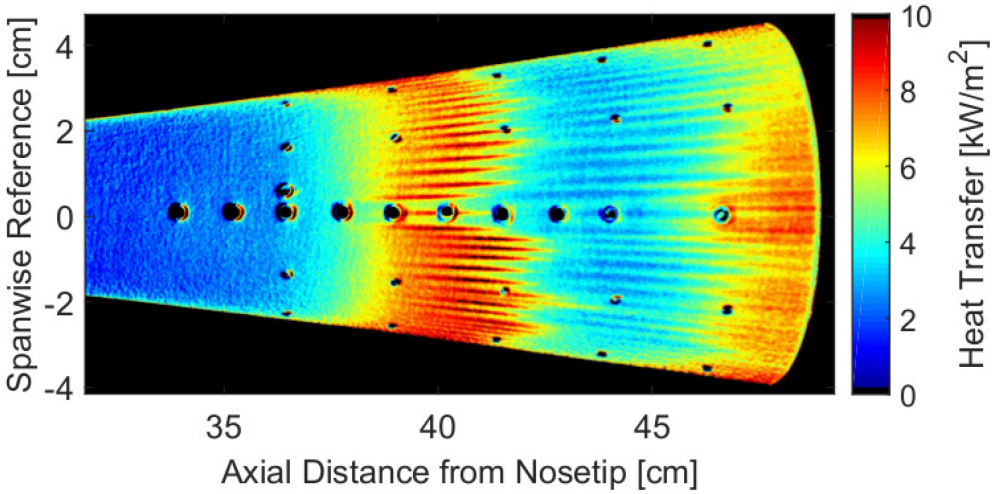

Figure 4-4: Heat Transfer Rates Showing the Characteristic Hot-Cold-Hot Pattern on the Flared Cone at a Re_∞ of 11.0 × 10^6/m.

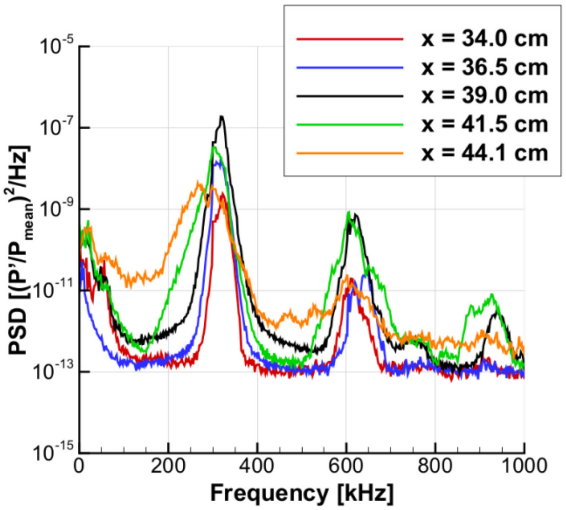

Figure 4-5: PSDs In the Streamwise Direction Showing the Non-linear Growth of the Second-mode Instability.

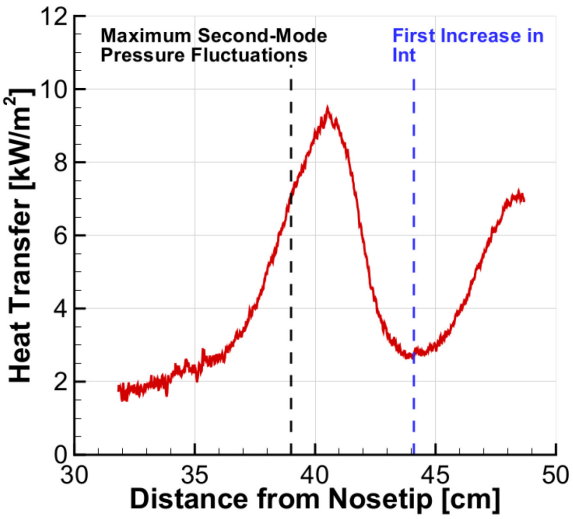

Figure 4-6: Streamwise Heat Transfer Profile Aligned with the Streaks of Heating.

4.2.2 Results with Roughness Elements

Pressure fluctuation measurements indicate that the streaks of heating occur when the second-mode instability is experiencing non-linear growth and saturation. Roughness elements were proposed as a method to control the non-linear growth and breakdown of the second-mode wave by forcing a specific wavenumber. Forcing different azimuthal wavenumbers could change the amplification rate resulting in different pressure fluctuation magnitudes prior to breakdown to turbulence. A major challenge was developing well controlled roughness elements that forced a desired wavenumber without causing roughness induced transition. The first experiments were performed using nail polish applied with a toothpick by Chou [19]. Luersen used a micro-syringe to better

control the volume of nail polish dispensed to create each dot, but variations in the height and width still existed. These methods were not well controlled, and TSP results were inconclusive as to whether the wavenumber was being controlled by the roughness elements [26, 27].

A new flared cone model was designed by Luersen with an interchangeable insert ring positioned between the nosetip and the frustum. He used the ring to test several different techniques for producing roughnesses. The first was rub-on transfer dots only 10 μm in height. These had no effect on the pattern of heating. A single diamond-shaped element with a height of 560 μm caused roughness induced transition directly downstream from the element. The technique that produced the most promising results was applying epoxy dots to the surface using a Nordson Electronic Fluid Dispenser. Epoxy roughness elements with a height of 533 μm were tested, but these again acted as a boundary-layer trip.

Work to create epoxy dots that did not result in roughness induced transition was continued by Chynoweth [25]. Creating epoxy roughnesses with heights of 200 μm and 300 μm altered the heating pattern without moving the location where transition begins. These results were promising, but further testing with newer, more viscous epoxy resulted in a loss of uniformity causing the dots to form in oblong shapes. A new, more repeatable method for creating roughness elements had to be developed.

The Rod Insertion Method (RIM) roughness was developed by Chynoweth [24, 28, 29]. In order to create a RIM insert, holes are drilled in an insert with the desired spacing between adjacent element. Brass rods with a known diameter are pressed into the holes and machined down to the final height. Figure 4-7 is a photograph of a RIM insert installed between the nosetip and frustum of the flared cone model.

Three different parametric studies were performed to investigate the effect of the varying the roughness height, diameter, and azimuthal spacing on the transition process. For RIM inserts that had 30 evenly spaced roughness elements with a diameter of 838 μm, it was found that elements with heights between 102 μm and 305 μm changed the azimuthal wavenumber of the streaks of heating, but the growth of the second-mode instability was similar to what was measured with a smooth wall. On average, the maximum magnitude prior to break-down was still approximately 28–30% of the mean surface pressure. Three RIM inserts were tested that had 30 elements with heights of 254 μm and roughness element diameters of 559, 838, and 1320 μm. The RIM insert with 1320 μm diameter elements suppressed the amplification of the second-mode instability and caused roughness induced transition. Maximum pressure fluctuations for inserts with roughnesses diameters of 559 and 838 μm were between 27 to 30%. Finally, three RIM inserts were created with roughness heights of 254 μm, diameters of 838 μm, and varying azimuthal wavenumbers of 35, 40, and 45. Based on DNS simulation, a wavenumber of 40 should force 80 streaks to form and result in the largest magnitude of the second-mode instability. Results showed that it did in fact induce 80 streaks to form, but Figure 4-8 shows that they form in a staggered pattern instead of beginning at a constant axial location. The maximum second-mode magnitude was within 20% of the smooth wall value for tests with the three different azimuthal wavenumber inserts. It could not be determined if 40 roughness elements actually resulted in the largest growth due to uncertainty in the PCB132A31 calibration process, but further testing with calibrated pressure sensors will resolve this issue. Combining the smooth wall and roughness results indicates that the maximum second-mode magnitude prior to breakdown to turbulence is approximately 30%. This result may be used to develop a magnitude based transition prediction method based on the work of Marineau[30].

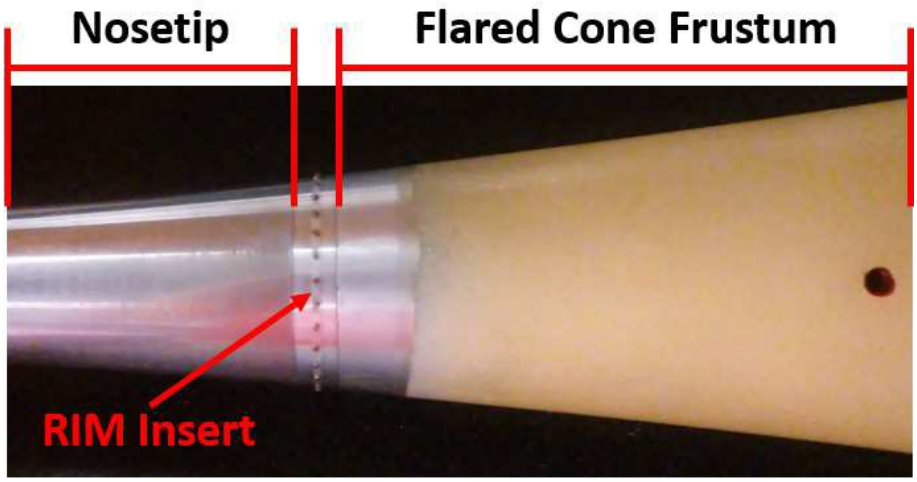

Figure 4-7: Photograph of RIM Insert Installed Between the Nosetip and the Frustum of the Flared Cone Model.

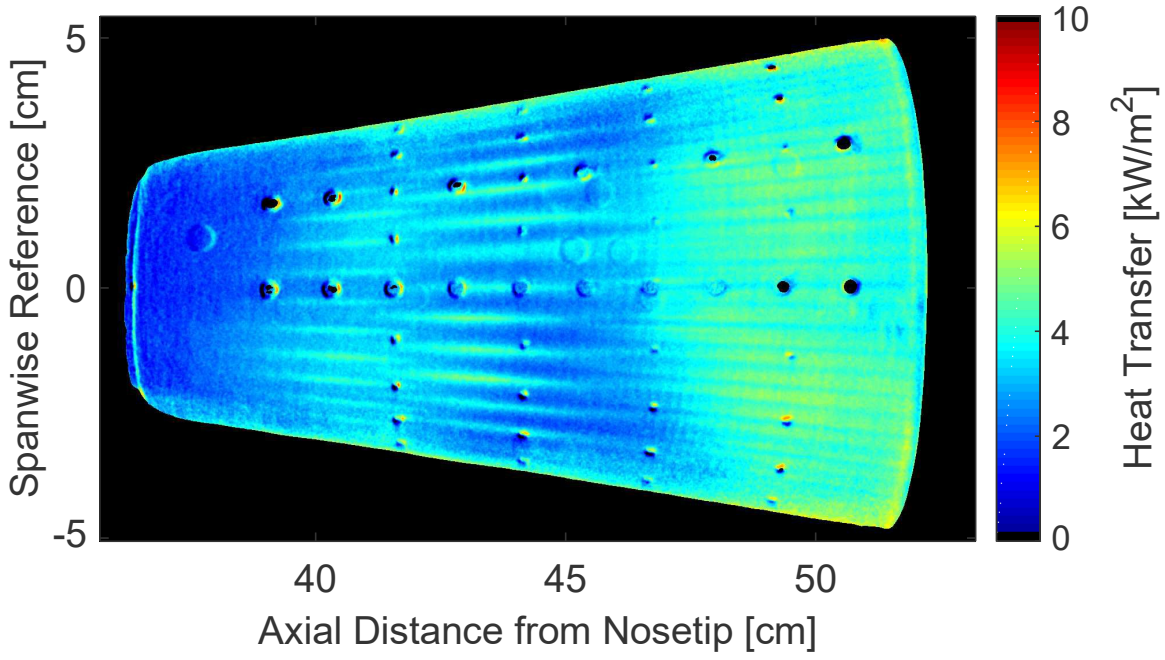

Figure 4-8: TSP Image at Re_∞ = 8.8 × 10^6/m with a RIM Insert Having an Azimuthal Wavenumber of 40 and Roughness Elements of Height and Diameter 254 μm and 838 μm , Respectively.

4.3 STABILITY ANALYSIS

A stability analysis was conducted, in conjunction with the experimental (Section 4.2) and direct numerical simulation (Section 4.4) investigations, to help elucidate the underlying physical mechanisms responsible for transition on the Mach 6 flared cone geometry. Unlike experiment, and to a lesser degree than direct numerical simulation, stability analysis makes a suite of simplifying assumption, and it is through the interpretation and modification of these assumptions that stability methods are able to probe the underlying physical phenomena of a system.

4.3.1 Methods

The stability analysis begins by considering a generic disturbance and decomposing the flow variables into a steady basic state plus a disturbance and assuming the basic state is a solution to the governing equations of motion. For simplicity we will consider the 2-D problem, assuming a 2-D basic state and 2-D disturbances. Substitution of this decomposition into the governing set of equations yields the equations describing the evolution of the disturbances.

$$\begin{aligned} \phi(x,y,t) &= \underbrace{\bar{\phi}(x,y)}_{\text{basic state}} + \underbrace{\phi'(x,y,t)}_{\text{disturbance}} \\ \phi &= [u,v,T,\rho]^T \end{aligned} \tag{4-1}$$

Here *x, y* are the wall-parallel and -normal coordinates, *t* is time, *u, v* are the wall-parallel and -normal velocity components, ρ is the density and *T* is the temperature. Different stability methods solve the disturbance equations under different sets of assumptions. Linear Stability Theory (LST) imposes the assumptions of infinitesimal (linear) disturbances and parallel flow upon which separable solutions may be found. That is, the basic state is assumed to be only a function of *y* and $\phi' = X(x)Y(y)T(t) = \hat{\phi}(y)e^{i(\alpha x-\omega t)}$. Here α and ω are the streamwise wavenumber and frequency, respectively, of the disturbance. Substitution of this form into the disturbance equations yields a generalized eigenvalue problem. Thus, LST describes the solution to the disturbance equations at a given location as a spectrum of linearly independent eigenmodes.

Another approach to solving the disturbance equations is the Parabolized Stability Equations (PSE) method [31, 32]. PSE takes advantage of the slow variation of the basic state along one spatial dimension to solve an initial value problem. A method-of-multiple-scales approach from Reference [33] is taken in which a disturbance is assumed of the form

$$\phi' = \underbrace{\tilde{\phi}(\bar{x},y)}_{\text{shape}}\underbrace{\Phi(x,t)}_{\text{wave}} \tag{4-2}$$

where the wave part satisfies

$$\frac{\partial \Phi}{\partial x} = i\alpha(\bar{x})\Phi \tag{4-3}$$

$$\frac{\partial \Phi}{\partial t} = -i\omega\Phi \tag{4-4}$$

Notice the introduction of a slow variable $\bar{x} = \frac{x}{Re}$ into the shape function and streamwise (x) complex exponential $\alpha(\bar{x})$, where $Re = \frac{U_e \delta_r}{\nu_e}$ is a Reynolds number based on characteristic values of edge velocity (U_e), edge kinematic viscosity (ν_e), and reference boundary-layer length scale (δ_r). PSE considers disturbances of the form

$$\phi' = \int_{-\infty}^{\infty} \underbrace{\tilde{\phi}(\bar{x}, y, \omega)}_{\text{shape}} \underbrace{A(\bar{x}, \omega) e^{-i\omega t}}_{\text{wave}} d\omega, \tag{4-5}$$

where the dependence of the shape function ($\tilde{\phi}$) and amplitude function (A) on ω has been made explicit. Motivated by the experimental observation of a finite disturbance bandwidth, we follow the wave packet formulation of Kuehl (2017 [34]) and assume an amplitude function $A(\bar{x}, \omega) = W(\omega) e^{i \int \alpha(\bar{x}, \omega) dx}$, where

$$W(\omega; \omega_0) = \frac{1}{\sigma_0 \sqrt{2\pi}} e^{-\frac{(\omega - \omega_0)^2}{2\sigma_0^2}} \tag{4-6}$$

is a Gaussian wave packet. Note, the traditional PSE approach assumes $W(\omega; \omega_0) = \delta(\omega - \omega_0)$.

Upon expansion of the streamwise derivatives it is found that the second spatial derivative $\frac{\partial^2 \tilde{\phi}}{\partial \bar{x}^2}$ is of highest order in a Re^{-1} expansion and the expansion may be consistently truncated resulting in the neglect of this term. This leaves the disturbance equation nearly parabolized (Li and Malik 1996 [35]) and an efficient marching solution may be sought. 3-D effects may be accounted for by either assuming $\bar{\phi} \neq \bar{\phi}(z)$ and including oblique mode via a Fourier expansion in the z direction or by allowing for z variations in the base flow and discretizing the z–y plane fully; the so-called BiGlobal or Planar LST/PSE approach [36–38]. In addition to those already mentioned, a number of other PSE codes have been developed in the USA including LASTRAC [39], STABL [40] and EPIC [41]. Here we will utilize JoKHeR which was developed at Texas A&M University [42]. The modal shape functions calculated with JoKHeR were validated in the Mach-6 Quiet Tunnel at Texas A&M on the Langley 93-10 flared cone design [43]. Kocianet al. [44] demonstrated the sensitivity of frequency content to experimental model alignment and Reed et al. [45] detailed verification and validation challenges, particularly concerning sensitivity to basic state calculations.

4.3.2 Results

As noted by Kuehl [34], the wave packet formulation accounts for proper re-distribution of energy between finite-bandwidth disturbances that the traditional PSE approach does not. The redistribution of energy onto "side-lobes" results in larger total disturbance amplitudes than those predicted by traditional PSE. Figure 4-9 shows calculations for 2-D second-modes initialized with amplitudes of $1e^{-6}$ (upper), $5e^{-7}$ (middle) and $1e^{-7}$ (lower) based on normalized temperature disturbance amplitude. Unlike experiment and to a lesser extent in DNS analysis, PSE is an approximate method in which assumptions are made with the intent to isolate and study specific physical processes. In this case, the wave packet methodology has been utilized to account for energy re-distribution into side-lobes, to model spectral broadening. In the traditional PSE case, the 270 and 330 kHz side-lobes are trivially amplified.

However, notice that due to the wave packet energy redistribution, those side- lobes grow to significant amplitude. These side-lobes model the spectral broadening observed in experiment. Spectral broadening, indicated by the shaded region enclosed by the vertical dashed lines in Figure 4-9, is found to begin between $0.4 - 0.42$ m downstream from the cone tip in the $1e^{-6}$ case, between $0.42 - 0.44$ m in the $5e^{-7}$ and between $0.44 - 0.46$ m in the $1e^{-7}$ case.

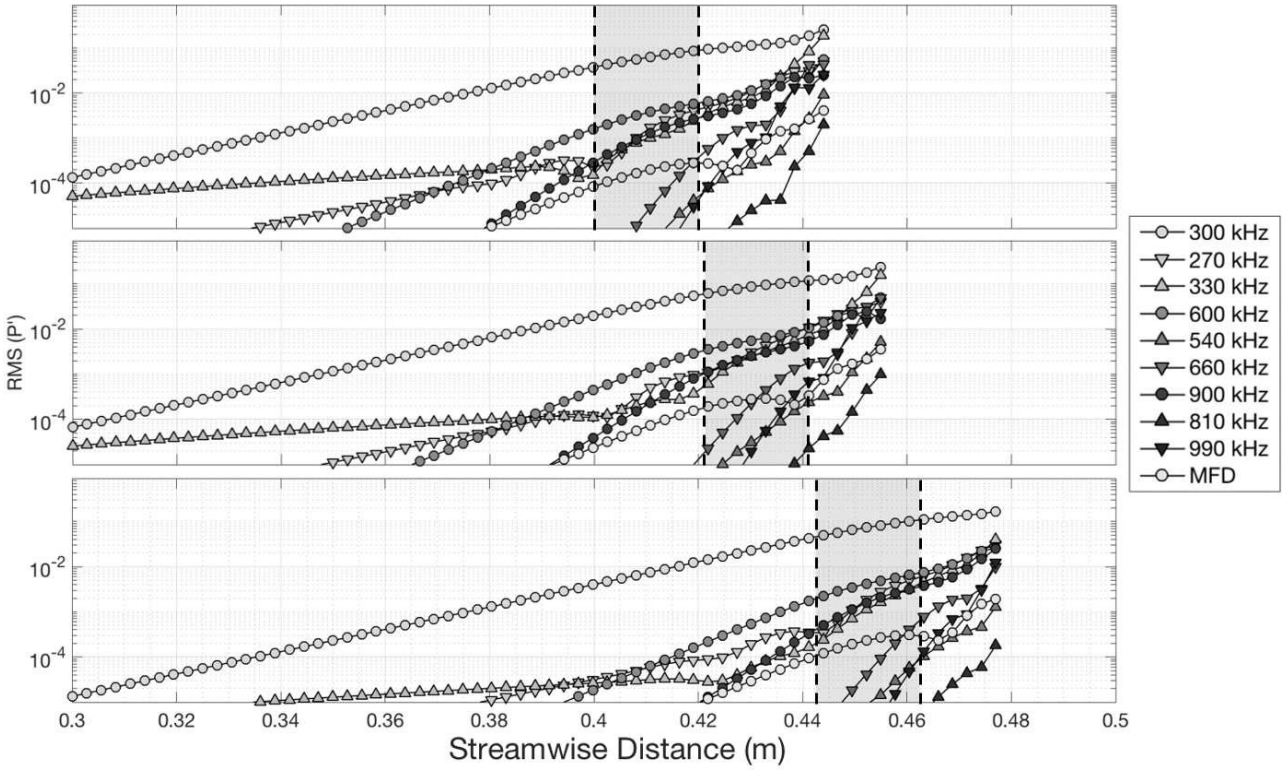

Figure 4-9: NPSE Calculations of Second-mode Growth on the Purdue Flared Cone for Initial Disturbance Amplitudes of $1e^{-6}$ (Upper), $5e^{-7}$ (Middle) and $1e^{-7}$ (Lower). The grey shaded region indicates the onset of spectral broadening.

The experimental results (above and in Chynoweth [25]) suggest spectral broadening begins between 0.4–0.42 m downstream of the cone tip, which appears consistent with initial disturbance amplitudes between $1e^{-6}$ and $5e^{-7}$. In addition, peak disturbance amplitudes of approximately 30% based on normalized pressure are found. This is consistent with the NPSE calculated amplitudes which reached into the 20–40% range for those initial amplitude cases that exhibit a similar onset of spectral broadening (Figure 4-10, left panel). Another useful comparison between the experimental and numerical data is to consider the amplitude ratio between the primary disturbances (primary mode and side lobes) and the first harmonics of those modes (i.e. primary/harmonic). Similar to the consideration of spectral broadening onset, this comparison provides information regarding the proper distribution of energy between modes in the numerical scheme. The experimental data shows primary to first harmonic amplitude ratios of approximately 20 prior to the onset of spectral broadening, dropping to 10 during spectral broadening and entering the single digits shortly afterwards. As seen in Figure 4-10 (right panel), the NPSE calculations recover similar amplitude ratio trends.

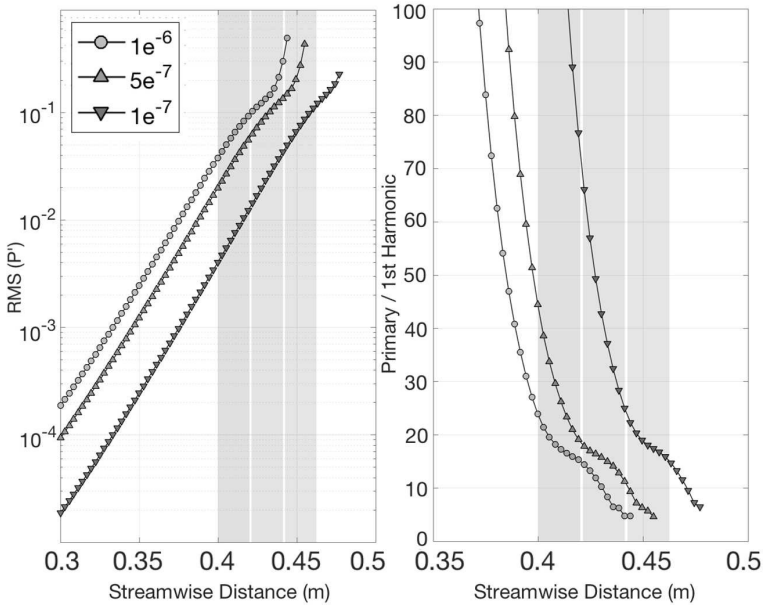

Figure 4-10: NPSE Calculations for $1e^{-6}$, $5e^{-7}$ and $1e^{-7}$ Initial Disturbance Amplitudes. Left: total primary disturbance amplitude (primary plus side-lobes). Right: primary to first harmonic amplitude ratio. grey shaded region indicates the onset of spectral broadening.

The agreement between these PSE trends (disturbance amplitude, onset of spectral broadening and primary to harmonic amplitude ratio) and experimental results is encouraging and suggest that PSE is a viable tool for studying the nonlinear pre-transitional zone. However, PSE is an approximate method and at the current level of approximation uncertainty remains. The results of Kuehl et al. [46] suggest the total disturbance amplitude will be sensitive to the number of modes utilized to represent the disturbance and preliminary results suggest sensitivity to both the number of side-lobes and their frequency distribution. This can be seen in Figure 4-11 where different distributions of side-lobes are considered. Notice that despite the total disturbance amplitude being the same in each case, variations in both amplitude and distribution remain. The resolution of these uncertainties will require further research, however in the present case, it is likely that the neglect of vortical and oblique disturbances has the most significant effect on numerical-experimental comparison via the energy transfer associated with the K-type breakdown scenario. In the traditional PSE case, inclusion of oblique and vortical disturbances is straight forward. In the wave packet formulation, their inclusion is ongoing research. In addition, evidence for the importance of vortical disturbances beyond the K-type energy transfer was provided by Kuehl and Parades [38]. It was shown that vortical modes distort the mean flow and fundamentally alter the second-mode behavior from 1-D disturbances to fully 2-D by modifying the acoustic waveguide in which the second-modes travel. This result is consistent with the recent thermoacoustic interpretation of second-mode instability provided by Kuehl [47].

It is interesting to note that as a consequence of the broadening spectrum, the PSE calculations predict the emergence of low frequency content (Batista and Kuehl 2016 [48]). Figure 4-12 illustrates a PSE calculation that includes a low-frequency disturbance corresponding to the difference between the primary disturbance frequency and the side-lobe frequencies. It is observed that after the spectrum broadens (after side-lobes emerge) that the low-frequency disturbance experiences significant growth. In this case, the low-frequency disturbance grows to approximately 2% amplitude. This result suggests that the emergence of low-frequency content in boundary

layer transition measurements may not be the result of "tunnel noise" but instead a fundamental consequence of finite-bandwidth primary mode disturbances. This is in contrast to the traditional belief that low-frequency "noise" is the cause of spectral broadening. In fact, these results suggest the opposite: that low-frequency content is the result of the spectral broadening which precedes the transition to turbulence.

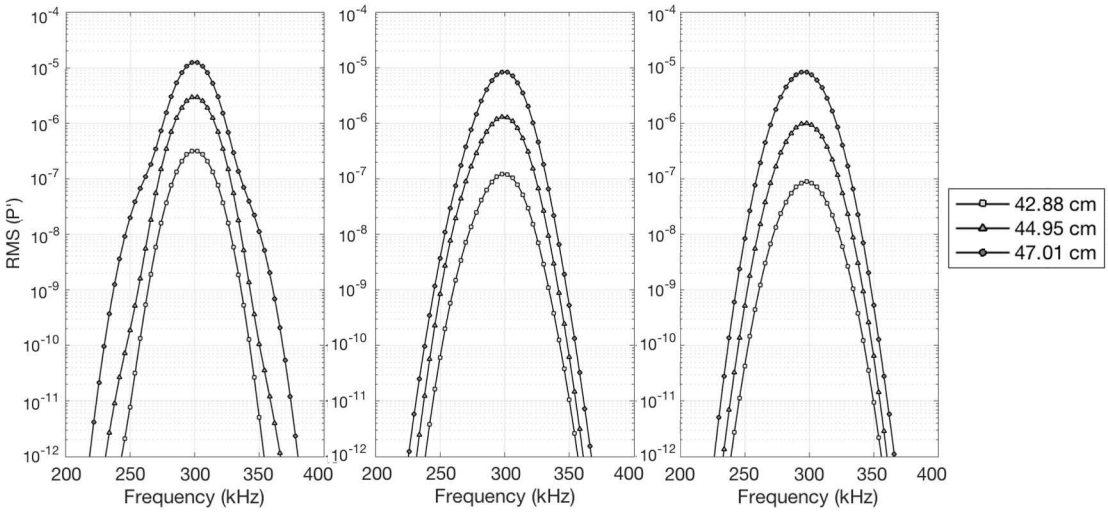

Figure 4-11: NPSE Calculated Disturbance Spectrum at Three Different Locations Spanning the Onset of Spectral Broadening for Initial Disturbance Amplitude of $5e^{-7}$. Left: 3 Modes Separated by 30kHz. Middle: 5 modes separated by 15kHz. Right: 7 modes separated by 10khz. total disturbence amplitude (primary plus side-lobes) is the same in each case.

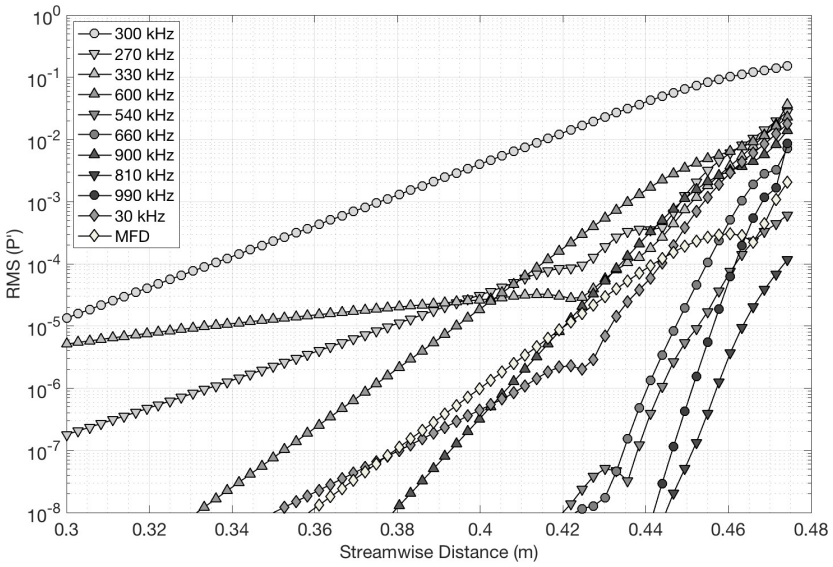

Figure 4-12: NPSE Calculations of Second-mode Growth on the Purdue Flared Cone for Initial Disturbance Amplitude of $1e^{-7}$ with the Inclusion of a Low-Frequency Disturbance.

4.4 DNS ANALYSIS

High-fidelity DNS were carried out to investigate the underlying nonlinear mechanisms of the streak pattern that has been observed on the surface of the flared cone in the experiments at the BAM6QT at Purdue University and simulations for straight and flared cone geometries [49–54]. The flow conditions and cone geometry of the flared cone experiments in the BAM6QT were used for the simulations. A synergistic approach between experiment (Section 4.2), stability analysis (Section 4.3) and DNS is used to further understand the complex laminar-turbulent boundary layer transition on the flared cone geometry.

For the DNS analysis, the mode terminology (n,m) is used as shorthand notation for (n x $f_{primary}$, m x $k_{c,domain}$), where $f_{primary}$ is the primary wave frequency and $k_{c,domain}$ is the azimuthal domain wave number. The primary wave frequency is usually chosen as the frequency leading to the maximum N-factors in the linear regime (pri- mary instability). For the breakdown simulations only a spanwise section of the cone is considered in azimuthal direction, as schematically shown in Figure 4-13. Consequently, the largest azimuthal wave number that is physically resolved in the simulations is $k_{c,domain} = 2\pi/\varphi_{domain}$, where φ_{domain} is the azimuthal extent of the computational domain.

Since no free-stream disturbances are considered in the simulations, a "controlled" set of disturbances is introduced into the computational domain through a blowing and suction slot at the wall (see close-up in Figure 4-13). Therefore, these simulations are referred to as "controlled" breakdown simulations as opposed to the natural breakdown observed in the BAM6QT experiments. Even in a quiet tunnel small level disturbances remain (tunnel noise), which are ingested by the boundary layer, subsequently amplified and ultimately cause laminar-turbulent transition. For the BAM6QT conditions, previous simulations [52, 53, 55] have shown that the so-called fundamental breakdown is a likely route to transition. This type of breakdown is initiated by forcing a large amplitude, two-dimensional primary wave, mode (1,0), and a small amplitude, three-dimensional secondary wave, mode (1,1), with the same frequency ($f_{primary}$) as the primary wave. Therefore, for initiating the "controlled" breakdown simulations, the primary wave frequency and the azimuthal wave number of the secondary wave have to be determined *a priori*.

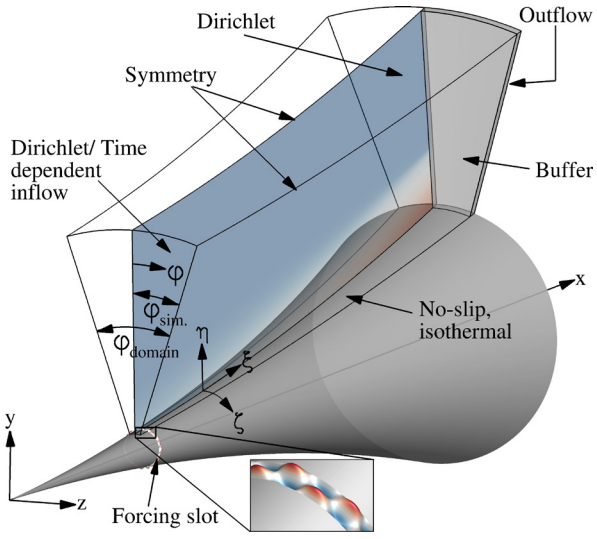

Figure 4-13: Schematic of The Computational Setup Used for "Controlled" Breakdown DNS.

The primary wave frequency is determined by mapping out the linear (primary instability) regime using short duration pulse simulations (for details see for example Hader & Fasel [52]). Experimental results for p_0 = 140 psi/ 965.27 kPa, T_0 = 420 K are readily available, so these conditions are used for the "controlled" breakdown simulation. The N-factors for these conditions, calculated according to van Ingen [56], are provided in Figure 4-14. For this set of flow conditions the maximum N-factor is obtained for f = 300kHz.

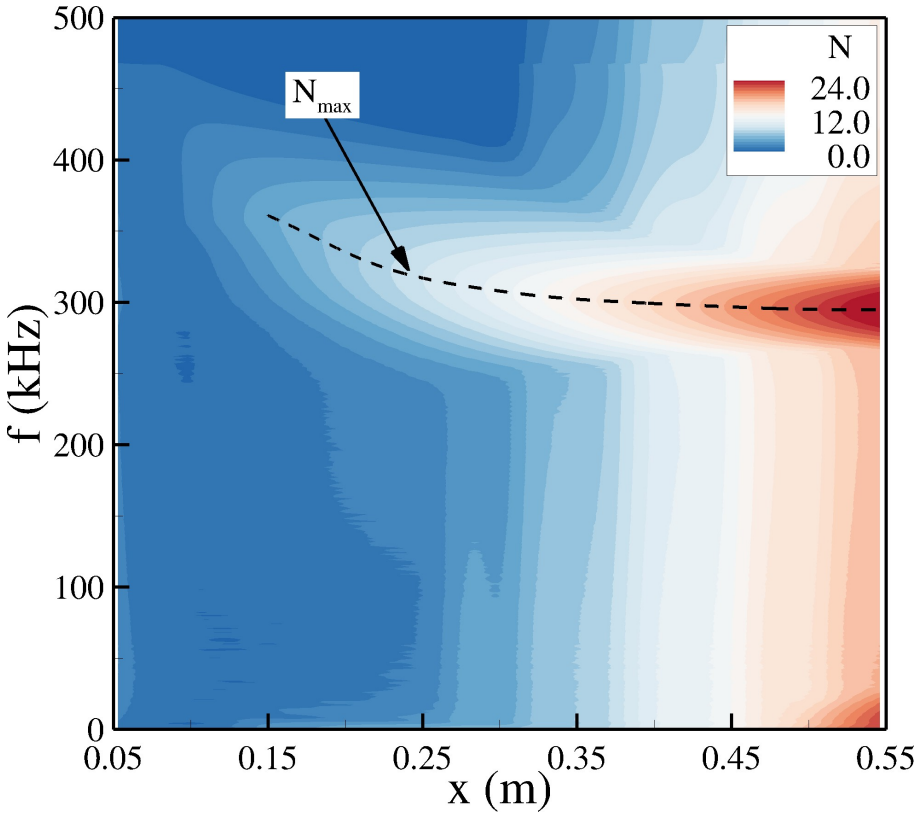

Figure 4-14: N-factors Obtained with an Axisymmetric, Low Amplitude, Short-duration Pulse Simulation for the Purdue Flared Cone (M = 6, p_0 = 140 psi, T_0 = 420 K).

The azimuthal wave number of the secondary wave is chosen based on a parameter study of the secondary instability mechanism. In previous studies Hader & Fasel [53] showed that for the BAM6QT conditions the fundamental resonance is stronger compared to the subharmonic resonance. To determine which azimuthal wave number (k_c) would then lead to the strongest fundamental resonance onset, low-resolution (in azimuthal direction) simulations were carried out. The azimuthal wave number in the simulations was varied by adjusting the azimuthal domain extent (φ_{domain}, see Figure 4-13).

In a typical resonance scenario shown in Figure 4-15, the primary wave grows exponentially until it reaches a large enough amplitude and then begins to saturate. Once the primary wave reaches sufficiently large amplitudes, a phase-speed locking process occurs between the primary and the secondary waves and then the secondary wave begins to deviate from its linear behavior, which is consistent with secondary linear stability theory [57]. The azimuthal wave number for which the secondary disturbance wave is most amplified after resonance onset is of particular interest because for the "controlled" breakdown simulations it is assumed that the disturbance waves that are dominant in the resonance onset also will prevail in the nonlinear breakdown.

The fundamental resonance onset calculations were carried out for a range of azimuthal wave numbers from $k_c = 5$ to $k_c = 200$ in increments of $\Delta k_c = 5$. The contours of the spatial growth rate and the wave angle are provided in Figure 4-16. Strong resonance is observed at $x \approx 0.3$ m. The fundamental resonance appears to be strongest for azimuthal wave numbers of about $k_c \approx 80$. The wave number for which the resonance onset is strongest shifts to larger values in downstream direction. The wave angle of the secondary wave, which experiences the strongest resonance onset, however, remains nearly constant at $\psi \approx 45^\circ$. Therefore, based on the primary and secondary instability investigations as discussed above, for the DNS of "controlled" fundamental breakdown, the frequency of the primary and the secondary wave was chosen as $f = 300$ kHz and for the azimuthal wave number of the secondary wave $k_c = 80$ was used.

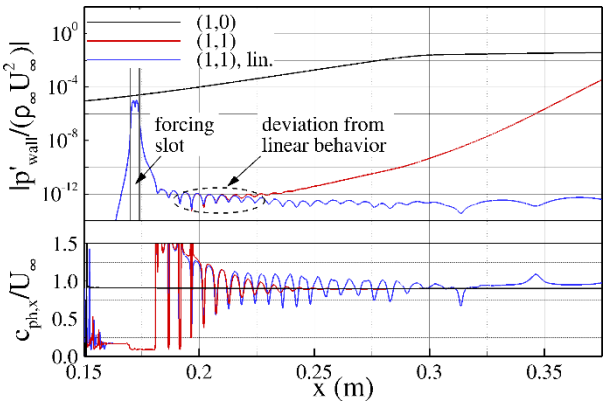

Figure 4-15: Wall Pressure Disturbance Amplitude and Phase Speed Development for a Fundamental Resonance Scenario.

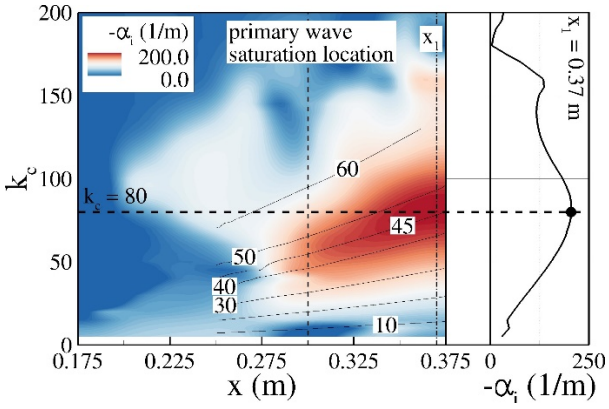

Figure 4-16: Spatial Growth Rate of the Secondary Disturbance Wave in Downstream Direction for Varying Azimuthal Wave Numbers (k_c) for the Fundamental Resonance Onset.

Subsequently a high-resolution "controlled" fundamental breakdown DNS was carried out. It was initiated with the primary and secondary wave parameters chosen as discussed above, using $n_x = 4750$ grid points in streamwise direction, $n_y = 350$ grid points in wall normal direction, and $n_z = 95$ grid points in azimuthal direction.

The time-averaged Stanton number, obtained from the "controlled" breakdown DNS, on the cone surface and a close-up of the "primary" streak location is shown in Figure 4-17a. Initially the time-averaged Stanton number on the cone surface is nearly uniform until there is a rise followed by the appearance of the "primary" streak pattern, which has also been observed in the experiments carried out at the BAM6QT using temperature sensitive paint (see Figure 4-2). Relatively little azimuthal variation of the Stanton number is observed until the "primary" streaks begin to appear. After a short downstream extent, the "primary" streaks disappear and the Stanton number remains nearly uniform in azimuthal direction before the flow begins to break down and a "secondary" streak pattern appears as can be observed in Figure 4-17a. The "secondary" streaks are weaker compared to the "primary" streaks. As a consequence, the peak surface heat flux of the "secondary" streaks observed in the breakdown region is much smaller compared to the upstream, "primary" streak region.

A close-up of the "primary" streaks is shown in the upper part of Figure 4-17b. In the lower part of Figure 4-17b the time-averaged downstream development of the Stanton number is provided. It is extracted at an azimuthal location aligned with the "primary" streaks ($\varphi = 0$ rad), and an azimuthal location in between two "primary" streaks ($\varphi = \pi/80$ rad). For reference, curves for a laminar and a turbulent estimate (according to

White [58])are given. The "overshoot" over the turbulent estimate for the Stanton number for an azimuthal location that cuts through the center of the "primary" streak is significant. The maximum Stanton number is reached at $x \approx 0.3941$ m. Before the "primary" streaks appear, the Stanton number curves for the time-averaged Stanton number development for different azimuthal locations and the azimuthally averaged Stanton number is almost indistinguishable. As soon as the "primary" streaks begin to establish, the curves deviate from one another but converge again further downstream when the streaks disappear. The behavior indicates that the appearance and disappearance of these "hot streaks" is directly linked to three-dimensional modes.

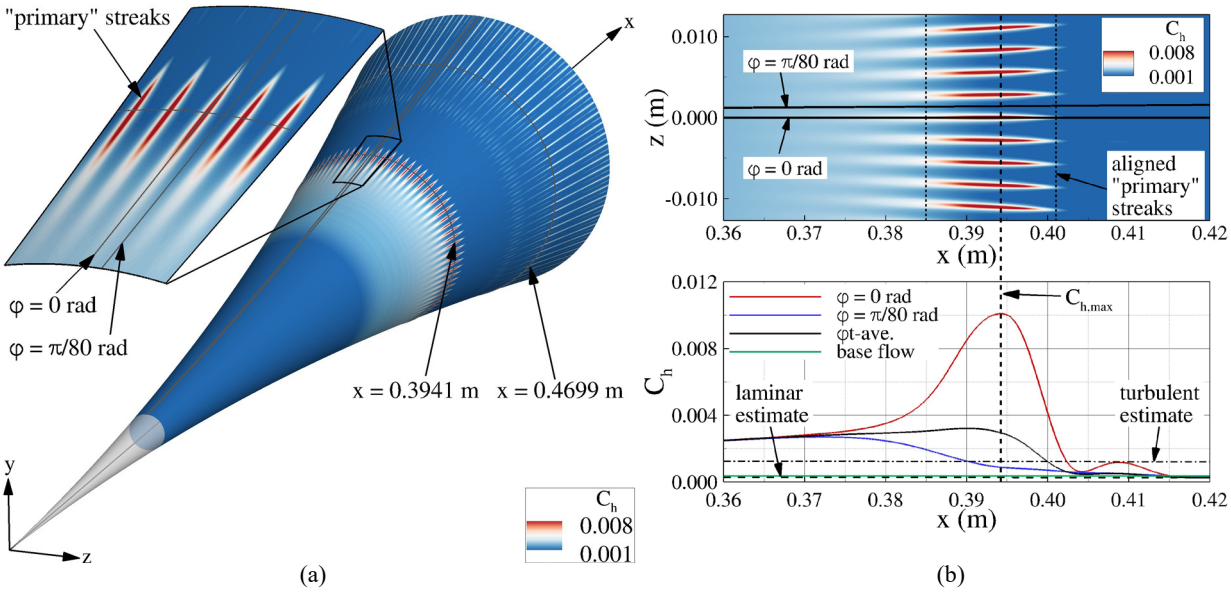

Figure 4-17: (a) Time-Averaged Stanton Number on the Surface of the Cone Surface and Location Markers Indicating Data Extraction Locations for Further Analysis, (b) Close-Up for "Primary" Streaks.

For a more quantitative analysis of the values obtained for the "primary" and "secondary" streaks, the time-averaged Stanton number development in downstream and azimuthal direction is plotted in Figure 4-18. The downstream development of the time-averaged Stanton number is shown in Figure 4-18a. For reference, the values for the laminar (undisturbed) base flow and the laminar and turbulent estimates derived for a straight cone geometry (White [58]) are provided again.

The downstream development of the Stanton number for $\varphi = 0$ rad begins to deviate from the laminar flow value at $x \approx 0.3$ m as can be seen in Figure 4-18a. Following the deviation is a significant "overshoot" over the turbulent estimate that is caused by the "primary" streaks before a sharp drop off occurs almost all the way back to the laminar value. Further downstream, another steep rise towards the turbulent value occurs when the "secondary" streaks begin to appear. The downstream development for $\varphi = \pi/80$ rad (location between streaks) exhibits a similar behavior, however with the main difference that the turbulent estimate "overshoots" are now much less for both the "primary" and "secondary" streaks when compared to the location that cuts through the streaks ($\varphi = 0$ rad).

In Figure 4-18 the azimuthal variation of the Stanton number at two downstream locations where the "primary" and "secondary" streaks were fully established, are plotted for $x = 0.3941$ m and $x = 0.5050$ m,

respectively. The azimuthal direction is normalized with the azimuthal extent of the domain, φ_{domain} (see Figure 4-13). For the fundamental breakdown simulation presented here the azimuthal extent of the computational domain was $\varphi_{domain} = 2\pi/80$. The Stanton number (Figure 4-18b) variations with respect to the normalized azimuthal direction are extended periodically for illustration purposes.

The results in Figure 4-18b show that at the azimuthal location that cuts through the "primary" streak (extracted at $x = 0.3941$ m) dominant peaks are also observed for the secondary streaks (extracted at $x = 0.5050$ m). As expected from the set-up of the "controlled" breakdown simulation using $k_c = 80$ for the secondary disturbance wave, exactly 80 "primary" streaks around the circumference of the cone can be observed. At the "secondary" streak location ($x = 0.5050$ m) additional peaks appear between the azimuthal locations where peaks occur for the "primary" streaks. However, the maxima of these streaks are much lower than those of the "secondary" streaks that are aligned with the "primary" streaks. Furthermore, the maxima of the secondary streaks are only about 30% of the maxima of the "primary" streaks. At this point, it is not understood why the additional streaks arise. This question will be subject to future investigations.

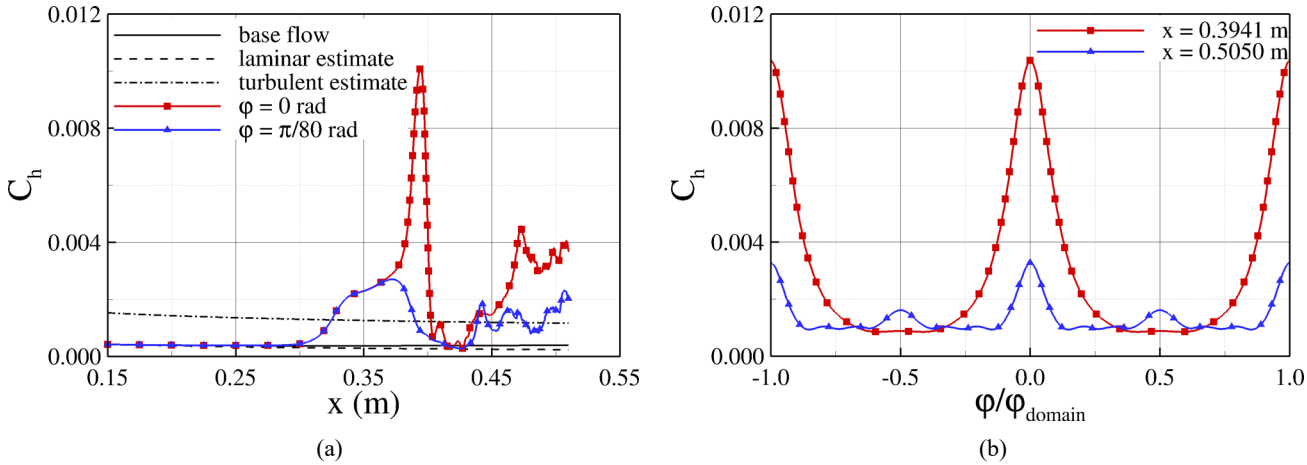

Figure 4-18: Time-Averaged Stanton Number Coefficient Development In Streamwise Direction (a) and in Azimuthal Direction (b).

To shed light on the underlying physical mechanism(s) leading to the formation of the streaks, in Figure 4-19 the time-averaged total flow and the time-averaged disturbance flow fields are plotted in cross-sections (perpendicular to the surface of the cone) at locations where the "primary" and the "secondary" streaks, respectively, are present.

Shown are contours of the time-averaged total temperature (base flow plus disturbance) together with streamlines, which were generated using the time-averaged disturbance flow field (u', v', w'). Time markers, displayed as dots, are seeded at an equidistant Δt along the streamlines to provide an indication how rapidly the fluid moves from one time instance to the next. The laminar boundary layer thickness of the steady base flow is marked for reference. In addition, in Figure 4-19, color contours of the time-averaged Stanton number on the cone surface are provided.

At the location where the "primary" streaks are present (Figure 4-19a) counter-rotating streamwise vortices are formed. These vortices appear to be confined within the boundary layer. The total temperature contours

show a strong modulation in azimuthal direction. These counter-rotating flow structures entrain "cooler" fluid from the free-stream, which is pushed towards the wall and lead to an accumulation of "warmer" fluid above the "primary" streaks. Hader & Fasel [52] showed that in the region where the "primary" streaks disappear the streamwise vortices are actually continuing but are lifted away from the wall. This causes the decrease of Stanton number on the surface of the cone back to its laminar value. As the flow progresses further into the nonlinear breakdown regime, smaller secondary streamwise structures begin to form, indicating that energy is transferred into higher azimuthal modes. At a location further downstream in Figure 4-19b, the streamwise vortices are pushed back towards the wall, which leads to the formation of the "secondary" streaks.

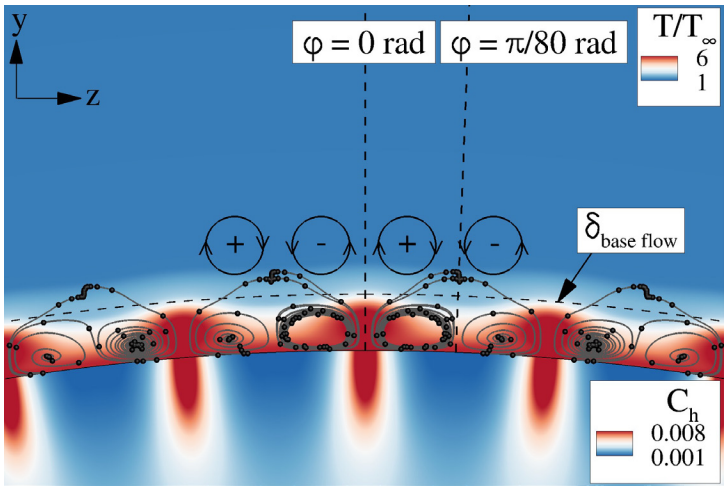

(a)

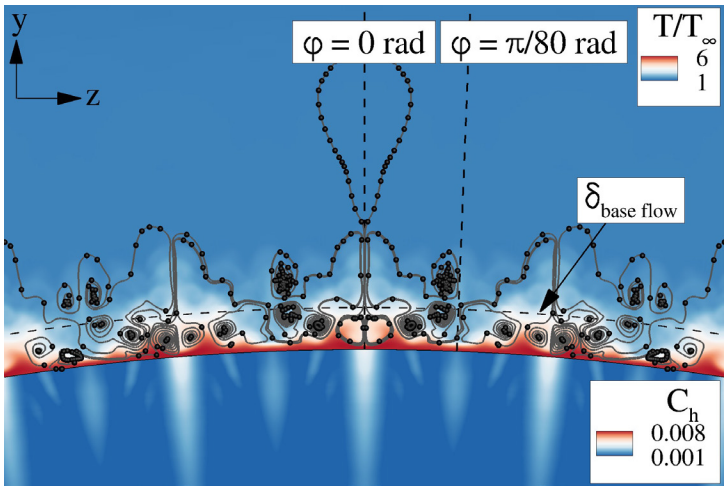

(b)

Figure 4-19: Time-averaged Temperature Contours and the Streamlines of the Disturbance Flow Field (u^t, v^t, w^t) and the Time-Averaged Stanton Number on the Surface of the Cone at (a) x = 0.3941 m, and (b) x = 0.4699 m.

Figure 4-20 contains the profiles for time-averaged u-velocity and temperature at x = 0.3941 m above the streaks (φ = 0 rad) and in between the streaks (φ = π/80 rad). The wall-normal velocity and temperature gradient increases are linked to a small "bulge" near the wall in the velocity and temperature profiles. Even though the boundary layer is thicker above the streaks, the overshoot of skin-friction and Stanton number is caused by that small "bulge" near the wall which is thought to be caused by the streamwise steady mode (0,1).

This bulge, which is only 0.02 mm thick at this axial station, would be very difficult to resolve experimentally with a hot wire or other instrumentation.

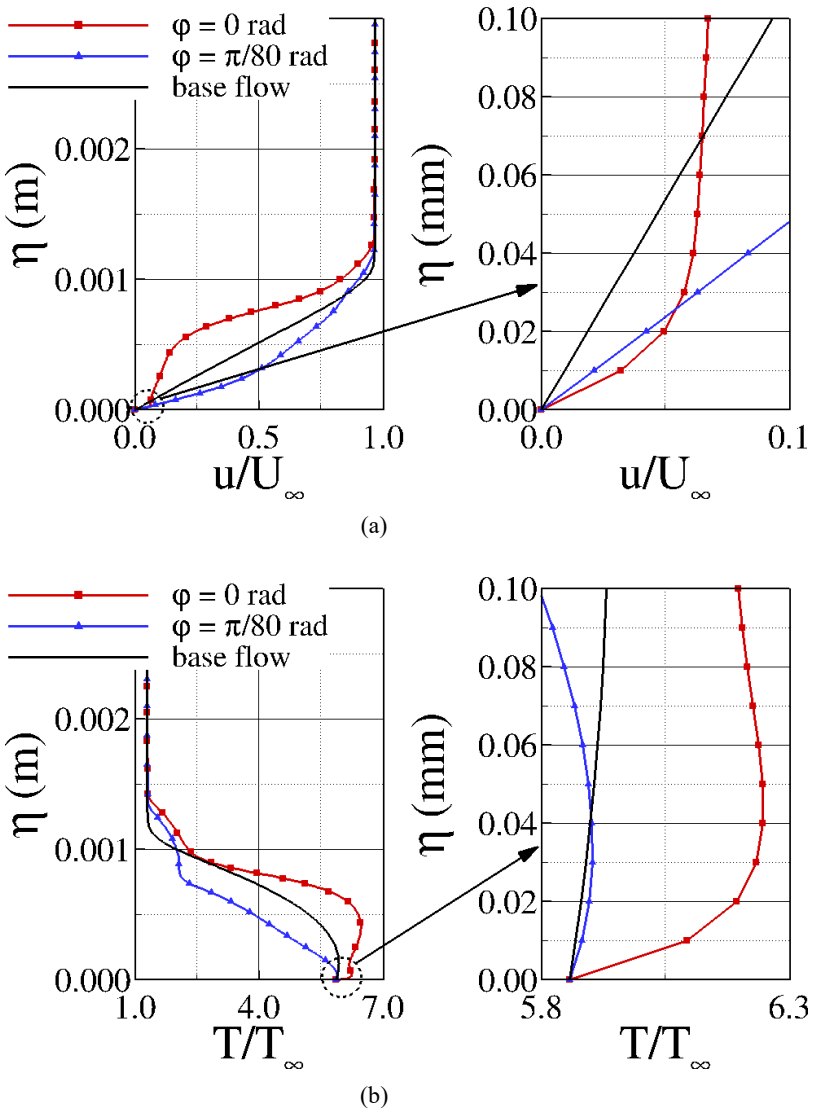

Figure 4-20: Time-Averaged and Base Flow Profiles of (a) U-velocity, (b) Temperature Extracted at x = 0.3941 m (maximum Stanton Number) at an Azimuthal Location Above the "Primary" Streaks (φ = 0 rad) and in Between Two Adjacent Streaks (φ = π/80 rad).

4.5 COMPARISON OF DNS AND EXPERIMENTAL RESULTS

If hypersonic boundary-layer transition prediction methods are to be improved, it is necessary to compare experimental results to DNS. Heat transfer and pressure fluctuation data were obtained experimentally at a unit Reynolds number of 11.0 x 10^6/m and "controlled" fundamental breakdown DNS were performed at 10.8 x 10^6/m. In order to compare results, the experimental heat transfer was converted to a dimensionless

Stanton number as described in Reference [24]. Figure 4-21 shows that primary and secondary streaks develop experimentally in a manner that is qualitatively similar to the streaks obtained with DNS. By extrapolating the number of streaks in a 60° field of view from experimental results, it is estimated that 78 streaks form around the circumference of the model. In the simulation 80 streaks form around the circumference.

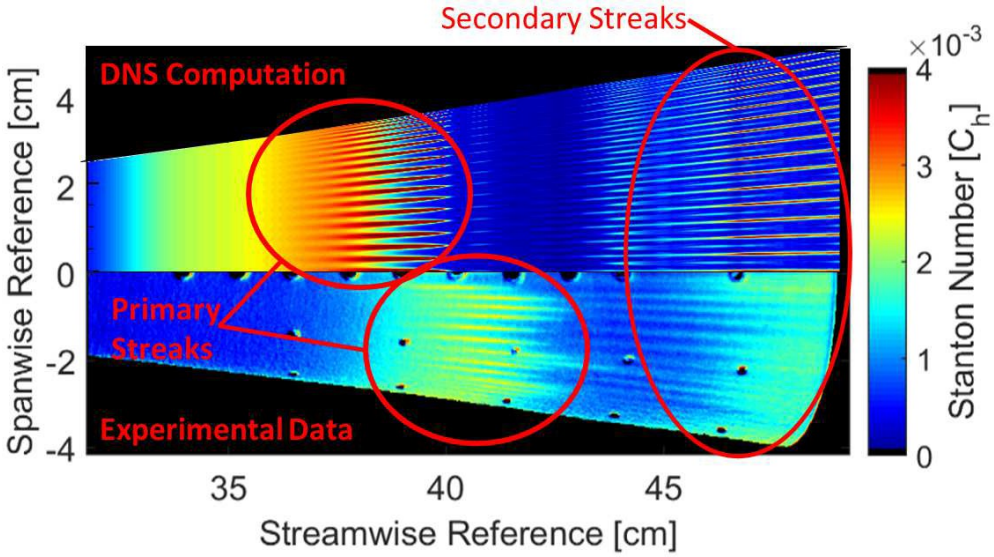

Figure 4-21: Global, Time-Averaged Stanton Number Comparison Showing Primary and Secondary Streaks in Both DNS and Experimental Results.

Streamwise Stanton number profiles were extracted along a ray through the primary streaks. The experimental profile in Figure 4-22 is the average of ten profiles extracted near the center of the global image. Computational values begin to deviate from laminar values near 30 cm and steadily increase until 37 cm where a sharp increase in Stanton number occurs. Experimentally the Stanton number deviates from laminar value further downstream at 35 cm from the nosetip. Unlike the computations, a massive overshoot does not occur. The maximum Stanton number in the primary streak region of the experiment is only 20% of the peak value observed for the "controlled" fundamental breakdown DNS.

Experimentally, the second-mode is measured on the flared cone and appears as an amplitude modulated wave train. To initiate the breakdown in the DNS the second-mode instability is forced using a 300 kHz two-dimensional primary wave and a pair of oblique waves with the same frequency (see Section 4.4). This forcing is perfectly periodic without amplitude modulation. This difference is clearly visible in Figure 4-23 which compares the experimental pressure fluctuations as measured by a PCB132A31 pressure sensor to the computational results at a distance of 39.0 cm from the nosetip.

Figure 4-24 shows the magnitude of the pressure fluctuations normalized by the surface static pressure at ten different streamwise locations. At the furthest upstream location, the computational fluctuations are almost 15 times larger than what is measured experimentally. These differences are most likely caused by the "controlled" disturbance forcing employed in the computations to initiate the laminar-turbulent transition process. Compared to the natural transition process caused by broadband free-stream disturbances in the experiment, the disturbance forcing in the simulations introduces only a single frequency at an initial forcing amplitude that is empirically determined such that breakdown can be observed in the computational domain. As a result, the initial amplitude

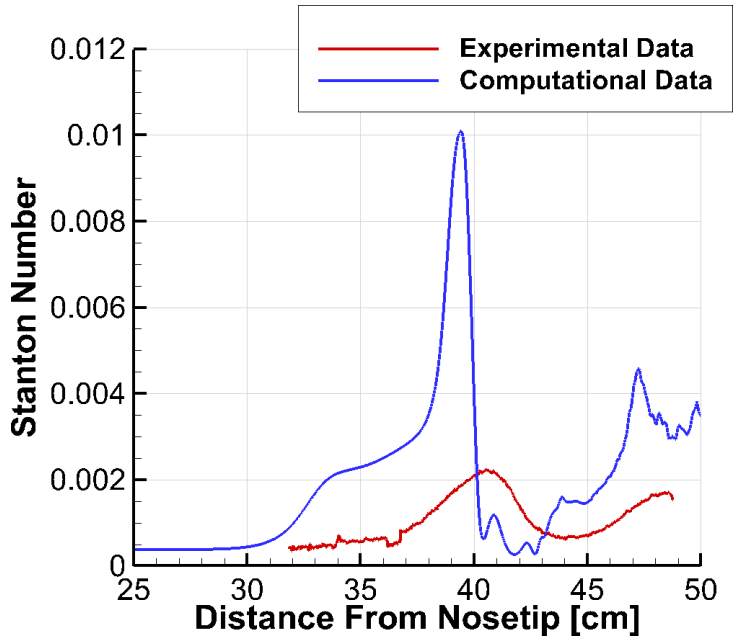

Figure 4-22: Comparison of Streamwise Stanton Number Profiles Following Streamlines Through the Primary Streaks.

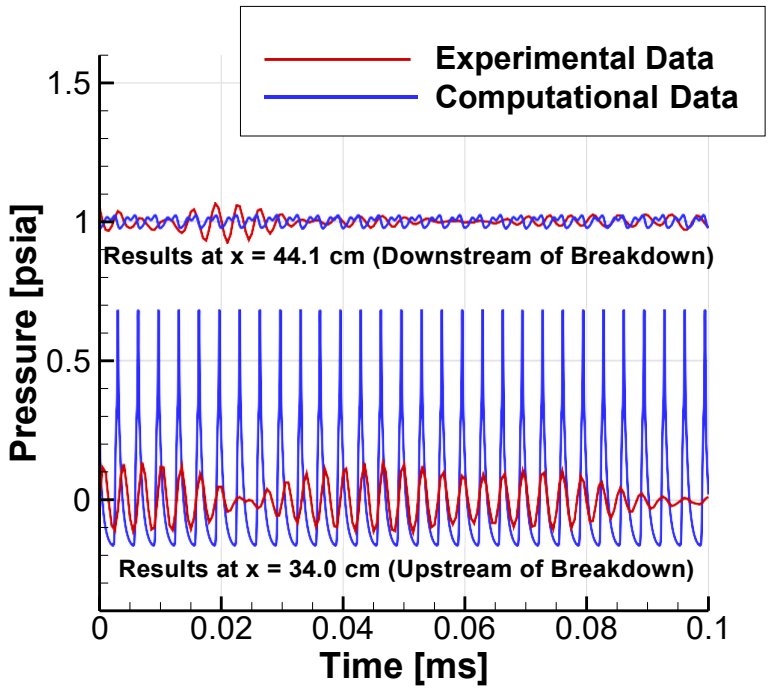

Figure 4-23: Pressure Signal from Experiments Showing Amplitude Modulation Versus the Periodic Forcing from Computations at Two Different Locations. Data At 44.1 cm are offset by 1 Psia.

of the forced disturbances can be smaller or higher than what occurs naturally. Additionally, the energy in the natural breakdown is most likely distributed over a wider range of frequencies (see Section 4.3) compared to the "controlled" breakdown DNS where it is initially concentrated in a single frequency. These discrepancies allow the second mode to reach much larger saturation amplitudes in the DNS compared to the experiment.

The pressure fluctuations increase until 39.0 cm from the nosetip when the maximum is measured for both cases. As the second-mode wave begins to break down after the maximum, similar pressure fluctuation magnitudes are measured. Computations with different initial amplitudes and an improved forcing approach to model the free-stream noise in the tunnel may help to rectify this difference.

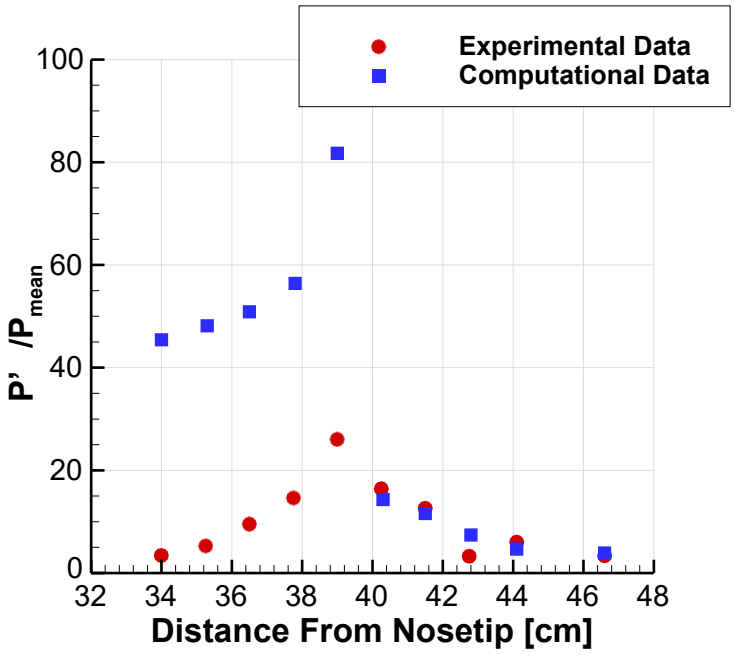

Figure 4-24: Second-Mode Pressure Fluctuation Magnitudes Comparing Experimental and Computational Results.

4.6 CONCLUSION

Accurately predicting transition caused by the second-mode instability remains an important aspect when designing hypersonic vehicles. Initial testing in the BAM6QT on 7° half-angle cones showed that transition to fully turbulent flow caused by the second-mode could not be measured under quiet flow conditions. A circular arc flared cone model was designed to accelerate the transition process such that the breakdown to turbulence could be observed on the model geometry in the experiments carried out at the BAM6QT. Initial testing in the BAM6QT showed that a unique hot-cold-hot heating pattern composed of streamwise streaks developed on the surface of the model. The measured disturbance spectra provide strong evidence that the flow breaks down all the way to turbulence in the experiments. A qualitatively similar heating pattern was also obtained using high-resolved "controlled" fundamental breakdown DNS. The peak Stanton number for the DNS are significantly larger compared to the peak value observed in experiments. These differences most likely arise due to the modeling assumptions of the "controlled" breakdown compared to the natural transition observed at BAM6QT.

Measurements at unit Reynolds numbers from 7.3 x 10^6/m to 12 x 10^6/m showed that the magnitude of the second-mode pressure fluctuations increased until they reached a maximum of nearly 30% of the mean surface pressure. These large second mode peak amplitudes were confirmed using NPSE calculations. The "controlled" breakdown DNS resulted in even larger peak amplitude (60%). This difference is most likely caused by the fact that in the BAM6QT natural, broadband transition is measured, whereas in the "controlled" breakdown DNS transition is initiated by continuously forcing a primary and secondary disturbance wave resulting in a different spectral content before the final breakdown to turbulence.

Increasing Re_∞ in the experiments did result in the heating pattern moving upstream on the surface of the model, the maximum pressure fluctuation prior to breakdown remained unaffected. It is important to compare experimental results with computations to better understand the physics of the transition process to improve modeling and prediction of boundary-layer transition. The two different methods currently being used are PSE stability analyses and DNS. Typically, stability analyses are performed by forcing a single discrete frequency, but experimentally it can be seen that the energy is spread across a wide bandwidth of frequencies. A wave-packet formulation of the Parabolized Stability Equations was implemented to account for the wide frequency bandwidth observed in experiments. This formulation allows for the transfer of energy to the side-lobes around the second-mode frequency that result in larger disturbance amplitudes that agree well with the amplitudes measured in the experiments when compared to the traditional PSE approach. The general trends using this method agree well with experimental results and predict the emergence of low frequency content.

The combined experimental and computational efforts helped to better understand the underlying physical mechanisms of the laminar-turbulent transition process on a flared cone geometry at Mach 6. It has been shown that the second mode reaches very large amplitudes when it saturates non-linearly, followed by a sudden nonlinear spectral broadening. The DNS results showed that the streaks are generated by steady streamwise modes. The streaks disappear when these vortical structures are lifted up, away from the wall. The reason for this "lift-up" process is currently not known and subject to future research. These steady streamwise streaks then break down and are pushed back towards the wall resulting in a reappearing streak pattern with an increased streak count in azimuthal direction. The qualitative similarities between the streak patterns observed in experiments and "controlled" fundamental breakdown DNS suggest that the natural transition in the BAM6QT is indeed caused by a fundamental breakdown process.

With an improved understanding of the transition process and streak development process flow control strategies can now be explored (active and passive) to either delay or accelerate transition depending on the application. Experiments using roughness elements have shown that the streak pattern can be modified by altering the azimuthal wave number of the dominant streamwise steady mode responsible for the streak development.

4.7 REFERENCES

[1] Saric, W.S., Reed, H.L., and White, E.B., "Stability and Transition of Three-Dimensional Boundary Layers," *Annual Review of Fluid Mechanics*, Vol. 35, 2003, pp. 413–430.

[2] Fedorov, A., "Transition and Stability of High-Speed Boundary Layers," *Annual Review of Fluid Mechanics*, Vol. 43, 2011, pp. 79–95.

[3] Schneider, S.P., "Effects of High-Speed Tunnel Noise on Laminar-Turbulent Transition," *Journal of Spacecraft and Rockets*, Vol. 38, No. 3, May–June 2001, pp. 323–333.

[4] Schneider, S.P., "Developing Mechanism-Based Methods for Estimating Hypersonic Boundary-Layer Transition in Flight: The Role of Quiet Tunnels," *Progress in Aerospace Sciences*, Vol. 72, January 2015, pp. 17–29.

[5] Mack, L.M., "Linear Stability Theory and the Problem of Supersonic Boundary Layer Transition," *AIAA Journal*, Vol. 13, No. 3, March 1975, pp. 278–289.

[6] Juliano, J., Schneider, S.P., Aradag, S., and Knight, D., "Quiet-Flow Ludwieg Tube for Hypersonic Transition Research," *AIAA Journal*, Vol. 46, No. 7, July 2008, pp. 1757–1763.

[7] Rufer, S.J. and Schneider, S.P., "Hot-Wire Measurements of Instability Waves on a Blunt Cone at Mach 6," *AIAA Paper 2005-5137*, June 2005.

[8] Rufer, S.J., *Hot-Wire Measurements of Instability Waves on Sharp And Blunt Cones at Mach 6*, PhD Dissertation, Purdue University School of Aeronautics & Astronautics, West Lafayette, IN, December 2005.

[9] Casper, K.M., Beresh, S.J., Henfling, J.F., Spillers, R.W., Pruett, B.O., and Schneider, S.P., "Hypersonic Wind-Tunnel Measurements of Boundary-Layer Transition on a Slender Cone," *AIAA Journal*, Vol. 54, No. 4, April 2016, pp. 1250–1263.

[10] Johnson, H.B., Alba, C.R., Bartkowicz, M.D., Drayna, T.W., and Candler, G.V., "Design Optimization of Hypersonic Vehicles for Boundary-Layer Stability," *AIAA Paper 2008-6221*, August 2008.

[11] Johnson, H.B. and Candler, G.V., "Hypersonic Boundary Layer Stability Analysis Using PSE-Chem," *AIAA Paper 2005-5023*, June 2005.

[12] Juliano, T., "Stability Computations on a Compression Cone," Tech. rep., Purdue University AAE 624 Final Report, December 2008.

[13] Wheaton, B.M., "Boundary Layer Stability on Circular-Arc Geometries at Mach 6," Tech. rep., Purdue University AAE 624 Final Report, December 2008.

[14] Chen, F.J., Malik, M.R., and Beckwith, I.E., "Boundary-Layer Transition on a Cone and Flat Plate at Mach 3.5," *AIAA Journal*, Vol. 27, No. 6, June 1989, pp. 687–693.

[15] Wheaton, B., Juliano, T., Berridge, D., Chou, A., Gilbert, P., Casper, K., Steen, L., Schneider, S., and Johnson, H., "Instability and Transition Measurements in the Mach-6 Quiet Tunnel," *AIAA Paper 2009-3559*, June 2009.

[16] Balakumar, P. and Kegerise, M.A., "Receptivity of Hypersonic Boundary Layers over Straight and Flared Cones," *AIAA Paper 2010-1065*, January 2010.

[17] Blanchard, A., *An Investigation of Wall-Cooling Effects on Hypersonic Boundary-Layer Stability in a Quiet Wind Tunnel*, PhD Dissertation, Old Dominion University, Dept. of Mechanical Engineering, Norfolk, VA, December 1995.

[18] Lachowicz, J., Chokani, N., and Wilkinson, S., "Boundary-Layer Stability Measurements in a Hypersonic Quiet Tunnel," *AIAA Journal*, Vol. 34, No. 12, December 1996, pp. 2496–2500.

[19] Ward, C.A., Wheaton, B.M., Chou, A., Gilbert, P.L., Steen, L.E., and Schneider, S.P., "Boundary-Layer Transition Measurements in a Mach-6 Quiet Tunnel," *AIAA Paper 2010-4721*, June 2010.

[20] Chou, A., *Characterization of Laser-Generated Perturbations and Instability Measurements on a Flared Cone*, Master's Thesis, Purdue University School of Aeronautics & Astronautics, West Lafayette, IN, December 2010.

[21] Casper, K.M., Beresh, S.J., and Schneider, S.P., "Pressure Fluctuations Beneath Instability Wavepackets and Turbulent Spots in a Hypersonic Boundary Layer," *Journal of Fluid Mechanics*, Vol. 756, September 2014, pp. 1058–1091.

[22] Ward, C.A., Wheaton, B.M., Chou, A., Berridge, D.C., Letterman, L.E., Luersen, R.P., and Schneider, S.P., "Hypersonic Boundary-Layer Transition Experiments in the Boeing/AFOSR Mach-6 Quiet Tunnel," *AIAA Paper 2012-0282*, January 2012.

[23] Willems, S., Ward, C.A., and Schneider, S.P., "Free Transition on a Slender Cone in a Quiet and a Conventional Wind Tunnel and the Effect of Ultrasonically Absorptive Materials." Presented at the 6th European Conference for Aeronautics and Space Sciences, June - July 2015.

[24] Chynoweth, B.C., *Measurements of Transition Dominated by the Second-Mode Instability at Mach 6*, PhD Dissertation, Purdue University School of Aeronautics & Astronautics, West Lafayette, IN, May 2018.

[25] Chynoweth, B.C., *A New Roughness Array for Controlling The Nonlinear Breakdown of Second-Mode Waves at Mach 6*, Master's Thesis, Purdue University School of Aeronautics & Astronautics, West Lafayette, IN, May 2015.

[26] Chou, A., Ward, C.A., Letterman, L.E., Luersen, R.P., Borg, M.P., and Schneider, S.P., "Transition Research with Temperature-Sensitive Paints in the Boeing/AFOSR Mach-6 Quiet Tunnel," *AIAA Paper 2011-3872*, June 2011.

[27] Luersen, R.P., *Techniques for Application of Roughness for Manipulation of Second-Mode Waves on a Flared Cone at Mach 6*, Master's Thesis, Purdue University School of Aeronautics & Astronautics, West Lafayette, IN, December 2012.

[28] Chynoweth, B.C., Ward, C.A., Greenwood, R.T., McKiernan, G.R., Fisher, R.A., and Schneider, S.P., "Measuring Transition and Instabilities in a Mach 6 Hypersonic Quiet Wind Tunnel," *AIAA Paper 2014-2643*, June 2014.

[29] Sweeney, C.J., Chynoweth, B.C., Edelman, J.B., and Schneider, S.P., "Instability and Transition Experiments in the Boeing/AFOSR Mach 6 Quiet Tunnel," *AIAA Paper 2016-0355*, January 2016.

[30] Marineau, E.C., "Prediction Methodology for Second-Mode-Dominated Boundary-Layer Transition in Wind Tunnels," *AIAA Journal*, Vol. 55, No. 2, February 2017, pp. 484–499.

[31] Herbert, T., *Parabolized Stability Equations. Special Course on Progress in Transition Modelling*, Vol. 793, AGARD Rep., 1994.

[32] Herbert, T., "Parabolized Stability Equations," *Annual Review of Fluid Mechanics*, Vol. 29, 1997, pp. 245–283.

[33] Nayfeh, A.H., *Perturbation Methods*, Wiley-VCH Verlag GmbH & Co. KGaA, 2004.

[34] Kuehl, J., "Discrete and Finite Bandwidth Frequency Distributions in Nonlinear Stability Applications," *Physics of Fluids*, Vol. 29, 2017, pp. 024101.

[35] Li, F. and Malik, M.R., "On the Nature of PSE Approximation," *Theoretical and Computational Fluid Dynamics*, Vol. 8, 1996, pp. 253–273.

[36] Paredes, P., Theofilis, V., Rodriguez, D., and Tendero, J.A., "The PSE-3D Instability Analysis Methodology for Flows Depending Strongly on Two and Weakly on the Third Spatial Dimension," *AIAA Paper 2011-3752*, June 2011.

[37] Theofilis, V., "Global Linear Instability," *Annual Review of Fluid Mechanics*, Vol. 43, 2011, pp. 319–352.

[38] Kuehl, J. and Paredes, P., "Görtler Modified Mack-modes on a Hypersonic Flared Cone," *AIAA Paper 2016-0849*, January 2016.

[39] Chang, C., "The Langley Stability and Transition Analysis Code (LASTRAC) Version 1.2 User Manual," No. 213233, 2004.

[40] Johnson, H. and Candler, G., "Hypersonic Boundary Layer Stability Analysis using PSE-Chem." *AIAA Paper 2005-5023*, June 2005.

[41] Oliviero, N.B., *EPIC: A New and Advanced Nonlinear Parabolized Stability Equation Solver*, Master's Thesis, Texas A&M University, West Lafayette, IN, December 2012.

[42] Kuehl, J., Perez, E., and Reed, H.L., "JoKHeR: NPSE Simulations of Hypersonic Cross Instability," *AIAA Paper 2012-0921*, January 2012.

[43] Hofferth, J., Saric, W., Kuehl, J., Perez, E., Kocian, T., and Reed, H., "Boundary-Layer Instability and Transition on a Flared Cone in a Mach 6 Quiet Wind Tunnel," *International Journal of Engineering Systems Modelling and Simulation*, Vol. 5, No. 1/2/3, 2013.

[44] Kocian, T., Perez, E., Oliviero, N., Kuehl, J., and Reed, H., "Hypersonic Stability Analysis of a Flared Cone," *AIAA Paper 2013-0667*, January 2013.

[45] Reed, H.L., Perez, E., Kuehl, J., T.Kocian, and Oliviero, N., "Verification and Validation Issues in Hypersonic Stability and Transition Prediction," *Journal of Spacecraft and Rockets*, Vol. 52, 2014, pp. 29–37.

[46] Kuehl, J., Reed, H.L., Kocian, T.S., and Oliviero, N.B., "Bandwidth Effects on Mack-Mode Instability," *AIAA Paper 2014-2777*, June 2014.

[47] Kuehl, J.J., "Thermoacoustic Interpretation of Second-Mode Instability," *AIAA Journal*, 2018, pp. 1–8.

[48] Batista, A. and Kuehl, J., "A Mechanism for Spectral Broadening and Implications for Saturation Amplitude Estimates," *AIAA Paper 2017-3635*, June 2017.

[49] Laible, A. and Fasel, H.F., "Numerical Investigation of Hypersonic Transition for a Flared and a Straight Cone at Mach 6," *41st AIAA Fluid Dynamics Conference and Exhibit*, 2011, AIAA 2011-3565.

[50] Terwilliger, N., *Numerical Investigation of Boundary Layer Instability Modes on a compression cone at Mach 6*, Master's thesis, The University of Arizona, 2011.

[51] Sivasubramanian, J. and Fasel, H.F., "Direct Numerical Simulation of Laminar-Turbulent Transition in a Flared Cone Boundary Layer at Mach 6," *54th AIAA Aerospace Sciences Meeting*, 2016, AIAA 2016-0846.

[52] Hader, C. and Fasel, H.F., "Laminar-Turbulent Transition on a Flared Cone at Mach 6," *AIAA Paper 2016-3344*, June 2016.

[53] Hader, C. and Fasel, H.F., "Fundamental Resonance Breakdown for a Flared Cone at Mach 6," *AIAA Paper 2017-0765*, January 2017.

[54] Hader, C. and Fasel, H.F., "Towards Simulating Natural Transition in Hypersonic Boundary Layers Via Random Inflow Disturbances," *Journal of Fluid Mechanics*, Vol. 847, 2018.

[55] Sivasubramanian, J. and Fasel, H., "Numerical Investigation of the Development of Three-Dimensional Wavepackets in a Sharp Cone Boundary Layer at Mach 6," *Journal of Fluid Mechanics*, Vol. 756, 2014, pp. 600–649.

[56] van Ingen, J., "The e^N Method for Transition Prediction. Historical Review of Work at TU Delft," *AIAA Paper 2008-3830*, June 2008.

[57] Herbert, T., "Secondary Instability of Boundary Layers," *Annual Review of Fluid Mechanics*, Vol. 20, No. 1, 1988, pp. 487–526.

[58] White, F.M., *Viscous Fluid Flows*, McGraw Hill, 3rd ed., 2006.

Chapter 5 - HIGH ENTHALPY EFFECTS ON HYPERSONIC BOUNDARY LAYER TRANSITION

Viola Wartemann, Alexander Wagner
German Aerospace Center (DLR)
GERMANY

Ross Wagnild
Sandia National Laboratories
UNITED STATES

Fabio Pinna, Fernando Miró Miró
von Karman Institute for Fluid Dynamics
BELGIUM

Hideyuki Tanno
Japan Aerospace Exploration Agency
JAPAN

Heath Johnson
VirtusAero LLC
UNITED STATES

5.0 NOMENCLATURE

f	Frequency, kHz
h	Enthalpy, $\mathrm{MJ/kg}$
M	Mach number
N	N-factor
p	Pressure, MPa
q	Flow / material quantity
Re_m	Unit Reynolds number
T	Temperature, K
u, v, w	Velocity in x-, y-, z-direction, $\mathrm{m/s}$
x, y, z	Coordinates, m
α, β	Wave numbers
σ	Growth rate, $1/\mathrm{m}$
ρ	Density, $\mathrm{g/m^3}$

Subscripts

e	Boundary layer edge quantity
w	Wall quantity
∞	Free stream quantity
0	Reservoir quantity

Superscripts

$\bar{}$	Base flow quantity
$\tilde{}$	Disturbance flow quantity
$\hat{}$	Eigenfunction

5.1 INTRODUCTION

Laminar to turbulent transition in high speed boundary layers is of high importance for re-entry vehicles since early transition can increase the surface heat transfer by a factor of 3 to 8 [1, 2]. The uncertainty on the transition location usually leads to an oversized thermal protection system, adding extra costs and reducing the payload of a hypersonic system. The second mode instability, commonly referred to as second mode or Mack mode [3], is the dominant boundary layer instability for essentially 2D boundary layers at high local Mach number ($Ma_e > 4$) and/or cold walls [3]. Therefore, the second mode is the main focus of the investigations in this chapter. High speed vehicles and re-entry vehicles operate in a high enthalpy range. In this range, real gas effects occur, which can include molecular rotation, molecular vibration, chemical dissociation and exchange, electronic excitation, radiation and ionization. In this chapter, the high enthalpy effects on second mode instabilities are investigated. The numerical investigations are performed with three different stability codes, which are compared against each other: the NOLOT code of the DLR, the STABL code from VirtusAero and the VESTA code of VKI, which are described in Section 5.3.The stability results are compared against low and high enthalpy experiments, which were performed on a blunted 7° half-angle cone model. The two high enthalpy shock tunnels (HEG and HIEST), in which the experiments were conducted, are described in Section 5.2. The mean flow as well as the stability calculations themselves are performed with and without real gas effects to isolate the high enthalpy effect on the instability. Currently, the NOLOT stability code is limited to caloric or thermal perfect gas assumptions. Thus, an essential element of this chapter is to assess the effect of real gas effects during the stability analysis.

5.2 GROUND TEST FACILITY AND CONE TEST ARTICLE

The experimental data referred to in the present study were obtained in two free-piston driven reflected shock tunnels, the DLR High Enthalpy Shock Tunnel Göttingen (HEG) [4] and the JAXA High Enthalpy Shock tunnel (HIEST) [5]. Similar test conditions were chosen with respect to unit Reynolds number, Mach number and total enthalpy. Table 5-1 provides a low enthalpy test condition from HEG and two comparable high enthalpy test conditions of both tunnels. The HEG conditions of Table 5-1 were derived by nozzle computations using the DLR TAU code [6–8] in combination with a one temperature model, thus, assuming thermal equilibrium, which was shown to be a reasonable approach [9, 10]. The HIEST test conditions were calculated using a two temperature model. As shown in Table 5-1 the translational-rotational and vibrational temperatures are almost identical which supports the before mentioned assumption. The model wall temperature for all tests is assumed to be isothermal at 293 K.

All tests were conducted on separate 7° half-angle blunted cones with a nose tip radius of $2.5\,\mathrm{mm}$ and an overall length of about $1\,\mathrm{m}$. Each model was supported by a sting at a nominal angle of attack of $0°$. Further, both models were equipped with thermocouples and PCB flush mounted pressure transducers. The latter transducer

Table 5-1: HEG and HIEST Test Conditions Used in the Present Study.

Condition	HEG-Low-E	HEG-High-E	HIEST-High-E
p_0 [MPa]	7.1	38.8	46.8
T_0 [K]	2680	6690	6370
h_0 [MJ·kg^{-1}]	3.1	11.6	10.9
M_∞ [-]	7.35	6.09	6.05
T_∞ (1T) [K]	264	1268	-
T_{vib} (2T) [K]	-	T_∞	1192
T_{rot} (2T) [K]	-	T_∞	1185
ρ_∞ [g·m^{-3}]	10.7	17.1	19
u_∞ [m·s^{-1}]	2399	4354	4246
Re_m [m^{-1}]	$1.55 \cdot 10^6$	$1.52 \cdot 10^6$	$1.71 \cdot 10^6$

have a response time of $\approx 1\,\mu$s and were used to capture the second mode frequencies for later comparison with stability analysis. On the cone model used in HIEST the PCB transducers were positioned between $0.412\,$m to $1.012\,$m, measured from the sharp tip, with a spacing of $0.04\,$m [11]. On the HEG model the PCB transducers were placed at $0.650\,$m, $0.785\,$m and $0.965\,$m from the sharp tip [12].

5.3 NUMERICAL METHODS

5.3.1 Mean Flow Solver

The laminar base flows $\bar{q}$, which are required for the stability analysis, are calculated by different CFD solvers, which are not described in detail here. For NOLOT the DLR TAU code is applied, which is a three-dimensional parallel hybrid multi-grid code and has been validated for hypersonic flows (see e.g. [6–8]). The base flow calculations account for real gas effects, based on non-equilibrium gas modeling with 5 species for air: N_2, O_2, NO, N, O. Different assumptions are applied: thermal equilibrium and chemical non-equilibrium (one temperature models) and thermochemical non-equilibrium (two and three temperature model). Constant free stream conditions, which are listed in Table 5-1, are used. Additional mean flow calculations with a perfect gas assumption are performed to isolate the real gas effects. Figure 5-1 shows the Mach number distribution of the low-enthalpy test case (see also Table 5-1: HEG-Low-E) as an example of the base flow calculations, including for the rear part a zoom of the grid.

The stability simulations obtained with the VESTA toolkit are based on mean flow computations with the second order finite volume solvers CFD++® (see for instance Peroomian and Chakravarthy [13]) and COOLFluiD (Lani *et al.* [14], Degrez *et al.* [15]). Grid convergence studies were conducted for each code as described in Section 5.4.1.1.

The VirtusAero STABL software contains a structured, axisymmetric CFD solver, which solves the reacting Navier-Stokes equations and is maintained by Dr. Heath Johnson [16]. This flow solver is based on the finite-volume formulation. The inviscid fluxes are based on the modified Steger-Warming flux vector splitting method

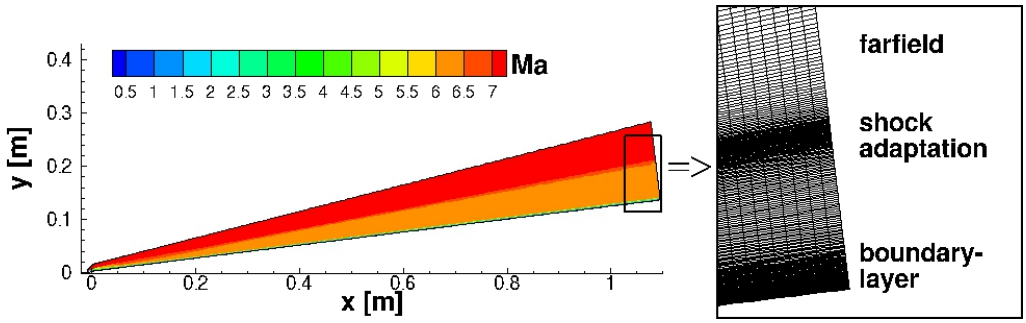

Figure 5-1: Example of Mean Flow: HEG-Low-E Test Case (CFD Solver: TAU).

and are second-order accurate with a MUSCL limiter as the TVD scheme. The viscous fluxes are second order accurate. The time integration method is the implicit, first-order DPLR method. The simulated gas is a mixture of ideal gases using N2, O2, NO, N, and O in chemical and thermal non-equilibrium. The viscosity law uses Blottner curve fit data for species viscosities and the Wilke mixing rule for mixture viscosity. The heat conductivity is calculated using Euckens relation.

5.3.2 LST / PSE Solver

The equations of the stability codes are derived from the conservation equations of mass, momentum and energy, which govern the flow of a viscous, compressible gas. All flow and material quantities are decomposed into a steady laminar base flow $\bar{q}$ and an unsteady disturbance flow $\tilde{q}$

$$q(x, y, z, t) = \bar{q}(x, y) + \tilde{q}(x, y, z, t). \tag{5-1}$$

The laminar mean flows $\bar{q}$ are calculated by different CFD codes (see previous Section) and can be used without and with chemistry. The disturbance $\tilde{q}$ is represented as a harmonic wave

$$\tilde{q}(x, y, z, t) = \hat{q}(x, y) \exp[i(\alpha x + \beta z - \omega t)] + c.c. \tag{5-2}$$

with the complex-valued amplitude function $\hat{q}$.

The stability codes applied in this chapter are: the NOnLocal Transition analysis code (NOLOT [17]) of the German Aerospace Center, the Stability and Transition Analysis for hypersonic Boundary Layers code (STABL [16]) of VirtusAero and the VKI Extensible Stability and Transition Analysis (VESTA) toolkit [18], [19], [20] of the von Karman Institute. All codes can be used for Linear Stability Theory (LST) as well as Parabolized Stability Equations (PSE) analyses. Both approaches are applied in this chapter. In contrast to STABL and VESTA [21], which can account for real gas effects, NOLOT is limited to a calorically or thermally perfect gas.

The stability analyses performed using the STABL software suite are calculated with the PSE-Chem solver [16]. PSE-Chem solves the reacting, two-dimensional, axisymmetric, linear parabolized stability equations (PSE) to

predict the amplification of disturbances as they interact with the boundary layer. The PSE-Chem solver includes finite-rate chemistry and translational-vibrational energy exchange.

The VESTA code is made of different components dealing with the different aspects of the stability equations solution: derivation of a generic set of equations, generation of an automated implementation and a set of solution algorithms associated to different ansatz. The toolkit has been tested against several cases available in the literature such as the one in Malik [22], Arnal [23] and Özgen and Kırcalı[24]. Several solvers are available within VESTA, namely LST, PSE and BiGlobal. They are all able to cope with different regimes from incompressible to compressible flows with LST and PSE dealing with chemical reactions.

5.4 RESULTS

Three test cases are chosen for the analyses of the chemical effects on the second mode: a low enthalpy experiment is conducted as reference case and two high enthalpy experiments as main test cases for the investigations of the chemical effects. See also Table 5-1.

5.4.1 Low Enthalpy Test Case (HEG)

The chosen reference test case is an experiment, which was performed in HEG. This low enthalpy test case, HEG-Low-E, was conducted at a total enthalpy of 3.1 MJ/kg (Table 5-1), at which the gas can be assumed to be calorically perfect.

5.4.1.1 Grid Convergence

Different axisymmetric grids are used for the base flow calculations: non-adapted grids as well as adapted grids. For the shock adapted grids with additional modulation of the outer grid limits, it is possible to reduce the number of points compared to the non-adapted grids. Apart from the number of grid points, also the wall normal distance of the first grid points has an effect.

Figure 5-2 shows the grid convergence study using the TAU code in combination with the NOLOT code. The calculated growth rates σ of the second mode is given as a function of the x-coordinate (axial distance measured from the blunt nose for this diagram as for all following pictures), for the described cone of Section 5.2 and a comparable low-enthalpy free stream condition as HEG-LOW-E of Table 5-1. Grid point clustering is applied towards the nose, the wall of the cone and the shock. Figure 5-2 demonstrates that the two finest grids deliver the same growth rates. For the following NOLOT investigations, the number of grid points is with about a half million between the two finest shown grids of Figure 5-2.

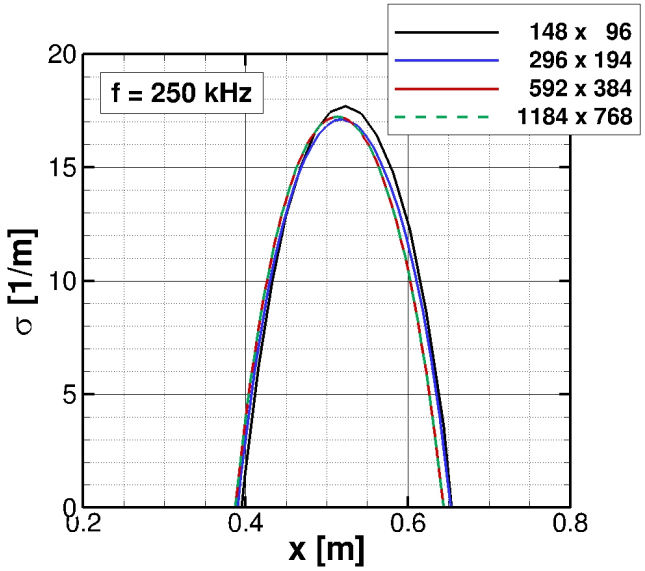

Figure 5-2: LST, NOLOT: $\sigma = \mathrm{f}(\mathrm{x})$ - Grid Convergence Study with Perfect Gas Assumption.

Due to the use of different CFD solvers, the grid convergence study has to be done for each of them, separately. For the STABL code, Wagnild [25] summarized a detailed grid convergence study using a comparable geometry as well as comparable free stream conditions. Different grids up to a cell count of over 15 million cells were investigated. Based on these previous grid studies a grid of 1215 $\times$ 350 (about a half million grid points) is chosen. The following VESTA results based on a 1 million grid (2600 $\times$ 450). The VESTA grid study is summarized in Wartemann et al. [26].

5.4.1.2 Chemical Influence (HEG-Low-E)

In this subsection, PSE calculations performed with NOLOT are shown: in Figure 5-3a the calculated N-factors of the second mode as a function of the x-coordinate (axial distance measured from the blunt nose) for a frequency range from 200 up to 300kHz are depicted. The dashed lines in gray are based on perfect gas calculations, whereas the black lines are based on thermochemical non-equilibrium gas modeling (see also Section 5.3.1). Almost identical results were obtained confirming the assumption of calorically perfect gas for the low enthalpy test case.

As mentioned in Section 5.2, PCB sensors were used in the HEG experiments to measure the pressure fluctuations in the boundary layer, which are associated with second mode instabilities. From Figure 5-3a the N-factors can be extracted at the transducer positions as shown in Figure 5-3b for the three PCB sensor positions of the experiment. The calculated second mode is amplified in the streamwise direction. Due to the increase of the boundary layer thickness in the downstream direction and the relation between the boundary layer thickness δ and the second mode wavelength, $\lambda \approx 2\delta$, the typical shift towards lower frequencies can be observed.

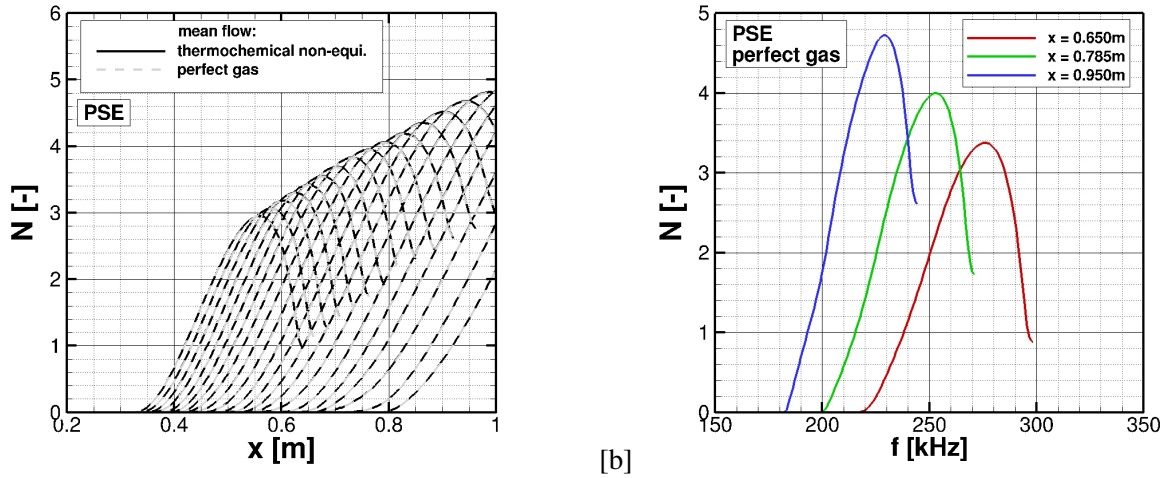

[a] [b]

Figure 5-3: HEG-Low-E, PSE, NOLOT: a) N = f(x), b) N = f(f).

5.4.1.3 LST Comparison: VESTA / NOLOT (HEG-Low-E)

The first comparison of this subsection is visible in Figure 5-4.a and illustrates the LST calculations of VESTA (dashed lines with symbols) and NOLOT (solid lines). To be consistent in the comparison the base flow as well as the LST calculations of both codes are based on the perfect gas assumption. The codes predict comparable results with small deviations: VESTA predicts slightly higher maximum N-factors while the frequency range shifts to higher values. Looking at the three maxima, for the N-factors as well as the frequencies, the discrepancy between both codes is less than 1.5%. This is an acceptable / typical deviation, using different mean flow solvers as well as LST solvers. The main reason for the differences is the application of different mean flow solver. Using the same grid and same mean flow solver (in this case: CFD++) delivers almost the same distributions, visible in Figure 5-4.b. The small distinctions at the first and last maximum are caused by less extracted data points of the VESTA results for the maxima positions (the symbols marks the extracted data points of VESTA).

Figure 5-4.c demonstrates the effect of a physical model using a local thermodynamic equilibrium (LTE) approach. An LTE approach assumes the flow to be in a thermal and chemical equilibrium. For the VESTA base flow calculation the COOLFluiD code is applied, which uses the common LTE approach. That means all chemical reactions take place infinitely fast. To have a consistent LTE approach, the VESTA LST calculations are also based on the LTE assumption. Additionally, Figure 5-4.c depicts the VESTA perfect gas outcome of Figure 5-4.a/b (using CFD++ for the mean flow simulation). Of course, the expected differences between the VESTA results due to the different approaches are clearly visible in Figure 5-4.c. The frequency range is similar, but the maximal N-factors show high deviations: the maximum N-factors compared to the perfect gas solution are about 15% lower.

Nevertheless, as already mentioned in Section II, the HEG is a free-piston driven reflected shock tunnel with an expanded flow. The time required to reach an equilibrium condition, is defined by the density and local

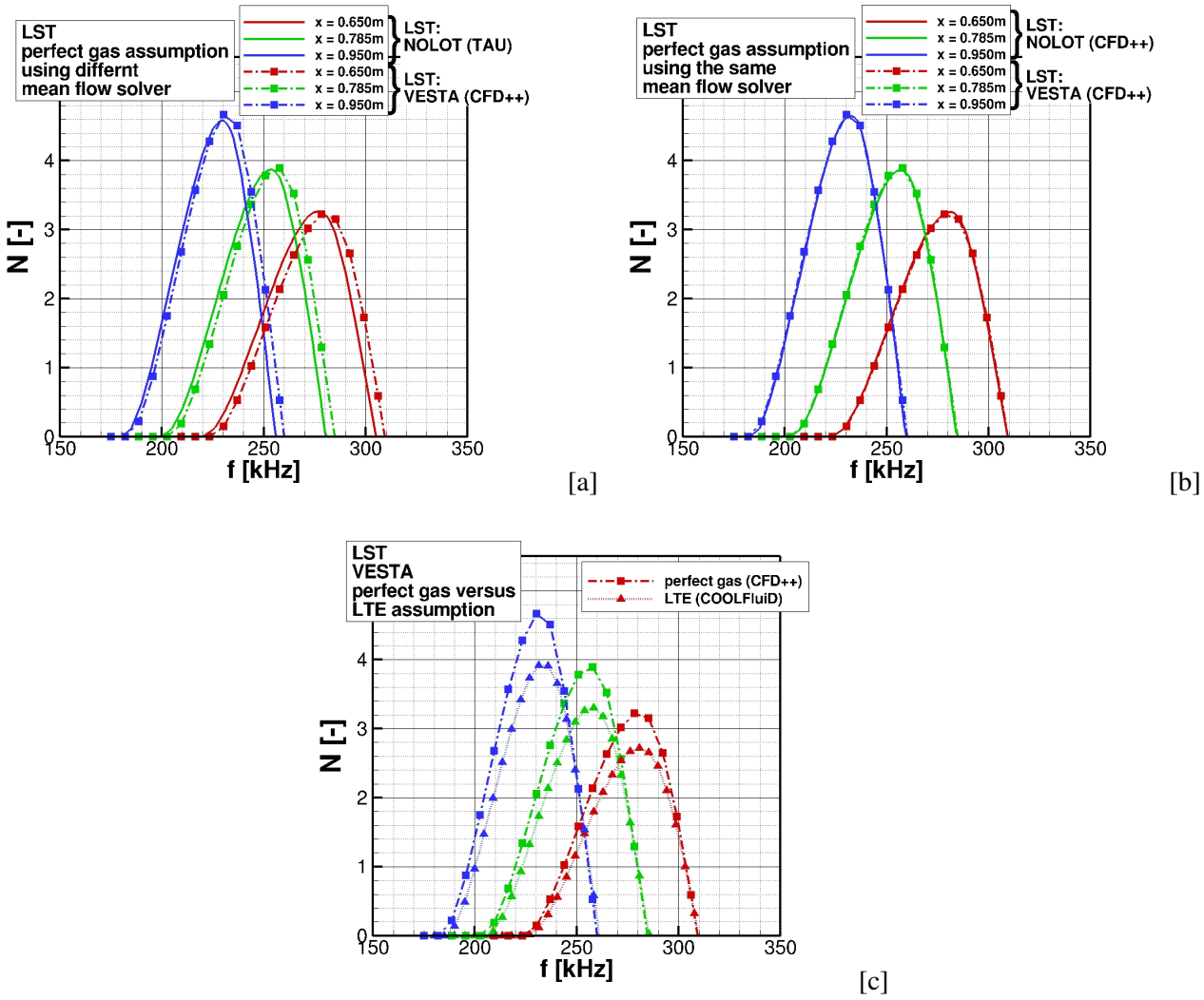

Figure 5-4: HEG-Low-E, LST, Comparison NOLOT and VESTA: N = f(f).

temperature. Therefore, depending on the ratio of the relaxation time to a characteristic timescale of the flow, the chemical and thermal relaxation processes can be either in non-equilibrium or in equilibrium [4], depending on the test condition. For HEG test conditions with high enthalpy, a non-equilibrium approach is suggested for CFD calculations. For low enthalpy test cases, as the investigated case of this subsection, also a perfect gas approach is possible (see previous Section 5.4.1.2).

5.4.1.4 PSE Comparison: STABL / NOLOT (HEG-Low-E)

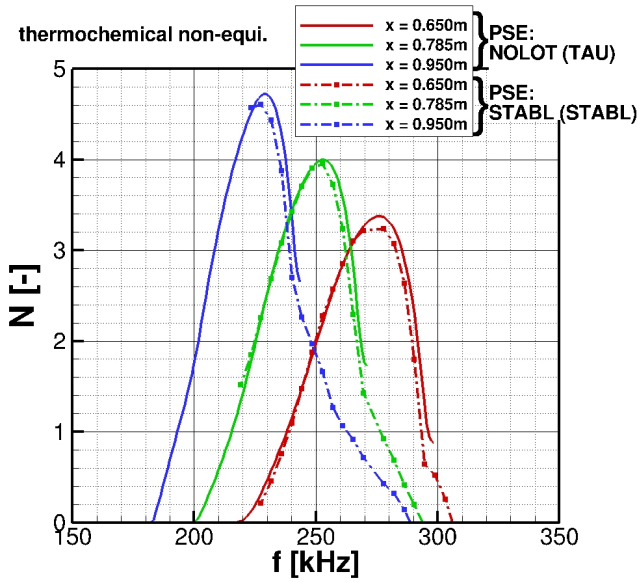

Figure 5-5: HEG-Low-E, PSE, Comparison NOLOT and STABL: N = f(f).

Previous investigations of the same geometry with a similar low enthalpy free stream condition, based on a comparison of the experimental / calculated growth rate of the second modes, show that it is possible to apply LST instead of PSE [27]. Nevertheless, LST neglects the nonparallel nature of the boundary layer as well as nonlinear effects. Thus, PSE is in general the preferable method.

The N-factor of the PSE calculations and consequently the differences between PSE and LST, depend on the chosen parameter for the PSE N-factor calculations, such as velocity or disturbance energy. For all PSE results in this chapter, the N-factors are derived based on the disturbance energy.

Figure 5-5 shows that the STABL results (dashed lines with symbols) are in a good agreement with the NOLOT calculations (solid lines). The mean flow as well as the stability calculations of STABL are performed with thermochemical non-equilibrium based on a two temperature approach. In contrast, due to the limitation of the NOLOT code, only the base flow simulation used thermochemical non-equilibrium. The differences between the code predictions are in the range of 1% comparing the maximum N-factors and the corresponding frequencies at the three sensor locations. These small deviation are in a similar range as these of the previous code to code

comparison of Section 5.4.1.3 (Figure 5-4.a), which were mainly caused by the use of the distinct mean flow solvers and not caused by the use of different PSE solvers, or in case of Figure 5-5, the use of different chemistry approaches for the stability calculations. Consequently, the results of fig. 5-5 confirmed, as expected for the low enthalpy case, the chemical effects are negligible.

5.4.1.5 Comparison to Experiment: HEG-Low-E

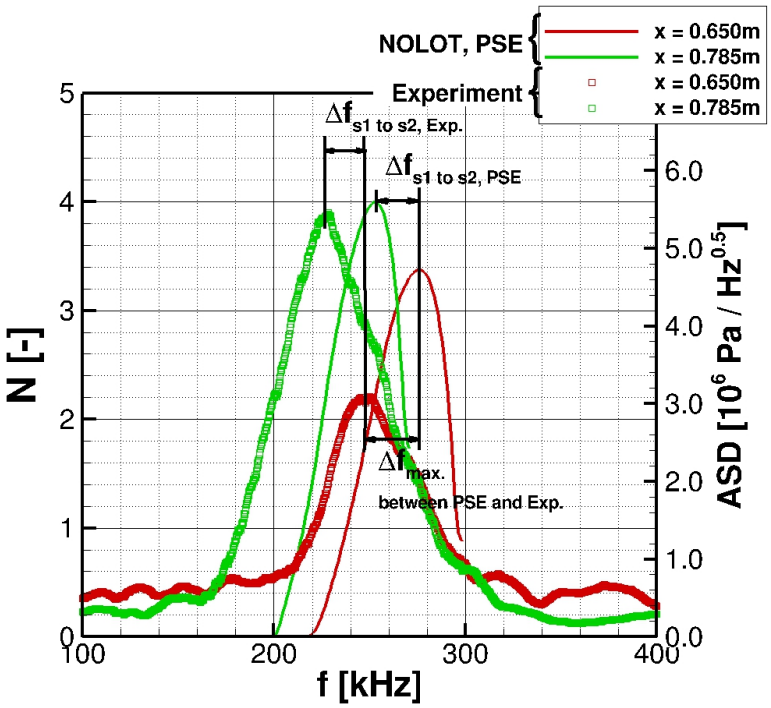

Figure 5-6: HEG-Low-E, Comparison NOLOT (N-factor) and Experimental Data (ASD).

For the second mode comparison of the numerical data with the measurements, two requirements are necessary. First, the second mode at the PCB sensor position has to be strong enough, meaning it has to be higher than the background noise level. Second, the flow at the sensor position has to be laminar. In the current case, the measured second mode at the last position (x = 950mm) is in the transition region. Thus, for the comparison with the measured second mode, the first and second sensor positions (x = 0.650 m, red color; x = 0.785 m, green color) are used. For the comparison with the experimental data, the results of the NOLOT code of the previous Section are used.

Figure 5-6 shows the measured amplitude spectral density (ASD) marked as symbols. N-factors, which are based on PSE NOLOT calculations, as a function of the frequency are shown as lines. The differences of the peak frequencies are in the range of 10%. However, the frequency shift between the first and the second sensor positions is within about 22kHz for both the experiment and the computations, $\Delta f_{s1\ to\ s2,\ \mathrm{Exp.}} = \Delta f_{s1\ to\ s2,\ \mathrm{PSE}}$. Thus, a satisfactory agreement is observed, despite with a small frequency shift.

Several analyses were performed to investigate this frequency shift: Wagner et al. [28] investigated the influence of small deviations of the nose radius on the second mode. A change in the nose radius of 10% results in a frequency shift of about 10%. However, the nose is well proven for this test case. Further, Wagner et al. [28] investigated the influence of small variations of the angle of attack on the transition location and the second mode development. In two subsequent tests on the same model as used in the present study the angle of attack was varied in a range of $0.2°$, which a conservative estimation of angle of attack uncertainties. The analysis shows a negligible effect on the transition process and the second mode frequencies.

The good agreement in $\Delta f_{s1\ to\ s2}$ of the comparison makes small inaccuracies in the free stream condition the most likely reason for the Δf_{max}. In Wartemann et al. [29] the influence of usual measurement inaccuracies in the determination of the free stream conditions on the maximum frequency of the second modes are investigated using a $3°$ half-angle sharp cone. In reference [27], an investigation on the geometry used in the present study revealed, that a change of unit Reynolds number of about 5% results in a frequency shift of about 10%.

5.4.2 First High Enthalpy Test Case (HEG-High-E)

This Section summarizes the comparison of the first high enthalpy test case: HEG-High-E with a total enthalpy of 11 MJ/kg.

5.4.2.1 PSE Comparison: STABL / NOLOT (HEG-High-E)

Figure 5-7 summarizes the PSE code to code analysis. The mean flow as well as the stability calculation of STABL, dashed lines with symbols, are performed with thermochemical non-equilibrium based on a two temperature model. For NOLOT (lines), different approaches are applied: data in Figure 5-7a are based on a calorically perfect gas assumption using a specific heat ratio of 1.4 for base flow as well as stability calculations. As expected, for the high enthalpy case major differences are visible. For all sensor positions a shift of the frequency range can be observed. Including chemistry reduces the boundary layer stability and increases the calculated N-factors. The deviations of the N-factors at the maximum of each sensor position between the two approaches depend strongly on the sensor position itself: for the first sensor, almost the same maximum N-factor is predicted, while for the second position, the deviation increases to a ΔN_{max} of around 10% and for the last sensor position up to over 10%. Figure 5-7b considers variations of the specific heat ratio. One result of the calculations of the complete nozzle is, that the specific heat ratio κ is reduced to 1.33. Using this reduced κ for the calorically perfect gas simulation delivers the values in Figure 5-7b. This numerical test approach does not affect the frequency range. Looking at the frequencies, the same differences between STABL and NOLOT as in Figure 5-7a are visible. Due to the dependency on the position, the maximum N-factor at the first sensor position is overestimated from NOLOT, the second position is similar to the STABL results, and the last sensor is underestimated. Thus, only an upgrade to thermochemical non-equilibrium base flow simulations make senses, which is summarized in Figure 5-7c. Minor differences between STABL and NOLOT are still visible especially for the downstream sensor positions. The differences of the N-factor at the maximum for the last sensor is about 3%. Consequently, real gas effects have a higher effect on the mean flow, than on the stability calculations itself. The application of the thermochemical non-equilibrium for the base flow in combination with the perfect gas

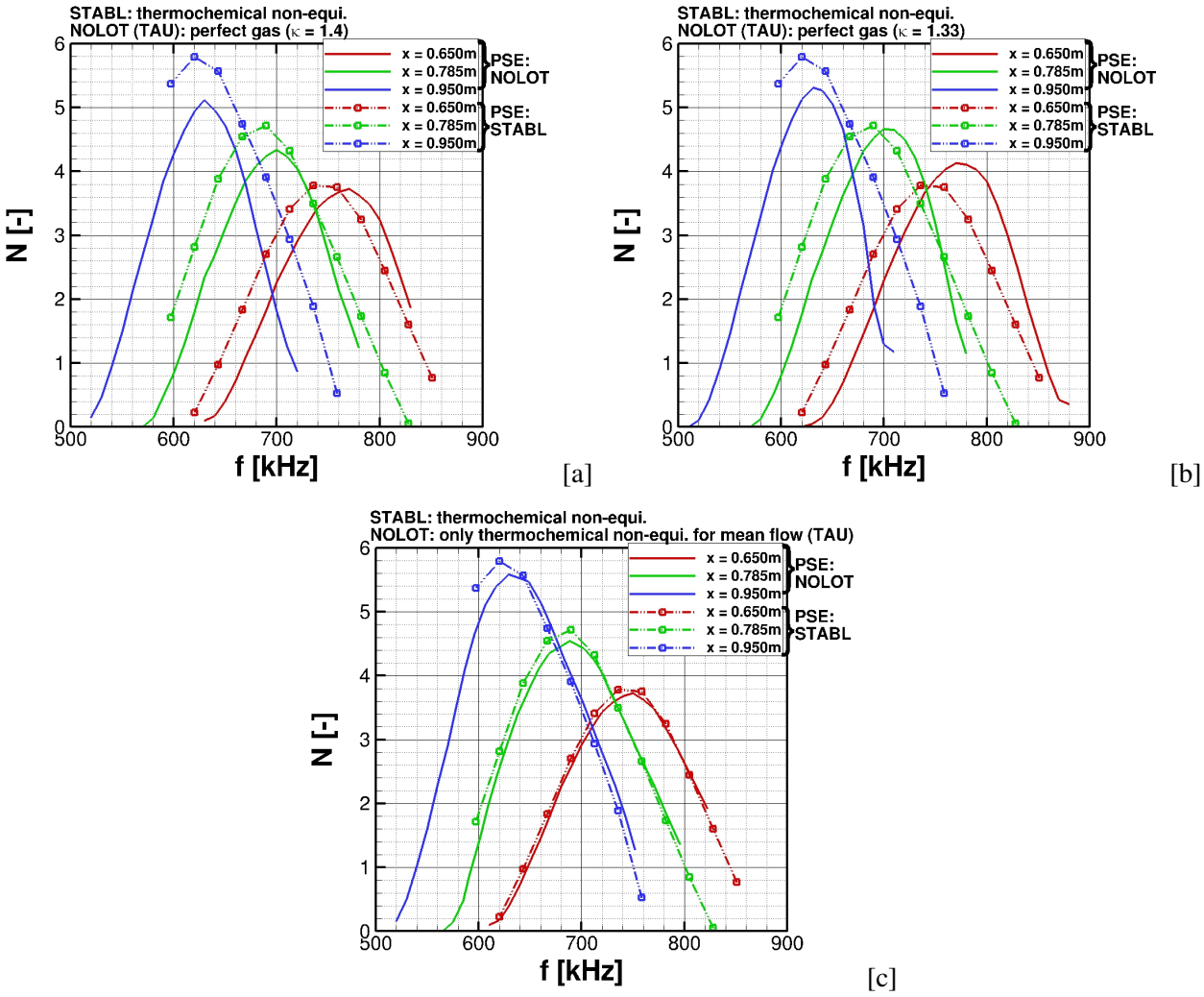

Figure 5-7: HEG-High-E, PSE, Comparison NOLOT and STABL: N = f(f).

assumption for the stability calculations result in a satisfactory agreement for the present test case. However, the error, due to the perfect gas assumption, propagates in streamwise direction and increases the discrepancy.

5.4.2.2 Comparison to Experiment: HEG-High-E

The code to code comparison of the previous Section is based on a generic test case using the nominal free-stream conditions of Table 5-1 to perform the simulations of the mean flow. For the comparison with the experimental data, the base flow simulation includes the nozzle, test camber and cone model.

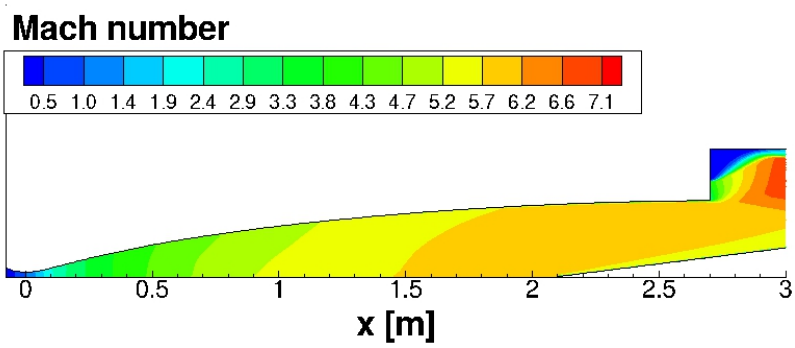

Figure 5-8: Base Flow Calculations of HEG-High-E Test Case (CFD Solver: TAU).

The grid is axially-symmetric and has about four million points clustered to the laminar walls and the shock. Based on the nozzle calibration of Wagner [9], the nozzle boundary layer is set turbulent. Due to the thermocouple measurements of the experiment, the boundary layer of the cone is known to be completely laminar. A thermochemical non-equilibrium approach based on a three temperature model is used. Figure 5-8 illustrates the Mach number distribution in the numerical nozzle - cone set up.

The second mode at the first PCB sensor position is not strong enough and still in the range of the background noise level. Thus, Figure 5-9 shows the measured amplitude spectral density (symbols) as function of the frequency for the second and third PCB sensor. The N-factors are based on NOLOT calculations using the mean flow simulation of Figure 5-9.

The numerically predicted N-factor distribution is in relatively good agreement with the measured data, but with visible differences. Although the nozzle, the test Section, and the cone model are simulated together, there are still uncertainties in the free stream conditions, which could explain the remaining differences. Nevertheless, the numerical results are in a satisfactory agreement with the experimental data.

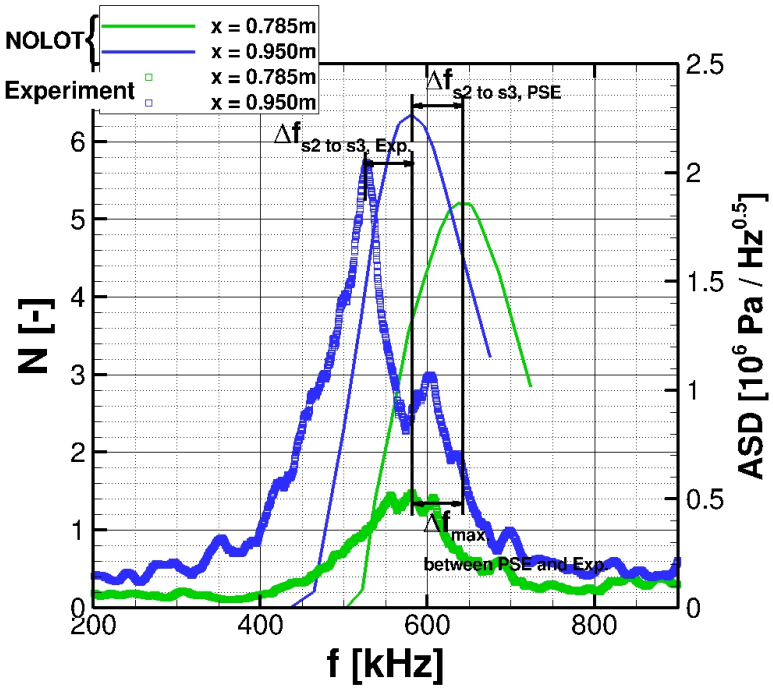

Figure 5-9: HEG-High-E, Comparison NOLOT (N-factor) and Experimental Data (ASD).

5.4.3 Second High Enthalpy Test Case (HIEST-High-E)

This Section summarizes the comparison of the second high enthalpy test case: HIEST-High-E with a total enthalpy of 10.9 MJ/kg. These test conditions for the second high-enthalpy case are chosen because of their similarity to the HEG-High-E test case, with respect to unit Reynolds number, Mach number and total enthalpy.

5.4.3.1 PSE Comparison: STABL / NOLOT (HIEST-High-E)

Figure 5-10a summarizes the PSE code to code analysis. The mean flow as well as the stability calculations of STABL, dashed lines with symbols, are performed with thermochemical non-equilibrium based on a two temperature model. For NOLOT (solid lines) the mean flow is also simulated with the thermochemical non-equilibrium approach based on a two temperature model in combination with the perfect gas assumption for the NOLOT stability calculations. Due to the increase of the error in streamwise direction, which was described in Section 5.4.2, the last sensor position was chosen for the code to code comparison to provoke the worst case with maximal deviation for the present test case.

The predicted frequency range is similar to the previous test case (HEG-HIGH-E) due to the similarity of the free stream conditions, the total enthalpy and the wind tunnel model. The difference of the maximum N-factors

as well as the corresponding most amplified frequency between NOLOT and STABL are found to be approximately 3%. This confirms the validity of the selected approach for the NOLOT analyses.

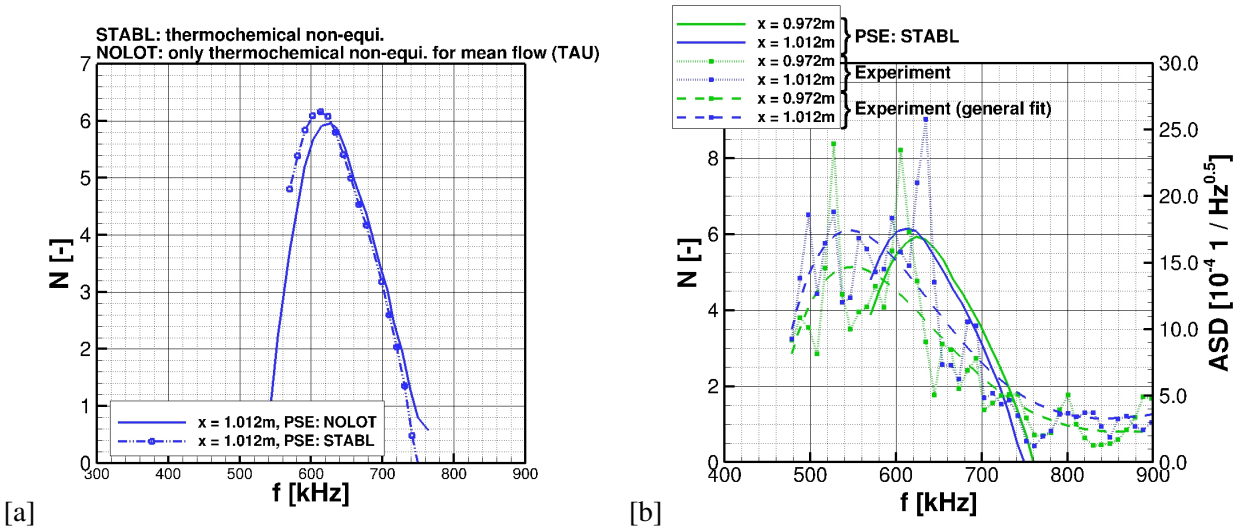

Figure 5-10: HIEST-High-E, Comparison a) NOLOT STABL and b) STABL (N-factor) Experimental Data (ASD).

5.4.3.2 Comparison to Experiment: HIEST-High-E

The last two sensor positions are chosen for the comparison conducted in this Section. Figure 5-10b shows the measured amplitude spectral density (ASD) marked as symbols. N-factors, which are based on PSE STABL calculations of the previous Section, are shown as solid lines. The last two sensors of the HIEST-High-E case are with x = 0.972m and x = 1.012m very close together. Thus, the shift of frequencies due to the thickening of the boundary layer is only clearly visible for the stability results. The predicted frequencies of the second modes are in a similar frequency range as the experimental PCB data. Due to the scatter of the PCB data for this short-duration wind tunnel, the dashed lines show general fits of the ASD functions. Compared to the numerical data, the differences are about 10% for the frequencies at the maxima, which were already discussed in the previous Section (see Section 5.4.2).

5.5 CONCLUSION

In the scope of the present study different stability codes were compared: the NOnLocal Transition analysis code (NOLOT) of the German Aerospace Center (DLR), the Stability and Transition Analysis for hypersonic Boundary Layers code (STABL) of VirtusAero and the VKI Extensible Stability and Transition Analysis code (VESTA) of the von Karman Institute.

The code to code comparison revealed good agreement for the low enthalpy reference case. The deviations of the maximum N-factors and corresponding frequencies are around 1% and are expected to be mainly caused by using different CFD solvers for the mean flow computations. Since the gas can be considered being calorically perfect, the results obtained by using an thermochemical non-equilibrium approach for the mean flow and the stability code are almost identical to the approach of considering thermochemical non-equilibrium for the mean flow only.

The focus of this chapter is the high enthalpy test cases. The main results of the code to code comparison at high enthalpy are the following:

- Real gas effects reduce the boundary layer stability and thus increase the N-factors.
- If real gas effects are of importance, it is essential to model those in the mean flow computations.
- For the present test cases only minor effects, with acceptable errors, were observed considering or neglecting real gas effects in the stability analysis.
- Nevertheless, it is important to remember that errors can built up with increasing flow length.

The comparison to the experiments shows a good agreement to the numerical data regarding the predicted/ measured frequency shift between two sensor position: for example: $\Delta f_{s1\ to\ s2,\ \mathrm{Exp.}} = \Delta f_{s1\ to\ s2,\ \mathrm{PSE}}$ was almost the same for the low enthalpy references case. The differences of the frequency at the maxima Δf_{max}, comparing the maximum N-factors with measured PCB data, are about 10%. Thus a satisfactory agreement is observed, despite with the mentioned frequency shift. Inaccuracies in the free stream conditions are the most likely reason for these deviations since the predicted N-factors are extremely sensitive towards small changes of the free stream condition and the corresponding base flow calculations.

5.6 ACKNOWLEDGEMENTS

Sandia National Laboratories is a multi-mission laboratory managed and operated by National Technology and Engineering Solutions of Sandia, LLC., a wholly owned subsidiary of Honeywell International, Inc., for the U.S. Department of Energy's National Nuclear Security Administration under contract DE-NA0003525.

5.7 REFERENCES

[1] Schneider, S., "Flight Data for Boundary Layer Transition at Hypersonic and Supersonic Speeds," *Journal of Spacecraft and Rockets*, Vol. 36, No. 1, 1999, pp. 8–20.

[2] Schneider, S., "Hypersonic Laminar-Turbulent Transition on Circular Cones and Scramjets Forebodies," *Process in Aerospace Sciences*, Vol. 40, No. 1-2, 2004, pp. 1–50.

[3] Mack, L.M., "Boundary Layer Linear Stability Theory," *AGARD - Special Course on Stability and Transition of Laminar Flow*, Vol. R-709, 1984, pp. 2–1 – 2–71.

[4] Hannemann, K., Martinez Schramm, J., and Karl, S., "Recent Extensions to the High Enthalpy Shock Tunnel Göttingen (HEG)," *2nd International Atmospheric Reentry Association Days*, Arcachon, France, October 2008.

[5] Itho, K., Ueda, S., Komuro, T., Sato, K., Tanno, H., and Takahashi, M., "Hypervelocity Aerothermodynamic and Propulsion Research Using a High Enthalpy Shock Tunnel HIEST," *9th International Space Planes and Hypersonic Systems and Technologies Conference*, Vol. 12, 1999, pp. 93–98.

[6] Reimann, B. and Hannemann, V., "Numerical Investigation of Double-Cone and Cylinder Experiments in High Enthalpy Flows Using the DLR TAU Code," *48th AIAA Aerospace Sciences Meeting Including the New Horizons Forum and Aerospace Exposition*, 2010.

[7] Schwamborn, D., Gerhold, T., and Heinrich, R., "The DLR Tau-code: Recent Applications in Research and Industry," *European Conference on Computational Fluid Dynamics ECCOMAS CFD*, 2006.

[8] Mack, A. and Hannemann, V., "Validation of the Unstructured DLR-TAU-Code for Hypersonic Flows," *32nd AIAA Fluid Dynamics Conference and Exhibit*, St. Louis, Missouri, 2002, AIAA 2002-3111.

[9] Wagner, A., *Passive Hypersonic Boundary Layer Transition Control Using Ultrasonically Absorptive Carbon-Carbon Ceramic with Random Microstructure*, Ph.D. thesis, Katholieke Universiteit Leuven, 2014.

[10] Takahashi, M., Kodera, M., Itoh, K., Komuro, T., Sato, K., and Tanno, H., "Influence of Thermal Non-Equilibrium on Nozzle Flow Condition of High Enthalpy Shock Tunnel HIEST," *AIAA Paper-2009-7267*, 2009.

[11] Tanno, H., Komuro, T., Sato, K., Itoh, K., and Takahashi, M., "Measurement of Surface Pressure Fluctuation in Hypersonic High-Enthalpy Boundary Layer on a 7-Degree Cone Model," *41st AIAA Fluid Dynamics Conference and Exhibit*, 2011.

[12] Wagner, A., Kuhn, M., Martinez Schramm, J., and Hannemann, K., "Experiments on Passive Hypersonic Boundary Layer Control Using Ultrasonically Absorptive Carbon/Carbon Material with Random Microstructure," *Experiments in Fluids*, Vol. 54, 2013, pp. 1–10.

[13] Peroomian, O. and Chakravarthy, S., "A 'Grid-Transparent' Methodology for CFD," *35th Aerospace Sciences Meeting and Exhibit*, Reno,NV, 1997, AIAA 97-0724.

[14] Lani, A., Villedieu, N., Bensassi, K., Kapa, L., Panesi, M., and Yalim, M.S., "COOLFluiD: an Open Computational Platform for Multi-Physics Simulation," *21st AIAA Computational Fluid Dynamics Conference*, San Diego, CA, 2013, AIAA 2013-2589.

[15] Degrez, G., Lani, A., Panesi, M., Chazot, O., and Deconinck, H., "Modelling of High-Enthalpy, High-Mach Number Flows," *Journal of Physics D: Applied Physics*, Vol. 42, 2009, pp. 1–16, Course Note 143.

[16] Johnson, H.B. and Candler, G.V., "Hypersonic Boundary Layer Stability Analysis Using PSE-Chem," *35th AIAA Fluid Dynamics Conference and Exhibit*, Toronto, Ontario, Canada, 2005, AIAA Paper 2005-5023.

[17] Hein, S., Bertolotti, F.P., Simen, M., Hanifi, A., and Henningson, D., "Linear Nonlocal Instability Analysis - the Linear NOLOT Code," Tech. Rep. IB-223-94 A56, DLR, 1994.

[18] Pinna, F., "VESTA toolkit: a Software to Compute Transition and Stability of Boundary Layers," *43rd Fluid Dynamics Conference, Fluid Dynamics and Co-located Conferences*, 2013.

[19] Pinna, F. and Groot, K., "Automatic Derivation of Stability Equations in Arbitrary Coordinates and for Different Flow Regimes," *44th AIAA Fluid Dynamics Conference*, 2014.

[20] Pinna, F., *Numerical Study of Stability of Flows from Low to High Mach Number*, Ph.D. thesis, Sapienza Università di Roma, 2012.

[21] Pinna, F. and P. Rambaud, P., "Linear Stability Analysis of Hypersonic Boundary Layer," *7th Aerothermodynamics Symposium*, 2011.

[22] Malik, M.R., "Numerical Methods for Hypersonic Boundary Layer Stability," *Journal of Computational Physics*, Vol. 86, No. 2, 1990, pp. 376–413.

[23] Arnal, D., "Boundary Layer Transition: Special Course on Progress in Transition Modelling," *AGARD Report*, Vol. R-793, No. 761, 1994, pp. 2–1 – 2–61.

[24] Özgen, S. and Kırcalı, S., "Linear Stability Analysis in Compressible, Flat-Plate Boundary-Layers," *Theoretical and Computational Fluid Dynamics*, Vol. 22, 2008, pp. 1–20.

[25] Wagnild, R.M., *High Enthalpy Effects on Two Boundary Layer Disturbances in Supersonic and Hypersonic Flow*, Ph.D. thesis, University of Minnesota, 2012.

[26] Wartemann, V., Wagner, A., Wagnild, R., Pinna, F., Miró Miró, F., and Tanno, H., "Code to Code Comparison on Hypersonic High Enthalpy Transitional Boundary Layers," *2018 AIAA Aerospace Sciences Meeting*, Kissimmee, Florida, 2018, AIAA 2018-0351.

[27] Wartemann, V., *Mack-Moden-Dämpfung Mittels Mikroporöser Oberflächen im Hyperschall*, Ph.D. thesis, Technische Universität Braunschweig, 2014.

[28] Wagner, A., Hannemann, K., Wartemann, V., Tanno, H., and Ito, K., "Free Piston Driven Shock Tunnel Hypersonic Boundary Layer Transition Experiments on a Cone Configuration," *RTO - Hypersonic Laminar-Turbulent Transition Conference*, 2012.

[29] Wartemann, V., Lüdeke, H., Willems, S., and Gülhan, A., "Stability Analyses and Validation of a Porous Surface Boundary Condition by Hypersonic Experiments on a Cone Model," *7th Aerothermodynamics Symposium*, Brugge, Belgium, 2011.

Chapter 6 - CHARACTERIZATION OF FREESTREAM DISTURBANCES IN CONVENTIONAL HYPERSONIC WIND TUNNELS

Lian Duan
Missouri University of Science and Technology
UNITED STATES

Meelan M. Choudhari and Amanda Chou
NASA Langley Research Center
UNITED STATES

Federico Munoz and Rolf Radespiel
TU Braunschweig
GERMANY

Thomas Schilden and Wolfgang Schröder
RWTH Aachen University
GERMANY

Eric C. Marineau
AEDC White Oak
UNITED STATES

Katya M. Casper
Sandia National Laboratories
UNITED STATES

Ross S. Chaudhry and Graham V. Candler
University of Minnesota
UNITED STATES

Kathryn A. Gray and Steven P. Schneider
Purdue University
UNITED STATES

6.0 NOMENCLATURE

C_p	heat capacity at constant pressure, J/(K·kg)
E	hot-wire voltage, J/C
H	hot-wire variables, dimensionless
M	Mach number, $M = u/a$, dimensionless
M_r	relative Mach number, $M_r = (U_\infty \quad U_b)/a_\infty$, dimensionless
Re_τ	friction Reynolds number, $Re_\tau = \rho_w u_\tau \delta/\mu_w$, dimensionless
R	wind-tunnel nozzle radius, m
R	ratio of transfer functions with two pitot probe geometries, dimensionless
R	correlation function in modal analysis, dimensionless
S	ratio of transfer functions with two pitot probe geometries, dimensionless

T	temperature, K
T_r	recovery temperature, K
T_0	total temperature, K
U_∞	freestream velocity, m/s
U_b	bulk propagation speed of freestream acoustic disturbances, m/s
a	speed of sound, m/s
f	frequency, Hz
k	transfer function, dimensionless
$\dot{m}$	mass flow rate, $\dot{m} = \rho u$, kg/(m^2·s)
p	pressure, Pa
P	total pressure, Pa
r	radial coordinate, m
r	transfer function with respect to preshock density in modal analysis, dimensionless
s	entropy, J/K
u_τ	friction velocity, m/s
x	streamwise direction of the right-hand Cartesian coordinate, m
x_t	axial distance from throat, m
y	spanwise direction of the right-hand Cartesian coordinate, m
z	wall-normal direction of the right-hand Cartesian coordinate, m
z_n	normal distance from the wall, m
α	frequency-specific wavenumber in the streamwise direction, m ^{1}
β	frequency-specific wavenumber in the vertical direction, m ^{1}
γ	specific heat ratio, dimensionless
δ	boundary layer thickness, m
δ^*	displacement thickness, m
μ	dynamic viscosity, kg/(m·s)
ϕ	randomly-selected phase, dimensionless
ρ	density, kg/m^3
θ	coefficient in hot-wire modal analysis, dimensionless
ζ	coefficient in hot-wire modal analysis, dimensionless
ω	angular frequency, rad/s

Subscripts

ac	acoustic
en	entropy
rms	root mean square
t	transducer-measured quantities
vo	vortical
w	wall variables
∞	freestream variables
0	stagnation quantities
1	preshock quantities of a pitot probe
2	post-shock quantities of a pitot probe

Superscripts

$+$	inner wall units
$\overline{(\cdot)}$	averaged variables
$(\cdot)'$	perturbation from averaged variables

6.1 INTRODUCTION

Prediction of boundary-layer transition is a critical part of the design of hypersonic vehicles because of the large increase in skin-friction drag and surface heating associated with the onset of transition. Testing in conventional (noisy) wind tunnels has been an important means of characterizing and understanding the boundary-layer transition (BLT) behavior of hypersonic vehicles. Because the existing low disturbance, i.e., quiet, facilities operate only at Mach 6, moderate Reynolds numbers, fairly small sizes, and low freestream enthalpy, conventional facilities will continue to be employed for testing and evaluation of hypersonic vehicles, especially for ground testing involving other Mach numbers, higher freestream enthalpies, and larger models. To enable better use of transition data from conventional facilities and more accurate extrapolation of wind-tunnel results to flight, one needs an in-depth knowledge of the broadband disturbance environment in those facilities as well as of the interaction between the freestream disturbances with laminar boundary layers.

Freestream disturbances in conventional high-speed wind tunnels are usually composed of acoustic disturbances, vorticity disturbances and fluctuations of flow entropy. The acoustic disturbances are mainly generated within the high-speed, turbulent boundary layers along the nozzle walls and radiated into the wind tunnel test section [1]. The intensity of the acoustic disturbances increases rapidly with flow Mach number; and hence, these disturbances are likely to dominate the overall disturbance environment at Mach numbers of 2.5 or above [2–5] and can strongly affect the transition processes. Theoretical models for acoustic radiation from a supersonic boundary layer were developed by Phillips [6] and Ffowcs-Williams [7], who attributed a major cause of the acoustic radiation to eddy Mach waves from boundary layer turbulence convecting supersonically with respect to the free stream. A lack of adequate knowledge concerning the boundary layer turbulence restricted the theoretical predictions to just the intensity of the freestream acoustic fluctuations. Fluctuations of freestream vorticity and entropy stem from the flow state in the tunnel settling chamber and the subsequent changes imposed by the wind tunnel nozzle. Figure 6-1 gives a schematic of the origin of freestream disturbances in a supersonic/hypersonic wind tunnel.

The freestream disturbances in conventional tunnels can impact not only the transition location, but possibly the transition mechanism as well, and their effect on transition cannot be quantified in terms of a single metric corresponding to the root mean square (rms) amplitude, as indicated by the measurements at Purdue University [8] and AEDC Tunnel 9 [9]. Unfortunately, existing measurements mostly provide data in terms of rms values alone, i.e., without an evaluation of the disturbance spectra up to the high frequencies observed in transitional hypersonic boundary layers. Although a number of investigators have reported measurements of freestream disturbance intensity in high-speed facilities at both supersonic and hypersonic Mach numbers (see, for example, [10–14]), these measurements are largely limited to single-point information (e.g., freestream pitot pressure fluctuations) and the measurements by Laufer [3, 15] still reflect one of the few datasets that are detailed enough to be suitable for comparison or model development.

Recently, new probes and new instrumentation have become available to the research community that greatly help the physical characterization of freestream disturbance levels [16, 17]. The new experimental data measured with fast PCB132 pressure sensors are able to cover a spectral range of disturbances that were previously not achieved by using hot-wire probes. Progress in direct numerical simulation (DNS) as well as the rapid deployment of high-performance computing facilities across the US and around the world provide the opportunity to address the problem of the generation of random acoustic disturbances at the nozzle walls and the transfer of those disturbances to the location of a pitot-mounted sensor, making the numerical rebuilding of transition

experiments possible. The progress in both experimental and numerical techniques has resulted in a significantly improved knowledge base pertaining to the nature and spectral contents of wind tunnel freestream disturbances and holds the potential to bridge the gap between quiet tunnels, conventional wind tunnels, and flight.

The current paper summarizes the coordinated experimental and numerical work undertaken by the NATO STO AVT-240 specialists group to characterize the freestream disturbances in conventional hypersonic ground facilities. Definitive progress has been made possible by coordinating international research efforts in this difficult but important area. Specifically, tunnel noise has now been measured with freestream Pitot probes mounted with new, fast PCB132 pressure transducers that allow single-point noise characterization up to and above the second-mode frequencies in most tunnels. DNS of acoustic radiation from the nozzle wall have been conducted to provide additional multi-point information of the acoustic disturbance field that would help guide the application of receptivity theories based on more realistic input concerning the disturbance environment. The computed freestream acoustic disturbance field including the acoustic angle has also been used to define inflow conditions for computations of hypersonic flow around a Pitot probe, which yield a transfer function that relates the transducer-measured (postshock) spectrum to the (preshock) freestream disturbance spectrum. Such a transfer function can be used to directly correct for the effect of Pitot probe geometry on the measurement. The additional multi-sensor measurements with both Pitot and hot-wire probes can provide further details related to the modal content of freestream disturbances in a facility. All in all, the coordinated experimental and numerical work can be integrated to provide as much information as possible on tunnel noise, with the purpose of developing a “tunnel-like” disturbance field for input into transition computations. Although much work remains to be done to achieve that goal, such international research efforts will eventually enable improved ground-to-flight scalability of the laminar-turbulent transition data from conventional high-speed wind-tunnel facilities.

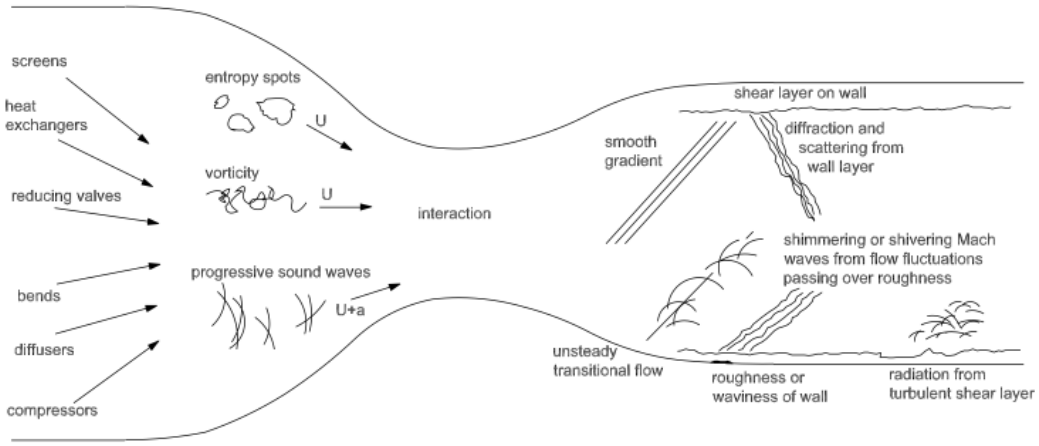

Figure 6-1: Schematic of Freestream Disturbances in Supersonic/Hypersonic Wind Tunnels (Adapted from Schneider [18]).

The paper is structured as follows. Measurements of freestream disturbances in various high-speed facilities with new probes and new instrumentation as well as closely related DNS are outlined in Section 6.2. Section 6.3 presents DNS studies for synthesizing the naturally occurring, random acoustic disturbances induced by tunnel wall turbulence. Section 6.4 is focused on numerical rebuilding of tunnel freestream disturbances from the measurement of intrusive probes. Section 6.5 outlines a summary of the overall findings and a general vision for future research.

6.2 TUNNEL FREESTREAM DISTURBANCE MEASUREMENT

Measurements of freestream disturbances in multiple high-speed facilities at hypersonic Mach numbers have been reported with new probes and new instrumentation. Tunnel noise has now been measured with new, fast PCB132 pressure sensors that allow noise characterization up to 1 MHz, which is above the second-mode frequencies in most tunnels. Enabled by the coordinated international research effort, a comparison of tunnel noise measurements in different hypersonic wind tunnels is made that allows for cross-validation and, more importantly, sheds light on whether tunnel-to-tunnel noise variation follows a relatively simple pattern as suggested by Pate's correlation [19, 20].

Figure 6-2 shows the power spectral density (PSD) of freestream pitot-pressure fluctuations measured in multiple high-speed facilities. The measurement data covers a wide range of tunnel conditions, including the Hypersonic Ludwieg Tube Braunschweig (HLB), the Purdue Boeing/AFOSR Mach-6 Quiet Tunnel (BAM6QT), the NASA 20-Inch Mach 6, the Sandia Hypersonic Wind Tunnel at Mach 8 (HWT-8), and the AEDC Tunnel 9; these wind tunnels generate freestream Mach numbers ranging from Mach 6 to 14. The PSD are computed with pressure signals measured by Kulite® sensors in the low-frequency range up to $f \approx 20$ kHz and by PCB PIEZOTRONICS, Inc. sensors in the high-frequency range up to $f \approx 1$ MHz. The frequency range measured by the PCB® sensors covers that of second-mode waves. For all the cases, the freestream pitot-pressure spectrum has a similar rate of spectral roll-off at high frequencies. A spectral slope of $f^{-3.5}$ provides a good fit to the data over the second-mode frequency range. The data suggests that the freestream disturbance spectrum relevant to second-mode-dominated boundary-layer transition may be modeled with a constant-slope model of $\Phi \sim f^{-m}$. Such a model has been used by Marineau [21] who proposed a new amplitude method for predicting second-mode-dominated boundary-layer transition in hypersonic wind tunnels. Marineau's amplitude method was found to reduce the error between the measured and predicted start of transition, compared with predictions based on a constant transition N factor [21]. Because of measurement difficulties at high frequencies and the nontrivial transfer function associated with measurement probes, physics-based transition models of this type cannot rely solely upon the measurement database and synergistic numerical simulations are also important in developing more accurate and reliable models for the tunnel disturbance environment. Direct computations of acoustic freestream disturbances are discussed in Section 6.3 below, whereas the recovery of actual freestream disturbances from probe measurements is addressed in Section 6.4.

6.3 DIRECT SIMULATION OF TUNNEL ACOUSTIC DISTURBANCES

An important component of the recent progress in tunnel-noise characterization is to use DNS for synthesizing the naturally occurring, random acoustic disturbances created within the tunnel wall turbulence. Given that in unheated conventional hypersonic tunnels with adequate flow conditioning, the freestream disturbance environment is dominated by acoustic radiation from tunnel-wall turbulent boundary layers (TBL) [2–5] (Figure 6-3), DNS can be used to resolve both the tunnel-wall boundary layer and the near field of acoustic fluctuations radiated by the boundary layer, thus allowing access to tunnel-noise quantities that are difficult to obtain otherwise and for clarifying the physics of noise generation in conventional hypersonic facilities.

The research teams of Missouri S&T and NASA Langley developed a systematic strategy that first established the feasibility of DNS in the context of a canonical, single-wall boundary layer (Figure 6-4) across a range

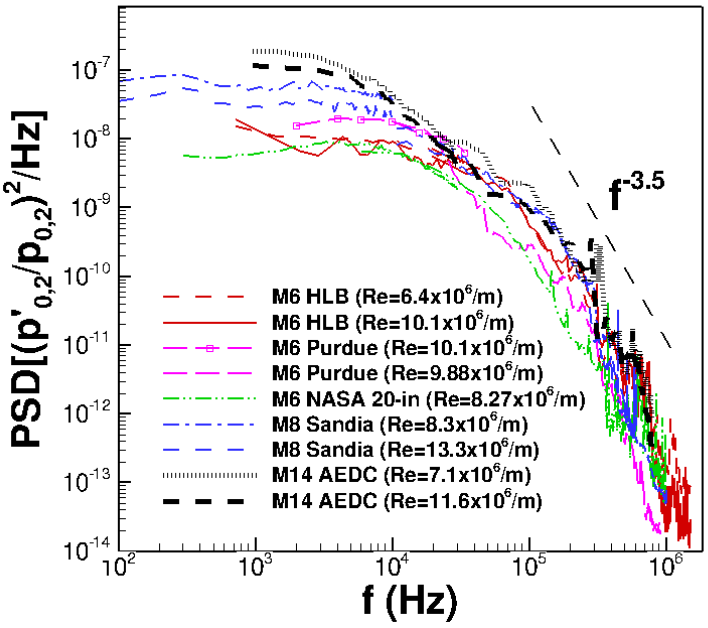

Figure 6-2: The Pressure Transducer Models and the Freestream Locations for Pitot-pressure Measurements are Listed as Follows: HLB Mach 6 (Kulite® & PCB® : x_t = 2.69 **m,** r = 0.1 **m); Purdue BAM6QT-noisy (Kulite® :** x_t = 2.3368 **m,** r = 0 **m & PCBR :** x_t = 2.2098 **m,** r = 0 **m); NASA 20-Inch Mach 6 (Kulite® & PCBR : =** x_t = 2.25 **m,** z = 0.09042 **m); Sandia HWT-8 (Kulite® & PCB® :** x_t = 2.3368 **m,** r = 0 **m); AEDC Tunnel 9 Mach 14 (Kulite® & PCB® :** x_t = 13.97 **m,** r = 0.38 **m).**

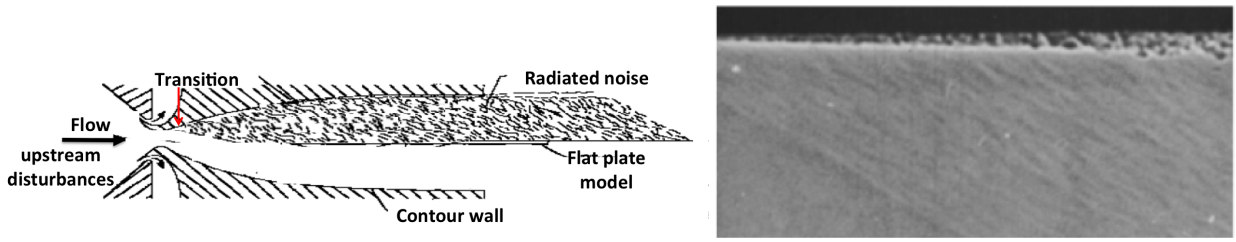

(a) (b)

Figure 6-3: (*a*) Sketch of the Test Core of a Mach 3.5 Wind Tunnel and Radiated Noise from the Tunnel-wall Turbulent Boundary Layer (Adapted from Beckwith & Miller [22]); (*b*) Experimental Image of a Shadowgraph for a Mach 3.5 Boundary Layer, which Shows that the Acoustic Nearfield in the Freestream Region Consists of Randomly Spaced Wavepackets (Courtesy of NASA Langley).

of Mach numbers [23–27]. The DNS of acoustic radiation from a single-wall boundary layer circumvented the difficulties associated with the reflection/reverberation of acoustic waves from all sides of a wind tunnel nozzle and, thus, helped clarify the physical process of acoustic noise generation. The physical realism and accuracy of the DNS flow fields have been established by comparison with existing experimental results at similar flow conditions. In particular, the coordinated experimental and numerical work undertaken by the international specialists group has led to the first successful comparison between numerical predictions and wind tunnel measurements of surface pressure fluctuations underneath a hypersonic TBL, with the experimental

data measured on the nozzle walls of the Purdue BAM6QT, Sandia HWT-8, and AEDC Tunnel 9 (Figure 6-5). Very good agreement of wall-pressure PSD between the DNS and the nozzle-wall measurements has been achieved at Mach 6 and 8. The DNS-predicted PSD deviates from the measured PSD at low frequencies for the Mach 14 case. The large disparity in Karman Reynolds numbers during the experiment and the DNS may have contributed to the discrepancy in wall pressure PSD; however, further work is necessary to identify the precise reasons and to resolve the differences at low frequencies. The cause of the spurious peak at a $f \approx 40$ kHz in the wall-pressure PSD measured at Mach 14 is unknown and is currently under investigation.

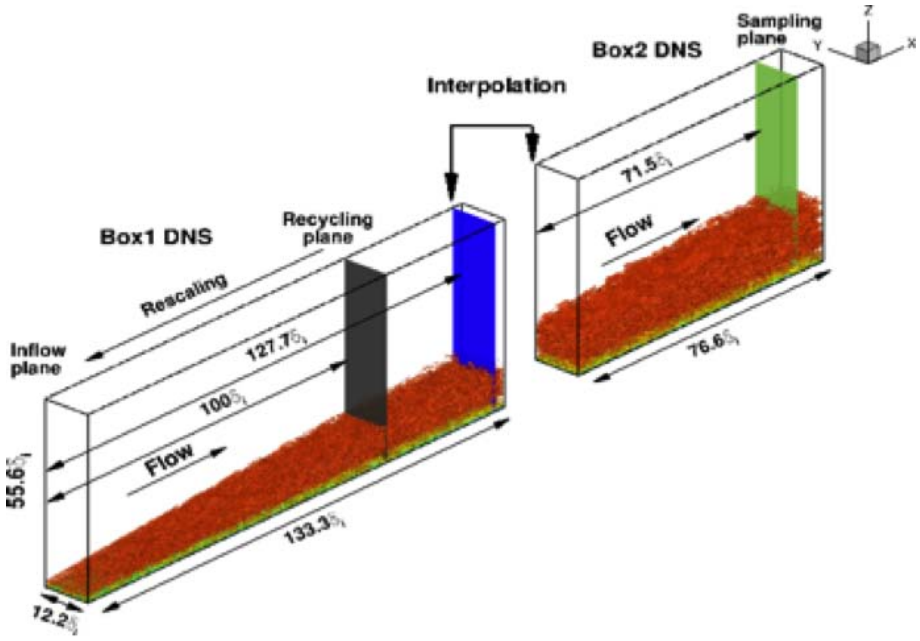

Figure 6-4: Computational Domain and Simulation Setup for DNS of a Mach 14 Turbulent Boundary Layer with Flow Conditions Representative of the Nozzle Exit of AEDC Tunnel 9 (from Figure 1 [24]).

The DNS provided access to tunnel-noise quantities that are difficult to obtain otherwise, including high-frequency PSD (Figure 6-6a), propagation speed (Figure 6-6b), the inclination angle of the prominent acoustic structures (Figure 6-7a), spatial and temporal correlations (Figure 6-7b), and acoustic sources (Figure 6-8). DNS showed that tunnel noise consists of a field of broadband, stochastic acoustic waves that have a finite spatiotemporal coherence and propagate at oblique angles to the free stream, rather than as a deterministic train of time harmonic, planar waves as commonly assumed in receptivity studies; the acoustic sources that give rise to the pressure fluctuations in the free stream are located mostly in the inner layer of the tunnel-wall turbulent boundary layer and are strongly influenced by wall cooling, as seen from the differences in peak source location in Figure 6-8 (see Ref. [23] for an explanation of this behavior); the inclination angle of the prominent structures associated with acoustic fluctuations within the freestream region, visualized by instantaneous contours of the density gradient as shown in Figure 6-7a, is similar to the Mach angle for the relative Mach number M_r (between the sources and the free stream). The findings are consistent with the classic theory of "eddy Mach-wave radiation" and the early measurements of freestream noise by Laufer [3] during his unique wind tunnel experiments.

After the feasibility of the DNS was established in the context of a single flat wall, the DNS conditions were extended to those within a confined enclosure to mimic the typical case of multiple tunnel walls in an experiment.

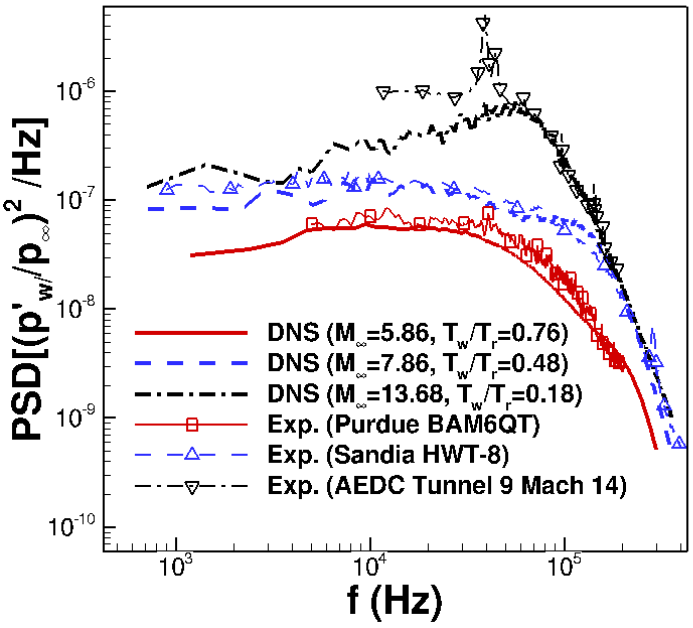

Figure 6-5: The Pressure Transducer Models and the Axial Locations for Surface-pressure Measurements are Listed as Follows: Purdue BAM6QT (PCB® : x_t = 2.679 m; Re = 9.69 x 10^6/m); Sandia HWT-8 (Kulite®: x_t = 2.2024 m & PCB®: x_t = 2.679 m; Re = 9.69 x 10^6/m); AEDC Tunnel 9 Mach 14 (PCB®: x_t = 11.83 m; Re = 7.2 x 10^6/m).

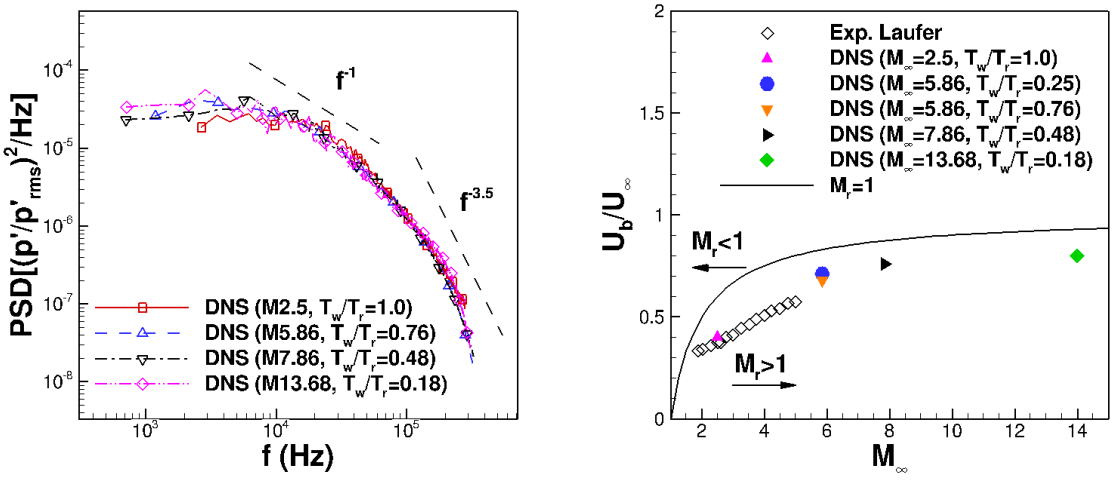

(a) (b)

Figure 6-6: (*a*) Power Spectral Density and (*b*) Bulk Propagation Speed of the Freestream Acoustic Pressure Fluctuations as a Function of the Freestream Mach Number. The Bulk Propagation Speed is Estimated as the Ratio between the Streamwise Spatial Distance between Probe Pairs, and the Time Lags corresponding to the Peak of the Cross-correlation Curve.

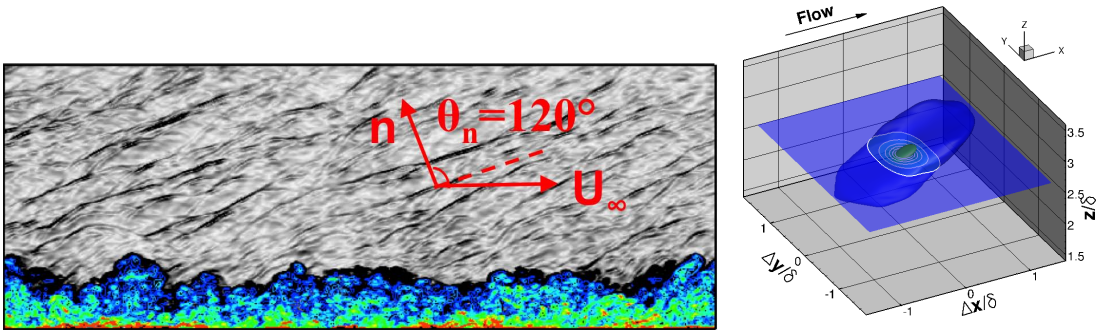

(a) (b)

Figure 6-7: Freestream Acoustic Structures Radiated from a Mach 5.86 Turbulent Boundary Layer at a Wall-to-recovery Temperature Ratio of $T_w/T_r = 0.76$ [26]. (*a*) Instantaneous Flow Visualization, with the Freestream Acous-tic Wave Front Visualized by the Grey Contours of the Density Gradient. (*b*) Three-dimensional Isosurfaces of the Spatial Correlation Coefficient to Illustrate Statistically Significant 3-D Acoustic Structures in the Free Stream.

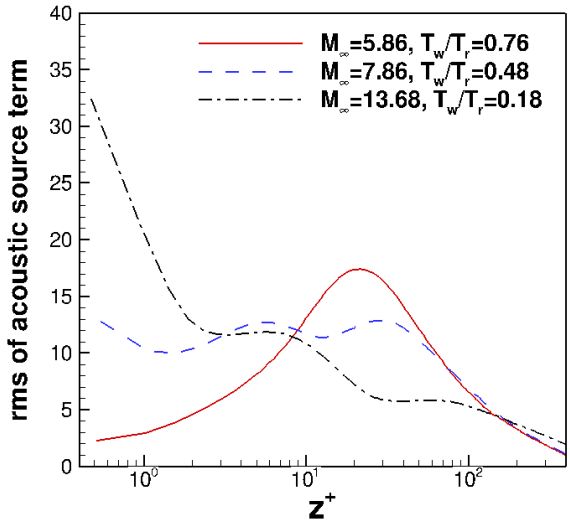

Figure 6-8: Acoustic Source Terms, $\partial u_i/\partial x_j \;\; \partial u_j/\partial x_i$, Normalized by δ^2/U_∞^2, of Hypersonic Turbulent Boundary Layers that Give Rise to the Acoustic Pressure Fluctuations in the Free Stream. The RMS of the Source Terms are Normalized by δ^2/U_∞^2, and z^+ is the Wall-normal Distance Normalization by Local Viscous Length. The Acoustic Source Terms are Defined according to the Acoustic Analogy by Phillips [6].

DNS were carried out in stages corresponding to increasing complexity and computational cost, progressing from internal noise within a double-wall (channel) configuration [28] to an axisymmetric cylinder [29], and finally, a full-scale nozzle of a hypersonic wind tunnel (Figure 6-9). These simulations have shed light on the effect of geometry on the noise field and, in the future, would help enable practical applications of the simulation data for freestream disturbances in the context of actual wind-tunnel experiments. Detailed results of DNS with multiple tunnel walls were reported in Ref. [28–30].

The most recent outcome of these DNS studies was the simulation of acoustic disturbances within the nozzle of a Mach 6 Hypersonic Ludwieg Tube, Braunschweig (HLB), at the Technical University of Braunschweig (TUB). The DNS are carried out in two stages involving overlapping streamwise domains as shown in Figure 6-9. The selected DNS domain covers the origin of most of the acoustic sources responsible for generating freestream noise in the test section, as it includes the portion of the nozzle with high freestream Mach numbers, and, thus, with large intensity of noise radiation. The DNS inflow is extracted from a precursor Reynolds-Averaged Navier-Stokes (RANS) calculation that simulates the full-domain HLB geometry, including the storage tube, the fast acting valve, the de Laval nozzle and the test section. The flow conditions of the DNS are representative of the operational conditions of HLB with $P_{0,\infty} = 7.3$ bar, $T_{0,\infty} = 470$ K, and the flow conditions are relevant to transition measurement. As seen at the top of Figure 6-9, the HLB configuration starts from the storage tube ahead of the nozzle throat, which is located at $x \approx 1.41$ m. The nozzle spans from $x \approx 1.41$ m to $x \approx 3.8$ m, followed by the test section. The DNS domain starts slightly downstream of the nozzle throat at $x = 2.0$ m with a local freestream Mach number of $M_\infty = 3.85$ and ends in the test section region at $x = 4.15$ m, with a freestream Mach number of $M_\infty = 5.88$. Good comparison was achieved for the freestream Mach number distribution along the nozzle axis among DNS, RANS, and theory (Figure 6-10). The DNS methodologies, including numerical methods, boundary conditions, and grid resolutions, are similar to those described in Ref. [30].

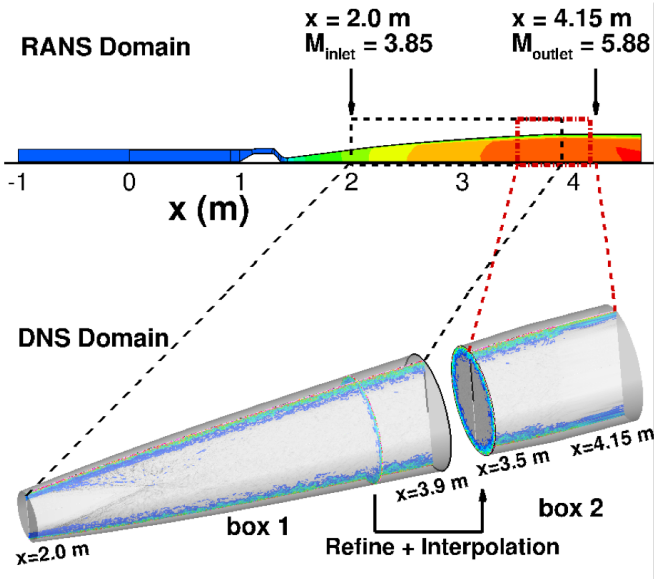

Figure 6-9: DNS of Acoustic Disturbances within the Nozzle of Mach 6 Hypersonic Ludwieg Tube at the Technical University of Braunschweig. The Flow Conditions of the DNS are Representative of the Operational Conditions of HLB with $P_{0,\infty} = 7.3$ bar, $T_{0,\infty} = 470$ K.

Figure 6-11 shows an instantaneous visualization of the density gradient associated with the radiated acoustic field. The prominent structures associated with acoustic fluctuations within the freestream region exhibit a preferred orientation of $\theta = 28^\circ \pm 2^\circ$ with respect to the nozzle centerline within the streamwise-radial plane. The preferred orientation is determined by inspecting instantaneous planar visualizations of the contours of the density gradient. This inclination angle in HLB is similar to that for a single flat plate (Figure 6-7), considering that the nozzle wall upstream of the nozzle exit also forms an angle of approximately 3° with respect to the axis. The density gradients reveal the omnidirectional origin of the acoustic field within a given cross-section of the nozzle, which adds to the stochastic nature of the wave front pattern at a given axial location. Because of the

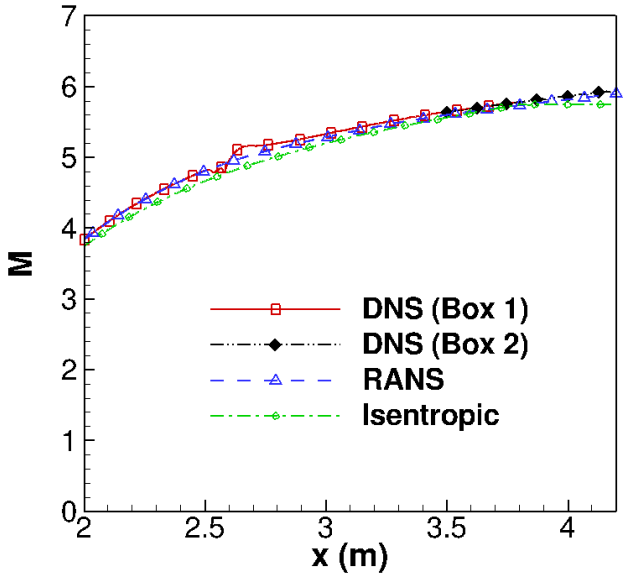

Figure 6-10: Comparison of Mach Number Distribution along the HLB Nozzle Axis among DNS, RANS, and Theory.

limited length of the nozzle and shallow acoustic propagation angles (with respect to the flow direction), the number of acoustic reflections from the nozzle wall that contribute to the acoustic signal at the nozzle exit plane is expected to be small. Thus, additional simulations are required to establish the relative contribution from those acoustic reflections, i.e., the reverberation effect.

Figure 6-12 shows that the rms pressure fluctuation field is nearly homogeneous outside the boundary layer, with a value of approximately 2.1% of the mean freestream pressure near the nozzle exit ($x = 3.8$ m). The above value of p'_{rms}/p_∞ outside the nozzle-wall boundary layer ($z_n/\delta > 1$) is significantly higher than that induced by the turbulent boundary layer over a single flat plate at a similar freestream Mach number. This increase in the noise intensity is believed to be caused by the combined effect of acoustic radiation arriving from different azimuthal segments of the axisymmetric nozzle wall. For both the nozzle and the flat plate, the DNS results show a similar frequency content and bulk propagation speed of freestream pressure fluctuations (Figure 6-13).

The current simulations described in this section have paved the way for improved simulations including a larger section of the nozzle and the full test section downstream of the nozzle exit. Additionally, further analysis is required to establish the dependence of noise characteristics on the tunnel operating conditions such as the reservoir conditions and the unit Reynolds number; experimental measurements of the nozzle boundary layer profiles are needed to provide further validation of the DNS and offer important scaling parameters to extrapolate noise characteristics to a different tunnel condition.

6.4 RECOVERY OF TUNNEL FREESTREAM DISTURBANCES

Another area of the internationally coordinated research effort is to recover tunnel noise spectrum from pitot-probe measurements and characterize the modal contents of tunnel freestream disturbances by modal analysis.

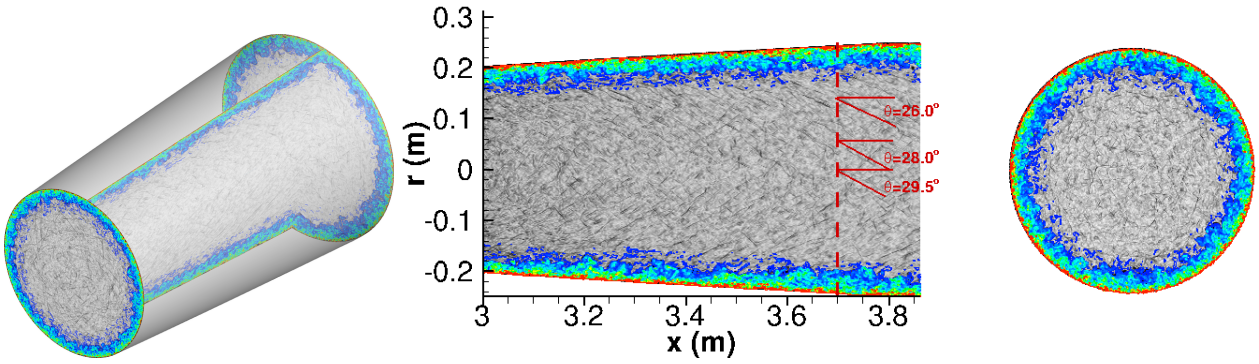

(a) (b)

Figure 6-11: Numerical Schlieren Images (i.e., Density Gradient Contours) of Radiated Acoustic Waves within the Nozzle of HLB. (a) Three Dimensional Volume, $3.0 < x < 3.8$ m; (b) Streamwise-radial Plane ($3.0 < x < 3.8$ m) and Cross Section at $x = 3.7$ m. θ is the Inclination Angle of the Prominent Structures Associated with Acoustic Fluctuations within the Freestream Region; the Vertical Dashed Line Indicates the Axial Location of the Selected Cross Section Visualized in the Right Panel of (b).

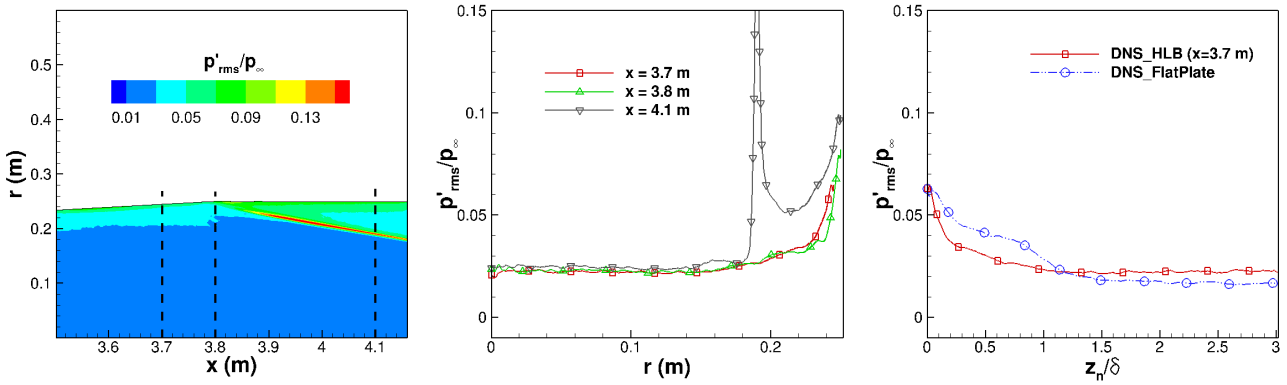

(a) (b) (c)

Figure 6-12: RMS Pressure Fluctuation Profile Induced by the Turbulent Boundary Layer over the HLB Nozzle Wall. (a) Streamwise-radial Contour of p'_{rms}/p_∞; (b) p'_{rms}/p_∞ as a Function of Radial Coordinate r at Multiple Streamwise Locations; (c) Comparison of p'_{rms}/p_∞ Induced by the Turbulent Boundary Layer over the HLB Nozzle Wall and a Single Flat Plate at the Same Freestream Conditions. $r = 0$ Corresponds to the Nozzle Axis; and the Vertical Dashed Lines in (a) Indicate the Streamwise Locations of the Selected Line Plots in (b). z_n is the Wall-normal Distance.

Freestream disturbances in a hypersonic wind tunnel pass through the bow shock and the stagnation region of a pitot probe before being measured by the transducer. Therefore, the relationship between the freestream disturbance spectrum and the transducer-measured spectrum, defined as the transfer function, was characterized to recover tunnel freestream spectrum from pitot-probe measurements. In addition, the pitot-probe transfer function was combined with hot-wire measurements to decompose freestream disturbances into the three Kovasznay's modes (i.e., acoustic, entropy, and vorticity modes) [31].

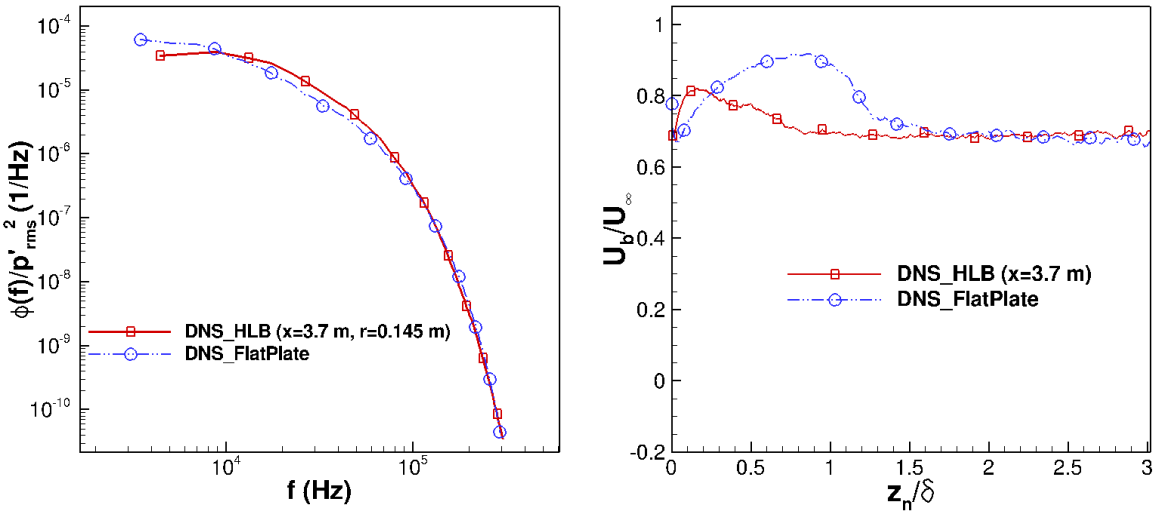

(a) (b)

Figure 6-13: Power Spectral Density and Bulk Propagation Speed of Freestream Acoustic Disturbances Induced by a Turbulent Boundary Layer over the HLB Nozzle Wall and a Single Flat Plate at the Same Freestream Conditions. The Bulk Propagation Speed is Defined according to Equation (3.7) in Ref [26]).

6.4.1 Recovery of Freestream Disturbance Spectrum From Hypersonic Pitot-Probe Measurements

Researchers have previously attempted to account for the difference between a pitot-probe-measured spectrum and a freestream spectrum, including the so-called quasisteady analysis by Harvey et al. [32] and the unsteady analysis by Stainback and Wagner [33]. The quasisteady analysis was found to significantly underpredict the pitot probe fluctuations. The unsteady analysis of Stainback and Wagner only accounts for the sound-wave mode of freestream disturbances and yields a transfer function that is independent of frequency and probe geometry, thus cannot be used to relate the transducer-measured spectrum to the freestream spectrum.

To derive a transfer function for recovering the PSD of preshock static pressure, the research team of the University of Minnesota constructed a method to compute the transfer function by using DNS of flow around pitot probes with imposed freestream disturbances. Pitot probe geometries corresponding to recent characterizations of hypersonic facilities were considered at a variety of freestream conditions and disturbance types. All disturbance types are parameterized by a single fluctuating quantity q', which is pressure p' for acoustic disturbances and temperature T' for entropy disturbances. The imposed freestream disturbances were assumed to consist of N discrete-frequency disturbances with the following form:

$$q'(t) = \sum_{k=1}^{N} q'_k \cos(\alpha_k x + \beta_k z - \omega_k t + \phi_k) \, ,$$

in which α and β are frequency-specific wavenumbers in the streamwise and vertical directions, respectively, defined by

$$\alpha_k = \frac{\omega_k \cos\theta}{u \cos\theta + c}$$

$$\beta_k = \frac{\omega_k \sin\theta}{u\cos\theta + c} \, .$$

A subscript k indicates a frequency-specific value, and ϕ_k is a randomly-selected phase. Mean flow quantities are denoted with an overline, and the free stream is assumed to be homogeneous in the spanwise direction. The normalized power spectral density is

$$PSD_k = \frac{1}{2}\left(\frac{q'_k}{q}\right)^2 \, .$$

In a simulation, the pressure within the transducer radius is first area-averaged to yield the pressure timetrace measured by the transducer. The timetrace of area-averaged pressure is then Fourier-decomposed to yield the transducer-measured PSD. The transfer function χ is defined as the ratio of transducer-measured PSD to freestream PSD,

$$\chi(f) = \frac{PSD_{t,k}}{PSD_{\infty,k}} \, ,$$

in which a subscript t indicates transducer-measured, and ∞ indicates free stream. DNS of flow around pitot probes were first conducted by the Minnesota team to characterize transfer functions for flow-parallel acoustic and entropic disturbances [34]. Flow-parallel acoustic disturbances are those whose wavenumber vector is either aligned with ($\theta = 0°$) or opposite to ($\theta = 180°$) the bulk flow, commonly referred to as fast or slow acoustic waves. The transfer functions for flow-parallel acoustic disturbances were found to exhibit a geometry-dependent resonance. For the current work, the Minnesota team conducted subsequent DNS for freestream acoustic disturbances inclined at $\theta = 120°$, with probe geometries and flow conditions corresponding to those in the Purdue BAM6QT facility. The incident angle of $120°$ is similar to the angle of acoustic radiation from the nozzle-wall turbulent boundary layer (Figure 6-7).

Figure 6-14 shows the DNS predictions for the transfer functions of angled acoustic disturbances ($\theta = 120°$) with and without area averaging and their comparison with flow-parallel slow acoustic disturbances ($\theta = 180°$) computed previously [34]. The transfer function exhibits a geometry-dependent resonance; the acoustic disturbance angle has a large effect on the transfer function, resulting in a smaller resonant frequency and a lower amplification factor for angled freestream acoustic disturbances than for flow-parallel freestream disturbances. Because of phase interference on the face of the Pitot probe at high frequencies, the transfer function for angled acoustic disturbances shows a dependence on the area of the active sensing element, as indicated by the difference in face-averaged and stagnation-point transfer functions. Moreover, destructive interference can occur when the disturbance wavelength is similar to or smaller than the size of the transducer, causing an essentially zero transfer function at high frequencies ($f \gtrsim 200$ kHz for a transducer radius of 0.83 mm as shown in Figure 6-14) when face average is applied across the entire face of the transducer.

The DNS predictions for transfer functions were compared to experimental measurements in the Purdue BAM6QT facility. The pitot probe geometries used in the experiments include four geometries; each uses the same sensing element with different flush-mounted shrouds to investigate the effect of probe geometry (Table 6-1). Figure 6-15 gives a picture of the probes used in the experiments. The experimental data were collected during two different weeks, referred to as Entry 1 and Entry 2. Given that the freestream disturbance spectra PSD_∞ cannot be directly measured in an experiment, comparisons between DNS and experiments were done in terms of the ratio of transfer functions, S, with two different probe geometries:

$$S_{a,b}(f) \equiv \frac{\chi_a}{\chi_b} = \frac{PSD_a}{PSD_b}$$

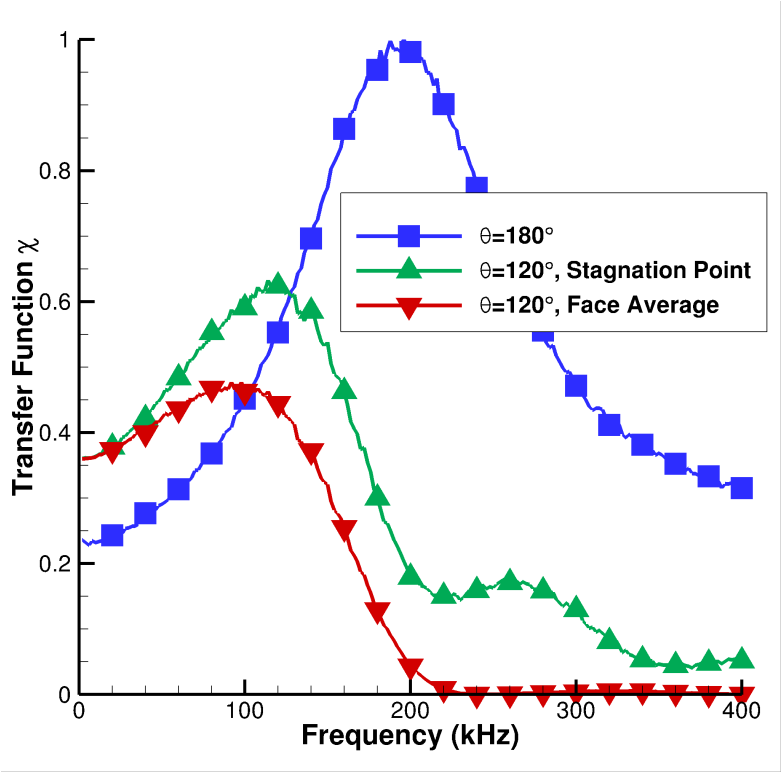

Figure 6-14: Transfer Function for No-sleeve Pitot Probe Geometry with Angled Freestream Acoustic Disturbances, Flow-parallel Slow Acoustic Disturbance Included for Comparison.

The quantity S is defined as the ratio between probes and is a frequency-dependent function. Figure 6-16 shows the ratio of each sleeved geometry to the no-sleeve geometry for both simulation and experiment. For example, $R_{large} \equiv S_{large-sleeve,no-sleeve}$. The DNS for $\theta = 0°$ corresponds to that reported in Chaudhry and Candler [34]. At this angle, the ratio of transfer functions shows a peaky behavior caused by resonance due to an acoustic disturbance reflecting between the shock and the Pitot probe face, and this resonance is further amplified by the focusing effect of shock curvature. Such a peaky behavior in transfer functions at $\theta = 0°$ was discussed and justified in the previous publication [34]. For all the Reynolds numbers and probe geometries in Figure 6-16, the angled acoustic disturbances ($\theta = 120°$) produce a much better match to experimental data than flow-parallel fast acoustic disturbances ($\theta = 0°$) [34]. The results suggest that, with judiciously imposed freestream disturbances, the method of computing the transfer function using DNS of flow around Pitot probes holds the potential to ultimately be used to replace the unsteady approach of Stainback and Wagner [33] for recovering freestream disturbance spectrum from stagnation pressure spectrum for hypersonic Pitot probes. Experiments and DNS also suggest an unexpected dependence of transfer functions on sleeve geometries and Reynolds numbers. The cause for such dependence is unknown and is currently under investigation.

6.4.2 Kovasznay Modal Decomposition

To better characterize the nature and origin of freestream disturbances in a high-speed wind tunnel, a new modal decomposition method was proposed to decompose wind-tunnel freestream disturbances into three modes of

Table 6-1: Pitot Probe Geometries Used to Characterize Freestream Disturbance Levels in the Purdue BAM6QT Facility.

Probe Name	Transducer Radius	Total Radius
No Sleeve	0.83 mm	0.83 mm
Small Sleeve	0.83 mm	1.50 mm
Medium Sleeve	0.83 mm	3.00 mm
Large Sleeve	0.83 mm	3.60 mm

(a) No-sleeve Case, Entry 1

(b) Sleeves Used in Entry 1

(c) No-sleeve Case, Entry 2

(d) Sleeves Used in Entry 2

Figure 6-15: Pictures of Pitot Probe Geometries Used in the Experiments.

covarying physical properties: an acoustic or sound-wave mode (isentropic variation of pressure, density, and temperature as well as that of the coupled irrotational velocity field); an entropy mode (isobaric variation of entropy, density, and temperature, also mentioned as entropy or temperature spottiness); and a vorticity mode

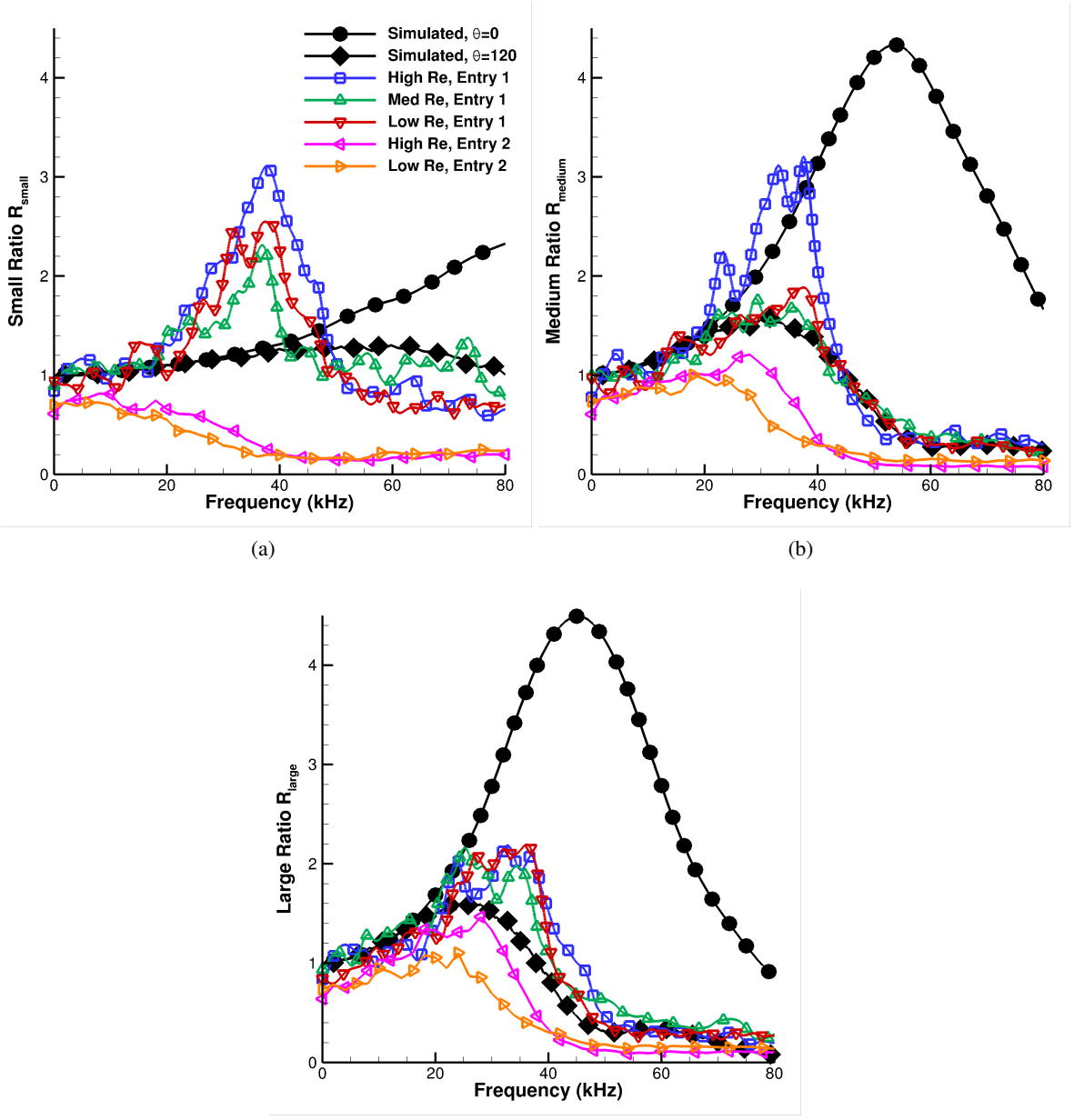

Figure 6-16: Ratio of Transfer Functions R with Two Pitot Probe Geometries, Comparing Experiment to Simulation. High Re: $Re \approx 11.5 \times 10^6$/m; Med Re: $Re \approx 8.64 \times 10^6$/m; Low Re: $Re \approx 3.01 \times 10^6$/m.

(variation of the solenoidal component of the velocity field, which is known as simple "turbulence" at low speeds). The concept and analytics of modal analysis goes back to Kovasznay [31] and Morkovin [1].

Early experimental investigations by Kovasznay [31], Morkovin [1], and Laufer [2], using hot-wire measurements, made use of the analytics to characterize supersonic wind tunnel flows. Later, Stainback and Wagner [33] conducted hot-wire and pitot probe measurements and compared resulting pressure fluctuations. Since hot-wire

measurements yield fluctuations of static pressure and pitot probes measure total pressure, Stainback and Wagner [33] introduced an ansatz for the transfer function relating preshock static and post-shock total pressure fluctuations. Logan [35] proposed a new hot-wire modal analysis by considering separate static pressure fluctuation measurements using nonintrusive laser-induced fluorescence (LIF). The method of Logan was afterwards applied by Masutti et al. [14], Wu et al. [36], and Schilden et al. [37] among others using pitot probes and applying the transfer function by Stainback and Wagner [33]. Static pressure fluctuations due to vorticity and entropy fluctuations are neglected. They are generated during the interaction of the aforementioned disturbances with the shock wave upstream of the pitot probe [38, 39].

Another experimental and numerical approach using purely stagnation point probes (SPP) was introduced by Schilden et al. [37]. This modal decomposition method was based on total pressure and stagnation point heat flux fluctuations to decompose freestream disturbances via a sensitivity matrix containing transfer functions between the measured quantities and acoustic and entropy mode computed in DNS. Schilden and Schröder [40] showed that the proposed method is limited to a very low Strouhal number of the incident disturbances, i.e., the heat flux probe has to be very small to perceive essential postshock entropy modes. At this point, the hot-wire is a promising alternative to the rather large SPP since it is basically a very small heat flux probe. On the other hand, the transfer functions of Schilden and Schröder [40] or Chaudhry and Candler [34] relating post-shock total pressure to preshock acoustic and entropy disturbances could be used to replace the transfer function of Stainback and Wagner [33] in the hot-wire method. Therefore, the hot-wire and SPP modal decomposition methods can be merged.

The research teams of RWTH Aachen and TU Braunschweig proposed an improved technique for conducting combined modal analysis with data provided by hot-wire and pitot probe. Instead of using the transfer function of Stainback and Wagner [33], a sensitivity matrix containing the transfer functions between freestream disturbances and hot-wire and pitot data is used. The new combined modal decomposition method is described as follows:

6.4.2.1 Data Acquisition

The voltage applied to a hot-wire E at constant temperature varies to compensate changes of heat loss due to flow disturbances. The heat loss is sensitive to mass flow $\dot{m} = \rho u$ and total temperature T_0. The corresponding transfer functions $k_{\dot{m}}$ and k_{T_0} in

$$\frac{dE}{E} = k_{\dot{m}} \frac{d\dot{m}}{\dot{m}} + k_{T_0} \frac{dT_0}{T_0} \tag{6-1}$$

are unknown. Voltage data postprocessing yields normalized rms values $< \cdot >$ (NRMS) of mass flow fluctuations $< \dot{m} >$, total temperature $< T_0 >$, and their correlation $R_{\dot{m},T_0}$ [31, 36]. For the later modal decomposition, the three quantities are combined to two hot-wire variables

$$< H_{p,s} >^2 = \beta^2 < \dot{m} >^2 + < T_0 >^2 \quad 2\beta R_{\dot{m},T_0} \tag{6-2}$$

$$< H_{p,u} >^2 = \alpha^2 < \dot{m} >^2 + < T_0 >^2 + 2\alpha R_{\dot{m},T_0} \, . \tag{6-3}$$

The coefficients α and β are a function of the Mach number M and the heat capacity ratio γ.

A pitot probe measures total pressure p_0, which contains acoustic pressure dp and entropy fluctuations ds

$$\frac{dp_0}{p_0} = \frac{r_{ac}}{\gamma}\frac{dp}{p} + r_{en}\frac{ds}{C_p} \; . \tag{6-4}$$

The transfer functions r_{ac} and r_{en} in Equation 6-4 are formulated with respect to the preshock density fluctuations

$$r_i = \frac{dp_0}{p_0}\frac{\rho_\infty}{d\rho_i} \; . \tag{6-5}$$

The ratio of preshock average density and post-shock total pressure normalizes the transfer functions. Introducing NRMS values and neglecting any correlation between acoustic and entropy waves, Equation 6-4 becomes

$$< P >^2 = \left(\frac{r_{ac}}{\gamma}\right) < p >^2 + r_{en}^2 < s >^2 \; . \tag{6-6}$$

$< P >=< p_0 >$ denotes the data of the pitot pressure measurements, which are plugged into the modal decomposition method.

6.4.2.2 Modal Decomposition

Following the procedure of Logan [35], we start with the mass flow rate, the equation of state for ideal gas and the energy equation for inviscid flows, differentiate, and rewrite the system of equations for NRMS values to gain

$$< H_{p,u} >^2 = \alpha^2 < p >^2 + \theta^2 < u >^2 + 2\alpha\theta R_{p,u} \tag{6-7}$$

$$< H_{p,s} >^2 = \zeta^2 < p >^2 + \theta^2 < s >^2 \tag{6-8}$$

under the aforementioned assumption of uncorrelated acoustic and entropy modes. The coefficients ζ and θ again depend on the Mach number and the heat capacity ratio. The remaining correlation term in Equation 6-7 can be expressed as a perfectly correlated slow acoustic wave $R_{\rho,u} = - < p >^2 / \gamma M$. Finally, the velocity fluctuations $< u >$ have to be split into the acoustic mode and vorticity mode contributions. Assuming no correlation between these disturbance types, $< u >^2 = < u_{ac} >^2 + < u_{vo} >^2$ holds. The velocity fluctuations $< u_{ac} >$ are again expressed by the pressure fluctuations of a slow acoustic wave. The complete system of equations of the modal decomposition can be written as

$$< H_{p,u} >^2 = \psi^2 < p >^2 + \theta^2 < u_{vo} >^2 \tag{6-9}$$

$$< H_{p,s} >^2 = \zeta^2 < p >^2 + \theta^2 < s >^2 \tag{6-10}$$

$$< P >^2 = \left(\frac{r_{ac}}{\gamma}\right) < p >^2 + r_{en}^2 < s >^2 \; . \tag{6-11}$$

In Equation 6-9, ψ is a function of Mach number and heat capacity ratio. The first two equations resemble the original equations of Logan [35]. The vorticity mode definition, i.e., velocity fluctuations $< u >^2$ minus the contribution of the acoustic wave $< u_{ac} >^2$, is incorporated. The last equation is extracted from the SPP

method. The transfer functions r_{ac} and r_{en} are computed in DNS and capture the frequency dependence present in SPP measurements. The consideration of the frequency dependence is crucial to apply Eqs. 6-9, 6-10, & 6-11 to bandpass filtered data. In short, the modal analysis can be written $F_w = SF_\infty$ by using $F_w = (< H_{p,u} >^2 , < H_{p,s} >^2, < P >^2)^T$ and $F_\infty = (< p >^2, < s >^2, < u_{vo} >^2)^T$. S is the sensitivity matrix containing the transfer functions between freestream disturbances and hot-wire and pitot data.

6.4.2.3 SPP and Combined Hot-Wire Freestream Disturbances

Experimental data of F_w, i.e., SPP data $< P >$ and combined hot-wire data $< H_{p,u} >$ and $< H_{p,s} >$, were measured at three radial positions in HLB at varying unit Reynolds numbers from 5×10^6/m to 18×10^6/m. The measurement locations are on the centerline, and 50 mm and 100 mm off the centerline. In Figure 6-17, the left-hand sides of Eqs. 6-10 and 6-11 are shown. According to the final system of equations of the modal decomposition only the acoustic and entropy mode contribute to $< H_{p,s} >$ and $< P >$. Bandpass filtered data at unit Reynolds number $Re = 5 \times 10^6$/m are shown in Figure 6-17a to illustrate the frequency effect. The acoustic and entropy noise in the wind tunnel leads to different trends in $< H_{p,s} >$ and $< P >$. Whereas the total pressure decays exponentially with increasing frequency, the combined hot-wire variable shows a spectral decay of type $f^{\ m}$ using a log-log scale (not shown here). The centerline data always contain the most intense disturbances. The dependence on unit Reynolds number in Figure 6-17b is very small at a frequency of $f = 102$ kHz. To apply the previously derived modal decomposition method to the measured freestream disturbance variables F_w, we want to determine all transfer functions in the sensitivity matrix S, thus accounting for frequency dependence and the inclination of incident acoustic waves.

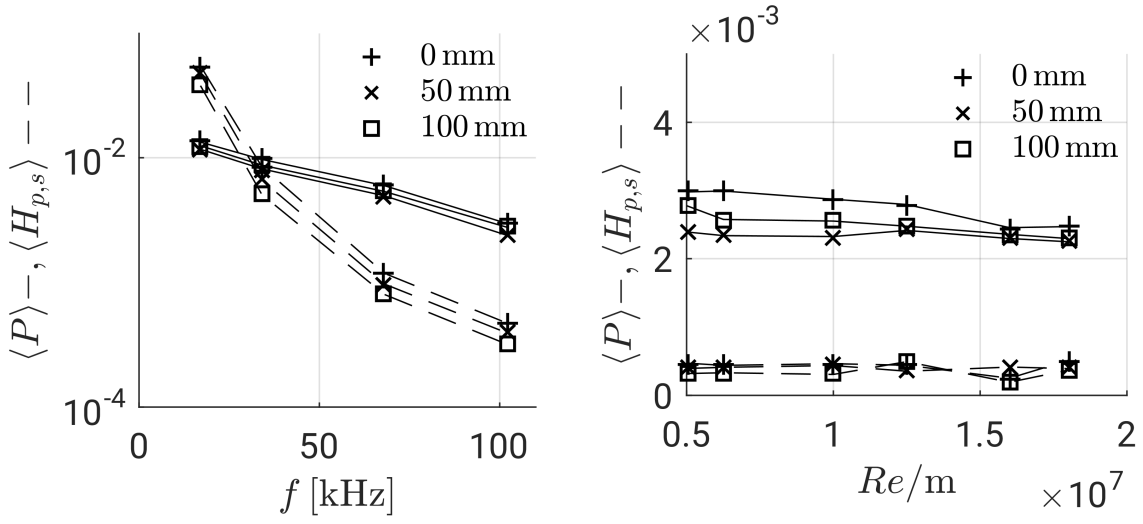

(a) (b)

Figure 6-17: Experimental Bandpass Filtered Hot-wire $< H_{p,s} >$ and SPP $< P >$ Data from the Hypersonic Ludwieg Tube of the Technical University Braunschweig. The Dashed Line Represents the Hot-wire Data, the Solid Line the SPP data. The Symbols Indicate the Distance to the Centerline of the Wind Tunnel: (a) Effect of Frequency at Unit Reynolds Number $Re = 5 \times 10^6$/m; (b) Effect of Unit Reynolds Number at $f = 102$ kHz.

6.5 SUMMARY AND CONCLUSION

This paper outlines some of the coordinated experimental and numerical work by the NATO STO AVT-240 specialists group that yielded freestream disturbance data that is physically relevant for transition processes in hypersonic flows. New freestream disturbance measurements with fast-response pressure transducers mounted on a variety of probes were performed and provided spectral data up to the high frequencies of relevance to second-mode instabilities. DNS of high-speed turbulent boundary layers and their acoustic radiation were conducted to allow direct computation of the stochastic disturbance field within the free stream. The DNS studies of acoustic radiation have overcome difficulties in experimental measurements and provided access to both flow and acoustic quantities that are difficult to obtain otherwise, including the acoustic disturbance angle, the propagation speed, and the acoustic sources. DNS of flow around a pitot probe were performed to cover the transfer of disturbances to the detailed location of the flow sensor as mounted in the probe, resulting in the recovery of freestream disturbance spectrum from the transducer-measured spectrum. In particular, the DNS study showed that the acoustic angle has a large effect on the pitot-probe transfer function, and the results for angled disturbances, with an incident acoustic angle similar to that of acoustic radiation from the nozzle wall, agreed much more closely with the experimental measurements. A new modal decomposition method was proposed to decompose hot-wire and pitot-probe measurements of freestream disturbances into the three Kovasznay modes (i.e., acoustic, entropy, and vorticity modes). By replacing the pitot-probe transfer function by Stainback and Wagner [33] with the DNS-predicted pitot-probe transfer function by Schilden and Schröder [40], the new combined modal decomposition method can yield rms values of modal amplitudes within a selected frequency band. In all, the joint effort of the specialists group has resulted in a significantly improved knowledge base pertaining to the nature and spectral contents of wind tunnel freestream disturbances, with the purpose of quantifying the stochastic input to the receptivity process in a broadband disturbance environment of conventional, cold-flow hypersonic wind tunnels. Because of the need to employ conventional tunnels for a majority of ground testing involving large-scale models, such knowledge base is essential for the reliable extrapolation of wind tunnel data to in-flight transition.

We also wish to emphasize that the objective of the current research was to investigate the building block components to facilitate further progress, and much work remains to be done to achieve the ultimate goal of developing a disturbance field algorithm as input for transition computations. Follow-on studies should include boundary-layer receptivity to a “tunnel-like” disturbance field (i.e., the response of a laminar boundary layer to acoustic disturbances radiated from nozzle wall) that relates the freestream disturbance field to the initial amplitude of instability waves in the laminar boundary layer. Such receptivity computations can then be used to calibrate a tunnel noise model that reflects the observed dependence of transition onset on the facility disturbance environment. In addition to studying boundary-layer receptivity, further Pitot probe simulations with more generalized inflow freestream disturbances are necessary to generate a simplified model of the transfer function that could ultimately be used to replace the unsteady approach of Stainback and Wagner [33] for recovering input disturbance spectrum for transition computations from Pitot probe measurement.

6.6 ACKNOWLEDGMENTS

This work was sponsored by the Air Force Office of Scientific Research (under grants FA9550-14-1-0170, FA9550-17-1-0250, and FA9550-12-1-0167). Partial support was also provided by the Office of Naval Research

(under grant N00014-17-1-2347). Computational resources were provided by the DoD High Performance Computing Modernization Program, the NASA Advanced Supercomputing Division, and the NSF PRAC program (NSF ACI-1640865). Eric Marineau would like to acknowledge the Test Resource Management Center T&E / S&T HSST program for their funding as part of the Center of Testing Excellence. The views and conclusions contained herein are those of the authors and should not be interpreted as necessarily representing the official policies or endorsements, either expressed or implied, of the funding agencies or the U.S. Government. Sandia National Laboratories is a multimission laboratory managed and operated by National Technology and Engineering Solutions of Sandia, LLC., a wholly owned subsidiary of Honeywell International, Inc., for the U.S. Department of Energy's National Nuclear Security Administration under contract DE-NA0003525. This paper describes objective technical results and analysis. Any subjective views or opinions that might be expressed in the paper do not necessarily represent the views of the U.S. Department of Energy or the United States Government.

6.7 REFERENCES

[1] Morkovin, M.V., "On Transition Experiments at Moderate Supersonic Speeds," *Journal of the Aeronautical Sciences*, Vol. 24, No. 7, 1957, pp. 480–486.

[2] Laufer, J., "Aerodynamic Noise in Supersonic Wind Tunnels," *Journal of Aerospace Sciences*, Vol. 28, No. 9, 1961, pp. 685–692.

[3] Laufer, J., "Some Statistical Properties of the Pressure Field Radiated by a Turbulent Boundary Layer," *Physics of Fluids*, Vol. 7, No. 8, 1964, pp. 1191–1197.

[4] Pate, S.R., "Measurements and Correlations of Transition Reynolds Numbers on Sharp Slender Cones at High Speeds," *AIAA Journal*, Vol. 9, No. 6, 1971, pp. 1082–1090.

[5] Stetson, K.F., "Nosetip Bluntness Effects on Cone Frustrum Boundary-Layer Transition in Hypersonic Flow," AIAA Paper 1983-1763, 1983.

[6] Phillips, O.M., "On the Generation of Sound by Supersonic Turbulent Shear Layers," *Journal of Fluid Mechanics*, Vol. 9, 1960, pp. 1–28.

[7] Ffowcs-Williams, J.E. and Maidanik, G., "The Mach Wave Field Radiated by Supersonic Turbulent Shear Flows," *Journal of Fluid Mechanics*, Vol. 21, 1965, pp. 641–657.

[8] Schneider, S.P., "Effects of High-Speed Tunnel Noise on Laminar-Turbulent Transition," *Journal of Spacecraft and Rockets*, Vol. 38, No. 3, 2001, pp. 323–333.

[9] Marineau, E.C., Moraru, C.G., Lewis, D.R., Norris, J.D., Lafferty, J.F., and Johnson, H.B., "Investigation of Mach 10 Boundary Layer Stability of Sharp Cones at Angle-of-attack, part 1: Experiments," AIAA Paper 2015-1737, 2015.

[10] Kendall, J.M., "Supersonic Boundary Layer Transition Studies," *JPL Space Program Summary*, Vol. 3, 1970, pp. 43–47.

[11] Donaldson, J. and Coulter, S., "A Review of Free-Stream Flow Fluctuation and Steady-State Flow Quality Measurements in the AEDC/VKF Supersonic Tunnel A and Hypersonic Tunnel B," AIAA Paper 1995-6137, 1995.

[12] Lafferty, J.F. and Norris, J.D., "Measurements of Fluctuating Pilot Pressure, Tunnel Noise in the AEDC Hypervelocity Wind Tunnel No. 9," AIAA Paper 2007-1678, 2007.

[13] Bounitch, A., Lewis, D.R., and Lafferty, J.F., "Improved Measurements of "Tunnel Noise" Pressure Fluctuations in the AEDC Hypervelocity Wind Tunnel No. 9," AIAA Paper 2011-1200, 2011.

[14] Masutti, M., Chazot, E., and Carbo, M., "Disturbance Level Characterization of a Hypersonic Blow-Down Facility," *AIAA Journal*, Vol. 50, No. 12, 2012, pp. 2720–2730.

[15] Laufer, J., "Sound Radiation from a Turbulent Boundary Layer," *Proceedings of the Marseille Conference on Turbulence*, CNRS Report 108, 1962.

[16] Schneider, S.P., "Experiment of the Two-Dimensional Roughness Effect on Hypersonic Boundary-Layer Transition," *Journal of Spacecraft and Rockets*, Vol. 43, No. 4, 2006, pp. 731–738.

[17] Parziale, N.J., Shepherd, J.E., and Hornung, H.G., "Free-stream Density Perturbations in a Reflected-Shock Tunnel," *Experiments in Fluids*, Vol. 55, No. 1665, 2014, pp. 1–10.

[18] Schneider, S.P., "Development of Hypersonic Quiet Tunnels," *Journal of Spacecraft and Rockets*, Vol. 45, No. 4, 2008, pp. 641–664.

[19] Pate, S.R., "Dominance of Radiated Aerodynamic Noise on Boundary-Layer Transition in Supersonic-Hypersonic Wind Tunnels," Tech. rep., Tech. Rep. AEDC-TR-77-107, Arnold Engineering Development Center, 1978.

[20] Pate, S.R., "Effects of Wind Tunnel Disturbances on Boundary-Layer Transition with Emphasis on Radiated Noise," AIAA Paper 1980-0431, 1980.

[21] Marineau, E.C., "Prediction Methodology for Second-Mode-Dominated Boundary Layer Transition in Hypersonic Wind Tunnels," *AIAA Journal*, Vol. 55, No. 2, 2017, pp. 484–499.

[22] Beckwith, I.E. and Miller, C.G., "Aerothermodynamics and Transition in High-Speed Wind Tunnels at NASA Langley," *Annual Review of Fluid Mechanics*, Vol. 22, 1990, pp. 419–439.

[23] Zhang, C., Duan, L., and Choudhari, M.M., "Effect of Wall Cooling on Boundary Layer Induced Pressure Fluctuations at Mach 6," *Journal of Fluid Mechanics*, Vol. 822, 2017, pp. 5–30.

[24] Zhang, C., Duan, L., and Choudhari, M.M., "Acoustic Radiation from a Mach 14 Turbulent Boundary Layers," AIAA Paper 2016-0048, 2016.

[25] Duan, L., Choudhari, M.M., and Wu, M., "Numerical Study of Pressure Fluctuations due to a Supersonic Turbulent Boundary Layer," *Journal of Fluid Mechanics*, Vol. 746, 2014, pp. 165–192.

[26] Duan, L., Choudhari, M.M., and Zhang, C., "Pressure Fluctuations Induced by a Hypersonic Turbulent Boundary Layer," *Journal of Fluid Mechanics*, Vol. 804, 2016, pp. 578–607.

[27] Duan, L. and Choudhari, M.M., "Analysis of Numerical Simulation Database for Pressure Fluctuations Induced by High-Speed Turbulent Boundary Layers," AIAA Paper 2014-2912, 2014.

[28] Zhang, C. and Duan, L., "Acoustic Radiation from High-Speed Turbulent Boundary Layers in a Tunnel-like Environment," AIAA Paper 2015-0836, 2015.

[29] Huang, J., Zhang, C., Duan, L., and Choudhari, M.M., "Direct Numerical Simulation of Hypersonic Turbulent Boundary Layers inside an Axisymmetric Nozzle," AIAA Paper 2017-0067, 2017.

[30] Huang, J., Duan, L., and Choudhari, M.M., "Direct Numerical Simulation of Acoustic Noise Generation from the Nozzle Wall of a Hypersonic Wind Tunnel," AIAA Paper 2017-3631, 2017.

[31] Kovasznay, L.S.G., "Turbulence in Supersonic Flow," *Journal of Aeronautical Sciences*, Vol. 20, 1953, pp. 657–674.

[32] Harvey, W.D., Bushnell, D.M., and Beckwith, I.E., "Fluctuating Properties of Turbulent Boundary Layers for Mach Numbers up to 9," NASA TN D-5496, 1969.

[33] Stainback, P.C. and Wagner, R.D., "A Comparison of Disturbance Levels Measured in Hypersonic Tunnels using a Hot-wire Anemometer and a Pitot Pressure Probe," AIAA Paper 1988-1003, 1972.

[34] Chaudhry, R.S. and Candler, G.V., "Computing Measured Spectra from Hypersonic Pitot Probes with Flow-Parallel Freestream Disturbances," *AIAA Journal*, Vol. 55, No. 12, 2017, pp. 4155–4166.

[35] Logan, P., "Modal Analysis of Hot-Wire Measurements in Supersonic Turbulence," AIAA Paper 1988-0423, 1988.

[36] Wu, J., Zamre, P., and Radespiel, R., "Flow Quality Experiment in a Tandem Nozzle Wind Tunnel at Mach 3," *Experiments in Fluids*, Vol. 56, No. 1, 2015, pp. 20–37.

[37] Schilden, T., Schröder, W., Ali, S.R.C., Schreyer, A.M., Wu, J., and Radespiel, R., "Analysis of Acoustic and Entropy Disturbances in a Hypersonic Wind Tunnel," *Physics of Fluids*, Vol. 28, No. 5, 2016, pp. 056104.

[38] McKenzie, J.F., "Interaction of Linear Waves with Oblique Shock Waves," *Physics of Fluids*, Vol. 11, No. 11, 1968, pp. 2350–2362.

[39] Anyiwo, J.C. and Bushnell, D.M., "Turbulence Amplification in Shock-Wave Boundary-Layer Interaction," *AIAA Journal*, Vol. 20, No. 7, 1982, pp. 893–899.

[40] Schilden, T. and Schröder, W., "Numerical Analysis of High Speed Wind Tunnel Flow Disturbance Measurements using Stagnation Point Probes," *Journal of Fluid Mechanics*, Vol. 833, 2017, pp. 247–273.

Chapter 7 – NOSETIP BLUNTNESS EFFECTS ON TRANSITION AT HYPERSONIC SPEEDS: EXPERIMENTAL AND NUMERICAL ANALYSIS

Pedro Paredes
National Institute of Aerospace
UNITED STATES

Meelan M. Choudhari and Fei Li
NASA Langley Research Center
UNITED STATES

Joseph S. Jewell and Roger L. Kimmel
U.S. Air Force Research Laboratory
UNITED STATES

Eric C. Marineau
AEDC White Oak
UNITED STATES

Guillaume Grossir
von Karman Institute for Fluid Dynamics
BELGIUM

7.1 INTRODUCTION

Laminar-turbulent transition of boundary-layer flows can have a strong impact on the performance of hypersonic vehicles because of its influence on the surface skin friction and aerodynamic heating. Therefore, the prediction and control of transition onset and the associated variation in aerothermodynamic parameters in high-speed flows is a key issue for optimizing the performance of the next-generation aerospace vehicles. Although many practical aerospace vehicles are blunt, the mechanisms that lead to boundary-layer instability and transition on blunt geometries are not well understood as yet. A detailed review of boundary layer transition over sharp and blunt cones in a hypersonic freestream is given by Schneider [1]. As described therein, both experimental and numerical studies have shown that the modal growth of Mack-mode instabilities (or, equivalently, the so called second-mode waves) is responsible for laminar-turbulent transition on sharp, axisymmetric cones at zero angle of attack. Studies have also shown that increased nosetip bluntness has a stabilizing effect on the amplification of Mack-mode instabilities, which is consistent with the observation that the onset of transition is displaced downstream as the nose bluntness is increased. However, while the boundary layer flow continues to become more stable with increasing nose bluntness, experiments indicate that the downstream movement in transition actually slows down and eventually reverses as the nose bluntness exceeds a certain critical range of values. The observed reversal in transition onset at large values of nose bluntness is contrary to the predictions of linear stability theory, and therefore, must be explained using a different paradigm. While no satisfactory explanation has been proposed as yet, one of the physical effects that have been suspected to cause this transition reversal is the role of surface roughness.

Earlier measurements related to the effect of nose bluntness on frustum transition over hypersonic blunt cones have been thoroughly documented by Stetson [2]. He concluded that the details of the nose tip flow played an important role in the transition reversal process, even though the onset of transition occurred significantly farther downstream over the frustum of the cone. Stetson [2] also observed that the measured transition locations within this regime were not easily reproducible across different runs. At a fixed set of freestream conditions, transition onset was found to vary across a wide range of frustum stations, and at times, the boundary layer flow remained laminar over the entire cone. Nonaxisymmetric transition patterns were observed even at zero angle of attack, and the measured length of the transition zone was much larger than that for cones with smaller values of nose bluntness. Finally, Stetson observed that frustum transition in the transition-reversal regime was highly sensitive to surface roughness in the nosetip region. For smaller nosetip bluntness prior to transition reversal, the surface finish on the nosetip (or the frustum) appeared to have no effect on frustum transition. Polishing the blunt nosetip before the wind tunnel run for the large bluntness cones resulted in either higher frustum transition Reynolds numbers or a completely laminar flow over the model. Primarily on the basis of this last observation, Stetson speculated that frustum transition for large bluntness cones was dominated by disturbances originating near the nosetip. Therefore, roughness-induced transient growth appears to be a reasonable explanation for the transition-reversal phenomena in large bluntness cones at high speeds.

Historically, the term “bypass transition” has been used to identify transition paths that cannot be explained via modal amplification of small-amplitude disturbances [3]. Well-known examples of bypass transition include the transition due to high levels of freestream disturbances, as for example, in turbomachinery, or the subcritical transition observed in Poiseuille pipe flow experiments [4–6], transition due to distributed surface roughness on flat plates [7, 8] or cones [9], and subcritical transition observed on spherical forebodies [10–13]. Because of the strongly favorable pressure gradient over blunt bodies such as hemispherical nose tips and spherical segment capsules, the laminar boundary layer is highly stable; and hence, the observed onset of transition on such bodies has been known as the “blunt-body paradox”. In recent years, the phenomenon of transient, nonmodal amplification of disturbance energy has emerged as a possible explanation for many cases of bypass transition. Mathematically, the transient, nonmodal growth is associated with the nonorthogonality of the eigenvectors corresponding to the linear disturbance equations. Physically, the main growth mechanism corresponds to the lift-up effect [14–16], which results from the conservation of horizontal momentum in the course of spanwise varying wall-normal displacement of the fluid particles. The actual growth in any given scenario is determined by the details of the external disturbance environment. However, an upper bound on the magnitude of energy gain via transient growth can be predicted by using the so-called optimal growth theory, which is typically formulated to maximize the disturbance growth across a specified interval of streamwise locations. Regardless of the flow Mach number [17, 18], the disturbances experiencing the highest magnitude of transient growth have been found to be stationary streaks that arise from initial perturbations in the form of streamwise vortices. Schmid & Henningson [19] and Schmid [20] provide a thorough review of the transient growth theory and the earlier results from the literature.

Reshotko & Tumin [21] were able to successfully correlate the transition data from several wind tunnel experiments involving subcritical, nose tip transition by using a semiempirical correlation derived from the optimal transient growth theory, which provides an upper bound on the magnitude of transient growth under suitable constraints. Reshotko & Tumin [21] extended the ideas from Anderson et al. [22], who had investigated subcritical transition in a flat plate boundary layer due to moderate to high levels of freestream turbulence (FST) and had derived a correlation based on the optimal growth of boundary layer disturbances generated by the FST. Based on the hypothesis that a similar disturbance growth could also be initiated by distributed surface roughness over hypersonic blunt forebodies, Reshotko & Tumin [21] were able to develop a semiempirical transition

correlation by linking a critical disturbance amplitude required for the onset of transition with the roughness height parameter via a gain function based on the optimal growth framework. Even though the relevance of the linear, optimal disturbance growth concept to realistic, rough nose tips remains to be established, their work provides the first physics-based model toward a potential resolution of the blunt-body paradox. Unlike other established models based on empirical curve fits that are valid for a specific subclass of datasets, Reshotko & Tumin's optimal-growth-based transition criterion has been able to provide a reasonable correlation with the measurements in various wind tunnel and ballistic range facilities and for a broad range of surface temperature ratios. In follow-on work, Paredes et al. [23, 24] have revised the Reshotko & Tumin correlation by including the effects of nonparallel basic state evolution, curvature terms, and the variation of both inflow and outflow locations for the transient growth interval. Their results indicate that application of a more thorough theoretical framework reveals certain new features of optimal growth characteristics that were not indicated by the parallel framework used in the previous correlation. However, despite these changes, the constants in the transition correlation remain close to their original values.

Not withstanding the questions related to the physical relevance of optimal growth theory, the successful correlation of much of the available data by the Reshotko & Tumin correlation raises the possibility that a similar framework could also correlate (or, perhaps, explain) the observations of transition reversal over blunt cones. That possibility was investigated during a collaborative effort under the NATO STO group AVT-240 on Hypersonic Boundary-Layer Transition Prediction focused on the problem of blunt cone transition and the potential role of transient growth in the transition reversal phenomenon. While the problems of blunt-body paradox and transition reversal over blunt cones share a key similarity by way of transition onset in the absence of (significant) modal instability, they also exhibit two major differences. First, the onset of transition in the latter case is typically observed over the frustum of the cone, as opposed to the nose tip in the case of blunt body paradox. As such, the transient growth characteristics of blunt cone boundary layers are also expected to be different, and in fact, more complex than those over a blunt nose without any frustum. Besides investigating the transient growth features over blunt cones, the NATO group's effort also included wind tunnel measurements in both U.S. and Europe, and a preliminary study related to the effects of an azimuthally-periodic array of roughness elements located near the sonic location over the nose tip. The current paper provides an overview of the collaborative work including both theoretical analysis and experimental measurements. The layout of the paper is as follows. First, experimental transition measurements over blunt cones at hypersonic freestream speeds from the literature are summarized and compared in Section 7.2. In Section 7.3, we apply the transient growth analysis to hypersonic blunt cones for selected flow conditions that match the experimental studies relevant to the NATO effort [2, 25]. Those results were used to determine the azimuthal spacing between roughness elements for the experimental measurements of roughness effects within the transition reversal regime. Section 7.4 outlines the preliminary findings from that experiment, while the summary and conclusions are presented in Section 7.5.

7.2 OVERVIEW OF TRANSITION MEASUREMENTS OVER BLUNT CONES

The effect of nosetip bluntness on boundary-layer transition is often assessed by plotting the transition Reynolds number as a function of the nosetip radius Reynolds number where both Reynolds numbers are based on the freestream conditions. Figure 7-1(a) presents the Reynolds number at the start of transition (Re_{ξ_T}) as a function of the nosetip Reynolds number (Re_{R_N}) for the experiments by Stetson [2] in the Air Force Research Laboratory (AFRL) Mach 6 high-Reynolds-number facility with R_N = sharp (A1), 0.5 (A2), 1.0 (A3), 1.5 (A4), 2.0 (A5), 2.5 (A6), 5.1 (A7), 7.6 (A8), 10.2 (A9), 12.7 (A10), and 15.2 mm (A11) cones; and by Aleksandrova et al.

[26] in the Central Aerohydrodynamic Institute (TsAGI) UT-1M Ludwieg tube with with R_N = 0.5 (B1),1 (B2), 2 (B3), 3 (B4), 4 (B5), 5 (B6), 6 (B7), 7 (B8), 8 (B9), 10 (B10), 12 (B11), and 14 mm (B12) cones. Both data sets are at a nominal freestream Mach number of 6 on straight 8° half-angle cones. The data from Stetson displays two distinct regions referred to as "small bluntness" where the transition location moves downstream with increased bluntness, and "large bluntness" where the transition location rapidly moves upstream. The data from Aleksandrova et al. [26] (indicated by star symbols) has a positive slope (small bluntness behavior) up to a critical Re_{R_N} of 1.3 x 10^5. Beyond this critical value, the transition appears to depend on uncontrolled disturbances due to nosetip roughness. In the critical region, groups of points clustered by nosetip radii of 3, 4, 5, 12, and 14 mm exhibit a decrease in the transition Reynolds number with an increasing nosetip Reynolds number, which is indicative of transition reversal. With the exception of the sharp and the 0.5 mm nosetips that consist of steel inserts, the cone model and nosetip inserts were made of AG-4 composite material. The roughness height of the AG-4 material was not specified by the authors, but is expected to be rougher than polished steel. The shape of the transition front, which was quantified using temperature-sensitive paint, revealed turbulent wedges at Reynolds numbers above the critical value. The authors attribute the formation of such wedges to the presence of uncontrolled nosetip roughness. The experiments from Aleksandrova et al. [26] illustrate that surface roughness has a significant effect on the emergence of the transition reversal. In Stetson's Mach 6 experiments [2], the nominal model surface finish had a root-mean-square (rms) value of 15 μin. (0.38 μm) and blunt nosetips were polished before each run. The polished nosetips most likely explain why the small bluntness behavior was extended to nosetip Reynolds numbers slightly above 9.0 × 10^5 in Stetson's experiments. The sensitivity of frustum transition to roughness at high nosetip Reynolds numbers was investigated by Stetson by adding 45 – 50 μin. (1.14 – 1.27 μm) rms roughness on the 0.6 in. (15.2 mm) nosetip. The added roughness caused early frustum transition.

Figure 7-1(b) presents the Reynolds number at the start of transition as a function of the nosetip Reynolds number for three sets of experiments at nominal freestream Mach numbers between 9 and 10 on straight slender cones. The plot includes the experiments of Stetson [2] in Tunnel F at Mach 9 on 7° half-angle cones with R_N = sharp (C1), 1.5 (C2), 4.5 (C3), 7.5 (C4), 10.5 (C5), 14.0 (C6), 22.5 (C7), 55.4 (C8); of Marineau et al. [25] in Tunnel 9 at Mach 10 on 7° half-angle cones with R_N = 0.15 (D1), 5.1 (D2), 9.5 (D3), 12.7 (D4), 25.4 (D5), and 50.1 mm (D6); and that of Softley et al. [27, 28] in the G.E. shock tunnel on 5° half-angle cones with R_N = 0.25 (E1),0.51 (E2), 1.3 (E3), 12.7 (E4), 19.1 (E5), and 25.4 mm (E6). As seen at Mach 6, the Mach 10 data also displays the small bluntness and large bluntness regions. The boundary between the large bluntness and small bluntness occurs at varying Reynolds numbers of approximately, respectively, for 1.2 x 10^5, 3.9 x 10^5, and 9.0 x 10^5, respectively for Softley, Marineau, and Stetson. The reason for the variation in the critical Reynolds numbers among the three data sets is not clear, since the respective experiments report similar surface finishes of 30, 32, and 40 μin. (0.76, 0.81, and 1.02 μm). Just like Stetson, Softley and Marineau also polished the nosetip prior to each run, but from the results it appears that the polished surface finish might have been smoother in Stetson's experiment.

As noted by Stetson [29], the use of "small bluntness" and "large bluntness" when discussing nosetip bluntness effects can be misleading, as the bluntness effect is related not only to the physical dimensions of the nosetip, but also to where transition occurs with respect to the nosetip. As discussed by Muir and Trujillo [30], the nosetip Reynolds number does not properly account for the various effects of the nosetip radius and unit Reynolds numbers. Stetson and Rushton [31] introduced the entropy-swallowing length as a parameter to relate the transition location to nosetip bluntness effects. Using Rotta's correlation [32], the entropy-swallowing length is found to be a function of $(Re_\infty)^{1/3}$ and $(R_N)^{4/3}$. One disadvantage of the entropy-swallowing length as a correlation parameter is that it cannot be easily defined for arbitrary geometries. Moreover, the blunt cone data is usually correlated by normalizing the transition locations (location or Reynolds numbers) on blunt cones by the transition length on sharp cones in order to remove unit Reynolds number effects. Such an approach cannot be extended to arbitrary geometries.

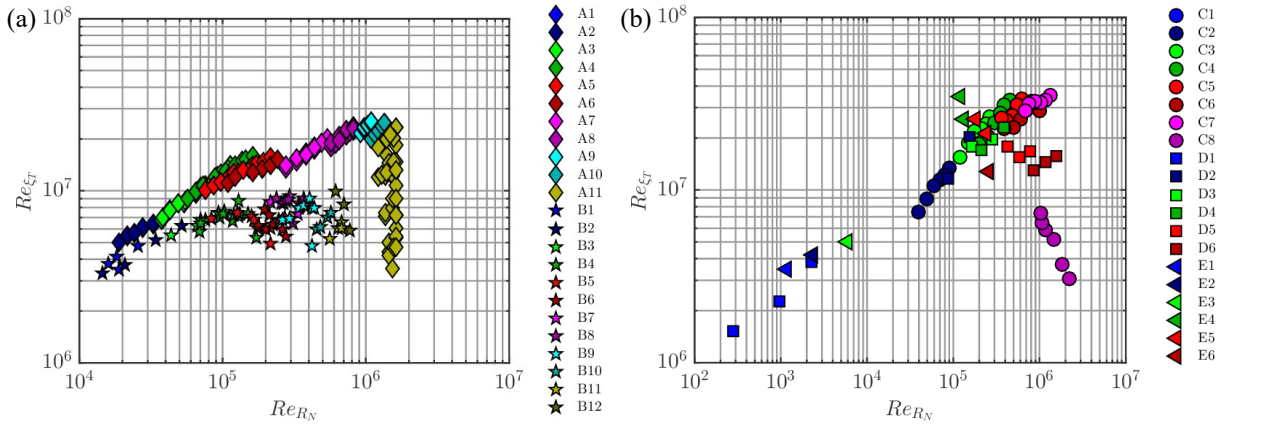

Figure 7-1: Transition Reynolds Number based on Free Stream as a Function of the Nose Reynolds Number at (a) Mach 6 and (b) Mach 9 to 10, which Illustrates the Effect of Bluntness and the Transition Reversal.

Boundary-layer stability calculations have tried to explain the transition behavior in hypersonic blunt cones. The effect of bluntness on the second-mode instability was first investigated by Malik et al. [33] and Herbert and Esfahanian [34] and more recently by Marineau et al. [25, 35] and Jewell and Kimmel [36]. These recent studies include parabolized stability equation (PSE) analysis of the historical Stetson Mach 6 and Mach 9 blunt cone experiments using the STABL software suite [37]. The stability analyses agree that the transition reversal cannot be predicted by only considering Mack's second-mode instability mechanism. This is because increased bluntness stabilizes the second mode by moving the neutral point downstream due to local edge Mach number and local unit Reynolds number reductions within the entropy layer. This implies that the transition location based on Mack's second-mode amplification keeps moving downstream and eventually transition does not occur as the bluntness increases. In addition, the boundary-layer stability studies found that the first mode is also not destabilized by bluntness, so that it cannot be responsible for the transition reversal.

Even if transition reversal cannot be predicted with linear stability computations of the first and second modes, an approach combining the measurements and computations data will still be useful to evaluate where and when the transition process is no longer dominated by the second mode. Figure 7-2 presents a compilation of second-mode transition N -factors N_T as a function of the nosetip Reynolds number Re_{R_N} for the Mach 6 experiments of Stetson [2] from Ref. [36] (diamonds), Mach 9 experiments of Stetson [2] from Ref. [35] (circles) and Mach 10 experiments of Marineau et al. [25] (squares). For values of Re_{R_N} below 1×10^4, N_T increases with Re_{R_N} as a result of the increase in the unit Reynolds number. This behavior can be linked to an increase in the critical second-mode frequency f_T, which implies a lower tunnel noise content near f_T. This effect, first discussed by Marineau et al. [25] and Marineau [35], has recently been modeled by Balakumar and Chou [38] with direct numerical simulations (DNS) of the Tunnel 9 Mach 10 experiments. The approach includes the measured freestream noise spectrum and an empirical correlation (see Marineau et al. [25]) to determine the breakdown amplitude of the second mode. The sharp cone nosetip radius was not specified in either Stetson Mach 6 or Mach 9 experiments. To include these sharp cone data points in Figure 7-2, the sharp nosetips were assumed to have the same radius as the sharp Tunnel 9 cone. A variation in the sharp cone nosetip radius does not change the trends, as it simply shifts the point left or right. For Re_{R_N} between approximately 4×10^4 and 1×10^5, a steep decrease in N_T with Re_{R_N} is observed.

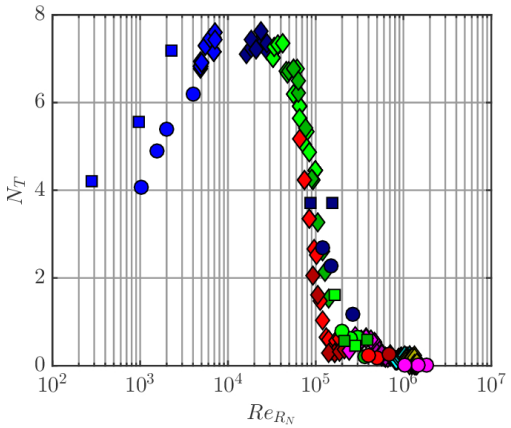

Figure 7-2: Computed Second-Mode *N* -Factors at the Experimental Transition Location (Start of Transition) as a Function of the Nosetip Reynolds number. The Same Symbols and Colors as in Figure 7-1 Are Used to Indicate the Nosetip Radius.

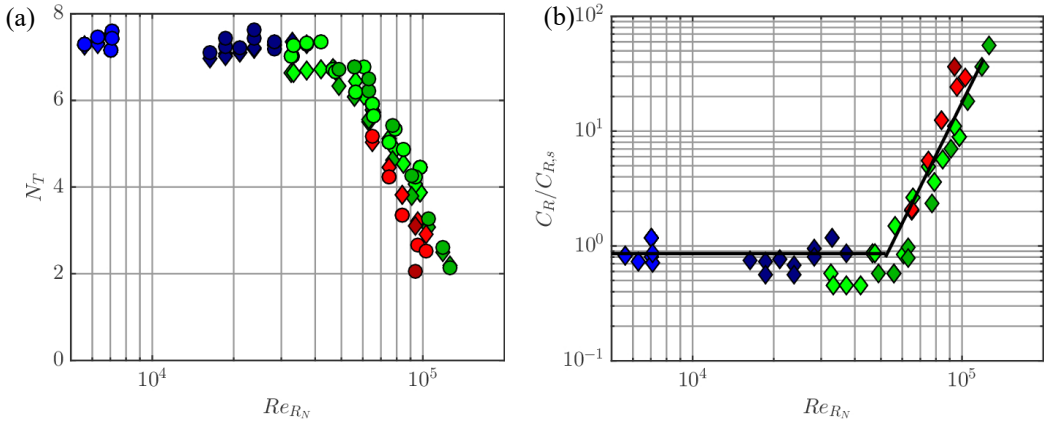

Figure 7-3: Effect of Bluntness on (a) Transition *N*-Factors and (b) Receptivity for Stetson Blunt Cone Experiments at Mach 6. The Same Symbols and Colors as in Figure 7-1 Are Used to Indicate the Nosetip Radius.

Somewhere in this region, the transition process appears to not be dominated by second-mode amplification. Note that the departure from second-mode-dominated transition occurs prior to transition reversal. The decrease of N_T with bluntness was discussed by Marineau [35] and attributed to a decrease of the second-mode breakdown amplitudes and to an increase in the initial amplitudes. The decrease in the breakdown amplitudes is linked to the lower edge Mach number whereas the increase in the initial amplitudes is related to the decrease in the critical second-mode frequency f_T as well as an increase in the receptivity coefficient with Re_{R_N}. For these conditions, the measured and estimated transition N-factors and the estimated receptivity coefficients are shown in Figures 7-3(a) and 7-3(b), respectively.

In contrast to Stetson's blunt cone experiments, which measured just the transition location, Marineau et al. [25] also measured the boundary-layer instabilities by using a large number of high-frequency response pressure sensors (PCB®-132). These measurements captured the evolution of the pressure fluctuations over the surface of the cone. Figure 7-4 presents a map of the logarithm of the pressure power spectral density (log(PSD)) at $Re_\infty \approx 17 \times 10^6$ m^{-1} for $R_N = 0.15$, 5.1, 9.5, 12.7, 25.4, and 50.8 mm. For $R_N \geq 5.1$ mm, the transition occurs before the entropy layer is swallowed. This leads to a significant reduction of the edge Mach number

compared to the sharp cone case. For the 5.1 mm nosetip in Figure 7-4(b), the edge Mach number varies from 4.4 to 4.8 between the neutral point and the start of transition. The bluntness significantly delays the appearance of the second-mode waves and increases the distances over which growth and breakdown occur. As a result of these two factors, the transition location is moved further downstream on the blunt cone (from 0.25 m on the sharp cone to 0.68 m on the 5.1 mm cone, based on heat transfer measurements). In addition, the second-mode frequencies are significantly lower on the blunt cone due to the increased boundary-layer thickness. As the nosetip radius increases from 5.1 mm to 9.5 mm, the transition location moves further downstream and the unstable second-mode frequencies are further decreased. The increase from 9.5 mm to 12.7 mm has a minor effect on the transition location, which indicates that reversal is near. For the 12.7 mm nosetip, the start of transition occurs prior to significant growth of the second mode. This indicates that transition was not initiated by the second-mode instability. However, further downstream within the transitional region, the second-mode amplitudes keep increasing up to the downstream end of the cone. The 25.4 and 50.8 mm nosetips are in the reversal regime as the transition location has moved upstream compared to those at the smaller radii. In addition, transition occurs before the appearance of second-mode waves. This makes sense, as the edge Mach number at the start of transition for the 25.4 mm and 50.8 mm radii are 3.3 and 3.2 respectively, which are too low for second-mode growth. The results for 25.4 mm and 50.8 mm nosetips also reveal that the mechanism responsible for the transition reversal has a weak pressure signature, as no significant variation in the pressure PSD is found.

The use of fast-response heat flux sensors can help to characterize the transition mechanisms on blunt cones. For instance, time-resolved heat transfer measurements performed at Mach 9 by Zanchetta [39] in the Imperial College Gun Tunnel on a 5° half-angle cone revealed that in the reversal regime, transitional events are formed in the near-nose region and convect downstream. The formation frequency of the events was linked to the severity of the roughness environment. In certain cases, second-mode instability waves and these transition events were occurring concurrently; and the experiments indicated that the second mode was responsible for the completion of transition. Recent laser-induced-fluorescence-based (LIF) schlieren measurements from Grossir et al. [40] on a blunt 7° half-angle cone at Mach 11.9 in the von Karman Institute Longshot hypersonic wind-tunnel revealed disturbances with shapes quite different from the usual second-mode rope structures. The disturbances that extend above the edge of the boundary layer are seen in Figure 7-5 for the 4.75 mm nosetip radius. These disturbances, that were not present on schlieren images for sharper cones, could be a manifestation of the blunt cone transition mechanism leading to the heat transfer fluctuation measured by Zanchetta [39].

In summary, the experimental and numerical studies agree that frustum transition in the reversal regime cannot be accounted for via linear, modal instability analysis. Furthermore, the experimental observations agree that frustum transition on large bluntness cones is highly sensitive to wall roughness and appears to be dominated by disturbances that originate in the vicinity of the nosetip. Therefore, roughness-induced transient growth emerges as the primary candidate for the experimentally-observed trend in laminar-turbulent transition.

7.3 TRANSIENT GROWTH ANALYSIS FOR HYPERSONIC BLUNT CONES

This section presents the transient growth analysis of blunt circular cones with conditions selected to match a subset of the configurations from the experiments conducted by Stetson [2] in the Air Force Research Laboratory (AFRL) Mach 6 High Reynolds Number facility and by Marineau [25] in the Arnold Engineering Development Complex (AEDC) Tunnel 9 at Mach 10. Modal instability analysis for the AFRL configurations has been already performed by Jewell & Kimmel [36], and Marineau [25] has described similar analysis for the AEDC

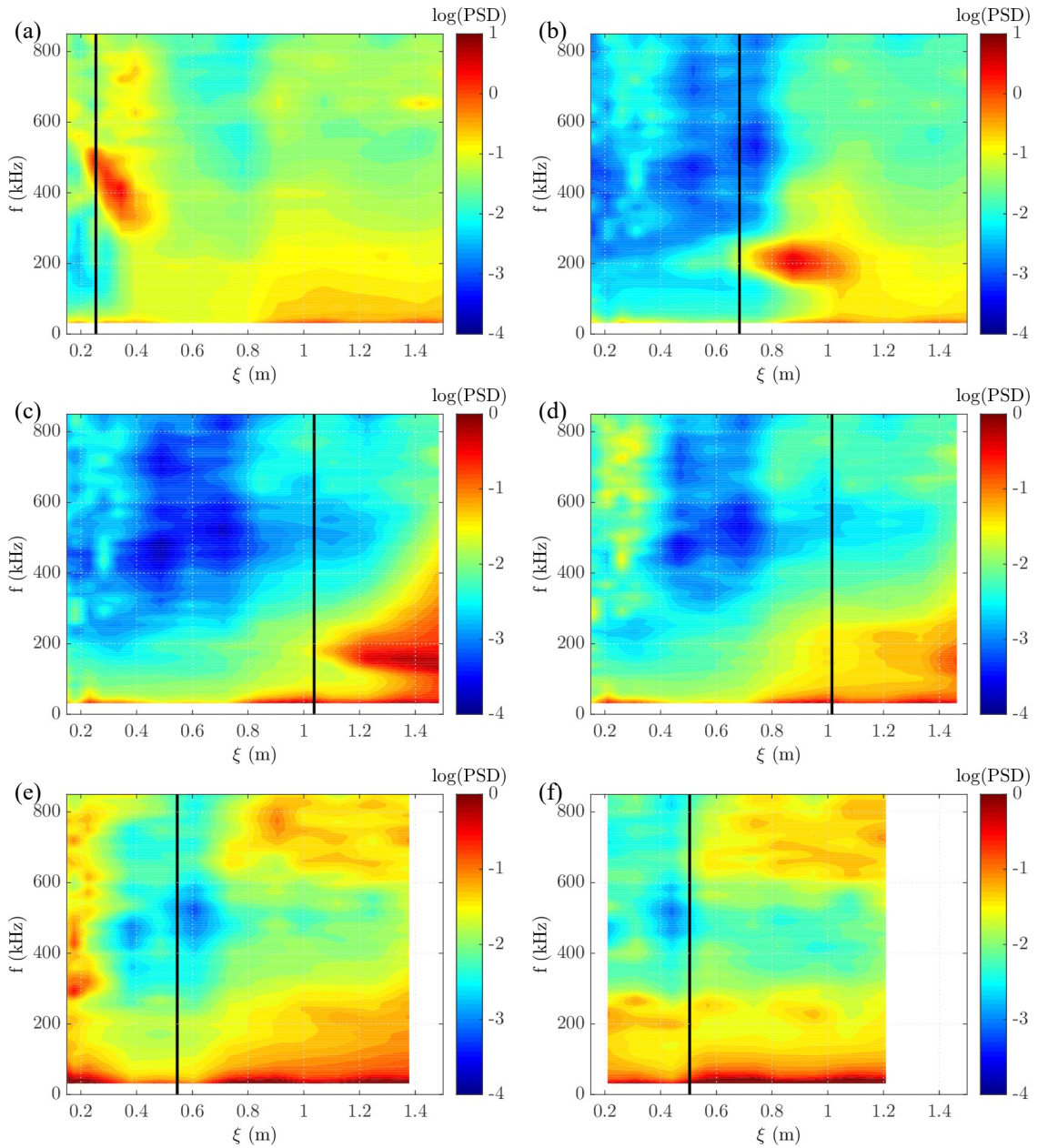

Figure 7-4: Contour Map of the Logarithm of the Pressure Power Spectral Density log(PSD) for Cones with (a) R_N = 0.15 mm (ξ_T = 0.254 m), (b) R_N = 5.1 mm (ξ_T = 0.683 m), (c) R_N = 9.5 mm (ξ_T = 1.037 m), (d) R_N = 12.7 mm (ξ_T = 1.015 m), (e) R_N = 25.4 mm (ξ_T = 0.546 m), and (f) R_N = 50.8 mm(ξ_T = 0.504 m), at $Re_\infty \approx 17 \times 10^6$ m^{-1} at Mach 10 in Tunnel 9. The Vertical, Black Line Denotes the Measured Transition Location.

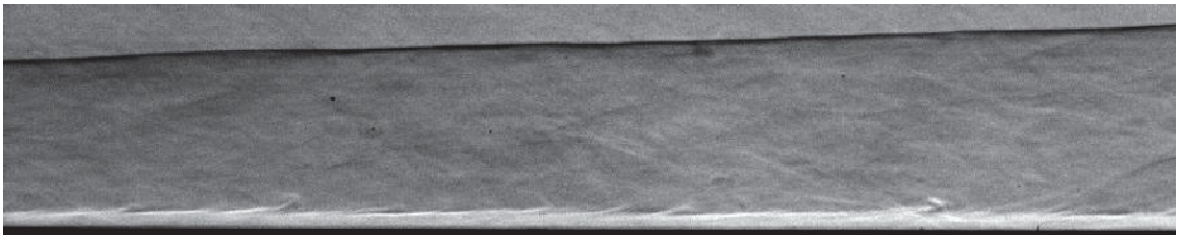

Figure 7-5: LIF-based Schlieren Flow Visualization on 4.75 mm Radius Nosetip 7° Half-Angle Cone in VKI at M_∞ = 11.9 and Re_∞ = 11.6 x 10^6 m^{-1}. Fields of View Extend from x = 625 mm until the End of the Cone at 806 mm. Disturbance Extending Past the Boundary-Layer Thickness are Visible.

configurations. They found that both first-mode and Mack-mode waves were either damped or weakly unstable for the present configurations; and therefore, transition reversal cannot be predicted with the modal analysis. Another modal instability mechanism that might play a role in the transition reversal is the entropy-layer instability [41, 42]. However, although not shown here, our analysis did not revealed any substantially amplified entropy-layer modes for the configurations of interest. Therefore, the transient growth mechanism is investigated as a potential cause for the transition reversal. First, the basic state solutions are presented in Subsection 7.3.1. Second, the transient growth theory is briefly introduced in Subsection 7.3.2. Then, a detailed transient growth analysis of the selected blunt cones configurations is presented in Subsection 7.3.3.

7.3.1 Laminar Boundary Layer over Blunt Cones

The basic states used in the present analysis correspond to the laminar boundary layer flow over the selected blunt cone configurations. The laminar boundary layer flows were computed by Jewell & Kimmel [36] and Marineau [25] with reacting, axisymmetric Navier-Stokes equations on a structured grid. The solver was a version of the NASA data parallel-line relaxation (DPLR) code [43], that is included as part of the STABL-2D software suite, as described by Johnson [44] and Johnson et al. [45]. This flow solver employs a second-order-accurate finite-volume formulation. The inviscid fluxes are based on the modified Steger-Warming flux vector splitting method with a monotonic upwind scheme for conservation laws (MUSCL) limiter. The time integration method is the implicit, first-order data parallel line relaxation (DPLR) method. The effects of chemistry and molecular vibration are negligible at the present flow conditions. Thus, the high enthalpy effects are omitted from the calculations. The viscosity law used is the Sutherland's law and the heat conductivity is calculated using Eucken's relation. Additional details about the basic state solution and the grid convergence study are given by Jewell & Kimmel [36] for the AFRL configurations and by Marineau [25] for the AEDC configurations.

7.3.1.1 AFRL Configurations

The AFRL Mach 6 facility operates at stagnation pressures p0 from 700 to 2100 psi (4.83 to 14.5 MPa). The working fluid is air and is treated as ideal gas because of the relatively low temperature and pressure. The blunt cones used in the experiments have a half-angle of 8° and a base radius of 2.0 in. (0.0508 m). A total of 196 experiments encompassing 108 unique conditions comprised the Stetson [2] Mach 6 results. Table 7-1 shows the details of the four configurations selected for the present analysis. The present analysis uses the 7° half-angle variable-bluntness cone that is currently used in the experiments in the AFRL Mach 6 facility. The thermal wall condition is isothermal with a constant wall temperature equal to $\bar{T}_w = 300.0$ K.

Table 7-1: Details of the Four AFRL Configurations Used in the Present Study. The Wall Temperature is $\bar{T}_W$ = 300 K. The Measured Transition Locations, ξ_T, Are Extracted from Ref. [46].

R_N (mm)	Re_∞ x 10^6 (m^{-1})	M_∞	$\bar{T}_\infty$	$\bar{T}_w/\bar{T}_{w,ad}$	ξ_T (m)
5.080	91.4	5.9	76.74	0.57	0.161
15.24	91.4	5.9	76.74	0.57	0.051
15.24	60.9	5.9	76.74	0.57	0.227
15.24	30.5	5.9	76.74	0.57	–

The streamwise evolution of the boundary layer thickness δh and edge Mach number M_e is plotted in Figure 7-6. The boundary-layer edge, $\eta_e = \delta_h$, is defined as the wall-normal position where $h_t/h_{t,\infty} = 0.995$, with h_t denoting the total enthalpy, i.e., $h_t = h + 0.5(\bar{u}^2 + \bar{v}^2 + \bar{w}^2)$, where h is the static enthalpy. The evolution of boundary layer thickness δ_h within the nose region and along the entire geometry is shown in Figures 7-6 (a) and 7-6 (b), respectively. The boundary layer thickness is nearly constant from the stagnation point up to $\varphi \approx 30°$, which is characteristic of stagnation boundary layer flow. From $\varphi \approx 45°$, the boundary layer thickness grows monotonically up to the end of the cone, as shown in Figure 7-6 (b). Figures 7-6 (a) and 7-6 (b) also show that the boundary layer thickness for the smaller nose radius (R_N = 9.53 mm) cone is smaller than for the larger nose radius (R_N = 15.24 mm) cone with the same freestream conditions (Re_∞ = 91.4 x 10^6 m^{-1}). Figures 7-6 (c) and 7-6 (d) show the evolution of the edge Mach number in the nose region and in the entire cone, respectively. The edge Mach number is determined by inviscid theory to the leading order, and therefore, the evolution within the nose is nearly coincident for the four configurations (Figure 7-6 (c)). However, the edge Mach number evolution is clearly distinguishable from the smaller to the larger nose radius cases when it is plotted against the streamwise coordinate for the entire geometry (Figure 7-6(d)). The sonic location, which coincides with the peak of the streamwise mass-flux within the nose [23, 24], is found at $\varphi = 41.4°$. The edge Mach number remains below M_e = 3 along the entire geometry for the large nose radius cones and only becomes slightly larger than M_e = 3 at the end of the cone for the smaller nose radius case.

7.3.1.2 AEDC Configurations

The Air Force AEDC Hypervelocity Wind Tunnel No. 9 (Tunnel 9) is a hypersonic, nitrogen gas, blowdown wind tunnel with interchangeable nozzles that allow for testing at Mach numbers of 7, 8, 10, and 14 over a 0.177 x 10^6 m^{-1} to 158.8 x 10^6 m^{-1} unit Reynolds number range. A detailed description of the facility can be found in Ref. [25]. The blunt cones used in the experiments of Marineau et al. [25] had a base diameter of 15 in. (0.381 m) and interchangeable nose tips with radius of 0.152 mm to 50.80 mm. The test matrix for the 24 run test program is provided in Ref. [25]. The working fluid is nitrogen. Table 7-2 shows the details of the four configurations selected for the present analysis. The used thermal wall condition is isothermal with a constant wall temperature equal to $\bar{T}_w$ = 300.0 K. The four configurations share a similar freestream unit Reynolds number of Re_∞ 17.5 x 10^6 m^{-1} and a freestream Mach number of $M_\infty \approx 9.78$. The nose radius values varies from R_N = 9.53 mm to R_N = 50.8 mm.

The boundary layer thickness δ_h and edge Mach number M_e for the four configurations are plotted in Figures 7- 7(a) and 7-7(b), respectively. As observed in the comparison of the AFRL configurations of Figure 7-6(b), despite the same freestream conditions, the boundary layer thickness in the frustum part of the cone is larger for larger nose radius values. Also, the edge Mach number is larger for the smaller nose radius cases, although remains smaller than M_e= 4.5 for the four configurations.

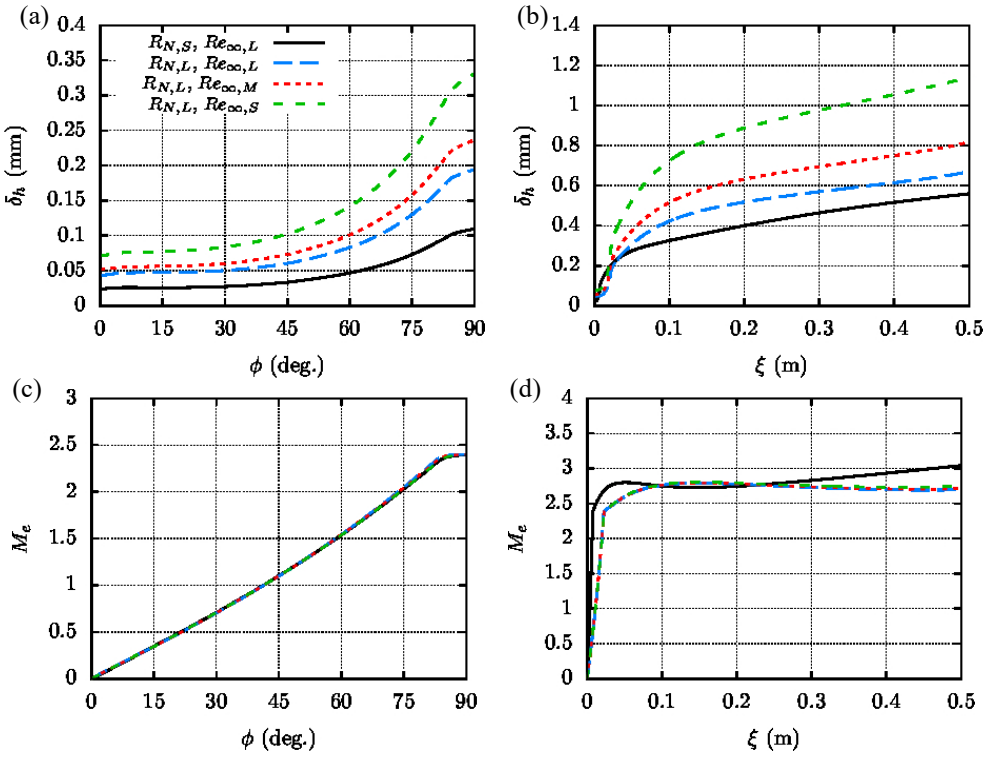

Figure 7-6: Streamwise Evolution of (a,b) Boundary Layer Thickness and (c,d) Edge Mach Number of the Laminar Boundary Layer Flows over the AFRL Configurations. The Legend Refers to $R_{N,S}$ = 5.08 mm, $R_{N,L}$ = 15.24 mm, $Re_{\infty,L}$ = 91.4 x 10^6 m^{-1}, $Re_{\infty,M}$ = 60.9 ×10^6 m^{-1}, $Re_{\infty,S}$ = 30.5 ×10^6 m^{-1}.

Table 7-2: Details of the Four AEDC Configurations Used in the Present Study. The Wall Temperature Is $\bar{T}_w$ = 300 K. The Measured Transition Locations, ξ_T, Are Extracted from Ref. [25].

R_N (mm)	$R_{e\infty}$ (m^{-1})	M_∞	$\bar{T}_\infty$	$\bar{T}_w/\bar{T}_{w,ad}$	ξ_T (m)
9.530	17.6 x 10^6	9.797	51.01	0.340	1.037
12.70	17.4 x 10^6	9.795	51.17	0.339	1.015
25.40	17.3 x 10^6	9.791	51.13	0.340	0.546
50.80	17.6 x 10^6	9.777	51.27	0.340	0.504

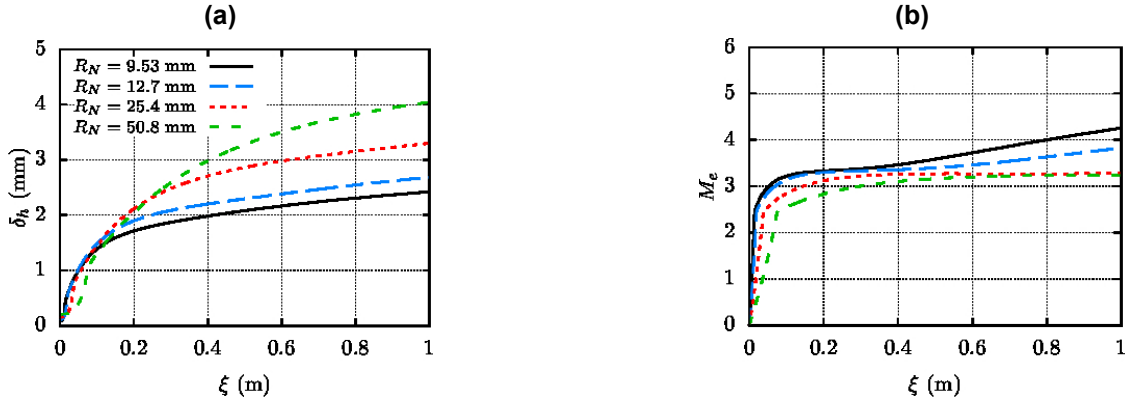

Figure 7-7: Streamwise Evolution of (a) Boundary Layer Thickness and (b) Edge Mach Number of the Laminar Boundary Layer Flows over the AEDC Configurations.

7.3.2 Transient Growth Theory

Transient growth analysis is performed using the linear PSE as explained in the literature [18, 23, 47–49]. The analysis focuses on stationary perturbations because, despite of the speed regime, they experience the largest transient growth. For completeness, the present section outlines the methodology, which bears strong similarities with the optimization approach based on the linearized boundary layer equations [17, 22, 50]. The advantage of the PSE-based formulation is that it is also applicable to more complex base flows where the flow evolves along the streamwise direction and the boundary layer approximation may not hold. The PSE approach can also be easily extended to unsteady disturbances. While infinite Reynolds number asymptotic results cannot be directly computed using this technique, good agreement is achieved between the two methodologies for incompressible and compressible regimes as shown by Paredes et al. [18].

In the PSE context, stationary perturbations have the form

$$\tilde{\mathbf{q}}(\xi,\eta,\zeta) = \hat{\mathbf{q}}(\xi,\eta)\exp\left[\mathrm{i}\left(\int_{\xi_0}^{\xi}\alpha(\xi')\,\mathrm{d}\xi' + \mathbf{m}\zeta - \omega\mathbf{t}\right)\right] + \text{c.c.}, \tag{7-1}$$

where c.c. denotes complex conjugate. The suitably nondimensionalized, orthogonal, curvilinear coordinate system (ξ, η, ζ) denotes streamwise, wall-normal, and azimuthal coordinates and (u, v, w) represent the corresponding velocity components. Density and temperature are denoted by ρ and T. The streamwise and azimuthal wavenumbers are α and m, respectively; and ω is the angular frequency of the perturbation.

The Cartesian coordinates are represented by (x, y, z). The vector of perturbation fluid variables is $\tilde{\mathbf{q}}(\xi, \eta, \zeta, t) = (\tilde{\rho}, \tilde{u}, \tilde{v}, \tilde{w}, \tilde{T})^T$ and the vector of amplitude functions is $\hat{\mathbf{q}}(\xi, \eta) = (\hat{\rho}, \hat{u}, \hat{v}, \hat{w}, \hat{T})^T$. The vector of basic state variables is $\bar{\mathbf{q}}(\xi, \eta) = (\bar{\rho}, \bar{u}, \bar{v}, \bar{w}, \bar{T})^T$.

Upon introduction of the perturbation form (7-1) into the linearized NS equations together with the assumption of a slow streamwise dependence of the basic state and the amplitude functions, thus neglecting the viscous derivatives in ξ, the PSE are recovered as follows

$$\mathbf{L}\hat{\mathbf{q}}(\xi,\eta) = \left(\mathbf{A} + \mathbf{B}\frac{\partial}{\partial\eta} + \mathbf{C}\frac{\partial^2}{\partial\eta^2} + \mathbf{D}\frac{\mathbf{1}}{\mathbf{h_1}}\frac{\partial}{\partial\xi}\right)\hat{\mathbf{q}}(\xi,\eta) = \mathbf{0}. \tag{7-2}$$

The linear operators **A**, **B**, **C** and **D** are given by Pralits et al. [47] and h_1 is the metric factor associated with the streamwise curvature. The system of Equations (7-2) is not fully parabolic due to the term $\partial\hat{p}/\partial\xi$ in the streamwise momentum equation [51–54]. However, for purely stationary disturbances ($\omega = 0$ and $\alpha = 0$), this term can be dropped from the equations as justified in Refs. [48, 55]. For nonstationary perturbations ($\omega \neq 0$), a commonly adopted solution is to replace $\partial\hat{p}/\partial\xi$ by $\Omega_{PNS}\partial\hat{p}/\partial\xi$, where Ω_{PNS} is the Vigneron parameter [56– 58]. This parameter was originally introduced for the integration of the parabolized Navier-Stokes equations (PNS) , and is determined by

$$\Omega_{PNS} = \min(1, M_\xi^2), \tag{7-3}$$

where M_ξ is the local streamwise Mach number. The Vigneron approximation ensures numerical stability of the marching scheme by suppressing upstream influence within the solution. For locally supersonic flow, the equations are not altered because $\Omega_{PNS} = 1$. For a disturbance field with $\alpha \neq 0$,a portion of the elliptic behavior is absorbed in the wave part via the term $i\alpha\hat{p}$ and the residual upstream influence can be suppressed by choosing a sufficiently large marching step [53], without having to invoke the Vigneron approximation.

The optimal initial disturbance, $\tilde{\mathbf{q}}_0$, is defined as the initial (i.e., inflow) condition at ξ_0 that maximizes the objective function, J, which is defined as a measure of disturbance growth over a specified interval $[\xi_0, \xi_1]$. The definitions used in the present study correspond to the outlet energy gain $J = G^{out}$ and mean energy gain $J = G^{mean}$ and are defined as

$$G^{out} = \frac{E(\xi_1)}{E(\xi_0)}, \tag{7-4}$$

$$G^{mean} = \frac{1}{\xi_1 - \xi_0}\frac{\int_{\xi_0}^{\xi_1} E(\xi')\,d\xi'}{E(\xi_0)}, \tag{7-5}$$

where E denotes the energy norm of $\tilde{\mathbf{q}}$. The energy norm is defined as

$$E(\xi) = \int_\eta \hat{\mathbf{q}}(\xi,\eta)^{\mathbf{H}}\mathbf{M_E}\hat{\mathbf{q}}(\xi,\eta)\,\mathbf{h_1}\,\mathbf{h_3}\,d\eta, \tag{7-6}$$

where h_3 is the metric factor associated with the azimuthal curvature, $\mathbf{M}_E$ is the energy weight matrix and the superscript H denotes conjugate transpose. The selection of $J = G^{out}$ corresponds to the "outlet energy gain" that is commonly used in studies of the optimal-perturbation problem [22, 50]. The selection of $J = G^{mean}$ defines the "mean energy gain" and corresponds to the optimization of the mean energy. This latter definition accounts for a possible overshoot in the disturbance energy evolution that are not accounted for by the former definition and is found to be present in hypersonic blunt forebodies [23, 24], as well as in the nosetip of blunt cones as documented in what follows.

The choice of the energy norm is known to influence the optimal initial perturbation as well as the magnitude of energy amplification [17, 49, 59]. Here, we use the positive-definite energy norm derived by Mack [60] and used by Hanifi et al. [61] for transient growth calculations, which is defined by

$$\mathbf{M}_E = \mathrm{diag}\left[\frac{\bar{T}(\xi,\eta)}{\gamma\bar{\rho}(\xi,\eta)M^2}, \bar{\rho}(\xi,\eta), \bar{\rho}(\xi,\eta), \bar{\rho}(\xi,\eta), \frac{\bar{\rho}(\xi,\eta)}{\gamma(\gamma-1)\bar{T}(\xi,\eta)M^2}\right]. \tag{7-7}$$

Additionally, the kinetic energy norm is also used for optimization in this paper. The kinetic energy of a perturbation is defined by

$$K(\xi) = \int_\eta \hat{\mathbf{q}}(\xi,\eta)^{\mathbf{H}}\mathbf{M_K}\hat{\mathbf{q}}(\xi,\eta)\,\mathbf{h_1}\,\mathbf{h_3}\,\mathrm{d}\eta, \tag{7-8}$$

where

$$\mathbf{M}_K = \mathrm{diag}\left[0, \bar{\rho}(\xi,\eta), \bar{\rho}(\xi,\eta), \bar{\rho}(\xi,\eta), 0\right]. \tag{7-9}$$

To differentiate when the total energy norm E or the kinetic energy norm K are used, a corresponding subscript is added to the energy gain, resulting in four options for the objective function: G_E^{out}, G_E^{mean}, G_K^{out} and G_K^{mean}. In the present study, the transient growth amplification is also expressed in terms of the logarithmic amplification ratio, the so-called N-factor, based on the total energy norm, which is defined as

$$N_E = \frac{1}{2}\ln\left(\mathrm{G_E^{out}}\right) = -\int_{\xi_0}^{\xi} \alpha_\mathrm{i}(\xi')\,\mathrm{d}\xi' + 1/2\ln\left[\hat{\mathrm{E}}(\xi)/\hat{\mathrm{E}}(\xi_0)\right]. \tag{7-10}$$

Furthermore, the present study uses the N-factor based in other disturbance magnitude norms, as the kinetic energy, N_K, maximum temperature, N_T, or maximum streamwise velocity, N_u. These definitions are equivalent to that of Equation (7-10), but with their respective norms.

The variational formulation of the problem to determine the maximum of the objective functional J leads to an optimality system [18], which is solved in an iterative manner, starting from a random solution at ξ_0 that must satisfy the boundary conditions. The PSE, $\mathbf{L}\tilde{\mathbf{q}} = \mathbf{0}$, are used to integrate $\tilde{\mathbf{q}}$ up to ξ_1, where the final optimality condition is used to obtain the initial condition for the backward adjoint PSE integration, $\mathbf{L}^\dagger\tilde{\mathbf{q}}^\dagger = c_{mean}F(\tilde{\mathbf{q}})$, where $c_{mean} = 0$ for the outlet energy gain optimization and $c_{mean} = 1$ for the mean energy gain optimization, and $F(\tilde{\mathbf{q}})$ is a function of the direct solution [47]. At ξ_0, the adjoint solution is used to calculate the new initial condition for the forward PSE integration with the initial optimality condition. The iterative procedure finishes when the value of G has converged up to a certain tolerance, which was set to 10^{-4} in the present computations.

Nonuniform stable high-order finite-difference schemes [62, 63] of sixth order are used for discretization of the PSE along the wall-normal coordinate. The discretized PSE are integrated along the streamwise coordinate by using second-order backward differentiation. The number of discretization points in both directions was varied in selected cases to ensure convergence of the optimal gain predictions. The wall-normal direction was discretized using $N_y = 161$, with the nodes being clustered toward the wall [63]. No-slip, isothermal boundary conditions are used at the wall, i.e., $\hat{u} = \hat{v} = \hat{w} = \hat{T} = 0$. The amplitude functions are forced to decay at the farfield boundary by imposing the Dirichlet conditions $\hat{\rho} = \hat{u} = \hat{w} = \hat{T} = 0$, unless otherwise stated. The farfield boundary coordinate is set just below the shock layer. Verification of the present optimal growth module against available transient growth results from the literature is shown in Ref. [18].

In what follows, we study the axisymmetric boundary layer over circular cones in hypersonic freestream flows. The freestream conditions and geometries are selected to match a subset of configurations used in the experiments conducted at AFRL [2, 36] and at AEDC [25]. For this problem, the computational coordinates (ξ, η, ζ),are defined as an orthogonal body-fitted coordinate system. The metric factors are defined as

$$h_1 = 1 + \kappa\eta, \tag{7-11}$$

$$h_3 = r_b + \eta \cos(\theta), \tag{7-12}$$

where κ denotes the streamwise curvature, r_b is the local radius, and θ is the local half-angle along the axisymmetric surface, i.e., $\sin(\theta) = dr_b/d\xi$. For our study, the half angle, θ, is 7° and $\kappa = 0$ in the frustum region. The end of the nose and beginning of the frustum is denoted as the juncture location that is defined as $\xi_j = R_N\pi/2$. The streamwise coordinate within the nosetip region is represented by an angular coordinate defined as $\phi = \xi/R_N$. The nosetip Reynolds number, $Re_{R_N} = \bar{\rho}_\infty \bar{u}_\infty R_N/\mu_\infty$ is used to scale the energy gain. The length scale $L_{R_N} = R_N/\sqrt{Re_{R_N}}$ is used to normalize the spanwise disturbance wavelength defined as $\lambda = 2\pi rb/m$.

7.3.3 Transient Growth Results

For a nonselfsimilar boundary layer such as the boundary layer over blunt cones, both the initial and final locations must be varied in order to obtain the overall picture of the optimal growth characteristics [23]. A special feature of the transient growth analysis for the blunt cones of interest is that the results naturally split into two parts, one that deals with transient growth intervals that are limited to the nose region, where the results are expected to resemble those for the hemisphere forebody reported by Paredes et al. [23], and a second one that deals with transient growth intervals that extend into the frustum region, where transition is observed in the experiments. Detailed transient growth results are first presented for the AFRL configurations in Subsections 7.3.3.1 and 7.3.3.2. Because stationary disturbances usually yield the highest transient growth overall, a majority of the analysis in Section 7.3 is focused on the zero frequency case. However, motivated by the findings of Cook et al. [64], who performed a resolvent analysis of a similar blunt cone configuration at hypersonic conditions and reported significant nonmodal growth of planar, traveling waves inside the entropy layer, the transient growth analysis is extended to traveling disturbances in Subsection 7.3.3.3. Finally, a brief summary of results is presented for the AEDC configurations in Subsection 7.3.3.4.

7.3.3.1 Transient Growth Interval Within the Nose Region

Herein, transient growth results with initial and final disturbance locations within the nose region for the AFRL configurations introduced in Table 7-1 are investigated. The optimal mean total energy gain (G_E^{mean}) and optimal mean kinetic energy gain (G_K^{mean}) for the $R_N = 15.24$ mm and $Re_\infty = 91.4 \times 10^6$ m^{-1} case are plotted in Figures 7-8(a) and 7-8(b), respectively. Figure 7-8(a) shows that the highest total energy gain occurs for relatively short optimization intervals in the vicinity of the stagnation point, as indicated by the black line nearly parallel to the lower boundary of the plot. However, the kinetic energy budget for these perturbations initiated near the stagnation point is rather small. This fact is confirmed by the optimal mean kinetic energy gain (G_K^{mean}) plot of Figure 7-8(b). The optimal kinetic energy gain exhibits a maximum in the interior of the domain at $\phi_0 = 42.4°$ that nearly coincides with the sonic location, $\phi_{Me=1} = 41.4°$. These results indicate the same features as the results reported by Paredes et al. [23] for a hypersonic hemisphere forebody.

The optimal growth results for a specified inflow location ξ_0 of the flow are characterized in terms of the combination of azimuthal wavenumber m and outflow location ξ_1 that lead to the maximum value of the energy gain.

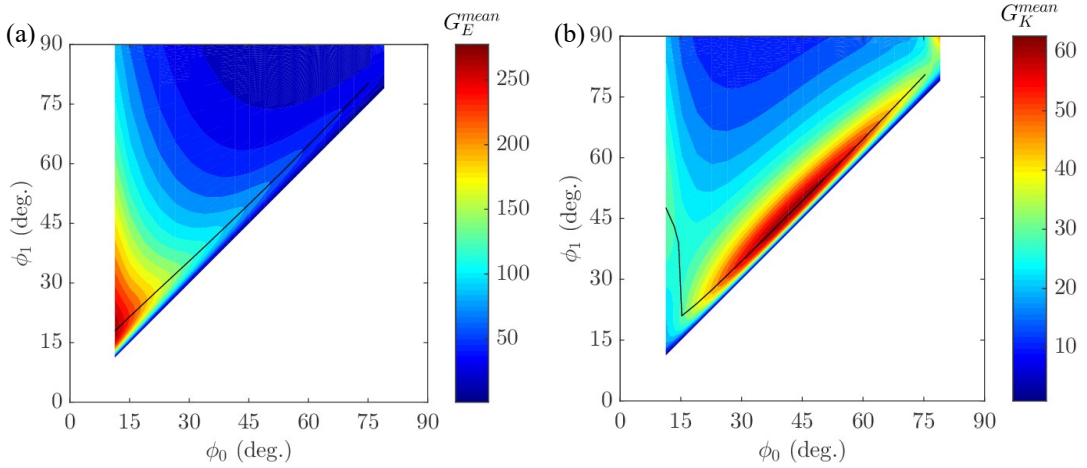

Figure 7-8: Contours of (a) Optimal Mean Total Energy Gain G_E^{mean} and (b) Optimal Mean Kinetic Energy Gain G_K^{mean} within the Nose Region of the R_N = 15.24 mm and Re_∞ = 91.4 x 10^6 m^{-1} Case. The Solid Line in the Contour Plot Indicates the Value of φ_1 Corresponding to Maximum Energy Gain for a Given φ_0.

Thus, the effect of nosetip radius R_N on the maximum value of the optimal energy gain, optimal wavenumber, and optimal growth interval, is analyzed next. Figure 7-9 shows the optimal total and kinetic energy gains as a function of the inflow location (Figures 7-9(a) and 7-9(d)), as well as the corresponding azimuthal wavenumber (Figures 7-9(b) and 7-9(e)) and the optimal growth interval (Figures 7-9(c) and 7-9(f)). Results are shown for the R_N = 5.08 mm and R_N = 15.24 mm cones at the same freestream unit Reynolds number of Re_∞ = 91.4 x 10^6 m^{-1}. Figure 7-9(a) shows that both the total and kinetic energy gains are larger for the larger nose radius, although as shown in Figure 7-9(d), the scaling is not perfectly linear because, as indicated by Paredes et al. [24], small deviations from the linear scaling occur as a result of the differences in the ratio of boundary-layer thickness to the radius of the surface curvature. Figure 7-9(b) shows that the optimal azimuthal wavenumber is nearly twice as large for the larger nose radius cone in comparison with the case of the smaller nose radius. The scaling of the initial disturbance wavelength with L_{R_N} plotted in Figure 7-9(e) shows a reasonable scaling with the boundary layer thickness. On the other side, the optimal growth interval plotted in Figure 7-9(c) does not scale with L_{R_N} (or R_N) as shown in Figure 7-9(f), presumably because the ratio of boundary-layer thickness to the radius of the surface curvature plays an important role for this parameter.

7.3.3.2 Transient Growth Along the Frustum Region

Next, transient growth across spatial intervals that extend into the frustum region is studied in detail for the AFRL configurations. In this case, we find it more convenient to plot the transient growth amplification in terms of the N -factor based on the total energy norm defined in Equation (7-10). Figures 7-10(a) shows the N -factor contours for initial and final locations on the frustum for the R_N = 5.08 mm AFRL cone at Re_∞ = 91.4 x 10^6 m^{-1}. Similar results for the larger nose radius, R_N = 15.24 mm, are shown in Figure 7-10(b). The N -factor values are larger for the smaller nose radius cone except for initial and final locations near the juncture of the cone, i.e., beginning of the frustum. The N_E values are larger than 5.5 in the studied range of parameters for the smaller nose radius case (Figure 7-10(a)). For the larger nose radius case, the N_E values are larger than 4.5 in the range of ξ_0 and ξ_1 values studied here, although the N_E = 3.5 value is reached at smaller values of ξ_1 than for the smaller radius case when the initial disturbance location is near the juncture location $\xi_0 \approx \xi_j$.

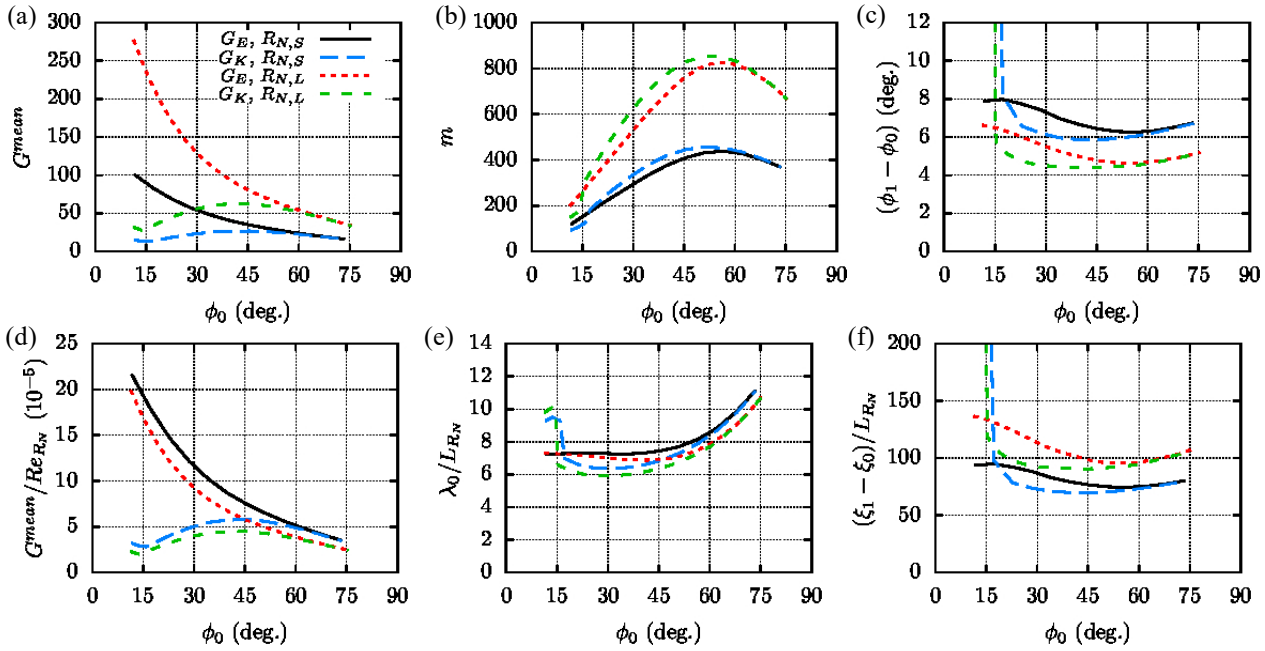

Figure 7-9: (a), (d) Optimal Mean Energy Gain and Corresponding (b), (e) Azimuthal Wavenumber and (c), (f) Optimization Interval within the Nose rRegion for $R_{N,S}$ = 5.08 mm and $R_{N,L}$ = 15.24 mm Cones at Same Freestream Unit Reynolds Number, Re_∞ = 91.4 x 10^6 m^{-1}.

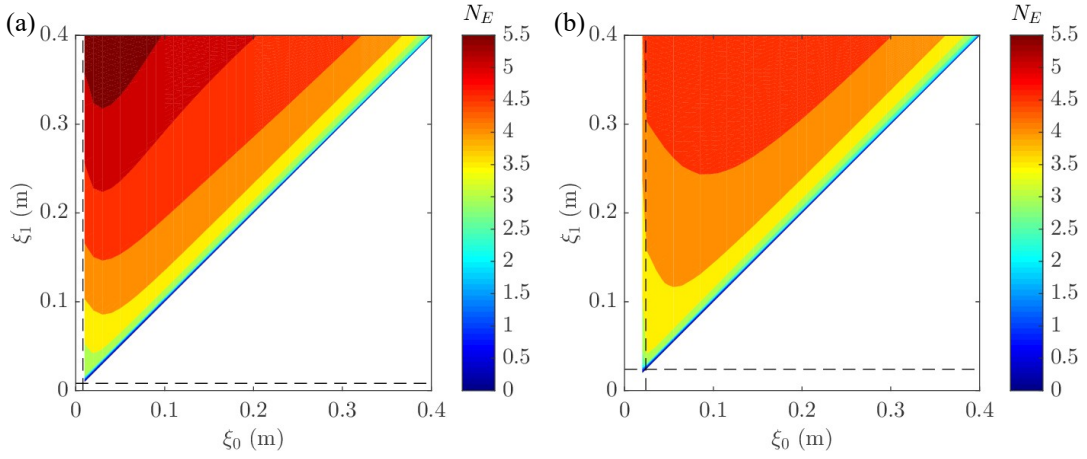

Figure 7-10: Contours of N -Factor Values Defined as NE = 1/2ln $\left(G_E^{out}\right)$ in the Frustum Region of the (a) R_N = 5.08 mm and (b) R_N = 15.24 mm Cones. The Juncture Location ξ_j is Marked with a Vertical and a Horizontal Dashed Line. The Freestream Unit Reynolds Number is Re_∞ = 91.4 ×10^6 m^{-1}.

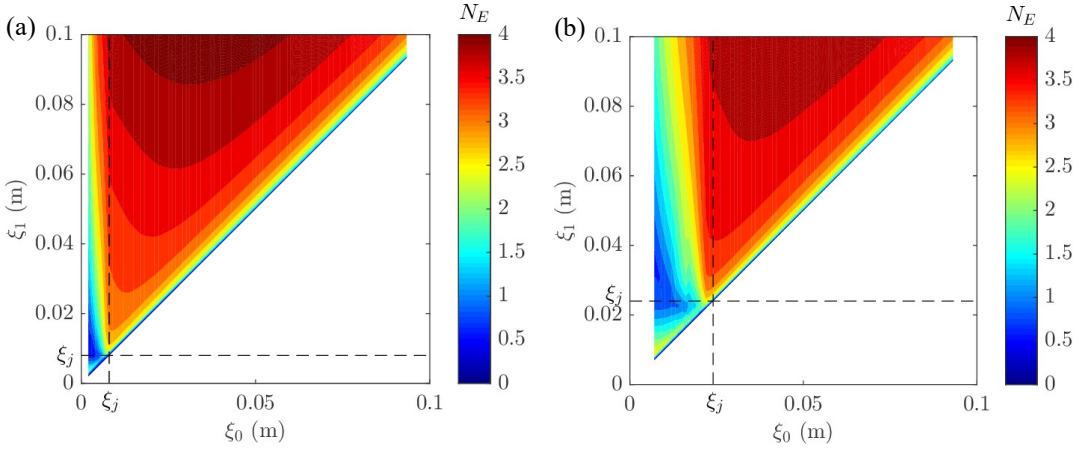

Figure 7-11: Contours of *N* -Factor Values Defined as $N_E = 1/2\ln\left(G_E^{out}\right)$ in the Vicinity of the Nose Region of the (a) R_N = 5.08 mm and (b) R_N = 15.24 mm Cones. The Juncture Location ξ_j is Marked with a Vertical and a Horizontal Dashed Line. The Freestream Unit Reynolds Number is $Re_\infty = 91.4 \times 10^6$ m^{-1}.

Figures 7-11(a) and 7-11(b) show a magnified view of the N-factor contours from Figures 7-10(a) and 7-10(b), respectively, for initial and final locations in the vicinity of the juncture between the nose and the frustum of the cone. Both figures show different behavior of the transient growth amplification for disturbances initiated within the nose region ($\xi_0 < \xi_j$) and those that are initiated downstream of the juncture location ($\xi_0 \geq \xi_j$). The disturbances initiated in the nose have a maximum for very short optimal growth intervals, as previously shown in Figure 7-9. For larger optimal growth intervals, the transient growth amplification first decreases and then increases again for $\xi_1 > \xi_j$. On the other side, disturbances initiated downstream of the nose ($\xi_0 \geq \xi_j$) experience a monotonic increase in energy gain factor as ξ_1 is increased. Remarkably, disturbances initiated in the vicinity of the juncture location ($\xi_0 \approx \xi_j$) experience a quite rapid growth for the blunter case and short transient growth intervals (Figure 7-11(b)), resulting in relatively significant values of N_E just downstream of the juncture location.

The AFRL experiments investigated the effect of an azimuthally-periodic array of roughness elements mounted near the sonic point at $\varphi = 45°$. To help gain some insight into the role of transient growth as a mechanism for roughness effects, we next examine the details of transient growth disturbances initiated in the nose region at $\varphi_0 = \xi_0/R_N = 45°$, which coincides with the location of the roughness array. A description of the experimental findings is deferred to Section 7.4. Figure 7-12 shows the mean total energy gain and corresponding azimuthal wavenumber as a function of the optimal growth interval, $\Delta\xi = \xi_1 - \xi_0$, for the four AFRL configurations shown in Table 7-1. Figure 7-12(a) shows that the trend previously observed for $\xi_0 < \xi_j$ at $Re_\infty = 91.4 \times 10^6$ m^{-1} (Figure 7-11(b)) also applies at other Reynolds numbers. Specifically, the optimal energy gain has a maximum immediately downstream of the inflow station and then decays up to a plateau zone before increasing again for longer transient growth intervals. For the same freestream unit Reynolds number, the initial peak in optimal energy gain is larger for the larger nose radius cone than for the smaller nose radius case, but this situation is reversed for larger optimal growth intervals ($\Delta\xi > 0.02$ m). Figure 7-12(b) shows that the three regions translate into a discontinuous evolution of the corresponding azimuthal wavenumber. The scaling of the optimal mean total energy gain with Re_{R_N} (Figure 7-12(c)) and of the corresponding initial azimuthal wavelength with L_{R_N} (Figure 7-12(d)) is reasonable for the cases with the same nose radius R_N = 15.24 mm and different freestream unit Reynolds numbers, but not for the smaller nose radius case (R_N = 5.08 mm) and outside the nose region.

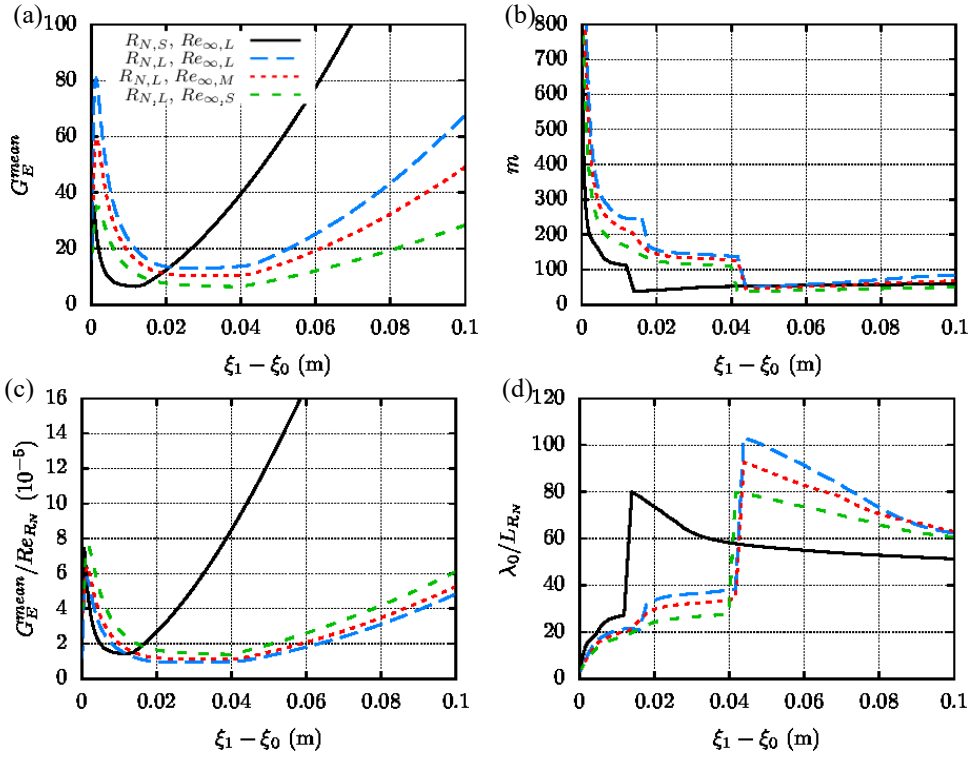

Figure 7-12: (a), (c) Optimal Mean Energy Gain and Corresponding (b), (d) Azimuthal Wavenumber with Initial Disturbance Location ϕ_0 = 45° (ξ_0 = 0.04 m for the R_N = 5.08 mm Cone and ξ_0 = 0.012 m for the R_N = 15.24 mm Cone). The Legend Refers to $R_{N,S}$ = 5.08 mm, $R_{N,L}$ = 15.24 mm, $Re_{\infty,L}$ = 91.4 x 10^6 m^{-1}, $Re_{\infty,M}$ = 60.9 x 10^6 m^{-1}, $Re_{\infty,S}$ = 30.5 x 10^6 m^{-1}.

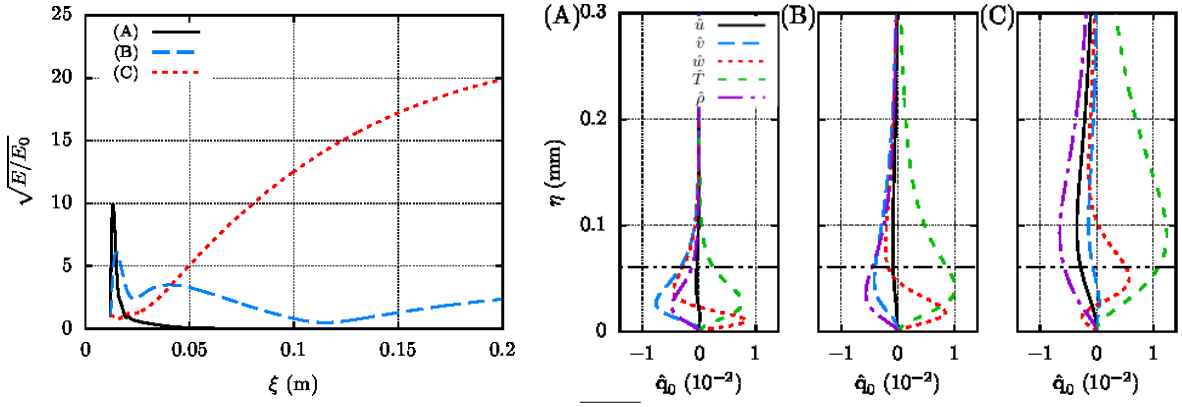

Figure 7-13: Evolution of the Disturbance Amplitude $\sqrt{E/E0}$ and Corresponding Initial Optimal Perturbations for the R_N = 15.24 mm and Re_∞ = 91.4 x 10^6 m^{-1} Configuration. The Selected Optimization Intervals and Azimuthal Wavenumbers are (A) $\Delta\xi$ = 0.0030 m and m = 420; (B) $\Delta\xi$ = 0.023 m and m = 150; and (C) $\Delta\xi$ = 0.091 m and m = 80. The Initial Disturbance Location is Set at the Nosetip at φ_0 = 45° that Corresponds to ξ_0= 0.012 m. The Horizontal, Dash-Double Dot Lines Indicates the Edge of the Boundary Layer based on Total Enthalpy, $\eta = \delta_h$.

Figure 7-13 shows further details of the transient growth disturbances initiated in the nose at $\varphi_0 = 45°$ for the blunter cone at the highest Re_∞ configuration (R_N = 15.24 mm and Re_∞ = 91.4 x 10^6 m^{-1}). Three cases based on the trends observed in Figure 7-12 are plotted; namely, (A) $\Delta\xi$ = 0.0030 m and m = 420; (B) $\Delta\xi$ = 0.023 m and m = 150; and (C) $\Delta\xi$ = 0.091 m and m = 80. The case (A) corresponds to the first peak in mean energy gain that is larger for the larger nose radius cone (Figure 7-12 (a)). The evolution of the disturbance amplitude $\sqrt{E/E0}$ for the case (A) shows a rapid rise to its peak value within a rather short distance from the initial disturbance location and a slower subsequent decay with values lower than 1 for streamwise locations in the frustum region. The initial optimal perturbation plotted in Figure 7-13 is mostly contained within the boundary layer thickness; and hence, such initial disturbance profiles are better suited for excitation via surface roughness than some other cases where the initial profiles extend well outside of the boundary layer. The disturbance amplitude evolution of the case (B) has a smaller initial peak and then remains below 6 along the streamwise domain plotted in Figure 7-13. The initial optimal perturbation associated with this case (B) is similar to that in case (A), but the peaks of the perturbation variables are located somewhat farther from the wall, which presumably makes this perturbation less likely to be excited via surface roughness. The energy gain evolution for case (C) ($\Delta\xi$ = 0.091 m, m = 80) shows rather small disturbance amplification near the inflow location and then a monotonic amplification up to ξ = 0.2 m. Figure 7-13 shows that the optimal initial perturbation shape in case (C) is more complex than that for cases (A) and (B), because the perturbation profiles for wall-normal and spanwise velocity components have two and three peaks instead of one and two peaks, respectively. Also, the perturbation profiles have a larger wall-normal extension and the peaks of these profiles are located farther from the wall. In summary, the results shown in Figure 7-13 indicate that roughness-induced perturbations at φ_0 = 45° can experience transient growth in a short interval within the nose region. The transient growth streaks can lead to the onset of nonstationary streak instabilities that typically amplify rather rapidly and induce transition shortly after their onset; see Refs. [65–70] for details on secondary instability of streaks in high-speed boundary layers.

Previously, disturbances initiated in the vicinity of the juncture location, $\xi_j = R_N\pi/2$, were found to experience a larger growth for the larger nose radius cone and relatively short transient growth intervals. This finding is further investigated here. Figure 7-14 shows the mean gain in total energy and corresponding azimuthal wavenumber as a function of the optimal growth interval, $\Delta\xi = \xi_1 - \xi_0$, for the four AFRL configurations shown

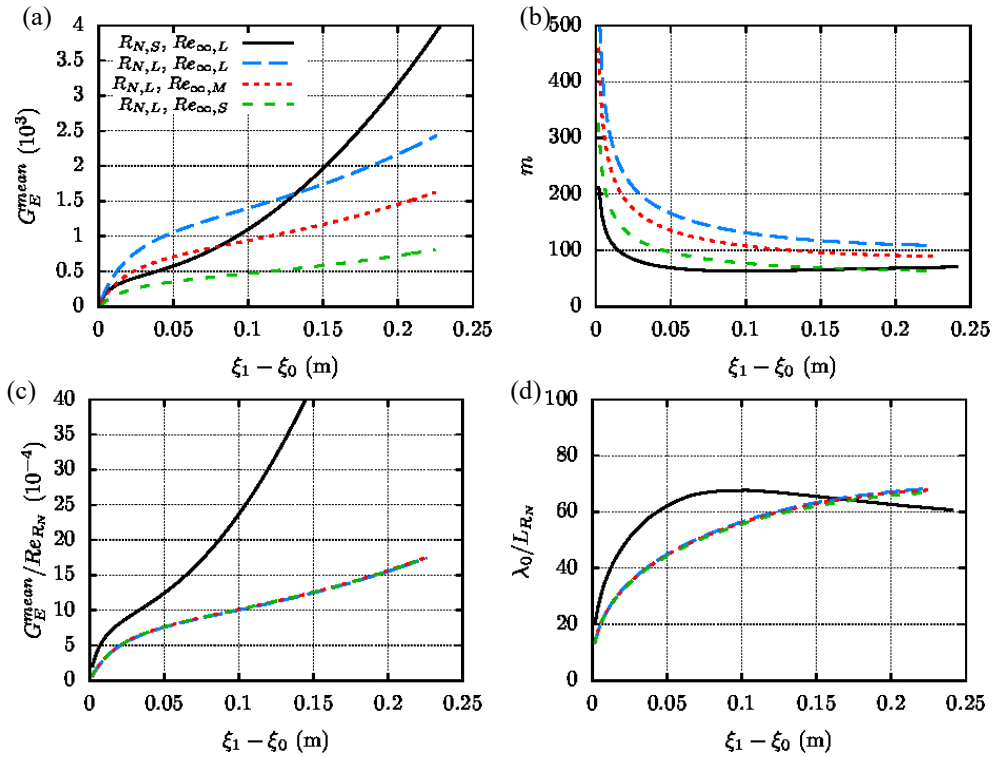

Figure 7-14: (a), (c) Optimal Mean Energy Gain and Corresponding (b), (d) Azimuthal Wavenumber with Initial Disturbance Location Set in the Juncture at $\xi_0 = \xi_j = R_N \pi/2$ (ξ_0 = 0.008 m for R_N = 5.08 mm and ξ_0 = 0.024 m for R_N = 15.24 mm.) The Legend Refers to $R_{N,S}$ = 5.08 mm, $R_{N,L}$ = 15.24 mm, $Re_{\infty,L}$ = 91.4 × 10^6 m^{-1}, $Re_{\infty,M}$ = 60.9 × 10^6 m^{-1}, $Re_{\infty,S}$ = 30.5 x10^6 m^{-1}.

in Table 7-1. Figure 7-14(a) shows in details that the trend observed in Figure 7-11(b) is for Re_∞ = 91.4 x 10^6 m^{-1} is also found at other Reynolds numbers. Specifically, the energy gain has a monotonic increasing evolution as $\Delta\xi$ is increased, and the energy gain is larger for larger nose radius for relatively short optimization intervals ($\Delta\xi$ < 0.13 m). The difference between the energy gain values for the two nose radii (R_N = 5.08 and 15.24 mm) and same freestream unit Reynolds number (Re_∞ = 91.4 x 10^6 m^{-1}) reaches about a factor of 2 for $\Delta\xi$ = 0.05 m. The azimuthal wavenumbers associated with the optimal energy gain values of Figure 7-14(a) are shown in Figure 7-14(b). The azimuthal wavenumber quickly decreases and as the length of the transient growth interval increases, albeit at a decreasing rate. Compared to the large bluntness cases (R_N = 15.24 mm), the smaller radius case (R_N = 5.08 mm, Re_∞ = 91.4 x 10^6 m^{-1}) shows a notable, different behavior of both the optimal energy gain and the associated azimuthal wavenumbers. This difference is clearly observed in the scaled mean energy gain and scaled initial wavelength plotted in Figures 7-14(c) and 7-14(d), respectively. The large nose radius cases (R_N = 15.24 mm) show a perfect scaling of both properties as the unit Reynolds number is varied, but the scaled values corresponding to the small radius case (R_N = 5.08 mm) are clearly different from the blunt nose cases. The reason for this poor scaling of the transient growth parameters with nose radius could be due to the lack of selfsimilarity of the boundary layer profiles near the nose.

Figure 7-15 shows further details of the transient growth disturbances initiated at the juncture location for the R_N = 15.24 mm and Re_∞ = 91.4 x 10^6 m^{-1} configuration. The three cases shown in Figure 7-15 for the R_N = 15.24 mm case correspond to (A) $\Delta\xi$ = 0.0295 m and m = 200; (B) $\Delta\xi$ = 0.0668 m and m = 150; and (C) $\Delta\xi$ = 0.2066 m and m = 110. Figure 7-15 shows that the peak in disturbance amplitude moves slightly

downstream as the optimal growth interval becomes longer from case (A) to case (C). This peak is barely reached at the end of the cone length for the case (C). The optimal initial perturbations associated with the three cases are plotted in Figure 7-15. The wall-normal extension and the peaks of these profiles are located closer to the wall for shorter optimal growth intervals, which makes them more closely related to roughness-induced perturbations. A wall-mounted device is not expected to generate a perturbation with the wall-normal extension of the optimal perturbation corresponding to case (C). Although not shown here, equivalent results for the small radius case (R_N = 5.08 mm, Re_∞ = 91.4 x 10^6 m^{-1}) and an optimal growth interval of $\Delta\xi$ = 0.0295 m show a peak disturbance amplitude equal to approximately one half of the peak value corresponding to the large radius cone (R_N = 15.24 mm, Re_∞ = 91.4 x 10^6 m^{-1}) plotted in Figure 7-15. Similar to results for disturbances initiated near the sonic location, these results with $\xi_0 = \xi_j$ indicate that roughness-induced perturbations can experience greater transient growth for larger nosetip bluntness at the same freestream conditions. Therefore, transition onset could be driven by roughness-induced transient growth if the streak amplitude required for streak instabilities is reached.

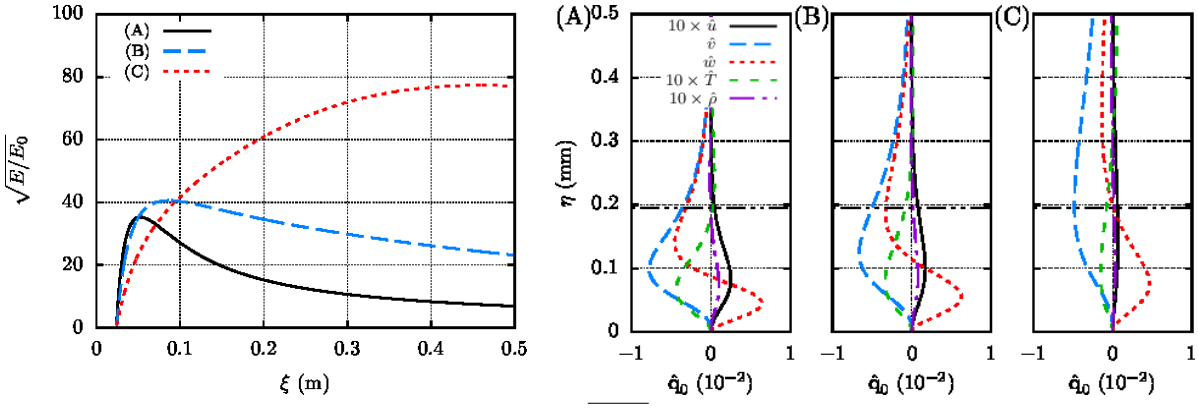

Figure 7-15: Evolution of the Disturbance Amplitude $\sqrt{E/E_0}$ for the R_N = 15.24 mm and Re_∞ = 91.4 x 10^6 m^{-1} Configuration. The Selected Optimization Intervals and Azimuthal Wavenumbers are (A) $\Delta\xi$ = 0.0295 m and m = 200; (B) $\Delta\xi$ = 0.0668 m and m = 150; and (C) $\Delta\xi$ = 0.2066 m and m = 110. The Initial Disturbance Location Is Set at the Juncture $\xi_0 = \xi_j$ that Corresponds to ξ_0 = 0.024 m. The Horizontal, Dash-Double Dot Lines Indicates the Edge of the Boundary Layer based on Total Enthalpy, $\eta = \delta_h$.

7.3.3.3 Transient Growth of Traveling Disturbances Along the Frustum Region

Next, we present salient findings pertaining to the nonmodal growth of traveling disturbances over the frustum region of the AFRL cone for the case of R_N = 5.08 mm and Re_∞ = 91.4 x 10^6 m^{-1}. A detailed parameter study of traveling mode disturbances is deferred to Paredes et al. [71]. The procedure used for the transient growth analysis of traveling disturbances is the same as that used earlier for the stationary disturbances with α = 0, except with the addition of the streamwise pressure gradient term that is approximated with Equation (7-3) based on the work by Vigneron et al. [56] for PNS equations. For the results presented herein, we confine our attention to a transient growth interval of (ξ_0; ξ_1) = (0.04; 0.161) m. The selected outflow location corresponds to the transition location measured by Jewell et al. [46] as indicated in Table 7-1, whereas the inflow location was chosen on the basis of a parameter study, which showed that the maximum energy gain occurs for ξ_0 = 0.04 m for most combinations of frequency and azimuthal wavenumber.

Figure 7-16 shows the contours of the N-factor based on the total energy gain, N_E, as a function of the frequency, F , and azimuthal wavenumber, m. The outlet energy gain is selected as the objective function for the optimal growth analysis. One may observe that the maximum energy gain of $N_E = 4.59$ is achieved by a stationary, three-dimensional perturbation with $F = 0.0$ kHz and $m = 82$. This stationary disturbance is the same as that studied previously in Section 7.3.3.2. Additionally, Figure 7-16 shows a second, local maximum ($N_E = 3.27$) in the N -factor contours for planar traveling waves with $F = 340.0$ kHz, $m = 0$. Additional results not presented herein for sharper cones ($R_N = 1.524$ and 2.54 mm) have indicated that the energy gain associated with this local maximum for traveling disturbances increases with the nose bluntness. Those results also showed that, unlike the case considered in Figure 7-16, the peak N-factor for traveling disturbances is not always associated with planar waves.

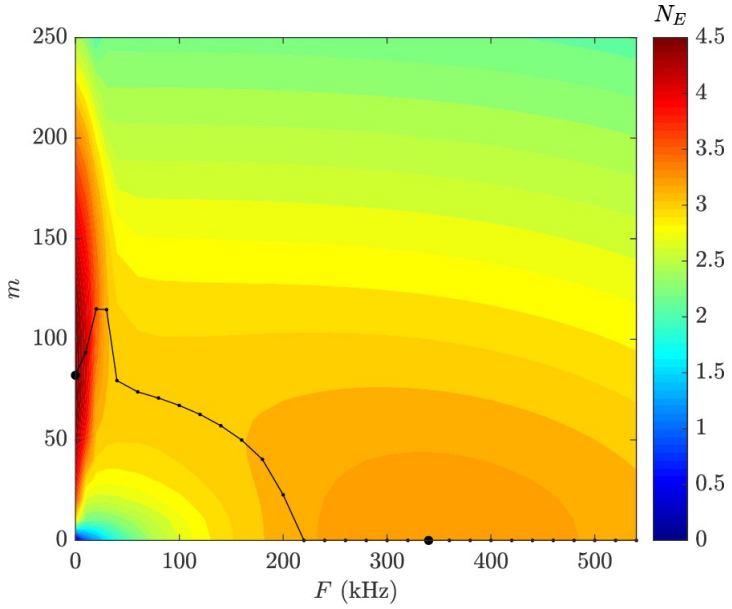

Figure 7-16: Contours of N-Factor Values Defined as $N_E = 1/2\ln\left(G_E^{out}\right)$ in the Azimuthal Wavenumber versus Frequency Plane in the Frustum Region of the $R_N = 5.08$ mm Cone with $Re_\infty = 91.4 \times 10^6$ m^{-1}, $\xi_0 = 0.04$ m and $\xi_1 = \xi_T = 0.161$ m. The Isocontours Represents N-Factor Increments of $\Delta N_E = 0.1$. The Solid Black Line Denotes the Azimuthal Wavenumber Corresponding to Maximum N_E. The Large Black Circles Denote the (F, m) Combination for Maximum N_E in Both Axes.

Figures 7-17 and 7-18 show further details concerning the streamwise evolution of the optimal traveling disturbance ($F = 340.0$ kHz, $m = 0$, $(\xi_0; \xi_1) = (0.04; 0.161)$ m and $J = \left(G_E^{out}\right)$). Figure 7-17 illustrates the axial growth in the disturbance amplitude in terms of the N-factors based on the total energy (N_E), kinetic energy (N_K), maximum temperature fluctuation (N_T), and the maximum of the streamwise velocity fluctuation N_u, respectively. To check the grid convergence of the solution obtained on the basis of $\alpha = 0$ and the PNS approximation, results were obtained with two different streamwise grids with $n_\xi = 8192$ and $n_\xi = 16384$, respectively. To confirm that the Vigneron parameter does not have a significant influence on the N-factor evolution, additional results were obtained by marching the PSE equations with the same initial condition. The PSE solution is obtained without invoking the Vigneron PNS approximation (i.e., with $\alpha \neq 0$ and $\Omega_{PNS} = 1$). The number of streamwise points required to obtain grid converged results with $\alpha \neq 0$ is approximately two orders of magnitude lower than the number of grid points required to resolve the entire wave form via $\alpha = 0$. The agreement between the various results is excellent, indicating that the prediction accuracy is not compromised by either physical or numerical approximation. An important characteristic of the traveling mode growth is the

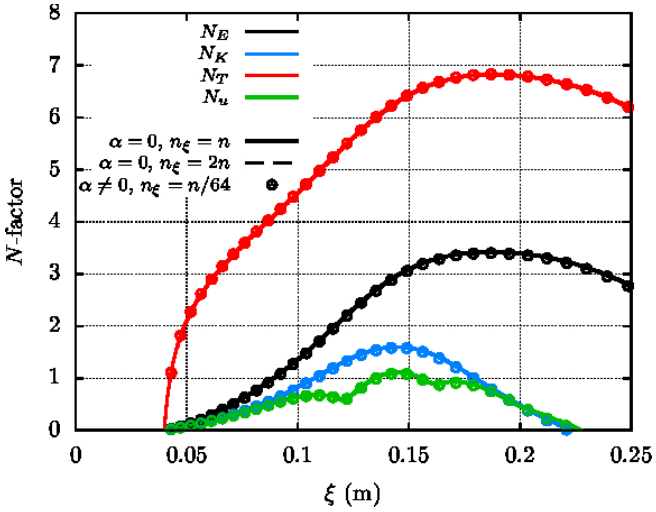

Figure 7-17: *N*-Factor Evolution of the Optimal Disturbance with F = 340 kHz, m = 0, ξ_0 = 0.04 m, and ξ_1 = 0.161 m, for the R_N = 5.08 mm Cone with Re_∞ = 91.4 x 10^6 m^{-1}. The Solid and Dashed Lines Represent the Solution with α = 0 and PNS Approximation of Equation (7-3) with n_ξ = n = 8192 Points and n_ξ = 2n, Respectively. The Symbols Denote the Solution with $\alpha \neq 0$ and No PNS Approximation (Ω_{PNS} = 1).

large difference between the growth factors for the temperature and streamwise velocity perturbations, respectively. The maximum N -factor based on the temperature perturbation is N_T = 6.82, whereas that based on the streamwise velocity perturbation is substantially lower, N_u = 1.11. This difference is also reflected in the evolution of the total disturbance energy and the disturbance kinetic energy, indicating that the transient growth of the traveling disturbances is mainly reflected in the thermodynamic perturbations. The optimum initial disturbance at the inflow location is dominated by velocity fluctuations, which are an order of magnitude larger than the temperature fluctuations. However, the rapid growth in temperature perturbation immediately downstream of the inflow location allows the velocity and temperature perturbation to become comparable to each other. Indeed, Paredes et al. [71] have pointed out that, because of the sustained higher growth in temperature perturbation over the remaining portion of the transient growth interval (albeit at a reduced pace in comparison with the inflow region), the temperature fluctuations become the dominant component of the outflow disturbance at $\xi = \xi_1$. On the basis of initial value analysis of transient nonmodal growth in compressible Poiseuille flows, Xie et al. [72] argued that the pressure-velocity coupling at higher Mach numbers played an important role in influencing the evolution of disturbances that are nearly aligned with the mean flow direction. However, the role of temperature fluctuations was not directly investigated. Therefore, further work will be necessary to establish whether or not the physical mechanisms discussed therein also play a role in the transient growth of planar disturbances observed in this paper.

The streamwise evolution in the mode shape of the optimal disturbance is plotted in Figure 7-18. The normalized temperature $\tilde{T}/\max(\tilde{T})$ and streamwise velocity $\tilde{u}/\max(\tilde{u})$ are mostly contained between the boundary-layer edge δ_h and the entropy-layer edge, δ_S, which is defined as the location where the local entropy increment with respect to the freestream value, i.e., $\Delta S = c_p \ln(\bar{T}/\bar{T}_\infty) - R_g \ln(\bar{p}/\bar{p}_\infty)$, is 0.25 times the entropy increment at the wall ($\Delta S(\xi, \eta = \delta_S) = 0.25 \Delta S_{wall}$). The disturbance is initially tilted against the flow direction and increases in magnitude while rotating downstream. This behavior strongly resembles the Orr mechanism for the transient growth of planar disturbances [73, 74], which has been widely studied for incompressible flows [20, 75]. Nonmodal growth based on the Orr mechanism is attributed to an energy extraction from the mean

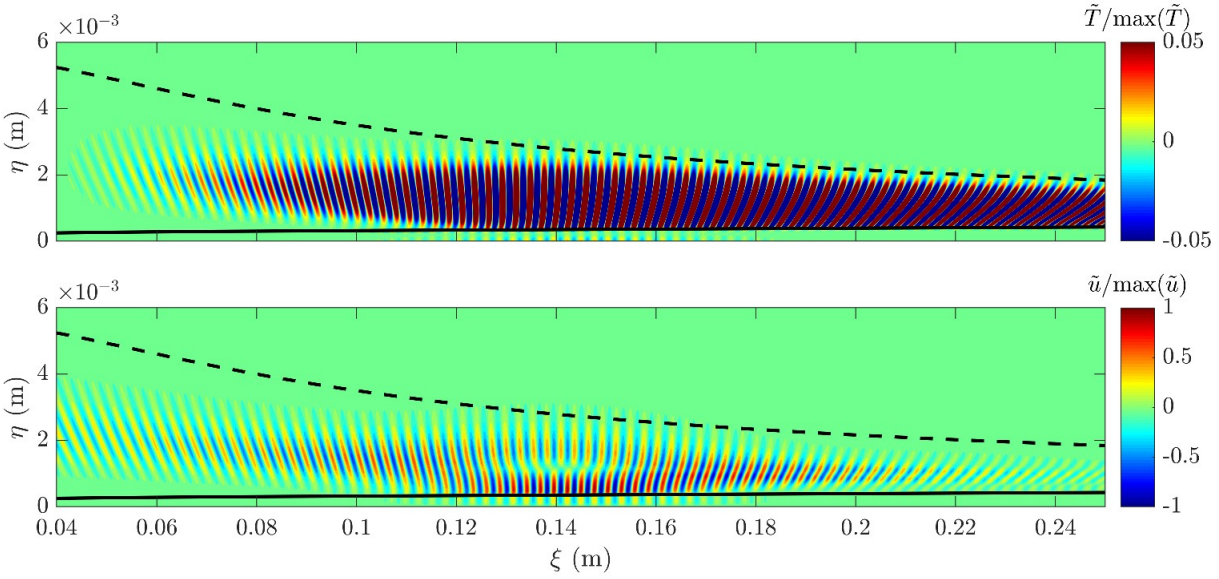

Figure 7-18: Contours of Normalized Temperature and Streamwise Velocity Components of the Optimal Disturbance with F = 340 kHz, m = 0, ξ_0 = 0.04 m, and ξ_1 = 0.161 m, for the R_N = 5.08 mm Cone with Re_∞ = 91.4 x 10^6 m^{-1}. The Solid, Black Line Indicates the Edge of the Boundary Layer, δ_h. The Dashed, Black Line Indicates the Edge of the Entropy Layer δ_S.

shear by transporting momentum down the mean momentum gradient through the action of the Reynolds stress associated with the perturbation field. However, the energy amplification observed in this compressible case is mainly attributed to the temperature perturbation within the entropy layer. Similar to the LIF-based schlieren images of Figure 7-5, the peak disturbance magnitude at any axial location is observed outside of the mean boundary layer edge. However, additional work is required to establish a more definitive link between the experimental observations and the nonmodal growth mechanism reported herein. Furthermore, because the traveling mode structure in Figure 7-18 has a relatively weak signature within the boundary layer region, its role in initiating boundary layer transition also remains to be clarified. Similarly, nonlinear simulations of these traveling instabilities, e.g., by means of nonlinear PSE, could provide some insights into the potential breakdown mechanism and the minimum initial amplitude of the optimal disturbance that would likely result in the onset of transition at the measured transition location.

7.3.3.4 Transient Growth on AEDC Configurations

Transient growth results for the AFRL cones showed that disturbances initiated in the vicinity of the juncture between the nosetip and the frustum of the cone can experience a rather strong transient amplification in a short streamwise distance. This amplification is stronger for the larger nose radius case at the same freestream conditions. Based on that observation, results for the AEDC configurations are focused on disturbances initiated at the juncture of the cones to study the trend with this different set of flow and geometry parameters. Figure 7-19(a) shows the evolution of optimal gain in mean energy gain as a function of the optimal growth interval for disturbances initiated at the juncture location. Again, as the nose radius of the cone is increased, the optimal energy

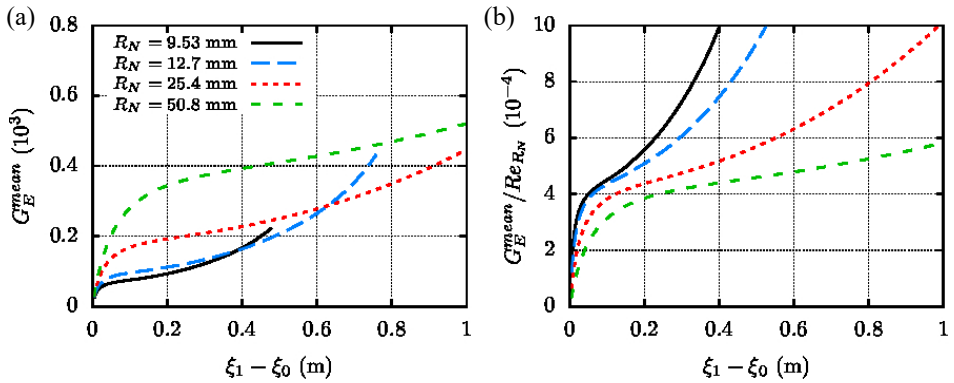

Figure 7-19: Optimal Mean Energy Gain with Initial Disturbance Location Set at the Juncture $\xi_0 = \xi_j = R_N \pi/2$ for the AEDC Configurations (ξ_0 = 0.015 m for R_N = 9.53 mm, ξ_0 = 0.020 m for R_N = 12.7 mm, ξ_0 = 0.040 m for R_N = 25.4 mm, and ξ_0 = 0.080 m for R_N = 50.8 mm). The Freestream Unit Reynolds Number Is $Re_\infty \approx 17.5 \times 10^6$ m^{-1}.

gain becomes notably larger. Figure 7-19(b) indicates that the scaled energy gain values, G_E^{mean}/Re_{R_N}, are smaller for larger nose radius cases, indicating a nonlinear increase in optimal energy gain with increasing nose bluntness. This trend is similar to the trend in Figure 7-14(c) for the AFRL configurations.

7.4 ROUGHNESS EFFECTS ON LAMINAR-TURBULENT TRANSITION ON BLUNT CONES

Between 1978 and 1982, K. F. Stetson performed a total of 196 sharp- and blunt-cone experiments on a thin-walled 8° half-angle, 4 in. (0.1016 m) diameter base cone at zero angle of attack in the AFRL Mach 6 High Reynolds Number facility. These measurements were initially reported in a 1983 paper [2] and recently Jewell & Kimmel [36] performed a computational analysis indicating that neither the Mack second mode nor the first mode were likely to be the dominant instability mechanism for nosetips with radius larger than 1 mm, for which transition was nevertheless consistently observed once sufficient freestream Reynolds numbers were reached. Alternate physical mechanisms may explain these results, and include transient growth or mean flow distortion from roughness.

More recently, experiments have been performed in the same facility on a 7° half-angle variable-bluntness cone at zero angle of attack with similar nosetip bluntness values, which have also been shown to transition from laminar to turbulent flow without significant predicted amplification of first- or second-mode instability for smooth nosetips with radius larger than 1 mm and sufficient freestream Reynolds numbers [46]. A subset of the smooth cases, with R_N = 5.08 mm and R_N = 15.24 mm, have been repeated with 15 μm laser-machined roughness elements of approximately cubical shape located on the circle at 45 degrees from the apex of the spherical tip, which is near the sonic line for zero angle of attack. The array of roughness elements has been designed following the transient growth results of Subsection 7.3.3. The number of roughness elements has been selected to match the disturbance azimuthal wavenumber that lead to significant transient growth at the same conditions. Specifically, 210 roughness elements were mounted on the small radius cone (R_N = 5.08 mm) and 420 roughness elements on the large radius cone (R_N = 15.24 mm). A picture of the small radius nosetip with the array of roughness elements is shown in Figure 7-20.

Figure 7-20: Nosetip of R_N = 5.08 mm with 210 Equally Spaced 15 μm Cubical Roughness Elements that Were Laser-Machined Circumferentially at 45° from the Apex of the Spherical Tip.

The presence of roughness elements on the R_N = 5.08 mm cone had little discernible effect on the experimentally observed transition location or heating levels across the operating conditions of the Mach 6 High Re Facility. In contrast, roughness elements of the same shape and dimension on the R_N = 15.24 mm cone had a profound effect on transition above a critical Reynolds number. This effect is illustrated in Figures 7-21(a) and 7-21(b), which present surface heat flux distributions measured by Medtherm coaxial thermocouples from pairs of rough and smooth experiments, with roughness-height Re_{kk} values matched to within 3% between the two sets. In Figure 7-21(a), the rough (Re_∞ = 66.5 × 10^6 m^{-1}, k/δ_h = 0.381, Re_{kk} = 294) and smooth (Re_∞ = 66.0 x 10^6 m^{-1}) surface heat transfer values for the R_N = 5.08 mm cone overlap. In Figure 7-21(b), the rough (Re_∞ = 75.8 x 10^6 m^{-1}, k/δ_h = 0.225, Re_{kk} = 287) and smooth (Re_∞ = 76.9 x 10^6 m^{-1}) cases for the R_N = 15.24 mm cone are quite different, with the rough tip resulting in nearly immediate transition onset, while the equivalent smooth tip results in laminar flow nearly to the end of the cone. This result indicates that the onset of transition in this data is associated with the combined effects of bluntness and roughness.

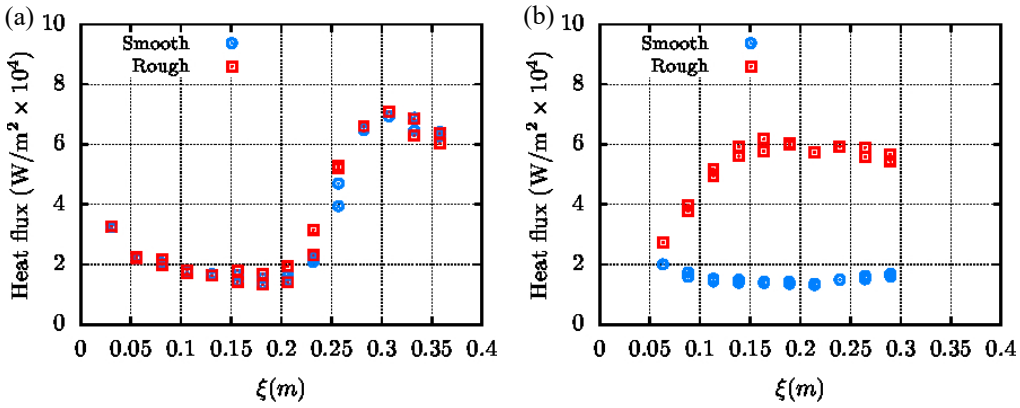

Figure 7-21: Heat Flux Distributions for a 7° Half-Angle Cone at M_∞ = 5.9 with Nosetip of (a) R_N = 5.08 mm and (b) R_N = 15.24 mm for a Smooth Tip and a Tip with a Row of Equally Spaced 15 μm Cubical Roughness Elements.

7.5 SUMMARY AND CONCLUDING REMARKS

A collaborative effort by the NATO STO group AVT-240 on Hypersonic Boundary-Layer Transition Prediction was devoted to bluntness effects on transition over circular cones at zero angle of attack. This paper presented an overview of that work, which consisted of transition measurements on blunt cones models with varying degrees of nosetip bluntness, measurements pertaining to the combined effects of nose bluntness and controlled surface roughness on the nose tip, and theoretical analysis of optimal transient growth on blunt cones.

The following observations can be made on the basis of wind tunnel measurements at freestream Mach numbers from 6 to 12:

1) The recent measurements are consistent with the known trend of an initially downstream movement in the transition onset location as the nosetip bluntness is increased. This trend confirms the stabilizing effect of nose bluntness on the amplification of Mack mode, i.e., second-mode instability waves.

2) The measurements also confirm the well-known observation concerning a reversal in the above trend at sufficiently large values of the nosetip Reynolds number and the transition reversal phenomenon cannot be explained via the hydrodynamic stability paradigm, due to the absence of an adequately significant modal amplification of first-mode, second-mode, and entropy-layer instabilities.

3) Experimental measurements indicate that, in the transition reversal regime, boundary layer transition over the frustum of the cone is highly sensitive to wall roughness. The onset of transition appears to be dominated by disturbances that originate in the vicinity of the nosetip, suggesting roughness-induced transient growth as a likely cause for laminar-turbulent transition.

Optimal transient growth analysis has been conducted for the laminar flow based on the solution of the Navier-Stokes equations over a 7° half-angle variable-bluntness cone at zero angle of attack with bluntness and freestream conditions corresponding to a subset of the experiments of Stetson [2] at the AFRL Mach 6 High Reynolds Number facility and $Re_\infty = 30.5-91.4 \times 10^6$ m^{-1} and of Marineau et al. [25] at the AEDC Tunnel 9 facility with the Mach 10 nozzle and $Re_\infty \approx 17.5 \times 10^6$ m^{-1}. Some interesting findings in regard to the transient growth of both stationary and traveling disturbances have been uncovered in the course of this study. Estimates of maximum possible transient growth are obtained through a dual optimization [23, 24] that varies both the initial and final locations of the transient growth interval. The following conclusions may be drawn on the basis of the transient growth analysis:

1) The optimal growth results can be naturally divided into two parts. The first part deals with transient growth intervals limited to the nose region, and second part applies to optimal growth intervals that extend to the frustum region that encompasses the range of measured transition locations.

2) Results for optimal growth intervals within the nose region are similar to the findings by Paredes et al. [23] for a hemispherical forebody. Specifically, the highest predicted growth in total energy corresponds to relatively short transient growth intervals in the vicinity of the stagnation point, but the kinetic energy growth associated with these perturbations is rather small. The maximum growth in disturbance kinetic energy is found for perturbations initiated near the sonic point at an angle of

42.4° from the apex of the spherical tip. Furthermore, the wall-normal profiles of optimal initial perturbations associated with the maximum energy gain are concentrated within the boundary layer thickness, i.e., close to the wall. More important, at a fixed set of freestream conditions, increased nose bluntness results in higher transient amplification within the nose region.

3) Based on the transient growth analysis for both AFRL and AEDC configurations, one may conclude that stationary disturbances that are initiated in the vicinity of the juncture between the nosetip and the frustum also exhibit a greater transient amplification for larger values of nosetip bluntness, but only for relatively short optimization intervals. Furthermore, for the large nosetip bluntness, the wall-normal extension of the optimal initial perturbations is small, indicating that wall roughness may be able to induce such perturbations.

4) The transient growth analysis of traveling disturbances showed significant growth of planar waves that peak between the boundary-layer and entropy edges. The temperature component of the disturbance can reach significant N -factors at the measured transition location, $N_T \approx 7$, while the streamwise velocity component is barely amplified, $N_u \approx 1$.

We note that the actual generation (i.e., receptivity) of the transient growth disturbances has not been addressed in this paper. Disturbance profiles resulting from realistic external disturbances usually result in a suboptimal transient growth. In that regard, the present results based on optimal initial, disturbances may be viewed as providing an upper bound on the nonmodal amplification due to either spanwise periodic, roughness-induced, stationary disturbances or freestream traveling waves.

Finally, the roughness effects on transition reversal over a 7° half-angle blunt cone at hypersonic flow are experimentally investigated in the AFRL Mach 6 High Reynolds Number facility. Transition measurements were made with an azimuthally periodic array of 15 μm, laser-machined roughness elements of approximately cubical shape located at 45° from the apex of the spherical tip, which nearly coincides with the sonic location. The roughness array spacing ($m = 210$ for $R_N = 5.08$ mm and $m = 420$ for $R_N = 15.24$ mm) was designed to match the disturbance azimuthal wavenumber that is predicted to induce large transient growth under the respective conditions. The following observations can be made on the basis of these measurements:

1) The roughness array on the small nosetip bluntness cone showed no effect on the transition location at $Re_\infty \approx 66 \times 10^6$ m^{-1} (i.e., $k/\delta_h = 0.381$, $Re_{kk} = 294$).

2) On the other hand, the experiments conducted with the large nosetip bluntness with $Re_\infty \approx 76 \times 10^6$ m^{-1} (i.e., $k/\delta_h = 0.225$, $Re_{kk} = 287$) showed a prominent effect of the roughness elements on the transition onset, moving the transition front close to the nosetip, whereas the smooth tip baseline for the same blunter cone has resulted in a laminar flow over the majority of the cone.

3) The above findings indicate that the transition onset is associated with the combined effects of bluntness and roughness.

Finally, we note that wakes behind sufficiently large discrete roughness elements can sustain large modal amplification of streak instabilities as shown by Choudhari et al. [65, 67]; but the level of amplification is sensitive to the roughness parameters and other flow details [66]. Because the measured onset of transition during the

AFRL experiments was within a short distance behind the roughness array, wake instability may have played a role in the large upstream shift in transition location; and we are currently investigating that possibility via more detailed computations. However, a broader set of measurements involving controlled surface roughness would be useful in determining whether or not naturally occurring micro-roughness over the model surface may have been responsible for the observed transition reversal in other blunt cone experiments. Effects of roughness location in the vicinity of the nosetip and the juncture location would be an important aspect of such a parametric study. Flow visualizations accompanied by dynamic measurements, i.e., high frequency response heat transfer or pressure measurements, in the region between the controlled surface roughness and the onset of transition would go a long way in providing valuable clues regarding the physical mechanisms at play. Finally, performing parallel measurements in both quiet and conventional wind tunnel facilities, or in flight test experiments, would provide further information regarding the role of both the freestream disturbances and the nonmodal growth of traveling disturbances within the entropy layer during transition reversal phenomenon.

7.6 ACKNOWLEDGMENTS

Part of this research was sponsored by the NASA Transformational Tools and Technologies (TTT) Project of the Transformative Aeronautics Concepts Program (TACP) of the Aeronautics Research Mission Directorate (ARMD). A portion of the computational resources supporting this work were provided by the NASA High-End Computing (HEC) Program through the NASA Advanced Supercomputing (NAS) Division at Ames Research Center. The authors would like to thank Test Resource Management Center (TRMC) Test and Evaluation/Science and Technology (T&E/S&T) Program for their support. E. C. Marineau's work was funded by T&E/S&T Program through the High Speed Systems Test (HSST) area as part of the Center of Testing Excellence (CoTE). We also acknowledge Benxin Wu and his group at Purdue University for laser-machining the nose tip roughness elements. J. S. Jewell was supported by the NRC Research Associateship for part of this work.

7.7 REFERENCES

[1] Schneider, S., "Hypersonic Laminar-Turbulent Transition on Circular Cones and Scramjet Forebodies," *Progress in Aerospace Sciences*, Vol. 40, 2004, pp. 1–50.

[2] Stetson, K., "Nosetip Bluntness Effects on Cone Frustum Boundary Layer Transition in Hypersonic Flow," AIAA Paper 83-1763, 1983.

[3] Morkovin, M., Reshotko, E., and Herbert, T., "Transition in Open Flow Systems – A Reassessment," *Bull. Am. Phys. Soc.*, Vol. 39, 1994, pp. 1882.

[4] Reshotko, E., "Boundary Layer Transition, Instability and Control," AIAA Paper 94-0001, 1994.

[5] Reshotko, E. and Tumin, A., "Spatial Theory of Optimal Disturbances in a Circular Pipe Flow," *Phys. Fluids*, Vol. 13, 2001, pp. 991–996.

[6] Avila, K., Moxey, D., De Lozar, A., Avila, M., Barkely, D., and Hof, B., "The Onset of Turbulence in Pipe Flow," *Science*, Vol. 333, 2011, pp. 192–196.

[7] Reshotko, E., "Preliminary Experimental Study of Disturbances in a Laminar Boundary Layer Due to Distributed Surface Roughness," AIAA Paper 81-1224, 1981.

[8] White, E., "Transient Growth of Stationary Disturbances in a Flat Plate Boundary Layer," *Physics of Fluids*, Vol. 14, No. 12, 2002, pp. 4429–4439.

[9] Sharp, N. and White, E., "Roughness-Induced Transient Growth on a Hypersonic Blunt Cone," AIAA Paper 2014-0432, 2014.

[10] Murphy, J. and Rubesin, M., "Re-Evaluation of Heat-Transfer Data Obtained in Flight Test of Heat-Sink Shielded Re-Entry Vehicles," *Journal of Spacecraft Rockets*, Vol. 3, No. 1, 1966, pp. 53–60.

[11] Reshotko, E. and Tumin, A., "The Blunt Body Paradox: A Case for Transient Growth," *Laminar-Turbulent Transition: IUTAM Symposium, Sedona/AZ September 13 – 17, 1999*, edited by H. Fasel and W. Saric, Springer Berlin Heidelberg, Berlin, Heidelberg, 2000, pp. 403–408.

[12] Schneider, S., "Hypersonic Boundary-Layer Transition on Blunt Bodies with Roughness," AIAA Paper 2008-0501, 2008.

[13] Hollis, B., "Blunt-Body Entry Vehicle Aerothermodynamics: Transition and Turbulent Heating," *Journal of Spacecraft Rockets*, Vol. 49, No. 3, 2012, pp. 435–449.

[14] Case, K., "Stability of Inviscid Plane Couette Flow," *Physics of Fluids*, Vol. 3, 1960, pp. 143–148.

[15] Stuart, J., "The Production on Intense Shear Layers by Vortex Stretching and Convection," NATO AGARD Report No. 514. (also: National Phys. Lab. Aeronaut. Res. Rep. 1147), 1965.

[16] Landahl, M., "A Note on Algebraic Instability of Inviscid Parallel Shear Flows," *Journal of Fluid Mechanics*, Vol. 98, 1980, pp. 243–251.

[17] Tumin, A. and Reshotko, E., "Optimal Disturbances in Compressible Boundary Layers," *AIAA Journal*, Vol. 41, 2003, pp. 2357–2363.

[18] Paredes, P., Choudhari, M., Li, F., and Chang, C.L., "Optimal Growth in Hypersonic Boundary Layers," *AIAA Journal*, Vol. 54, No. 10, 2016, pp. 3050–3061.

[19] Schmid, P. and Henningson, D.S., *Stability and Transition in Shear Flows*, Springer, New York, 2001.

[20] Schmid, P., "Nonmodal Stability Theory," *Annunal Review of Fluid Mechanics*, Vol. 39, 2007, pp. 129–162.

[21] Reshotko, E. and Tumin, A., "Role of Transient Growth in Roughness-Induced Transition," *AIAA Journal*, Vol. 42, 2004, pp. 766–770.

[22] Andersson, P., Berggren, M., and Henningson, D., "Optimal Disturbances and Bypass Transition in Boundary Layers," *Physics of Fluids*, Vol. 11, 1999, pp. 134–150.

[23] Paredes, P., Choudhari, M., and Li, F., "Blunt-Body Paradox and Transient Growth on a Hypersonic Spherical Forebody," *Physical Review Fluids*, Vol. 2, 2017, pp. 053903.

[24] Paredes, P., Choudhari, M., and Li, F., "Blunt-Body Paradox and Improved Application of Transient Growth Framework," *AIAA Journal*, 2018, accessed June 13, 2018. doi: https://doi.org/10.2514/1.J056678.

[25] Marineau, E., Moraru, C., Lewis, D., Norris, J., Lafferty, J., Wagnild, R., and Smith, J., "Mach 10 Boundary-Layer Transition Experiments on Sharp and Blunted Cones," AIAA Paper 2014-3108, 2014.

[26] Aleksandrova, E., Novikova, A., Utyzhnikov, S., and Fedorov, A., "Experimental Study of the Laminar Turbulent Transition on a Blunt Cone," *Journal of Applied Mechanics and Technical Physics*, Vol. 55, No. 3, 2014, pp. 375–385.

[27] Softley, E., Graber, B., and Zempel, R., "Experimental Observation of Transition of the Hypersonic Boundary Layer," *AIAA Journal*, Vol. 7, No. 2, 1969, pp. 254–263.

[28] Softley, E., "Boundary Layer Transition on Hypersonic Blunt, Slender Cones," AIAA Paper 69-0705, 1969.

[29] Stetson, K., "Hypersonic Boundary Layer Transition Experiments," AFWAL-TR-80-3062, 1980.

[30] Muir, J. and Trujillo, A., "Experimental Investigation of the Effects of Nose Bluntness, Free-Stream Unit Reynolds Number, and Angle of Attack on Cone Boundary Layer Transition at a Mach Number of 6," AIAA Paper 72-0216, 1972.

[31] Stetson, K. and Rushton, G., "Shock Tunnel Investigation of Boundary Layer Transition at M=5.5," *AIAA Journal*, Vol. 5, 1967, pp. 899–906.

[32] Rotta, N., "Effects of Nose Bluntness on the Boundary Layer Characteristics of Conical Bodies at Hypersonic Speeds," NYU-AA-66-66, 1966.

[33] Malik, M., Spall, R., and Chang, C.L., "Effect of Nose Bluntness on Boundary Layer Stability and Transition," AIAA Paper 90-0112, 1990.

[34] Herbert, T. and Esfahanian, V., "Stability of Hypersonic Flow over a Blunt Body," AGARD CP-514. Paper 28. Theoretical and experimental methods in hypersonic flows., 1994.

[35] Marineau, E., "Prediction Methodology for Second-Mode-Dominated Boundary-Layer Transition in Hypersonic Wind Tunnels," *AIAA Journal*, Vol. 55, No. 2, 2017, pp. 484–499.

[36] Jewell, J. and Kimmel, R., "Boundary Layer Stability Analysis for Stetson's Mach 6 Blunt Cone Experiments," *Journal of Spacecraft Rockets*, Vol. 54, No. 1, 2017, pp. 258–265.

[37] Johnson, H. and Gandler, G., "Hypersonic Boundary Layer Stability Analysis using PSE-Chem," AIAA Paper 2005-5023, 2005.

[38] Balakumar, P. and Chou, A., "Transition Prediction in Hypersonic Boundary Layers using Receptivity and Freestream Spectra," *AIAA Journal*, Vol. 56, No. 1, 2018, pp. 193–208.

[39] Zanchetta, M., *Kinetic heating and transition studies and hypersonic speeds*, Ph.D. thesis, Imperial College of Science, Technology and Medicine, London, 1996.

[40] Grossir, G., Pinna, F., Bonucci, G., Regert, T., Rambaut, P., and Chazot, O., "Hypersonic Boundary Layer Transition on a 7 Degree Half-Angle Cone at Mach 10," AIAA Paper 2014-2774, 2014.

[41] Dietz, G. and Hein, S., "Entropy-Layer Instabilities over a Blunted Flat Plate in Supersonic Flow," *Physics of Fluids*, Vol. 11, No. 1, 1999, pp. 7–9.

[42] Fedorov, A. and Tumin, A., "Evolution of Disturbances in Entropy Layer on Blunted Plate in Supersonic Flow," *AIAA Journal*, Vol. 42, No. 1, 2004, pp. 89–94.

[43] Wright, M., Candler, G., and Bose, D., "Data-Parallel Line Relaxation Method for the Navier-Stokes Equations," *AIAA Journal*, Vol. 36, No. 9, 1998, pp. 1603–1609.

[44] Johnson, H., *Thermochemical interactions in hypersonic boundary layer stability*, Ph.D. thesis, University of Minnesota, 2000.

[45] Johnson, H., Seipp, T., and Candler, G., "Numerical Study of Hypersonic Reacting Boundary Layer Transition on Cones," *Physics of Fluids*, Vol. 10, No. 10, 1998, pp. 2676–2685.

[46] Jewell, J., Kennedy, R., Laurence, S., and Kimmel, R., "Transition on a Variable Bluntness 7-Degree Cone at High Reynolds Number," AIAA Paper 2018-1822, 2018.

[47] Pralits, J., Airiau, C., Hanifi, A., and Henningson, D., "Sensitivity Analysis using Adjoint Parabolized Stability Equations for Compressible Flows," *Flow, Turbulence and Combustion*, Vol. 65, 2000, pp. 321–346.

[48] Tempelmann, D., Hanifi, A., and Henningson, D., "Spatial Optimal Growth in Three-Dimensional Boundary Layers," *Journal of Fluid Mechanics*, Vol. 646, 2010, pp. 5–37.

[49] Tempelmann, D., Hanifi, A., and Henningson, D., "Spatial Optimal Growth in Three-Dimensional Compressible Boundary Layers," *Journal of Fluid Mechanics*, Vol. 704, 2012, pp. 251–279.

[50] Luchini, P., "Reynolds-Number-Independent Instability of the Boundary Layer over a Flat Surface: Optimal Perturbations," *J. Fluid Mech.*, Vol. 404, 2000, pp. 289–309.

[51] Li, F. and Malik, M., "Mathematical Nature of Parabolized Stability Equations," *R. Kobayashi (Ed.), Laminar-Turbulent Transition, Springer*, 1994, pp. 205–212.

[52] Li, F. and Malik, M., "On the Nature of the PSE Approximation," *Theoretical and Computational Fluid Dynamics*, Vol. 8, No. 4, 1996, pp. 253–273.

[53] Li, F. and Malik, M., "Spectral Analysis of Parabolized Stability Equations," *Computers & Fluids*, Vol. 26, No. 3, 1997, pp. 279–297.

[54] Haj-Hariri, H., "Characteristics Analysis of the Parabolized Stability Equations," *Studies Applied Mathematics*, Vol. 92, 1994, pp. 41–53.

[55] Bagheri, S. and Hanifi, A., "The Stabilizing Effect of Streaks on Tollmien-Schlichting and Oblique Waves: A Parametric Study," *Physics of Fluids*, Vol. 19, 2007, pp. 078103–1–4.

[56] Vigneron, Y., Rakich, J., and Tannehill, J., "Calculation of Supersonic Viscous Flow over Delta Wings with Sharp Supersonic Leading Edges," AIAA Paper 78-1137, 1978.

[57] Chang, C., Malik, M., Erlebacher, G., and Hussaini, M., "Compressible Stability of Growing Boundary Layers using Parabolized Stability Equations," AIAA Paper 1991-1636, 1991.

[58] Chang, C.L., "Langley Stability and Transition Analysis Code (LASTRAC) Version 1.2 User Manual," NASA TM-2004-213233, 2004.

[59] Zuccher, S., Tumin, A., and Reshotko, E., "Parabolic Approach to Optimal Perturbations in Compressible Boundary Layers," *Journal of Fluid Mechanics*, Vol. 556, 2006, pp. 189–216.

[60] Mack, L.M., "Boundary Layer Stability Theory," Tech. Rep. Jet Propulsion Laboratory Report 900-277, California Institute of Technology, Pasadena, CA, 1969.

[61] Hanifi, A., Schmid, P., and Henningson, D., "Transient Growth in Compressible Boundary Layer Flow," *Physics of Fluids*, Vol. 8, 1996, pp. 826–837.

[62] Hermanns, M. and Hernández, J., "Stable High-Order Finite-Difference Methods Based on Non-Uniform Grid Point Distributions," *International Journal for Numerical Methods in Fluids*, Vol. 56, 2008, pp. 233–255.

[63] Paredes, P., Hermanns, M., Le Clainche, S., and Theofilis, V., "Order 10^4 Speedup in Global Linear Instability Analysis using Matrix Formation," *Computer Methods in Applied Mechanics and Engineering*, Vol. 253, 2013, pp. 287–304.

[64] Cook, D., Thome, J., Brock, J., Nichols, J., and Candler, G., "Understanding Effects of Nose-Cone Bluntness on Hypersonic Boundary Layer Transition using Input-Output Analysis," AIAA Paper 2018-0378, 2018.

[65] Choudhari, M., Li, F., and Edwards, J., "Stability Analysis of Roughness Array Wake in a High-Speed Boundary Layer," AIAA Paper 2009-0170, 2009.

[66] Choudhari, M., Li, F., Chang, C., Edwards, J., Kegerise, M., and King, R., "Laminar-Turbulent Transition Behind Dicrete Roughness Elements in a High-Speed Boundary Layer," AIAA Paper 2010-1575, 2013.

[67] Choudhari, M., Li, F., Chang, C., Norris, A., and Edwards, J., "Wake Instabilities Behind Discrete Roughness Elements in High Speed Boundary Layers," AIAA Paper 2013-0081, 2013.

[68] Paredes, P., Choudhari, M., and Li, F., "Nonlinear Transient Growth and Boundary Layer Transition," AIAA Paper 2016-3956, 2016.

[69] Paredes, P., Choudhari, M., and Li, F., "Transition Due to Streamwise Streaks in a Supersonic Flat Plate Boundary Layer," *Physical Review Fluids*, Vol. 1, No. 8, 2016, pp. 083601–1–23.

[70] Paredes, P., Choudhari, M., and Li, F., "Transient Growth and Streak Instabilities on a Hypersonic Blunt Body," AIAA Paper 2017-0066, 2017.

[71] Paredes, P., Choudhari, M., Li, F., Jewell, J., Kimmel, R., and Marineau, E., "Nonmodal Growth of Traveling Waves on Blunt Cones at Hypersonic Speeds," *Physical Review Fluids*, 2018, (in preparation).

[72] Xie, Z., Karimi, M., and Girimaji, S., "Small Perturbation Evolution in Compressible Poiseuille Flow: Pressure-Velocity Interactions and Obliqueness Effects," *Journal of Fluid Mechanics*, Vol. 814, 2017, pp. 249–276.

[73] Orr, W., "The Stability Or Instability of the Steady Motions of a Perfect Liquid and of a Viscous Liquid. Part I: A Perfect Liquid," *Proceedings of the Royal Irish Academy A*, Vol. 27, 1907, pp. 9–68.

[74] Orr, W., "The Stability Or Instability of the Steady Motions of a Perfect Liquid and of a Viscous Liquid. Part II: A Viscous Liquid," *Proceedings of the Royal Irish Academy A*, Vol. 27, 1907, pp. 69–138.

[75] Butler, K. and Farrell, B., "Three-Dimensional Optimal Perturbations in Viscous Shear Flow," *Physics of Fluids*, Vol. 4, No. 8, 1992, pp. 1637–1650.

Chapter 8 - NUMERICAL INVESTIGATION OF ROUGHNESS EFFECTS ON TRANSITION ON SPHERICAL CAPSULES

Stefan Hein and Alexander Theiss
German Aerospace Center (DLR)
GERMANY

Antonio Di Giovanni and Christian Stemmer
Technical University of Munich
GERMANY

Thomas Schilden and Wolfgang Schröder
RWTH Aachen University
GERMANY

Pedro Paredes
National Institute of Aerospace
UNITED STATES

Meelan M. Choudhari and Fei Li
NASA Langley Research Center
UNITED STATES

Eli Reshotko
Case Western Reserve University
UNITED STATES

8.0 NOMENCLATURE

c	damping function
c_T	power-law exponent
d	Cartesian cell length, µm
f_i	disturbance frequency for unsteady computations, $1/\mathrm{s}$
$g(\xi, \zeta, \eta, t)$	generic flow variable
k	peak-to-valley roughness height, µm or m
h_t	total enthalpy, $\mathrm{J/kg}$
h_ξ, h_ζ	streamwise (nondimensional) and azimuthal (in m) metric factors, respectively
m_ζ	nondimensional azimuthal wavenumber
m, n	time and space indices in the spatiotemporal analysis, respectively
p	pressure, $\mathrm{N/m^2}$
$\overline{\mathbf{q}}$	basic flow vector
$\tilde{\mathbf{q}}$	unsteady perturbation vector
$\hat{\mathbf{q}}$	vector of amplitude functions
r_b	local radius, m

This chapter corresponds to an article published in a special issue of the Journal of Spacecraft and Rockets.

$s, \hat{s}$	streamwise coordinate with reference to the stagnation point, mm or m
t	time, s
(u, v, w)	velocity components along streamwise, azimuthal, and wall-normal directions, m/s
$A_{m,n}(\xi)$	amplitude of the spatiotemporal mode
D	face diameter, m
E	energy norm based on total energy, $\mathrm{J/m^2}$
G	energy gain
$G_{m,n}(\xi, \eta)$	azimuthal wavenumber-frequency spectra
J	objective function
K	energy norm based on kinetic energy, $\mathrm{J/m^2}$
L	twice the edge length of a roughness element, µm
Ma	Mach number
M, N	number of time and space samples, respectively
N_E, N_K	N-factor, i.e., integrated logarithmic amplification factor, based on E and K, respectively
R	face radius, m
R_a	surface mean roughness, µm
R_s	spherical-segment radius, m
Re_{δ^*}	Reynolds number based on displacement thickness and flow conditions at the boundary-layer edge, $\bar{\rho}_e \bar{u}_e \delta^* / \bar{\mu}_e$
Re_θ	Reynolds number based on boundary-layer momentum thickness, $\bar{\rho}_e \bar{u}_e \theta / \bar{\mu}_e$
Re_{kk}	roughness Reynolds number based on roughness height and flow conditions at this height, $\bar{\rho}_k \bar{u}_k k / \bar{\mu}_k$
Re_k	roughness Reynolds number with dynamic viscosity evaluated at wall temperature, $\bar{\rho}_k \bar{u}_k k / \bar{\mu}_w$
Re_R	freestream Reynolds number based on capsule-face radius
Re/l	freestream unit Reynolds number, $1/\mathrm{m}$
T	temperature, K
$\hat{U}_m(\xi, \zeta, \eta)$	time Fourier transform of the streamwise velocity
β	dimensional azimuthal wavenumber, $1/\mathrm{m}$
γ	ratio of specific heats
δ	boundary-layer thickness, µm or m
δ^*	boundary-layer displacement thickness, µm or m
(ξ, ζ, η)	streamwise, azimuthal, and wall-normal coordinates, mm or m, (in Section 8.4: ζ in rad.)
θ	boundary-layer momentum thickness, µm or m
κ_ξ	streamwise curvature, $1/\mathrm{m}$
λ	azimuthal wavelength, mm or m
μ	dynamic viscosity, $\mathrm{kg/(m \cdot s)}$
ρ	density, $\mathrm{kg/m^3}$
ϕ	angular coordinate, deg.
χ	inclination of the local tangent to the body surface, deg.
$\mathbf{A}$, $\mathbf{B}$, $\mathbf{C}$, $\mathbf{D}$, $\mathbf{L}$	PSE matrix operators
$\mathbf{M}$	energy weight matrix

Subscripts

$()_0$	inlet disturbance location
$()_1$	outlet disturbance location

$()_e$	value at the boundary-layer edge
$()_k$	value at the roughness height
$()_L$	left adjacent cell
$()_R$	right adjacent cell
$()_w$	value at the wall
$()_{opt}$	optimal value
$()_{tr}$	transition location
$()_\infty$	freestream value

Superscripts

$()^{mean}$	mean energy gain
$()^{out}$	outlet energy gain
$()^\dagger$	adjoint
$()^H$	conjugate transpose

8.1 INTRODUCTION

Vehicles flying at hypersonic Mach numbers are exposed to a significant amount of heat load, and thus, often require a thermal protection system (TPS). Since heat transfer rates of a turbulent boundary layer are much higher compared to the laminar state, the location of laminar-turbulent transition is a crucial design parameter for the TPS. The mechanisms of laminar-turbulent transition on the windward side of blunt bodies like reentry capsules are not well understood so far. However, experiments have shown that surface roughness plays an important role during the transition process [1, 2]. Based on systematic studies of the roughness effects on blunt-body transition, different empirical correlations have been proposed in the literature [3, 4].

Blunt reentry capsules with a sphere-cone shaped forebody like the Mars Science Laboratory (MSL) support modal growth of boundary-layer instabilities on the conical part of the heat shield strong enough to trigger laminar-turbulent transition [5–7]. Configurations where the forebody consists of a spherical segment only, like the Apollo capsule or the Orion Crew Exploration Vehicle (CEV), require a much higher Reynolds number for the onset of modal disturbance growth [8]. Owing to the strong bow shock, the boundary-layer edge Mach number remains subsonic or slightly supersonic on the spherical heat shield, which excludes the possibility of second-mode amplification. Due to the spherical body shape, there is a sustained, strongly favorable pressure gradient that has a highly stabilizing effect on the first-mode instabilities. Moreover, although the flow is strongly accelerated, the crossflow velocity component inside the boundary layer remains small because of the weak curvature of the boundary-layer edge streamlines. Therefore, crossflow-mode amplification is not relevant either, and the Görtler-type instability is precluded due to the convex surface curvature. Nevertheless, laminar-turbulent transition is observed on such configurations, even at Reynolds numbers for which, according to the linear stability theory, no modal disturbance growth can be found. This phenomenon is denoted as “blunt-body paradox” in the literature [9].

In situations where the flow does not support modal disturbance amplification, transient growth is still a possible scenario for significant disturbance growth [10]. Basically, a linear superposition of modal disturbances may exhibit transient growth in amplitude despite the fact that each individual mode is decaying in the downstream

direction. The transient amplification becomes possible only because the individual modes are nonorthogonal to each other, which is a consequence of the non-normality of the underlying governing equations. The overall nonmodal growth strongly depends on the initial shape of the disturbance. Therefore, an optimization procedure is typically used to identify the optimal initial condition that leads to the maximum transient growth, excluding the question of a physical realizability of the initial disturbance. Hence, such optimal transient-growth studies provide an upper limit on the nonmodal disturbance growth.

Transient disturbance growth has been proposed in literature as a possible cause for laminar-turbulent transition, in particular for those cases where modal disturbance amplification is too weak. Reshotko & Tumin [11] considered nosetip transition and used optimal transient-growth results to derive a correlation for roughness-induced transition in the near vicinity of the stagnation point of blunt geometries. Their correlation uses the same parameters as these purely empirical correlations [3, 4], which relate the momentum thickness Reynolds number at the transition-onset location with the surface-roughness height and the ratio of surface to boundary-layer edge temperatures. However, the exponents describing the roughness and surface temperature effects are derived from physical considerations together with optimal transient-growth theory. The correlation of Reshotko & Tumin will be denoted as "RT-correlation" from here on. The RT-correlation was able to reproduce the trends of the various data sets used to derive the empirical correlations. However, the optimal transient-growth approach of Reshotko & Tumin included some simplifying assumptions. Therefore, Paredes et al. [12] used an improved framework of optimal transient-growth analysis that removed the shortcomings of the approach of Reshotko & Tumin and applied it to the scale model of the Orion CEV geometry studied in the Mach 6 ACE wind tunnel at Texas A&M University (TAMU) [13, 14]. In these experiments, the effect of uniformly-distributed surface roughness on transition onset was systematically studied. For the comparatively small Reynolds numbers considered in this experiment, the necessary roughness height to trigger transition in the stagnation flow region was in the order of 0.7 to 1.5 boundary-layer thicknesses [14]. Despite the significant effects of the nonsimilar boundary layer on the transient-growth characteristics, Paredes et al. found that the transient-growth scaling with respect to Reynolds number and the ratio of surface to edge temperature did not change significantly after the improved framework was applied. Since the RT-correlation depends only on those two scalings, the modified correlation remained close to the original correlation of Reshotko & Tumin despite the improvements in the calculation of optimal growth factors. Thus, both correlations based on optimal transient-growth analysis reproduce equally well the trends observed for roughness-induced transition at the stagnation-flow region of spherical blunt forebodies. On the other hand, Paredes et al. [12] also pointed out that the magnitude of transient growth up to the measured transition locations at the experiments at TAMU was rather small, which raises questions regarding the relevance of the optimal growth paradigm.

Additional experimental studies [8, 15, 16] on laminar-turbulent transition in the boundary layer of a blunt Apollo-like capsule were performed at Mach 5.9 in the Hypersonic Ludwieg tube at the Technische Universität Braunschweig (HLB) in the unit Reynolds number range of $Re/l \approx 6 \times 10^6$ /m to $Re/l \approx 20 \times 10^6$ /m. Infrared (IR) thermography was used to monitor laminar and transitional surface heating. IR measurements based on a standard IR coating with a mean roughness of $R_a \approx 10\,\mu$m revealed the appearance of transitional surface heating at $Re/l \approx 15 \times 10^6$ /m. For a highly polished surface with $R_a \approx 0.5\,\mu$m, no indication of transition was found within the unit Reynolds number range of the HLB. As expected, linear stability analyses for the nominally smooth surface showed that the laminar boundary layer is highly stable. Much larger unit Reynolds numbers would be required for the onset of modal boundary-layer instability growth [8]. Numerical studies on modal disturbance growth in the wake of discrete roughness elements at unit Reynolds number conditions of the experiment showed that roughness element heights well above the mean roughness of the IR coating are required for the onset of a noteworthy modal disturbance growth in the wake flow [17, 18]. For further stud-

ies of the distributed surface-roughness effects, a specifically designed micron-sized surface-roughness patch of 20 mm $\times$ 20 mm was fabricated and placed at the center of the capsule forebody [16], i.e. at some distance downstream of the stagnation point region. The patch consists of uniformly-spaced rectangular micron-sized roughness elements. It features a similar R_a value as the surface with the standard IR coating but has a roughness structure that is well defined, reproducible, and also amenable to numerical studies. The roughness patch triggered laminar-turbulent transition in recent experiments in the HLB at unit Reynolds numbers that are similar to those required in the case of the standard IR coating, but the onset of transition depends on the position of the capsule model in the wind-tunnel test section [16]. If the capsule model with increased roughness height due to the patch is positioned such that its stagnation point region is located closer to the centerline of the test section, transition is observed for $Re/l \gtrapprox 15 \times 10^6$ /m. In the transitional region, several broadband peaks appear in the hot-wire spectra above 100 kHz. If the stagnation flow region is moved further away from the wind-tunnel centerline, then no transition is observed. Due to peculiar design characteristics of the HLB, the freestream disturbance level near the center is moderately higher than that outside the centerline zone. The roughness heights of the standard IR coating and of the roughness patch normalized with a characteristic boundary-layer length scale were significantly lower than those of the sandgrit coatings considered in the experiments of Leidy et al. [13, 14].

One of the main objectives of the present paper is to assess the potential for nonmodal disturbance growth on the forebody of the HLB capsule by using optimal transient-growth theory. Specifically, the effects of surface temperature and unit Reynolds number on the optimal transient growth are investigated and compared with the results for the TAMU capsule at a similar Mach number but lower Reynolds numbers [12]. Furthermore, the steady disturbance flow field introduced by the roughness patch on the HLB capsule and its interaction with additional unsteady disturbances is studied by direct numerical simulations (DNS) in order to investigate possible modal or nonmodal disturbance growth mechanisms either in the vicinity of the roughness patch or in the wake region behind the patch. The different numerical approaches used are briefly introduced in Section 8.2 and the blunt body configurations considered are described in Section 8.3. The optimal transient-growth results for the HLB capsule are presented in Section 8.4 and compared to corresponding data for the TAMU capsule. The additional data set for the HLB capsule is used to further substantiate the value of the power-law exponent of the wall to boundary-layer edge temperature ratio of the correlation for roughness-induced transition that was originally proposed by Reshotko & Tumin [11] and the slightly different value recently derived by Paredes et al. [12] based on optimal transient-growth data for the TAMU capsule. In Section 8.5, the results of direct numerical simulations are presented that attempt to replicate the conditions of the HLB capsule experiment with the specifically tailored roughness patch. The experimental results for the HLB and TAMU capsules among others are discussed in further detail in a companion paper by Radespiel et al. [16].

8.2 METHODOLOGIES

This section introduces the different methodologies used in this paper. First, a brief overview of the linear optimal transient-growth theory based on parabolized stability equations is given, where an initial disturbance is sought that maximizes an objective function. The following subsection highlights the methods used for the direct numerical simulation.

8.2.1 Optimal Transient-Growth Theory

The optimal transient-growth analysis is performed using the framework of linear parabolized stability equations (PSE) as elucidated in the literature [19–22]. The method is outlined here for the sake of completeness.

8.2.1.1 Governing Equations

In the PSE concept, the stationary three-dimensional disturbance $\tilde{\mathbf{q}}$ can be written as

$$\tilde{\mathbf{q}}(\xi,\zeta,\eta) = \hat{\mathbf{q}}(\xi,\eta)\exp\left(i\beta\zeta\right) + c.c., \tag{8-1}$$

where $c.c.$ denotes the complex conjugate and $\hat{\mathbf{q}}(\xi,\eta) = \left[\hat{\rho},\hat{u},\hat{v},\hat{w},\hat{T}\right]^T$ represents the vector of amplitude functions, containing the density and temperature fluctuations $(\hat{\rho},\hat{T})$, as well as the velocity disturbances $(\hat{u},\hat{v},\hat{w})$ in the streamwise (ξ), azimuthal (ζ), and wall-normal direction (η), respectively. The wavenumber along the azimuthal (ζ) direction is β and the disturbance azimuthal wavelength is defined as $\lambda\left(\xi\right) = 2\pi/\beta$.

Introducing the perturbation form from Equation 8-1 into the linearized Navier-Stokes equations and assuming a slow streamwise variation of the basic state and of the amplitude functions to neglect the viscous derivatives in the streamwise direction, the nonlocal linear stability equations are obtained and can be written in the form

$$\mathbf{L}\hat{\mathbf{q}}(\xi,\eta) = \left(\mathbf{A} + \mathbf{B}\frac{\partial}{\partial\eta} + \mathbf{C}\frac{\partial^2}{\partial\eta^2} + \mathbf{D}\frac{\partial}{\partial\xi}\right)\hat{\mathbf{q}}(\xi,\eta) = 0. \tag{8-2}$$

The linear operators $\mathbf{A}$, $\mathbf{B}$, $\mathbf{C}$, and $\mathbf{D}$ are provided in Ref. [23] along with a more detailed explanation on the derivation of the PSE. The parabolized stability equations (Equation 8-2) are integrated in the downstream ξ-direction using a marching procedure. Even though the system has been 'parabolized', some ellipticity remains and information is allowed to propagate upstream, which in turn can cause numerical instabilities if the step size in ξ becomes too small. Chang et al. [24] identified the $\partial\hat{p}/\partial\xi$-term as the most relevant source of remaining ellipticity, however, this term is of higher order for transient-growth problems [25, 26] and, therefore, will be omitted for the present work.

8.2.1.2 Optimality System

In the optimal transient-growth framework, a set of perturbation profiles at an initial location, $\tilde{\mathbf{q}}_{\mathbf{0}} = \tilde{\mathbf{q}}_{\xi_0}$, are sought that maximize a suitably defined objective function, $J\left(\tilde{\mathbf{q}}\right)$, which is a measure of disturbance energy gain within the optimization interval $[\xi_0,\xi_1]$. There are two definitions of the energy gain that are commonly used for optimal-perturbation problems [19, 22, 27]; namely the outlet energy gain,

$$J = G^{out} = \frac{E\left(\xi_1\right)}{E\left(\xi_0\right)}, \tag{8-3}$$

and the mean energy gain,

$$J = G^{mean} = \frac{1}{\xi_1-\xi_0}\frac{\int_{\xi_0}^{\xi_1} E\left(\xi'\right)\mathrm{d}\xi'}{E\left(\xi_0\right)}, \tag{8-4}$$

where E denotes the energy norm of $\tilde{\mathbf{q}}$. In this work, we use the positive-definite energy norm, proposed by Chu [28], Mack [29], and Hanifi et al. [30], defined as

$$E\left(\xi\right)=\frac{1}{\lambda}\int_{\zeta}\int_{\eta}\tilde{\mathbf{q}}\left(\xi,\zeta,\eta\right)^{H}\mathbf{M_{E}}\tilde{\mathbf{q}}\left(\xi,\zeta,\eta\right)h_{\xi}h_{\zeta}\mathrm{d}\eta\mathrm{d}\zeta, \tag{8-5}$$

where the superscript H denotes conjugate transpose and h_{ξ}, h_{ζ} are metric factors associated with the streamwise and azimuthal curvature, respectively. The total energy weight matrix, $\mathbf{M_{E}}$, includes all five state variables and is defined by

$$\mathbf{M_{E}}=\mathrm{diag}\left[\frac{\bar{T}\left(\xi,\eta\right)}{\bar{\rho}\left(\xi,\eta\right)\gamma Ma^{2}},\bar{\rho}\left(\xi,\eta\right),\bar{\rho}\left(\xi,\eta\right),\bar{\rho}\left(\xi,\eta\right),\frac{\bar{\rho}\left(\xi,\eta\right)}{\gamma\left(\gamma-1\right)\bar{T}\left(\xi,\eta\right)Ma^{2}}\right]. \tag{8-6}$$

An overbar denotes meanflow quantities, γ is the ratio of specific heats and Ma is the Mach number. Additionally, an energy norm, which is solely based on the kinetic energy of the disturbance is also used in this paper. The energy weight matrix, in this case, reduces to

$$\mathbf{M_{K}}=\mathrm{diag}\left[0,\bar{\rho}\left(\xi,\eta\right),\bar{\rho}\left(\xi,\eta\right),\bar{\rho}\left(\xi,\eta\right),0\right]. \tag{8-7}$$

To distinguish when the objective function is maximized for the total energy E or the kinetic energy K of a disturbance, a corresponding subscript is added to the objective function, resulting in four different possible options: J_{E}^{out}, J_{K}^{out}, J_{E}^{mean}, and J_{K}^{mean}.

An adjoint-based optimization algorithm is applied to determine the maximum of the objective functional J, employing the intrinsic parabolic nature of the equations. Starting from an initial guess at ξ_0 the direct PSE, $\mathbf{L}\tilde{\mathbf{q}}=0$, are used to march the solution $\tilde{\mathbf{q}}$ from $\xi=\xi_0$ to $\xi=\xi_1$, where the final optimality condition is used to obtain the initial condition for the backward integration of the adjoint PSE, $\mathbf{L}^{\dagger}\tilde{\mathbf{q}}^{\dagger}=\mathrm{RHS}$, where $\mathrm{RHS}=0$ in case of outlet energy gain optimization (J^{out}) and $\mathrm{RHS}=2\mathbf{M}^{H}\tilde{\mathbf{q}}$ for the mean energy optimization (J^{mean}). A new initial condition for the forward problem is obtained from the adjoint solution at ξ_0 employing the initial optimality condition. The optimization procedure is terminated when the value of J has converged to a prescribed tolerance, which was set to 10^{-4} in the present computations. In this work, we have used the continuous, as well as the discrete adjoint approach for integrating $\tilde{\mathbf{q}}^{\dagger}$ from ξ_1 to ξ_0, revealing no impact of the adjoint method on the optimal disturbance growth. All results shown in this paper have been computed by applying the continuous adjoint approach.

8.2.1.3 Spatial Discretization and Boundary Conditions

The PSE are discretized with a stable high-order finite-difference scheme (FD-q) [31] of sixth order along the wall-normal direction. The perturbations are integrated along the streamwise coordinate by using second-order backward differentiation and a constant step size. The number of discretization points was varied in both spatial directions to ensure grid convergence of the optimal transient-growth results, whereas clustering of grid points toward the wall was performed. No-slip, isothermal boundary conditions are imposed at the wall, i.e., $\hat{u}=\hat{v}=\hat{w}=\hat{T}=0$. At the upper boundary, which is located just below the shock layer, homogeneous Dirichlet conditions, $\hat{\rho}=\hat{u}=\hat{v}=\hat{T}=0$, and a Neumann boundary condition for the wall-normal velocity component, $\hat{w}_{\eta}=0$, are prescribed.

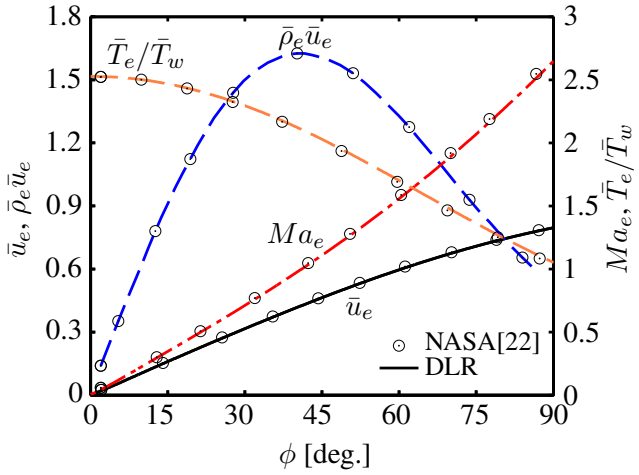

Figure 8-1: Streamwise Evolution of Basic Flow Variables at the Edge of the Boundary Layer for the Hemisphere.

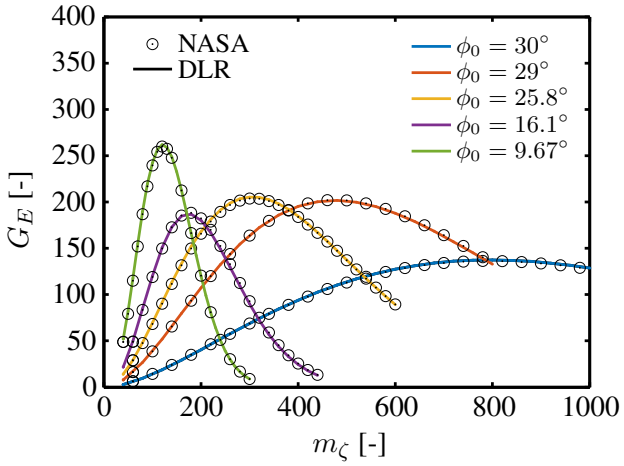

Figure 8-2: Total Energy Gain G_E at $\phi_1 = 32.2°$ Optimized for $J = G^{out}$.

8.2.1.4 Cross-Comparison of the Optimal Transient-Growth Codes

The nonmodal disturbance growth results presented in this paper have been computed with two different codes. The optimal-growth framework developed by NASA is used for the computations for the TAMU ACE capsule configuration and has been extensively verified [21]. On the other hand, a newly developed optimal transient-growth code by DLR is employed for characterizing the nonmodal growth properties of the boundary layer on the HLB capsule. A more detailed overview of the two different capsule configurations is given in Section 8.3.

The boundary-layer flow over a hemisphere at $Ma = 7.32$ is considered to cross-verify the two different transient-growth implementations used in this work. Details on the basic flow computations by NASA were reported by Li et al. [32], and the nonmodal disturbance growth characteristics of the boundary layer in downstream direction are given in Ref. [22]. Figure 8-1 depicts the streamwise evolution of basic flow variables at the edge of the boundary layer along the angular coordinate ϕ ($\phi = \xi/R_s$ with R_s being the radius of the hemisphere). The boundary-layer edge is defined as the wall-normal position where the total enthalpy reaches 99.5% of the freestream value ($h_t/h_{t,\infty} = 0.995$). The basic state computed by DLR uses the numerical framework described in Theiss et al. [8]. Figure 8-2 shows the optimal outlet energy gain based on the total energy of the disturbance, G_E, at a fixed output location, $\phi_1 = 32.2°$, and varying inflow positions, ϕ_0, as a function of the azimuthal wavenumber, m_ζ, for the basic state computed by DLR. An excellent agreement of the predicted gain from both codes is observed.

8.2.2 Direct Numerical Simulations

The numerical method used by RWTH solves the compressible Navier-Stokes equations in space and time [33]. The computational domain is discretized by an unstructured hierarchical Cartesian mesh whose cells are arranged in an octree structure. The domain decomposition for parallel computations is based on the Hilbert space-filling

curve and subtree workloads to distribute subtrees of the hierarchical octree of equal loads to processors [34]. The governing equations are integrated using a finite-volume method [35]. The boundaries of the computational domain are embedded in the Cartesian mesh and modeled employing cut cells [33]. Small cut cells are treated using an interpolation and flux-redistribution scheme [35].

For the spatial discretization, an advection upstream splitting method (AUSM) is used. The advection Mach number on the cell surface is the mean of the extrapolated Mach numbers from the adjacent cells $Ma_{1/2} = 0.5\,(Ma_L + Ma_R)$. The same formulation holds for the pressure on the cell surface. The cell-center gradients are computed using a second-order accurate least-squares reconstruction scheme [33]. Shock capturing is achieved by adding additional numerical dissipation at the shock position. The temporal integration is based on a 5-stage second-order accurate Runge-Kutta scheme. For supersonic flows, the code has been employed and validated for the flow past a cone and around a blunt stagnation point probe [36, 37].

The DNS by the Technical University of Munich (TUM) are performed using the Navier Stokes Multi Block solver (NSMB). NSMB is an MPI-parallelized, finite-volume code for structured grids with a wide variety of numerical schemes; and it has been extensively tested in studies of hypersonic flows [38, 39]. The spatial discretization is based on a 4th-order, central difference scheme, whereas a 4th-order Runge-Kutta method is used for time integration. Artificial numerical dissipation is added to capture the shock and to suppress spurious oscillations.

8.3 CONFIGURATIONS

8.3.1 TAMU Capsule

The first configuration for which transient-growth results are presented corresponds to a blunt, spherical-section forebody at 28° angle of incidence with respect to the free stream. The forebody configuration models the Orion CEV capsule geometry [40]. The face diameter is $D = 2R = 0.0762\,\text{m}$ and the remaining dimensions are scaled according to Hollis [40], resulting in a sphere of radius $R_s = 0.09144\,\text{m}$. The flow conditions at Mach 6 match those of a wind-tunnel experiment in the Actively Controlled Expansion (ACE) tunnel at the National Aerothermochemistry Laboratory (NAL) of Texas A&M University [13, 14]. Paredes et al. [12] performed transient growth calculations for four freestream unit Reynolds numbers, namely, $Re/l = 3.4 \times 10^6$ /m, 4.4×10^6 /m, 5.4×10^6 /m, and 6.4×10^6 /m. The freestream temperature was set to $\bar{T}_\infty = 54.69\,\text{K}$ and the surface temperature was equal to $\bar{T}_w = 391.0\,\text{K}$. To investigate the effects of surface temperature on the transient-growth characteristics, computations were also performed for additional, cooler surface temperatures corresponding to $\bar{T}_w = 300.0\,\text{K}$, 195.5 K, and 130.33 K, respectively, with the unit Reynolds number held fixed at $Re/l = 4.4 \times 10^6$ /m.

The basic state, laminar boundary-layer flow over the forebody was computed by using a second-order accurate algorithm as implemented in the finite-volume compressible Navier-Stokes flow solver VULCAN-CFD (see Ref. [41] and http://vulcan-cfd.larc.nasa.gov for further information about the solver). Further details about the laminar basic flow computations are given in Ref. [12].

8.3.2 HLB Capsule

The second capsule studied in this work corresponds to an Apollo-shaped capsule with a spherical-section forebody ($D = 0.17\,\text{m}$ and $R_s = 0.204\,\text{m}$) at an angle of attack of AoA = 24°. Laminar basic flow computations are performed for Mach 5.9 freestream conditions that match the experiments of Ali et al. [15] in the Hypersonic Ludwieg Tube at the TU Braunschweig (HLB). Overall, four different unit Reynolds numbers have been computed, namely $Re/l = 10 \times 10^6$ /m, 12.5×10^6 /m, 16×10^6 /m, and 18×10^6 /m with the freestream temperature set to $\bar{T}_\infty = 59.03\,\text{K}$ and prescribed surface temperature of $\bar{T}_w = 295\,\text{K}$. To also assess the impact of surface temperature on the nonmodal disturbance growth characteristics, additional simulations have been performed at fixed freestream conditions for $Re/l = 10 \times 10^6$ /m and modified surface temperatures with $\bar{T}_w = 170\,\text{K}$, 245 K, and 395 K, respectively.

The laminar basic flow was computed with the second-order accurate, three-dimensional, finite-volume, compressible Navier-Stokes flow solver FLOWer [42] on a block-structured grid. More details about the numerical settings and the employed grid are given in Ref. [8].

8.3.3 Comparison of Boundary-Layer Edge Data for the Two Capsules

Figure 8-3 shows a three-dimensional view of the HLB capsule forebody. Mach number isocontours in the symmetry plane and the Reynolds number based on momentum thickness, Re_θ, with boundary-layer edge streamlines on the capsule forebody are plotted for $Re/l = 10 \times 10^6$ /m and $\bar{T}_w = 295\,\text{K}$. The thick dashed lines indicate the sonic lines. Only one half of the model was used in the basic flow computations, exploiting the azimuthal symmetry of the flow field. Due to the strong bow shock, the boundary-layer edge Mach number falls within the subsonic to transonic range and the flow continuously accelerates from the stagnation point at $\xi = 0$ toward the capsule shoulder. In this work, we focus on the leeward symmetry region above the stagnation point, where transition has been observed in experiments [8, 14]. The HLB capsule has been investigated at higher unit Reynolds numbers, and its diameter is about twice the size of the Orion CEV model. The angle of attack differs also, but due to the spherical forebody, the boundary-layer edge values normalized with the respective freestream values are very similar for the two flow configurations as depicted in Figure 8-4. Boundary-layer edge quantities along the symmetry plane for the HLB capsule at $Re/l = 10 \times 10^6$ /m and $\bar{T}_w = 395\,\text{K}$ are compared to those for the TAMU capsule at $Re/l = 4.4 \times 10^6$ /m and $\bar{T}_w = 391\,\text{K}$. In accordance with Section 8.2.1.4, the boundary-layer edge is determined from the total enthalpy criterion ($h_t/h_{t,\infty} = 0.995$). For both capsule geometries, the mass flux, $\bar{\rho}_e \bar{u}_e$, increases with growing distance from the stagnation point and reaches its maximum at the sonic point, $Ma_e = 1$, in agreement with the inviscid flow theory.

8.3.4 Hemisphere Approximation

To ease the computational effort in the case of unsteady DNS, a reduction of the domain size is performed in the simulations of TUM as shown in Figure 8-5. First, the flow over a hemisphere is considered. The flow over the hemisphere well represents the flow over the HLB capsule with angle of attack with minor restrictions outside of the area of interest. Second, results for the laminar steady flow on the whole hemispheric forebody (full domain) are used to generate inflow profiles for a restricted computational domain. The grid resolution of the

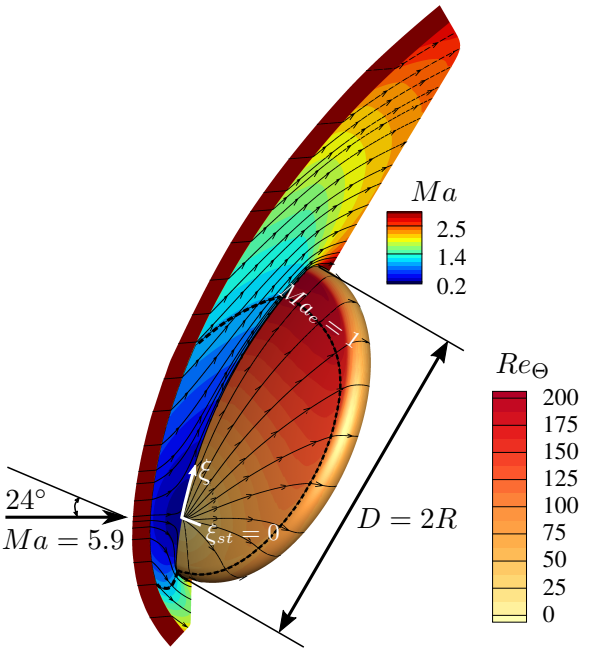

Figure 8-3: Three-Dimensional View of the HLB Capsule Forebody.

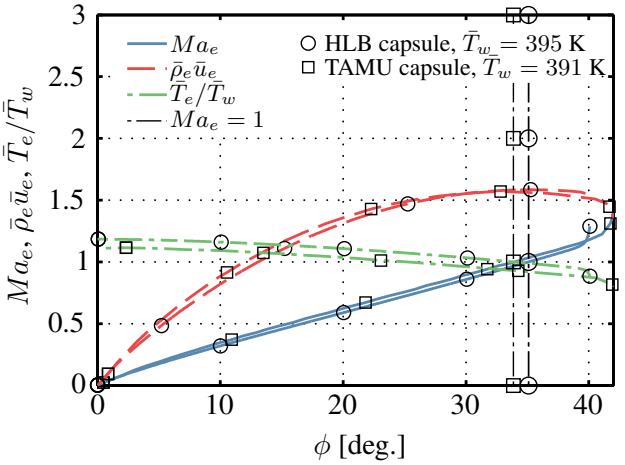

Figure 8-4: Streamwise Evolution of Boundary-Layer Edge Quantities along the Symmetry Plane.

restricted domain can be increased to match the resolution requirements imposed by the presence of the rough wall. Simulations for the smooth configuration are conducted on the entire hemisphere (full domain), whereas simulations for roughness investigations are conducted on a restricted domain. The box in Figure 8-5a shows the position of the restricted domain. The roughness position is indicated by the red square in Figure 8-5b.

The steady base flow for the entire hemisphere with smooth surface is computed on an axisymmetric two-dimensional grid. The grid consists of about $76,000$ points clustered around the shock location and inside the boundary layer. To provide similar outflow boundaries as in the case of the reentry capsule, the hemisphere ends with a shoulder resembling the one of the HLB capsule.

For both the 3D capsule and the axisymmetric 2D hemisphere, boundary-layer streamwise velocity and temperature profiles at different positions are shown in Figure 8-6 for a unit Reynolds number of $Re/l = 18 \times 10^6$ /m. The profiles on the 3D capsule geometry are extracted along the symmetry plane. The origin of the streamwise coordinates s and $\hat{s}$ is set on the stagnation point of the respective configuration. A clear match of the profiles is observed for the two configurations. In particular, the equivalence of the two flows is obtained by comparing velocity and temperature profiles on the capsule at a given position s with the ones on the hemisphere at $\hat{s} = s + \Delta s$, with s and $\hat{s}$ being the streamwise coordinates on the two geometries with origin on the respective stagnation points. On the capsule, the distance between the stagnation point and the rotation axis is $s = 60.5$ mm. In the vicinity of this position, the flow corresponds to the one on the hemisphere at $\hat{s} = 77.4$ mm. Details on the restricted domains and further comparisons between the capsule and the hemisphere boundary layer in presence of roughness are discussed in Section 8.5.2.1.

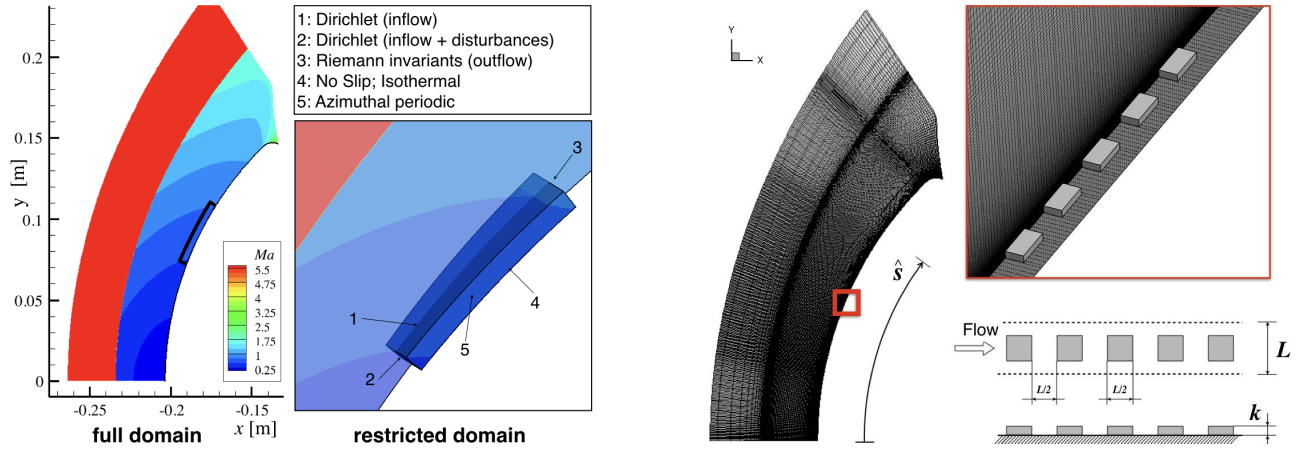

a) b)

Figure 8-5: Simulation Domains with a) the Specified Boundary Conditions and b) Computational Grid with Close-Up on the Roughness Position.

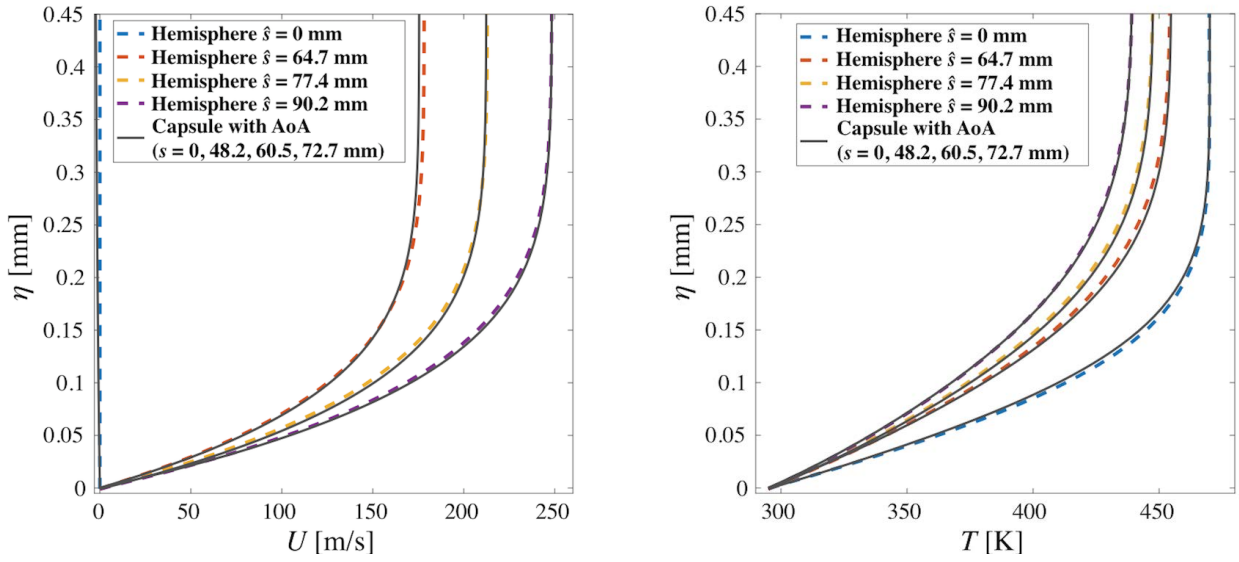

a) b)

Figure 8-6: Comparison of a) Boundary-Layer Velocity and b) Temperature Profiles for the Smooth Hemisphere and the HLB Capsule Geometry with $\mathrm{AoA} = 24°$.

8.4 RESULTS ON OPTIMAL TRANSIENT GROWTH

Optimal transient-growth results are presented for the HLB capsule with an emphasis on the effects of unit Reynolds number and wall temperature on the nonmodal growth characteristics and optimal optimization parameters, namely, spanwise wavelength and optimization interval length. For each parametric study, the transient-growth characteristics will be compared to the findings for the TAMU capsule presented in Ref. [12]. Subsequently, the implications of optimal growth results on the transition correlation of Reshotko & Tumin [11] and Paredes et al. [12] are investigated.

In this work, we assume that the spanwise disturbance wavelength, $\lambda\left(\xi\right)$, increases in proportion to the distance from the stagnation point. This ensures a constant wavenumber in the azimuthal direction, m_ζ, at each streamwise position, as it was also used in the axisymmetric case for the hemisphere in Section 8.2.1.4. Note that the dimensional spanwise wavenumber of Equation 8-1 turns into the nondimensional, azimuthal wavenumber m_ζ. However, this assumption may not hold for the fully three-dimensional flows investigated in this work. In general, a physically accurate specification of azimuthal-wavenumber variation along a prescribed trajectory in a fully three-dimensional flow remains an open question in the literature for both, modal and nonmodal disturbance growth. For the TAMU capsule, Paredes et al. [12] have examined the effect of different strategies for specifying the streamwise variation in spanwise disturbance wavelength on the transient-growth characteristics for the boundary layer along the leeward line of symmetry. In their study, the authors tested a constant wavelength approach, a variation based on streamline divergence, and the assumption of axisymmetric flow. Their calculations revealed only a minor impact of the chosen wavelength variation on the optimal transient growth across the optimization interval that led to the highest gain. The assumption of axisymmetric flow for the azimuthal-wavelength variation resulted in the strongest growth of disturbance energy, and hence, can be considered as the strategy that provides the upper bound for nonmodal disturbance growth on the geometries regarded in this work. Under the assumption of axisymmetric flow, the metric factors yield in

$$h_\xi = 1 + \kappa_\xi \eta, \tag{8-8}$$

$$h_\zeta = r_b + \eta \cos\left(\chi\right), \tag{8-9}$$

where κ_ξ denotes the streamwise curvature ($\kappa_\xi = 1/R_s$), r_b is the local radius ($r_b = R_s \sin\left(\phi\right)$), and χ specifies the inclination of the local tangent to the body surface ($\sin\left(\chi\right) = \mathrm{d}r_b/\mathrm{d}\xi$).

8.4.1 Effects of Unit Reynolds Number and Energy Norm

Paredes et al. [12] pointed out that, in order to apply the optimal transient-growth predictions toward transition correlations for nonsimilar boundary-layer flows such as the HLB and TAMU capsules, both the initial and final locations of the transient-growth interval must be varied in addition to the azimuthal wavenumber of the disturbance. First, we address the impact of energy norm (total energy vs. kinetic energy only) on the gain based on outlet energy (Equation 8-3) at $Re/l = 10 \times 10^6$ /m and $\bar{T}_w = 295\,\mathrm{K}$. The maximum gain within all possible optimization intervals $[\phi_0, \phi_1]$ ($\max_{[\phi_0,\phi_1]} G$) at the corresponding optimal azimuthal wavenumber, $m_{\zeta,opt}$, is plotted for the total energy norm in Figure 8-7a and for the kinetic energy norm in Figure 8-7b with $J = G^{out}$, respectively. The black dot indicates the location of the optimal interval where the highest gain occurs, $[\phi_0, \phi_1]_{opt}$. The black line denotes the value of ϕ_1 corresponding to maximum G_E and G_K for a given

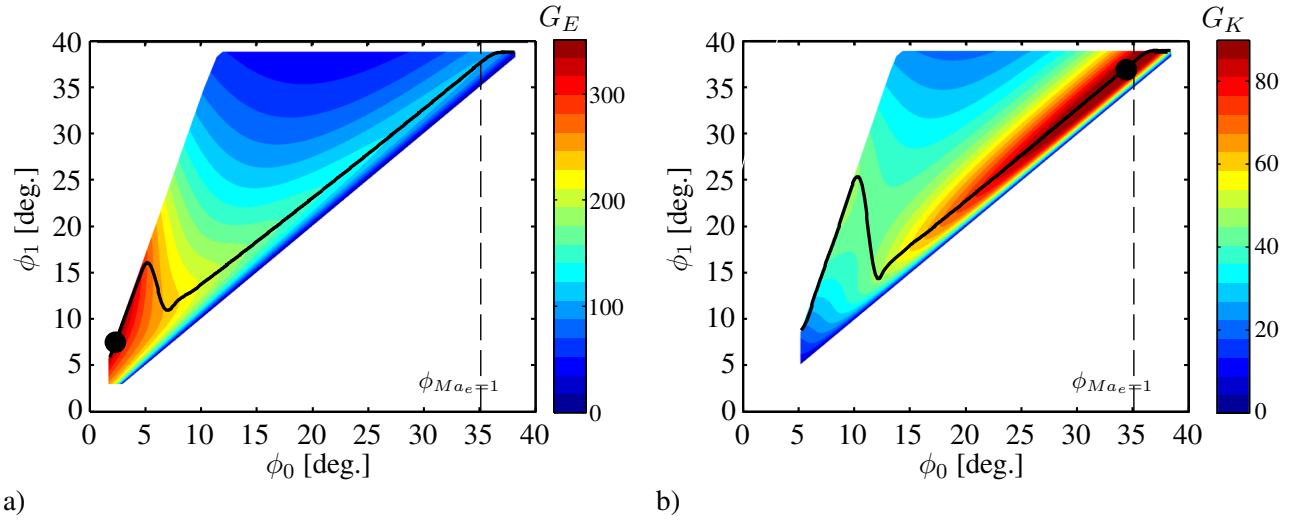

a) b)

Figure 8-7: Isocontours of Maximum Gain in Interval $[\phi_0, \phi_1]$, $\max_{[\phi_0,\phi_1]} G$, for an Optimization of a) Total Energy Gain J_E^{out} and b) Kinetic Energy Gain J_K^{out}.

ϕ_0. The region included in the figure is limited by the line of zero length optimization interval $\phi_1 = \phi_0$ with $G = 1$ on the diagonal, and a line on the left that delimits the region of the $[\phi_0, \phi_1]$ space that is omitted because the initial disturbance profiles at ϕ_0 peak above the boundary-layer edge and do not exhibit sufficient decay in wall-normal direction (especially the wall-normal velocity component), which in turn prevents the adjoint-based optimization algorithm to converge toward a satisfactory result. However, the excluded portion of the plot is not considered to be important for the present analysis because perturbations with an extended wall-normal support are unlikely to be excited by surface roughness. The maximum disturbance energy gain in the case of J_E^{out} occurs close to the stagnation point, which is in line with the observations for a hemisphere in hypersonic flow [22, 27] and the TAMU capsule with $\bar{T}_w/\bar{T}_e < 1$ [12]. When the norm for the optimization is based on the kinetic energy alone (J_K^{out}), the location of the maximum gain shifts further downstream toward the vicinity of the sonic point as depicted in Figure 8-7b ($\phi_{Ma_e=1} \approx 35°$, see also Figure 8-4), which again is in close agreement with previous observations for blunt body configurations [12, 22].

From here on, the overall nonmodal growth characteristics of the flow are presented in terms of optimal combination of azimuthal wavenumber, $m_{\zeta,opt}$, and optimal optimization interval length, $[\phi_0, \phi_1]_{opt}$, that lead to the maximum value of the energy gain for a specific initial location. In the following, the impact of unit Reynolds number on the optimal transient-growth characteristics is discussed with respect to objective functions based on outlet energy and mean energy, respectively. The former objective function maximizes the disturbance energy at a prescribed outlet location ϕ_1 (see Equation 8-3), whereas $J = G^{mean}$ maximizes the integral energy in the interval $[\phi_0, \phi_1]$ (see Equation 8-4), which can lead to a higher possible overshoot in the disturbance energy evolution in comparison to $J = G^{out}$.

Figure 8-8 depicts the evolution of the maximum disturbance energy gain along the angular coordinate for the four possible optimization options (J_E^{out}, J_E^{mean}, J_K^{out}, and J_K^{mean}) at different unit Reynolds numbers and $\bar{T}_w = 295\,\mathrm{K}$. Note that the region below $\phi_0 < 6°$ for G_E and $\phi_0 < 11°$ for G_K is omitted, respectively. In those areas, the length of the optimization interval is limited by the boundaries of the parameter space depicted in

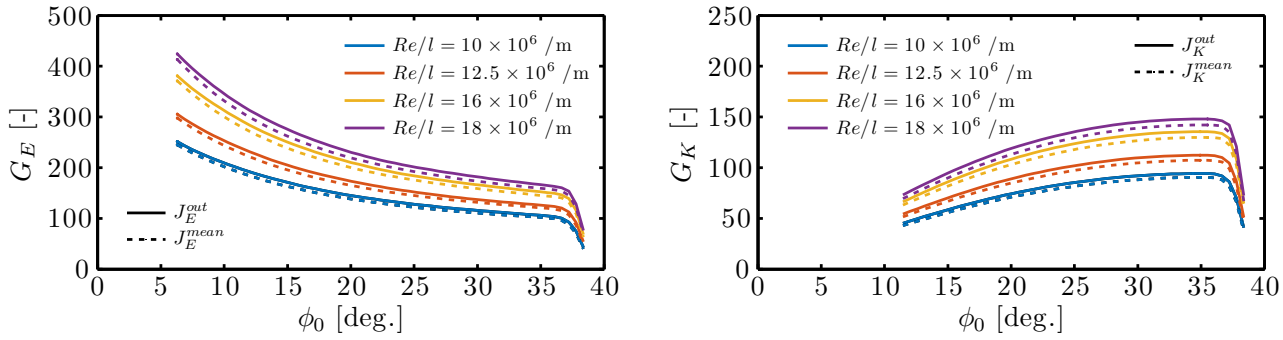

a) b)

Figure 8-8: Streamwise Evolution of the Maximum Optimal Disturbance Energy Gain, $\max_{[\phi_0,\phi_1]} G$, Based on a) Total Energy and b) Kinetic Energy.

Figure 8-7. In the case of mean energy gain as the objective function for optimization, the length of the optimal optimization interval is much longer than when the objective function corresponds to the outlet energy gain. Therefore, a meaningful comparison of both objective functions with regard to the highest possible disturbance energy gain is not feasible below the mentioned regions. For all cases shown in Figure 8-8, maximizing the outlet energy, J^{out}, leads to the highest possible disturbance energy gain within $[\phi_0, \phi_1]_{opt}$ at $m_{\zeta,opt}$. On that account, all of the results presented below to define the upper bound of optimal transient growth for the HLB capsule will pertain only to the objective function based on outlet energy gain ($J = G^{out}$). For all unit Reynolds numbers considered here, the total energy gain of the perturbations reduces with increasing distance from the stagnation point, whereas the kinetic energy gain grows toward the shoulder of the capsule, which in turn implies an increasing share of the overall energy. The sudden decay in energy gain at $\phi_0 \approx 37°$ for both energy norms, G_E and G_K, is attributed to the shortened optimization interval length at the end of the simulation domain (see Figure 8-7).

From the optimal transient-growth analysis for boundary-layer flows over flat plates, the disturbance energy gain at high Reynolds numbers is known to scale with the body-length Reynolds number Re_L [27, 43]. Figure 8-9 indicates the nearly linear scaling of the optimal total disturbance energy gain (G_E) with the unit Reynolds number ($Re_R = R \cdot Re/l$). The results shown in Figure 8-9 are for J_E^{out} and $\bar{T}_w = 295$ K. Because the dimension of the body is kept constant when the unit Reynolds number is varied, the observed small deviations from the linear trend are attributed to the differences in the ratio of boundary-layer thickness to the radius of surface curvature. The linear-like unit Reynolds number dependency of the optimal disturbance energy gain is also reported for the TAMU capsule [12].

The transient-growth amplification with regard to the logarithmic amplification ratio, i.e., N-factor, for $\bar{T}_w = 295$ K is shown in Figure 8-10 in terms of N-factor envelope curves and $\max_{[\phi_0,\phi_1]_{opt}}(N)$ optimized for J^{out} with optimal outlet energy norms based on total and kinetic energy, respectively. The N-factors based on the total energy norm N_E and kinetic energy norm N_K are defined as

$$N_E(\xi) = 1/2 \ln\left[E(\xi)/E(\xi_0)\right], \quad N_K(\xi) = 1/2 \ln\left[K(\xi)/K(\xi_0)\right]. \tag{8-10}$$

The vertical dashed lines in Figure 8-10 indicate the transition locations for the experiments of Ali et al. [15]. The N-factor at the observed transition location based on the norm for total disturbance energy and kinetic energy

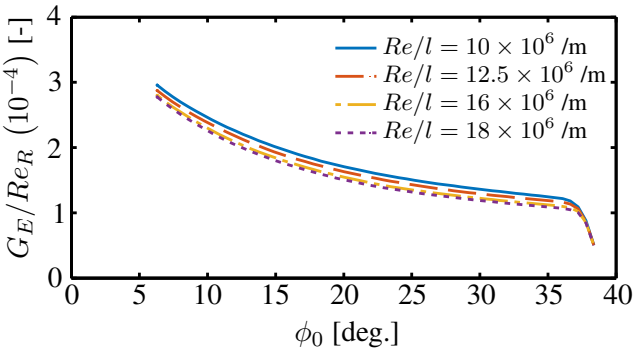

Figure 8-9: Impact of Unit Reynolds Number on the Maximum Total Energy Gain, $\max_{[\phi_0,\phi_1]} G_E$. The Energy Gain is Scaled with Re_R.

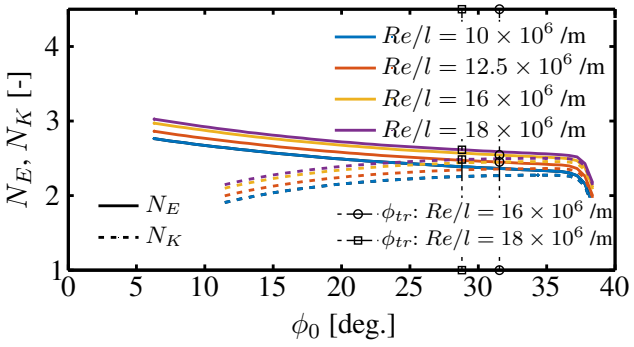

Figure 8-10: Impact of Unit Reynolds Number on the Maximum N-factor, $\max_{[\phi_0,\phi_1]} N$.

are $N_E = 2.54$ and $N_K = 2.45$ at $Re/l = 16 \times 10^6$ /m and $N_E = 2.61$ and $N_K = 2.48$ at $Re/l = 18 \times 10^6$ /m, respectively.

The optimal transient-growth results in Figures 8-8–8-10 have been presented at the optimal parameters of spanwise wavelength and optimization interval. Figure 8-11a depicts the optimal spanwise wavelength for J_E^{out} in terms of boundary-layer thickness along the initial optimization locations for the HLB capsule with $\bar{T}_w = 295$ K and for four different Reynolds numbers. In addition, the optimal parameters for the TAMU capsule with $\bar{T}_w = 391$ K are also plotted at the unit Reynolds numbers from Ref. [12]. For both capsule geometries, the optimal disturbance wavelength displays a good scalability with the boundary-layer thickness. The optimal wavelength with respect to the boundary-layer thickness varies in the range of $(\lambda/\delta)_{opt} \approx [1.6, 2.7]$ for the HLB capsule and $(\lambda/\delta)_{opt} \approx [2.2, 3.0]$ for the TAMU capsule (in the region without domain boundary effects) and is not too different from the findings of Reshotko & Tumin [11] with $(\lambda/\delta)_{opt} \approx [3, 3.5]$ for the flat plate and $(\lambda/\delta)_{opt} \approx 3.2$ for stagnation point flows. Although the predicted optimal wavelengths are similar for both configurations, the small difference may have been caused by the different wall temperatures used in the two studies ($\bar{T}_{w,HLB} = 295$ K, $\bar{T}_{w,TAMU} = 391$ K) and the resulting ratios of wall temperature to boundary-layer edge temperature ($(\bar{T}_w/\bar{T}_e)_{HLB} < 1$ and $(\bar{T}_w/\bar{T}_e)_{TAMU} \approx 1$). The impact of the $\bar{T}_w/\bar{T}_e$-ratio on the optimal parameters for nonmodal disturbance growth will be addressed in the next subsection. Figure 8-11b shows the length of the optimal transient-growth interval as a function of the initial location for the HLB and TAMU capsules at the respective unit Reynolds numbers. Even though the dimension of the TAMU capsule is only about one half the size of the HLB capsule, the optimal length of the transient-growth interval is nearly the same for both geometries ($(\xi_1 - \xi_0)_{opt} \approx 1.0$ cm) and decreases slightly with the unit Reynolds number. The relatively short optimal optimization length is consistent with the findings of Theiss et al. [17, 18] for the laminar wake flow development behind an isolated roughness element on the forebody of the HLB capsule. The authors have shown that due to the strongly favorable pressure gradient [44], the laminar wake flow experiences growth and decay of the streak amplitude (and also modal disturbance growth) only within a few roughness diameters downstream of the element. Although not shown here, choosing J_E^{out} as the objective function, the boundary layer on both capsule forebodies undergoes optimal nonmodal disturbance growth within 30–40 boundary-layer thicknesses depending on the angular coordinate, which is about fifteen times shorter in comparison to the findings of Reshotko & Tumin [11] for flat plate flows.

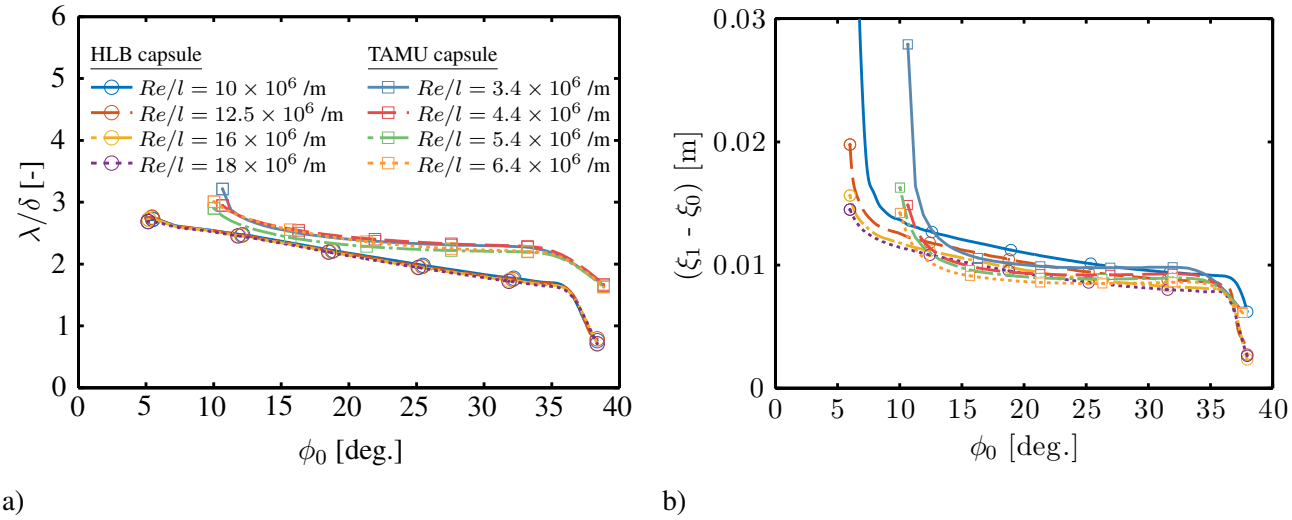

a) b)

Figure 8-11: Impact of Unit Reynolds Number on a) Optimal Spanwise Disturbance Wavelength and b) Optimal Optimization Interval Length.

8.4.2 Effect of Wall Temperature

The effect of the wall temperature on the optimal disturbance growth based on the total and kinetic energy norm is shown in Figure 8-12 for the TAMU capsule with $Re/l = 4.4 \times 10^6$ /m optimized for the outlet energy gain. The corresponding results for the HLB capsule with $Re/l = 10 \times 10^6$ /m are plotted in Figure 8-13. In accordance with previous findings in the literature [9, 11, 20, 27, 45–47], the disturbance energy gain increases with wall-cooling, whereas the effect is more pronounced in the case of the total energy norm, especially in the vicinity of the stagnation point. The disturbance energy gain based on total and kinetic energy norms is higher for the HLB capsule due to the larger body-length Reynolds number by a factor of about five. The share of the kinetic energy on the total energy of the disturbance increases with $\bar{T}_w/\bar{T}_e$ and for $\bar{T}_w/\bar{T}_e \approx 1$ (HLB capsule: $\bar{T}_w = 395$ K, TAMU capsule: $\bar{T}_w = 391$ K; see also Figure 8-4) the total energy mainly consists of kinetic energy, i.e., at $\phi_0 = 35.5°$: $G_E = 70.6$, $G_K = 69.7$ for the HLB capsule and $G_E = 10.3$, $G_K = 9.9$ for the TAMU capsule, respectively.

The effect of wall temperature on the optimal spanwise wavelength and the optimal optimization interval for both capsules is shown in Figures 8-14a and 8-14b, respectively. The objective function is J_E^{out}. The optimal azimuthal wavelength scaled by the boundary-layer thicknesses decreases slightly with wall cooling for both capsule configurations. The results for the TAMU capsule at $Re/l = 4.4 \times 10^6$ /m fall within the range of the HLB capsule data for $Re/l = 10 \times 10^6$ /m when $(\bar{T}_w/\bar{T}_e)_{TAMU} < 1$. On the other hand, the optimal optimization length increases slightly with wall-cooling ($(\xi_1 - \xi_0)_{opt} \approx 1.1$ cm) along with a higher deviation from the mean value.

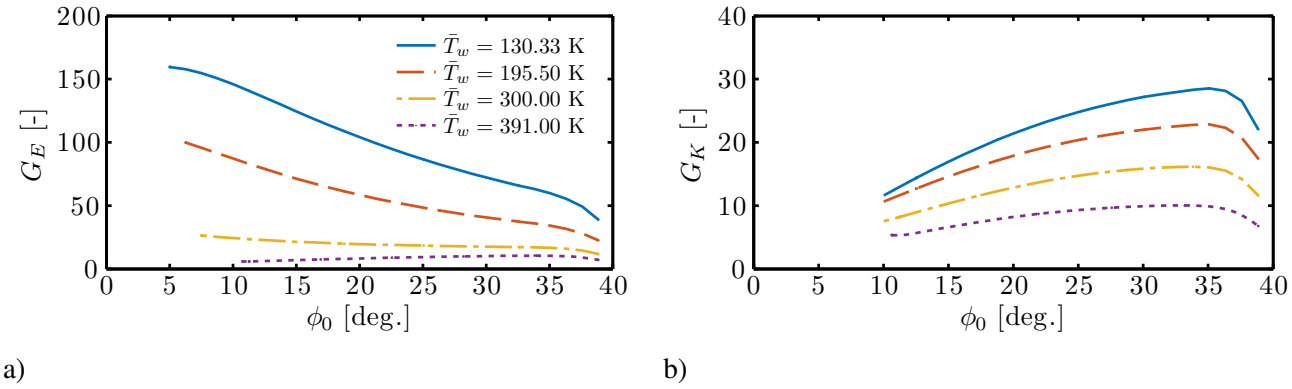

Figure 8-12: Streamwise Evolution of the Maximum Optimal Disturbance Energy Gain, $\max_{[\phi_0,\phi_1]} G$, Based on a) Total Energy and b) Kinetic Energy for the TAMU Capsule.

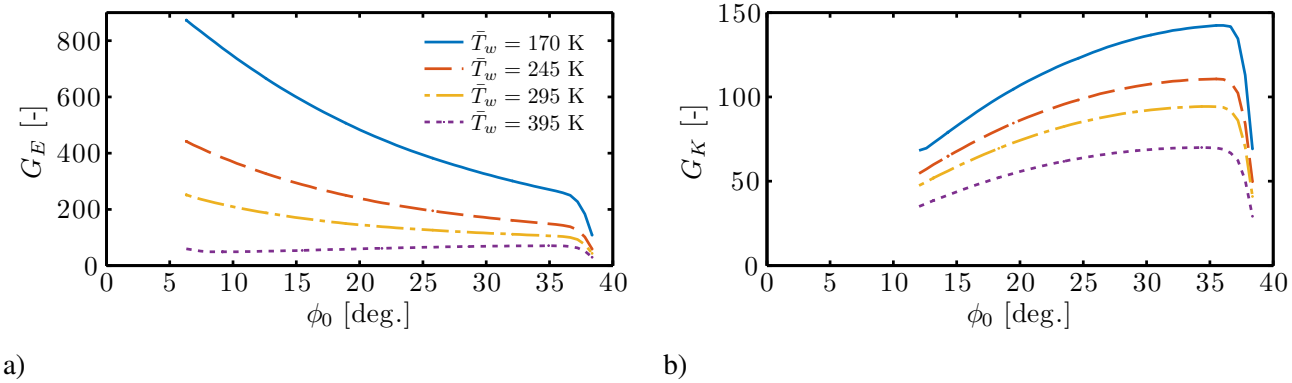

Figure 8-13: As in Figure 8-12, but for the HLB Capsule.

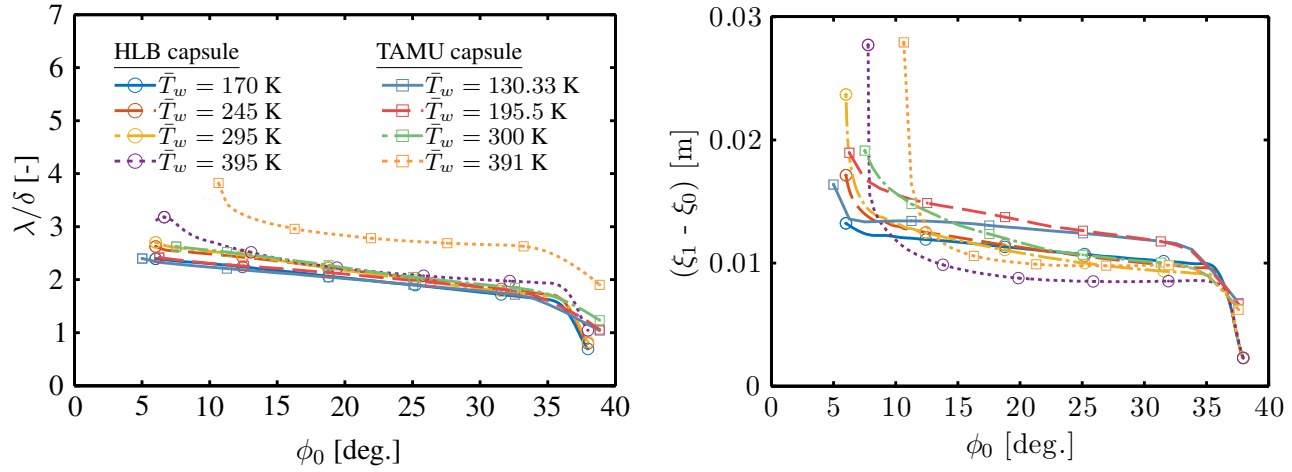

a) b)

Figure 8-14: Impact of Wall Temperature on a) Optimal Spanwise Disturbance Wavelength and b) Optimal Optimization Interval Length.

8.4.3 Revision of Transient-Growth-Based Transition Correlation

Recently, Paredes et al. [12] revisited the distributed roughness-induced transition correlation of Reshotko & Tumin [11], which is the only physics-based model that tackles the blunt-body paradox. The RT-correlation is defined as

$$Re_\theta \left(\frac{k}{\quad}\right) \left(\frac{\bar{T}_e}{\bar{T}_w}\right)^{1.27} = 434, \tag{8-11}$$

where denotes the momentum thickness, Re_θ is the Reynolds number based on , and k is the roughness height. Reshotko & Tumin [11] assumed that an energy norm at the transition location is related to the roughness-induced energy through the transient-growth energy gain factor G with $E_{tr} = GE_{in}$. Further assumptions are that the input energy scales with $E_{in} = \bar{\rho}_k \bar{u}_k^2$ where the roughness-induced disturbance velocities are proportional to the roughness height, $\bar{u}_k/\bar{u}_e \propto k/$ and the wall-cooling ratio $\bar{T}_e/\bar{T}_w$ is equivalent to $\bar{\rho}_k/\bar{\rho}_e$. As a result, the input energy can be approximated to $E_{in} = \left(\bar{T}_e/\bar{T}_w\right)(k/\ )^2$. Furthermore, the gain is assumed to scale with the length Reynolds number (as shown in Figure 8-9) or with the square of a thickness Reynolds number. Thus, the energy at the transition location results in

$$(E_{tr})^{1/2} = \left(\frac{G^{1/2}}{Re_\theta}\right) Re_\theta \left(\frac{k}{\quad}\right) \left(\frac{\bar{T}_e}{\bar{T}_w}\right)^{0.5}. \tag{8-12}$$

Assuming a power-law variation of the scaled optimum transient energy gain with respect to the surface-to-edge temperature ratio,

$$\left(\frac{G^{1/2}}{Re_\theta}\right) \propto \left(\frac{\bar{T}_w}{\bar{T}_e}\right)^{c_T}, \tag{8-13}$$

Reshotko & Tumin [9, 11] in the vicinity of $\bar{T}_w/\bar{T}_e \approx 0.5$ obtained a value for the power-law exponent of $c_T = -0.77$, which finally yields Equation 8-11. For their analysis they used optimal transient-growth computations based on local, parallel theory and self-similar boundary-layer flow without curvature effects. Furthermore,

the initial optimization position and the spanwise wavenumber also remained unchanged. Paredes et al. [12] applied an advanced framework to improve the shortcomings of the optimal transient-growth computations by Reshotko & Tumin [9, 11]; namely, nonlocal transient growth computations including curvature effects for full Navier-Stokes basic state solutions of the TAMU capsule at varying wall temperatures $(\bar{T}_w/\bar{T}_e)_{TAMU} < 1$. The initial ($\xi_{in} = \xi_0$) and final locations ($\xi_{tr} = \xi_1$), as well as the spanwise wavenumber were also optimized. Based on the improved framework, Paredes et al. [12] revised the original RT-correlation and also assumed a power-law variation for the optimum transient energy gain with respect to the surface-to-edge temperature ratio

$$\left(\frac{G^{1/2}}{Re_{\theta_0}}\right)\left(\frac{\bar{\rho}_{e,0}\bar{u}^2_{e,0}}{\bar{\rho}_{e,tr}\bar{u}^2_{e,tr}}\right)^{1/2} \propto \left(\frac{\bar{T}_w}{\bar{T}_{e,0}}\right)^{c_T}. \tag{8-14}$$

In their analysis, they computed the c_T-value for several possible transition onset locations, ϕ_{tr}, based on the optimal parameter combinations $(\lambda_{opt}, m_{\zeta,opt}, (\phi_{tr} - \phi_0)_{opt})$ for each of the different wall temperatures involved ($\bar{T}_w/\bar{T}_e < 1$) and for maximizing the total energy gain (J_E^{out}). Moreover, three assumed variations in spanwise disturbance wavelength were also considered. As a result, the set of exponents were nearly insensitive to the assumed λ-variation and all c_T-values were averaged, resulting in a mean value of $c_T \approx -0.81$, which is remarkably close to the value computed by Reshotko & Tumin [9, 11] based on parallel flow transient-growth calculations. For that reason, the following revised RT-correlation of Paredes et al. [12] only slightly deviates from the originally proposed correlation (Equation 8-11)

$$Re_\theta\left(\frac{k}{\theta}\right)\left(\frac{\bar{T}_e}{\bar{T}_w}\right)^{1.31} = 455. \tag{8-15}$$

The purpose of this section is not to provide an additional transient-growth-based transition correlation, but rather to check if the presented nonmodal growth data for the HLB capsule will result in a similar power-law exponent, c_T, as derived based on the TAMU capsule data. The results shown in Figure 8-13a are used to estimate the best-fit exponent through the relation given in Equation 8-14. Note, that only results were considered when $\bar{T}_w/\bar{T}_e < 1$, in particular, $\bar{T}_w = 170\,\text{K}$, $245\,\text{K}$, and $295\,\text{K}$. Figure 8-15 depicts the variation of the c_T-value at selected transition onset locations for the HLB capsule with $Re/l = 10 \times 10^6\,/\text{m}$. In addition, the results for the TAMU capsule at $Re/l = 4.4 \times 10^6\,/\text{m}$ with the spanwise disturbance wavelength variation based on axisymmetric flow (the same assumption as used in this work) are also shown. The angular coordinate for the HLB capsule data is shifted by $\Delta\phi \approx 1.3°$ to match the boundary-layer edge Mach number conditions on the TAMU capsule (see Figure 8-4). The averaged power-law exponent for the HLB capsule data is $c_{T,HLB} = -0.813$ and therefore in very good agreement with the equivalent TAMU capsule value of $c_{T,TAMU} = -0.809$.

8.5 DNS RESULTS FOR ROUGHNESS PATCHES

To investigate the effect of micron-sized roughness on the capsule boundary layer, direct numerical simulations (DNS) of the supersonic flow around the HLB capsule and the corresponding hemisphere are performed considering finite patches of distributed roughness. The roughness patch geometry for these simulations is deduced from capsule experiments in the HLB [16] and will be quantified subsequently. The generic roughness mimics the Nextel Velvet Coating that allows for infrared surface temperature measurements and showed to have a distinct influence on transition [8]. The Reynolds number based on the height of the roughness is $Re_{kk} = \mathcal{O}(1)$,

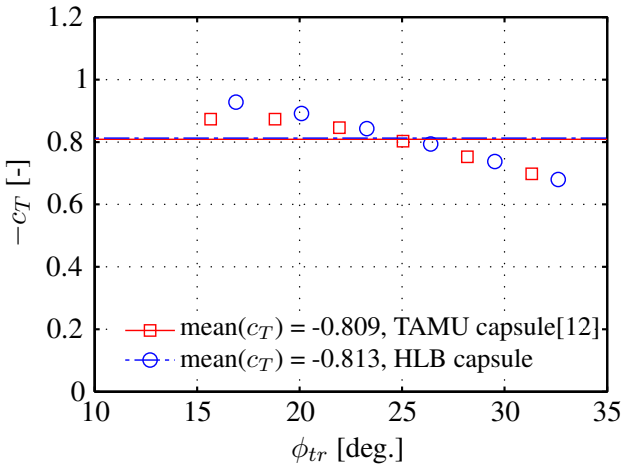

Figure 8-15: Best-Fit Power-Law Exponent of Wall-to-Edge Temperature Ratio for ○: HLB Capsule and □: TAMU Capsule.

Table 8-1: Freestream Conditions for the Configurations with Rough Wall.

Case	Geometry	Ma [−]	p_∞ [Pa]	T_∞ [K]	T_w [K]	Re/l [1/m]	AoA [°]
1	HLB Capsule	5.9	478	59	295	$6.25 \cdot 10^6$	24
2	Hemisphere	5.9	478	59	295	$6.25 \cdot 10^6$	0
3	Hemisphere	5.9	1377	59	295	$18.0 \cdot 10^6$	0

which is well below the critical value. Thus, immediate transition can be excluded [18, 48]. The possible presence of modal as well as nonmodal growth mechanisms in the roughness wake is investigated in Section 8.5.2. Three studies are presented and compared. Freestream conditions for the different simulations are listed in Table 8-1. First, the steady flow at $Re/l = 6.25 \times 10^6$ /m over two different roughness patches located on the HLB capsule is analyzed by RWTH. The computational domain contains capsule, shock wave, and roughness patch. The flow disturbances in the vicinity of the two roughness patches are analyzed and compared. Second, a roughness patch located on the hemisphere from Section 8.3.4 is investigated by TUM. The wake of the roughness is analyzed for modal instabilities at $Re/l = 18 \times 10^6$ /m, and unsteady DNS imposing pressure disturbances are performed to investigate the interaction of roughness and forced disturbance modes.

8.5.1 HLB Capsule Roughness Simulations By RWTH

The roughness patches are located in the center of the spherical forebody of the generic Apollo-like "HLB capsule" in Figure 8-3. The origin of the spherical coordinate system is set in the center of the roughness patch, with ξ, ζ, and η being the streamwise, spanwise, and wall-normal direction, respectively. At the given location, the Mach number at the edge of the boundary layer is $Ma_e = 0.5$. For the current Reynolds number $Re/l = 6.25 \times 10^6$ /m, the boundary-layer thickness, displacement thickness, and momentum loss thickness are $\delta = 492\,\mu$m, $\delta^* = 89.2\,\mu$m, and $\quad = 74.3\,\mu$m, respectively. In this section, the boundary-layer edge is defined as the wall normal distance where the flow has 99 % of the total enthalpy of the freestream. The Reynolds number based on the displacement thickness is $Re_{\delta^*} = 109.65$. The roughness patch elements protrude 20 µm

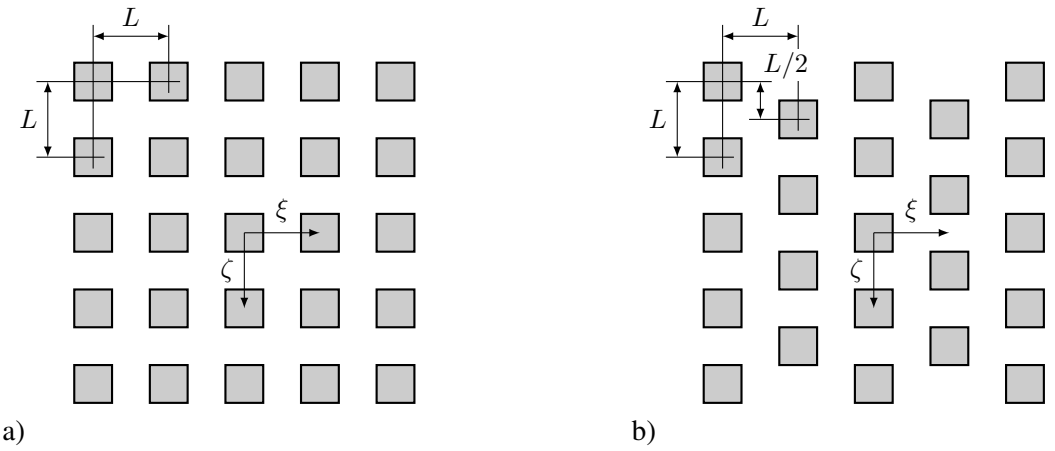

Figure 8-16: Schematic of the Distributed Roughness: a) "Aligned"; b) "Staggered".

into the boundary layer, which is 4% of the boundary-layer thickness and 22% of the displacement thickness. The corresponding roughness Reynolds numbers are $Re_{kk} = 5.82$ and $Re_k = 6.02$, respectively.

The geometry of the aforementioned finite roughness patches is illustrated in Figure 8-16, where the flow direction at the boundary-layer edge is from left to right. Each of the patches consists of a certain number of identical single roughness elements having a square base of $100\,\mu\text{m} \times 100\,\mu\text{m}$ and a height of $20\,\mu\text{m}$. Two patterns of elements are considered. In Figure 8-16a, the "aligned" or "checkerboard" configuration with 5×5 elements is depicted. Based on the flow direction, neighboring elements in the spanwise direction form rows, whereas columns are found in the streamwise direction. This configuration possesses infinite channels between the columns of elements. The spacing between the elements in both streamwise and spanwise direction is $L = 200\,\mu\text{m}$. The "staggered" configuration is shown in Figure 8-16b. The second and fourth row of elements are reduced by one element and misaligned in the spanwise direction by $L/2$. The projected area in the streamwise direction is gapless. The base area of both patches is $0.9\,\text{mm} \times 0.9\,\text{mm}$.

To resolve the micron-sized roughness patch, the unstructured Cartesian grid is massively refined in the vicinity of the roughness patch. The regions of constant grid resolution around the patch are evidenced in Figure 8-17, where thin lines indicate a change of grid resolution of the Cartesian mesh. The streamwise and normal variation of the grid is shown in Figure 8-17a, whereas the variation in the ζ-direction is sketched in Figure 8-17b. Note that instead of the single elements of the roughness patch, the thick line depicts the extent of the complete patch. Furthermore, the capsule surface is sketched flat. The gray dashed line in Figure 8-17a indicates the surface of the spherical forebody. The Cartesian cell length in the innermost region with the highest resolution is $\Delta d = 1.945\,\mu\text{m}$, and it is doubled from region to region. An example of the change in resolution (scaled by a factor of 2) is given in Figure 8-17a at the outermost frame. In total, the mesh contains 300×10^6 cells and 30×10^6 cells are clustered in the refined vicinity of the roughness patch.

The streamwise velocity deficit with respect to the smooth configuration u' downstream of the second and third rows of the elements, i.e., at $\xi = -L/2$ and $\xi = L/2$, is shown in Figure 8-18. In each figure, the staggered and the aligned configurations are shown in the left and right half plane, respectively. Differences between the configurations are restricted to the region close to the wall, i.e., for $\eta < 0.1\,\text{mm}$. Downstream of the staggered

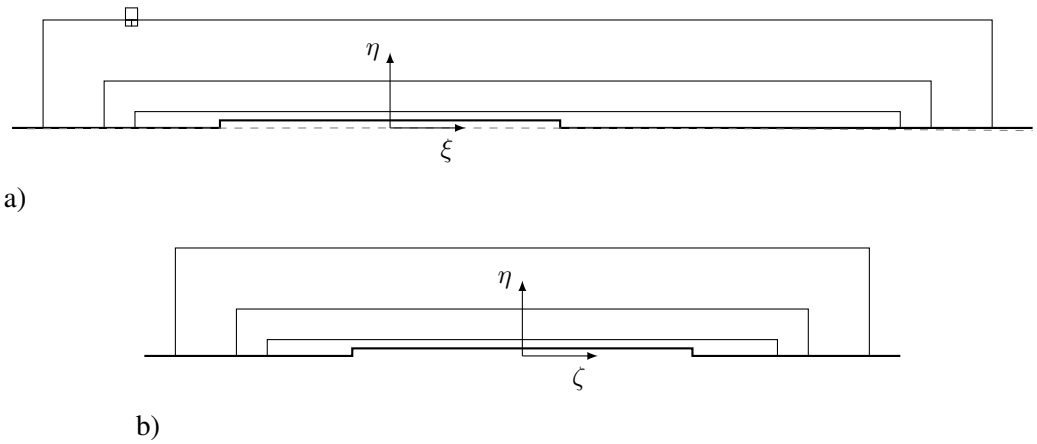

Figure 8-17: Grid Topology in the Vicinity of the Roughness Patch: a) $\xi - \eta$ Plane at $\zeta = 0$; b) $\zeta - \eta$ Plane at $\xi = 0$.

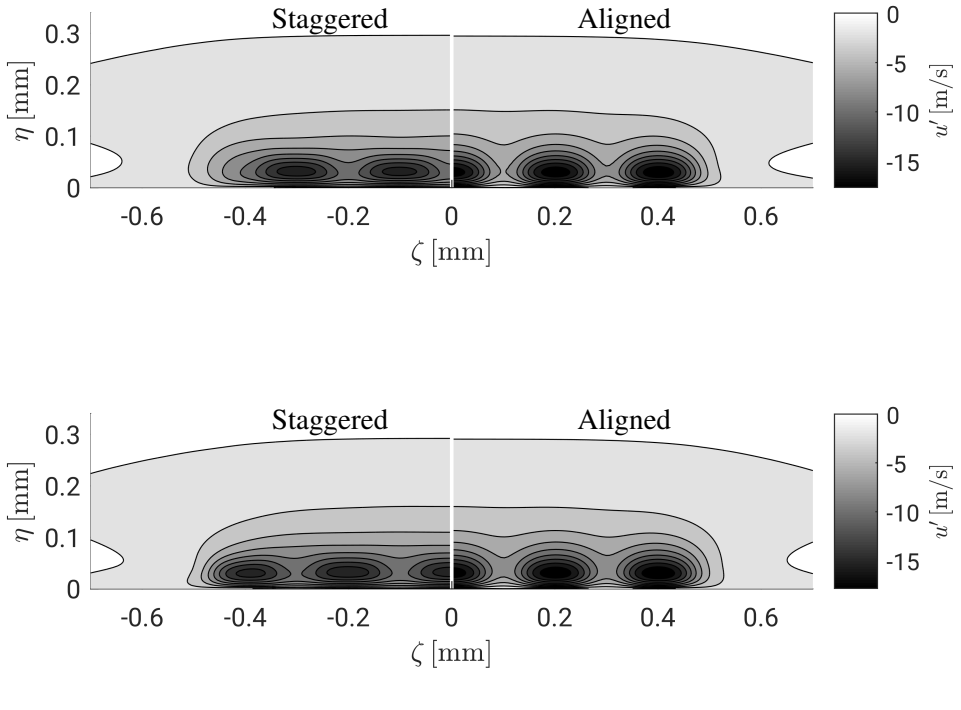

Figure 8-18: Streamwise Velocity Deficit u': a) at $\xi = -L/2 = -100\ \mu$m; b) at $\xi = L/2 = 100\ \mu$m.

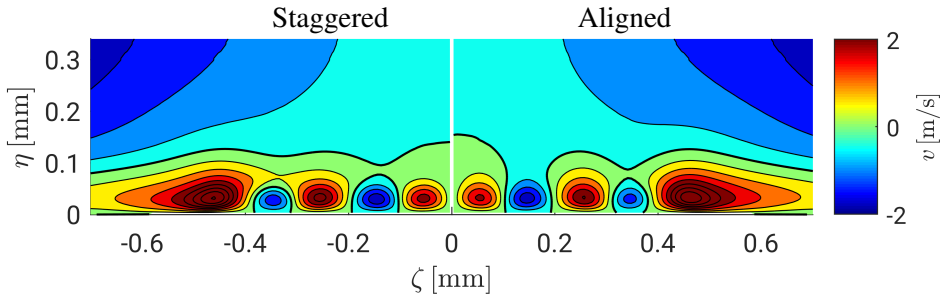

Figure 8-19: Velocity in Spanwise Direction Downstream of the Last Row of Elements at $\xi = 2.5\,L = 500\,\mu$m.

second row in Figure 8-18a, the highest velocity deficit occurs downstream of the elements slightly above the top of the element at $\eta \approx 30\,\mu$m. Note that it is more intense in the aligned configuration. In the channel between the elements, higher velocities, i.e., a lower velocity deficit, are evident in the aligned configuration. This statement also holds downstream of the identically aligned third row in Figure 8-18b. Inside the patch, the difference in the streamwise velocity between the flow-channel and the post-element location is higher for the aligned configuration.

The spanwise velocity component normal to the symmetry plane is evidenced in Figure 8-19 downstream of the roughness patch. Again, the staggered and aligned roughness elements are compared. The velocity component of the aligned configuration in the positive half-plane is multiplied by -1 to yield a better comparison. The thick line indicates $v = 0$. The overall pattern for both cases is identical, but the inward flow, i.e., the bright peaks in Figure 8-19, is stronger for the staggered configuration. This can be attributed to the inward flow generated by the sum of the elements acting as a finite patch. This discussion is resumed in the subsequent analysis in Section 8.5.2 on the infinite extent of the rows of roughness elements located on the hemisphere.

8.5.2 Hemisphere Roughness Simulations By TUM

The TUM-DNS were carried out on a restricted 3D domain extracted on the hemisphere geometry for $\hat{s} \in [74, 116]$ mm. Details of the restricted domain and the roughness patch are shown in Figure 8-5. The roughness patch of the hemisphere consists of 5 squared elements in the streamwise direction. The size of each element and the streamwise spacing are described in Section 8.5.1. The patch is centered at $\hat{s} = 77.4$ mm. Dirichlet boundary conditions are applied at the inflow, Riemann invariants are used at the outflow and azimuthal-periodic boundary conditions are used in the spanwise direction. By using periodic boundary conditions, the domain can be limited in spanwise direction to one single roughness periodicity (L). As a result, a considerable reduction of the domain size and, consequently, of computational cost is achieved. The grid of the restricted domain consists of about 29×10^6 points (1320 points in the streamwise and 220 in the wall-normal direction clustered at the roughness location and 100 points equally spaced in the spanwise direction).

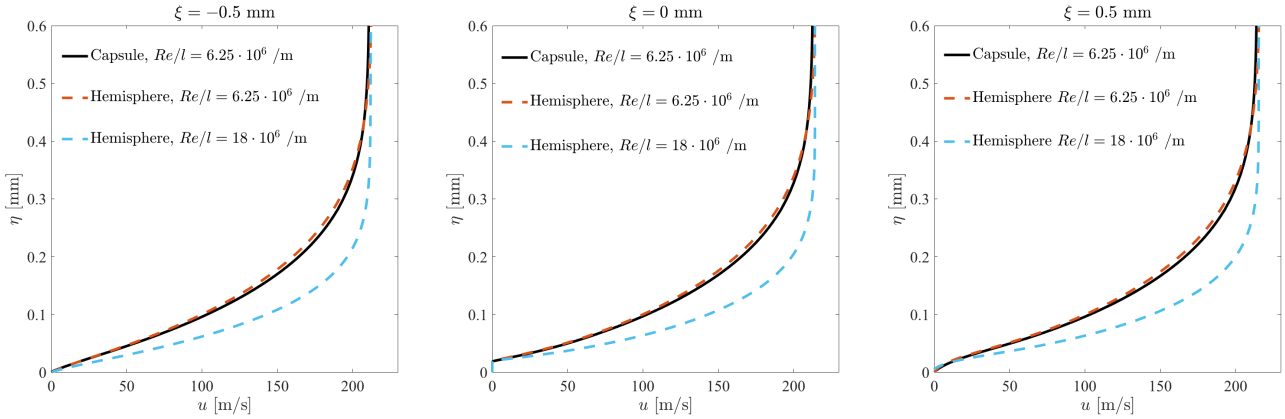

Figure 8-20: Comparison of the Streamwise Velocity Profiles of the Boundary Layer for the Hemisphere and the HLB Capsule Geometry with $\mathrm{AoA} = 24°$.

8.5.2.1 Steady Simulations

For the case of $Re/l = 6.25 \times 10^6$ /m, we compare the results with the ones presented in Section 8.5.1 for the HLB capsule configuration. We found that the presence of the roughness on the hemisphere has a similar effect on the flow as in the case of the HLB capsule. In particular, since several roughness elements are present in the spanwise direction in the case of the HLB capsule, the flow in the vicinity of the symmetry plane presents the same periodicity features as in the case of the rough hemispherical geometry. The profiles of the streamwise velocity at three different positions are shown in Figure 8-20. Profiles are extracted at spanwise coordinate $\zeta = 0$ mm. The roughness patch is centered on $\xi = 0$ mm, whereas $\xi = -0.5$ mm and $\xi = 0.5$ mm refer to positions at 0.5 mm before and after the roughness patch, respectively. A good match can be observed at all three positions. Moreover, Figure 8-21 shows a contour map for the spanwise component of the velocity in the $\zeta - \eta$ plane at the position $\xi = 2.5L = 0.5$ mm downstream of the last roughness row. Contour lines are used for the capsule results and color shading for the hemisphere results. Contour level spacing is 0.3 m/s. For clarity, the dashed line shows the projection of the roughness elements. Also in this case, the spanwise velocity data for the hemisphere and the capsule are similar.

Results for the base flow at $Re/l = 18 \times 10^6$ /m are also shown in Figure 8-20. Compared to the case with lower unit Reynolds number, a less stable boundary layer is expected; and a higher roughness height to boundary-layer thickness ratio is found, in particular, $k/\delta = 0.069$ and $Re_{kk} = 25$.

Further numerical studies on the hemispherical geometry (not shown here) have been undertaken to investigate the influence of the patch length in the streamwise direction. In fact, compared to the experiments in the HLB, the roughness in the present analysis has a smaller spatial extension. However, we found that further lengthening of the rough region in the streamwise direction, obtained by adding roughness elements upstream of the patch, has a negligible influence on the flow downstream of the patch. Therefore, no significant influence is expected on the stability properties of the wake developing downstream of the last roughness element.

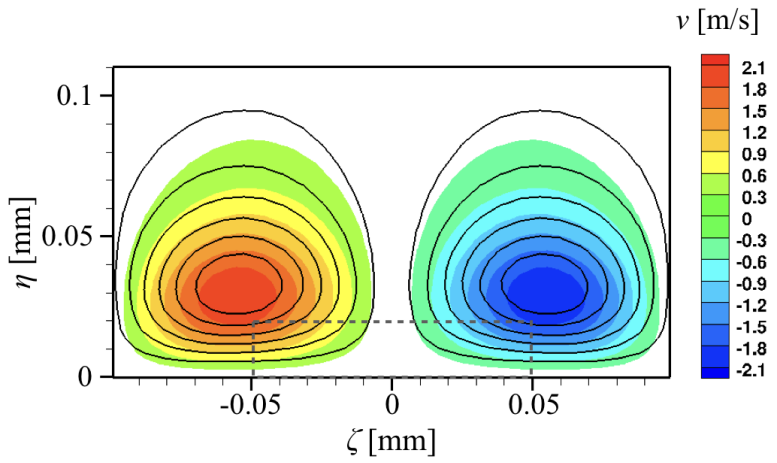

Figure 8-21: Contour Map for the Spanwise Velocity at the Position $\xi = 2.5L = 0.5$ mm.

8.5.2.2 Unsteady Simulations

For the case of $Re/l = 18 \times 10^6$ /m, the base flow downstream of the roughness patch has been analyzed with the help of spatial two-dimensional linear stability analysis (LST-2D). The code used to perform LST-2D has already been validated and tested in the case of wake flow instability behind isolated roughness elements [17, 18]. No modal instability could be found in the boundary layer downstream of the roughness patch.

To investigate the presence of possible nonmodal instability mechanisms (i.e., transient growth), time-varying pressure disturbances are introduced at the inflow of the restricted domain (side 2 in Figure 8-5a) and the development of unsteady disturbances is analyzed by means of unsteady DNS. The disturbance is defined as a superposition of 5 spatial modes with random amplitude A_n and phase ϕ_n,

$$p'(\zeta,\eta) = c(\eta) \cdot \sum_{n=1}^{5} A_n \cos\left(\frac{2\pi n}{\lambda_\zeta}\zeta + \phi_n\right), \tag{8-16}$$

where λ_ζ equals the spanwise length of the domain at the inflow position. The function $c(\eta) = e^{-(\eta/\delta)^3}$, with δ being the boundary-layer thickness, guarantees that the perturbation vanishes outside the boundary layer. Experimental investigations at HLB have revealed that relevant frequencies over the rough-wall capsule for large Reynolds numbers lie in the range 100 – 300 kHz [16]. Based on this observation, three different frequencies are investigated in the present analysis: $f_1 = 167$ kHz, $f_2 = 250$ kHz, and $f_3 = 333$ kHz. The resulting inflow condition for the pressure at $\xi = -3.4$ mm is given by:

$$p(\xi_0,\zeta,\eta,t) = \bar{p}(\xi_0,\zeta,\eta) + p'(\zeta,\eta) \sum_{m=1}^{3} \cos(2\pi f_m t), \tag{8-17}$$

where ξ_0 is the streamwise coordinate value of the inflow boundary and $\bar{p}(\xi_0,\zeta,\eta)$ is the pressure distribution of the steady base flow.

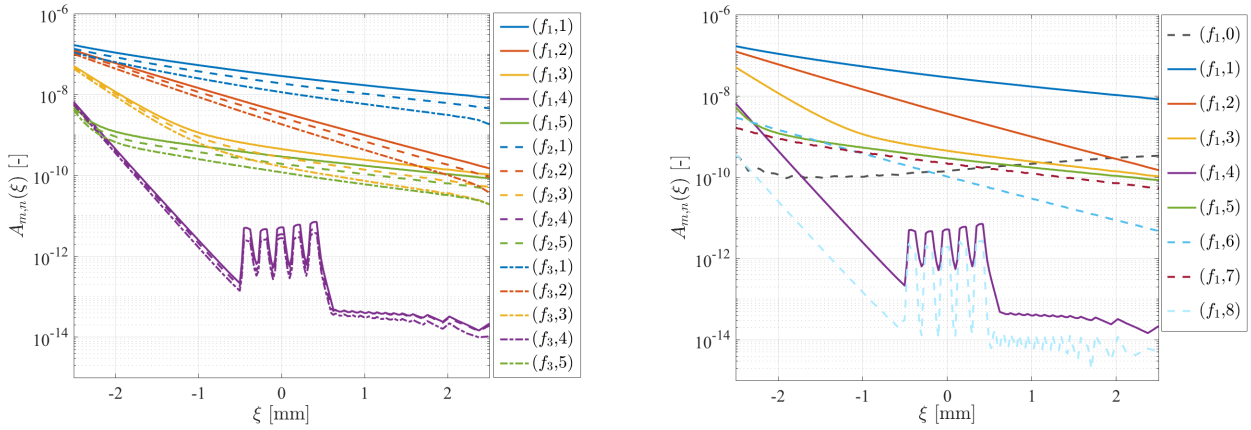

Figure 8-22: Evolution of the Amplitude of Different Spatiotemporal Fourier Modes along the Streamwise Coordinate for the Streamwise Component of the Velocity.

Simulations over a long enough time interval corresponding to multiple periods of the forcing field are needed for the transient effects to vanish and we verified the convergence of the spectrum across the entire simulation domain. The spatiotemporal analysis is conducted by performing a two-dimensional fast Fourier transform (FFT). Any flow variable $g(\xi, \zeta, \eta, t)$ is thus decomposed into spanwise wavenumber-frequency spectra, $G_{m,n}(\xi, \eta)$:

$$g(\xi, \zeta, \eta, t) = \sum_{m=0}^{M-1} \sum_{n=0}^{N-1} G_{m,n}(\xi, \eta) \exp[i2\pi(n\zeta/N + mt/M)], \tag{8-18}$$

where M and N are the number of time and space samples, respectively. The amplitude $A_{m,n}(\xi)$ of the modes (m, n) is defined as the maximum value of $|G_{m,n}(\xi, \eta)|$ at the position ξ.

Figure 8-22 shows the amplitude of the perturbed modes with regard to the streamwise component of the velocity as well as the evolution of higher modes for the frequency f_1. Values are normalized with the edge velocity at the inflow. The origin of the streamwise coordinate, $\xi = 0\,\text{mm}$, is set on the center of the roughness patch. Qualitatively similar results are found for the other frequencies and they are not shown here.

As predicted by LST-2D analysis, no amplified modes are found for the analyzed frequencies. In addition, no evidence of possible transient growth could be found for the considered disturbances. Even though a rapid disturbance growth at the roughness location is evident for the modes $(\cdot, 4)$ and $(\cdot, 8)$, their contribution to the total disturbance energy is small.

The absolute value of the time Fourier transform of the streamwise velocity $|\hat{U}_m(\xi, \zeta, \eta)|$ at different streamwise positions is shown in Figure 8-23 for $f_1 = 167\,\text{kHz}$. The absolute values are normalized on a scale of 0 to 1 and values below 0.2 are blanked out. The black isolines indicates the streamwise-velocity distribution and the red line the projection of the roughness element. For clarity, the roughness height and the boundary-layer edge are marked in the figure. At the inflow, the maximum value of the disturbance is found at a height of about $\eta = 0.07\,\text{mm}$, corresponding to about 0.14δ. Further downstream, viscous effects are responsible for a strong damping of the disturbance in the region close to the wall and the disturbance maximum moves to about $\eta = 0.2\,\text{mm}$. As the roughness does not produce a significant perturbation at this height, no significant interaction can be observed with the incoming unsteady disturbance.

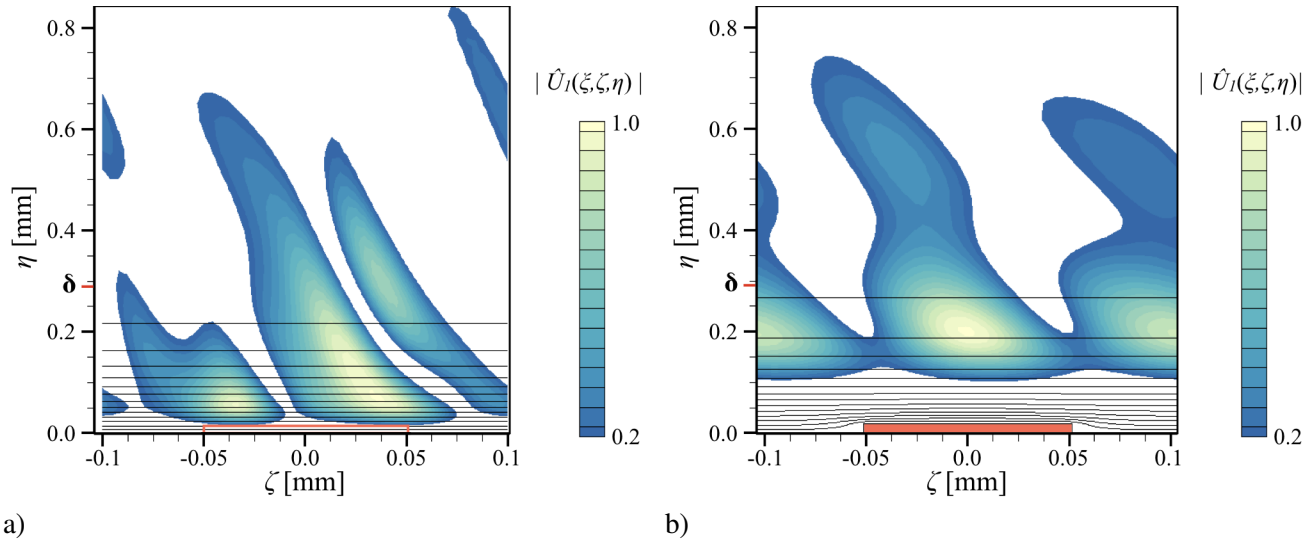

Figure 8-23: Time Fourier Transform of the Streamwise Velocity for $f_1 = 167$ kHz: a) at the Inflow ($\xi = -3.4$ mm); b) at the Roughness Position ($\xi = 0$ mm).

8.6 SUMMARY AND CONCLUSIONS

Optimal transient-growth results for the capsule experiment in the hypersonic Ludwieg tube at the Technische Universität Braunschweig (HLB) at Mach 5.9 were presented and compared with predictions by Paredes et al. [12] for a similar experiment at Mach 6 in the Actively Controlled Expansion (ACE) tunnel at Texas A&M University (TAMU). The angle of attack in the two setups was different, but due to the spherical-segment forebody of both capsule models, the normalized boundary-layer edge data are still very much comparable. In each of the two sets of data, the unit Reynolds number only varied by a factor of about two. Both sets cover a Reynolds number range based on capsule diameter that extends over more than one order of magnitude, however. The maximum gain in energy is higher for the HLB capsule owing to the higher Reynolds numbers but still remains rather moderate in comparison with the amplification factors that correlate the onset of transition in other flows with modal instabilities. Similar trends were observed for the two setups, e.g., concerning the spanwise wavelength normalized by the boundary-layer thickness of the optimal disturbances and the relatively short optimal optimization interval length. In particular, the surface-temperature dependence of the optimal transient-energy gain is very much comparable. Therefore, the value of the power-law exponent of the wall to boundary-layer edge temperature ratio of the correlation for roughness-induced transition that was originally proposed by Reshotko & Tumin [11] and the slightly different value recently derived by Paredes at al. [12] based on optimal transient-growth data for the TAMU capsule are further substantiated by the HLB capsule data at higher Reynolds numbers.

In some of the HLB experiments, a patch of well-defined micron-sized surface roughness had been applied to the capsule model. The effect of this roughness patch on the boundary-layer flow field was replicated by direct numerical simulations (DNS). A hemisphere geometry has been introduced to reduce the size of the simulation domain and, thus, the computational costs of some of these DNS. We compared the flow on the capsule at angle of attack in the vicinity of the symmetry plane with the one on the hemisphere for both the smooth and the

rough-wall geometry and showed that the flow over the hemisphere is similar to the flow over the capsule. In particular, a good match of velocity and temperature profiles is observed.

The stationary disturbance flow field introduced by the well-defined roughness patch was simulated, and its instability characteristics were analyzed. In the case of $Re/l = 18 \times 10^6$ /m where transitional surface heating in the HLB experiment was observed, 2D linear eigenvalue analysis (LST-2D) based on partial differential equations did not reveal any modal instability. Unsteady DNS have been undertaken to investigate possible nonmodal instability mechanisms. Unsteady pressure disturbances are introduced in the domain at three different frequencies ($f_1 = 167$, 200, and 333 kHz) and a spatiotemporal Fourier analysis has been performed on the entire domain. Neither modal amplification nor transient growth of disturbances could be found. In particular, the height of the roughness elements has been shown to be too small for the roughness wake to amplify the incoming unsteady disturbances.

In summary, we considered several potential mechanisms to explain laminar-turbulent transition on the spherical forebody of blunt reentry capsules. At the conditions of the wind-tunnel experiments, modal disturbances are strongly damped in the boundary layer of the nominally smooth configuration, as shown in Ref. [8]. The complementary studies on the upper limit of nonmodal disturbance growth by using optimal transient-growth theory revealed that the maximum transient gain in energy for stationary disturbances is rather moderate. The maximum transient growth in total energy is found in a relatively short distance downstream of the stagnation point. Roughness-induced transient growth of stationary disturbances is unlikely to serve as the primary cause for the observed onset of transition for the rather low surface-roughness values of the HLB experiment. The direct numerical simulations supplemented by the LST-2D studies on the effects of the roughness patch showed that the modifications of the steady flow field due to the patch are too weak to trigger modal disturbance growth in its wake. Present DNS did not reveal any noteworthy nonmodal disturbance growth in the wake flow. Therefore, a plausible explanation for the observed transition onset in experiment for low surface-roughness values under conditions investigated in the HLB experiment remains to be found and further studies on the interaction of freestream disturbances with small surface roughness are required.

Very recent HLB experiments have yielded transition data for sandgrit-type coatings with significantly increased roughness heights. This data is in good agreement with the correlations derived from transient-growth scalings [49]. However, single discrete roughness elements of comparable height have already been found to produce a large enough deformation of the mean flow to support a significant modal growth within the wake of the roughness elements [17, 18]. Hence, future numerical studies for distributed surface roughness at increased roughness heights should take into account the effects of the distributed surface roughness on the mean flow and its modal and nonmodal (transient) disturbance growth characteristics.

8.7 ACKNOWLEDGMENTS

Part of this work has been funded by the German Research Foundation (DFG) within the HYPTRANS PAK742. The support is gratefully acknowledged. Computing resources were provided by the High Performance Computing Center Stuttgart (HLRS), the Jülich Supercomputing Center and the Leibniz Supercomputing Centre Munich (LRZ). The work of the NASA authors was performed jointly under the NASA Transformational Tools and Technologies project and the NASA Hypersonic Technologies Project.

8.8 REFERENCES

[1] Schneider, S.P., "Effects of Roughness on Hypersonic Boundary-Layer Transition," *Journal of Spacecraft and Rockets*, Vol. 45, No. 2, 2008, pp. 193–209.

[2] Schneider, S.P., "Summary of Hypersonic Boundary-Layer Transition Experiments on Blunt Bodies With Roughness," *Journal of Spacecraft and Rockets*, Vol. 45, No. 6, 2008, pp. 1090–1105.

[3] Reda, D.C., "Review and Synthesis of Roughness-Dominated Transition Correlations for Reentry Applications," *Journal of Spacecraft and Rockets*, Vol. 39, No. 2, Mar - Apr 2002, pp. 161–167.

[4] Hollis, B.R., "Correlation of Recent and Historical Rough-Wall Transition Data on Hemispherical Nosetips," *33rd AIAA Aerodynamic Measurement Technology and Ground Testing Conference, AIAA AVIATION Forum*, AIAA Paper 2017-3986, 2017.

[5] Johnson, H.B., Candler, G.V., and Wright, M.J., "Boundary Layer Stability Analysis of Mars Science Laboratory Aeroshell," *44th AIAA Aerospace Sciences Meeting and Exhibit, Aerospace Sciences Meetings*, AIAA Paper 2006-0920, 2006.

[6] Chang, C.L., Choudhari, M.M., Hollis, B.R., and Li, F., "Transition Analysis for the Mars Science Laboratory Entry Vehicle," *41st AIAA Thermophysics Conference*, AIAA Paper 2009-4076, 2009.

[7] Theiss, A., Lichtmess, M., and Hein, S., "Local Stability Analysis of Laminar-Turbulent Transition on Blunt Generic Re-Entry Capsules," *New Results in Numerical and Experimental Fluid Mechanics X, Notes on Numerical Fluid Mechanics and Multidisciplinary Design*, Vol. 132, 2014.

[8] Theiss, A., Hein, S., Heitmann, D., Ali, S.R.C., and Radespiel, R., "Numerical and Experimental Investigation of Laminar-Turbulent Boundary Layer Transition on a Blunt Generic Re-Entry Capsule," *44th AIAA Fluid Dynamics Conference, AIAA AVIATION Forum*, AIAA Paper 2014-2353, 2014.

[9] Reshotko, E. and Tumin, A., "The Blunt Body Paradox — a Case for Transient Growth," *Laminar-Turbulent Transition*, Springer, 2000, pp. 403–408.

[10] Schmid, P.J. and Henningson, D.S., *Stability and Transition in Shear Flows*, Springer, 2001.

[11] Reshotko, E. and Tumin, A., "Role of Transient Growth in Roughness-Induced Transition," *AIAA Journal*, Vol. 42, No. 4, Apr 2004, pp. 766–770.

[12] Paredes, P., Choudhari, M.M., and Li, F., "Blunt-Body Paradox and Improved Application of Transient-Growth Framework," *AIAA Journal*, Vol. 56, No. 7, Jul 2018, pp. 2604–2614.

[13] Leidy, A.N., Reshotko, E., Siddiqui, F., and Bowersox, R.D.W., "Characterizing the Transient Growth Mechanism on a Hypersonic Blunt Body at a High Angle of Attack," *46th AIAA Fluid Dynamics Conference*, AIAA Paper 2016-3951, 2016.

[14] Leidy, A.N., Reshotko, E., Siddiqui, F., and Bowersox, R.D.W., "Transition Due to Roughness on Blunt Capsule: Comparison With Transient Growth Correlation," *Journal of Spacecraft and Rockets*, Vol. 55, No. 1, Jan.-Feb. 2018, pp. 167–180.

[15] Ali, S.R.C., Radespiel, R., and Theiss, A., "Transition Experiment With a Blunt Apollo Shape Like Capsule in Hypersonic Ludwieg Tube," *63. Deutscher Luft- Und Raumfahrtkongress 2014*, Paper 2014-340270, 2014.

[16] Radespiel, R., Ali, S.R.C., Bowersox, R.D.W., Leidy, A.N., Tanno, H., Kirk, L.C., and Reshotko, E., "Experimental Investigation of Roughness Effects on Transition on Blunt Spherical Capsule Shapes," *2018 AIAA Aerospace Sciences Meeting, AIAA SciTech Forum*, AIAA Paper 2018-0059, 2018.

[17] Theiss, A., Hein, S., Ali, S.R.C., and Radespiel, R., "Wake Flow Instability Studies Behind Discrete Roughness Elements on a Generic Re-Entry Capsule," *46th AIAA Fluid Dynamics Conference, AIAA AVIATION Forum*, AIAA Paper 2016-4382, 2016.

[18] Theiss, A. and Hein, S., "Investigation on the Wake Flow Instability Behind Isolated Roughness Elements on the Forebody of a Blunt Generic Reentry Capsule," *Progress in Flight Physics*, edited by D. Knight, Y. Bondar, I. Lipatov, and P. Reijasse, EDP Sciences, 2017.

[19] Pralits, J., Airiau, C., Hanifi, A., and Henningson, D., "Sensitivity Analysis Using Adjoint Parabolized Stability Equations for Compressible Flows," *Flow, Turbulence and Combustion*, Vol. 65, No. 3–4, 2000, pp. 321–346.

[20] Tempelmann, D., Hanifi, A., and Henningson, D.S., "Spatial Optimal Growth in Three-Dimensional Compressible Boundary Layers," *Journal of Fluid Mechanics*, Vol. 704, Jul 2012, pp. 251–279.

[21] Paredes, P., Choudhari, M.M., Li, F., and Chang, C.L., "Optimal Growth in Hypersonic Boundary Layers," *AIAA Journal*, Vol. 54, No. 10, Oct 2016, pp. 3050–3061.

[22] Paredes, P., Choudhari, M.M., and Li, F., "Blunt-Body Paradox and Transient Growth on a Hypersonic Spherical Forebody," *Physical Review Fluids*, Vol. 2, No. 5, May 2017, pp. 053903–1–24.

[23] Hein, S., Bertolotti, F., Simen, M., Hanifi, A., and Henningson, D., "Linear Nonlocal Instability Analysis - The Linear NOLOT Code," Tech. Rep. DLR-IB 223-94 A56, Deutsches Zentrum für Luft- und Raumfahrt e. V. (DLR), Germany, 1994.

[24] Chang, C.L., Malik, M., Erlebacher, G., and Hussaini, M., "Compressible Stability of Growing Boundary Layers Using Parabolized Stability Equations," *22nd Fluid Dynamics, Plasma Dynamics and Lasers Conference*, AIAA Paper 91-1636, 1991.

[25] Tempelmann, D., Hanifi, A., and Henningson, D.S., "Spatial Optimal Growth in Three-Dimensional Boundary Layers," *Journal of Fluid Mechanics*, Vol. 646, Mar 2010, pp. 5–37.

[26] Levin, O. and Henningson, D.S., "Exponential vs Algebraic Growth and Transition Prediction in Boundary Layer Flow," *Flow, Turbulence and Combustion*, Vol. 70, No. 1–4, 2003, pp. 183–210.

[27] Zuccher, S., Tumin, A., and Reshotko, E., "Parabolic Approach to Optimal Perturbations in Compressible Boundary Layers," *Journal of Fluid Mechanics*, Vol. 556, May 2006, pp. 189–216.

[28] Chu, B.T., "On the Energy Transfer to Small Disturbances in Fluid Flow (Part I)," *Acta Mechanica I*, Vol. 1, No. 3, 1965, pp. 215–234.

[29] Mack, L.M., "Boundary Layer Stability Theory," Tech. Rep. JPL Report 900-277, Jet Propulsion Laboratory, California Institute of Technology, Pasadena, CA, Nov 1969.

[30] Hanifi, A., Schmid, P.J., and Henningson, D.S., "Transient Growth in Compressible Boundary Layer Flow," *Physics of Fluids*, Vol. 8, No. 3, Mar 1996, pp. 826–837.

[31] Hermanns, M. and Hernández, J.A., "Stable High-Order Finite-Difference Methods Based on Non-Uniform Grid Point Distributions," *International Journal for Numerical Methods in Fluids*, Vol. 56, No. 3, 2007, pp. 233–255.

[32] Li, F., Choudhari, M.M., Chang, C.L., and White, J., "Effects of Injection on the Instability of Boundary Layers Over Hypersonic Configurations," *Physics of Fluids*, Vol. 25, 2013, pp. 104107–1–15.

[33] Hartmann, D., Meinke, M., and Schröder, W., "An Adaptive Multilevel Multigrid Formulation for Cartesian Hierarchical Grid Methods," *Computers & Fluids*, Vol. 37, No. 9, 2008, pp. 1103–1125.

[34] Lintermann, A., Schlimpert, S., Grimmen, J.H., Günther, C., Meinke, M., and Schröder, W., "Massively Parallel Grid Generation on HPC Systems," *Computer Methods in Applied Mechanics and Engineering*, Vol. 277, 2014, pp. 131–153.

[35] Schneiders, L., Hartmann, D., Meinke, M., and Schröder, W., "An Accurate Moving Boundary Formulation in Cut-Cell Methods," *Journal of Computational Physics*, Vol. 235, 2013, pp. 786–809.

[36] Schilden, T., Schröder, W., Ali, S.R.C., Wu, J., Schreyer, A.M., and Radespiel, R., "Analysis of Acoustic and Entropy Disturbances in a Hypersonic Wind Tunnel," *Physics of Fluids*, Vol. 28, 2016, pp. 056104–1–25.

[37] Schilden, T. and Schröder, W., "Numerical Analysis of High Speed Wind Tunnel Flow Disturbance Measurements Using Stagnation Point Probes," *Journal of Fluid Mechanics*, Vol. 833, 2017, pp. 247–273.

[38] Hoarau, Y., Pena, D., Vos, J.B., Charbonnier, D., Gehri, A., Brazak, M., Deloze, T., and Laurendeau, E., "Recent Developments of the Navier Stokes Multi Block (NSMB) CFD Solver," *54th AIAA Aerospace Sciences Meeting, AIAA SciTech Forum*, AIAA Paper 2016-2056, 2016.

[39] Stemmer, C., Birrer, M., and Adams, N.A., "Disturbance Development in an Obstacle Wake in a Reacting Hypersonic Boundary Layer," *Journal of Spacecraft and Rockets*, Vol. 54, No. 4, 2017, pp. 945–960.

[40] Hollis, B.R., Berger, K.T., Horvath, T.J., Coblish, J.J., Norris, J.D., Lillard, R.P., and Kirk, B.S., "Aeroheating Testing and Predictions for Project Orion Crew Exploration Vehicle," *Journal of Spacecraft and Rockets*, Vol. 46, No. 4, Jul 2009, pp. 766–780.

[41] Litton, D., Edwards, J., and White, J., "Algorithmic Enhancements to the VULCAN Navier-Stokes Solver," *16th AIAA Computational Fluid Dynamics Conference*, AIAA Paper 2003-3979, 2003.

[42] Raddatz, J. and Fassbender, J.K., "Block Structured Navier-Stokes Solver FLOWer," *MEGAFLOW - Numerical Flow Simulation for Aircraft Design*, Springer Berlin Heidelberg, 2005, pp. 27–44.

[43] Andersson, P., Berggren, M., and Henningson, D.S., "Optimal Disturbances and Bypass Transition in Boundary Layers," *Physics of Fluids*, Vol. 11, No. 1, Jan 1999, pp. 134–150.

[44] Theiss, A., Leyh, S., and Hein, S., "Pressure Gradient Effects on Wake Flow Instabilities Behind Isolated Roughness Elements on Re-Entry Capsules," *7th European Conference for Aeronautics and Space Sciences (EUCASS), Paper FP-594*, 2017.

[45] Tumin, A. and Reshotko, E., "Spatial Theory of Optimal Disturbances in Boundary Layers," *Physics of Fluids*, Vol. 13, No. 7, Jul 2001, pp. 2097–2104.

[46] Tumin, A. and Reshotko, E., "Optimal Disturbances in Compressible Boundary Layers," *AIAA Journal*, Vol. 41, No. 12, Dec 2003, pp. 2357–2363.

[47] Zuccher, S., Shalaev, I., Tumin, A., and Reshotko, E., "Optimal Disturbances in the Supersonic Boundary Layer Past a Sharp Cone," *AIAA Journal*, Vol. 45, No. 2, Feb 2007, pp. 366–373.

[48] Klebanoff, P.S., Cleveland, W.G., and Tidstrom, K.D., "On the Evolution of a Turbulent Boundary Layer Induced by a Three-Dimensional Roughness Element," *Journal of Fluid Mechanics*, Vol. 237, 1992, pp. 101–187.

[49] Radespiel, R., Ali, S.R.C., Bowersox, R.D.W., Leidy, A.N., Tanno, H., Kirk, L.C., and Reshotko, E., "Experimental Investigation of Roughness Effects on Transition on Blunt Spherical Capsule Shapes," *Journal of Spacecraft and Rockets*, Vol. 56, No. 2, Mar - Apr 2019, pp. 405–420.

Chapter 9 - EXPERIMENTAL INVESTIGATION OF ROUGHNESS EFFECTS ON TRANSITION ON BLUNT SPHERICAL CAPSULE SHAPES

Rolf Radespiel and Syed R.C. Ali
Technische Universität Braunschweig
GERMANY

Rodney Bowersox and Andrew Leidy
Texas A&M University
UNITED STATES

Hideyuki Tanno
JAXA Kakuda Space Center
JAPAN

Lindsay C. Kirk
NASA Johnson Space Center
UNITED STATES

Eli Reshotko
Case Western Reserve University
UNITED STATES

9.0 NOMENCLATURE

b	wall thickness
c	specific heat
D, d	diameter of the wind tunnel model
E	voltage
f	frequency
H	enthalpy
h	convective heat transfer coefficient
k	peak-to-valley roughness height
M	Mach number
PSD	power spectral density
Q	heat flux rate
R	radius of the model
R_a	mean surface roughness
Re	Reynolds number
R_d	Reynolds number based on model diameter
Re_{kk}	Reynolds number based on roughness height and flow conditions at this height
Re/l	Unit Reynolds number of freestream flow

Re_θ	Reynolds number based on boundary layer momentum thickness
St	Stanton number
T	temperature
t	time
u	streamwise velocity
x, y, z	Cartesian coordinates
θ	momentum thickness of boundary layer
κ	thermal conductivity
ν	kinematic viscosity
ρ	density

Subscripts

$conv$	convective
e	at boundary layer edge
$mean$	mean value
p	at constant pressure
RMS	root mean square
tr	transitional
∞	freestream
w	wall
0	at stagnation point

9.1 INTRODUCTION

Heat transfer on hypersonic vehicles with blunt nose geometries during re-entry or at sustained hypersonic flight is important for designing the thermal protection system. Turbulent heat transfer is generally much larger than laminar heating. Therefore, the onset of turbulent flow due to boundary-layer transition must be predicted during design phases of the vehicle. This is a difficult task since important flow parameters such as Reynolds number, stagnation enthalpy and wall temperatures vary largely along the flight trajectory. Hence, sensitivity of the flow with respect to vehicle details that augment transition processes present for an ideally smooth vehicle varies largely, too. One of these parameters is surface roughness. Roughness can be an inherent feature of the surface material used for thermal protection, but it often changes during flight, due to chemical interactions of the surface materials with the high-temperature near-wall flow, resulting in a range of complex roughness manifestations.

Computational prediction methods for boundary-layer transition of hypersonic flow over blunt shapes which take these effects into account based on first principles are not yet available. Present computational design tools use theoretical considerations and assumptions to simplify the computation task. Also, the computations usually involve uncertainties due to the numerical approximation of the continuous problem. Therefore, detailed experiments in a suited flow environment are needed for validating prediction methods and for verifying new vehicle designs. While experiments by well-documented flight tests could be considered as an ultimate proof of

validation, this approach is generally not feasible, due to extremely high cost and specific uncertainties related to flight-testing as well. Therefore, wind tunnel testing in hypersonic facilities must be used. Unfortunately, hypersonic wind tunnels large enough to allow transition experiments of blunt shapes at reasonably high Reynolds numbers usually have significant flow distortions in their test section flow. These distortions are primarily comprised of acoustic noise originating from the high-velocity nozzle boundary layer. However, they also contain fluctuations of flow total temperature due to temperature variations in the tunnel flow reservoir before the nozzle, and vorticity disturbances due to turbulence generated in the tunnel settling chamber.

Generic blunt noses shapes are often spherical. The boundary layer of hypersonic flows over spherical nose shapes does generally not exhibit modal instabilities such as Tollmien-Schlichting modes, up to very high Reynolds numbers. This holds true for blunt bodies with spherical noses also at significant angles of attack. However, experiments indicate that transition on such blunt shapes appears under many circumstances. Note that blunt windward shapes combined of sphere segments and cone portions behave differently, as they exhibit modal instabilities.

Heat flux augmentation around the stagnation point and transition onset in wind tunnels were investigated by a number of researchers for nominally smooth capsule shapes at hypersonic speeds [1], [2]. Using models of different size and correlations between heat transfer sensors, Marineau et al. [2] emphasize the importance of vortical disturbance size originating from the freestream relative to model size and the vortex augmentation by vortex stretching. Ali et al. [3] measure similar phenomena, however they also observe significant sensitivity to small, subcritical surface roughness at roughness heights typical for instrumented wind tunnel models. For isolated roughness elements on blunt shapes, there exist a large number of experiments, see Ref. [4] as an example. While these protuberances often trip the boundary layer state from laminar to turbulent, they can also generate modal instabilities, which grow in the mean-flow wake of these disturbances. Ref. [5] presents the analysis of such wake instabilities in the accelerated boundary layer of an Apollo-shape capsule at angle of attack, indicating a rather short stream-wise extent of eigenmode growth, compared to flat-plate results, and presents corresponding measured surface fluctuations. The influence of flow enthalpy on transition with and without roughness elements is of particular interest. Here, first results from the HIEST facility became available over recent years [6], with corresponding computations indicating relative boundary layer parameters [7]. The latter indicate good correlation with unit Reynolds number.

Most representative for the effect surface roughness during hypersonic flight is distributed roughness. Distributed roughness generates streamwise vortices, which are rather independent of freestream disturbances. These vortices possibly grow in the area close to the stagnation point. A candidate mechanism for this is transient growth. Transient growth describes the superposition of slightly damped, non-orthogonal modes of the boundary layer. For suited boundary layer parameters, the resulting disturbing magnitudes may become large. Reshotko and Tumin [8], [9] considered the theory of optimal disturbances for compressible stagnation point flow. They find that optimal boundary layer disturbances are stationary streamwise vortices of zero frequency and with particular spanwise wave numbers. Hence, transient growth can be significant in transition to turbulence for blunt shapes with otherwise stable modes. It bypasses eigenmode growth and therefore, leads directly to parametric instabilities and mode interactions of large boundary layer disturbances, followed by breakdown. This is called roughness induced transition. Ref. [9] analyzed growth calculations of axisymmetric stagnation point flow for the effects of roughness height, wall-to-edge temperature ratio and surface curvature. The resulting model is

$$Re_{\theta,tr} = 180 \left(\frac{k}{-}\right)^{-1} \left(\frac{T_e}{2T_w}\right)^{-1.27} \tag{9-1}$$

for which the scaling coefficient was based on carefully analyzed wind tunnel data [10], [11]. The validity of this model obviously breaks for large roughness heights, as the flow disturbances created by large roughness would directly bypass any linear growth mechanism. More recently, new experiments became available which can be used to substantiate the theoretical findings. Hollis performed wind tunnel experiments with a range of distributed sand grain and patterned roughness setups for various blunt nose shapes [12] and he derived further empirical correlations [13]. Leidy et al. set up dedicated transition experiments in support of the transient-growth based correlation [14]. Further substantiation can be expected from numerical computations that go beyond the limitations associated with transient growth theory, for example solutions of the parabolized stability equations, PSE, and direct numerical simulations, DNS. The Research Group AVT 240 of the Science Technology Organization has performed significant research works in numerical analysis of Apollo-type capsule shapes, as presented in a companion paper [15]. This confirmed the theory-based relationship of the Equation 9-1 remarkably well. Boundary layer transition on blunt, spherical nose shapes often depends on freestream disturbances of the facility, as noted above. Hence, new approaches and results in analyzing freestream disturbances in hypersonic wind tunnel facilities are presented in another companion paper [16].

The present contribution reviews experimental investigations of roughness effects on boundary layer transition on capsule geometries with spherical windward geometries, also performed as part of the Research Group AVT 240. We describe experiments in three wind tunnel facilities. The ACE Tunnel of Texas A&M University, USA, provided Mach 6 experiments with distributed roughness at relatively low Reynolds numbers, $2.5 \cdot 10^5 < Re_d < 5 \cdot 10^5$, with d denoting the capsule diameter. Observed boundary layer transition are compared to correlations based on transient growth theory. Larger Reynolds numbers, $1 \cdot 10^6 < Re_d < 3 \cdot 10^6$, could be assessed in the hypersonic Ludwieg tube of TU Braunschweig, Germany. These experiments varied fluctuation levels of the freestream. Transition is already observed at rather low, subcritical roughness values in the order of 20 μm (peak to valley) on a 170 mm capsule model. Roughness induced transition is obtained for larger roughness of around 100-250 μm. Additionally, disturbance levels within the shock layer, close to the edge of the boundary layer, were measured by hot-wire anemometry. Effects of total flow enthalpy on transition with isolated roughness were investigated in the HIEST facility of JAXA, Japan. Here, a model insert with roughness elements for tripping transition to turbulence was employed and flow total enthalpy along with Reynolds number was varied.

9.2 TRANSITION EXPERIMENTS IN ACE WIND TUNNEL

9.2.1 Experimental Setup

Tests were conducted at Mach 6 on a thin-walled, scaled model of the Orion CEV mounted in the Actively Controlled Expansion (ACE) wind tunnel at a 28 degree angle of attack. ACE is an open-circuit hypersonic blowdown pressure-vacuum tunnel that can achieve Mach 5-8. The Mach number on the method of characteristics designed nozzle is adjusted by changing the throat height. ACE has a maximum run time of 40 seconds and a unit Reynolds number range is $0.3 - 10 \cdot 10^6$ /m.

The stainless steel model is comprised of a conical base and a 7.62 cm diameter spherical cap with a wall thickness of 0.76 mm. The cap was coated in samples of aluminum oxide sandgrit to give the face five different quasi-uniform distributed roughness heights. It was also spray-painted with six coats of high-temperature black spray paint to minimize the infrared reflectivity of the surface. The roughness height for each sample was char-

acterized using a laser profilometer. The laser scans were processed according to the 30 % exceedance criteria described by Batt and Legner [11]. The thermal properties of the face were approximated using the method of layers which assumes that thermal capacities and resistances of different materials are additive and the surface emissivity is unity. The roughness heights and associated thermal properties for each sandgrit sample are given in Table 9-1.

Surface temperature measurements on the capsule face were sampled continuously throughout the run at 60 Hz using a FLIR SC3000 IR camera. The gallium arsenide detector is sensitive to longwave infrared radiation within the range of 8-9 micrometers and has 320 $\times$ 240 pixel resolution. The camera was positioned facing 30 degrees downstream from normal to the tunnel sidewall at a distance of 32.8 cm from the center of the capsule face. The configuration is given in Figure 9-1. Data were collected in ThermaCAM Researcher and opened in ExaminIR, where .tif files containing temperature values at each pixel were generated for every frame.

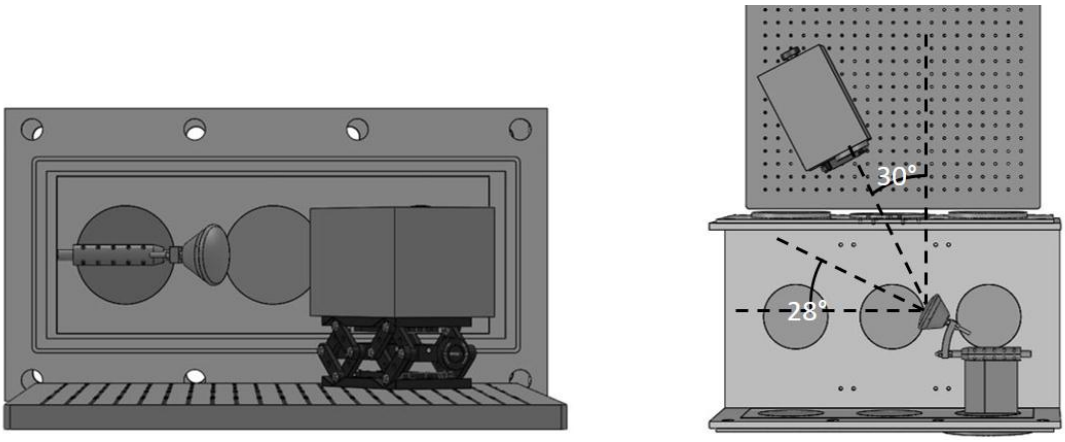

Figure 9-1: Experimental Setup Side (Left) And Top (Right) Views

Table 9-1: Capsule Thermal Properties Based On Roughness Height

Grit	Roughness Height	ρcb ($\frac{\mathrm{J}}{\mathrm{m^2/K}}$)	κd ($\frac{\mathrm{W}}{\mathrm{K}}$)
G36	665	3870	1.07E-3
G46	487	3750	1.08E-3
G60	370	3560	1.12E-3
G80	271	3530	1.13E-3
G120	150	3460	1.18E-3
smooth	3.6	3150	4.67E-3

9.2.2 Method

Tunnel runs were conducted at four unit Reynolds numbers: $3.4 \cdot 10^6$ /m, $4.5 \cdot 10^6$ /m, $5.5 \cdot 10^6$ /m, and $6.6 \cdot 10^6$/m, with the six surface roughness heights listed in Table 9-1, making for a test matrix of 24 different conditions. Average tunnel conditions for all of the runs are listed in Table 9-2. The mean temperature varied by less than $\pm$ 5K and the Reynolds number by less than $\pm 3\%$ over the 15 second time range considered for each run. The

Table 9-2: Mean Tunnel Conditions

Re/l (1/m)	Re_d	M_∞	T_0 (K)
3.4E6	2.6E5	6.03	432
4.5E6	3.4E5	5.95	435
5.5E6	4.1E5	5.92	436
6.6E6	4.9E5	5.92	438

temperature maps generated by the IR camera were transformed using a ray tracing code to view the capsule head-on. Centerline profiles were established using the new coordinate system, with y being the coordinate along the centerline, and y/R defined as -1 at the centerline point on the most upstream side of the face, and y/R defined as 1 on the most downstream centerline point on the face. From the temporally uninterrupted surface temperature data, the convective heat flux is given by Equation 9-2.

$$\dot{Q} = \rho c b \frac{\partial T}{\partial t} - \kappa b \nabla^2 T \tag{9-2}$$

where ρ is material density, c is specific heat, b is the effective capsule wall thickness, T is surface temperature, t is time, κ is thermal conductivity. The temporal temperature derivative term was approximated for each pixel through a linear fit for frames between 12-27 seconds. These values were multiplied by the constants specific to roughness, listed in the second column of Table 9-2, to get the first term of the convective heat flux. Since the capsule has a thin wall that is backed by air, the assumptions were that wall normal temperature gradient through the material is zero and no heat is lost to the inside of the shell. The lateral conductive term in Eq. (2), was found to account for less than 5% of the convective heat flux, so it was removed from consideration for simplicity. The convective heat flux allowed for the calculation of the Stanton number by Equation 9-3.

$$St = \frac{\dot{Q}_{conv}}{\rho_\infty u_\infty c_p \left(T_0 - T_w\right)} \tag{9-3}$$

where ρ_∞ is the freestream density, u_∞ is the freestream velocity, c_p is the specific heat measured at constant pressure, and T_0 and T_w are the total freestream and wall temperatures, respectively. Normalization of the Stanton number by a value from the upstream side of the face allowed for the identification of the approximate transition location on the runs where transition was present. This normalizing quantity was typically the maximum centerline Stanton number value on the upstream side.

9.2.3 Results

The normalized Stanton number centerline plots presented in Figure 9-2 align the similarly shaped curves and highlight the points in which some curves diverge from the group. In this figure, it is clear that there is much

overlap in the data points of different roughness sizes at the lowest Reynolds numbers, $Re_d \approx 2.6 \cdot 10^5$ and $Re_d \approx 3.4 \cdot 10^5$. However, at the highest Reynolds numbers, $Re_d \approx 4.1 \cdot 10^5$ and $Re_d \approx 4.9 \cdot 10^5$, larger roughness data points diverge from the smaller roughness points at some downstream value on the capsule face. The beginning of this data point divergence signifies a difference in the rate of heat transfer, which is believed to be the onset of transition from laminar to turbulent flow. Commonality in the centerline profile divergence location as well as elevated heating on the downstream side of the capsule face for the largest two roughness sizes (G36 and G46) at $Re_d \approx 4.9 \cdot 10^5$ and the largest roughness size at $Re_d \approx 4.1 \cdot 10^5$ suggests that the boundary layer transitioned on the upstream side of the capsule face. The onset of transition for these test cases is estimated to occur at a centerline position of y/R between -0.45 and -0.30. Other profiles show potential for transition farther downstream. These three cases include the largest roughness size at $Re_d \approx 3.4 \cdot 10^5$ as well as G60 and G46 at $Re_d \approx 4.9 \cdot 10^5$ and $Re_d \approx 4.1 \cdot 10^5$, respectively. Table 9-3 summarizes the conditions for all runs that showed elevated downstream heating.

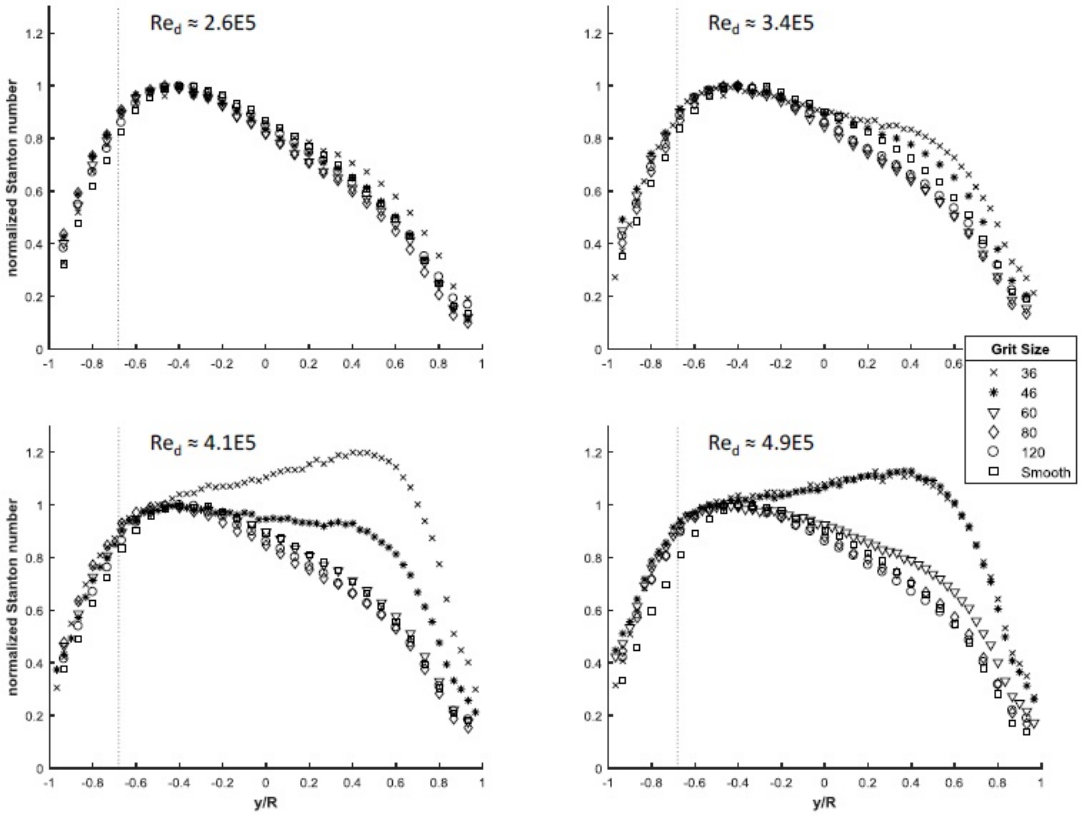

Figure 9-2: Normalized Stanton Number Plots Along the Centerline for the Entire Test Matrix

Figure 9-3 gives Stanton number maps for these six runs and a comparison laminar run. The Stanton number range differs across the maps to highlight the salient features. The three maps on the left represent the runs where transition first occurs most upstream on the capsule face and elevated heating persists downstream from

Table 9-3: Flow Conditions for Runs with Elevated Downstream Heating

Run	Grit	Re_d	k/Θ	k/δ	y/R	$T_w(K)$	$T_e(K)$ [a]	$U_e(m/s)$ [a]	$\rho_e(kg/m^3)$ [a]	Re_θ
2790	36	4.9E5	17.0	1.51	−0.42	394	413	126	0.121	25.4
2788	36	4.1E5	16.6	1.46	−0.36	393	413	141	0.0995	23.6
2789	36	3.3E5	14.0	1.15	0.17	386	400	244	0.0669	34.3
2786	46	5.0E5	12.3	1.08	−0.38	394	413	135	0.120	27.5
2783	46	4.1E5	11.6	0.99	−0.22	392	410	175	0.0930	29.9
2775	60	4.9E5	8.3	0.69	−0.03	390	404	222	0.101	44.5

[a] Boundary layer edge values were estimated from the computational simulations reported in Leidy et al. [14]

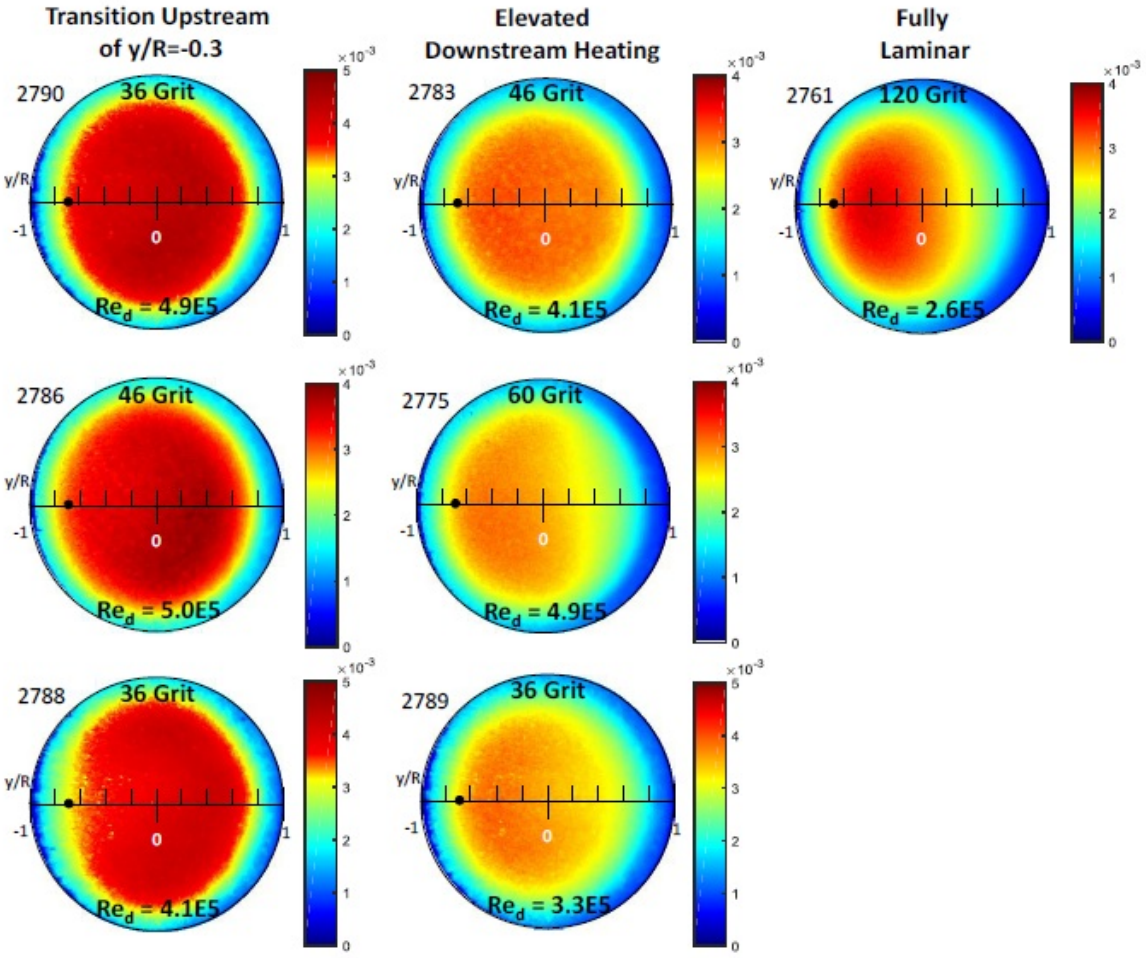

Figure 9-3: Stanton Number Maps for First To Transition (Left), other Elevated Downstream Heating (Center), and Fully Laminar (Right) Cases

the point of transition. The Stanton number peaks on the downstream side for all three of these runs. The three maps in the center represent the runs where heating is elevated above the laminar baseline, but transition occurs farther downstream than for the runs shown on the left. The downstream Stanton number for these three runs never exceeds the upstream maximum. The right map corresponds to a run that resulted in only laminar flow. More information on the experimental specifics and detailed results can be found in Leidy et al. [14].

9.3 TRANSITION EXPERIMENTS IN HLB WIND TUNNEL

9.3.1 Experimental Setup

Transition experiments were performed in the hypersonic Ludwieg tube at Technische Universität Braunschweig (HLB). This blow down tunnel was initially calibrated by Estorf et al. [17] and has been used for various experiments of freestream disturbances [18],[19]. The tunnel comprises the partly heated storage tube, the Ma = 6 Laval-nozzle, the test section of 500 mm in diameter and finally, the dump tank. Before a run, the fast acting valve upstream of the nozzle seals the high-pressure and low pressure parts from each other. Upon valve opening, the high-pressure air expands along the nozzle for about 80 ms, which is the testing time of the tunnel. The unit Reynolds number (Re/l) can be varied between 3-30 $\cdot 10^6$/ m. Figure 9-4 displays disturbance level in the test section measured with a stagnation probe, showing the effects of unit-Reynolds number probe position. The data reveal that normalized pitot pressure fluctuation at tunnel axis are the highest for all unit Reynolds numbers. It is believed that the wake of the tunnel valve, mounted centrally in the tunnel settling chamber, contributes to the locally increased disturbance level.

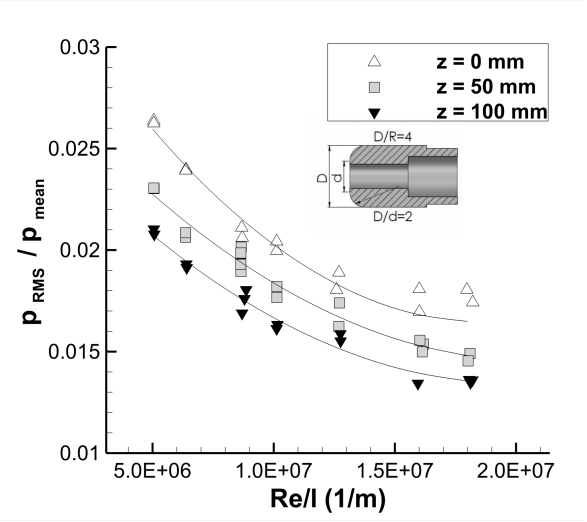

Figure 9-4: Normalized Pitot Pressure Fluctuation for Three Z-Positions and Variation of Unit Reynolds Number

For all conducted measurements the Apollo capsule model was installed at an angle of attack of 24 deg. The 170 mm diameter capsule model comprises of a central disc and a movable outer ring. This allows for rotating

installed sensors around the model axis, and hence for providing variable space-correlations between sensors. For the present transition experiment, the model was equipped with flush-mounted coaxial thermocouple (TE) sensors in positions that are sketched in Figure 9-5 (a and b). These sketches show two measurement configurations. In subfigure 9-5 (a), thermocouples are located downstream of a quadratic patch of deterministically arranged and orientated roughness elements (RN). The roughness patch was located at the capsule center. It has a size of 20 $\times$ 20 mm. Another line of TE elements is placed diagonally to the roughness patch, with the same sensor spacing. Note that the sensor P4 was not available in the diagonal configuration. Furthermore, P1, P3 & P4 are designed for housing miniature hot-wire inserts, which can be manually adjusted for different wall-normal heights above the capsule surface. Note that the wire supports were glued to the instrumentation holes in order to avoid wire oscillations caused by tunnel startup loads. Subfigure 9-5 (b) displays the setup of stochastically distributed roughness elements as a band over the entire capsule front with 7 thermocouples employed. Subfigure 9-5 (c) depicts the locations of the model with respect to the tunnel axis. In the model reference position, the vertical distance between center point of capsule and tunnel axis is 37 mm. In the tunnel axis position, tunnel and model axes coincide.

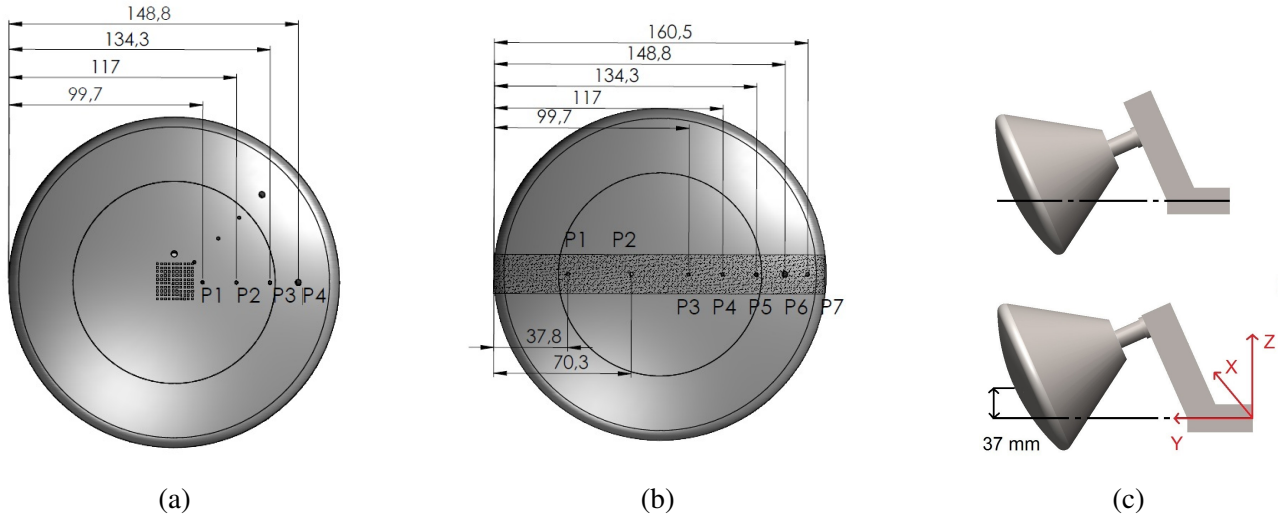

Figure 9-5: Capsule Model Front with Sensor Positions for Deterministic Roughness (a), Stochastically Distributed Roughness (b), and Model Locations with Respect to the Tunnel Axis at Reference and Tunnel Axis(c).

The subcritical, deterministic roughness patch was manufactured by the Fraunhofer Institute for Surface Engineering and Thin Films, located in Braunschweig, Germany. The institute is capable of producing 3D micrometer-scale surface structures very precisely by applying the technique of photolithography. In the first step, a photoresist is flooded homogeneously over the surface. The resist is tempered at 110 °C for hardening. The resist is then exposed to UV-light while a flexible exposure mask is fixed above the resist. The exposure mask defines the surface roughness arrangement as it provides selective reaction with a developer additive. Eventually, at the positions where the mask shutters the light, one obtains the intended 3-D micrometer structures. The final dimensions of the produced cuboidal elements shown in Figure 9-6 (a) displays an edge length of 100 μm and the element height is 23 μm. The equidistant spacing between the elements is also 100 μm. Figure 9-6 (a) at the top, displays a photo of the manufactured roughness patch recorded via laser microscope.

Moreover, the line plot in Figure 9-6 (a) displays a geometry measurement of a single disturbance element. It turns out that quite good agreement between the manufactured element and the design data is achieved.

For investigating roughness induced transition with larger roughness heights, two roughness patches with stochastically arranged elements were prepared. One of them employed spherical particles with a nominal diameter of 100 μm made of polyamide (Vestosint©). The other used angular-shaped metallic particles with a nominal size of 177 μm. The roughness patches were applied as follows: After putting small covers over the thermocouple sensors, black paint was sprayed on the surface to generate an adhesive layer of almost constant thickness. Next, particles were applied on the adhesive layer from above, by using a trickle device. After paint drying and removal of non-bonded particles, another layer of paint was applied to enclose the particles. Finally, the thermocouple covers were removed and local steps caused by the paint around the sensor recesses as well as along the lateral boundaries of the roughness patch were carefully removed by applying local sanding.

The characteristic heights for both stochastically distributed roughness patches were determined similarly as described in Section 9.2.1 and detailed in Leidy et al. [14]. Peak-to-valley heights were derived from surface roughness scans with a laser-microscope system Keyence VK-X100K that allows obtaining window samples with specific dimensions. The surface scans were acquired at three different positions with a size of 1.4 $\times$ 1.4 mm for the roughness patch with small particles and at two positions with a size of 3.8 $\times$ 1.0 mm for the patch with larger particles. Five roughness profiles were extracted in streamline direction from each scan, each covering approximately 5 peaks/valleys for the small-particle samples and 8 peaks/valleys for the samples with large particles. Figure 9-6 (b) presents samples of these profiles. The profiles were manually positioned such that large peak-to-valley values of the scan were precisely captured. The 30% exceedance criteria [11] was applied on the measured peak-to-valley heights for the data of each scan to obtain numerical k-values. Finally, the k-values for different surface scans were averaged. As a result, the roughness patch with small particles is characterized by a k-value of 99 μm, whereas the larger particles lead to a k-value of 253 μm. These k-values served for extracting roughness Reynolds numbers, Re_{kk}, along the roughness patch from Navier-Stokes-solver computation data by DLR-Göttingen [20]. Typically, Re_{kk} increases with unit Reynolds number and streamwise position on the capsule front. Figure 9-6 (c) shows that the deterministic roughness elements are always subcritical. Figure 9-6 (d) displays Re_{kk}-values of the two stochastic roughness patches at a moderate high unit Reynolds number. Obviously, by varying Reynolds number and particle size a large variation of Re_{kk}-values is possible. Note, that critical values for transition tripping by single roughness elements are in the range $Re_{kk} \approx$ 400 - 700 [21].

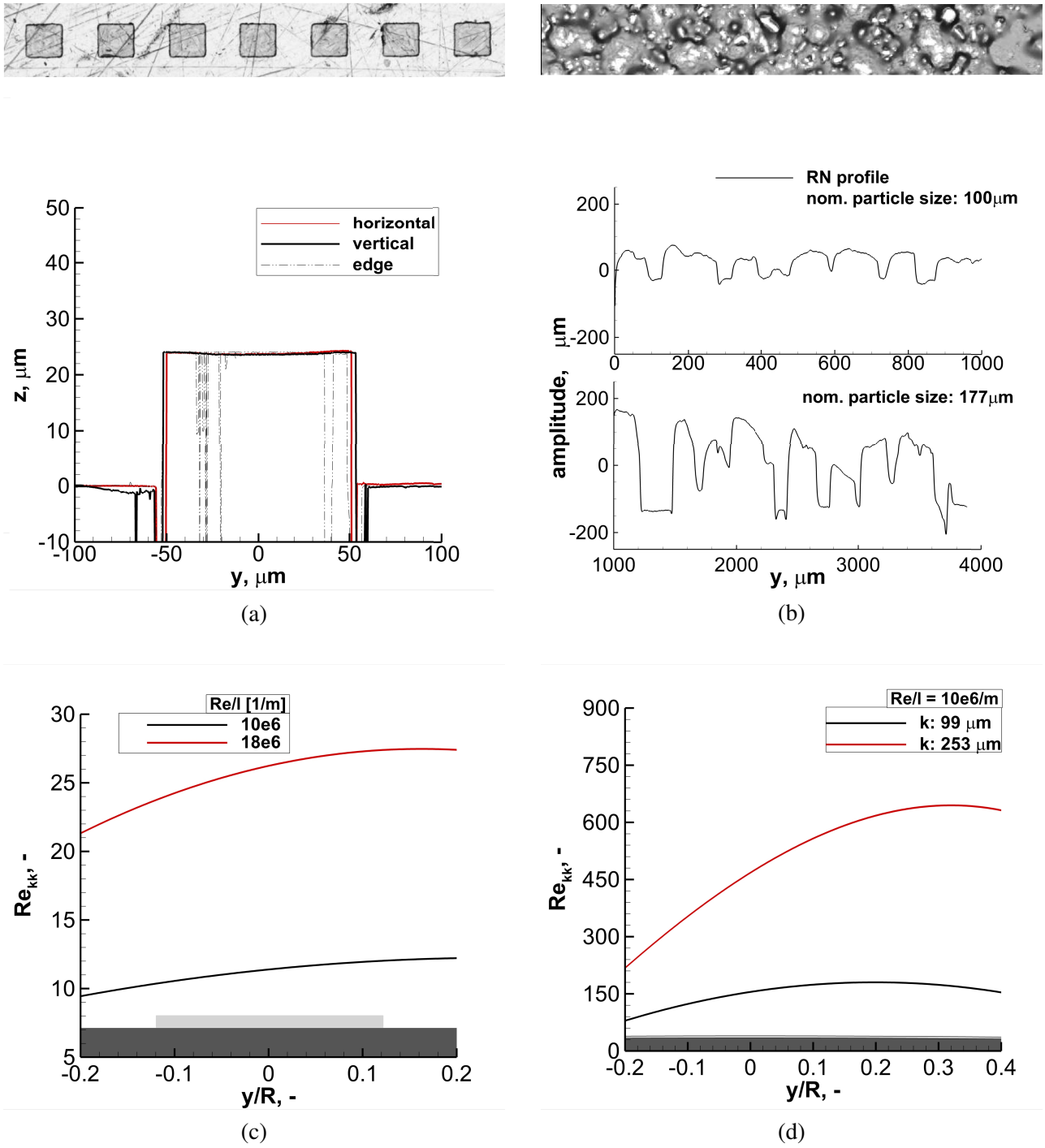

Figure 9-6: Photo of Deterministic Roughness Elements Taken by Laser Microscope and Measured Size of One Single Roughness Element (a), Photo of Stochastic Roughness Elements and Measured Roughness Profiles (b), Re_{kk} Distribution for Low and High Re/l Case in Plane of Symmetry of Deterministic Roughness Patch (c), Re_{kk} Distribution for Two k-values of Stochastic Roughness Calculated in Plane Of Symmetry (d).

9.3.2 Methods

Transition experiments were conducted for both capsule locations in the test section, thereby varying the disturbance level of the tunnel freestream relative to the capsule stagnation region. The role of the subcritical, deterministic roughness patch was to represent the surface quality used in previous experiments with non-sanded paint for infrared imaging which had a mean average roughness (R_a) of 10 μm. Transition experiments with the larger, stochastical roughness served to introduce roughness induced transition on the capsule front.

Transition data were obtained with TE (Type E: chromel-constantan) sensors used to acquire the time signal of the mean surface temperature. A commonly known relation for heat conduction into a semi-infinite slab allows the calculation of the occurring mean heat flux density from the temperature time trace [22]. After completion of TE measurements, hot-wire data were acquired for the cases of the smooth capsule surface and the deterministic roughness, to obtain a more detailed characterization of disturbances within the boundary and in the shock layer close to the boundary layer edge. The high dynamic response of the hot wire system gives access to the fluctuation behavior of disturbances. The hot wire was operated with high overheat ratios, τ, of 0.9 which makes the wire predominately sensitive to massflow, (ρu). While hot wire raw data for high-speed flows may be decomposed into (T_o) - and (ρu) - fluctuations [23], this is not valid for the subsonic capsule flow present in the shock layer. We note that only at P4 the flow reached edge Mach numbers larger than one, according to the corresponding flow simulations [20]. Nonetheless, hot wire data contain information on impact of freestream disturbances, effect of subcritical roughness present and finally, on the difference between fluctuations inside the boundary layer and outside the boundary layer edge.

The measurement data were sampled with an M2i.4652 transient recorder (company Spectrum) with a sampling frequency of 3 MHz in 16 bit format. The measured voltage fluctuations via hot wire are displayed as power spectra density (PSD) obtained by the discrete Fourier transform of the signal. The PSD is based on selected 30 ms of the sampled data where the flow condition is steady and no sharp spikes in the time trace appear. To improve the quality of the spectra, it was divided into 2048 data points per segment with an overlap of 75%. These segments were multiplied by a normalized Blackman-Harris window to reduce leakage effects and finally averaged over the number of individual spectra. The frequency resolution is then Δf = 1.46 kHz.

9.3.3 Results

In this section the experimental results are presented in two steps. Firstly, the TE data for two tunnel positions are compared for the smooth capsule surface and for the configurations with applied roughness patches. In the second part, hot wire data are presented in form of normalized PSD obtained at position P4 for the configuration depicted in Figure 9-5 (a).

Figure 9-7 compares the non-dimensional heat flux along the capsule symmetry line for the smooth capsule and for subcritical roughness two with a Navier-Stokes computation at relatively high $Re/l = 18 \cdot 10^6$/m. Note, that the stagnation point is located at around y/R = -0.7. The infrared (IR) data represent an update of the results reported in Theiss et al. [20]. The mean roughness of the paint for IR measurement was about 3.5 μm. While the limited field of view of the IR camera did not allow for measuring surface temperatures for $y/R < 0.5$, IR data and simulation agree very well on the leeward part of the capsule surface. Also, TE data is displayed for the clean and aligned roughness configurations. For the clean configuration, the TE heat flux is very close to IR

data and simulation which indicates an excellent reliability of the experimental methods for heat flux. The blue square elements represent a run with subcritical roughness setup at tunnel axes where for position P4 transition onset becomes visible.

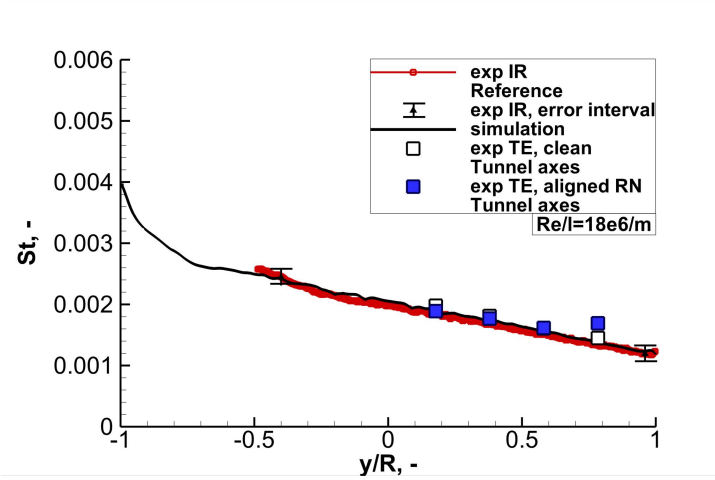

Figure 9-7: Stanton Number Distribution along Symmetry Line for Clean and Subcritical Roughness (RN) Setup. IR Measurement on Painted Surface of the Plastic Capsule Model.

The evaluation of transition measurements with TE sensors is shown in Figure 9-8 and Figure 9-9. The measurement points without roughness patch (clean) show no sign of transition onset, according to Figure 9-8 (a) and (b). Here, the rows of roughness elements as shown in Figure 9-6 (a) point in streamwise direction which is denoted as aligned roughness. Besides that, one can observe the impact of different capsule location corresponding to a spatial distribution of freestream noise level on the measured heat flux that results in higher heat flux values obtained at tunnel axis position compared to reference position. Also, no transition onset is observed for the subcritical roughness patch with the model at the reference position. However, the configuration with subcritical, aligned roughness at tunnel axis in Figure 9-8 (d) generates transition onset for unit Reynolds numbers of $16 \cdot 10^6$ /m and higher. As the sensor spacing is relatively coarse, transition onset is first observed at P4 for moderate Re/l. At increased Reynolds numbers, transition onset moves upstream as expected. The results show a clear effect of model position on heat flux rise due to transition. Hence, this transition phenomenon cannot not be characterized solely as roughness induced transition, since freestream disturbances contribute to the transition process as well. At this point we characterize the phenomenon as roughness augmented transition.

Transition results with the patches of stochastical roughness elements are shown in Figure 9-9 (a-c). Heat flux data obtained with the smaller roughness height, k = 99 μm, indicate first transition onset for a unit Reynolds number of $8.25 \cdot 10^6$ /m (not shown here). For lower Re/l runs heat flux augmentation far downstream at sensor position P6 and P7 was observed. Transition onset moves upstream with increasing Re/l, as seen in subfigure 9-9 (a). At Re/l of $12.5 \cdot 10^6$ /m, the high heat flux values obtained at the most downstream measurement positions indicate a fully turbulent boundary layer. Subfigure 9-9 (b) presents samples of heat flux results for the roughness patch with larger roughness height, k = 253 μm. Transition onset occurs on the capsule luv side, even at the lowest unit Reynolds number. Note that the highest Reynolds number, at which transition onset can be resolved for k = 253 μm with the present location of thermocouples, is about $10 \cdot 10^6$ /m. Subfigure 9-9 (c) displays the effect of capsule position in the wind tunnel and hence, the effect of freestream disturbances

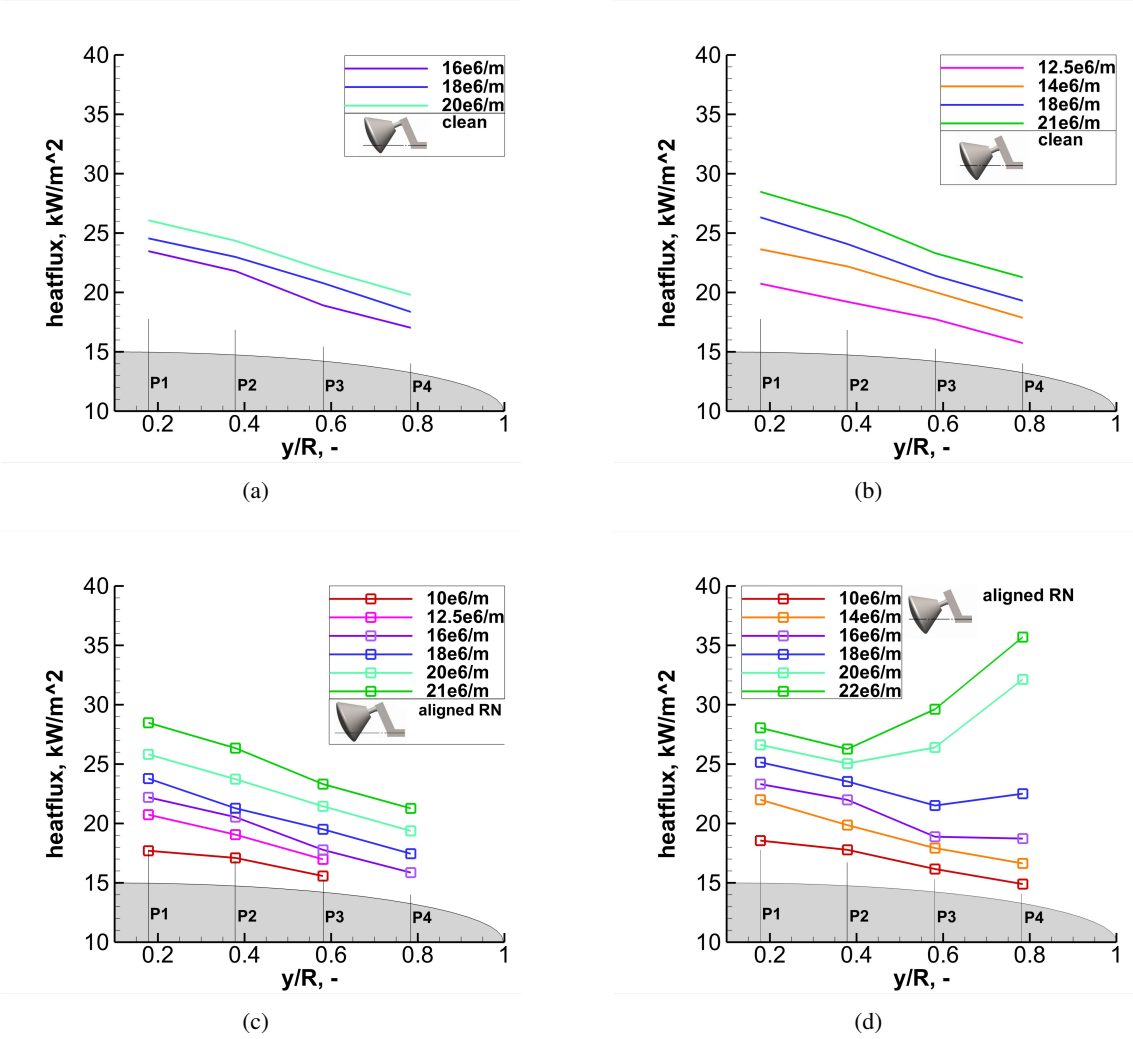

Figure 9-8: Heat Fluxes On Smooth Surface (a,b) and with Subcritical, Roughness, k=23 μm (c,d).

on boundary layer transition. This yields evidence that the observed transition onset is dominated by roughness since the capsule position appears to have little effect on the heat flux.

The extraction of a precise location of transition onset from the measured sets of discrete heat flux data appeared as a particular challenge. Closer inspection of the data points in subfigures 9-9 (a,b) reveal that information about the assumed region of transition onset is typically contained in the heat flux data of three sensors, one representing still laminar flow and two indicating the transitional rise of heat flux. The numerical extraction process is complicated by the fact that the thermocouple reading of laminar heat flux at the rough surface carries some additional scatter relative to the smooth surface, as the sensor is located in a small recess of the roughness layer. One way to reduce uncertainty due to the scatter of the laminar reading is to introduce additional data form numerical flow simulations. Therefore, a number of 12 additional data points along an arc length of 10 % of the capsule diameter, located just upstream of the assumed laminar sensor, were extracted from the numerical flow

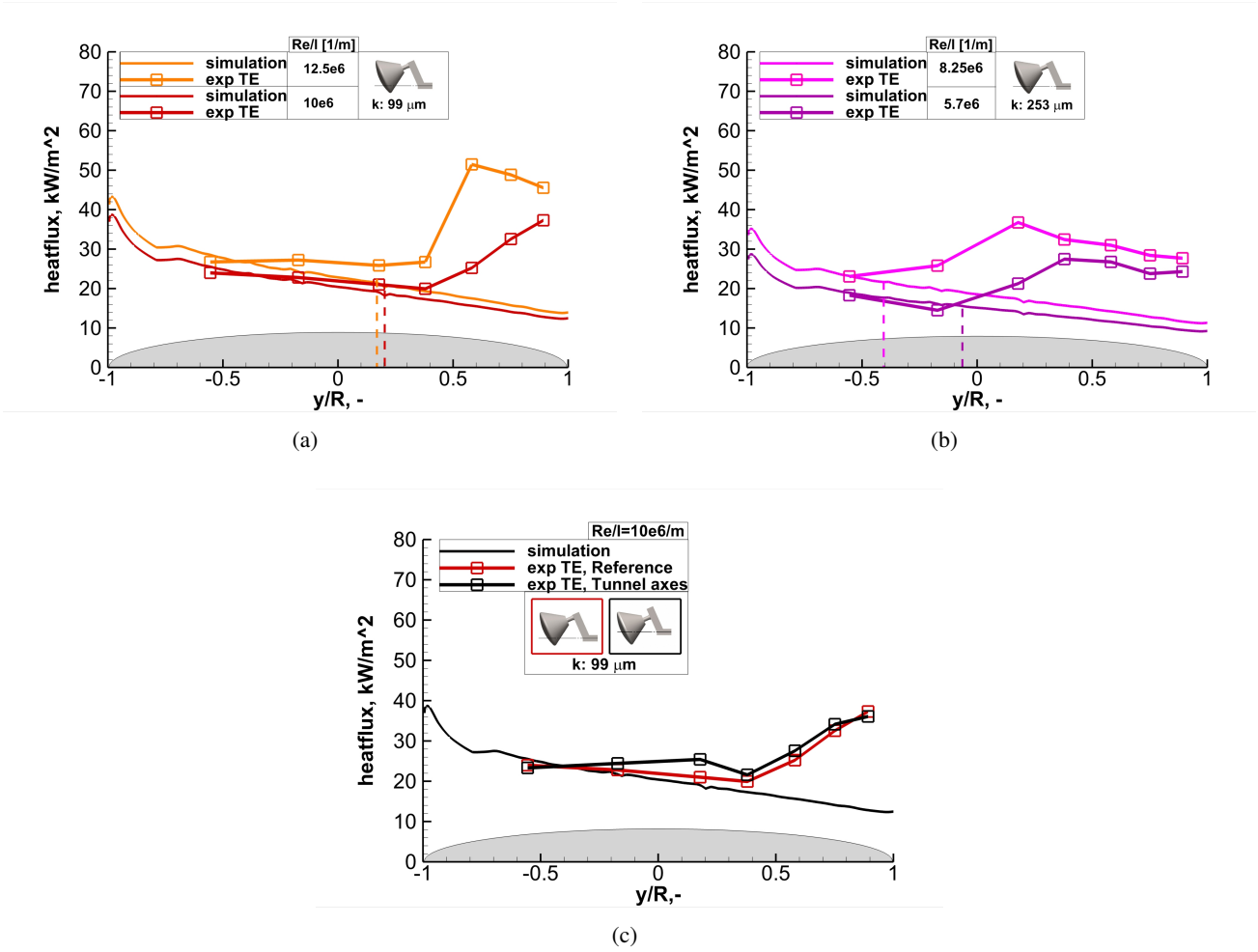

Figure 9-9: Heat Fluxes with Stochastic Roughness, k = 99 μm (a), k = 253 μm (b), and Tunnel Position Variation for k = 99 μm (c).

solution, to represent the laminar flow better. Then a polynomial best fit was applied on the new data set that now included the heat flux of 12 numerical simulation points and the three thermocouple results. To determine location of transition onset, a 5 % deviation criteria was applied to the difference between the simulation curve and the polynomial curve.

Hot wire measurements constituted the second part of the investigations. For this purpose the capsule was instrumented with a hot wire at the position P4 for the capsule configuration presented in Figure 9-6 (a). The hot wire signal is presented in form of normalized PSD spectra. The capsule model was positioned at tunnel axis, where the thermocouple measurements showed transition onset at the sensor location P4 for Re/l = 16·10^6 /m, with the subcritical roughness patch. Voltage fluctuations were normalized with the mean voltage of the hot wire system during the selected test interval. Figure 9-10 illustrates the obtained spectra for clean surface and with subcritical, deterministic roughness, measured within the boundary layer at 0.5 mm above the surface. Until 100 kHz both spectra appear very similar. The spectrum of the clean surface drops smoothly beyond that frequency

until it vanishes in electronical noise at about 200 kHz.In contrast for the roughness patch configuration, three broadband peaks of fluctuation appear in the frequency ranges of 100 – 140 kHz, 140 – 180 kHz and 220 – 250 kHz. The first two peaks exhibit a moderate Reynolds-number dependency as seen in Figure 9-12, whereas the high-frequency peak is insensitive to Re/l changes. At this point, no statement can be made, whether the first two peaks are physically connected, as they appear to overlap around 140 kHz. The shape of the fluctuation peaks indicates broadening with Reynolds number. We speculate that the high-frequency peaks represent roughness-induced fluctuations of vortical structures within the boundary layer. The vortical structures develop from vorticity modes of the freestream, subject to strong acceleration downstream the stagnation point. Further hot-wire data analysis should also characterize signal behaviours in transitional flows at higher Reynolds numbers, by extracting the possible growth of turbulent spots. Hot-wire data obtained in the shock layer 1.5

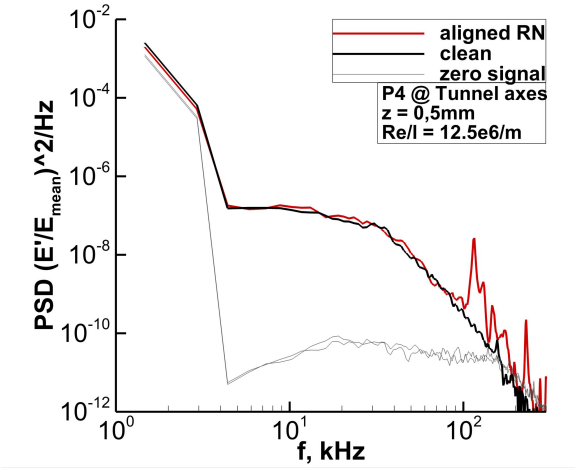

Figure 9-10: PSD of Hot Wire Signal, Comparing Clean Versus Subcritical Roughness Patch Configuration

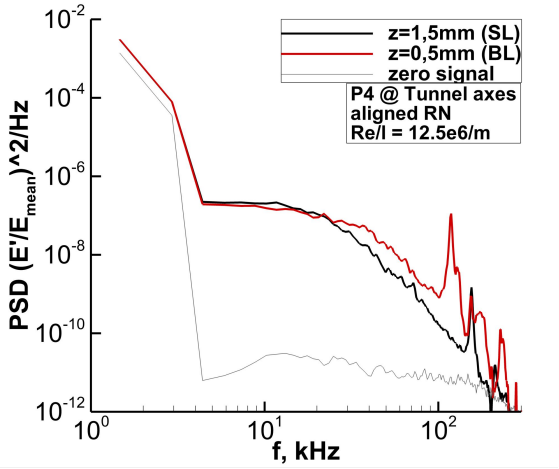

Figure 9-11: PSD of Hot Wire Signal, Comparing BL and SL Position

mm away from the wall are compared to boundary layer data as shown in Figure 9-11, for one exemplary run at $Re/l = 12.5 \cdot 10^6$ /m. The measured fluctuations starts to differ from 20 kHz on, where the boundary-layer spectra show higher fluctuations. Furthermore, one observes only two broad-band peaks in the shock layer, which are smaller than the peaks in the boundary layer. These peaks of the shock layer show little effect of the Reynolds number on peak frequency, while some spectral broadening also occurs, according to Figure 9-13. Future repeated measurements should be used to confirm these findings and provide high-frequency disturbances at further measurement points in the capsule flow field.

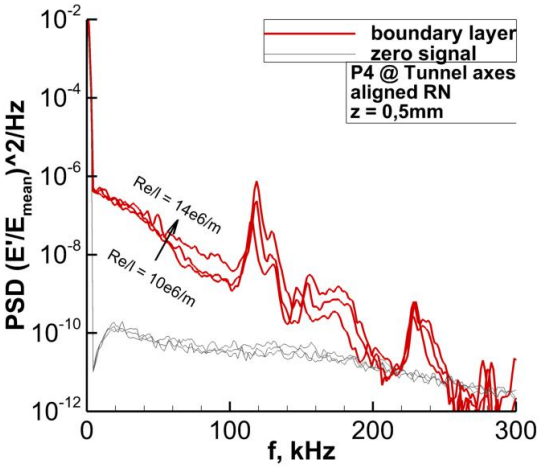

Figure 9-12: PSD of Hot Wire Signal Obtained in Boundary Layer, Variation Of Re/l

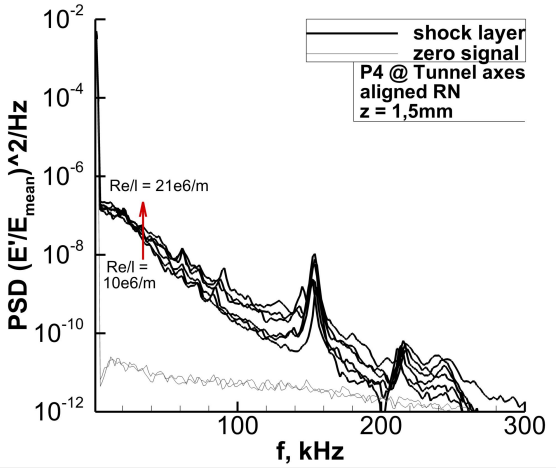

Figure 9-13: PSD of Hot Wire Signal Obtained in Shock Layer, Variation Of Re/l

9.4 TRANSITION EXPERIMENTS IN HIEST FACILITY

An aeroheating measurement test campaign on a capsule model with laminar and turbulent boundary layers was performed in the free-piston shock tunnel JAXA-HIEST [24]. A 250 mm-diameter 6.4 %-scale Apollo CM capsule model was used. To measure heat flux distribution, the model was equipped with miniature co-axial chromel-constantan thermocouples on its heat shield surface. In order to promote boundary layer transition, a boundary layer trip insert with 'pizza box' shaped isolated roughness elements of variable height was employed. Heat flux records with and without roughness elements were obtained for a 28 deg angle of attack under stagnation enthalpies from H_0 = 3.6 MJ/kg to 21 MJ/kg and stagnation pressures from P_0 = 27 MPa to 52 MPa. Under these conditions, the unit Reynolds number varied from 0.84 - 4.8·10^6 /m.

9.4.1 Experimental Setup

Figure 9-14 presents the layout and picture of the free-piston shock tunnel HIEST. This tunnel was originally built to obtain the aerothermodynamic characteristics of the Japanese reentry vehicle HOPE. The tunnel can produce higher stagnation conditions and longer test times than any other free-piston facility because it was originally designed to operate in a 'tuned' condition [25]. The tunnel can be operated at stagnation pressures P_0 up to 150 MPa and stagnation enthalpies H_0 up to 25 MJ/kg with test times of 2 ms or longer. In the present test campaign, the HIEST contoured nozzle was used, which is 2.8 m long and has an exit diameter of 800 mm. Nozzle flow calibration was discussed in a previous report [26]. From H_0 = 3.5 MJ/kg to 20 MJ/kg, the nozzle calibration tests showed that a steady test core flow diameter prevails up to 400 mm, in which the deviation of the free-stream Pitot pressure is less than 6%. Since the test duration depends on the stagnation condition, the test duration is 7 ms or longer in low-enthalpy conditions (H_0 = 3.5 MJ/kg or lower). The relation between the free-stream Re number and the stagnation enthalpy with the HIEST contoured nozzle is shown in Figure 9-15.

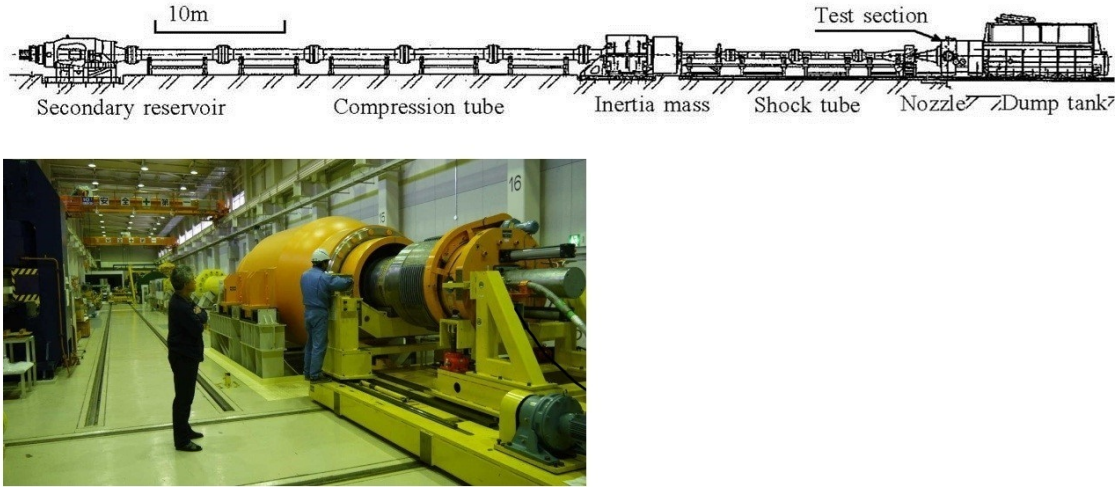

Figure 9-14: Free-Piston Shock Tunnel HIEST

Table 9-4: Free-Stream Condition

Condition	P_0	H_0	T_0	T_∞	P_∞	ρ_∞	U_∞	Ma_∞	Re/l
–	(MPa)	(MJ/kg)	(K)	(K)	(kPa)	(kg/m^3)	(m/s)	–	–
A	3.1E1	3.6	3.0E3	2.7E2	2.5	3.2E-2	2.5	7.7	4.8E6
B	2.7E1	5.1	3.9E3	4.4E2	2.6	2.1E-2	3.0	7.2	2.6E6
C	5.2E1	6.3	4.5E3	5.8E2	5.8	3.4E-2	3.3	6.9	3.8E6
D	5.2E1	9.0	5.7E3	9.6E2	7.1	2.5E-2	3.9	6.4	2.4E6
E	4.3E1	1.3E1	7.1E3	1.4E3	6.5	1.6E-2	4.6	6.1	1.4E6
F	8.3E1	1.3E1	7.3E3	1.4E3	12.6	2.9E-2	4.6	5.9	2.4E6
G	4.2E1	2.1E1	9.0E3	2.0E3	6.7	1.0E-2	5.6	6.0	8.4E5

Table 9-5: Flow Condition at the Trip Insert T_w = 300 K (const.)

Condition	T_e	H_w	H_e	Ma_e	δ		Re_θ	Re_{kk}	Re_{kk}	Re_{kk}
–	(K)	(J/Kg)	(J/Kg)	–	(m)	(m)	–	0.3mm	0.6mm	0.8mm
A	3.0E3	4.9E5	4.1E6	5.2E-1	6.4E-4	1.1E-4	1.2E2	3.4E2	6.1E2	8.1E2
B	3.3E3	5.6E5	5.1E6	5.3E-1	8.7E-4	1.3E-4	1.1E2	3.0E2	5.3E2	6.9E2
C	3.7E3	5.3E5	6.2E6	5.3E-1	6.9E-4	9.7E-4	1.5E2	4.9E2	9.0E2	1.2E3
D	4.5E3	5.7E5	8.8E6	5.3E-1	7.6E-4	1.1E-4	1.8E2	4.2E2	7.3E2	9.5E2
E	5.7E3	6.7E5	1.3E7	5.3E-1	9.3E-4	1.5E-4	1.1E2	2.7E2	4.6E2	5.9E2
F	5.9E3	5.7E5	1.2E7	5.3E-1	6.8E-4	1.1E-4	1.5E2	4.7E2	8.3E2	1.1E3
G	6.8E3	7.9E5	2.1E7	5.3E-1	1.1E-3	1.7E-4	9.4E1	1.9E2	3.5E2	4.6E2

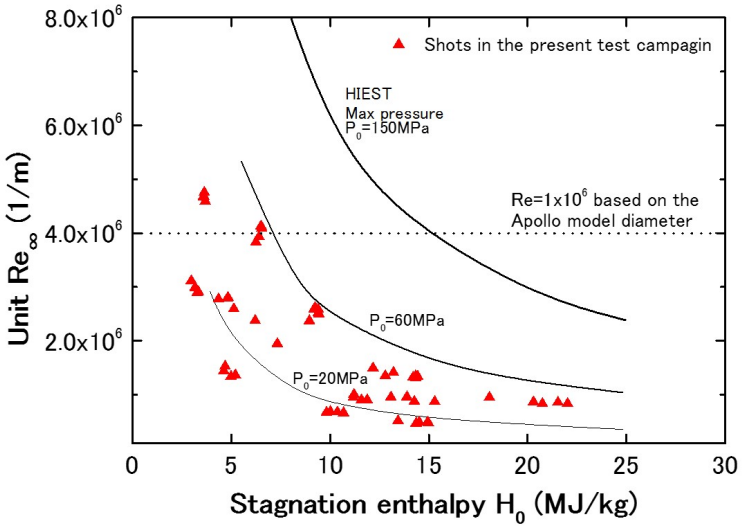

Figure 9-15: Unit Reynolds Number and Stagnation Enthalpy in the Present Test Campaign.

9.4.2 Methods

The diameter of the Apollo CM test model used in the test campaign was 250 mm, which is almost 6.4 % of the actual flight vehicle (Figure 9-16). On the windward surface of the model, 88 co-axial miniature thermocouples were mounted, and 12 co-axial miniature thermocouples and two Kulite Piezoresistive pressure transducers were mounted on the leeward surface (not shown in the figure). The thermocouples, originally developed at CalTech [27], [28], were chromel-constantan with a diameter of 2.0 mm (Figure 9-19). The left-hand picture in Figure 9-17 shows the heat shield surface of the Apollo CM test model. Coaxial thermocouples are displayed as dots on the surface. The other picture in Figure 9-17 presents the model installation in the HIEST test section with 28 deg angle of attack. To monitor the test free-stream, there are two permanent probes (Pitot pressure probe and heat flux probe) in the HIEST test section. Both of the two permanent probes are located 250 mm from the nozzle center.

For the present test campaign, natural boundary layer transition was not expected, except for the lowest enthalpy condition. The isolated roughness element was therefore required to promote boundary layer transition on the lee side of the heat shield (Figure 9-18). The roughness elements used were 'pizza box' shaped isolated roughness elements, which were used in several wind tunnel tests for CEV Orion development [29], [30]. The boundary layer thickness on the model heat shield surface was calculated for the test flow conditions by numerical simulations performed at NASA JSC [31]. The roughness height was determined to k = 0.2, 0.3, 0.6, 0.8, 1.1 and 1.3 mm according to the calculations. In the present test campaign, roughness heights of k = 0.3, 0.6 and 1.1 mm were used. All the roughness elements were machined on a trip insert made from copper alloy to prevent damage from aeroheating, and inserts were located 17 mm (y/D = 0.068) below the model's geometric centerline on its heat shield surface, a location that was also determined using data from a previous study.

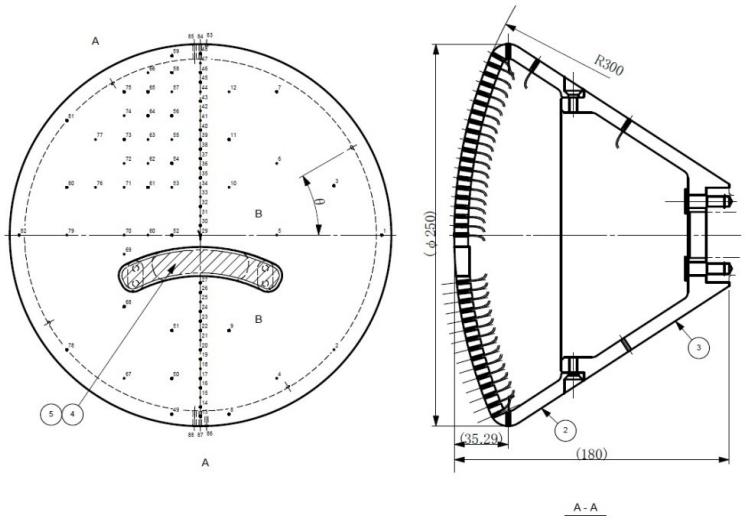

Figure 9-16: Drawing of the Apollo CM-AS202 Test Model, denoting Thermocouples Locations as Dots (Left).

9.4.3 Results

In HIEST, stagnation conditions in the nozzle reservoir (shock tube end) were calculated with an equilibrium computation code [32] from the shock speed and the shock tube initial conditions. For the stagnation condition, the free-stream condition was calculated with an axis-symmetrical JAXA in-house nozzle flow code [33]. Table 9-4 and Table 9-5 show all the free-stream conditions and flow condition at the trip insert, respectively.

Since heat flux measurements varied remarkably with H_0 and P_0 due to an unexpected heat flux augmentation [34], they cannot be directly compared with the results obtained under different flow conditions. Therefore, smooth surfaces (i.e. the trip insert without roughness elements) were also tested under each test condition to obtain reference heat flux distributions. As already shown in Figure 9-15, even when limited to low-enthalpy conditions, HIEST can produce Reynolds numbers sufficiently high to reach the onset of natural transition without any roughness elements. Figure 9-20 (a) shows a comparison between natural (smooth surface) and forced transition (roughness of k = 0.6 mm) measured at the lowest enthalpy under medium-pressure conditions (H_0 = 3.6 MJ/kg, P_0 = 31 MPa), at which the unit Reynolds number was $4.8{\cdot}10^6$ /m. Here, the variable y/D denotes the radial coordinate in the symmetry plane. It is interesting that the location where the heat flux increased without roughness (i.e. the natural transition point) is found at y/D = -0.16, which is upstream from the roughness element (y/D = -0.068). Yet in the heat flux distributions with roughness elements, a heat flux jump is observed at y/D = 0, which is the closest thermocouple location downstream from the roughness. Since the location of the heat flux increase point on a smooth surface often shows dispersion, even under identical flow conditions, the difference in location with and without roughness appears reasonable. Since the region downstream from y/D = 0.25 shows the same heat flux (not significantly different) both with and without roughness, it appears that the boundary layer changes to fully turbulent flow in both cases. It is therefore concluded that the roughness elements were effective under the present free-stream conditions and that a turbulent boundary layer was successfully established with k = 0.6 mm roughness elements.

Figure 9-17: Apollo Model with 'Pizza Box' Shaped Isolated Roughness Elements (k = 0.3 mm) and Model Installation in HIEST Test Section.

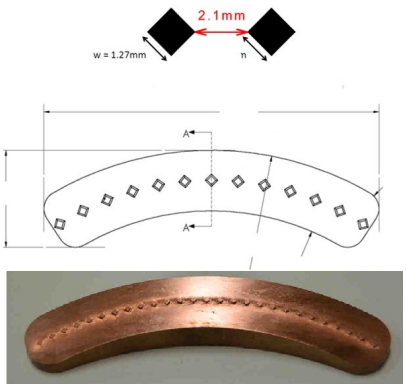

Figure 9-18: 'Pizza Box' Shaped Isolated Roughness Elements and a Trip Insert with 13 Roughness Elements (k = 0.8 mm).

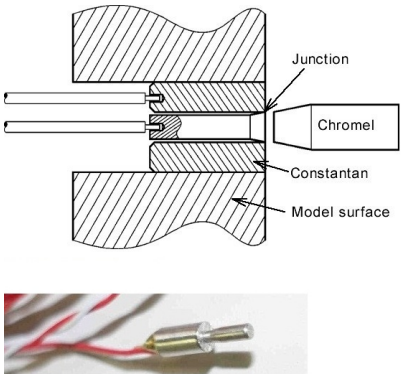

Figure 9-19: Cross Section Of The Coaxial Miniature Thermocouple With 2 mm Diameter And A Photo.

The effect of roughness height for flow condition B to F is now discussed, by comparing the measured heat flux distribution profiles. Figure 9-20 (b), (c) and (d) display the profiles of heat flux distribution up to H_0 = 9 MJ/kg, which show onset of turbulence flow in the presence of the roughness elements. In these figures, all the roughness elements are effective because the there is no significant difference in the heat flux downstream of different roughness elements (y/D = 0.2, or downstream). However, there is an undesirable heat flux overshoot in downstream regions near roughness elements. According to the comparison of heat flux distribution profiles, a roughness element with k = 0.3 mm is the best choice for tripping because it showed minimum overshoot. At the much higher H_0 with lower Reynolds number (Condition E: H_0 = 13 MJ/kg and Condition F: H_0 = 20 MJ/kg) shown in Figure 9-20 (e) and (g), a heat flux jump is found at the vicinity of roughness elements. However, the expected heat flux due to a turbulent boundary layer in the downstream region is not observed even with the highest roughness elements (k = 0.8 mm). At the maximum P_0 (Condition F) as shown in Figure 9-20 (f), the roughness elements are effective to induce the onset of transition, indicating that boundary layer tripping was achieved at H_0 = 12MJ/kg.

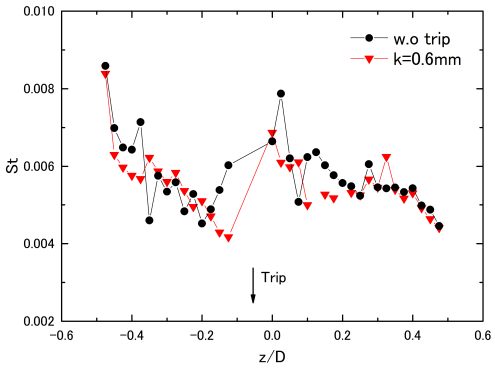
w.o trip
k=0.6mm
Trip
St
z/D

(a)

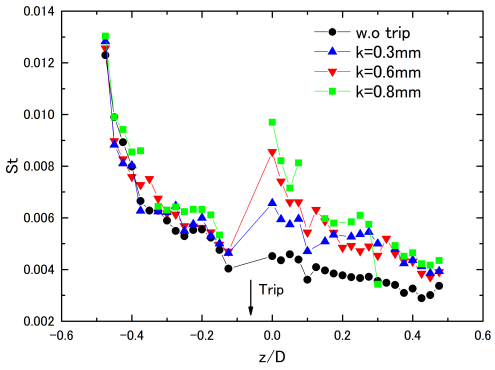
w.o trip
k=0.3mm
k=0.6mm
k=0.8mm
Trip
St
z/D

(b)

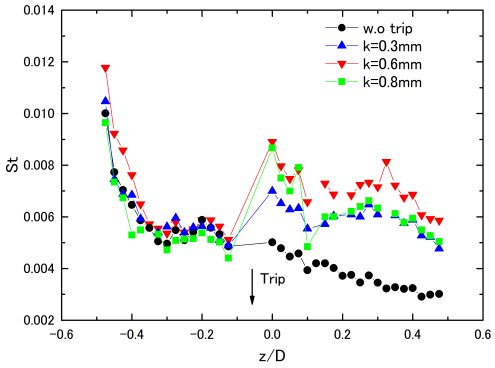
w.o trip
k=0.3mm
k=0.6mm
k=0.8mm
Trip
St
z/D

(c)

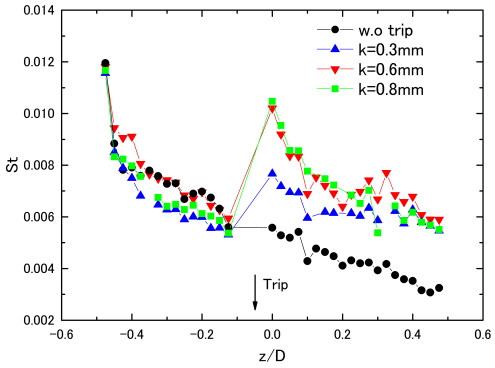
w.o trip
k=0.3mm
k=0.6mm
k=0.8mm
Trip
St
z/D

(d)

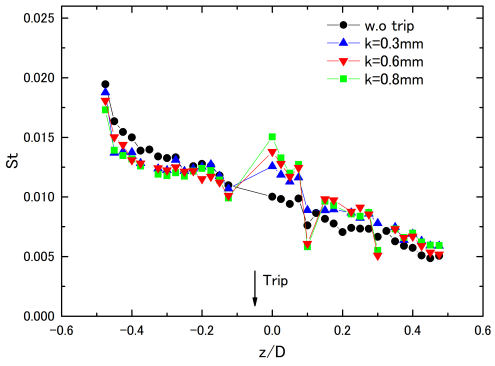
w.o trip
k=0.3mm
k=0.6mm
k=0.8mm
Trip
St
z/D

(e)

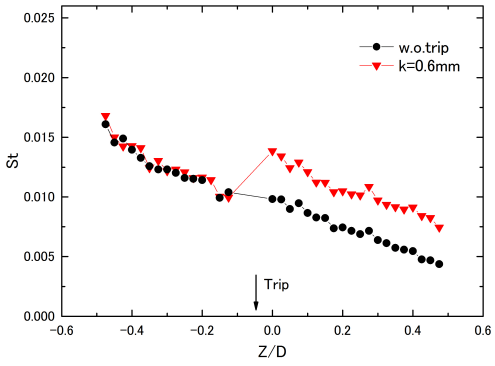
w.o.trip
k=0.6mm
Trip
St
Z/D

(f)

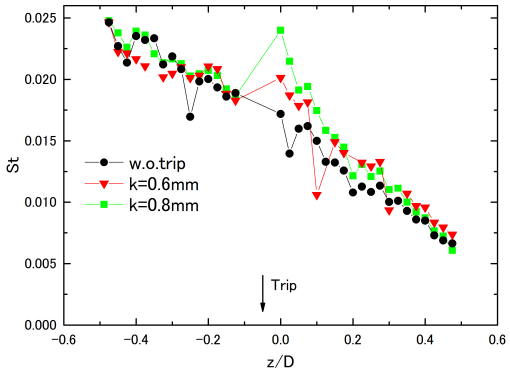

(g)

Figure 9-20: Heat Flux Distribution on Heat-Shield Surface with Isolated Roughness Elements.

9.5 ANALYSIS

The transient growth theory for stagnation point flow advanced by Reshotko and Tumin [9] has provided a successful correlation for the observed roughness-induced transition on spherical forebodies including the PANT experiments done in wind tunnels [10], [11] and the Reda experiment done in a ballistic range [35, 36] as Figure 9-21 shows. The transition on blunt entry shapes such as the Apollo and CEV configurations is also dominated by stagnation point flow. It has been shown that for these configurations at angle-of-attack, the flow is T-S stable and the crossflow is insignificant. Hence, a plausible mechanism for transition is roughness induced transient growth. The Reshotko-Tumin theory shows that the maximum transient growth occurs in the near vicinity of the stagnation point, at Mach numbers up to about 0.3. This is confirmed in the recent PSE studies of Parades et al. of NASA-Langley, and the even more recent studies of Theiss and Hein of DLR-Gottingen that are in agreement with the NASA-Langley studies [15]. All of the experiments done within the present work involve the Apollo/CEV windward geometry at angle-of-attack.

For the ACE Tunnel experiment (Chapter 9.2) and the HIEST experiment (Chapter 9.4) the angle-of-attack was 28 deg. For the HLB experiment (Chapter 9.3), the angle-of-attack was 24 deg. All reported measurements are evaluated along the center plane-of-symmetry of the models. Typical flow parameter of the experiments with distributed roughness are given in Table 9-6.

For the ACE experiment, the roughness was applied quasi-uniformly over the whole front surface of the model, consistent with what was done in the PANT and Reda experiments. Their results are reasonably well correlated by the Reshotko-Tumin theory. Their observed transition locations are between y/R of -0.45 and -0.30, upstream of the center point of the model. This was a somewhat difficult experiment because of the low Reynolds number range of the tunnel and also that the transient growth is weakest near adiabatic wall temperatures. Thus, the roughness heights needed to obtain the observed transitions on the model were of the order of 0.7 to 1.5 boundary-layer thickness.

Table 9-6: Flow Parameters of Transient-Growth Correlation in Selected Transition Experiments

Source	T_w/T_e	assumed value $180(T_e/2T_w)^{-1.27}$	transition onset Re_θ	transition onset $k/$
PANT	$0.45 - 0.55$	180	$20 - 96$	$1.7 - 30$
Reda	≈ 0.3	106	$32 - 189$	$0.57 - 3.4$
ACE, stochastic roughness	$0.95 - 0.96$	405	$23 - 45$	$8.3 - 17$
HLB, deterministic subcritical roughness	$0.69 - 0.74$	280	$220 - 240$	$0.45 - 4.6$
HLB, stochastic roughness	$0.63 - 0.71$	261	$40 - 148$	$1.87 - 4.7$

In the HLB experiments, two different types of roughness were applied. One roughness patch, 20 mm $\times$ 20 mm was placed about the geometric center of the 170 mm diameter model. The stagnation point for this model at 24 deg angle-of-attack is 59 mm upstream of the center of the model. At the beginning of the roughness patch, the local Mach number is 0.43 so that the roughness begins downstream of the region of maximum transient growth. The level of freestream disturbances could be varied during these experiments within a certain range by varying model position in the tunnel. Table 9-6 shows that relative roughness heights at transition and transition Reynolds numbers would cluster at the upper left corner of Figure 9-21, rather far away from the transient growth correlation. Based on the results, the authors assume that the observed transitions that occur about 20-25 mm downstream of the roughness patches are due to freestream disturbances in the tunnel, which interact with subcritical roughness. This set of experiments does not indicate roughness induced transition that can be assigned to transient growth correlation although transient growth may exist but is subordinated to modulated high freestream noise in the boundary layer that becomes enhanced at subcritical roughness patch location. The second set of roughness experiments in HLB was conducted with patches of larger roughness height. The roughness elements were stochastically distributed and covered a 30 mm wide band over the entire capsule front. Figure 9-21 confirms, that transition locations derived from these experiments, which employed two patches with different roughness height, correlate reasonably well with transient growth theory, while varying freestream disturbances by changing model position in the tunnel resulted in only a minor effect on transition.

The HIEST experiment had a different objective, namely to study the effectiveness of a trip located just upstream of the geometric center of the model. The trip is located at y/R = -0.034 where the local Mach number is about 0.53. This is well downstream of the region of maximum transient growth. Thus, the HIEST data cannot be classified with the Reshotko-Tumin correlation for transient growth. At the highest capsule Reynolds number of $1.2 \cdot 10^6$, transition is observed on the model even without a trip. For all lower capsule Reynolds numbers, without a trip, the flow remains laminar. For capsule Reynolds numbers between $0.6 \cdot 10^6$ and $1 \cdot 10^6$, with trips of height 0.3 mm to 0.8 mm, the boundary layer is tripped and turbulent heat transfer levels are sustained. So, in these cases, the trips can be considered as effective. For capsule Reynolds numbers of $0.4 \cdot 10^6$ and smaller, a heat flux jump was found just downstream of the trip but the heat fluxes returned to laminar levels. In these cases, the trip was not effective. As shown in Figure 9-22, for these cases where the trips were not effective, the Re_{kk} was as high as 590 for the 0.8 mm trip height, but the capsule Reynolds numbers were at the low end of all the tests. From Figure 9-22 it is seen that trip effectiveness depends primarily on capsule Reynolds number. However to be noted is that the stagnation enthalpies, H_e, all exceed 2 MJ/kg so that the air is no longer a perfect gas. As H_e increases, the surface temperature levels, T_w/T_e decrease while the roughness Reynolds numbers

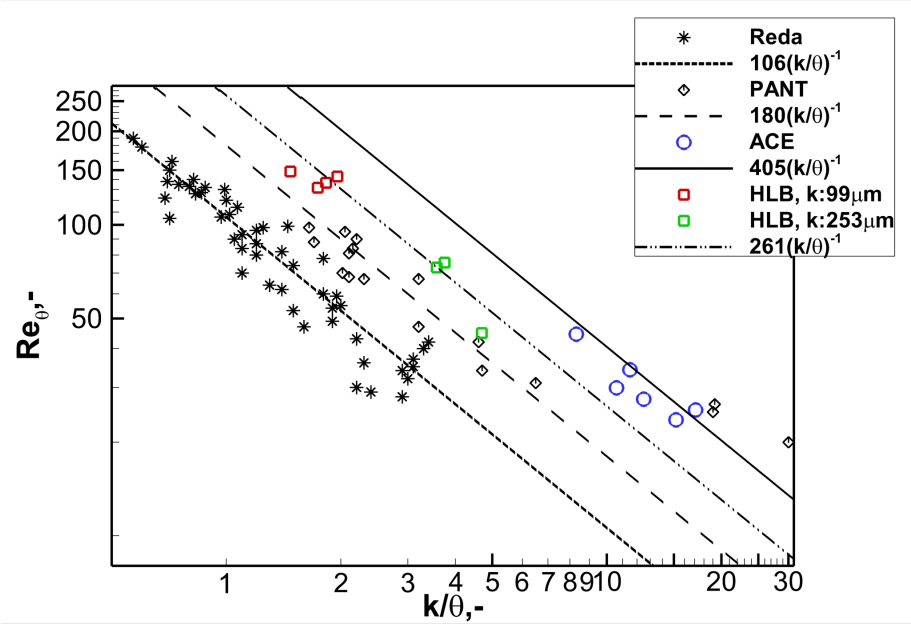

Figure 9-21: Transient Growth Based Transition Data Comparison

Re_{kk} increase slightly, these are effects of chemistry. So while trip effectiveness depends primarily on capsule Reynolds number, the effects of chemistry make tripping slightly more difficult.

9.6 CONCLUSION

The present contribution reviews recent experimental results of roughness effects on boundary layer transition on capsule geometries with spherical windward geometries. Experiments in three wind tunnel facilities are considered. The ACE Tunnel of Texas A&M University, USA, provided Mach 6 experiments with distributed roughness at relatively low Reynolds numbers, $2.5 \cdot 10^5 < Re_d < 5 \cdot 10^5$, with d denoting the capsule diameter. The observed boundary layer transition compared well with correlations based on transient growth theory, even though the roughness heights were in the order of boundary layer thickness. Larger Reynolds numbers, $1 \cdot 10^6 < Re_d < 3 \cdot 10^6$, could be assessed in the hypersonic Ludwieg tube, HLB, of TU Braunschweig, Germany. Transition is observed at rather low, subcritical roughness values in the order of 20 μm for a roughness patch placed about the geometric center of the capsule model. These experiments varied fluctuation levels of the freestream. The authors assume that the observed transitions that occur downstream of the subcritical roughness patch are due to freestream disturbances in the tunnel, which interact with small roughness heights. Additional experiments in the HLB facility with patches of larger roughness height support the relevance of transient growth theory for low-to-medium roughness heights, relative to boundary layer thickness. The effects of Reynolds numbers and total flow enthalpy on transition with isolated roughness were investigated in the HIEST facility of JAXA, Japan. Here, a model insert with roughness elements of varying height for tripping transition to turbulence was employed. The results are compared to known trip effectiveness correlations for isolated roughness.

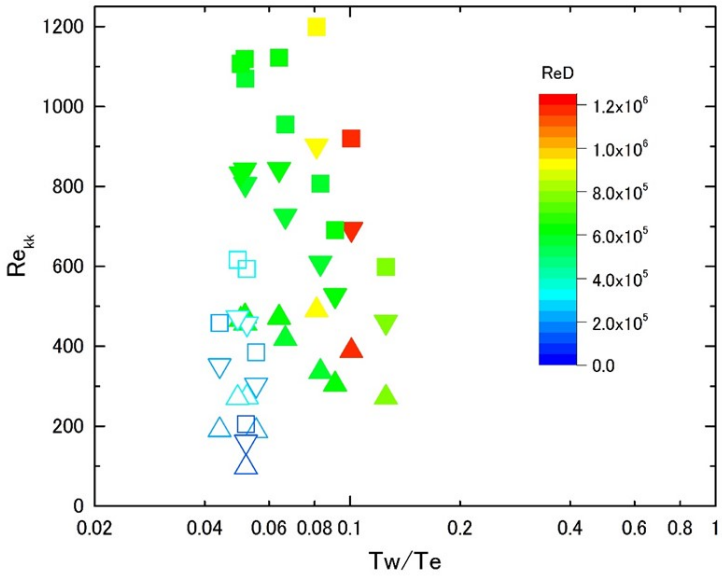

Figure 9-22: Trip Effectiveness for Various Stagnation Enthalpies and Capsule Reynolds Numbers. Filled Symbols Denote Effective Tripping.

Overall, the transient growth correlation seems to represent roughness-induced transition behavior on the ACE and HLB entry capsule shapes with roughness over the entire capsule surface. These experiment are however for perfect gases. Comparable experiments on roughness induced transition in a high-enthalpy facility are still needed to confirm the validity of transient-growth correlation for vehicle design.

9.7 ACKNOWLEDGMENTS

The authors of TU Braunschweig received funding by the German Research Association, DFG, within the HYP-TRANS PAK742 project and by EOARD, Award No. FA9550-16-1-0285.

9.8 REFERENCES

[1] Hollis, B., Berger, K., Horvath, T., Lillard, R., Coblish, J., Norris, J., and Kirk, B., "Aeroheating Testing and Predictions for Project Orion Crew Exploration Vehicle," *Spacecraft and Rockets*, Vol. 46 No.4, 2009.

[2] Marineau, E., Lewis, D., Lafferty, J., White, M., and Amar, A., "Investigation of Hypersonic Laminar Heating Augmentation in the Stagnation Region," *AIAA paper 2013-308*, 2013.

[3] Ali, S.R.C., Radespiel, R., and , A., "Transition Experiment with a Blunt Apollo Shape Like Capsule in Hypersonic Ludwieg Tube," *DLRK paper 2014-340270*, 2014.

[4] Amar, A., Horvath, T., Hollis, B., Berger, K., Berry, S., and Calvert, N., "Protuberance Boundary Layer Transition for Project Orion Crew Entry Vehicle," *AIAA paper 2008-1227*, 2008.

[5] Theiss, A., Hein, S., Ali, S.R.C., and Radespiel, R., "Wake Flow Instability Studies behind Discrete Roughness Elements on a Generic Re-Entry Capsule," *AIAA paper 2016-4382*, 2016.

[6] Tanno, H., Komuro, T., Sato, K., Itoh, K., Lillard, R., and Olejniczak, J., "Aeroheating Measurements of Apollo-Shaped Capsule with Boundary Layer Trip in the Free-Piston Shock Tunnel HIEST," *AIAA paper 2014-0434*, 2014.

[7] Kirk, L., Lillard, R., Olejniczak, J., and Tanno, H., "Boundary Layer Transition and Trip Effectiveness on an Apollo Capsule in the JAXA High Enthalpy Shock Tunnel (HIEST) Facility," *AIAA paper 2015-0209*, 2015.

[8] Reshotko, E. and Tumin, A., "The Blunt Body Paradox – A Case for Transient Growth," *Laminar-Turbulent Transition*, edited by H. Fasel and W. Saric, Springer, 2000, pp. 403–408.

[9] Reshotko, E. and Tumin, A., "Role of Transient Growth in Roughness-Induced Transition," *AIAA Journal*, Vol. 42 No.4, 2004.

[10] Batt, R.G. and Legner, H.L., "A Review and Evaluation of Ground Test Data on Roughness Induced Nosetip Transition," *Ballistic Missile Office/SYDT, Rept. BMD-TR-81-58, Norton AFB, CA*, 1980.

[11] Batt, R.G. and Legner, H.L., "A Review of Roughness-Induced Nosetip Transition," *AIAA Journal*, Vol. 21 No. 1, 1983.

[12] Hollis, B., "Distributed Roughness Effects on Blunt-Body Transition and Turbulent Heating Speeds," *AIAA paper 2014-0238*, 2014.

[13] Hollis, B., "Correlation of Recent and Historical Rough-Wall Transition Data on Hemispherical Nosetips," *AIAA paper 2017-3986*, 2017.

[14] Leidy, A.N., Reshotko, E., Siddiqui, F., and Bowersox, R.D.W., "Transition Due to Roughness on Blunt Capsule: Comparison with Transient Growth Correlation," *Journal of Spacecraft and Rockets*, Vol. 55, No. 2, 2017, pp. 167–180.

[15] Hein, S., Theiss, A., Di Giovanni, A., Stemmer, C., Schilden, T., Schröder, W., Paredes, P., Choudhari, M.M., Li, F., and Reshotko, E., "Numerical Investigation of Roughness Effects on Transition on Spherical Capsules," *Journal of Spacecraft and Rockets*, Vol. 56, No. 2, 2019, pp. 388–404.

[16] Duan, L., Choudari, M., Chou, A., Munoz, F., Ali, S., Radespiel, R., Schilden, T., Schröder, W., Marineau, E., Casper, K., Chaudhry, R., Candler, G., Gray, K., Sweeney, C., and Schneider, S., "Characterization of Wind Tunnel Freestream Disturbances in Conventional Hypersonic Wind Tunnels," *AIAA paper 2018*, 2018.

[17] Estorf, M., Wolf, T., and Radespiel, R., "Experimental and Numerical Investigations on the Operation of the Hypersonic Ludwieg Tube Braunschweig," *Proceedings 5th European Symposium on Aerothermodynamics for Space Vehicles*, Vol. ESA SP-563, 2005, 2004, pp. 579–586.

[18] Heitmann, D., Kähler, C., Radespiel, R., Rödiger, T., Knauss, H., and Krämer., E., "Disturbance-Level and Transition Measurements in a Conical Boundary Layer at Mach 6," *AIAA paper 2008-3951*, 2018.

[19] Ali, S.R.C., Radespiel, R., Schilden, T., and Schröder, W., "High-Frequency Measurements of Acoustic and Entropy Disturbances," *AIAA paper 2014-2644*, 2014.

[20] Theiss, A., Hein, S., Heitmann, D., Ali, S., and Radespiel, R., "Numerical and Experimental Investigation of Laminar-Turbulent Boundary Layer Transition on a Blunt Generic Re-Entry Capsule," *AIAA paper 2014-2353*, 2014.

[21] Bernardini, M., Pirozzoli, S., Orlandi, P., and Lele, S.K., "Compressible Boundary Layer Transition Induced by Isolated Roughness Elements," *Proceedings of CTR Summer Program 2012*, 2012, pp. 15–24.

[22] Schultz, D.L. and Jones, T.V., "Heat Transfer Measurements in Short Duration Facilities," *AGARD Rept. 165*, 1973.

[23] Laufer, J. and Mcclellan, R., "Measurements of Heat Transfer From Fine Wires in Supersonic Flows," *Journal of Fluid Mechanics*, Vol. 1, No.3, 1956, pp. 276–289.

[24] Itoh, K., Ueda, S., Tanno, H., Komuro, T., and Sato, K., "Hypersonic Aerothermodynamic and Scramjet Research Using High Enthalpy Shock Tunnel," *Shock Waves*, Vol. 12, 2002, pp. 93–98.

[25] Hornung, H. and Belanger, J., "Role and Techniques of Ground Testing for Simulation of Flows up to Orbital Speed," *AIAA paper 1990-1377*, 1990.

[26] Tanno, H., Komuro, T., Sato, K., Itoh, K., Yamada, T., Sato, N., and Nakano, H., "Heat Flux Measurement of Apollo Capsule Model in the Free-Piston Shock Tunnel HIEST," *AIAA paper 2009-7304*, 2009.

[27] Sanderson, S. and Sturtevant, B., "Transient Heat Flux Measurement Using a Surface Junction Thermocouple," *Rev. Sci. Inst.*, Vol. 73, No.7, 2002.

[28] Marineau, E. and Hornung, H., "Modeling and Calibration of Fast-Response Coaxial Heat Flux Gages," *AIAA paper 2009-737*, 2009.

[29] Berger, K., "Aerothermodynamic Testing of the Crew Exploration Vehicle in the LaRC 20-Inch Mach 6 and 31-Inch Mach 10 Tunnels," *AIAA paper 2008-1225*, 2008.

[30] Marineau, E., Laurence, S., and Hornung, H., "Apollo-Shaped Capsule Boundary Layer Transition at High-Enthalpy in T5," *AIAA paper 2010-446*, 2010.

[31] Kirk, L., Lillard, R., Olejniczak, J., and Tanno, H., "Boundary Layer Transition and Trip Effectiveness on an Apollo Capsule in the JAXA High Enthalpy Shock Tunnel (HIEST) Facility," *AIAA paper 2015-0209*, 2015.

[32] Prabhu, R. and Erickson, W., "A Rapid Method for the Computation of Equilibrium Chemical Composition of Air to 15000 K," *NASA TP-2792*, 1988.

[33] Takahashi, M., Kodera, M., Itoh, K., Komuro, T., Sato, K., and Tanno, H., "Influence of Thermal Non-Equilibrium on Nozzle Flow Condition of High Enthalpy Shock Tunnel HIEST," *AIAA paper 2009-7267*, 2009.

[34] Tanno, H., Komuro, T., Lillard, R., and Olejniczak, J., "Experimental Study of High-Enthalpy Heat Flux Augmentation in Shock Tunnels," *Journal of Thermophysics and Heat Transfer*, Vol. 29, No. 4, 2015.

[35] Reda, D.C., "Correlation of Nosetip Boundary-Layer Transition Data Measured in Ballistic Range Experiments," *AIAA Journal*, Vol. 19, No. 3, 1981, pp. 329–339.

[36] Reda, D.C., "Review and Synthesis of Roughness-Dominated Transition Correlations for Reentry Applications," *Journal of Spacecraft and Rockets*, Vol. 39, No. 2, 2002, pp. 161–167.

Chapter 10 - HIFIRE-1 AND -5 FLIGHT AND GROUND TESTS

Roger L. Kimmel, David W. Adamczak, Matthew P. Borg
Air Force Research Laboratory
UNITED STATES

Joseph S. Jewell
Air Force Research Laboratory and Spectral Energies, LLC
UNITED STATES

Thomas J. Juliano
University of Notre Dame
UNITED STATES

Scott A. Stanfield
Innovative Scientific Solutions, Inc.
UNITED STATES

Karen T. Berger
NASA Langley Research Center
UNITED STATES

10.0 NOMENCLATURE

f	frequency, units as noted
h	convective heating coefficient
h_{F-R}	reference convective heating coefficient
M	Mach number, dimensionless
N	dimensionless disturbance amplitude, $\ln(A/A_0)$, where A_0 is amplitude at lower neutral bound
Re_e	unit Reynolds number based on boundary layer edge conditions, per meter
Re_{RN}	Reynolds number based on freestream (upstream of bow shock) conditions and nose radius
Re_x	Reynolds number based on freestream (upstream of bow shock) conditions and axial length
$\mathrm{Re}_{x,tr}$	transition Reynolds number based on freestream (upstream of bow shock) conditions and axial length
T_w	wall temperature, K
T_0	stagnation temperature, K
t	time, seconds
x	axial length, units as noted
y	spanwise distance, units as noted
x_T	transition location, meters
α	angle-of-attack, degrees
Φ	azimuthal coordinate in wind-fixed reference frame, degrees
ϕ	azimuthal coordinate in body-fixed coordinate system, degrees

10.1 INTRODUCTION

The Hypersonic International Flight Research Experimentation (HIFiRE) program is a hypersonic flight test program executed by the Air Force Research Laboratory (AFRL) and the Australian Defence Science and Technology Group (DSTG). [1, 2] Its purpose is to develop and validate technologies critical to next generation hypersonic aerospace systems. Candidate technology areas include, but are not limited to, propulsion, propulsion-airframe integration, aerodynamics and aerothermodynamics, high temperature materials and structures, thermal management strategies, guidance, navigation, and control, sensors, and system components. The HIFiRE program consists of extensive ground tests and computation focused on specific hypersonic flight technologies. Each technology program culminates in a flight test.

Two HIFiRE flights focused on boundary layer transition. HIFiRE-1 created an extensive knowledge base regarding transition on axisymmetric bodies that was summarized in numerous prior publications. [3–17] HIFiRE-5 was devoted to measuring transition on a three-dimensional (3D) body. The results of this flight were summarized in a number of technical papers. [18–23] Preflight research was described in numerous publications.[24–40]

Both HIFiRE transition flight experiments were successful, with some minor anomalies. HIFiRE-1 launched 22 March 2010 at the Woomera Prohibited Area in South Australia. This vehicle entered the atmosphere at higher-than-intended angle-of-attack, but was otherwise successful. Low angle-of-attack (AoA) hypersonic transition data were obtained on ascent, and high AoA transition was measured during descent. The HIFIRE-5a mission launched 23 April 2012 from Andoya, Norway. [41–44] The second stage of HIFiRE-5a failed to ignite, preventing the payload from attaining hypersonic speeds. Despite the failure of the HIFiRE-5a second stage, the payload acquired supersonic transition data. However, since this did not satisfy mission objectives to acquire hypersonic transition measurements, a new payload, essentially identical to the first, was constructed and flown at Woomera, Australia, on 18 May 2016. This mission, HIFiRE-5b, was entirely successful.

The HIFiRE-1 and -5 primary experimental objectives were to measure transition on smooth bodies in hypersonic flight. Although previous flight tests had measured transition during hypersonic flight, these tests were subject to some ambiguity due to surface roughness, as-flown nosetip geometry, vehicle motion, ablation, wall temperature and so on. Schneider provides a survey paper of previous hypersonic flight tests. [45] The HIFiRE goal was to remove this ambiguity by flying heavily-instrumented test articles with smooth, unablating moldlines. The singular flight test product that could not be derived from ground test was transition measurements in a quiet environment. Transition locations measured in flight would be converted to transition Reynolds numbers and N-factors, and compared to ground test results to assess the influence of wind tunnel noise, and to provide some calibration of N-factor prediction methods. Subsequent sections of this paper will demonstrate that this goal was achieved, and will summarize conclusions regarding ground test and computation that could be derived from the flight data.

The HIFiRE research program obtained data on numerous aspects of hypersonic transition, including roughness-dominated transition and the phenomenology of transition in flight. To limit the scope of this paper, only smooth-body results are discussed, with a focus on comparison to ground test and computation. The research campaign also contributed a huge amount of computational work. For brevity, discussion of computational results is limited to a few select computations that help elucidate the flight and ground transition results.

10.2 FLIGHT EXPERIMENTS DESCRIPTION

The HIFiRE-1 and -5 configurations were described in prior papers. [16, 41] Both configurations consisted of an instrumented test article mounted atop a two-stage, ground-launched sounding rocket. The payloads remained attached to the second stage throughout flight. The vehicles were spun at a low rate to reduce trajectory dispersion. Cant-angle on the first and second-stage fins caused the vehicles to spin passively. Because of this, the vehicles were rolling throughout the entire trajectory. Both flights were launched with high elevations and flew lofted, ballistic trajectories, with short endoatmospheric flight times, and with relatively long exoatmospheric stages and high exoatmospheric apogees. Data were obtained on ascent and descent, with descent being the primary test window.

Neither flight possessed active control surfaces on the upper stage, and relied solely on the static aerodynamic stability of the stack to maintain low angle-of-attack during ascent. During relevant ascent flight periods, angle-of-attack was less than 0.5°. On both flights, cold-gas thrusters were used during exoatmospheric flight to orient the vehicle along the descent flight path vector, in order to minimize angle of attack during descent. This maneuver was unsuccessful for HIFiRE-1, and the payload reentered the atmosphere at a relatively high angle of attack. The AoA damped in an oscillatory manner so that $5^\circ < \alpha < 13^\circ$ during descent transition. The HIFiRE-5b exoatmospheric thruster maneuver was successful, so that AoA during descent transition was less than 1°. Considerable effort was expended to ensure that the HIFiRE-1 and -5 instrumentation and post-flight analysis were able to resolve the effects of the vehicle motion.

The 7-degree half-angle cone geometry was chosen for HIFiRE-1 since this configuration had been the basis of extensive test and analysis for many years. The HIFiRE-5 configuration was chosen as the test-article geometry based on extensive previous testing and analysis on elliptic cones. [46–53] This prior work [46–48] demonstrated that the 2:1 elliptic cone would generate significant crossflow instability at hypersonic flight conditions and potentially exhibit leading-edge transition. Figure 10-1, taken from [16] and [18] illustrates the HIFiRE-1 and -5 geometries.

Both payloads consisted of aluminum frusta that served as the primary test surfaces, and had solid, uninstrumented nosetips built-up from several materials. To account for the differential coefficients of thermal expansion of the nosetip materials, the tips possessed backward-facing steps at each material interface when cold. The steps were sized to approach zero height when the nosetip was at working temperature in the test window during descent. The nosetips of both vehicles were slightly blunted. References describe the nosetip details and detailed surface roughness measurements. [10, 16, 18] For both HIFiRE-1 and -5, roughness did not demonstrably affect transition, and nose-bluntness effects were limited primarily to the first 300 mm of the test article.

The bulk of the instrumentation on both flights consisted of Medtherm coaxial thermocouples, hand-contoured to the outer mold line of the vehicle. The HIFiRE-1 test surface contained two rays of thermocouples. The secondary side of the vehicle possessed a diamond-shaped, discrete roughness element to assess tripped transition, and the primary side of the cone was smooth. The HIFiRE-5 configuration had one side that contained a closeout panel with fasteners. The primary test surface on the other side was smooth and devoid of fasteners. Ground tests verified on both vehicles that roughness-induced transition would not contaminate the test surface flow. Post flight analysis confirmed that this indeed was the case.

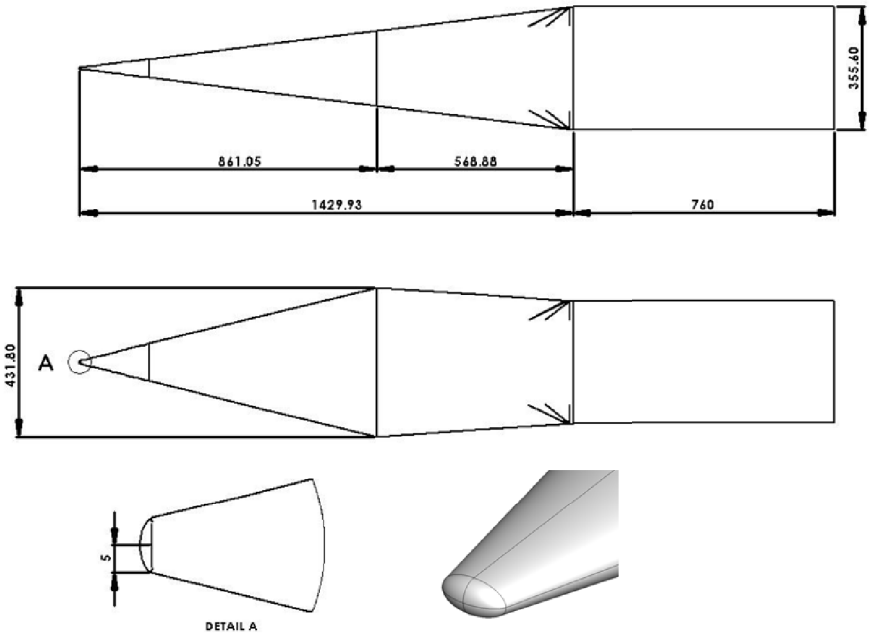

Figure 10-1: HIFiRE-1 (top, [16]) and HIFiRE-5 (Bottom, [18]) Flight Vehicles. Dimensions in mm.

10.3 SMOOTH-BODY, AXISYMMETRIC TRANSITION: HIFIRE-1

During ascent, flow over the HIFiRE-1 test article was turbulent immediately after launch. As the vehicle ascended, and Reynolds number dropped, transition moved aft over the vehicle. Ascent transition occurred in three phases. In phase one, for $t < 15$ s, roughness due to nosetip joint steps dominated transition. For $t > 15$ s, the combination of higher nose temperature, which reduced step heights, and lower Reynolds number and higher Mach number, which made the boundary layer less sensitive to roughness, lessened the influence of the steps. However, during phase two, $15 < t < 19$ s, nosetip roughness still appeared to affect transition somewhat, and transition behaved erratically. During phase three, $19 < t < 22$ s, transition on the primary test surface moved downstream in an orderly fashion, consistent with a smooth-body transition, with $10.4 \times 10^6 < \mathrm{Re}_x < 13.7 \times 10^6$. For $t > 22$ s during ascent, the primary test surface was entirely laminar. During phase three, AoA was estimated to be less than 0.5°, and the ratio of wall-temperature to stagnation-temperature was approximately 0.3. Flow downstream of the diamond-shaped trip on the secondary instrument ray remained turbulent until $t \approx 30$ s, after which it was laminar for the remainder of the ascent.

During phase three (smooth-body transition), transition occurred at conditions where Mack's second-mode was predicted to dominate. [54] Boundary layer stability analysis at intervals during $19 < t < 22$ s indicated second-mode N-factors at transition of $10.9 < N < 14.5$, with an average value of $N = 13.4$. The frequency corresponding to the peak N-factor at transition during this period was calculated to be $400 < f < 725$ kHz. The transition N-factor calculated for $t = 19$ s (N=10.9) was low and slightly out-of-family with transition N-factors at later times. For $20 < t < 22$ s, $13 < N < 14.5$.

The HIFiRE-1 ascent transition N-factors were broadly consistent with past hypersonic flight tests, that is to say, at the upper end of commonly-cited free-flight transition N-factors. Kimmel et al. [16] includes a brief comparison of HIFiRE-1 to previous tests. Stability calculations by multiple researchers for the Reentry-F and Sherman-Nakamura hypersonic flight tests indicated correlating transition N-factors of 3.7-15. [55, 56] The investigators ascribed much of this variation to uncertainty in the calculated boundary conditions. With the lowest Reentry-F transition N-factor excluded, correlating transition N-factors for these two flights ranged from 8-15.

The HIFiRE-1 transition measurements may be used, judiciously, to inform hypersonic transition design. The final transition prediction depends on the designers risk tolerance. Based on the above data, it is reasonable to conclude that for a smooth, axisymmetric body, where ablation is not dominant, $8 < N < 15$ would be reasonable correlating N-factors for second-mode transition in hypersonic flight. This is an aggressive stance and probably approaches an upper limit on attainable laminar Reynolds number for these bodies under optimistic conditions. Depending on the desired level of conservatism, lower transition Reynolds numbers might be appropriate to account for uncertainty in flight conditions, surface geometry, or the potential for other "bypass" transition mechanisms.

A practical design question is the uncertainty in the transition location to which this N-factor uncertainty equates. This is situational, depending on the slope of N-factor versus x-location. Transition x-location is subject to more uncertainty at low Reynolds numbers than at high Reynolds numbers, due to the presumed spread in transition N-factor, since N-factor increases more quickly with x at high Reynolds numbers. Reference [54] tabulates this sensitivity about the measured transition location for HIFiRE-1 at various times. Transition x location sensitivity varies from $0.034 < \Delta x/\Delta N < 0.096$ (meters per unit N), for $19 < t < 22$ s. Taking into account nonlinearity in the N-factor versus x distribution, $8 < N < 15$ equates to an uncertainty of 35% of the cone length for HIFiRE-1 at $t = 22$ s.

Another concern regarding the assumed transition N-factor is the disturbance level, and variations thereof, in flight. Not enough hypersonic flight tests exist to develop a statistical sample of how flight disturbances affect transition. An N-factor of 14 (typical for HIFiRE-1 ascent transition) represents a million-fold amplification. This is not to say that the freestream disturbances were one-millionth of the boundary layer disturbances at transition. Freestream disturbances had to be processed, presumably, through some receptivity process and some subsequent linear and nonlinear amplification. It suffices to say that initial disturbance levels were probably quite low, perhaps immeasurable, and small scale. The second mode wavelength at $t = 22$ s was on the order of several millimeters. Indeed, the ultimate source of flight disturbances is unknown, and may remain unknown. Bushnell speculated on numerous sources of initial disturbances. [57] Fedorov et al. [58] have calculated that thermal molecular fluctuations (Brownian motion) might have engendered transition on HIFiRE-1.

Since disturbances amplify so rapidly, changes in the initial disturbance field do not necessarily translate into large differences in the transition location, however. Assuming that a disturbance breaks down after one-million fold amplification ($N = 13.8$), another disturbance beginning at half the initial amplitude of the first, would have to undergo a two-million fold amplification ($N = 14.5$), assuming that the disturbances undergo the same amplification process and break down at the same amplitude. For HIFiRE-1 at $t = 22$ s, the difference between $N = 13.8$ and $N = 14.5$ equates to only a 67 mm difference in transition location.

Besides prediction of the absolute transition location, it appears that stability theory is well-suited to analyze parametric trends on HIFiRE-1-type configurations. During its period of second-mode transition, the HIFiRE-1

flight experienced only small parametric variations. Ground tests, however, covered a wider range of Mach number, Reynolds number and nose bluntness. Transition from two wind tunnels were well-correlated across the parameter range by an N-factor of 5.5, over a range $6 < M < 10$ and nose bluntness from sharp to 6.35 mm radius. Later tests and analysis of similar configurations suggest that a variable N-factor for wind tunnel data that takes wind tunnel noise into account might be a better prediction method. [59] It should also be noted that a constant N-factor prediction method did not fare so well for correlating transition on HIFiRE-1 at AoA in ground tests. [11]

One goal of the HIFiRE experiments was to compare ground test transition to flight test transition. Figure 10-2 illustrates heat transfer data obtained in two wind tunnels and in flight. The flight time of $t = 22$ s was chosen since it was the lowest Reynolds number at which clean transition data was obtained, and thus closer to the wind tunnel Reynolds numbers. Data were normalized with edge conditions to minimize Mach number differences. The disparity between ground and flight test transition is evident.

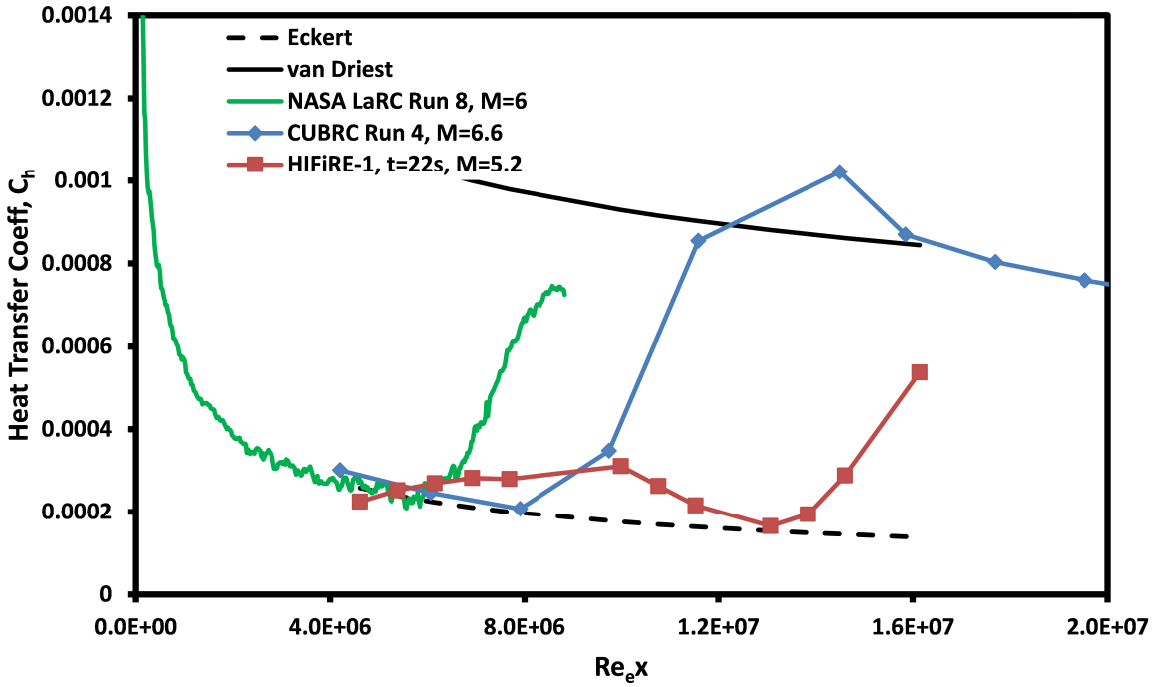

Figure 10-2: Heat Transfer Data from Wind Tunnels and Flight.

Since the actual flight conditions varied from the preflight tests, it was not possible to make a one-to-one comparison among the wind tunnel tests and flight data. The wind tunnel tests were conducted at higher Mach numbers and with T_w/T_0 ratios different from the ascent transition conditions. Also, Reynolds numbers based on nose radius were different. By considering parametric trends, however, some conclusions may be derived. Figure 10-3 illustrates transition Reynolds numbers for the HIFiRE configuration as a function of the nose radius Reynolds number. Table 10-1 lists conditions for these tests. For comparison, and to illustrate the transition trend with nose radius, Stetsons 8° cone transition data [60] (replotted from [61]) are included on the graph. Transition Reynolds numbers were normalized with edge conditions to minimize effects from differing Mach numbers and cone angles. Edge values were based on Taylor-Maccoll solutions for sharp cones.

Table 10-1: Ground Test Conditions.

	NASA Run 8	CUBRC Run 4	CUBRC Run 5	H2K Run 4	HIFiRE-1, $t = 22$ s	Stetson
M	6	6.6	7.2	7.1	5.2	6
Re/m	1.9E+07	1.7E+07	1.0E+07	9.3E+06	1.2E+07	var
Re_{RN}	22051	42968	25262	14880	30000	var
T_w/T_0	0.60	0.16	0.13	0.56	0.17	0.49

Despite the variations in conditions, the HIFiRE -1 flight data clearly trend higher than the wind tunnel data. The HIFiRE flight transition Reynolds number in Figure 10-3 is about 1.4 times higher than the Stetson Mach 6 data trend, and about twice the data trend for the HIFiRE-specific geometry.

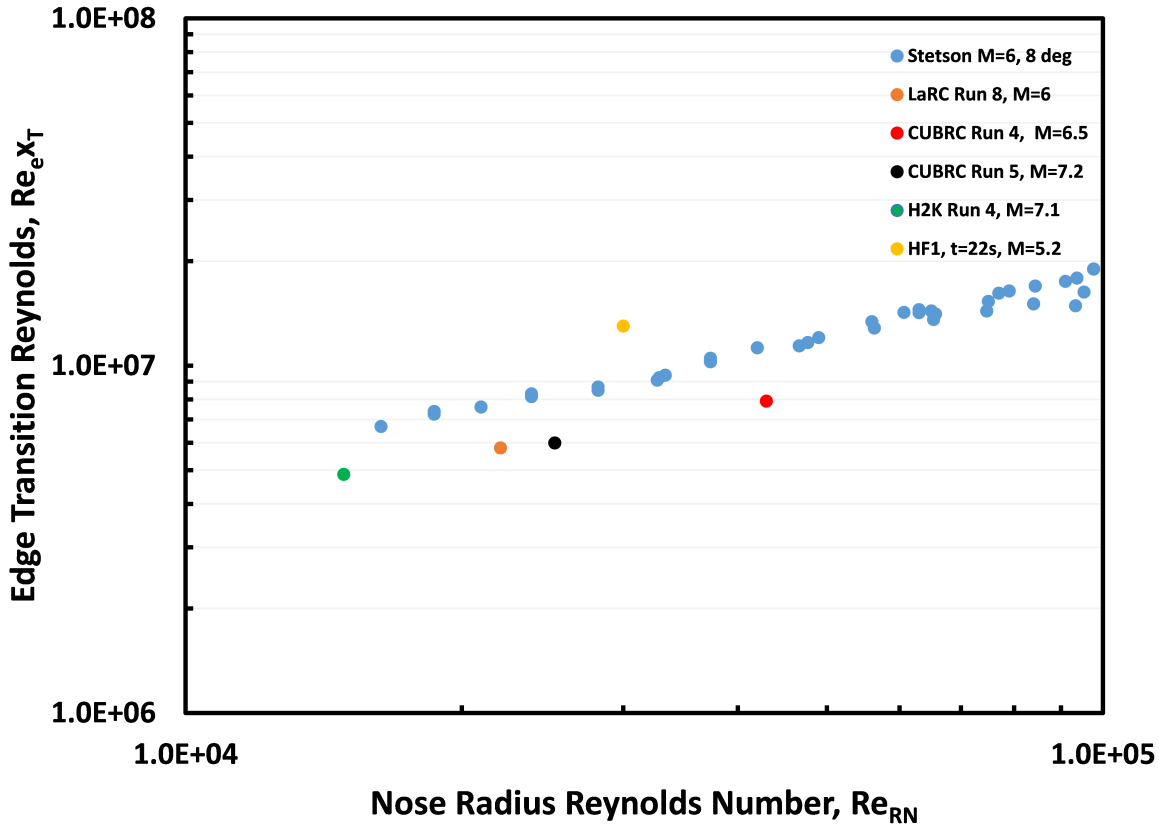

Figure 10-3: Transition Reynolds Number Based on Edge Conditions as Function of Nose Radius Reynolds Number.

Another potential confounding factor in comparing the wind tunnel to flight data is differences in wall cooling. However, Table 10-1 shows that the wind tunnel tests possessed wall temperature ratios either equivalent to or higher than the flight data. Assuming that transition was due to second-mode for all cases, decreasing T_w/T_0 for ground test, or increasing T_w/T_0 for the flight test, would only accentuate the differences between flight and wind tunnel transition Reynolds numbers, due to the destabilizing effect of wall-cooling on the second mode.

The effect of noise is clearer when N-factors are compared. The N-factor computations should take parametric differences between the flight and ground test into account. The correlating N-factors of 5.5 derived from wind

tunnel tests [11] compared to the $N = 13 - 14$ correlating values observed in flight clearly demonstrate the dominance of wind tunnel noise in ground test.

10.4 TRANSITION IN THREE-DIMENSIONAL FLOWS: HIFIRE-1 EXPERIMENTAL DATA

Both HIFiRE-1 and -5b flights provided information on hypersonic flight transition in fully three-dimensional flows. HIFiRE-5, because of its spanwise pressure gradient, possessed cross-flow even at zero AoA. HIFiRE-1 attained cross-flow data inadvertently during descent, due to its AoA. Although the HIFiRE-1 flight was not intended to acquire data at nonzero AoA, it was recognized that this might occur. To mitigate this risk, instrumentation was selected with sufficient frequency response to resolve fluctuations in the transition front due to vehicle attitude variations.

The HIFiRE-1 descent transition front was mapped out by determining the angular location and Reynolds number at which each transducer registered transition, as the spinning payload descended. The transition history recorded by each transducer may be visualized by assuming that the spatially nonuniform transition front was wind-fixed, and the transducer revolved beneath it. Early in the descent, at low Reynolds number, a transducer would indicate laminar flow continuously. As the Reynolds number increased, a transducer would register periods of laminar and turbulent flow during each revolution of the payload, due to the spatially nonuniform transition front. Finally, the transducer would be completely downstream of the transition front, and register continuously turbulent flow at all azimuthal locations. The highest bandwidth instrumentation, the Vatell heat transfer gauges and Kulite pressure transducers, registered the transition front with the highest temporal fidelity. The Medtherm coaxial thermocouples showed some evidence of the transition front nonuniformity, but this was greatly smeared due to their lower frequency response.

Transition data obtained in this fashion are presented as a function of transducer azimuthal location, relative to the windward attachment line, and Reynolds number based on freestream conditions and x-location. Formally, this presentation resembles typical x-ϕ maps of transition, for example those generated by Stetson. [62] It must be noted that HIFiRE-1 underwent significant variations in AoA and freestream Reynolds number over the region covered by this map. Nevertheless, this presentation of the data permits general features of the transition front to be compared to static wind tunnel data and CFD, and the conclusions derived from the data are not invalidated.

Figure 10-4 (from [17]) illustrates the HIFiRE-1 transition front during descent, and the transition front measured in the DLR H2K wind tunnel. [63–65] Several notable features are apparent in this figure. First, data collected from three Kulite transducers (called out as "PHBW" in the figure), a Vatell heat transfer gauge "HT3") and Medtherm coaxial gauges (dot-dash line, "Re_{TR}") are all consistent. Although the Medtherm gauges did not possess sufficient frequency response to resolve the transition front spatial nonuniformity, the transition location measured with the Medtherms falls at a Reynolds number that is the average transition Reynolds number observed with the higher bandwidth instruments.

Second, transition occurred at lower Reynolds numbers on the leeward centerline (Φ=180°), and higher Reynolds numbers on the attachment line (Φ=0°). This was expected and consistent with past wind tunnel results. [62, 66–68] A somewhat unexpected feature was that the highest transition Reynolds number occurred not on the windward or leeward symmetry meridians at Φ=0° and Φ=180°, but between them at about Φ=40° and

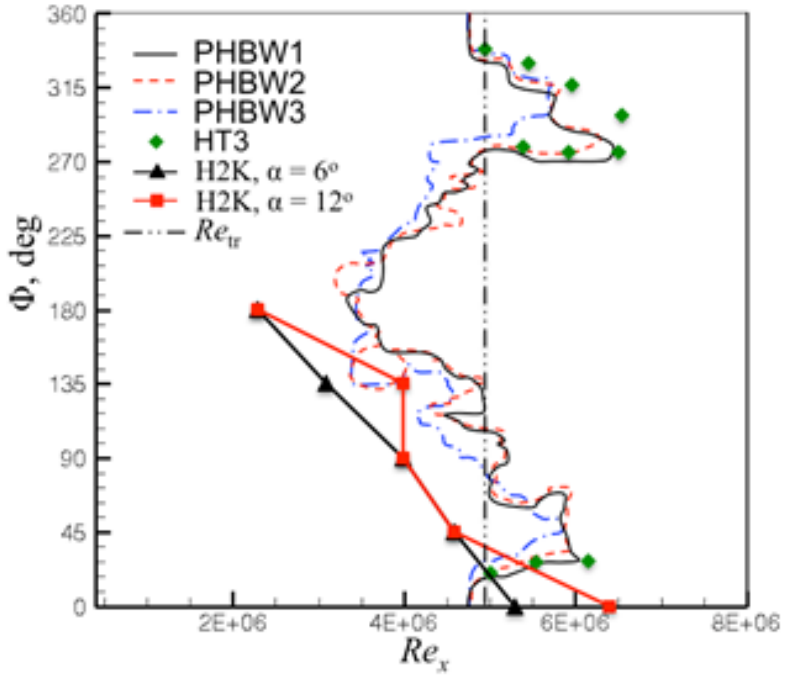

Figure 10-4: HIFiRE-1 Descent Transition Map [17].

Φ=300°. This multilobed transition front is probably the result of multiple transition processes, with traveling instabilities dominating transition on the windward and leeward meridians, and crossflow dominating between these meridians.

Third, the shape of the transition front measured in the H2K wind tunnel is somewhat similar to the shape of the flight transition front, with a low transition Reynolds number on the leeward meridian, and higher transition Reynolds number on the windward meridian. The H2K transition front does not appear to be sharply indented like the flight transition front, although the meager spatial resolution of the H2K measurements made this difficult to resolve.

Fourth, the leeward wind tunnel transition Reynolds numbers were lower than those measured in flight, as anticipated. Unexpectedly, however, wind tunnel transition on the windward meridian occurred at higher transition Reynolds numbers than in flight. Both this observation and the indented shape of the flight transition front are believed to be related to the higher wall-cooling of the flight article, as described below.

Various wind tunnel tests of smooth blunt cones, including the HIFiRE configuration itself, have shown contradictory trends of windward transition front movement with AoA. For HIFiRE-1 in H2K, the $\alpha = 6°$ and $\alpha = 12°$ windward transition Reynolds numbers (Re_x=5.3$\times 10^6$ and Re_x=6.4$\times 10^6$, respectively) were higher than the $\alpha = 0°$ transition Reynolds number (Re_x=3.9$\times 10^6$), in contrast to the flight test trends. Similarly, tests of HIFiRE-1 in the NASA Langley Research Center (NASA LaRC) 20-Inch Mach 6 wind tunnel at $\alpha = 0°, 3°$, and 5° showed transition moving downstream on the windward meridian as AoA increased, although the change was modest. [14] Tests of HIFiRE-1 at Calspan University of Buffalo Research Center (CUBRC), however, displayed trends contrary to the H2K and LaRC tests. At $\alpha = 0°$, 1°, 2°, and 5°, and M= 6.6 and 7.2 in CUBRC,

the windward transition front moved upstream with increasing AoA. [12] Some other wind tunnel tests have displayed upstream movement of the windward transition front with AoA on cones with small nose bluntness. In all of the ground test cases, leeward transition also moved upstream with increasing AoA, and thus remained upstream of windward transition, as it did in the HIFiRE flight results.

The nature of the disturbances, and their interaction with wind tunnel noise and wall temperature, offers a possible explanation for these observations. High-bandwidth pressure transducers in the H2K experiment showed a strong instability on the windward centerline consistent with a second-mode transition. Computations also predicted second-mode windward transition in flight. [54] Second-mode instability is affected by wind tunnel noise, creating a trend toward lower transition Reynolds numbers in ground test, all else being equal. [69] However, second-mode is destabilized by wall-cooling, and the flight vehicle wall was more highly cooled than in ground test. The ratio of wall-to-total-temperature, T_w/T_0, was 0.56 in the H2K test, compared to 0.18 in flight. It is possible that increased wall-cooling in the flight test more than compensated for lower noise in the flight environment, leading to lower windward transition Reynolds number in flight compared to ground test. Wall temperature ratio for the CUBRC tests, which showed upstream windward transition movement like the flight, was T_w/T_0=0.13, relatively close to the flight value of 0.18. Also, the indented transition front observed on HIFiRE-1 in flight has been observed in ground test on highly cooled models. [67, 68, 70, 71]

It should also be noted that for swept cylinders tested at Mach 3.5, wind tunnel noise did not appear to affect leading edge transition. [72] In analogy to the swept cylinder attachment line, the cone attachment line may exhibit a similar lack of sensitivity to wind tunnel noise.

The apparent lesser effect of wind tunnel noise on transition around the shoulders of the model (Φ=90° and 270° on HIFiRE-1) might also be explained by the presence of crossflow instabilities. The putative second-mode spectral peak observed on the windward centerline in the H2K test was less prominent, or in some cases absent, away from the windward meridian. Infrared images in H2K also showed streaks consistent with a crossflow-induced transition. This evidence strongly suggests that transition on the shoulder of the model was crossflow-dominated. Since stationary crossflow instabilities are presumed to be less sensitive to wind tunnel noise, this might account for the lesser impact of wind tunnel noise on the shoulder transition in the H2K test, compared to zero AoA tests.

Wall-cooling is expected to stabilize stationary crossflow to a limited extent, but this effect is probably minimal. Gosse, for example, showed that wall-cooling reduced the crossflow Reynolds number on a sharp 2:1 elliptic cone at Mach 8. [73] The higher shoulder transition Reynolds numbers on the flight article, compared to wind tunnel tests, might thus be due in part to increased wall-cooling, as well as lower noise.

10.5 TRANSITION IN THREE-DIMENSIONAL FLOWS: HIFIRE-5 EXPERIMENTAL DATA

The results of this section were presented in modified form in prior publications, [18, 74] and are recapitulated here for completeness.

HIFiRE-5 data analysis faced a challenge similar to HIFiRE-1, namely, merging transition records from multiple transducers at various times during descent. Similar to HIFiRE-1, transition events derived from all transducers

were synthesized into maps of the transition location in ϕ-Reynolds space. Also, like HIFiRE-1, this meant that when each transition event registered, the vehicle was at a different attitude. AoA was less than 1°, and the vehicle attitude did not have a major impact on transition Reynolds number on the centerline and leading edge meridians. However, at the maximum crossflow location, near the shoulder of the model (ϕ=45° on HIFiRE-5), transition was quite sensitive to yaw. Transition at the shoulder of the test article was promoted when that side was yawed into the wind. Therefore, some transducers registered multiple transition and laminarization events before recording continuously turbulent flow. The detailed effect of vehicle yaw is reserved for future analysis. The transition data presented in this section are based on first departure of a transducer from laminar heating. Therefore, they represent a transition Reynolds number for the most unstable attitude for that transducer.

Figure 10-5 (from [21]) shows flight transition Reynolds number as a function of spanwise location, at three different x-stations. This figure clearly shows three transitional lobes emanating from (top-to-bottom in the figure) leading edge, shoulder (ϕ= 45°) and centerline. Undoubtedly, multiple instabilities led to this multi-lobed transition. The transition pattern is similar at each x-station. For each lobe, the transition Reynolds number varied less than 10% with streamwise location. In the two regions of delayed transition (centered near ϕ=25° and 70°), the transition Reynolds number and the azimuthal location of maximum transition Reynolds number varied more. As discussed above, the transition Reynolds numbers in Figure 10-5 near the ϕ=45° region are more representative of the condition where that side is yawed into the wind.

Currently, there is no wind tunnel test directly replicating flight conditions. Several wind tunnel tests of HIFiRE-5 exist at Mach 6 and 7, and for a sharp 2:1 elliptic cone at M=8. HIFiRE-5 was tested at Purdue University, under quiet and noisy flow conditions [29–31, 33–35, 39], and at NASA LaRC [24, 36, 38], under noisy flow. The Purdue and LaRC tests used identically-scaled models. The sharp 2:1 elliptic cone was tested at M=8 under noisy conditions in Tunnel B of the Arnold Engineering Complex von Karman Facility (AEDC VKF-B). [46-48] Limited qualitative infrared imaging data were obtained at M=7 at CUBRC. [50]

The most comprehensive wind tunnel data were obtained in the Purdue Mach 6 quiet tunnel. Data included oil flows, temperature-sensitive paint, infrared imaging, and Kulite and PCB surface pressure measurements. Tests displayed stationary crossflow instabilities under quiet flow with oil flow, temperature-sensitive paint and IR. Figure 10-6 (from [34]) illustrates the heat transfer signature of stationary crossflow vortices and transition at M=6 and Re=12.3$\times 10^6$ /m under quiet flow. Stationary crossflow instabilities were only weakly evident under noisy flow. Traveling crossflow instabilities were measured in quiet flow, but could not be observed under noisy conditions. Kulite pressure transducer arrays permitted extraction of wave angle and phase velocity from traveling crossflow instabilities in quiet flow. Centerline and acreage transition was observed under both quiet and noisy conditions. The Purdue tunnel could not achieve a high-enough Reynolds number to produce leading edge transition under either noisy or quiet flow. Transition under quiet flow consisted of multiple lobes, with transition appearing most upstream on the centerline and the shoulder of the model. The lobe structure of the transition front was less well-defined under noisy flow, as discussed below.

Tests of HIFiRE-5 at LaRC under noisy flow focused on thermographic phosphor imagery. Noisy transition data were obtained for all locations on the model, from centerline to leading-edge, including data with sideslip and angle of attack. Testing at the Texas A&M University Actively-Controlled-Expansion wind tunnel explored wind tunnel noise effects. [32] Later testing in this tunnel showed transition patterns similar to those obtained in the Purdue tunnel, and evidence for stationary crossflow vortices. [75]

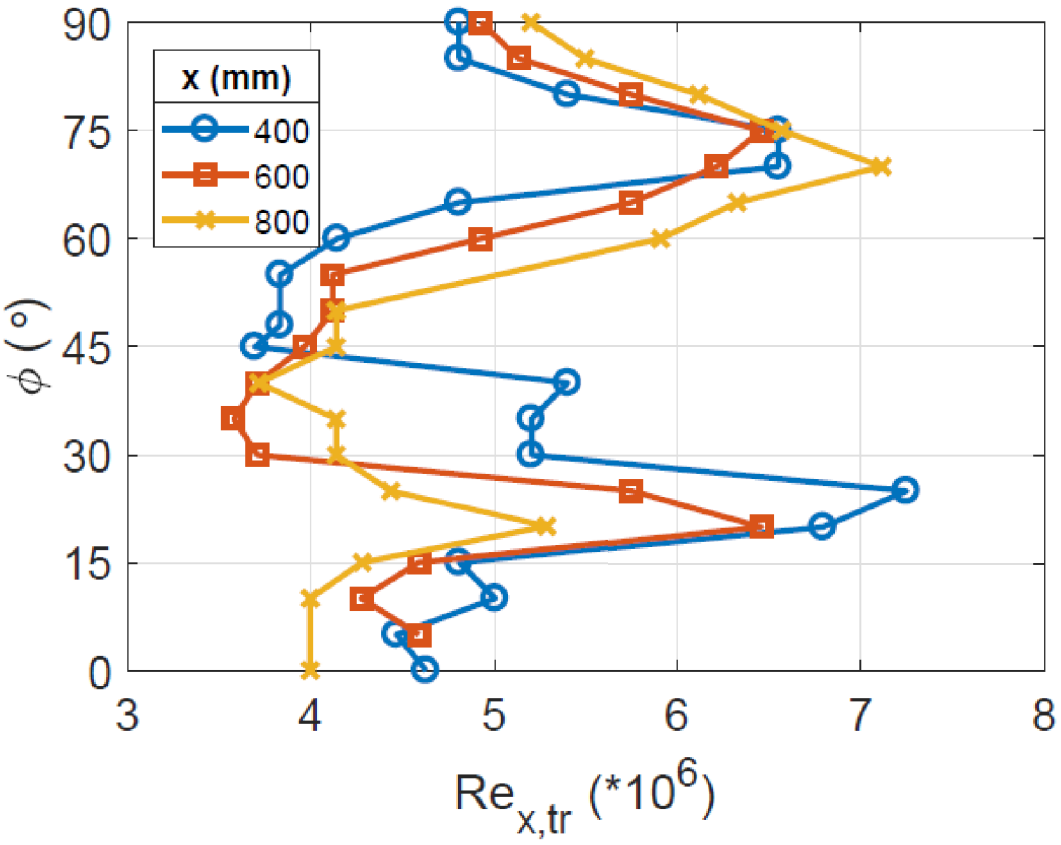

Figure 10-5: Transition Reynolds Numbers at Three Streamwise Locations (Reproduced from [21]).

Figure 10-7 (from [74]) compares flight and wind tunnel transition. Except for tests at CUBRC, no ground tests replicated flight T_w/T_0, which is suspected to be significant, especially for attachment line transition. Wall-cooling destabilizes second-mode instabilities, but reduces crossflow Reynolds number. [73] Despite the dissimilarities among these tests and flight conditions, some general conclusions may be drawn regarding HIFiRE-5 transition in the wind tunnel versus flight.

First, centerline transition occurred at relatively low Reynolds number in flight, as in ground test. The strongly inflected centerline velocity profile dominated transition here, making the boundary layer susceptible to rapidly-amplifying traveling instabilities. The scenario is probably similar to leeside transition on HIFiRE-1 at AoA. HIFIRE-5 flight centerline transition occurred at $\mathrm{Re}_x \approx 4.5\times10^6$ at Mach 7.8. HIFiRE-1 leeward transition occurred at $\mathrm{Re}_x \approx 3.2\times10^6$ at Mach 7.0. This is contrasted with HIFiRE-1 zero AoA transition at M=5.3, which took place at $\mathrm{Re}_x \approx 10^7$.

Second, for the wind tunnel cases, centerline transition under noisy flow occurred at much lower Reynolds numbers (about 1×10^6) than in flight (approximately 4.5×10^6). In quiet flow, centerline transition occurred at a Reynolds number of about 3.2×10^6, much closer to the flight value. This transition Reynolds number decrement due to tunnel noise, a factor of approximately 3, is comparable to that seen for HIFiRE-1 at α=0° and $M \approx 5.2$.

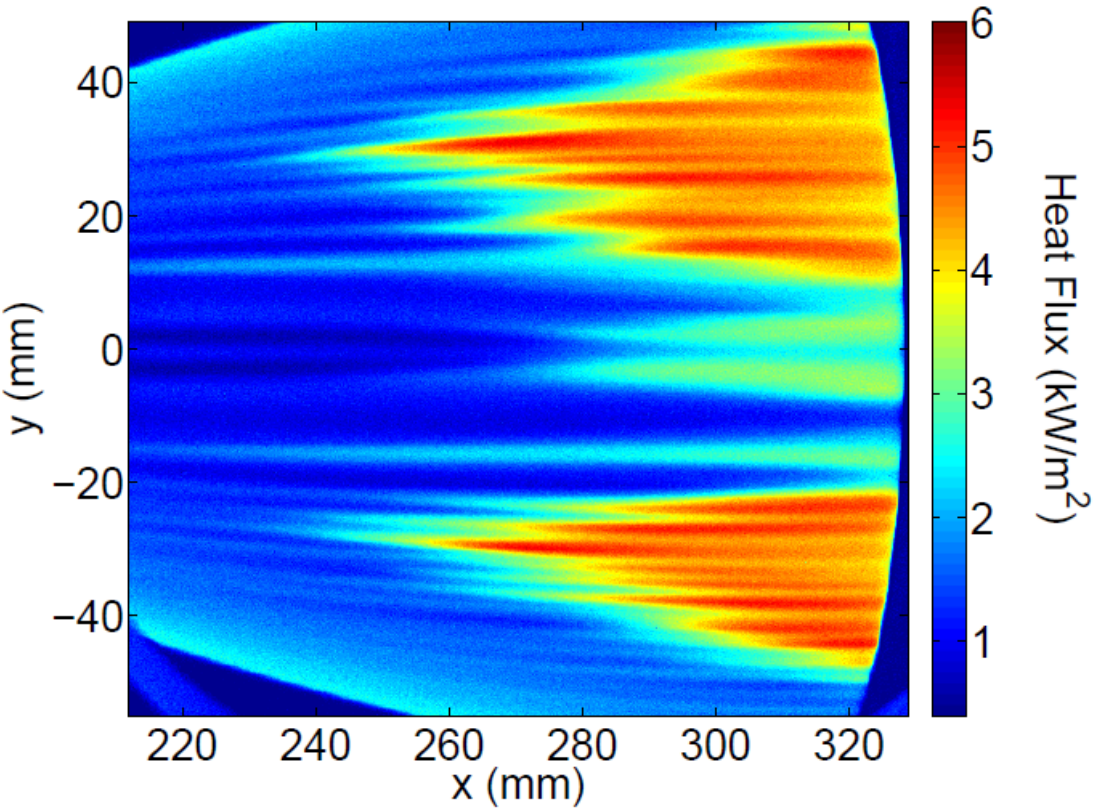

Figure 10-6: Heat Transfer for HIFiRE-5 Derived from Infrared Imaging, M=6, Re=12.3$\times 10^6$/m, Quiet Flow, Purdue Wind Tunnel (Reproduced from [34]).

Multiple centerline transition points for the LaRC data represent different unit Reynolds number cases, with higher transition Reynolds number corresponding to higher unit Reynolds number. This effect is often attributed to the spectral distribution of wind tunnel noise. [59]

Third, the distinct lobe near ϕ=45° present in flight and quiet wind tunnel flow was still evident in noisy flow. Linear stability calculations and wind tunnel tests indicated that transition near ϕ=45° was crossflow-dominated. TSP and IR imaging show that crossflow transition in the Purdue tunnel slightly preceded near-centerline transition in quiet flow, but under noisy flow, this was reversed, and near-centerline transition preceded crossflow transition. This earlier transition and lateral spreading of the near-centerline transition apparently made the transition-front indentation near ϕ=25° in quiet flow somewhat less prominent in noisy flow. The LaRC noisy tests also showed a transitional lobe near ϕ=45°. Figure 10-8 presents a thermographic phosphor image demonstrating this structure. Although a lobed structure was present in these images, the inboard portion of the transitional lobe was difficult to resolve from numerical heat transfer data, so Figure 10-7 shows only the outboard portion of the lobe for the LaRC data. The plot of the LaRC data incorporates both left and right sides of the model, creating some scatter due to left/right asymmetry. Although there is little overlap in the LaRC and the Purdue noisy data, the two data sets appear consistent. For comparison, Figure 10-9 shows heating contours ob-

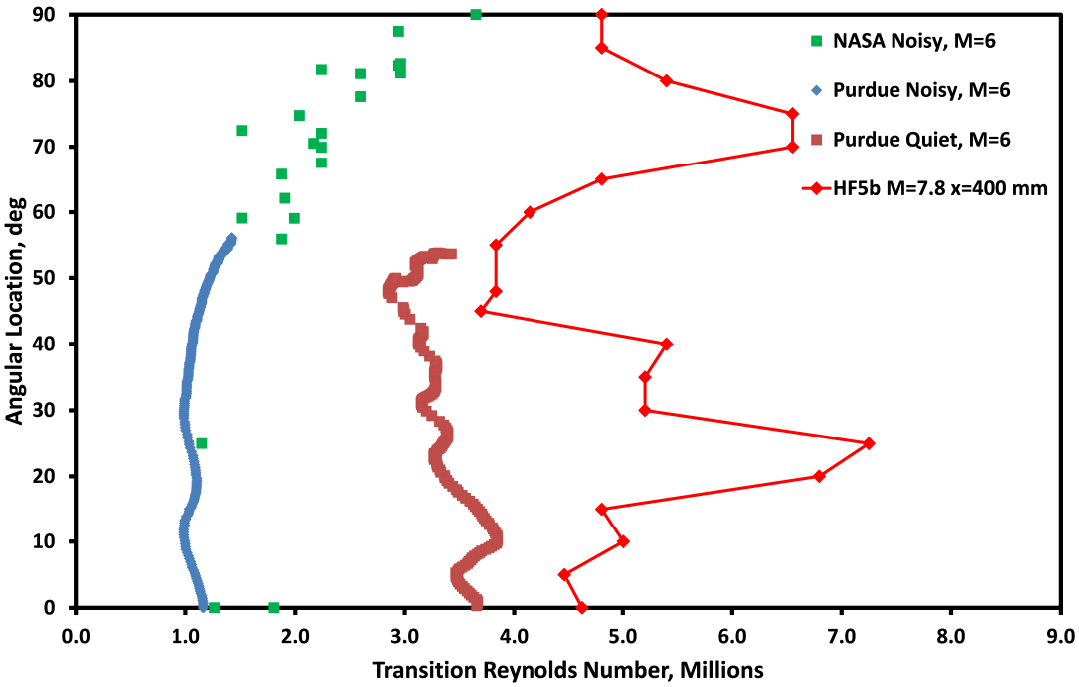

Figure 10-7: Noisy and Quiet Wind Tunnel Transition Compared to Flight Transition (Reproduced from [74]).

tained under noisy flow in the Purdue wind tunnel at conditions similar to those of the LaRC data in Figure 10-8. Since the Purdue and LaRC models were the same size, the similarity in the transition fronts is readily apparent.

The observation that wind tunnel noise affected near-centerline transition, which was dominated by traveling instabilities, slightly more than the crossflow transition, is consistent with the supposition that wind tunnel noise would affect traveling instabilities more strongly than stationary instabilities. That wind tunnel noise had this impact on crossflow transition is somewhat surprising, given the presence of stationary crossflow in this region. Traveling disturbances must develop somehow during the crossflow transition process however, as energy at zero frequency is distributed to nonzero frequencies, and wind tunnel noise may impact this process. Also, traveling crossflow waves were observed prior to transition in quiet flow, although the relative roles of traveling and stationary crossflow instability remains unclear. [33]

A fourth observation is that the flight case showed a distinct leading-edge transition lobe. Leading edge transition occurred in the LaRC tests, but it appeared to have a different character. Transition occurred on the leading edge, but it was the most downstream transition location on the model. Similar leading edge transition behavior occurred on the sharp elliptic cone at M=8. [48] In noisy flow, leading edge transition perhaps arose from spanwise contamination from adjacent turbulent regions. [36] Even so, wind tunnel noise did not seem to affect outboard (ϕ >50°) and leading edge transition as radically as centerline transition. In the LaRC tests, leading edge transition occurred at $\mathrm{Re}_x \approx 3.7\times10^6$, compared to about 4.5×10^6 in free flight. This result is somewhat reminiscent of the behavior of the HIFiRE-1 windward side transition when that test article was at angle of attack. In this case, windward transition Reynolds numbers in noisy flow were comparable to or even exceeded

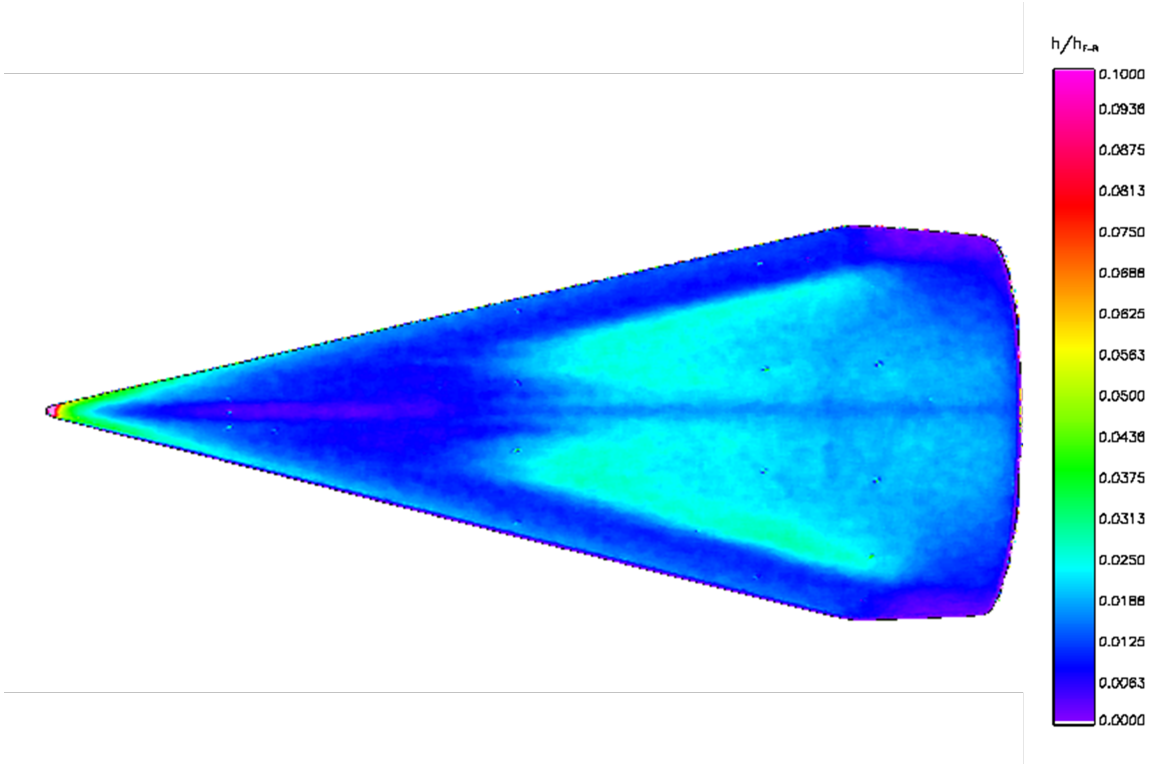

Figure 10-8: Heat Transfer Contours Derived from Thermographic Phosphor Image from LaRC Run 8. M=6, Re=9.5$\times 10^6$/m, α=0°. Enlarged Image Extracted from [36].

flight transition Reynolds numbers. At least part of this difference was ascribed to the higher wall cooling on the flight vehicle. [17]

The exception to these ground-test results for leading edge transition was the temperature-sensitive paint images obtained at CUBRC at about M=7. [28] In this study, at least one image showed a leading edge transition lobe where transition occurred at Reynolds numbers nearly identical to or lower than centerline transition.

That the multi-lobed transition front was observed both in flight and in the quiet wind tunnel, and that the same trends in crossflow transition were observed in wind tunnel and flight, is a powerful indication that the quiet tunnel accurately represented the flight transition mechanism. This further reinforces the notion that the flight transition was the result of modal instabilities, as observed in the wind tunnel.

10.6 TRANSITION IN THREE-DIMENSIONAL FLOWS: HIFIRE-1 AND -5 COMPUTATIONS

Boundary layer stability calculations for HIFiRE-1 at angle of attack were generally successful in replicating flight transition phenomenology. Li et al. [76] executed post-flight stability calculations for several points in the descent trajectory, labeled R1-R4, with increasing time (Table 10-2). Each point represented a significant event.

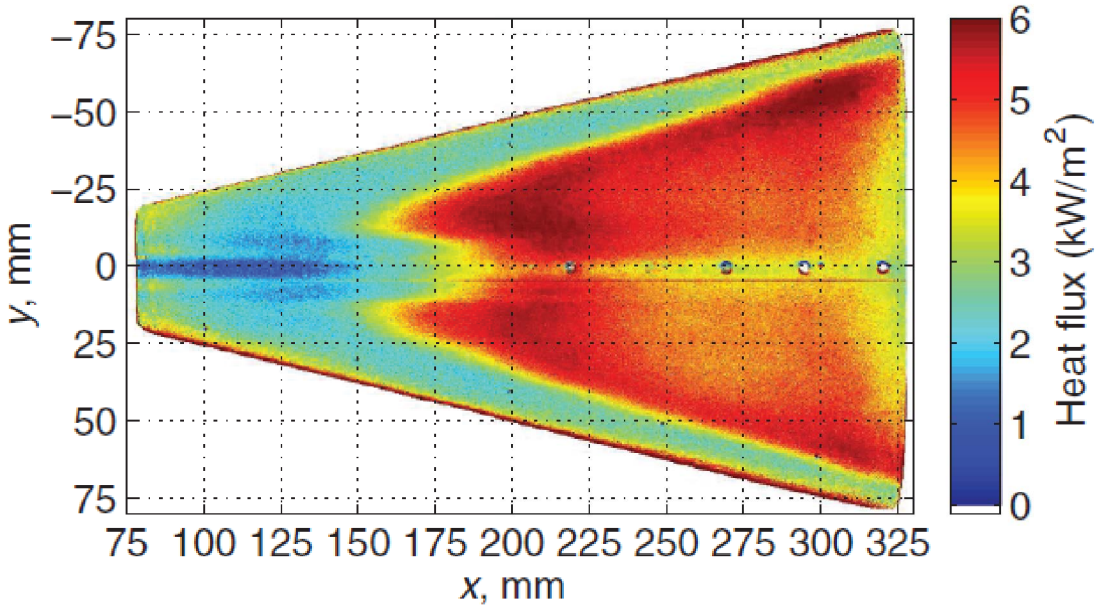

Figure 10-9: Heat Transfer Contours Derived from Temperature-Sensitive Paint Image from Purdue Wind Tunnel. M=6, Re=10.2$\times 10^6$/m, α=0°, Noisy Flow (Reproduced from [39]).

R1 (t=481.3 s) corresponded to a condition with fully laminar flow, but with periodic pressure fluctuations near the shoulder of the test article. These pressure fluctuations peaked at condition R2 (t=483.7 s). Conditions R3 and R4 were for the same time (t=485 s), but different angles of attack (α= 7.5° and 6.1° respectively). At conditions R3 and R4, flow had just become fully turbulent at all azimuthal locations at the x=850 mm, where most of the high bandwidth instrumentation was clustered.

Table 10-2: HIFiRE-1 Descent Analysis Cases (Transcribed from [76]).

Case	Time (s)	α (deg)
R1	481.3	13.6
R2	483.7	9.6
R3	485.0	7.5
R4	485.0	6.7

Parabolized Stability Equation (PSE) calculations for R1 predicted a maximum N-factor on the windward centerline of 6.4, consistent with the laminar flow observed in flight at this time. For point R2, the N-factor at x=850 mm was 14, consistent with the first appearance of transition in flight on the windward centerline at t=483.8 s. For condition R4, the N-factor at x=850 mm exceeded 14, consistent the observation of turbulent flow in flight at this time. Interestingly, the N-factor at the aft-most portion of the test article was 23 on the windward meridian, but only 9.5 on the leeward meridian. Li et al. [76] attributed the relatively slow instability growth on the leeward meridian to the structure of the mean flow there.

No attempt was made to develop a correlating N-factor for crossflow transition in flight, but the computational observations were broadly consistent with flight observations. Stationary crossflow calculations indicated an N-factor of 9.5-10 at x=850 mm for condition R1, which was shortly before flow at the shoulder of the test article became turbulent at this station. For condition R4, crossflow N-factors exceeding 14 were predicted for x=850 mm, with N-factors attaining a value of 23 at the end of the cone. These results were consistent with observations of fully laminar flow in flight at condition R1, and fully turbulent at R4.

Tufts et al. [23] executed post-flight linear PSE computations for HIFiRE-5, examining leading edge and crossflow stability. N-factor contours presented a lobed appearance similar to the transition front data. Traveling instabilities dominated the leading edge, and crossflow instability dominated the acreage. By comparing the computed N-factors to flight transition data, Tufts estimated the N-factors at transition on the acreage and leading edge to be 10 and 18, respectively. The acreage flight transition data were affected by model yaw angle, however, so the N=10 value is probably more indicative of conditions where that side of the model was yawed into the wind.

Tufts et al. [23] also executed PSE computations for some post-flight wind tunnel cases. Again, computed N-factor contours resembled the transitional lobes displayed in the wind tunnel tests. The N-factor of 10 that correlated the flight crossflow transition also appeared to correlate wind tunnel crossflow transition. Movement of the N=10 contour with AoA also resembled the transition front movement observed in the wind tunnel with AoA. Moyes, et al. [77] also using linear PSE, determined crossflow N-factors at transition of 5-8 for flight.

Choudhari et al. [24] performed pre-flight stability calculations for HIFiRE-5 at anticipated flight conditions. These calculations included computations of centerline instabilities, as well as attachment line and crossflow. Notably, these computations indicated a strongly unstable leading edge, with N-factors similar to the unstable centerline boundary layer. Given that the leading edge transition in flight occurred at nearly the same Reynolds number as the centerline transition, it seems plausible that the computed stability behavior on these meridians accurately represented flight.

Despite the high amplification predicted for the leading edge in flight, uncontaminated leading edge transition was observed only in CUBRC, where the ratio of wall to stagnation temperature was closer to the flight test. In analogy to the attachment line flow on the cone at angle of attack, it is suspected that cooling is highly destabilizing to the HIFiRE-5 leading edge.

10.7 CONCLUSIONS

Perhaps the most significant conclusion from the HIFiRE-1 and -5 research campaigns was the success of boundary layer stability theory in reproducing transition trends and patterns, implying that the stability calculations and wind tunnel tests reproduced at least some of the transition physics observed in flight. Although boundary layer instabilities were not directly measured in flight, the correlation between flight transition trends and those observed in ground test and computation is persuasive evidence that modal instabilities were responsible for transition in flight. This is not a trivial conclusion. Given the small scale and high frequency expected for these instabilities, it was not clear that the flight environment would provide sufficient excitation to generate them. Although N-factor correlations and ground test were able to replicate some trends from prior hypersonic flight tests, these predictions may have merely been simulants for some other, undetermined, instability process that

occurred in flight. We can now proceed with greater confidence to apply these tools to flight. Although these tools suffer recognized limits, they appear applicable to a wide range of flow scenarios.

The goal of using the HIFiRE flights to calibrate N-factor predictions and ground test was achieved, within the limits of the N-factor transition prediction approach. It is probably unrealistic to expect a single N-factor to correlate transition across a broad range of scenarios. Linear growth represents only a portion of the stability process. Variations in initial amplitudes, receptivity and nonlinear amplification probably all affect the best correlating N-factor. However, given the relatively high transition N-factors attained by the HIFiRE flights, the HIFiRE flight transition N-factors probably represent near-upper limits on attainable N-factors for smooth bodies. Since flight conditions, including disturbance levels and vehicle roughness, may vary from flight-to-flight, a statistical approach to transition prediction is probably warranted.

The subsidiary goal of calibrating ground test transition Reynolds numbers to flight was partially successful. In analogy to calibrating N-factor predictions, this goal was probably somewhat unrealistic, given the myriad parametric effects possible in ground test. This might be rectified in some cases by repeating ground tests with conditions tailored to flight. Despite this, some general conclusions could be reached. Axisymmetric, leeward and crossflow transition all showed lower transition Reynolds numbers or N-factors in the wind tunnel compared to flight. The impact of noise on HIFiRE-5 leading edge transition was not as great as for the other transition scenarios. Windward attachment line transition was an even more dramatic exception. HIFiRE-1 windward transition actually occurred at a lower Reynolds number in flight compared to the wind tunnel. The implication from this observation is that either attachment line transition is not as severely impacted by wind tunnel noise as the other transition mechanisms, or it is exceptionally sensitive to wall temperature differences. For attachment lines, the wind tunnel transition may not represent a “worst case” scenario, and designers should exercise due caution.

10.8 ACKNOWLEDGMENTS

A very large number of organizations and people contributed to the HIFiRE-1 and -5 research programs. The authors wish to thank the AFRL Aerospace Systems Directorate and its precursor organizations, and Ivett Leyva and her predecessors at the Air Force Office of Scientific Research, including John Schmisseur and Pon Ponnapan for their sponsorship. Douglas Dolvin of the AFRL Aerospace Systems Directorate provided program management. Flight tests were executed by the Air Vehicles Division, Brisbane, of the Defence Science and Technology Organisation and the Defence Science and Technology Group, Royal Australia Navy Ranges and Assessing Unit, Aerospace Operational Support Group, Royal Australian Air Force, White Sands Missile Range, DTI/Kratos, and DLR Moraba. Ground test support and analysis was provided by the NASA Langley Research Center, Purdue University, Texas A&M University and CUBRC. Many individuals, too numerous to mention, provided valuable advice and feedback.

10.9 REFERENCES

[1] Dolvin, D., “Hypersonic International Flight Research and Experimentation (HIFiRE) Fundamental Science and Technology Development Strategy,” Paper 2008-2581, AIAA, April 2008.

[2] Dolvin, D., "Hypersonic International Flight Research and Experimentation Technology Development and Flight Certification Strategy," Paper 2009-7228, AIAA, October 2009.

[3] Kimmel, R.L., Adamczak, D., Gaitonde, D., Rougeux, A., and Hayes, J.R., "HIFiRE-1 Boundary Layer Transition Experiment Design," AIAA paper 2007–0534, Jan. 2009.

[4] Wadhams, T.P., MacLean, M.G., Holden, M.S., and Mundy, E., "Pre-Flight Ground Testing of the Full-Scale FRESH FX-1 at Fully Duplicated Flight Conditions," AIAA paper 2007–4488, June 2007.

[5] Johnson, H.B., Alba, C.R., Candler, G.V., MacLean, M., Wadhams, T., and Holden, M., "Boundary Layer Stability Analysis of the Hypersonic International Flight Research Transition Experiments," *Journal of Spacecraft and Rockets*, Vol. 45, No. 2, March-April 2008, pp. 194–204.

[6] Holden, M.S., Wadhams, T.P., and MacLean, M., "Experimental Studies in the LENS Supersonic and Hypersonic Tunnels for Hypervelocity Vehicle Performance and Code Validation," AIAA paper 2008–2505, April 2008.

[7] Kimmel, R.L., "Aerothermal Design for the HIFiRE-1 Flight Vehicle," AIAA paper 2008–4034, June 2008.

[8] Casper, K.M., Wheaton, B.M., Johnson, H.B., and Schneider, S.P., "Effect of Freestream Noise on Roughness-Induced Transition at Mach 6," AIAA paper 2008–4291, June 2008.

[9] Casper, K.M., Wheaton, B.M., Johson, H.B., and Schneider, S.P., "Effect of Freestream Noise on Roughness-Induced Transition for a Slender Cone," *AIAA Journal of Spacecraft and Rockets*, Vol. 48, No. 3, May-June 2011, pp. 406–413.

[10] Kimmel, R.L., "Roughness Considerations for the HIFiRE-1 Vehicle," AIAA paper 2008–4293, June 2008.

[11] Alba, C.R., Johnson, H.B., Bartkowicz, M.D., Candler, G.V., and Berger, K.T., "Boundary-Layer Stability Calculations for the HIFiRE-1 Transition Experiment," *Journal of Spacecraft and Rockets*, Vol. 45, No. 6, November-December 2008, pp. 1125–1133.

[12] Wadhams, T.P., Mundy, E., MacLean, M.G., and Holden, M.S., "Ground Test Studies of the HIFiRE-1 Transition Experiment Part 1: Experimental Results," *Journal of Spacecraft and Rockets*, Vol. 45, No. 6, November-December 2008, pp. 1134–1148.

[13] MacLean, M.G., Wadhams, T.P., Holden, M.S., and Johnson, H.B., "Ground Test Studies of the HIFiRE-1 Transition Experiment Part 2: Computational Analysis," *Journal of Spacecraft and Rockets*, Vol. 45, No. 6, November-December 2008, pp. 1149–1164.

[14] Berger, K.T., Greene, F.A., Kimmel, R.L., Alba, C., and Johnson, H., "Erratum on Aerothermodynamic Testing and Boundary-Layer Trip Sizing of the HIFiRE Flight 1 Vehicle," *Journal of Spacecraft and Rockets*, Vol. 46, No. 2, March-April 2009, pp. 473–480.

[15] Adamczak, D., Alesi, H., and Frost, M., "HIFiRE-1: Payload Design, Manufacture, Ground Test, and Lessons Learned," AIAA paper 2009–7294, Oct. 2009.

[16] Kimmel, R., Adamczak, D., Paull, A., Paull, R., Shannon, J., Pietsch, R., Frost, M., and Alesi, H., "HIFiRE-1 Ascent-Phase Boundary-Layer Transition," *AIAA Journal of Spacecraft and Rockets*, Vol. 52, No. 1, feb 2015, pp. 217–230.

[17] Stanfield, S., Kimmel, R., Adamczak, D., and Juliano, T., "Boundary-Layer Transition Experiment During Reentry of HIFiRE-1," *AIAA Journal of Spacecraft and Rockets*, Vol. 52, No. 3, May-June 2015, pp. 637–649.

[18] Kimmel, R.L., Adamczak, D., Hartley, D., Alesi, H., Frost, M.A., Pietsch, R., Shannon, J., and Silvester, T., "HIFiRE-5b Flight Overview," AIAA paper 2017–3131, June 2017.

[19] Porter, K., Poggie, J., and Kimmel, R.L., "Laminar and Turbulent Flow Calculations for the HIFiRE-5b Flight Test," AIAA paper 2017–3132, June 2017.

[20] Jewell, J.S., Kimmel, R.L., Poggie, J., Porter, K.M., and Juliano, T.J., "Correlation of HIFiRE-5b Flight Data With Computed Pressure and Heat Transfer for Attitude Determination," AIAA paper 2017–3133, June 2017, doi: 10.2514/6.2017-3133.

[21] Juliano, T.J., Poggie, J., Porter, K.M., Jewell, J.S., Kimmel, R.L., and Adamczak, D.W., "HIFiRE-5b Heat Flux and Boundary-Layer Transition," AIAA paper 2017–3134, June 2017, doi: 10.2514/6.2017-3134.

[22] Borg, M.P. and Kimmel, R.L., "Ground Test Measurements of Boundary-Layer Instabilities and Transition for HIFiRE-5 at Flight-Relevant Attitudes," Paper 2017-3135, AIAA, June 2017.

[23] Tufts, M.W., Gosse, R., and Kimmel, R.L., "PSE Analysis of Crossflow Instability on the HIFiRE-5b Flight Test," AIAA paper 2017–3136, June 2017, doi: 10.2514/6.2017-3136.

[24] Choudhari, M., Chang, C.L., Jentink, T., Li, F., Berger, K., Candler, G., and Kimmel, R., "Transition Analysis for the HIFiRE-5 Vehicle," AIAA paper 2009–4056, June 2009, doi: 10.2514/6.2009-4056.

[25] Gosse, R., Kimmel, R., and Johnson, H., "Study of Boundary-Layer Transition on Hypersonic International Flight Research Experimentation 5," *AIAA Journal of Spacecraft and Rockets*, Vol. 51, No. 1, January 2014, pp. 151–162.

[26] Juliano, T.J. and Schneider, S.P., "Instability and Transition on the HIFiRE-5 in a Mach-6 Quiet Tunnel," AIAA paper 2010–5004, June 2010.

[27] Juliano, T.J., *Instability and Transition on the HIFiRE-5 in a Mach-6 Quiet Tunnel*, Ph.D dissertation, Purdue University (West Lafayette), August 2010, School of Aeronautics and Astronautics.

[28] Holden, M., Wadhams, T., MacLean, M., and Mundy, E., "Review of Studies of Boundary Layer Transition in Hypersonic Flows Over Axisymmetric And Elliptic Cones Conducted in the CUBRC Shock Tunnels," AIAA paper 2009-0782, Jan. 2009.

[29] Borg, M.P., Kimmel, R.L., and Stanfield, S., "HIFiRE-5 Attachment-Line Transition in a Quiet Hypersonic Wind Tunnel," Paper 2011-3247, AIAA, June 2011.

[30] Borg, M.P., Kimmel, R.L., and Stanfield, S., "Crossflow Instability for HIFiRE-5 in a Quiet Hypersonic Wind Tunnel," Paper 2012-2821, AIAA, June 2012.

[31] Borg, M.P., Kimmel, R.L., and Stanfield, S., "Traveling Crossflow Instability for HIFiRE-5 in a Quiet Hypersonic Wind Tunnel," Paper 2013-2737, AIAA, June 2013.

[32] Borg, M.P., Kimmel, R.L., Hofferth, J.W., Bowersox, R.D., and Mai, C.L., "Freestream Effects On Boundary Layer Disturbances for HIFiRE-5," Paper 2015-0278, AIAA, January 2015.

[33] Borg, M.P., Kimmel, R.L., and Stanfield, S.A., "Traveling Crossflow Instability for the HIFiRE-5 Elliptic Cone," *Journal of Spacecraft and Rockets*, Vol. 52, No. 3, May–June 2015, pp. 664–673, doi: 10.2514/1.A33145.

[34] Borg, M.P. and Kimmel, R.L., "Simultaneous Infrared and Pressure Measurements of Crossflow Instabiltiy Modes for HIFiRE-5," Paper 2016-0354, AIAA, January 2016.

[35] Borg, M.P. and Kimmel, R.L., "Measurements of Crossflow Instability Modes for HIFiRE-5 at Angle of Attack," Paper 2017-1681, AIAA, January 2017, doi: 10.2514/6.2017-1681.

[36] Berger, K., Ruger, S., Kimmel, R., and Adamczak, D., "Aerothermodynamic Characteristics of Boundary Layer Transition and Trip Effectiveness of the HIFiRE Flight 5 Vehicle," AIAA paper 2009-4055, June 2009.

[37] Lakebrink, M.T. and Borg, M.P., "Traveling Crossflow Wave Predictions on the HIFiRE-5 at Mach 6: Stability Analysis vs. Quiet Tunnel Data," AIAA paper 2016-0356, Jan. 2016.

[38] Kimmel, R.L., Adamczak, D., Berger, K., and Choudhari, M., "HIFiRE-5 Flight Vehicle Design," AIAA paper 2010–4985, June 2010.

[39] Juliano, T.J., Borg, M.P., and Schneider, S.P., "Quiet Tunnel Measurements of HIFiRE-5 Boundary-Layer Transition," *AIAA Journal*, Vol. 53, No. 4, April 2015, pp. 832–846.

[40] Dinzl, D. and Candler, G., "Direct Simulation of Hypersonic Crossflow Instability on an Elliptic Cone," *AIAA Journal*, Vol. 55, No. 6, June 2017, pp. 1769–1782.

[41] Kimmel, R.L., Adamczak, D., Juliano, T.J., and Paull, A., "HIFiRE-5 Flight Test Preliminary Results," AIAA paper 2013–0377, Jan. 2013, doi: 10.2514/6.2013-377.

[42] Juliano, T.J., Adamczak, D., and Kimmel, R.L., "HIFiRE-5 Flight Test Heating Analysis," AIAA paper 2014–0076, Jan. 2014.

[43] Jewell, J., Miller, J., and Kimmel, R., "Correlation of HIFiRE-5 Flight Data With Computed Pressure and Heat Transfer," AIAA paper 2015-2319, June 2015.

[44] Juliano, T.J., Adamczak, D., and Kimmel, R.L., "HIFiRE-5 Flight Test Results," *Journal of Spacecraft and Rockets*, Vol. 52, No. 3, May-June 2015, pp. 650–663, doi: 10.2514/1.A33142.

[45] Schneider, S.P., "Flight Data for Boundary-Layer Transition at Hypersonic and Supersonic Speeds," *Journal of Spacecraft and Rockets*, Vol. 36, No. 1, January-February 1999, pp. 8–20.

[46] Kimmel, R.L. and Poggie, J., "Transition on an Elliptic Cone at Mach 8," American Society of Mechanical Engineers ASME FEDSM97-3111, June 1997.

[47] Kimmel, R.L. and Poggie, J.J., "Three-Dimensional Hypersonic Boundary Layer Stability and Transition," WL-TR-97-3111, Air Force Research Laboratory Technical Report, Wright-Patterson Air Force Base, Ohio, Dec. 1997.

[48] Kimmel, R.L., Poggie, J.J., and Schwoerke, S.N., "Laminar-Turbulent Transition in a Mach 8 Elliptic Cone Flow," *AIAA Journal*, Vol. 37, No. 9, September 1999, pp. 1080–1087.

[49] Schmisseur, J., *Receptivity of the Boundary Layer on a Mach-4 Elliptic Cone to Laser-Generated Localized Freestream Perturbations*, Ph.D. thesis, Purdue University, Dec. 1997.

[50] Holden, M., "Experimental Studies of Laminar, Transitional, and Turbulent Hypersonic Flows Over Elliptic Cones at Angle of Attack," Technical report AFRL-SR-BL-TR-98-0142, Air Force Office of Scientific Research, Bolling Air Force Base, Washington D.C., Dec. 1998.

[51] Schmisseur, J., Schneider, S.P., and Collicott, S.H., "Receptivity of the Mach 4 Boundary Layer on an Elliptic Cone to Laser-Generated Localized Freestream Perturbations," AIAA paper 1998–0532, Jan. 1998.

[52] Schmisseur, J., Schneider, S.P., and Collicott, S.H., "Response of the Mach 4 Boundary Layer on an Elliptic Cone to Laser-Generated Freestream Perturbations," AIAA paper 1999–0410, Jan. 1999.

[53] Lyttle, I.J. and Reed, H., "Use of Transition Correlations for Three-Dimensional Boundary Layers Within Hypersonic Flows," AIAA paper 1995–2293, June 1995.

[54] Li, F., Choudhari, M., Chang, C.L., Kimmel, R., Adamczak, D., and Smith, M., "Transition Analysis for the Ascent Phase of HIFiRE-1 Flight Experiment," *AIAA Journal of Spacecraft and Rockets*, Vol. 52, No. 5, September-October 2015, pp. 1283–1293.

[55] Johnson, H. and Candler, G., "PSE Analysis of Reacting Hypersonic Boundary Layer Transition," AIAA paper 1999-3793, June 1999.

[56] Malik, M., "Hypersonic Flight Transition Data Analysis Using Parabolized Stability Equations with Chemistry Effects," *AIAA Journal of Spacecraft and Rockets*, Vol. 40, No. 3, May-June 2003, pp. 332–344.

[57] Bushnell, D., "Notes on Initial Disturbances Fields for the Transition Problem," *Instability and Transition*, edited by M. Hussaini and R. Voigt, Springer-Verlag, 1990, pp. 217–232.

[58] Fedorov, A. and Tumin, A., "Receptivity of High-Speed Boundary Layers to Kinetic Fluctuations," *AIAA Journal*, Vol. 55, No. 7, July 2017, pp. 2335–2348.

[59] Marineau, E., "Prediction Methodology for 2nd Mode Dominated Boundary Layer Transition in Hypersonic Wind Tunnels," *AIAA Journal*, Vol. 55, No. 2, February 2017, pp. 2335–2348.

[60] Stetson, K., Thompson, E., Donaldson, J., and Siler, L., "Laminar Boundary Layer Stability Experiments on a Cone at Mach 8, Part 1: Sharp Cone," AIAA paper 1983-1761, July 1983.

[61] Jewell, J. and Kimmel, R., "Boundary Layer Stability Analysis for Stetsons Mach 6 Blunt Cone Experiments," *AIAA Journal of Spacecraft and Rockets*, Vol. 54, No. 1, January-February 2017, pp. 258–265.

[62] Stetson, K., "Mach 6 Experiments of Transition on a Cone at Angle of Attack," *AIAA Journal of Spacecraft and Rockets*, Vol. 19, No. 5, September-October 1982, pp. 397–403.

[63] Willems, S., Gülhan, A., Juliano, T., and Schneider, S., "Laminar to Turbulent Transition on the HIFiRE-1 Cone at Mach 7 and High Angle of Attack," AIAA paper 2014–0428, Jan. 2014, doi: 10.2514/6.2014-0428.

[64] Juliano, T.J., Kimmel, R.L., Willems, S., Gülhan, A., and Schneider, S., "HIFiRE-1 Surface Pressure Fluctuations from High Reynolds, High Angle Ground Test," AIAA paper 2014–0429, Jan. 2014.

[65] Juliano, T.J., Kimmel, R.L., Willems, S., Gülhan, A., and Wagnild, R., "HIFiRE-1 Boundary-Layer Transition: Ground Test Results and Stability Analysis," AIAA paper 2015–1736, Jan. 2015.

[66] Stetson, K. and Rushton, G., "Shock Tunnel Investigation of Boundary-Layer Transition at M=5.5," *AIAA Journal*, Vol. 5, No. 5, May 1967, pp. 899–906.

[67] Marineau, E., Moraru, C., Lewis, D., Norris, J., Lafferty, J., Wagnild, R., and Smith, J., "Mach 10 Boundary-Layer Transition Experiments on Sharp and Blunted Cones," AIAA paper 2014-3108, June 2014.

[68] Holden, M.S., "Experimental Studies of the Effects of Asymmetric Transition on the Aerothermal Characteristics of Hypersonic Blunted Slender Cones," AIAA paper 1985–0325, Jan. 1985.

[69] Schneider, S.P., "Effects of High-Speed Tunnel Noise on Laminar-Turbulent Transition," *Journal of Spacecraft and Rockets*, Vol. 38, No. 3, May-June 2001, pp. 323–333.

[70] Holden, M., Bower, D., and Chadwick, K., "Measurements of Boundary Layer Transition on Cones at Angle of Attack for Mach Numbers from 11 to 13," AIAA paper 1995–2294, June 1995.

[71] DiCristina, V., "Three-Dimensional Boundary Layer Transition on a Sharp 8° Cone at Mach 10," *AIAA Journal*, Vol. 8, No. 5, May 1970, pp. 852–856.

[72] Creel, T., Beckwith, I., and Chen, F., "Transition on Swept Leading Edges at Mach 3.5," *Journal of Aircraft*, Vol. 24, No. 10, 1987, pp. 710–717.

[73] Gosse, R. and Kimmel, R., "CFD Study of Three-Dimensional Hypersonic Laminar Boundary Layer Transition on a Mach 8 Elliptic Cone," AIAA paper 2009-4053, June 2009.

[74] Kimmel, R., Adamczak, D., Hartley, D., Alesi, H., Frost, M., Pietsch, R., Shannon, J., and Silvester, T., "HIFiRE-5b Flight Overview," *Accpeted for publication in AIAA Journal of Spacecraft and Rockets*, 2018.

[75] Neel, I., Leidy, A., and Bowersox, R., "Preliminary Study of the Effect of Environmental Disturbances on Hypersonic Crossflow Instability on the HIFiRE-5 Elliptic Cone," AIAA paper 2017-0767, Jan. 2017.

[76] Li, F., Choudhari, M., Chang, C.L., White, J., Kimmel, R., Adamczak, D., Borg, M., Stanfield, S., and Smith, M., "Stability Analysis for HIFiRE Experiments," AIAA paper 2012–2961, June 2012.

[77] Moyes, A., Kocian, T., Mullen, T., and Reed, H., "Boundary Layer Stability Analysis of HIFiRE-5b Flight Geometry," AIAA paper 2017-4301, June 2017.

Chapter 11 - HYPERSONIC CROSSFLOW INSTABILITY

Travis Kocian, Alexander Moyes, and Helen Reed
Texas A&M University
UNITED STATES

Stuart Craig
University of Arizona
UNITED STATES

William Saric
Texas A&M University
UNITED STATES

Steven Schneider and Joshua Edelman
Purdue University
UNITED STATES

11.1 INTRODUCTION

The next generation of flight vehicles will be greatly dependent on the ability to create designs that achieve optimal levels of both mission performance and efficiency. This will require robust systems capable of operating under various flight conditions ranging from the subsonic to hypersonic flow regimes. A determining factor involved in the operation of every vehicle will be the ability to predict, and possibly even control, the onset of laminar-to-turbulent transition. This is complicated by the fact that the transition process itself is extremely complex with a large array of variables that interact with and modify either the receptivity process or the resulting pathways to transition in ways that must be understood [1].

Laminar-to-turbulent transition has significant effects on heat transfer, skin friction, and flow separation. Of particular interest is the desire to delay the transition process over the body of a hypersonic vehicle. The flight environment experienced at these high speeds often results in elevated levels of thermal heating. In severe cases, the heating is capable of reaching conditions that compromise the structural integrity of the surface of the vehicle and potentially even cause loss of control authority. Turbulent flow can produce heating rates that are higher than those of laminar flow by a factor of 6 or more, so a fundamental understanding of the laminar-turbulent transition process is critical for future designs [2]. Also of interest is the ability to trip the flow to turbulence, such as for propulsive efficiency. The most effective strategy for control is to capitalize on the flow physics and identify the relevant instability mechanisms.

Much of the foundation and physical description of the mechanisms and physics involved in hypersonic stability is provided by Mack [3] and Fedorov [4]. In the case of a three-dimensional (3-D) flowfield, several instabilities can be present including attachment-line instabilities, leading-edge contamination, first and second modes, crossflow instabilities, and Görtler instabilities [5]. Some areas of a 3-D flowfield may even see multiple instabilities co-exist at the same location.

Streamlines that are curved under the action of pressure gradients and wing sweep produce a resulting boundary-layer profile that is twisted. An imbalance between the centripetal acceleration and the pressure gradient within the boundary layer results in a flow component that is perpendicular to the direction of the local inviscid streamline. The combination of this flow component with the streamwise velocity results in the creation of a generalized inflection point, which is highly unstable. This situation may lead to the development of co-rotating vortices known as stationary crossflow, which is ultra sensitive to surface roughness. Also, it has been shown that the presence of stationary crossflow leads to early nonlinear distortion of the mean flow and the eventual growth of high-frequency secondary instabilities, leading to breakdown. In addition to stationary crossflow, theory also predicts that traveling crossflow (non-zero frequency) may appear. This mechanism has been measured in some hypersonic experiments, and its role in the crossflow-transition process (especially relative to flight) is still under investigation. Regarding crossflow, decades of collaboration among theory, computations, experiments, and flight tests have resulted in the identification of important factors for subsonic, transonic, and low supersonic flows [6–9].

Relating to transition, many of the first analysis techniques for boundary-layer stability used empirical data or formulated metrics in order to predict the behavior of various flows. The downfall of these methods is that they do not represent any physical processes. A good example of this is the transition location predicted using the parameter $\frac{Re_\theta}{M_e}$. Reshotko [10, 11] has determined the strong influence that density, and by extension altitude, has for this quantity which might be successfully used in correlating the altitude at which a given reentry vehicle will transition. However, $\frac{Re_\theta}{M_e}$ does not provide accurate trends involving Mach number, and it ignores important effects such as surface roughness, pressure gradients, and surface temperature. For cruise vehicles flying at constant altitude, this quantity is not relevant in helping to determine the x location of transition. A second example of a parameter that uses only the basic-state flowfield around a geometry to predict transition is the crossflow Reynolds number. This quantity is used for 3-D flows that are dominated by the stationary crossflow disturbance, such as on conical shapes. Reed & Haynes [12] emphasize caution when using this parameter to develop a correlation beyond the database involved in its formulation, as the crossflow Reynolds number is limited in applicability on general geometries. Even for relatively simple geometries, a large scatter is observed when a correlation is attempted using a moderately wide-ranging dataset [13].

A method which attempts to correlate transition location with the integrated growth of a linear stability analysis, known as the Smith-Van Ingen e^N method [14], has shown promising agreement with a variety of two-dimensional (2-D) experiments that consisted of a generally low level of environmental noise [15, 16]. This method, however, neglects the effects of receptivity, multiple mode interactions, and nonlinear effects. There is no constant value that exists that can be successfully applied to all generic cases in order to predict the location of transition. Changing to a new geometry or environment, such as to a different wind tunnel or to a flight situation, typically requires that a new value of N be used in order to align with the physically seen transition location.

Modern techniques, such as direct numerical simulations (DNS) and the nonlinear parabolized stability equations (NPSE) [17], have advanced to the point of being able to model the nonlinear development of stationary crossflow on a wide range of generic geometries. While a linear evaluation can be very useful and insightful in describing the relative growth of disturbances as long as laminar flow is maintained, a linear analysis is unable to properly model disturbance behavior under high amplitude conditions with large nonlinear effects. For example, in the latter stages of crossflow development, DNS is capable of producing the heat streaks seen in experiments [18, 19]. At the same time, NPSE can show the region of nonlinear saturation and captures the effect on skin-friction coefficient. Properly accounting for disturbance amplitude and interactions with other mechanisms present in the flowfield will lead to more accurate transition prediction criteria.

General conical geometries are proving to be important models in the study of hypersonic transition providing a wealth of information on the various relevant mechanisms associated with hypersonic design. For example, investigations of these geometry shapes at zero degrees angle of attack (AoA) have shown that the transition point moves with varying nose bluntness [20, 21], and Hofferth et al. [22] and Kocian et al. [23] captured the extreme sensitivities of the stability characteristics to model alignment in experiments. Continued and complementary research involving hypersonic experiments at yaw have identified multiple modes associated with different regions within a 3-D flowfield, including crossflow [24–27].

The challenges associated with hypersonic boundary-layer transition are multifaceted with many sensitivities from freestream effects, operating conditions, geometry, and surface conditions. Such a task requires the collaborative efforts of both experiments and computations in order to continue to progress the physical understanding of the various mechanisms and pathways to transition. The current study combines the efforts of two quiet wind tunnel experiments and a computational parabolized stability equations (PSE) analysis. This work is based on the findings of Kocian et al. [28]. Communication between the groups has been vital in ensuring the production of a converged set of conditions, measurements, and assumptions, and the combination of different facilities and PSE have shown to be highly complementary of one another in the analysis of the stationary crossflow instability at hypersonic speeds.

11.2 OBJECTIVES

As hypersonic flight-capable vehicles feature 3-D boundary layers, understanding, modeling, and controlling crossflow (and other associated) instabilities is of critical importance. This is combined with the need to reduce the uncertainty in knowing whether the flow is laminar or turbulent and how to either efficiently delay or enhance transition. The present authors, bringing both computational and experimental capabilities, are working together to determine relevant mechanisms and effects and, in the process, develop and validate physics-based models for the community. The geometry selected for this work is the generic 7° half-angle yawed straight cone which produces strong crossflow disturbances for study.

Experiments were conducted under quiet flow conditions in a range for which stationary crossflow reached the highly amplified and nonlinear stages of development. Table 11-1 shows the resulting flow conditions for the experiments as well as the corresponding computations.

Table 11-1: Comparison of Various Computational and Experimental Flow Variables used in the Present Analysis of the Yawed Straight Cone.

Flow Quantity	TAMU Experiments	Purdue Experiments	TAMU Computations
Re' $(10^6/\text{m})$	10.0	9.8	10.1
M	5.91	6	6
AoA (°)	5.6	6	6
T_∞ (K)	53.85	$50.0 - 51.83$	53.42
P_∞ (Pa abs.)	622.63	524.02	611.38
T_w (K)	400	300	300

The following sections will outline the progress made and key takeaways for research performed in the Boeing/AFOSR Mach-6 Quiet Tunnel (BAM6QT) at Purdue University, the Mach 6 Quiet Tunnel (M6QT) at Texas

A&M University (TAMU), and Euonymous Parabolized Instability Code (EPIC) computations from the Computational Stability and Transition (CST) laboratory at TAMU. Emphasis will be placed on findings for the primary stationary crossflow disturbance as well as disturbances measured within the vortex distorted flowfield. Comparisons between computations and experiments are made directly to validate the computational tools and provide physical explanations for the behavior seen in the wind tunnels. Measurement techniques, details of experimental setups, and methods of modeling the disturbance numerically are presented and may be used as guidance for any follow-on study involving the yawed cone, other configurations, or any application of the methodology to future endeavors.

11.3 EXPERIMENTS AT TEXAS A&M UNIVERSITY

11.3.1 Capabilities

11.3.1.1 Mach 6 Quiet Tunnel

Experiments were performed in the Mach 6 Quiet Tunnel at Texas A&M University. The facility was the result of an extensive design process at NASA Langley Research Center [29, 30] and was transferred to TAMU in 2005. The facility underwent an extensive recommissioning process and was shown by Hofferth et al. [31] to match its previous performance, featuring freestream fluctuation levels of $p'_{t2,rms}/p_{t2} \leq 0.05\%$ in the quiet core. For the present experiments, the tunnel was operated at $p_{t1} = 900$ kPa and $T_t = 430$ K, corresponding to $Re' = 10.0 \times 10^6$/m.

11.3.1.2 Cone Model

Experiments were performed on a right-circular cone with a semivertex angle of 7° (Figure 11-1). The TAMU model is 0.430 m in length and features a removable tip comprising the first 0.155 m. The model is internally heated in order to enforce an adiabatic wall condition. Measured wall temperatures varied from $T_w/T_{aw} \approx 0.99$ over the majority of the model and $T_w/T_{aw} \approx 0.96$ near the base. The model was placed at $5.6°$ yaw in the tunnel such that approximately the first 0.28 m of the model was located in the quiet core. The downstream portion was exposed to the high-noise region outside of this core. Based on the results, the high-noise region had little to no influence on the results of the study [27].

11.3.1.3 Measurement Technique

Measurements were made using a constant-temperature hot-wire anemometer (CTA) system. The temperature loading factor was set high ($\tau \approx 0.8$) such that the probes were sensitive primarily to mass flux [32, 33]. Probes were built in house and tuned in situ. A normalized calibration was applied in order to assign a normalized mass-flux value to each data point. The probe was positioned throughout the boundary layer using a custom-built traverse operating in cylindrical coordinates. Details of this system are given by Craig & Saric [27]. The

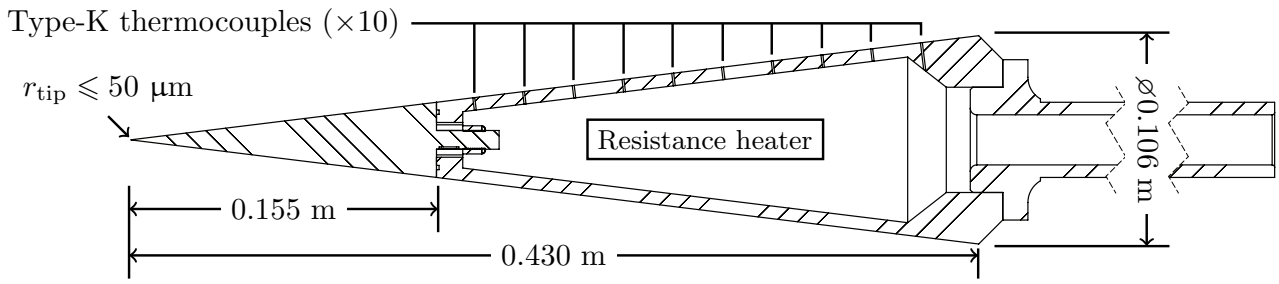

Figure 11-1: Schematic of the TAMU 7° Cone Model with Internal Heating (Image Attributed to Craig & Saric [27]).

traverse was used to move the probe in three dimensions about the model and generate contours of normalized mass flux at various locations along the cone axis.

11.3.2 Important Takeaways and Lessons Learned

The results of this study are summarized in depth in Craig & Saric [27], however, there were several key results. It is noted that the referenced work in this section used a cylindrical coordinate system where z was along the cone axis and is equivalent to x in the present work.

11.3.2.1 Qualitative Similarity to Low-Speed Flows

Crossflow instability is broadly and qualitatively very similar to its counterpart in low-speed flows. The stationary wave structure takes on the same overall shape as the low-speed case, albeit typically at larger wavelengths compared to δ. Figure 11-2 shows the first observation of the rollover of the crossflow vortices in a hypersonic flow. These stationary vortices cause $O(1)$ disturbances to the mean flow and lead to inflected profiles, both in r and in , and secondary instability. This similarity in the stationary structure is not unexpected due to insensitivity of the fundamental mechanism to Mach number. Quantitatively, however, these flows are quite different.

11.3.2.2 Quantitative Differences From Low-Speed Flows

Despite the qualitative similarities between low-speed and hypersonic crossflow, their quantitative behavior differs quite markedly. The type-I secondary instability in the hypersonic experiment is already measurable when the stationary wave saturates (Figure 11-3) and does not grow explosively.

This behavior may be explained by two plausible explanations. First, a brief period of neutral behavior is not unprecedented, as previously observed at low speeds by White & Saric [34]. However, if these experiments represented a hypersonic realization of this phenomenon, then it must play out over a ΔRe_x of at least an order of magnitude greater than the low-speed case. Alternatively, the behavior may turn out to be qualitatively different

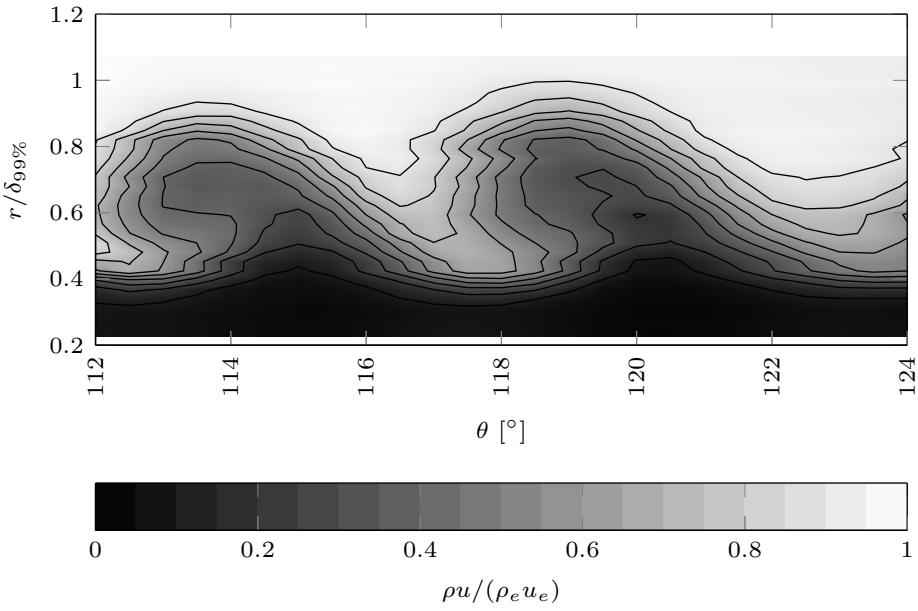

Figure 11-2: Contour of Normalized Mean Mass Flux Taken at $Re_x = 3.7 \times 10^6$ ($x = 0.370$ m) (Image Attributed to Craig & Saric [27]).

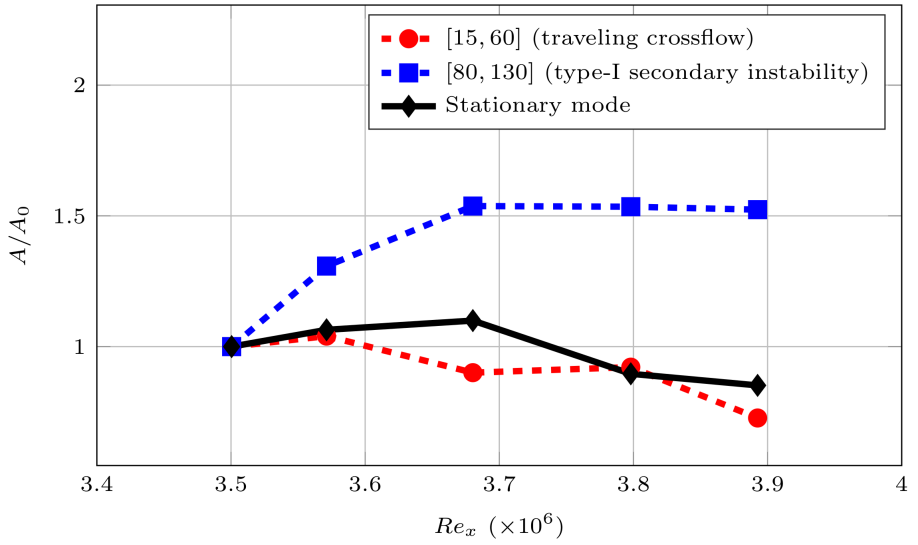

Figure 11-3: Mode Growth for Three Observed Modes. Amplitudes are Normalized by their Values at the Most Upstream Station (Image Attributed to Craig & Saric [27]).

from the low-speed case, where the onset of secondary instability portends rapid breakdown to turbulence. In either case, experiments will need to reach larger Re_x in order to explore which explanation is correct.

11.3.2.3 Effect of Tunnel Noise on Stability Behavior

Approximately half of the downstream portion of the measurement region in this experiment was subjected to elevated levels of freestream noise due to nozzle-wall transition. In order to affect the measurements, this noise must be linearly superposed or interacting nonlinearly with one of the modes. The noise typically has $f < 100$ kHz [22], which overlaps primarily with the traveling wave at these conditions, so a linear superposition would be expected to be primarily visible in this signal. The traveling wave signal does exhibit a small upward bump where the higher noise levels begin, though the effect is small. It was not possible to determine whether this is due to the freestream noise or was a feature of the instability. A bispectral analysis was also performed, and no evidence of nonlinear interaction was observed with any of the measured modes.

Without any other known mechanism of interaction with the unstable waves, it is therefore unlikely that heightened freestream noise plays a major role in crossflow-dominated transition as long as it occurs sufficiently downstream of the receptivity region.

11.4 EXPERIMENTS AT PURDUE UNIVERSITY

11.4.1 Capabilities

11.4.1.1 Purdue University Boeing/AFOSR Mach-6 Quiet Tunnel

The Boeing/AFOSR Mach-6 Quiet Tunnel at Purdue University is critical to the study of the hypersonic crossflow instability. The BAM6QT is a cold-flow Ludwieg tube with several special design features that maintain a laminar boundary layer on the nozzle wall. These features eliminate the large amounts of acoustic radiation introduced into the core flow from a turbulent boundary-layer's fluctuating displacement thickness. The expansion section is polished to a mirror finish and is elongated to reduce the growth of the Görtler instability. In addition, the boundary layer in the contraction is removed through a bleed slot just before the throat, enabling a fresh laminar boundary layer to form in the nozzle expansion.

The BAM6QT could maintain quiet Mach 6 flow up to $Re' = 12 \times 10^6/\text{m}$ for many years until the end of 2016, when performance dropped slightly to a maximum quiet Reynolds number of $Re' = 9.8 \times 10^6/\text{m}$. Multiple publications provide more information on the design and performance of the BAM6QT [35–37]. One important attribute of the BAM6QT is that the flow is quiet past the end of the nozzle to the maximum quiet pressure. This means that the nonlinear breakdown of instabilities on a model occurs under fully quiet conditions. Additionally, the BAM6QT can be run in noisy mode by closing the bleed valve. This allows a direct comparison between noisy and quiet flow in a single test facility.

Experiments in the BAM6QT make use of a range of instrumentation to measure boundary-layer transition. Temperature-sensitive paint (TSP) and infrared (IR) thermography can be used to measure the global temperature and heat-flux distributions on the model. PCB Piezotronics and Kulite pressure transducers are used to measure surface pressure fluctuations.

11.4.1.2 History of Crossflow Research At Purdue

Erick Swanson was the first student to study the crossflow instability in the BAM6QT [38]. He used oil-flow visualization and temperature sensitive paint to observe the developed stationary crossflow vortices. The vortices were measured in both noisy and quiet flow. Christopher Ward and Ryan Henderson continued Swanson's work. Ward [39] created interchangeable roughness inserts to be placed near the nosetip of the cone. These roughness inserts comprised patterns of discrete roughness elements which could be used to generate strong stationary crossflow vortices. Ward also measured traveling crossflow waves and their interaction with the stationary vortices. Henderson [40] focused on the stationary and traveling crossflow instabilities on cones at low angles of attack. Together, Ward and Henderson made the first measurements of a high-frequency secondary instability of the stationary crossflow waves using surface pressure sensors [25, 41].

11.4.2 Important Takeaways and Lessons Learned

Current work at Purdue has two thrusts. The first is to quantify the amplitudes of the stationary vortices using surface heat-transfer measurements. If the amplitude of the stationary vortices can be accurately described using surface heat-transfer, it will enable better computational comparisons. The amplitude of the stationary vortex is a critical input parameter to secondary instability studies and, therefore, to numerical investigations of turbulent breakdown for this flow. The second thrust at Purdue is to measure the nonlinear breakdown of the secondary instabilities in an attempt to create a mechanism-based transition prediction method for the stationary crossflow instability. At Purdue, all current crossflow measurements are taken on a 7° half-angle sharp circular cone at 6° angle of attack.

11.4.2.1 Stationary Vortex Measurements

Progress has been made in repeatably generating stationary vortices with isolated, patterned roughness elements near the nosetip. For more information, see Edelman [42] and Edelman & Schneider [43]. Figure 4 from Edelman [43] is reproduced here as Figure 11-4 and shows five runs under Mach 6 quiet flow with stagnation pressure $p_0 = 120 - 155$ psia. The vortex amplitude here is defined from the heat transfer as $A = q_{pp}/q_{mean}$, i.e. the peak-to-peak heat transfer on a single vortex normalized by the mean heat transfer across the vortex. This is not necessarily the ideal definition of the amplitude, and research is ongoing into better quantification.

In Figure 11-4, the amplitude starts at a low and roughly constant value near 20% of the mean heat transfer. It is possible that any growth of the vortex up to this point is obscured by a noise floor at 20%. TSP measurements, especially of low-amplitude features, can be relatively noisy. At an Re_x of about 3.5×10^6, the heat transfer starts to increase from the noise floor, reaching a peak of around 50% of the mean heat transfer level before decaying. Qualitatively, this behavior is similar to computations by Choudhari et al. [44], and quantitative comparisons are ongoing.

Current work is focused on calculating heat transfer from IR thermography. Preliminary results using IR appear to have lower noise or more clearly defined temperature peaks, but a robust heat-transfer reduction process is not yet available.

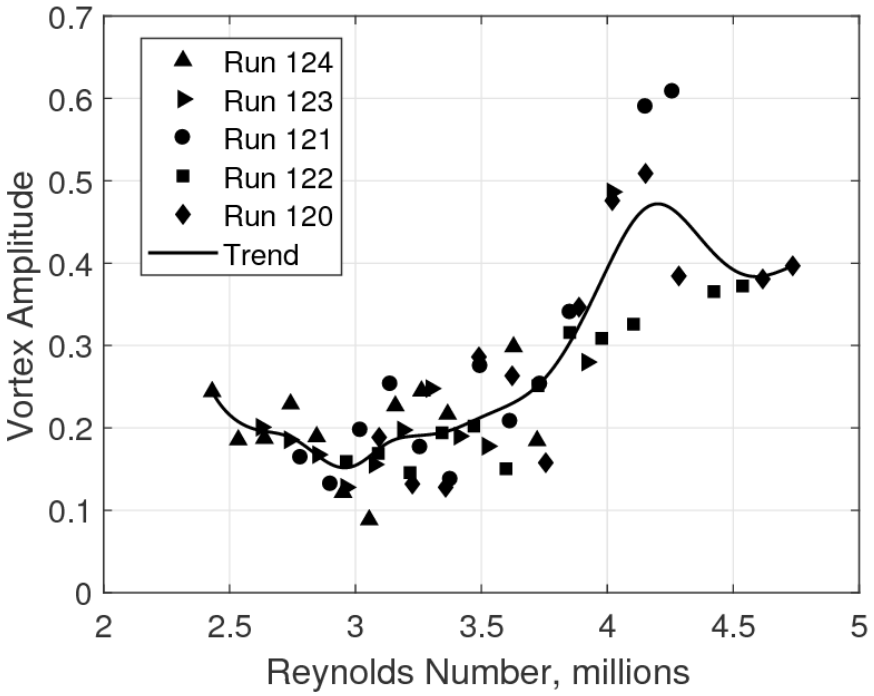

Figure 11-4: Vortex Amplitude Calculated from TSP-Inferred Heat Transfer Along a Single Vortex.

11.4.2.2 Secondary Instability Measurements

Many measurements have been made of the growth and breakdown of the secondary instabilities [42]. Figure 11 from Edelman & Schneider [43] has been reproduced here as Figure 11-5, and points of interest are connected to a possible boundary-layer state in the cartoon below the plot. These different states represent I: a region of growth and saturation of the vortex, II: the location where the secondary instability first appears and grows linearly, III: where turbulent intermittency begins, IV: the peak amplitude of the secondary instability, and V: a fully turbulent boundary layer (intermittency becomes 1). The amplitudes of the stationary vortex and secondary instability are shown along with the turbulent intermittency of the wall pressure signal. In this case, the secondary instability reaches a peak amplitude of about 15% of the local edge pressure at the same time that the stationary vortex peaks. The intermittency rises to 1 soon after the peak.

With a new model and measurement technique, fully described in Edelman [42], a map can be made of the surface pressure fluctuations associated with the secondary instability. Figure 11-6a shows an unwrapped IR image of the cone during a run. The streaks are the footprints of the stationary vortices. Figure 11-6b shows the map of the secondary instability pressure fluctuations. This map is made using several runs at the same Reynolds number with sensors at different locations and interpolating between the data points. The roughness elements used to generate the stationary vortices were in the same orientation for all the runs. There is a clear streaky pattern to the growth of the secondary instability, with lobes of high amplitude inclined at the same angle as the stationary vortices (note the azimuthal scale is different for 11-6a and 11-6b).

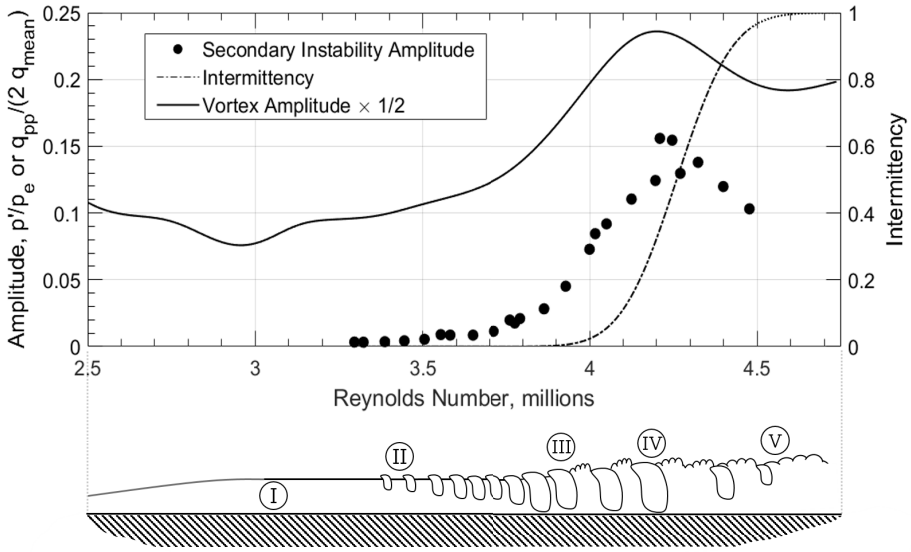

Figure 11-5: Comparison of the Primary and Secondary Instability Amplitude Developments.

The amplitudes shown in Figure 11-6b were calculated in a 200 kHz band centered on the peak frequency at each measurement point. The peak frequencies themselves are shown in Figure 11-6c. The same streaky behavior is observed in the frequencies, with higher frequencies concentrated in the same locations as the hot streaks in the IR. These correspond to the thin troughs between stationary vortices. The low-frequency lobes concentrate under the cold streaks in the IR which align with the upwellings of the vortices. In this case, the amplitude growth mostly occurs for the low-frequency modes between the hot streaks.

11.5 COMPUTATIONS AT TEXAS A&M UNIVERSITY

11.5.1 Capabilities

11.5.1.1 EPIC

EPIC is a quasi 3-D nonlinear parabolized stability equations capability developed at Texas A&M University that is capable of marching multiple disturbances and modeling the nonlinear interactions between them. In addition, EPIC accounts for the nonparallel and curvature effects of the boundary layer and geometry. A unique capability allows the spanwise wavelength of 3-D disturbances to evolve based on the local flowfield as they progress downstream along a marching path. The stability code is written in general orthogonal curvilinear coordinates and utilizes harmonic balancing to identify the nonlinear modal interactions. As well, the capability to run single disturbance linear stability theory (LST) and linear parabolized stability equations (LPSE) analyses are included within the EPIC code.

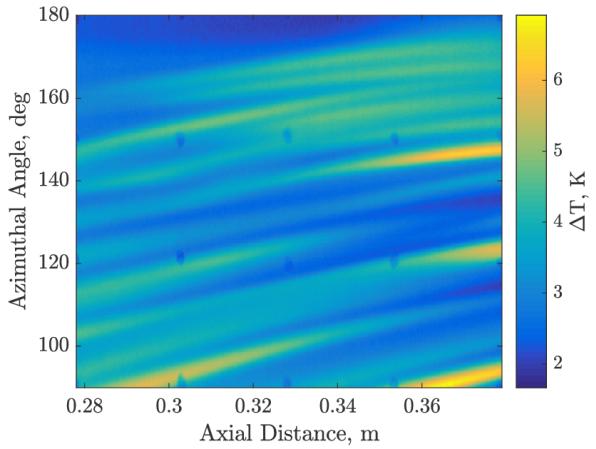

(a) Unwrapped IR Image of the Cone During a Run. Flow is from Left to Right.

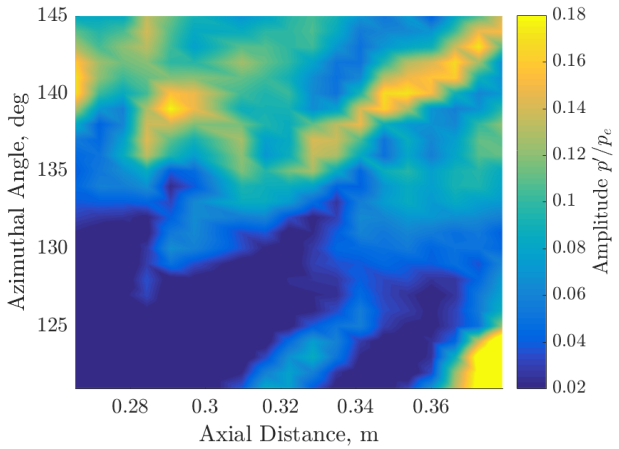

(b) Map of Surface Pressure Fluctuation Amplitudes Normalized by the Local Edge Pressure.

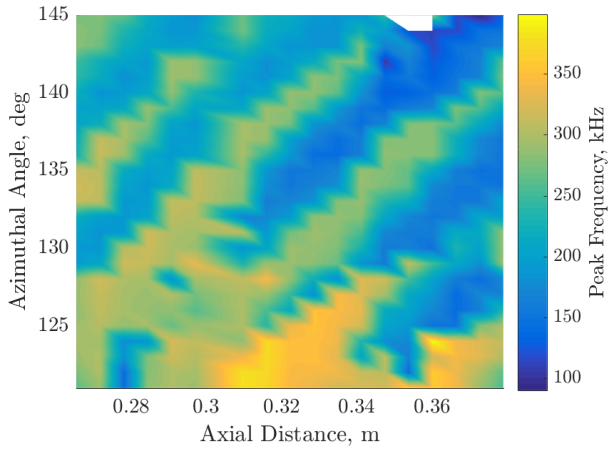

(c) Map of Peak Frequencies in the Pressure Spectra.

Figure 11-6: Quantities of Interest on a Pitched Cone, Unwrapped to an Axial-Azimuthal Grid.

For an NPSE analysis, the evolution of disturbances in the boundary layer is described by the disturbance equations that are obtained by decomposing the total flow into a basic state plus a disturbance and assuming that the basic state is a solution to the original equations of motion. Equation (11–1) shows the representation of disturbances for an NPSE calculation.

$$\phi'(\xi,\eta,\zeta,t) = \sum_{n=-\infty}^{\infty}\sum_{k=-\infty}^{\infty} \frac{A_{0_{(n,k)}}}{2}\hat{\phi}_{(n,k)}\left(\tilde{\xi},\eta\right) e^{i\left(\int \alpha_{(n,k)}(\tilde{\xi})\partial\xi + k\beta\zeta - n\omega t\right)} \tag{11–1}$$

Decomposing the flow in this manner allows a PSE (LPSE or NPSE) study to be conducted for varying initial disturbance conditions without needing to repeatedly solve the steady-state laminar basic-state flowfield.

Moreover, being a marching solution allows for computations to be performed at a fraction of the cost of methods such as DNS. The savings in computational time and resources is a critical advantage of using NPSE over more expensive methods, and the solutions have been shown to accurately reproduce crossflow in real flows [45]. NPSE is also capable of modeling the evolution of finite-amplitude disturbances, which is an important necessity because of the early onset of nonlinear effects displayed by stationary crossflow.

An in depth description of EPIC including the fundamental equations and assumptions is described in Oliviero [46]. Multiple geometries and a wide range of 2-D and 3-D instability mechanisms have been studied using the stability solver. Kocian et al. [23] validated LPSE calculations on a flared cone focusing on the second-mode mechanism with wind tunnel tests performed in the Texas A&M Mach 6 Quiet Tunnel. The second-mode mechanism was shown to be very sensitive to model alignment. Misalignment will create a discrepancy in boundary-layer thickness on opposite sides of a symmetric model, resulting in different frequencies becoming most amplified. Measuring this peak second-mode frequency is a recommended technique for experiments to align their models due to this sensitivity. Traveling and stationary crossflow have also been heavily examined for conical geometries, including circular and elliptic cones [27, 43, 47–50]. Stationary crossflow under both tunnel and flight flow conditions formed an amplification front that was strongest in regions of large spanwise pressure gradient and caused high frequency unstable secondary instabilities to develop within a highly nonlinear crossflow vortex [49]. The onset of secondary instabilities and increase in surface shear stress also aligned with transition location measurements taken from the recent HIFiRE-5b flight test [50].

11.5.1.2 Spatial Biglobal

In the study of secondary instabilities of nonlinearly distorted stationary crossflow, the ζ-direction gradients of the basic state are of the same order as the wall-normal variations. The analysis of such a modified basic state requires a multi-dimensional stability analysis. Spatial biglobal (SBG) analysis is the 2-D analogue of the classic spatial linear stability theory and resolves two inhomogeneous directions simultaneously on a plane while assuming the third direction is locally homogeneous or quasi-parallel. The disturbance quantities take the form

$$\phi'(\xi,\eta,\zeta,t) = \hat{\phi}(\eta,\zeta)e^{i(\alpha\xi-\omega t)} + c.c. \tag{11–2}$$

A complete review of multi-dimensional and global stability analysis techniques is given by Theofilis [51]. The present SBG code accompanying the EPIC solver was developed at Universidad Politécnica de Madrid, and details are provided by Paredes [52] and Paredes & Theofilis [53]. The SBG code has been used to detect secondary and other instability mechanisms in a modified base flow initially computed with a primary stationary crossflow disturbance in EPIC. These computations show the presence of four unstable mechanisms and the dominance of the type-I and type-II secondary instabilities [48].

11.5.2 Important Takeaways and Lessons Learned

11.5.2.1 Grid Architecture and Resolution

The very first step of any PSE analysis is to generate a converged and accurate base flow. Structured grids tend to be favored due to the accuracy advantage over an equally dense unstructured grid. It is also important to place a sufficient number of cells in regions associated with high gradients such as near the shock and boundary layer. Stability calculations have been shown to be very sensitive to variances in basic-state flow profiles. In the hypersonic flow regime, the boundary layers undergo very large changes within a height that is typically very small, and one needs to be sure that these values are highly resolved.

The yawed straight cone being used for this analysis has a length of 0.508 meters (20 inches) and half-angle of 7°. The structured grid used in the calculation of the basic state contains 369 points along the axial direction, 425 in the off-wall direction, and 399 azimuthally. Only half of the cone was modeled in order to take advantage of the symmetry of the flow and reduce computational cost. Details of the freestream conditions are provided in Oliviero et al. [54] and are listed in Table 11-1. Stability characteristics appear to be more sensitive to changes in grid density and architecture than flow values such as pressure. For this reason, the basic state is assumed to be converged once LPSE N-factors converge for different grids. A convergence study was performed by Kocian [55] for a representative conical geometry with a 3-D flowfield, and it was shown that placing $70 - 100$ points within the boundary layer of a grid with a similar cell count proved sufficient in obtaining an N-factor that varied by less than 1%.

11.5.2.2 Importance of Disturbance Path

The PSE method is a marching procedure and thus requires a defined path along which to march. Most commonly, inviscid streamlines are used as representative disturbance paths for Mack modes, stationary and traveling crossflow, and so forth. Extracting streamlines is relatively simple, but they are only a general approximation to use for disturbance trajectories.

For the stationary crossflow instability, a method has been devised which uses the mass flux of the basic-state quantities. Originally inspired by Kuehl et al. [56], the current method physically aligns the crossflow vortex paths such that the generalized inflection point, $\frac{\partial}{\partial \eta}\left(\bar{\rho}\frac{\partial \bar{w}}{\partial \eta}\right) = 0$, occurs at $\bar{\rho}\bar{w} = 0$. Here, $\bar{w}$ is the basic-state velocity component in the direction tangent to the surface and perpendicular to the marching direction. For hypersonic flow, this generalized inflection point within the boundary layer provides a dynamic (highly unstable) instability mechanism [3]. The exciting part of this method is that the direction of marching is predicted solely from the undisturbed basic-state profiles of a 3-D geometry prior to doing a stability analysis.

A comparison is made with the DNS results of Balakumar & Owens [18] and Gronvall et al. [19] for the yawed straight cone geometry. Balakumar & Owens generated stationary crossflow vortices with a ring of 40 periodically placed roughness elements while Gronvall et al. generated crossflow with a patch of random roughness near the windward portion of the cone. With $= 0^{\circ}$ and $= 180^{\circ}$ corresponding to windward and leeward, respectively, Figure 11-7a shows a comparison of the DNS paths along with the computed inflection-point paths.

The paths based on the generalized inflection point appear to agree well with the Gronvall et al. trajectories provided. The paths also agree well with those of Balakumar & Owens near the leeward plane, however there exists some deviation near the windward plane. The discrepancy is believed to be caused by the means with which the disturbances are created. It is possible that the discrete roughness elements may be locally modifying the basic state in a manner that influences the downstream progression of the crossflow vortices. Figure 11-7b then directly compares the various trajectory types used in PSE with the Balakumar & Owens DNS and shows the improvement of following the generalized inflection point over inviscid streamlines.

Streaks from stationary crossflow were observed using IR thermography in the BAM6QT and data corresponding to the disturbance trajectories were provided from Figure 11-6a. The range of experimental data was limited to the portion of the model visible through the viewing window. Crossflow vortices for the experiment were generated using 12 individual roughness elements spaced 9° apart. If extrapolated, this distribution would be equivalent to 40 elements around the full cone circumference. Figure 11-7c shows a comparison of paths calculated with the inflection-point method and those extracted from the IR images of the experiments.

The paths show excellent agreement with one another in the region available from the experiments. While one would not expect the data extracted from a wind tunnel experiment to be as smooth as data obtained numerically, the paths appear to have comparable slopes and trends with those predicted using the inflection-point method. In addition to providing an accurate path for modeling the evolution of the instability, the ability to predict the paths of the crossflow vortex can also be used to help define the optimal location for sensors in future experiments.

11.5.2.3 Modeling Crossflow Spanwise Wavelength

In a PSE analysis, assumptions are required in order to model the components of the spanwise wavenumber β. The imaginary part of the wavenumber is typically assumed to be zero, which signifies that all of the disturbance growth is occurring in the marching direction. This leaves the real portion of the spanwise wavenumber to be addressed which directly defines the spanwise wavelength of the disturbance at all stages along the disturbance path.

For the crossflow instabilities, a new method is proposed to model the spanwise wavelength while accounting for physical effects such as pressure gradient and the shape of the geometry. This is a generalization of a previous practice [54], and the new method assumes that if two crossflow waves are propagating downstream along two neighboring paths, then the change in surface distance, s, between the paths is indicative of the behavior of the wavelength. This value will change with each axial station as the two paths either approach each other or separate. By utilizing the ratio of the local distance with respect to that of the original position, a scale can be applied to the spanwise wavelength, λ, of any disturbance input into the PSE stability calculations. The definition of this scale factor, χ_2, is depicted in Equation (11–3).

$$\begin{aligned} \beta &= \frac{2\pi}{\lambda_0 \chi_2} \\ \chi_2 &= \frac{s_\perp}{s_{\perp_0}} \end{aligned} \tag{11–3}$$

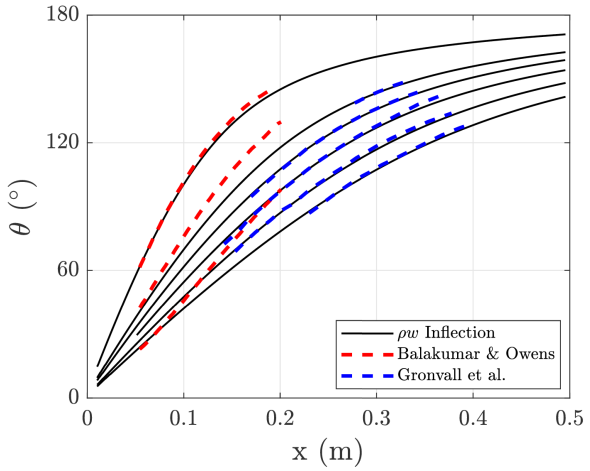

(a) Inflection-Point Method Paths and DNS Trajectories.

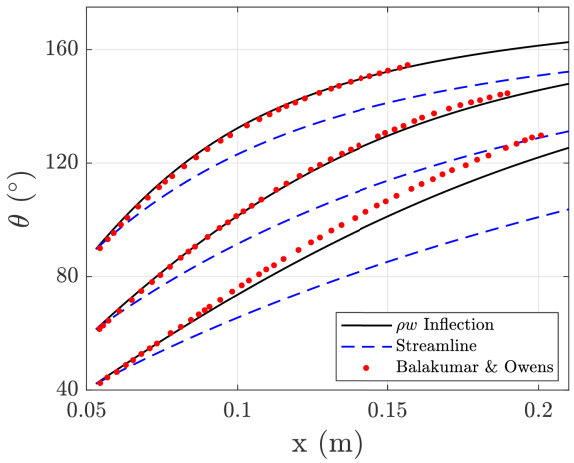

(b) Different Path Types and DNS Trajectories.

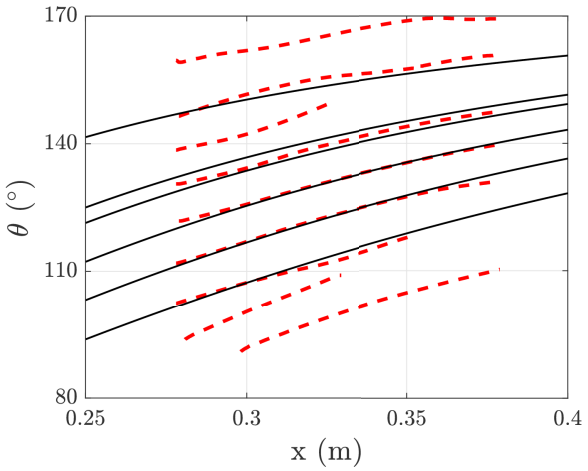

(c) Inflection-Point Method Paths (Black Lines) and Purdue Experiment Paths (Red Dashed Lines) (Figure 11-6a).

Figure 11-7: Verification and Validation of Inflection-Point Paths.

In order to satisfy the irrotationality condition of the wave, a correction is made to the local radius of curvature, $R_{\perp}$, as seen in Equation (11–4). This correction ensures that the total number of waves, k_c, that would be applied around the full geometry remains constant.

$$\begin{aligned} k_c &= \beta R_{art} \\ R_{art} &= R_{\perp_0} \chi_2 \end{aligned} \tag{11–4}$$

The scale factor is computed for three vortex paths from the yawed straight cone and converted to a local wavenumber using the ring of 40 roughness elements in the Balakumar & Owens [18] DNS as reference. Figure

11-8 compares the locally computed wavenumber with the number of waves extracted from three similar paths in the DNS. Of note is that the difference in compared wavenumbers is largest for path 3. This path is closest to the windward plane, and one would expect the discrepancy between the DNS paths and inflection-point paths in this region to influence the predicted wavenumber value.

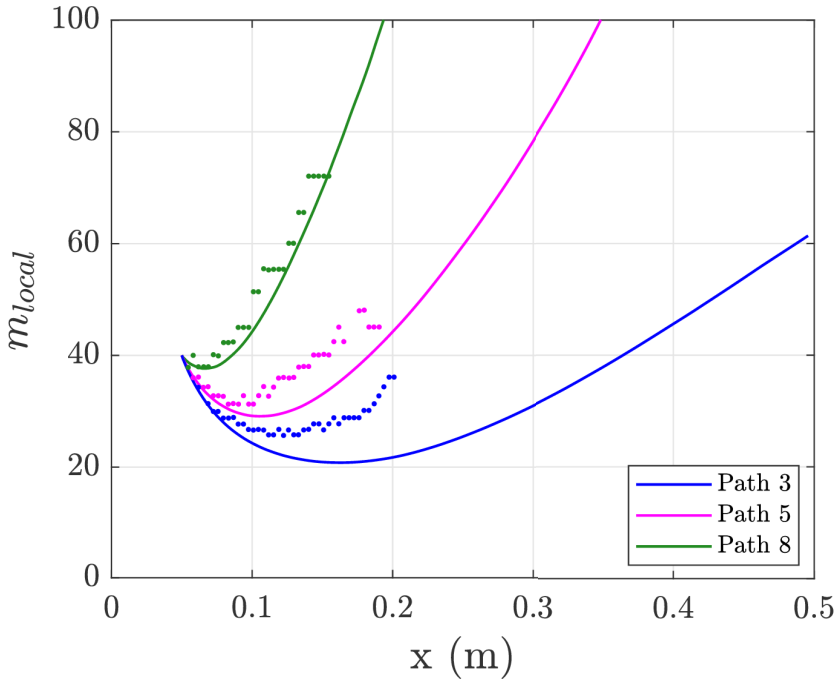

Figure 11-8: Predicted Number of Waves in Azimuthal Direction vs. DNS.

Further efforts were placed in validating the new method of modeling the spanwise wavelength. Craig & Saric [27] performed experiments on the same geometry under similar conditions and obtained hot-wire measurements of the stationary crossflow disturbance. The experiment geometry consisted of natural roughness and saw a local disturbance wavelength that would produce approximately 60 waves around the cone azimuth at measurement locations between $0.36 - 0.38$ meters and $\theta = 118^{\circ}$ from the windward plane. An LPSE analysis using χ_2 achieved a most amplified disturbance with a wavenumber of 57 at the measurement location. This solution is shown in Figure 11-9 and is in excellent agreement with the estimated number of waves from the experiment.

NPSE calculations were performed for stationary crossflow such that the local azimuthal wavenumber was 60 at the three locations of comparison. Disturbances were initialized at an axial location of $x = 0.2$ meters with u-amplitudes of 3×10^{-4} based on U_e. As the upstream condition from the experiments was unknown, this value was iterated to best match the resulting computational flowfield with the experimental flowfield. The flowfield was reconstructed by combining the velocity and density disturbances with the basic state and conducting a series of coordinate transformations to be consistent with the experimental measurements. Contours of ρu mass flux are shown in Figure 11-10 alongside experimental measurements where the top, center, and bottom images represent $x = 360$ mm, $x = 370$ mm, and $x = 380$ mm, respectively. The data for the center contour from the experiment is identical to that of Figure 11-2.

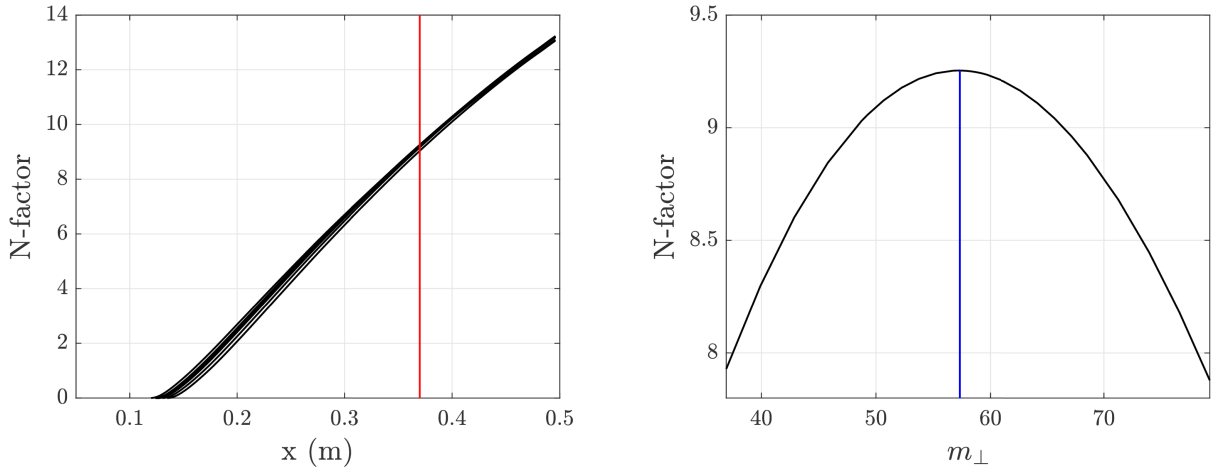

(a) N-Factors Along a Vortex Path Intersecting the Experiment Measurement Location at $x = 0.37$ m.

(b) N-Factor vs. Number of Waves Predicted by Equation (11–3) for the Measurement Location at $x = 0.37$ m.

Figure 11-9: Validation of Wavenumber Evolution.

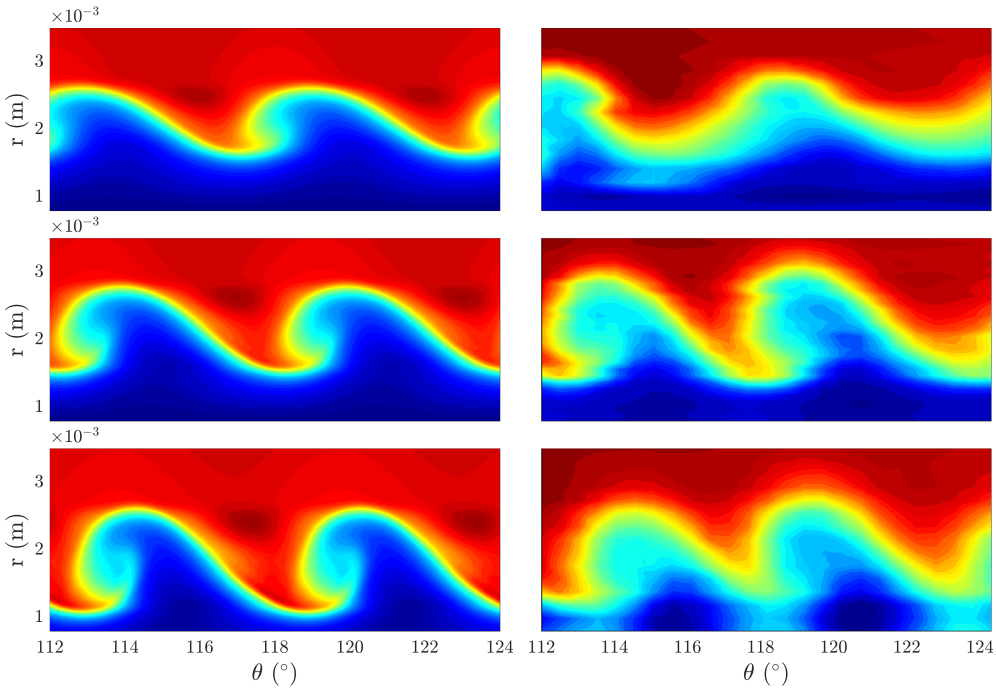

Figure 11-10: Development of Stationary Crossflow Vortices for NPSE Computations (Left) and the M6QT Experiment (Right) (Experiment Image Attributed to Craig & Saric [27]).

The experiments were also able to provide a measured root mean square (RMS) mass-flux profile at each of the axial locations. These profiles represent the disturbance mode shapes for crossflow at each station and can be compared with an equivalent RMS mode shape from the computations by combining the ρu mass-flux

disturbance modes from the NPSE computations with the basic-state quantities. The mode shapes from the experiments and computations in Figure 11-11 visually depict similar features including a two-lobed structure and relative maximum values.

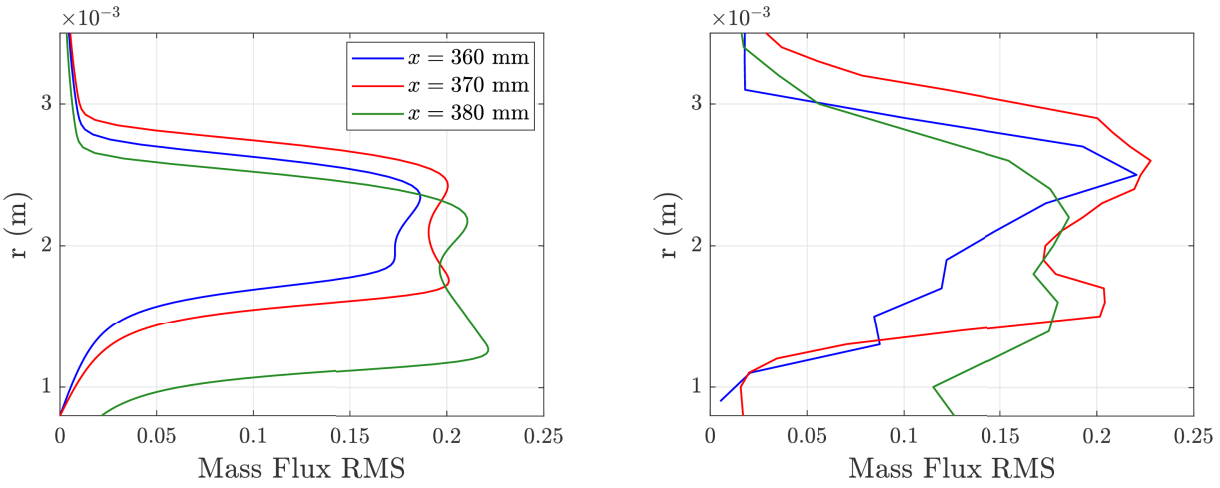

(a) NPSE Computations.

(b) M6QT Experiment.

Figure 11-11: Comparison of Computational and Experimental RMS Mode Shapes (Experiment Image Attributed to Craig & Saric [27]).

The combination of LPSE matching the approximated number of waves seen in the experiment and the similarities between the reconstructed flow and hot-wire measurements is a promising development in the validation of the PSE scale factor technique.

11.5.2.4 Initial Conditions and Secondary Instability Analysis

An example of the full progression of modal instability analysis on a representative geometry would include the stages of receptivity, linear growth, nonlinear growth, and finally secondary growth. The beginning stage of receptivity is an area that remains elusive and is a very important aspect for any PSE calculation. NPSE requires an initial condition containing information about frequency content, relative wavelengths, and disturbance amplitudes. To obtain these initial quantities, current PSE calculations must rely on amplitudes extracted from DNS computations or data provided by complementary experiments. Progress in receptivity models may also become beneficial in establishing the necessary initial conditions and complete the pathway ranging from receptivity to secondary analysis [57, 58].

Unstable high-frequency mechanisms begin to appear once the primary stationary crossflow disturbance enters the nonlinear stages of growth and reaches large amplitudes. These secondary instabilities, as well as distorted versions of traveling crossflow and second mode, form within different regions of the crossflow vortex and are driven by properties of the distorted flow such as spanwise gradient, normal gradient, and relative sonic line. Moyes et al. [48] provides a detailed overview of four unstable mechanisms within the crossflow modified base flow on the yawed straight cone geometry. The type-I and type-II secondary instabilities begin to experience rapid amplification and encompass a broad range of the frequency spectrum [49, 50].

Craig & Saric [27] used hot-wire anemometry inside of the M6QT to map out the disturbances within a modified crossflow boundary layer. The experiment was focused on a frequency range below 180 kHz, and by filtering the data they found traveling crossflow within the range $F = 15 - 60$ kHz and the secondary instability within a range $F = 80 - 130$ kHz. A SBG analysis was performed for a crossflow modified base flow on vortex paths that intersected the experiment measurement locations [48]. The development of the growth rates from six unstable modes, in addition to an LST analysis of the undisturbed base flow, are shown in Figure 11-12.

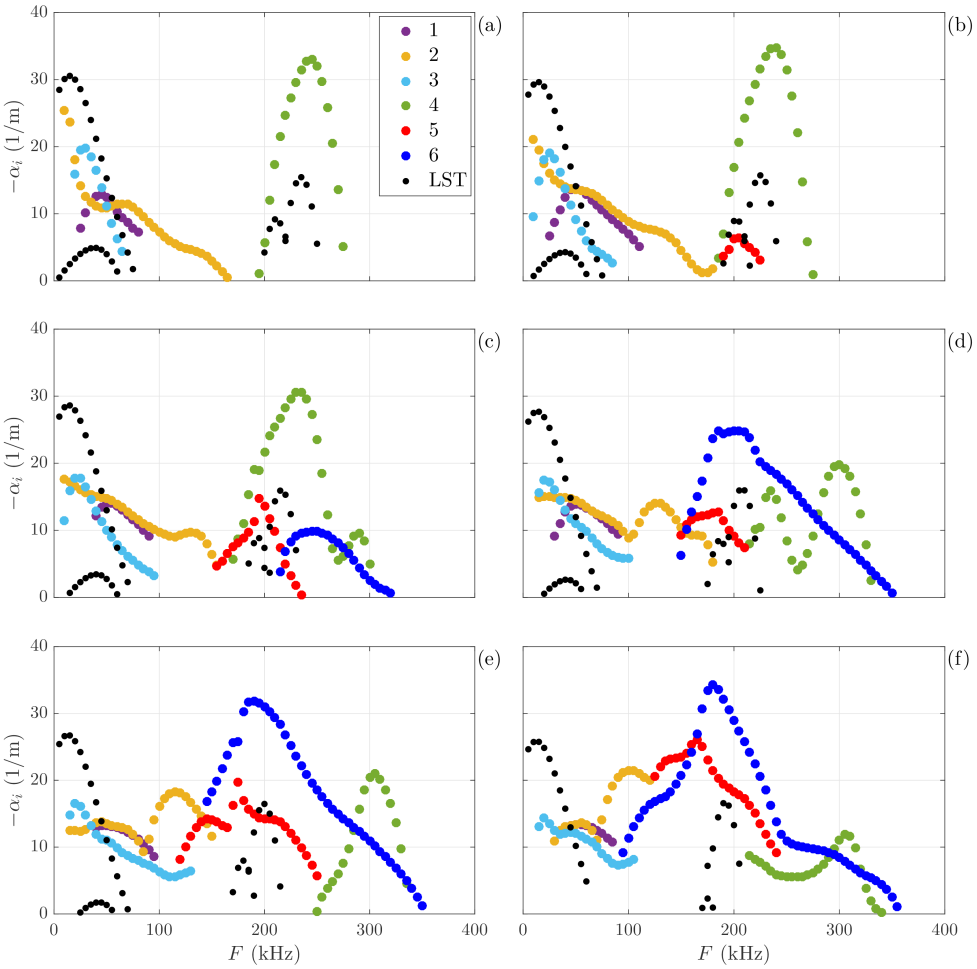

Figure 11-12: Growth Rates of Unstable Modes at (a) $x = 0.34$ m, (b) $x = 0.35$ m, (c) $x = 0.36$ m, (d) $x = 0.37$ m, (e) $x = 0.38$ m, and (f) $x = 0.39$ m (Image Attributed to Moyes et al. [48]).

The measured disturbances from the experiments for frequencies ranging from $F = 15 - 60$ kHz coincide with the families of modes 1, 2, and 3, which are modulated variants of traveling crossflow. The second range of measured frequencies, $F = 80 - 130$ kHz, instead appears to correspond to the growth rates of the type-I secondary instability. Also similar to the measurements from the experiment, the computations found that the traveling crossflow was concentrated mostly in the trough and slightly on the shoulder of the stationary vortex while the secondary instability was concentrated further up on the shoulder. The availability of data from the tunnel experiments helped to further validate the combination of NPSE and SBG through a means of identifying disturbance mechanisms, frequency bands, and physical location of disturbances.

In an experiment performed at the Boeing/AFOSR Mach-6 Quiet Tunnel at Purdue University, Ward et al. [25] measured multiple distinct frequency ranges at the wall using Kulite and PCB sensors. While the Craig & Saric [27] model had a natural surface roughness, Ward et al. included 50 evenly spaced discrete roughness elements (DREs) around the azimuth of the cone at an axial location of $x = 50.8$ mm. Based on Equation (11–3), a vortex path intersecting the measurement location at $x = 0.36$ m between $\theta = 115°$ and $\theta = 122.5°$ would lead to a local spanwise wavenumber of approximately $m_\perp = 14$. An NPSE analysis [48] was performed based on these conditions and resulted in the creation of a "flat-top" mass-flux crossflow vortex. Figure 11-13 shows the reconstructed total flow at axial locations of 0.395, 0.40, and 0.405 m.

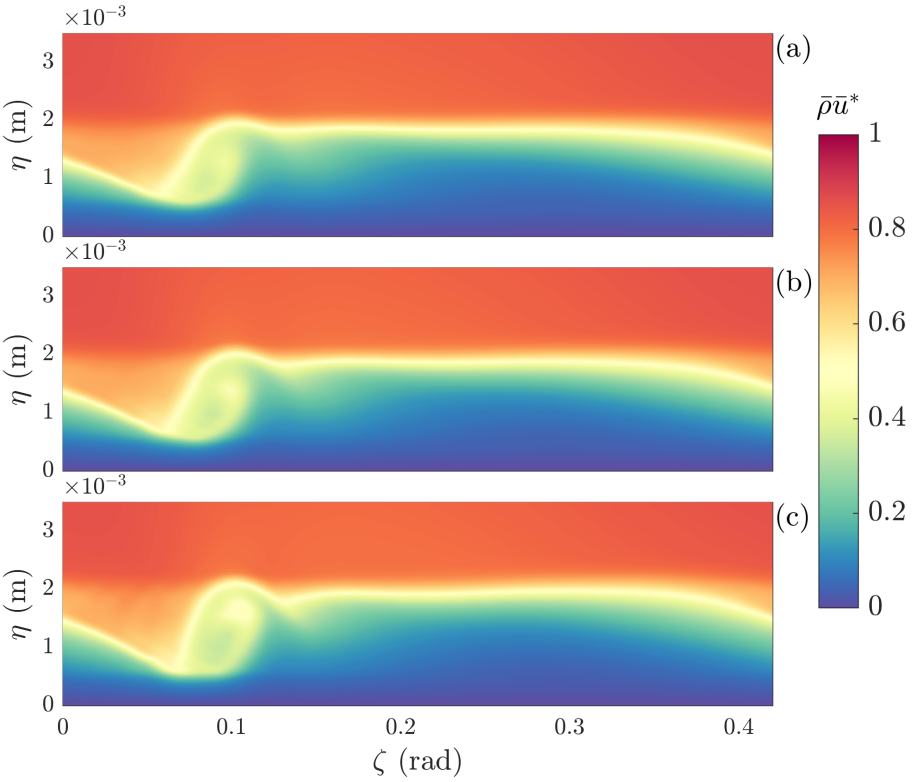

Figure 11-13: Reconstructed Flowfield ρu Mass-Flux Isocontours at (a) $x = 0.395$ m, (b) $x = 0.40$ m and (c) $x = 0.405$ m (Image Attributed to Moyes et al. [48]).

Ward et al. performed experiments with a rough Torlon insert and found that different frequency bands appeared and vanished as the azimuthal angle from the windward ray varied (Figure 11-14). The question remained as to whether the present frequencies were caused by second mode or if they were in fact secondary instabilities.

The modified basic states from Figure 11-13 result in crossflow wavelengths that span approximately $\theta = 24°$ of the cone azimuth, whereas the experiments measured a range of just 7.5°. A secondary instability analysis was performed at $x = 0.405$ m on the modified flowfield, and concentrations for disturbances including (a) modulated traveling crossflow at 15 kHz, (b) type-I at 125 kHz, (c) type-II at 375 kHz, and (d) modulated second mode at 140 kHz are shown in Figure 11-15. Included are locations of the critical layer (blue dotted line), relative sonic line (green dashed line), and azimuthal angles measured from the windward plane between $\theta = 115 - 122.5°$ (four magenta vertical dotted lines with increasing θ from left to right).

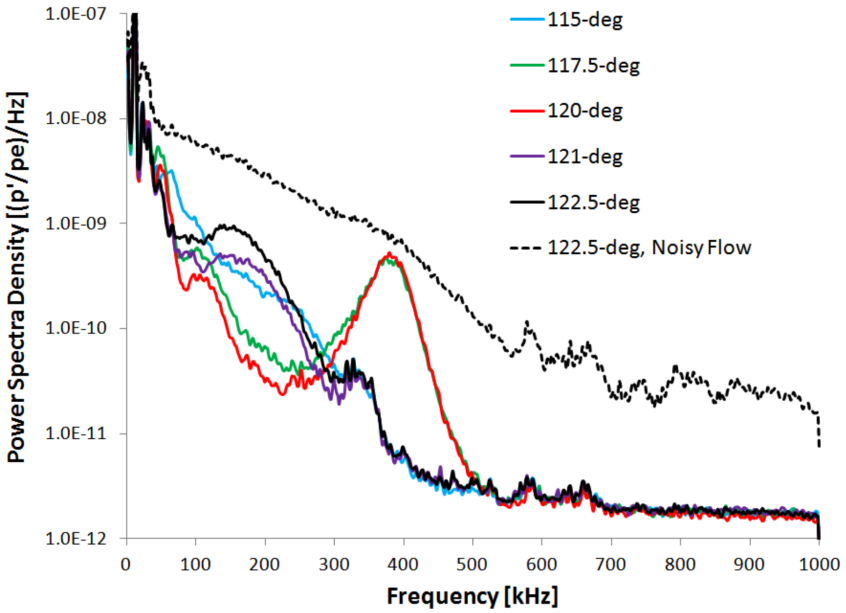

Figure 11-14: PSD of PCB Sensor 0.36 **m from the Nosetip.** $Re' = 10.8 \times 10^6$**/m,** $p_0 = 142$ **psia,** $T_0 = 425$ **K.**

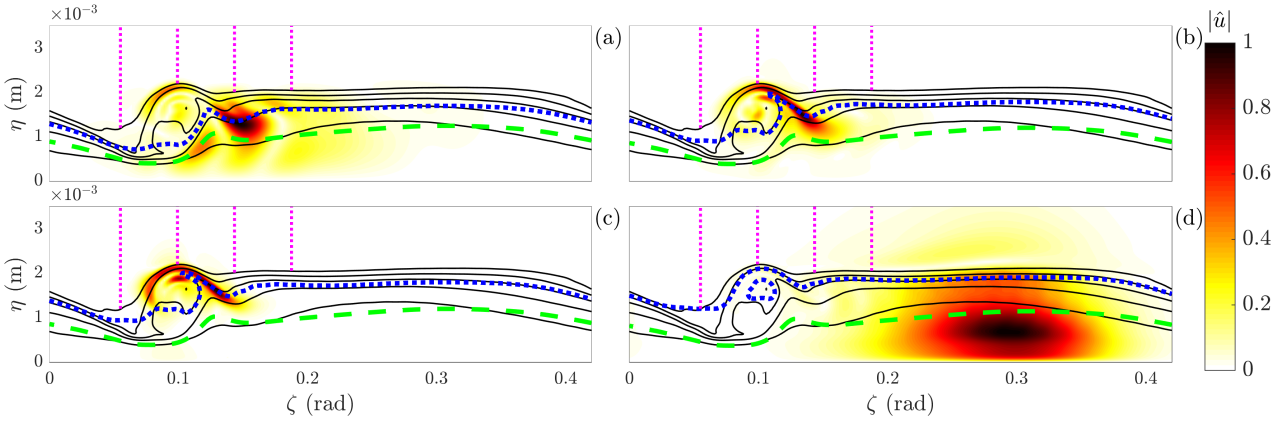

Figure 11-15: Isocontours of $|\hat{u}|$ **and Five Isolines of** ρu **Mass Flux (Black Solid Lines) (Image Attributed to Moyes et al. [48]).**

It is apparent that these modes produce disturbance concentrations in regions associated with significantly different azimuthal angles. A detailed comparison of the unstable frequency ranges from the spatial biglobal analysis with those observed in the experiments has been presented in Moyes et al. [48] (their table 3). Based on this analysis, Ward et al. are possibly measuring the modulated traveling crossflow, secondary instabilities, and second mode within the crossflow vortex. Furthermore, these modes appear at certain azimuthal angles and vanish at others, consistent with the findings of the matching frequency bands from the experiment.

11.6 CROSSFLOW FINDINGS

The research performed at Purdue University and Texas A&M University has led to the isolation of individual aspects of the stability problem for the crossflow mechanism, and analyses were conducted using techniques unique to each group. The information gained has led to a further appreciation of the sensitivities involved in a stability analysis and reinforced ideas on some of the more important factors that need to be addressed and accounted for when evaluating flows dominated by the crossflow instability. Some of the supported takeaways and lessons attained are extracted and discussed below.

11.6.1 Disturbance Trajectory

In order to study the growth of a crossflow vortex, an experiment needs to be able to trace the disturbance upstream. This can be accomplished if the vortex has become strong enough to produce heat streaks viewable from techniques such as IR thermography or temperature sensitive paint. By no means is this an easy task, however, as this requires having a sufficiently large viewing window or placing sensors at multiple stations along the crossflow trajectory, and it becomes difficult to differentiate disturbances from the surrounding tunnel noise at very small amplitudes. In order to validate computational calculations with data obtained from a wind tunnel test, care must be taken to ensure that the same vortex, and by extension the same vortex path, are being compared. The PSE method is a marching procedure that requires a predefined path to be provided in order to perform stability calculations. While inviscid streamlines have historically been the most common path type used for PSE analysis of stationary crossflow, they are not necessarily accurate in predicting the true trajectory of the crossflow mechanism [54]. In addition, there is no stability-based physical attribute associated with the use of streamlines and instead it is chosen due to its ease. Reed et al. [5] showed that it is important to use a proper marching path as growth rates and amplification vary depending on which direction one marches. The current computational and experimental work instead has led to the development, validation, and implementation in EPIC of a promising technique based purely on the generalized inflection point of the basic-state profiles in order to predict the disturbance trajectory [54].

11.6.2 Spanwise Wavelength

One of the key questions about stationary crossflow from a computational standpoint revolves around how to properly model the spanwise wavelength of the disturbance. The PSE method requires that a spanwise wavenumber be designated as an input where $\beta = \frac{2\pi}{\lambda}$. This wavenumber is a function of both axial and spanwise location and is directly influenced by both the geometric shape and pressure distribution of the vehicle. Past PSE methods have attempted to incorporate the wavelength into their algorithms by 1) assuming the wavelength is constant, 2) assuming the number of waves, k_c, around the geometry is constant and that λ scales directly with the spanwise radius of curvature, or 3) that λ scales with the local height of the boundary layer. However, it has been shown from multiple DNS calculations and wind tunnel experiments that these methods do not accurately model the wavelength evolution of a stationary vortex as it progresses downstream for generic cases [18, 19]. A new method has been proposed and implemented in EPIC which instead models the spanwise wavelength based on the behavior of neighboring vortex trajectories. Geometric vehicle divergence and spanwise pressure gradients

are now accounted for, and initial comparisons are very promising. As with the vortex path prediction, the spanwise wavelength evolution prediction is based solely on the basic-state profiles prior to any stability analysis.

11.6.3 Multiple Mechanisms

Mechanisms leading to hypersonic transition are complex and often difficult to measure or simulate. In a true physical setting this includes the presence of multiple disturbances within the boundary layer. Simulations often identify the mechanism predicted to most likely be the cause of breakdown for a particular flowfield and model that disturbance. However, real flows typically include the presence of different mechanisms and can lead to effects that would not be present in the linear calculation of a single mode. Multiple mechanism types, along with their harmonics, need to be accounted for using nonlinear analysis techniques such as NPSE, global methods, or DNS. The different mechanisms have the possibility of competing for dominance [47] or interacting with one another to generate a new effect [59–62]. One such example is the contest between traveling and stationary crossflow, which appears to directly correlate with the relative disturbance levels in the freestream. In some instances, mechanisms will only appear due to the presence of a large disturbance of a different type. The type-I and type-II secondary instabilities appear to reside within different locations of an amplified and developed crossflow vortex [25, 27, 48, 63]. This development may also lead to the existence of modified traveling crossflow and modified second-mode waves within the same vortex.

11.6.4 Surface Roughness

Surface roughness acts as a deterministic receptivity mechanism for stationary crossflow in environments with very low freestream amplitude fluctuations. From low-speed work, Müller & Bippes [64] performed experiments showing that the stationary transition pattern was fixed to the model despite translating the model with respect to the tunnel inflow. Radeztsky et al. [65] found that roughness is most effective at generating crossflow disturbances when located at or just upstream of the first neutral point, the transition location is very sensitive to roughness height, and the roughness is only effective when the diameter is greater than 10% of the most amplified stationary wavelength. In extension to hypersonics, some of the previously referenced experiments at Texas A&M and Purdue featured natural roughness and artificially generated discrete roughness, respectively, and coupled with EPIC analysis, the different roughness patterns were shown to directly affect the development and transition behavior of crossflow. Natural roughness [27] and discrete roughness elements [25] on a straight cone at 6° AoA produced downstream vortices of vastly different wavelengths under similar flow conditions, and these wavelengths were predicted by EPIC. In an experiment, it is critical to characterize the surface roughness of a test geometry in order to truly understand the problem that is being set up. This becomes even more important if there is to be an associated computational validation effort in order to know exactly what the input conditions should be for simulation.

Neither the distribution of surface roughness nor the freestream turbulence levels alone will indicate whether a traveling or stationary wave will be the most important disturbance introduced into the boundary layer. Rather, it is the interaction between roughness and turbulence level that will assign the corresponding disturbance frequencies, wavelengths, and amplitudes [66, 67]. Similar to the prior statement, it is also critical to characterize the freestream environment to assist receptivity modelers with providing initial conditions for stability analysis.

A measured turbulence level is not sufficient, and a characterization of both temporal and spatial content is desired.

11.6.5 Quiet Flow Wind Tunnels

Most of the ground-test data are obtained from operations in conventional wind tunnels and shock tunnels, which have much higher disturbance levels than in flight [36, 68]. The boundary layer on the wind-tunnel nozzle wall is usually turbulent, and this radiates high levels of noise onto the model. The impinging turbulence can alter the primary transition mechanism for a small-disturbance environment or bypass the modal growth pathway completely if the environment reaches high enough noise levels [69, 70]. Measurements of transition mechanisms should be conducted at noise levels comparable to flight in the same fashion practiced for low speed flows. Doing so requires laminar nozzle-wall boundary layers and will provide reliable and unambiguous data.

Presently, the ability to obtain quiet flow for hypersonic study exists only at Mach 6 and for moderate Reynolds numbers in cold flow [36]. Thus, no single wind tunnel is able to simulate the enthalpy, Mach number, Reynolds number, surface temperature, roughness, scale, freestream perturbations, and surface properties of ablating hypervelocity flight. This realization further supports the notion that measurements be obtained in a variety of facilities in conjunction with numerical analysis in order to identify the critical instability mechanisms and validate the computational capabilities. The parameter space of an experiment is too large to sort out individual effects based on transition measurements alone. Instead, experiments are encouraged to measure the mechanisms, freestream fluctuations, and transition location in collaboration with computations.

11.6.6 Similarities Between Flow Regimes

Much of the physical understanding of crossflow has stemmed from what was learned from computations and experiments in low speed flows. This flow regime contains a substantially larger amount of data and literature than the current focus of hypersonic flows. Hypersonics introduces an array of new flow physics such as shock/boundary-layer interactions, ablation, chemical reactions, and more. Despite this, the two flow regimes display some fundamental similarities for the crossflow instabilities.

At low speeds, traveling crossflow is a primary instability in low-amplitude regions, but becomes modulated once the flow enters into nonlinear regions [71]. While the traveling crossflow mechanism interacts with the present stationary crossflow, it does not appear to influence the shape of the stationary vortex through this interaction [71]. The traveling wave originally concentrates near the wall of the geometry [72], but gets lifted by the vortex into the low-momentum upwelling of the wave once the primary stationary crossflow disturbance becomes large and nonlinear [34]. Additionally, the type-II secondary instability appears to have approximately twice the frequency as the existing type-I instability. Moreover, surface roughness strongly influences the stationary crossflow features and evolution observed downstream. These behaviors are similar to those seen by the team in the hypersonic analysis of crossflow dominated geometries.

11.7 CONCLUSIONS

The NATO STO AVT-240: Hypersonic Boundary-Layer Transition Prediction project has enabled a team of experimentalists and computationalists to come together to study the crossflow instability characteristics of 3-D hypersonic configurations. A yawed straight cone served as a representative model for the flow physics and some of the findings are outlined below.

For a computational analysis:

- It is important to first ensure that the basic state being evaluated is highly converged due to the sensitivity of disturbances to small changes in the boundary layer.
- The trajectory of the mechanisms downstream also heavily influences the disturbance growth. Inviscid streamlines do not properly model this for stationary crossflow. Following a physics based attribute, the generalized inflection point in the basic-state crossflow profile, appears to be a more accurate representation.
- Defining an accurate behavior for crossflow spanwise wavelength which accounts for pressure gradients and geometric divergence has led to more direct comparison with experimentally measured mechanisms.
- Understanding the downstream evolution of spanwise wavelength has been shown to be important so that experiments or computations that generate crossflow with upstream roughness apply the appropriate spacing to achieve the desired results downstream.
- The nature and evolution of secondary instabilities should be a focal point in future studies regarding transition prediction due to their highly unstable nature and affinity for rapid growth. Also, looking at their relationship to the second mode would be important given the closeness in frequency.
- Determining the role of traveling crossflow (observed in the quiet-tunnel experiments) is important, especially for flight.

From an experimental standpoint:

- It was seen that, while the qualitative structure of stationary crossflow vortices is similar between low speed and hypersonic flows, there is a potential quantitative difference between the magnitude of growth for the type-I secondary instability.
- Experiments in the M6QT also showed that there is little to no influence from noise radiating off of the turbulent nozzle wall as long as it impacts the model sufficiently downstream of the receptivity region.
- Experiments at the BAM6QT stress the importance of accurately measuring the amplitude of stationary crossflow. A technique such as accurate surface heat-transfer measurements can be used to enable better direct validation efforts with computations and is also critical in the study of secondary instabilities.

In general, given the sensitivities involved in transition processes, the team benefited from close interactions between the experiments and computations. Each provides a different perspective when determining mechanisms, and each validates the other.

Collaboration between experiments and computations will become increasingly important in addressing the many questions that still exist regarding hypersonic disturbance flow physics. Both perspectives face obstacles that are challenging, whether it be creating new models to accurately formulate the problem or finding new ways of obtaining accurate measurement data. The advantages, however, are critical in fully explaining stability flow phenomena through the validation of results on parallel projects. Accomplishing this requires high levels of cooperation and coordination in order to guarantee that common geometries, flowfields, and initial conditions are all implemented.

Some of the planned feed-forward activities by the team include the following:

Research at Texas A&M will continue to utilize the combination of NPSE and spatial biglobal methods to investigate criteria gauged towards the prediction of transition onset and length. Additional capabilities for EPIC are also being developed such as the incorporation of thermochemical-nonequilibrium effects in hypersonic flows.

Future work at Purdue will continue to refine the measurement data and techniques available to obtain them. TSP, IR, and a traversing micro-pitot will be used to help determine the amplitudes of the stationary vortices given different roughness heights and spacings. Additional measurements will be taken of the secondary instability growth and breakdown for different roughness properties.

In order to address some of the challenges inherent in existing facilities, a new wind tunnel is under construction at the University of Arizona. This facility seeks to address two of the primary difficulties in studying laminar-turbulent transition: the stabilizing effect of compressibility and the limited achievable Reynolds number. The tunnel will be a Ludwieg tube with a nozzle diameter of 0.381 m (15 inches). In order to reduce the effect of compressibility and still retain the key hypersonic features of the above studies, the new facility will be designed for Mach 5 operation. Additionally, it will be designed for operation at $p_{t1} = 1380$ kPa (200 psia) and $T = 400$ K, corresponding to $Re' \approx 22 \times 10^6$/m. This large unit Reynolds number, combined with the large tunnel size, should allow the use of larger models with length Reynolds number $Re_x \approx 17 \times 10^6$. This facility will be operational in December 2018 in conventional mode, with quiet-flow upgrades to follow thereafter.

Boundary-layer stability and transition prediction are fields that have been studied for multiple decades, and there will likely be multiple decades more spent on extending the body of knowledge, modeling, predictive, and control capabilities. One prime opportunity exists in the upcoming AFOSR flight experiment designated BOLT [73–76]. The goal of this flight is to investigate the effects of new features, highly swept leading edges and a concave surface on the different mechanisms leading to transition (Figure 11-16).

11.8 FUNDING SOURCES

Kocian, Moyes, and Reed would like to acknowledge the support from Program Manager Ivett Leyva under U.S. Air Force Office of Scientific Research (AFOSR) grant FA9550-14-1-0365. The work provided by Edelman

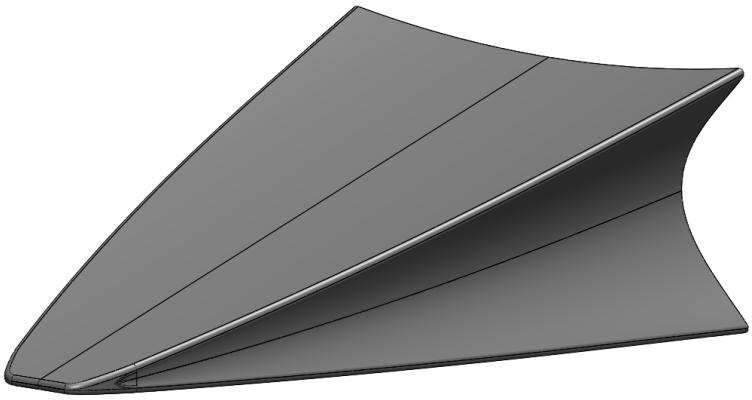

Figure 11-16: BOLT Model.

and Schneider was funded under AFOSR grant FA9550-12-1-0167, and some of this research was conducted with government support under and awarded by the U.S. Department of Defense, AFOSR, and the National Defense Science and Engineering Graduate Fellowship (32 CFR 168a). Funding was provided for the work of Craig and Saric by NASA and AFOSR through the National Center for Hypersonic Laminar-Turbulent Transition Research (AFOSR Grant FA9550-09-1-0341) and by the Texas A&M Foundation through the George Eppright 26 Chair in Engineering.

11.9 ACKNOWLEDGEMENTS

Kocian, Moyes, and Reed are grateful to Pointwise for providing the gridding software, NASA for providing the Data Parallel Line Relaxation (DPLR) flow solver, the Texas Advanced Computing Center (TACC) for providing the computational resources necessary for the basic state, Nicholas Oliviero for his contributions in the development of the EPIC stability code, and Pedro Paredes for his work in the development of the spatial biglobal code. Edelman and Schneider would like to thank Jeff Rigney for supplying the US3D solution and Jerry Hahn, Robin Snodgrass, and Jim Younts of the Purdue School of Aeronautics and Astronautics Machine Shop for their help in designing and fabricating the models.

11.10 REFERENCES

[1] Reed, H., Kimmel, R., Schneider, S., and Arnal, D., "Drag Prediction and Transition in Hypersonic Flow," *AGARD Interpanel (FDP&PEP) Symposium "Future Aerospace Technology in Service to Alliance"*, Paris, 14–18 April 1997.

[2] Wood, W. and Oliver, A., "Assessment of CFD Hypersonic Turbulent Heating Rates for Space Shuttle Orbiter," *AIAA 2011-3327*, 2011.

[3] Mack, L., "Boundary-Layer Linear Stability Theory," *AGARD Report 709: Special Course on Stability and Transition of Laminar Flow*, 1984, pp. 3.1–3.81.

[4] Fedorov, A., "Transition and Stability of High-Speed Boundary Layers," *Annual Review of Fluid Mechanics*, Vol. 43, 2011, pp. 79–95.

[5] Reed, H., Perez, E., Kuehl, J., Kocian, T., and Oliviero, N., "Verification and Validation Issues in Hypersonic Stability and Transition Prediction," *Journal of Spacecraft and Rockets*, Vol. 52, No. 1, 2015, pp. 29–37.

[6] Reed, H. and Saric, W., "Stability of Three-Dimensional Boundary Layers," *Annual Review of Fluid Mechanics*, Vol. 21, 1989, pp. 235–284.

[7] Bippes, H., "Basic Experiments on Transition in Three-Dimensional Boundary Layers Dominated by Crossflow Instability," *Progress in Aerospace Sciences*, Vol. 35, 1999, pp. 363–412.

[8] Arnal, D. and Casalis, G., "Laminar-Turbulent Transition Prediction in Three-Dimensional Flows," *Progress in Aerospace Sciences*, Vol. 36, No. 2, 2000, pp. 173–191.

[9] Saric, W., Reed, H., and White, E., "Stability and Transition of Three-Dimensional Boundary Layers," *Annual Review of Fluid Mechanics*, Vol. 35, 2003, pp. 413–442.

[10] Reshotko, E., "Is Re_θ/M_e a Meaningful Transition Criterion?" *AIAA Journal*, Vol. 45, No. 7, 2007, pp. 1441–1443.

[11] Reshotko, E., "Transition Issues for Atmospheric Entry," *Journal of Spacecraft and Rockets*, Vol. 45, No. 2, 2008, pp. 161–164.

[12] Reed, H. and Haynes, T., "Transition Correlations in Three-Dimensional Boundary Layers," *AIAA Journal*, Vol. 32, No. 5, 1994, pp. 923–929.

[13] Berkowitz, A., Kyriss, C., and Martellucci, A., "Boundary Layer Transition Flight Test Observations," *AIAA 77-125*, 1977.

[14] Reed, H., Saric, W., and Arnal, D., "Linear Stability Theory Applied to Boundary Layers," *Annual Review of Fluid Mechanics*, Vol. 28, 1996, pp. 389–428.

[15] Malik, M., "Hypersonic Flight Transition Data Analysis Using Parabolized Stability Equations with Chemistry Effects," *Journal of Spacecraft and Rockets*, Vol. 40, No. 3, 2003, pp. 332–344.

[16] Johnson, H. and Candler, G., "Analysis of Laminar-Turbulent Transition in Hypersonic Flight Using PSE-Chem," *AIAA 2006-3057*, 2006.

[17] Herbert, T., "Parabolized Stability Equations," *Annual Review of Fluid Mechanics*, Vol. 29, 1997, pp. 245–283.

[18] Balakumar, P. and Owens, L., "Stability of Hypersonic Boundary Layers on a Cone at Angle of Attack," *AIAA 2010-4718*, 2010.

[19] Gronvall, J., Johnson, H., and Candler, G., "Hypersonic Three-Dimensional Boundary Layer Transition on a Cone at Angle of Attack," *AIAA 2012-2822*, 2012.

[20] Malik, M., Spall, R., and Chang, C.L., "Effect of Nose Bluntness on Boundary Layer Stability and Transition," *AIAA 90-0112*, 1990.

[21] Tufts, M. and Kimmel, R., "Analysis of Windward Side Hypersonic Boundary Layer Transition on Blunted Cones at Angle of Attack," *AIAA 2017-0764*, 2017.

[22] Hofferth, J., Saric, W., Kuehl, J., Perez, E., Kocian, T., and Reed, H., "Boundary-Layer Instability and Transition on a Flared Cone in a Mach 6 Quiet Wind Tunnel," *International Journal of Engineering Systems Modeling and Simulation*, Vol. 5, 2013, pp. 109–124.

[23] Kocian, T., Perez, E., Oliviero, N., Kuehl, J., and Reed, H., "Hypersonic Stability Analysis of a Flared Cone," *AIAA 2013-0667*, 2013.

[24] Muñoz, F., Heitmann, D., and Radespiel, R., "Instability Modes in Boundary Layers of an Inclined Cone at Mach 6," *Journal of Spacecraft and Rockets*, Vol. 51, 2014, pp. 442–454.

[25] Ward, C., Henderson, R., and Schneider, S., "Possible Secondary Instability of Stationary Crossflow Vortices on an Inclined Cone at Mach 6," *AIAA 2015-2773*, 2015.

[26] Edelman, J., Chynoweth, B., McKiernan, G., Sweeney, C., and Schneider, S., "Instability Measurements in the Boeing/AFOSR Mach-6 Quiet Tunnel," *AIAA 2016-3343*, 2016.

[27] Craig, S. and Saric, W., "Crossflow Instability in a Hypersonic Boundary Layer," *Journal of Fluid Mechanics*, Vol. 808, 2016, pp. 224–244.

[28] Kocian, T., Moyes, A., Reed, H., Craig, S., Saric, W., Schneider, S., and Edelman, J., "Hypersonic Crossflow Instability," *Journal of Spacecraft and Rockets, Submitted for Publication*, 2018.

[29] Chen, F., Wilkinson, S., and Beckwith, I., "Görtler Instability and Hypersonic Quiet Nozzle Design," *Journal of Spacecraft and Rockets*, Vol. 30, No. 2, 1993, pp. 170–175.

[30] Blanchard, A., Lachowicz, J., and Wilkinson, S., "NASA Langley Mach 6 Quiet Wind-Tunnel Performance," *AIAA Journal*, Vol. 35, No. 1, 1997, pp. 23–28.

[31] Hofferth, J., Bowersox, R., and Saric, W., "The Mach 6 Quiet Tunnel at Texas A&M: Quiet Flow Performance," *AIAA 2010-4794*, 2010.

[32] Smits, A., Hayakawa, K., and Muck, K., "Constant Temperature Hot-wire Anemometer Practice In Supersonic Flows - Part 1: The Normal Wire," *Experiments in Fluids*, Vol. 1, No. 2, 1983, pp. 83–92.

[33] Semper, M., "Examining a Hypersonic Turbulent Boundary Layer at Low Reynolds Number," *PhD Dissertation, Texas A&M University*, 2013.

[34] White, E. and Saric, W., "Secondary Instability of Crossflow Vortices," *Journal of Fluid Mechanics*, Vol. 525, 2005, pp. 275–308.

[35] Schneider, S., "Design of a Mach-6 Quiet-Flow Wind-Tunnel Nozzle Using the e^N Method for Transition Estimation," *AIAA 98-0547*, 1998.

[36] Schneider, S., "Development of Hypersonic Quiet Tunnels," *Journal of Spacecraft and Rockets*, Vol. 45, No. 4, 2008, pp. 641–664.

[37] Steen, L., "Characterization and Development of Nozzles for a Hypersonic Quiet Wind Tunnel," *Masters Thesis, Purdue University*, 2010.

[38] Swanson, E., "Boundary-Layer Transition on Cones at Angle of Attack in a Mach-6 Quiet Tunnel," *Masters Thesis, Purdue University*, 2008.

[39] Ward, C., "Crossflow Instability and Transition on a Circular Cone at Angle of Attack in a Mach-6 Quiet Tunnel," *Masters Thesis, Purdue University*, 2014.

[40] Henderson, R., "Crossflow Transition at Mach 6 on a Cone at Low Angles of Attack," *Masters Thesis, Purdue University*, 2014.

[41] Chynoweth, B., Ward, C., Greenwood, R., McKiernan, G., Fisher, R., and Schneider, S., "Measuring Transition and Instabilities in a Mach 6 Hypersonic Quiet Wind Tunnel," *AIAA 2014-2643*, 2014.

[42] Edelman, J., "Secondary Instabilities of Hypersonic Stationary Crossflow Waves," *Masters Thesis, Purdue University*, 2016.

[43] Edelman, J. and Schneider, S., "Secondary Instabilities of Hypersonic Stationary Crossflow Waves," *AIAA Journal*, Vol. 56, No. 1, 2018, pp. 182–192.

[44] Choudhari, M., Li, F., Paredes, P., and Duan, L., "Computations of Crossflow Instability in Hypersonic Boundary Layers," *AIAA 2017-4300*, 2017.

[45] Haynes, T. and Reed, H., "Simulation of Swept-Wing Vortices Using Nonlinear Parabolized Stability Equations," *Journal of Fluid Mechanics*, Vol. 405, 2000, pp. 345–349.

[46] Oliviero, N., "EPIC: A New and Advanced Nonlinear Parabolized Stability Equation Solver," *Masters Thesis, Texas A&M University*, 2015.

[47] Borg, M., Kimmel, R., and Stanfield, S., "Traveling Crossflow Instability for the HIFiRE-5 Elliptic Cone," *Journal of Spacecraft and Rockets*, Vol. 52, No. 3, 2015, pp. 664–673.

[48] Moyes, A., Paredes, P., Kocian, T., and Reed, H., "Secondary Instability Analysis of Crossflow on a Hypersonic Yawed Straight Circular Cone," *Journal of Fluid Mechanics*, Vol. 812, 2017, pp. 370–397.

[49] Kocian, T., Moyes, A., Mullen, D., and Reed, H., "PSE and Spatial Biglobal Instability Analysis of Reduced Scale and Flight HIFiRE-5 Geometry," *AIAA 2017-0768*, 2017.

[50] Moyes, A., Kocian, T., Mullen, D., and Reed, H., "Boundary Layer Stability Analysis of HIFiRE-5b Flight Geometry," *Journal of Spacecraft and Rockets, Article in Advance*, 2018.

[51] Theofilis, V., "Global Linear Instability," *Annual Review of Fluid Mechanics*, Vol. 43, 2011, pp. 319–352.

[52] Paredes, P., "Advances in Global Instability Computations: From Incompressible to Hypersonic Flow," *PhD Dissertation, Universidad Politécnica de Madrid*, 2014.

[53] Paredes, P. and Theofilis, V., "Centerline Instabilities on the Hypersonic International Flight Research Experimentation HIFiRE-5 Elliptic Cone Model," *Journal of Fluids and Structures*, Vol. 53, 2014, pp. 36–49.

[54] Oliviero, N., Kocian, T., Moyes, A., and Reed, H., "EPIC: NPSE Analysis of Hypersonic Crossflow Instability on Yawed Straight Circular Cone," *AIAA 2015-2772*, 2015.

[55] Kocian, T., "Computational Hypersonic Boundary-Layer Stability and the Validation and Verification of EPIC," *PhD Dissertation, Texas A&M University*, 2018.

[56] Kuehl, J., Perez, E., and Reed, H., "JoKHeR: NPSE Simulations of Hypersonic Crossflow Instability," *AIAA 2012-0921*, 2012.

[57] Balakumar, P., "Receptivity of Hypersonic Boundary Layers to Acoustic and Vortical Disturbances," *AIAA 2015-2473*, 2015.

[58] Balakumar, P. and Chou, A., "Transition Prediction in Hypersonic Boundary Layers Using Receptivity and Freestream Spectra," *AIAA 2016-0847*, 2016.

[59] Klebanoff, P., Tidstrom, K., and Sargent, L., "The Three-Dimensional Nature of Boundary-Layer Instability," *Journal of Fluid Mechanics*, Vol. 12, No. 1, 1962, pp. 1–34.

[60] Herbert, T., "Secondary Instability of Boundary Layers," *Annual Review of Fluid Mechanics*, Vol. 20, 1988, pp. 487–526.

[61] Sivasubramanian, J. and Fasel, H., "Direct Numerical Simulation of Transition in a Sharp Cone Boundary Layer at Mach 6: Fundamental Breakdown," *Journal of Fluid Mechanics*, Vol. 768, 2015, pp. 175–218.

[62] Sweeney, C., Chynoweth, B., Edelman, J., and Schneider, S., "Instability and Transition Experiments in the Boeing/AFOSR Mach 6 Quiet Tunnel," *AIAA 2016-0355*, 2016.

[63] Kocian, T., Moyes, A., Mullen, D., and Reed, H., "PSE and Spatial Biglobal Instability Analysis of HIFiRE-5 Geometry," *AIAA 2016-3346*, 2016.

[64] Müller, B. and Bippes, H., "Experimental Study of Instability Modes in a Three-Dimensional Boundary Layer," *Fluid Dynamics of Three-Dimensional Turbulent Shear Flows and Transition, AGARD CP 438*, 1989, pp. 13.1–15.

[65] Radeztsky, Jr., R., Reibert, M., and Saric, W., "Effect of Isolated Micron-Sized Roughness on Transition in Swept-Wing Flows," *AIAA Journal*, Vol. 37, No. 11, 1999, pp. 1370–1377.

[66] White, E., Saric, W., Gladden, R., and Gabet, P., "Stages of Swept-Wing Transition," *AIAA 2001-0271*, 2001.

[67] Reed, H., Reshotko, E., and Saric, W., "Receptivity: The Inspiration of Mark Morkovin," *AIAA 2015-2471*, 2015.

[68] Beckwith, I. and Miller, III, C., "Aerothermodynamics and Transition in High-Speed Wind Tunnels at NASA Langley," *Annual Review of Fluid Mechanics*, Vol. 22, 1990, pp. 419–439.

[69] Schneider, S., "Effects of High-Speed Tunnel Noise on Laminar-Turbulent Transition," *Journal of Spacecraft and Rockets*, Vol. 38, No. 3, 2001, pp. 323–333.

[70] Casper, K., Johnson, H., and Schneider, S., "Effect of Freestream Noise on Roughness-Induced Transition for a Slender Cone," *Journal of Spacecraft and Rockets*, Vol. 48, No. 3, 2011, pp. 406–413.

[71] Fischer, T. and Dallman, U., "Primary and Secondary Stability Analysis of a Three-Dimensional Boundary-Layer Flow," *Physics of Fluids*, Vol. 3, 1991, pp. 2378–2391.

[72] Malik, M., Li, F., and Chang, C.L., "Crossflow Disturbances in Three-Dimensional Boundary Layers: Nonlinear Development, Wave Interaction, and Secondary Instability," *Journal of Fluid Mechanics*, Vol. 268, 1994, pp. 1–36.

[73] Wheaton, B., Berridge, D., Wolf, T., Stevens, R., and McGrath, B., "Boundary Layer Transition (BOLT) Flight Experiment Overview," *AIAA 2018-2892*, 2018.

[74] Berridge, D., McKiernan, G., Wadhams, T., Holden, M., Wheaton, B., Wolf, T., and Schneider, S., "Hypersonic Ground Tests In Support of the Boundary Layer Transition (BOLT) Flight Experiment," *AIAA 2018-2893*, 2018.

[75] Thome, J., Dwivedi, A., Nichols, J., and Candler, G., "Direct Numerical Simulation of BOLT Hypersonic Flight Vehicle," *AIAA 2018-2894*, 2018.

[76] Moyes, A., Kocian, T., Mullen, D., and Reed, H., "Pre-Flight Boundary-Layer Stability Analysis of BOLT Geometry," *AIAA 2018-2895*, 2018.

Chapter 12 – HYPERSONIC BOUNDARY LAYER CROSS FLOW TRANSITION – CHARACTERISTICS AND CONTROL

Thomas Corke
University of Notre Dame
UNITED STATES

tcorke@nd.edu

Alexander Arndt
University of Notre Dame
UNITED STATES

Alexander.J.Arndt.13@nd.edu

Eric Matlis
University of Notre Dame
UNITED STATES

ematlis@nd.edu

Ian Neel
Texas A&M University
UNITED STATES

neel480@email.tamu.edu

Rodney Bowersox
Texas A&M University
UNITED STATES

bowersox@tamu.edu

ABSTRACT

The paper focuses on a topic area of the NATO AVT-240 Working Group on Hypersonic Boundary Layer Transition dealing with the 3-D boundary layer cross-flow instability that is expected to be dominant mechanism of turbulent transition on hypersonic lift-generating shapes. The model geometries of interest are a 7° half-angle right-circular cone at a 6° angle of attack, and a 2:1 elliptic cone at a 0° angle of attack. The focus is on the prediction and control of turbulent transition in these cases, as well as the sensitivity to initial conditions including surface roughness, and free-stream acoustic disturbance levels. Potential interactions between stationary and the traveling cross-flow modes that might play a role in transition are highlighted. The cited results primarily originate from experiments in three different Mach 6 facilities of different designs. This provides an opportunity to investigate the effect of different free-stream characteristics on cross-flow transition.

12.1 INTRODUCTION

At its heart, hypersonics represents the fullest integration of the mediums of air and space, with elements of both aeronautics and astronautics. Hypersonic technologies, especially the ability for powered and sustained hypersonic flight in the atmosphere, holds the promise of revolutionizing civil and military intercontinental transportation. It could also have a dramatic impact on future space launches, by replacing rocket engines with air breathing scram-jet engines while in the atmosphere. Achieving this will require a maturation of hypersonic flight technologies and subsequent transition of the research towards practical applications. A critical element for this is the prediction and control of boundary layer laminar-to-turbulent transition. Predicting transition with any certainty in this Mach number regime will require a combination of experiments, and advanced simulation and modeling capabilities.

Interest in air-breathing flight at hypersonic speeds necessitates research on boundary layer turbulence transition in that flight regime. The fluid dynamic mechanisms of transition from laminar to turbulent flow is of both fundamental and practical importance since the onset of the turbulent boundary layer flow significantly increases the viscous drag and the surface heating, and determines critical boundary layer conditions at the inlet of scram-jet propulsion systems.

Turbulence transition on hypersonic *lifting* bodies is likely to be dominated by a mean cross-flow velocity component that is subject to a cross-flow instability. Much is known about the cross-flow dominated transition at subsonic and supersonic Mach numbers. In these Mach number regimes, validated flow simulation codes can predict the cross-flow instability mode characteristics, and with reasonable accuracy, the transition location. The understanding gained through coupled experiments and simulations has led to the development of a number of successful methods for cross-flow transition control. These have been validated up to supersonic Mach numbers, and should be valid at lower hypersonic Mach numbers where gas dissociation effects are minimal. A similar coordinated effort on cross-flow transition and control is needed for higher hypersonic Mach numbers that are projected for future air vehicles and air-breathing launch systems.

With regards to cross-flow transition, the NATO AVT-240 Working Group selected two common generic shapes: a 7° half-angle right-circular cone at a 6° angle of attack, and a 2:1 elliptic cone at a 0° angle of attack. These two geometries have been widely studied, with both exhibiting a mean cross-flow velocity component by which the dominant transition mechanism results from a cross-flow instability.

Fundamental knowledge of the linear and nonlinear cross-flow transition mechanisms on these two model shapes has been obtained through wind tunnel tests using well instrumented models with smooth surfaces in cold flows in two different facilities. An important difference between these facilities is that some have been optimized to reduce free-stream acoustic disturbances, so-called “quiet” tunnels, and others are conventional designs that are not designed to minimize acoustic disturbances. The contrast is important in understanding the receptivity of the cross-flow instability and turbulent transition to free-stream disturbances.

Receptivity is the process by which disturbances enter the boundary layer and provide an initial amplitude to boundary layer instabilities. These disturbances can be divided into modes such as entropy variation, vorticity, and acoustic or sound (irrotational velocity or pressure fluctuations)[1–3]. Conventional hypersonic tunnels are known to have elevated free-stream turbulence, owing to the high pressure piping supplying the facilities. At high Reynolds numbers the sidewalls of such tunnels undergo boundary layer transition feeding noise into the

free-stream along Mach line characteristics. This noise consists of sound waves which are seen to scale with M^4 [4]. The effect of this noise on the transition process is not well understood but has been seen to have a large effect.

With regard to the cross-flow instability, the traveling mode is predicted to have a higher growth rate than its stationary counterpart, but is not observed to be the dominant mechanism in flows with a low free-stream disturbance environment. Deyhle and Bippes [5] present a series of cross-flow experiments performed in a range of wind tunnels with varying free-stream disturbance environments. They found that cross-flow transition was dominated by traveling waves only for free-stream turbulence intensities above 0.20%. For lower turbulence levels, stationary waves dominated and tied to roughness on the model surface. Radeztsky et al. [6] found that transition was insensitive to acoustic disturbances, even at amplitudes greater than 100 dB. Thus, the variations observed by Deyhle and Bippes [5] were due primarily to variations in the vortical components of the free-stream fluctuations and not to acoustic modes [7]. Schneider [1] presents a good review and summary of the existing comparisons between quiet and noisy experimental data as well as flight experiments, and demon strates that trends in transition may even be reversed when tested under noisy conditions.

12.1.1 Right-Circular Cones

Experimental efforts have largely focused on straight cones at angle of attack and elliptic cones. Recently published results by Craig and Saric [8] provide insight into the cross-flow instability on a yawed cone in the low-disturbance Mach 6 Quiet tunnel at Texas A&M University (TAMU). Utilizing a model-fixed traverse, hot-wire boundary layer measurements were made across several runs, allowing for the study of both stationary and traveling cross-flow waves. Up to saturation, the growth and development of these instabilities were in agreement with low-speed theory and experiments. One difference observed when compared to White and Saric [9] is that secondary instabilities were not observed to grow rapidly and lead to breakdown immediately after developing. In conjunction with these experiments, numerous computational efforts have provided insight into the cross-flow instability for high speeds. The computational stability group at TAMU has utilized a toolkit which uses linear stability theory (LST), linear and nonlinear parabolized stability equations (LPSE,NPSE), and LST based on 2-D PDEs, called spatial BiGlobal (SBG) theory. LST and NPSE methods form the EPIC code which was developed in house at TAMU and is detailed in Oliviero et al. [10]. EPIC can be utilized for the initial linear growth of instabilities including cross-flow as assumptions of two homogeneous spatial directions and small disturbance amplitudes made for LST hold in this region. NPSE is able to account for and model the large amplitudes and nonlinearities of disturbances. SBG analysis allows for the analysis of the nonlinearly distorted modified basic state created by the stationary vortices. Moyes et al. [11] apply this toolkit to a hypersonic yawed circular cone. Their findings show qualitative and quantitative agreement with Craig and Saric [8] and provide insight into the results of another experiment performed in the Purdue BAM6QT. Similarity between secondary instabilities of incompressible and hypersonic stationary cross-flow are noted.

12.1.2 Elliptic Cones and HIFiRE-5 Research

Several modern experiments have focused in on the elliptic cone as a geometry of interest. A computational study by Kimmel et al. [12] in the mid 1990s identified the elliptic cone as a geometry ripe for study. Its shape naturally produces a favorable pressure gradient and amplifies the cross-flow instability with linear stability N-factors reaching a maximum near the shoulder of the cone. Along the centerline, highly inflectional profiles

warranting further study were identified. Poggie et al. [13] conducted experiments in Tunnel B at AEDC at M = 8 with surface mounted hot-film probes which revealed both stationary and traveling disturbances at frequencies in line with predictions from LST and computations. This work has expanded and become part of the **H**ypersonic **I**nternational **Fl**ight **R**esearch and **E**xperimentation (HIFiRE) program, a joint program between the AFOSR and the Australian DTSO. This program, described in Bowcutt et al. [14], is a series of flight tests aimed at examining several areas of interest to hypersonic flight.

The HIFiRE-5 flight model is a 2:1 elliptic cone designed to examine the cross-flow instability. A 7-degree minor axis half angle was chosen. The nose tip is defined by a 2.5 mm radius arc and keeps an elliptic cross section to its tip. Several ground based studies of the 2:1 elliptic cone geometry have been conducted in support of these flight tests [15–19], and several CFD analyses have been run [11, 20, 21]. Choudhari et al. [20] presents the initial CFD analysis performed on this geometry in support of the HiFIRE-5 program. Included are full scale and wind tunnel scale analyses for flight and the Purdue BAM6QT. The LST and PSE based analysis predicts moderate N-factors near the cone shoulder for both traveling and stationary cross-flow vortices. The pressure gradient from the model attachment line drives flow towards the centerline resulting in a mushroom shaped upwelling along the model centerline. More detailed analysis has been performed using more advanced modeling techniques such as those presented in Moyes et al. [11].

The ground based campaigns of Juliano et al. [22] and Borg and Kimmel [19] have examined a 38.1% scale model of the HF-5 geometry. Juliano et al. [22] performed a series of experiments using temperature sensitive paint to examine transition on the model surface. His experiments showed good agreement under quiet flow with the LST and PSE calculations of Li et al. [21] and Choudhari et al. [20]. Juliano analyzed the model center-line transition location and boundary layer frequency content utilizing temperature sensitive paint and surface mounted pressure transducers.

Borg and colleagues have run a series of campaigns focusing on various elements of the transition process on this geometry with an eye to supporting the design and flight test. Beginning with the model attachment line and its sensitivity to roughness, Borg has focused on the effect of free-stream disturbances, stationary cross-flow vortices, traveling cross-flow waves, and angle of attack effects [17–19, 23, 24].

Borg's studies have seen evidence of dominant stationary cross-flow under quiet flow with the accompanying presence of traveling cross-flow waves [25]. These tests utilized surface mounted Kulite pressure transducers to measure pressure fluctuations within the transitional boundary layer. Spectra from the Kulites revealed a peak centered near 45 kHz believed to be the traveling instability. The peak magnitude is seen to increase with increasing Re and then seen to broaden and fill all frequencies, indicating fully turbulent flow. Evidence of stationary vortices has been observed under noisy flow conditions in oil flow images but does not appear in either TSP or IR thermography. In addition, evidence of traveling cross-flow, in surface pressure transducer data, has not been seen under noisy flow.

Borg et al. [24] presented work conducted in the Purdue BAM6QT operated in noisy mode with bleed valves closed as well as the conventional TAMU ACE hypersonic tunnel to examine the effect of free-stream noise levels on the same test article. Although low frequency disturbances were observed in surface mounted Kulites, traveling cross-flow was not definitively identified. Comparisons of the spectral content measured from the Kulites revealed strong similarity between the BAM6QT in noisy mode and the conventional ACE facility. The exact cause of the transition under noisy flow or the effect of significantly varying noise levels was not obtained.

Borg et al. [19] and Juliano et al. [26] examined a newly constructed steel-tipped PEEK version of the 38.1% model geometry using simultaneous IR thermography and pressure measurements. Similar to the results from Borg and co-investigators [17, 24, 25], both stationary and traveling cross-flow were detected on the model under quiet flow but neither was observed under noisy flow, despite an observed region of increased heating near the cone shoulder. Borg and Kimmel [27] have also recently made measurements along the centerline using high frequency pressure transducers revealing spectral content of the centerline instability.

The computational stability group at TAMU has utilized the combination of modeling techniques to examine the stability of both the flight and reduced scale models of the HIFiRE-5 geometry. Kocian et al. [28] examined the 3-D cross-flow instabilities and nonlinear secondary instabilities on both the full and a wind tunnel scale HIFiRE-5 geometry. Type I & II secondary instabilities, traveling cross-flow, and Mack mode instabilities were identified and their growth rates and spectral extent examined. The results presented seem to explain the spectral broadening observed by Borg et al. [25] in the 0 – 200 kHz range of the Kulites utilized. Initially the traveling cross-flow instability dominates the spectral content with a peak centered near 45 kHz, but it is quickly surpassed in growth rate by type- I & II secondary instabilities in a broad frequency band that fills the 0 – 200 kHz spectral range. These techniques clearly form a powerful toolset for examining the transition process. The understanding gained can help inform experimental requirements, from necessary sensor response and placement, to need for characterization of critical areas.

12.1.3 Discrete Surface Roughness Transition Control

Linear theory predicts the growth of both traveling and stationary cross-flow modes. The traveling modes are more amplified. However the extreme sensitivity of the stationary modes to minute surface roughness usually makes them more dominant. Being stationary, they produce a distortion in the mean flow that can spawn a secondary inviscid instability the rapidly breaks down into turbulence.

The extreme sensitivity of the stationary mode to surface roughness is the basis for the use of discrete roughness elements (DREs) for cross-flow transition control. This feature was exploited by Corke and Knasiak [29] and Corke et al. [30] to excite selected wave numbers of cross-flow modes in the boundary layer over a rotating disk, which is a canonical three-dimensional flow that exemplifies the cross-flow instability. Its application to transition control was pioneered by Saric and Reed [31] who demonstrated that the application of micron-sized spanwise-periodic roughness could increase the transition to turbulence Reynolds number for boundary layer flows in which the cross-flow instability is the dominant mechanism. Saric et al. [32] and Radeztsky et al. [33] demonstrated that stationary cross-flow modes at the forced spanwise wavenumber exclusively appeared in the boundary layer. Super-harmonic wavenumbers of the forced wavenumber were also possible to appear, but lower wavenumbers were always completely suppressed. These observations led to the concept of exciting less amplified stationary cross-flow modes whereby the spanwise wavenumber of the forced mode had to be higher than those of the naturally amplified band. This would guarantee that no disturbance energy would cascade through nonlinear interactions to lower, more-amplified wavenumbers. Saric et al. [32] referred to this approach of cross-flow transition control as “subcritical forcing”. This was in reference to the most amplified spanwise wavenumbers being the “critical” wavenumbers, and forcing of the most amplified band being “critical forcing”.

Transition control comes by biasing the natural selection mechanism by raising the initial amplitude of the less-amplified cross-flow mode at the subcritical wavenumber, so that it initially dominates the instability growth

process. The growth of the forced mode inhibits the growth of the more amplified (critical wavenumber) stationary mode by modifying the basic state. Ultimately the forced mode decays and the flow eventually becomes turbulent. However, in swept wing experiments [31–33], the approach has been shown to produce a substantial increases in the transition Reynolds number.

Saric et al. [32] found that patterned surface roughness in the form of hemispherical "dots" with a height of 50 μm, provided an effective transition delay in low-speed swept wing experiments. Schuele, Corke and Matlis [34] found that circular indentations (dimples) worked equally as well and offered potentially better uniformity.

A majority of the experiments on cross-flow transition control have been conducted at subsonic and supersonic Mach numbers. These include Saric and Reed [31], Saric et al. [35] and Semionov et al. [36, 37] who investigated the effect of distributed roughness on swept wings at supersonic Mach numbers. Schuele, Corke and Matlis [34] performed experiments on a sharp-tipped 14° right-circular cone in a "quiet" tunnel at Mach 3.5. In that case, a subcritical spacing of discreet dimples near the cone tip increased the transition Reynolds by 40%.

While stationary cross-flow modes are exceedingly sensitive to surface roughness, traveling cross-flow modes are sensitive to vortical and possibly acoustic free-stream disturbances. Therefore their effect on cross-flow transition is an important topic of research. Any potential nonlinear interaction between stationary and traveling cross-flow modes is equally important.

Given this background, the overall objective is to present a "snap-shot" of the present understanding of cross-flow instability and transition to turbulence in hypersonic 3-D boundary layer, and our ability to control this process.

12.2 EXPERIMENTAL SETUPS

The following describes experimental setups that are designed to investigate (1) the role of free-stream turbulence and noise in the cross-flow instability process, and (2) the ability of patterned discrete roughness to control stationary cross-flow modes and subsequent transition to turbulence. The facilities used in this research include both conventional and "quiet" designs and therefore provides insight into the role these play in the development of the cross-flow instability.

12.2.1 TA&M Experiment: Quiet Mach 6 Tunnel

Experiments were performed in two facilities housed within the Texas A&M University National Aerothermochemistry and Hypersonics Laboratory (NAL); the Actively Controlled Expansion (ACE) tunnel and NASA Langley Mach 6 Quiet tunnel (M6QT). A photo of the NAL facilities is shown in Figure 12-1.

The ACE tunnel is a 9" x 14" (22.5 cm x 35.6 cm) test section, variable Mach number facility. The tunnel was designed so that the Mach number can be varied continuously by adjusting the throat height of its planar nozzle. The tunnel has been calibrated from Mach 5 to 7 and documented as uniform across the test section to within ± 1.5% at Mach 5 and ± 0.5% above Mach 6. For additional details, see Semper at al. [38].

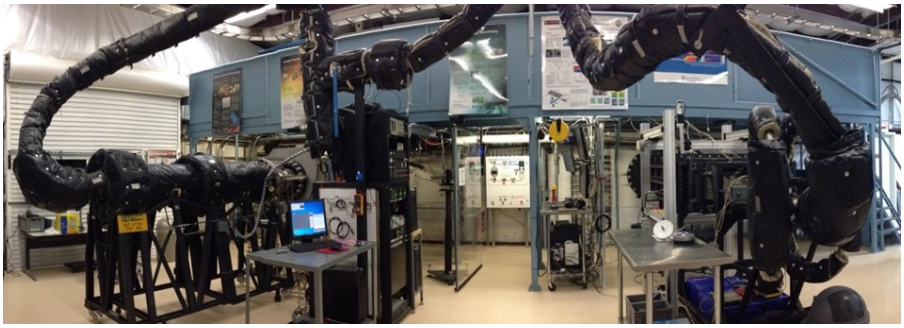

Figure 12-1: **NAL Facilities - Left: Mach 6 Quiet Tunnel (M6QT), Right: Actively Controlled Expansion Tunnel (ACE).**

The study leverages a unique characteristic of this facility that below Re/m ≈ 3 x 10^6, the tunnel wall boundary layers are laminar, and hence the free-stream turbulence levels are small. At Re/m > 3 x 10^6, the nozzle wall boundary layers transition to turbulence and free-stream pressure fluctuations increase. The free-stream fluctuations are believed to be dominated by noise radiating from the nozzle sidewalls. The free-stream disturbances versus Reynolds number are shown in Figure 12-2. The tunnel test section is provisioned with portholes on each of the test-section walls allowing for optical access and model mounting. A cage constructed of optical railing is installed surrounding the tunnel allowing for mounting of cameras, illumination sources, and traverse mechanisms.

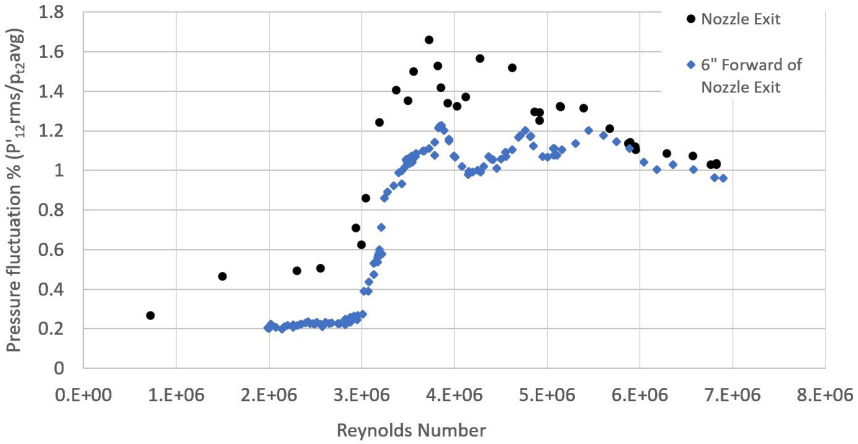

Figure 12-2: **Free-Stream Disturbance Levels in ACE.**

The Mach 6 Quiet tunnel is a low free-stream disturbance facility which was originally part of the NASA Langley hypersonic facility complex. The tunnel was relocated to TAMU in 2005 and an upgraded test section installed in 2008. The free-stream has been characterized and its quiet performance verified [39]. The nozzle exit diameter is 18.4 cm and is enclosed in a large enclosed free jet style test section. Within this test section a model fixed traverse system has been installed and utilized for free-stream and boundary layer surveys [8]. Test articles are typically placed well within the nozzle, attempting to take advantage of the test rhombus of on condition quiet flow defined by the limiting characteristic and the noise radiated from transition on the nozzle

sidewall. This limits the available optical access. Nevertheless previous efforts have successfully used IR thermography and focusing Schlieren on the portions of the model extending past the nozzle exit plane.

The model was a 38.1% scale model of the forebody of the HIFiRE-5 flight research vehicle. This particular model is of great interest because of the existing flight data as well as a number of ground tests at the same scale as detailed above. It's 2:1 elliptic cone geometry lends itself to the study of naturally developing cross-flow instability due to the inherent pressure gradient between the windward major axis and the leeward minor axis.

A monolithic PEEK cone model was constructed. This design was chosen to avoid steps or gaps on the model surface which may alter instability development in an uncontrolled way. PEEK was chosen because of the low thermal conductivity and high emissivity, which enabled IR thermometry. The model nose tip geometry was altered from the HIFiRE-5 design. Instead of a circular arc, the nose tip is defined by a modified super ellipse to eliminate a discontinuity in curvature at the junction of the nose tip and the rest of the cone. Such discontinuity has been shown to be a source of receptivity in low-speed flows [40]. In the finished model this change is likely within the margin of error in the machining process but was made as a "best practice" choice. A combination of a Keyance Laser profilometer and a Mitituyo contact profilometer was used to quantify the surface finish.

The instrumented improved model was run in the M6QT. This model has quite a large diameter base. It was uncertain that the model would be far enough into the nozzle to be inside the nozzle exit shock and also avoid the shockwave from the model impinging on the nozzle wall potentially leading to separation and nozzle unstart. These constraints meant that during a run the model was not fully within the quiet core of the tunnel. It is unknown what effect this impingement of radiated noise on the downstream portion of the model has on the development of the cross-flow instabilities on the model. Craig and Saric [8] argue that at least for their yawed cone, a similar impingement is far enough downstream on the model as to not effect the transition process and a bispectral analysis of hot-wire data supported this argument. A series of high speed Schlieren runs were conducted to examine the position of the shocks in this configuration. It was determined that the farthest the model could extend beyond the nozzle exit plane was 1.5". This location was used for the remainder of the runs. Figure 12-3 shows this configuration.

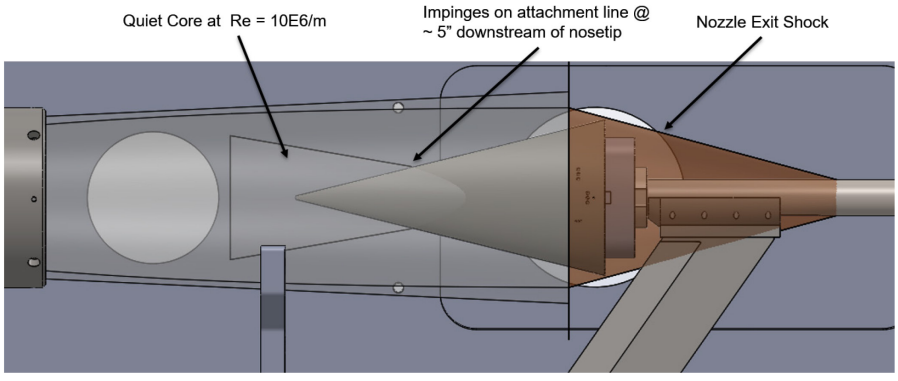

Figure 12-3: Improved Model in the M6QT, Drawing of Improved Model Mounted Within the M6QT. Estimated quiet core and nozzle exit shock are shown.

Infrared thermography, surface pressure measurements, and hot-wire anemometry were used to examine the development of instabilities on the cone. IR thermography has been successfully used in several studies to examine the location and extent of the onset of transition in both high- and low-speed flows [19, 41]. The model surface was imaged using a FLIR SC8100 IR Camera which is sensitive to wavelengths from 3 – 5 μm, and a resolution of 1,024 x 1,024. Time histories of model surface temperature were recorded at 15 Hz. from which surface heat flux and Stanton number was computed. A detailed description of the process can be found in Neel et al. [42, 43].

Surface pressure measurements were used to examine frequency spectra of fluctuations at points along the model surface. This utilized Kulite XCE-062-15A pressure transducers that were arranged in an array pattern that could differentiate traveling instability wave angles and phase speeds [13, 18]. These transducers have been characterized under a supersonic turbulent boundary layer and are expected to have a linear frequency response up to 30 – 40 % of their resonant frequency [44]. For higher frequency measurements, PCB 132B38 pressure transducers were utilized. These quoted resonant frequency of > 1 MHz, allowing measurements in the hundreds of kilohertz, the expected frequency range of the second mode, and potential secondary instabilities of the stationary cross-flow vortices. The sensors were placed to lie under streaks observed in the IR images. The locations of these two types of pressure transducers on the model are shown in the schematic in Figure 12-4.

Further PCB transducers were mounted at and on either side of the model centerline. An array of Kulites was placed with the center Kulite, Kulite 2, mirrored about the centerline in the same position as PCB 2. As mentioned previously this array is arranged following Borg and Kimmel [27]. It was intentionally placed in a more inboard location than on the model of Borg at al.[24] to investigate the more inboard observed transition under noisy flow. The resulting locations are presented in Figure 12-4.

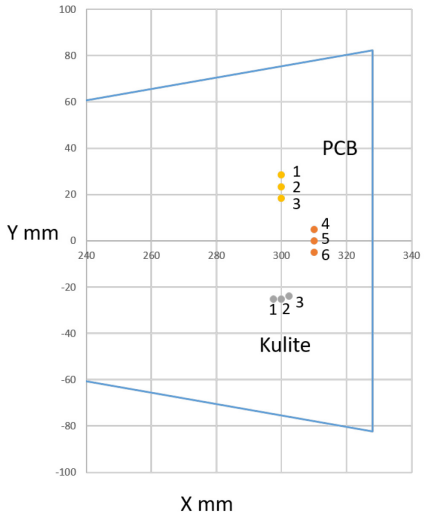

Figure 12-4: Sensor Locations – Diagram of Sensor Locations.

12.2.2 UND Experiment: Conventional Mach 6 Tunnel

The University of Notre Dame (UND) experiments [45] were conducted in the U.S. Air Force Academy (AFA) Mach 6 Ludwieg Tube facility. This is a conventional ("non-quiet") design. A schematic drawing of the facility is shown in Figure 12-5. The facility is "sister" design of the TU Braunschweig Ludwieg Tube, having the same valve, nozzle, test section and diffuser. These facilities use a specially designed plunger valve at the nozzle throat instead of a more conventional burst plate. The plunger valve is closed to pressurize the air in the driver tube. A control signal opens the valve to allow air from the pressurized charge tube to pass through the converging-diverging nozzle and test section. The valve can be closed after a pre-determined time interval so as to not completely exhaust the driver tube. The typical run time is ~100 ms. The time to recharge the tunnel for another run is ~15 min. The short recharge time allowed for numerous runs to be completed, which was an asset to sample a large matrix of spatial locations needed to document the basic state and instability development over the model.

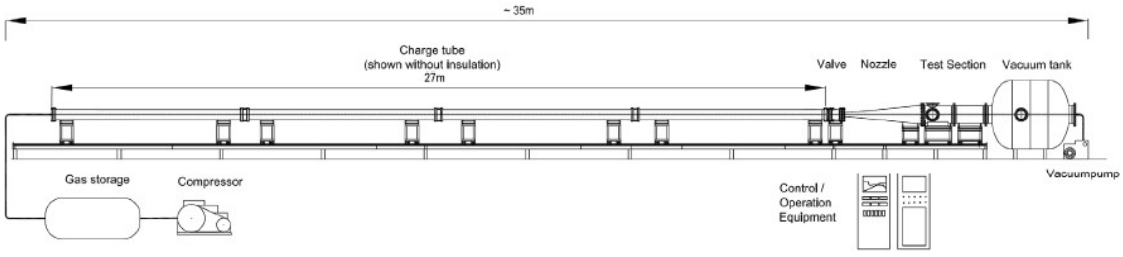

Figure 12-5: Schematic Drawing of the U.S. Air Force Academy Mach 6 Ludwieg Tube Facility.

The 0.5 m. diameter test section and range of unit Reynolds numbers of the AFA facility were ideal to utilize the same 14° cone model used by Schuele, Corke and Matlis [34]. As in their previous experiment, the cone model was equipped with a motorized 3-D traversing mechanism that mounted on the support sting. The traversing mechanism held a pair of closely spaced fast-response total pressure probes with a frequency response of 50 kHz. Figure 12-6 shows the cone model with the traversing mechanism in the AFA Mach 6 Ludwieg Tube test section.

A cone angle of attack of 6° was set to produce a mean cross-flow velocity component in the boundary layer over the cone by which the cross-flow instability was the dominant mechanism of turbulent transition. Similar 14° cone models have been examined experimentally at Mach 6 by Swanson and Schneider [46] at a 6° angle of attack, and by Craig and Saric [47] at a close, 5.6° angle of attack. Both experiments were in quiet tunnels. Li, Choudhari, Chang and White [48] performed stability analysis on a 14° cone at a 6° angle of attack at Mach. Thus this configuration is well represented in the literature.

Stability analysis of the basic cross flow for the cone model at the 6° angle of attack at Mach 6 by Li et al. [48] indicated that the most amplified stationary cross-flow modes were centered about an azimuthal wave number of approximately $m = 45$. This was in good agreement with experimental observations of Swanson and Schneider [46] and Craig and Saric [47]. This then corresponds to the "critical" wavenumber. Based on Saric et al. [32], the "subcritical" wavenumber for control of the stationary cross-flow mode would then be 1.5-times higher or $m = 68$.

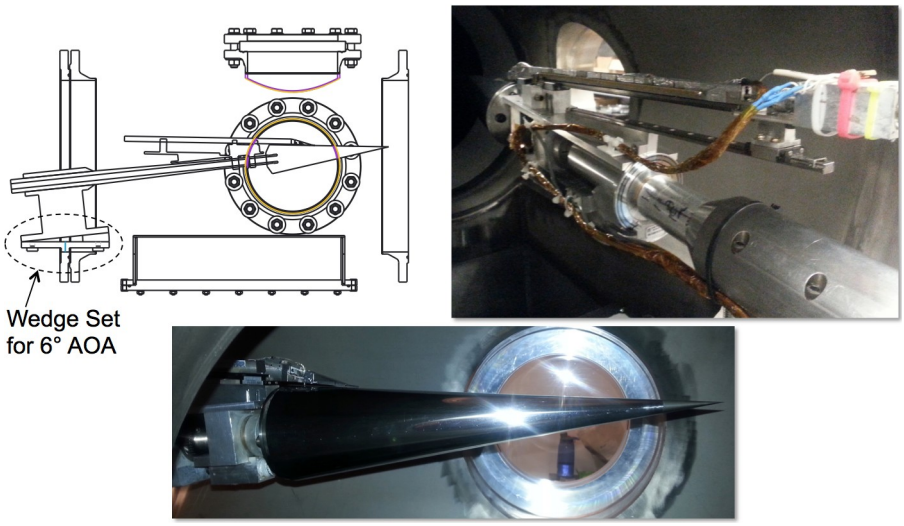

Figure 12-6: Schematic and Photographs of the Cone Model and 3-D Traversing Mechanism in the Air Force Academy Mach 6 Ludwieg Tube Test Section.

The streamwise location of the roughness array is determined by taking into account Branch I (N = 0) of the linear stability neutral curve for stationary cross-flow modes on the cone at a 6° angle of attack, as well as the theoretical vortex lines. These are shown for the cone at a unit Reynolds number of $10 \times 10^6 m^{-1}$ in Figure 12-7. Placing the roughness array too far upstream of Branch I would allow the controlled disturbances to decay, potentially below the background disturbance level. Placing them too far downstream would allow cross-flow modes excited by random roughness or free-stream disturbances to grow to larger amplitudes that minimize the effect of the roughness array. An equally important consideration on the placement of the roughness are the theoretical vortex lines, along which the disturbances generated by the roughness convect. To be effective, the axial location of the roughness array needs to intersect with the vortex lines that lead to the region where the linear theory N-factor curve reaches furthest upstream on the cone, indicating the most likely region where turbulent transition is expected to occur. For the cone at a 6° angle of attack this occurs in the azimuthal region on the lee side between 110° and 150° (where 0◦ is the windward stagnation line). Based on these two factors, the discrete roughness arrays were located $x_r = 1.27$ cm. from the tip of the cone.

The UND cone model utilized interchangeable nose tips representing different tip-roughness conditions. These tips were machined from Torlon (Polyamide-Imide (PAI)), which is a relatively hard polymer that can be polished. Following Schuele, Corke and Matlis [34], surface roughness patterns consisted of “dimples” that were produced by plunging a conical pin into the surface of the tip. An example of the dimple roughness is shown in Figure 12-8. This corresponds to the $m = 68$ subcritical azimuthal wave number designed to suppress cross-flow mode growth and turbulent transition. The hole diameter is approximately 80 μm and the ratio of the diameter to dimple centerline spacing is $d/\lambda \sim 0.6$. This ratio satisfies the discrete roughness criteria [49] that $d/\lambda \geq 0.5$.

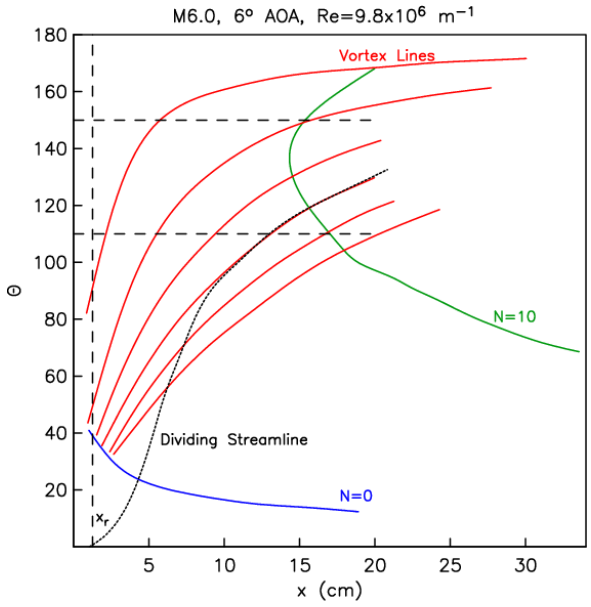

Figure 12-7: Linear Stability and Vortex Path Map Used in Determining Axial Location of Discrete Roughness for Cross-flow Transition Control Based on Li et al. [48].

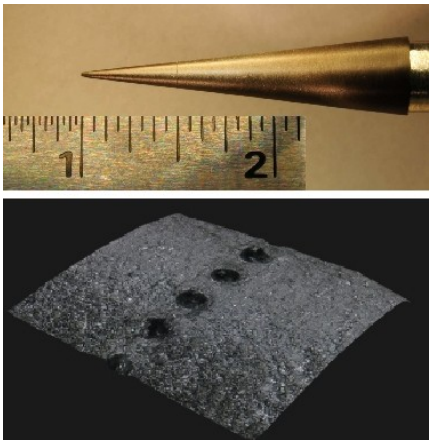

Figure 12-8: Photograph of a Removable Cone Tip with Representative "Dimples" Located at x_r = 1.27 cm. (0.5 in.) From the Tip.

12.3 KEY RESULTS

12.3.1 TA&M Experiment: Basic Flow and Effect of Free-Stream Disturbances

The following results are a subset of detailed experimental campaigns given in Neel at al. [43]. The experiments were conducted in the ACE facility at Mach 6 for the full range of Reynolds numbers. The model was placed at 0° AOA. It was allowed to remain at room temperature until the beginning of the run. For each run, the model wall temperature was measured to be approximately 310K. To quantify freestream disturbance effects, the model position was varied with the nose tip located 2.5 in. downstream of nozzle exit, 0.5 in. upstream of the nozzle exit, and 6 in. upstream of the nozzle exit. For a given Reynolds number, the upstream positions were in a lower disturbance environment. This was observed to produce more distinct streaks in the thermal image leading into the elevated heating. This was in contrast to the furthest back position where the thermal image revealed a more washed out or diffused front. This is documented in Figure 12-9.

Neel et al. [43] compared the present ACE IR images to similar results from the Purdue Mach 6 tunnel results [16] when operated noisy. One notable difference between the present and Purdue noisy results is the identification of stationary streaks emanating from the leading-edge and merging into the transition region. It is likely that the Purdue temperature sensitive paint did not have the fidelity to resolve these structures.

The instability and evolution, with increasing Reynolds number, under conventional tunnel disturbances, are presented in Figures 12-10 and 12-11. PSDs of the fluctuating pressure measured by Kulite sensors with the model at the furthest downstream position are shown in Figure 12-10. These show a broad peak in the 10 – 20 kHz range that was seen before in noisy runs in the BAM6QT and ACE [24]. There is also evidence of a broad-

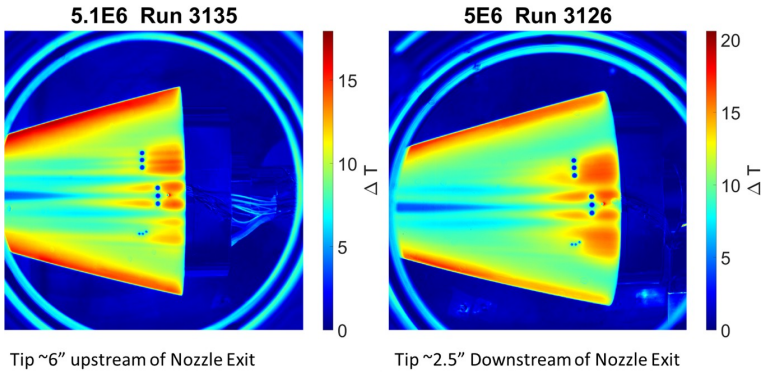

Figure 12-9: Comparison of Heating Between Model Locations - Comparison of Heating from the Upstream-most Station to the Downstream-most Location. Colored by ΔT from Beginning of the Run in the ACE Tunnel.

band disturbance centered near 150 kHz for the low Reynolds number conditions (less than about 4×10^6). However, 150 kHz is outside of the expected linear frequency range of the transducers. The three shoulder-located PCB PSD traces shown in Figure 12-11 confirm the growth of a band of frequencies in the range of 100 – 400 kHz for Reynolds number less than about 5×10^6. The center of this band shifts to higher frequencies with increasing Re, which is the expected trend for an instability scaling with boundary layer height. The peak frequency varied with PCB location. There is also a wave centered near 20 – 80 kHz, which is the expected frequency band of the traveling cross-flow mode [25]. This frequency is also present in the M6QT results (as discussed later). Broadband turbulence occurred for Re/m greater than about 5×10^6.

PSDs of the fluctuating pressure measured by Kulite sensors with the model at the most upstream position to help quantify freestream disturbance effects. The results are shown in Figures 12-12 and 12-13. Qualitatively, the wave structure results are similar to those in Figures 12-10 and 12-11. However, the magnitudes for the upstream measurements are smaller, which is consistent with the lower freestream disturbance levels. Hence, moving the model upstream resulted in more well defined stationary structures, but with PSD waves that strongly resembled the ones further downstream, where the model was exposed to significantly lower disturbances, as shown in Figure 12-2. The observed spectral peaks are summarized in Table 12-1, with modal interpretation based on the numerical simulations of Kocian et al. [28] also summarized in Table 12-1. The M6QT data are discussed in the next paragraph.

Table 12-1: Observed Excited Spectral Bands in the Shoulder Cross-flow Region.

Frequency	TAMU ACE (all locations)	TAMU M6QT	Mode
0	IR Therm; Re/m= 3.0 – 8.2 × 10^6	IR Therm; Re/m= 6.0 – 10.0 × 10^6	Stationary
10 – 20 kHz	Kulites 1-3; Re/m= 2.0 – 6.0 × 10^6	Not Observed	Unknown
20 – 80 kHz	PCB 1,2; Re/m= 2.0 – 4.0 × 10^6	PCB 1-3; Re/m= 6.0 – 11.6 × 10^6	Traveling
100 – 400 kHz	PCB 1-3; Re/m= 2.0 – 5.0 × 10^6	PCB 1,2; Re/m= 7.2 – 10.0 × 10^6	Secondary

Examples of IR images and pressure sensor data obtained in the M6QT are shown in Figure 12-14. The IR images show distinct differences from the conventional (noisy) ACE tunnel. For example, nearly streamwise

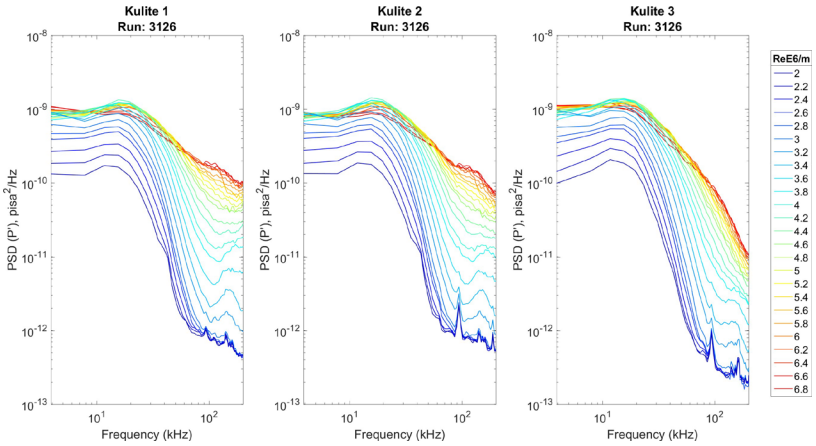

Figure 12-10: PSD of Kulite Sensor Data Run 3126 - PSD of Fluctuating Pressure for Each Kulite for Run 3126 at the Exit of the ACE Tunnel.

streaks that extend over a large portion of the surface are clearly visible. These are believed to be due to stationary cross-flow vortices generated by upstream surface roughness. As the Re is increased, these streaks are seen to increase in temperature with a distinct front appearing. The PSD functions of the fluctuating pressures measured by Kuilte sensors are shown in Figure 12-15. The Mach 6 Quiet Tunnel data are qualitatively different than those measured in the ACE tunnel. In particular, the 10 – 20 kHz band wave is absent, and instead there is clear wave in the 20 – 80 kHz range. A peak near 45 – 50 kHz is visible in Kulites 1 and 2, but not 3. This is consistent with the expectation that the spectral content varies with location with respect to the stationary structures. The PSD functions of the fluctuating pressures measured by PCB sensors are shown in Figure 12-16. The data show a small peak near 45 – 50 kHz, which is the expected frequency band of the traveling cross-flow mode [25]. Visible in the PCB 1 data is a broad region of growth with an accompanying sharp peak near 200 kHz. This peak, to a lesser degree, is visible in the spectra from PCBs 2 and 3. Based on comparison with the simulations, the spectral peak appears to correspond to the secondary instability associated with crossflow. It appears to grow rapidly from Re/m of 7.2 – 10.0 x 10^6. There also appears to be higher frequency content in the 500 – 800 kHz range for PCBs 1 and 2. This too may be a secondary instability. The spectra for PCBs 4-6 along the model centerline show three basic excited frequency bands centered near 40, 120 and 220 kHz. All of the excited bands are summarized in Table 12-1 (Column 3). Broadband turbulence occurred for Re/m greater than about 10 × 10^6, which is near the quiet operation of the tunnel.

12.3.2 UND Experiment: Basic Flow and Effect of Discrete Roughness

12.3.2.1 Basic Flow.

Normally the basic flow would be documented by measuring wall-normal profiles of mean (time-averaged) quantities to compare to numerical solutions of the Navier-Stokes equations. However, the short run times did not allow more than one spatial sampling point per tunnel run. Therefore the basic flow was indirectly verified by documenting the stability characteristics and comparing those to analysis such as that of Li et al. [48].

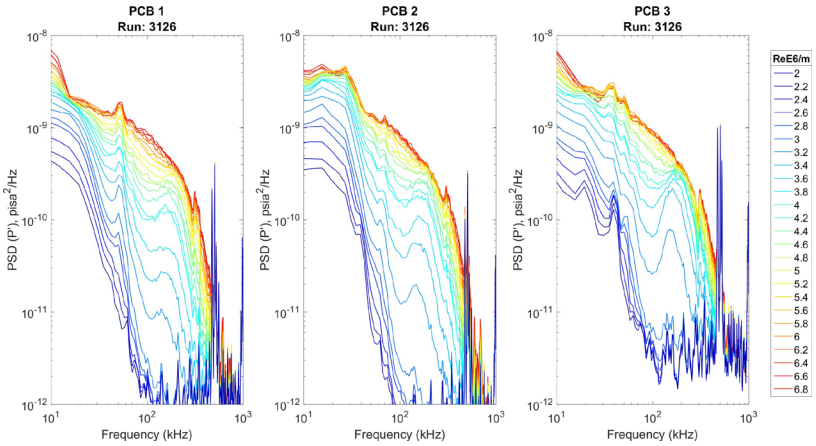

Figure 12-11: **PSD of PCB 1-3 Sensor Data Run 3126 – PSD of Fluctuating Pressure for Shoulder PCB Cluster for Run 3126 at the Exit of the ACE Tunnel.**

The first objective was to verify that stationary cross-flow were observable under the conditions of the AFA facility. The key issue is that the AFA Ludwieg tube is a conventional design rather than a *quiet* design. Previously, stationary cross-flow modes *have never been observed in conventional hypersonic wind tunnels*, where large acoustic disturbances are present. The possible reason is the potential dominance of traveling cross-flow modes, which are more amplified than the stationary modes, and sensitive to free-stream disturbances [50].

Following Schuele, Corke and Matlis [34], the presence of stationary cross-flow modes was first verified using surface oil-flow visualization [45]. The motion of the oil was recorded during the 80ms run time of the facility using a high-speed video camera. During the run, the oil pattern would reach a steady pattern that revealed the presence of the stationary cross-flow mode. Figure 12-17 shows a sample image for the cone at a 6° angle and a unit Reynolds number of 10×10^6 m^{-1}. Spectral analysis in the denoted interrogation region was performed on images like this to determine the spatial wave numbers in the visualization patterns. The azimuthal wave number distribution for the baseline (smooth tip) flow is shown in Figure 12-18. The dashed line at $m = 45$ represents the center of the band of most amplified stationary cross-flow modes based on Li et al. [48]. The dot-dashed line indicates the axial location on the cone where transition would occur based on a linear theory N-factor of 10.

Figure 12-18 indicates a broad distribution of energy at wave numbers that are approximately centered on $m = 45$ which is consistent with the linear theory predictions. The energy in this band of wave numbers diminishes beyond the axial location of the N = 10 line. This indicates that the coherent stationary pattern is lost beyond this x-location, possibly as a result of turbulent transition.

12.3.2.2 Discrete Roughness.

Two different discrete roughness cone tips were used to (1) verify the receptivity of the stationary cross-flow mode to the critical and subcritical mode number roughness, and (2) to demonstrate if the subcritical mode number roughness would increase the transition Reynolds number in a similar manner as found by Schuele, Corke and Matlis [34] in a Mach 3.5, quiet tunnel. The first evidence of this came from surface flow visualization. The result is presented in wave number spectra shown in Figures 12-19 and 12-20.

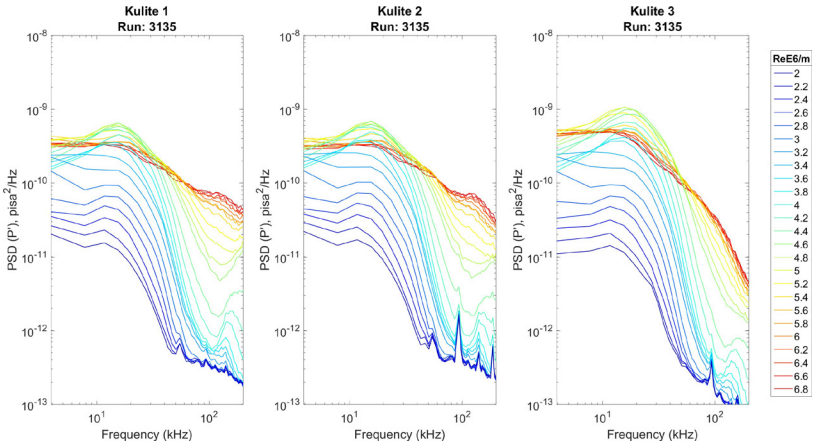

Figure 12-12: PSD of Kulite Sensor Data Run 3135 – PSD of Fluctuating Pressure for Each Kulite for Run 3135 at the Upstream Location in the ACE Tunnel.

Figure 12-19 shows the wave number spectrum for the case with the critical ($m = 45$) roughness cone tip. The contrast with the baseline (smooth tip) case in Figure 12-18 is striking. This shows a dominant peak in the wave number spectrum at $m = 45$ that indicates that the stationary pattern in the surface visualization was highly correlated with the roughness mode number.

The wave number spectrum for the subcritical ($m = 68$) roughness cone tip is shown in Figure 12-20. Comparing the wave number spectrum to that with the critical ($m = 45$) roughness tip, one now observes energy at wave numbers around $m = 68$ that was not previously evident. A peak in the wave number spectra is still observed around the most amplified $m = 45$ mode but its amplitude has been reduced by approximately 30% with the subcritical roughness.

The wave number spectra of the surface flow visualization also offers a first glimpse of the effect the subcritical roughness might have on the transition. If transition is defined as a loss of coherence of the stationary pattern, then for the critical ($m = 45$) roughness this appears to occur very close to the axial location where the N = 10 is drawn. In contrast, for the subcritical ($m = 68$) roughness, well defined spectral peaks in wavenumbers exist well beyond the N = 10 transition line. Further evidence will come from off-wall measurements.

The off-wall measurements involved a fast-response total pressure probe with a frequency response of 50 kHz [45]. The frequency response was important not only because of the short (80 ms) run times, but also because the most amplified *traveling* cross-flow modes were predicted [48] to be centered at 35 kHz. The voltage time series proportional to total pressure were sampled at 100 kHz to resolve up to the maximum frequency response of the probe.

Total pressure time series were sampled at discrete (θ, x) locations at a fixed height above the surface of the cone. The data samples at each location represented one run of the facility. In total, there were on the order of 350 runs to generate the data presented in the following figures. For efficiency, the sampled locations were grouped in a range of azimuthal locations where transition was first expected to occur based on an N-factor of

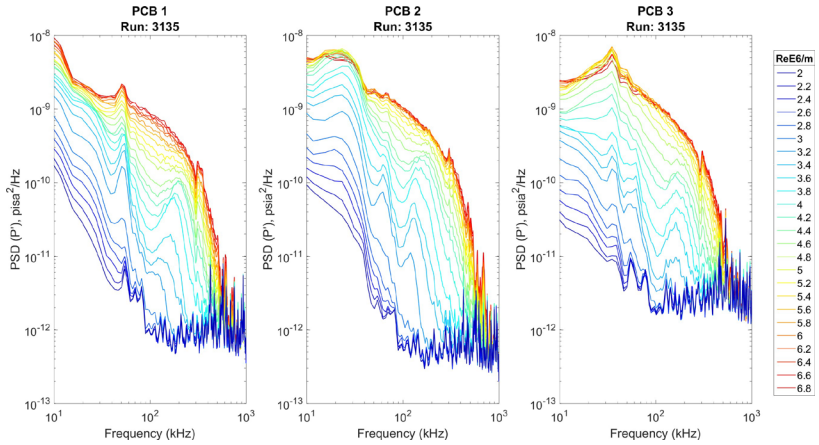

Figure 12-13: PSD of PCB 1-3 Sensor Data Run 3135 – PSD of Fluctuating Pressure for Shoulder PCB Cluster for Run 3135 at the Upstream Location in the ACE Tunnel.

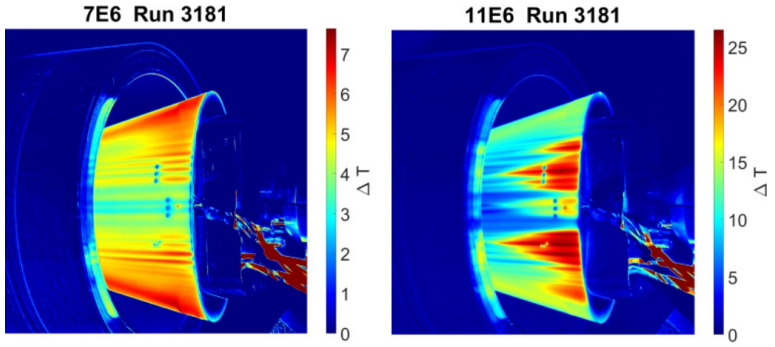

Figure 12-14: Surface Temperature in M6QT.

10 that was indicated in Figure 12-7. Figure 12-21(a) shows the azimuthal variation in the total pressure with the critical (m=45) roughness that is indicative of the mean flow distortion produced by the stationary cross-flow mode. The stationary cross-flow mode produces an azimuthal thickening and thinning of the boundary layer. Because of the measurements were at a fixed height above the cone surface, the negative pressures correspond to the thickened portion of the boundary layer, and the positive pressures to the thinned portions. In terms of the azimuthal angle, the m = 45 mode has an azimuthal wavelength of 8°, which is fairly close to the observed angle between the centers of the pressure minima at the upstream regions. Evidence of this azimuthal wave number is further reinforced by the wave number spectra of this total pressure distribution that is shown in Figure 12-21(b). This shows a dominant peak at m = 45. The energy in the m = 45 mode decays to a minimum near the axial location where the N = 10 factor predicts transition to occur. This agrees well with the wave number spectra that was derived from the flow visualization and shown in Figure 12-19.

The azimuthal variation in the total pressure indicative of the mean flow distortion produced by stationary cross-flow modes with the subcritical (m=68) roughness is shown in Figure 12-22(a). The contrast is immediately

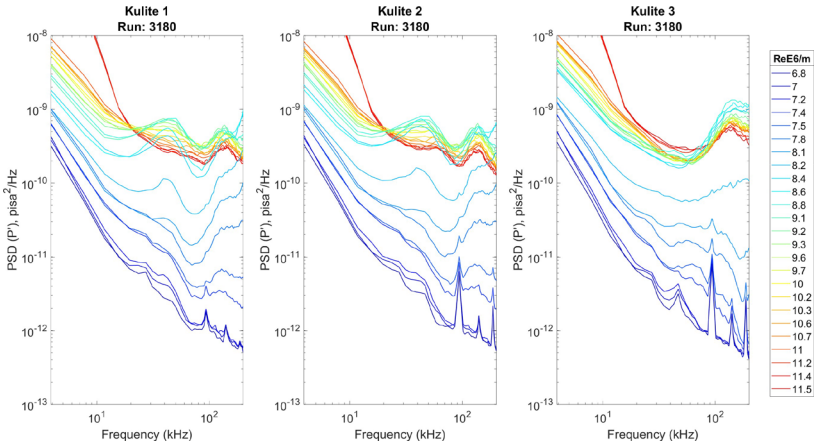

Figure 12-15: PSD of Kulite Sensor Data Run 3180 – PSD of Fluctuating Pressure for Each Kulite for Run 3180.

apparent and reflects the higher azimuthal wave number (smaller azimuthal wave length) that results from the closer spaced discrete roughness at the tip. For reference, the m = 68 mode has an azimuthal wavelength of 5.3°. The wave number spectra of the total pressure distribution for this roughness condition is shown in Figure 12-22(b). This shows a dominant peak at m = 68. Further downstream, the peak appears to shift to higher wave numbers on the order of 100. This is consistent with Saric et al. [32] where subcritical roughness with azimuthal wave numbers of 1.5-times that of the critical roughness value would not generate subharmonic mode numbers.

The dominant peak in the wave number spectra with the subcritical roughness extends well downstream of the N = 10 line, indicating that the transition Reynolds number has increased. As further evidence, the method of Schuele, Corke and Matlis [34] was used to estimate transition location. This involved following the x-trajectory of a minimum in the total pressure distributions in Figures 12-21(a) and 12-22(a). The actual trajectories are shown by the dotted curves in those two figures. As previously mentioned, the pressure minima are indicative of a region of local thickening of the boundary layer. Such regions are known to develop an off-wall inflectional shear layer and subsequent inviscid instability that quickly leads to turbulence.

The x-development of the total pressure along the two pressure minima for the critical and subcritical roughness is shown in Figure 12-23. Estimates of the transition location were performed by two approaches. The first, shown in blue, followed a Preston tube approach in which a linear curve is fit to the rise in the total pressure near the wall that would accompany transition. The x-location where the linear curve intersects a common reference level is designated as the transition location. Based on this approach, the subcritical roughness resulted in a 25% increase in the transition location.

The second approach is based on the loss in the coherence of the mean flow distortion. This would be evident as saturation and abrupt decay in the axial development of the total pressure. Based on this approach, shown in red, the subcritical roughness pattern resulted in a 15% increase in the transition location. This approach can be considered as an indication of the *late stage* of transition, whereas the Preston tube approach can be considered to be an indication of the *early stage*.

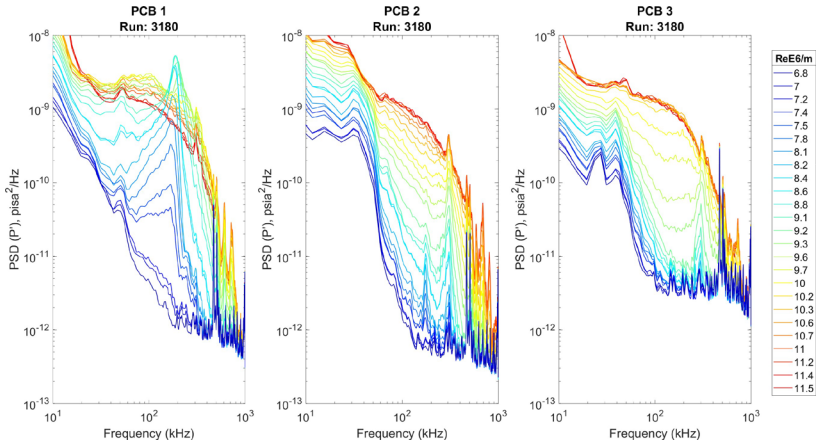

Figure 12-16: **PSD of PCB 1-3 Sensor Data Run 3180 – PSD of Fluctuating Pressure for Shoulder PCB Cluster for Run 3180.**

As mentioned, the total pressure Pitot probes had a frequency response that was capable of detecting the traveling cross-flow modes. Figures 12-24 and 12-25 show spectra of off-wall total pressure fluctuations at increasing x locations for a single azimuthal angle for the critical and subcritical roughness cone tips. Both these show a broad peak that is centered near 30 kHz that was predicted to be the frequency of the most amplified traveling cross-flow modes [48]. The azimuthal wave number of the most amplified traveling mode is predicted [48] to be $m = 40$.

The peak values of the spectra of the traveling disturbances, for all of the measured (θ, x) locations for the two tip roughness cases, were used to compile a view of the spatial amplitude distribution for the traveling cross-flow modes. These are shown for the critical $m = 45$ roughness cone tip in Figure 12-26, and for the subcritical $m = 68$ roughness cone tip in Figure 12-27. Examination of these reveals the presence of features with different azimuthal wave numbers. To interpret these, one needs to consider possible interactions between the traveling and stationary cross-flow modes.

Physically the traveling cross-flow modes ride (convect) over the stationary modes which then has the potential to modulate and interact with the traveling modes. Corke and Matlis [51] and Corke, Matlis and Othman [30] documented a nonlinear (quadratic) sum and difference interactions between traveling and stationary cross-flow modes in 3-D boundary layers over a rotating disk. The question is if there is similar interaction occurring in this instance.

Considering the critical $m = 45$ roughness cone tip, the stationary modes occur at $m = 45$. This mode will be designated as $(0, 45)$, where the first index is the frequency, and the second is the azimuthal wave number. Li et al. [48] determined the most amplified traveling cross-flow mode occurred with a mode number of $m = 40$. This mode will be designated as $(f_t, 40)$. The first interaction between these two modes will be through a sum and difference, namely

$$(0, 45) \pm (f_t, 40) = (f_t, 85) \text{ and } (f_t, 5). \tag{12-1}$$

Both $(f_t, 85)$ and $(f_t, 5)$ are traveling modes with the same frequency as the primary traveling mode, which is the energy peak that was used to generate Figures 12-26 and 12-27.

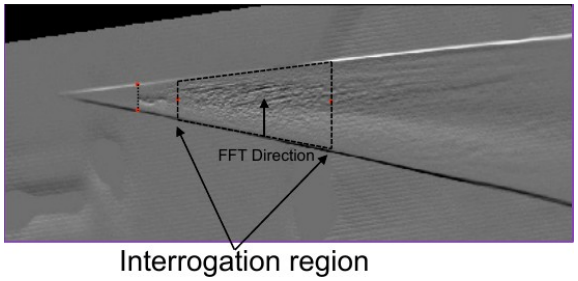

Figure 12-17: Sample Processed Image of Oil Flow Surface Visualization. Cone at 6° AoA at Mach 6 and Unit Reynolds Numbers of 10 ×10^{6}m^{-1}. From Matlis, Arndt and Corke [45].

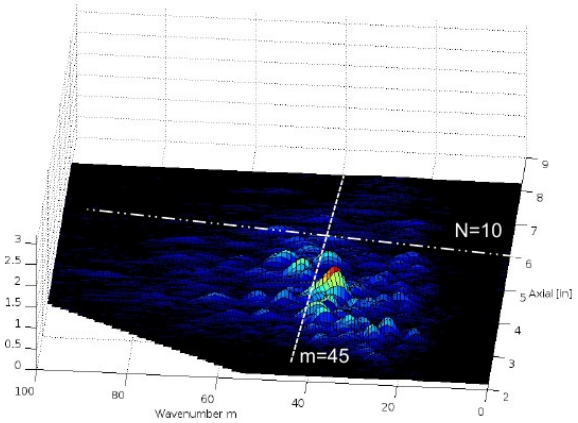

Figure 12-18: Azimuthal Wave Number Spectrum Axial Distribution Based on Flow Visualization for Baseline Cone (Smooth Tip) Condition. Cone at 6° AoA at Mach 6 and Unit Reynolds Numbers of 10 × 10^{6}m^{-1}. From Matlis, Arndt and Corke [45].

Now (f_t, 85) has an azimuthal wave angle of approximately 4°, and (f_t, 5) has an azimuthal wave angle of 72°. The latter is larger than the azimuthal extent of the measurements. However the former, (f_t, 85), is distinguishable in the spatial amplitude distribution in Figure 12-26.

Also observable is a spatial amplitude distribution with an azimuthal wavenumber that matches that of the discrete roughness, $m = 45$. This is not realizable through a quadratic interaction to produce (f_t, 45). Therefore it is most likely due to a *linear* superposition that leads to a modulation of the traveling mode amplitude as it rides over the stationary mean flow distortion.

For the case with the subcritical, $m = 68$ roughness cone tip, the sum and difference interaction would be

$$(0, 68) \pm (f_t, 40) = (f_t, 108) \text{ and } (f_t, 28). \tag{12-2}$$

Here (f_t, 108) would have an azimuthal wave angle of approximately 3°, and (f_t, 28) an azimuthal wave angle of approximately 13°. Both again are traveling modes with the same frequency as the primary traveling mode. Both of these are evident in the spatial amplitude distribution shown in Figure 12-27.

As before, a spatial amplitude distribution with an azimuthal wavenumber that matches that of the discrete roughness, $m = 68$, is also observable. This again is most likely due to a linear superposition that produces a modulation of the traveling mode amplitude as it rides over the stationary mean flow distortion produced by the $m = 68$ roughness.

Interactions such as these have the potential to be very important to the development of the traveling cross-flow modes. Further sum and difference interactions between these modes will produce other cross-flow modes *including stationary* cross-flow modes that can quickly lead to turbulence. As a result, this interaction between

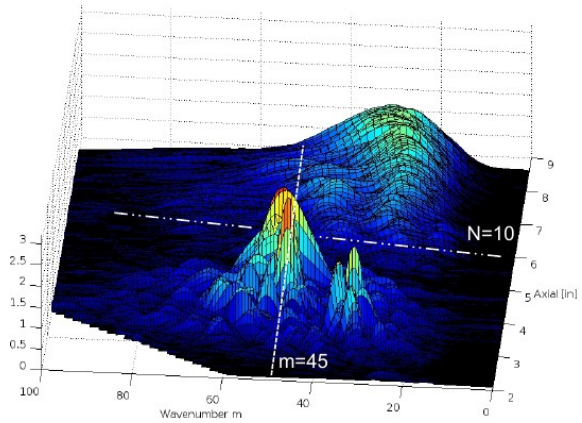

Figure 12-19: Azimuthal Wave Number Spectra Based on Flow Visualization for Cone with Critical (*m* = 45) Roughness Tip. Cone at 6° AoA at Mach 6 and Unit Reynolds Numbers of 1 x $10^6 m^{-1}$. From Matlis, Arndt and Corke [45].

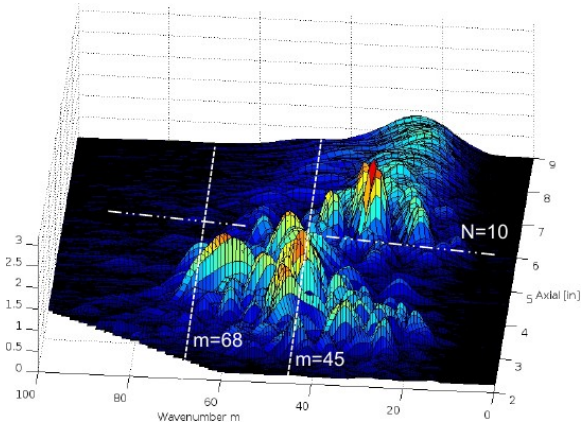

Figure 12-20: Azimuthal Wave Number Spectra Based on Flow Visualization for Cone with Subcritical (*m* = 68) Roughness Tip. Cone at 6° AoA at Mach 6 and Unit Reynolds Numbers of 1 x $10^6 m^{-1}$. From Matlis, Arndt and Corke [45].

the initial stationary and traveling cross-flow modes might be the mechanism for how free-stream disturbances affect cross-flow mode transition and account for the difference between the transition Reynolds number in conventional (noisy) and quiet wind tunnels.

12.4 DISCUSSION OF RESULTS

The surface flow visualization and off-wall azimuthal surveys of the total pressure revealed the same picture of the mean flow distortion produced by the stationary cross-flow modes that developed in the boundary layer over the right-circular cone at the 6° angle of attack. These measurements confirmed the receptivity of the cross-flow mode to the discrete roughness in a conventional (non-quiet design) environment.

The design of the roughness was identical in all characteristics to that used by Schuele, Corke and Matlis [34] in a quiet Mach 3.5 tunnel. The passive roughness consisted of micron-size indentations (dimples) that were located near the cone tip, just upstream of the first neutral growth branch of stationary cross-flow modes, based on linear stability theory. The roughness dimples encircled the cone tip with a uniform spacing that defined the azimuthal wavenumber of the roughness. The disturbances produced by the roughness dimples was expected to follow the theoretical vortex path lines to the azimuthal region where turbulent transition was predicted to first occur based on linear theory N-factors. For the cone at a 6° angle of attack, this was expected to be in the range of azimuthal angles from 110° to 150°, measured from the windward stagnation line. As a result, although the dimples encircled the cone tip, only those that intersected with the theoretical vortex path lines at the axial location of the roughness were active.

Two azimuthal wavenumbers of roughness were investigated. One that was in the band of the initially most-amplified (critical) wavenumbers of stationary cross-flow modes. The other that was at a 1.5 times higher (subcritical) wavenumber. The critical wavenumber roughness was intended to represent a controlled baseline

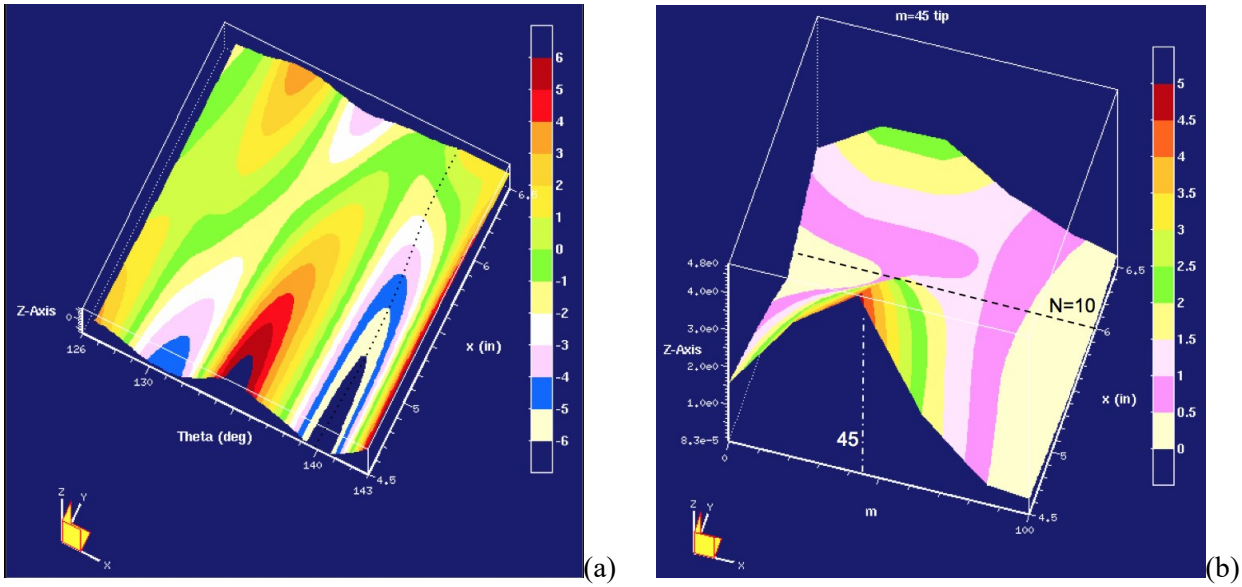

(a) (b)

Figure 12-21: Azimuthal Total Pressure Distributions at a Constant Height Above the Surface (a) and Corresponding Wave Number Spectra (b) for the Case with the Critical (*m* = 45) Roughness Cone Tip. From Matlis, Arndt and Corke [45].

that would favor a single wavenumber stationary cross-flow mode. The subcritical wavenumber roughness was intended to suppress the growth of initially amplified stationary cross-flow modes and thereby increase the transition Reynolds number in a scenario first documented at subsonic Mach numbers by Saric et al. [32].

A smooth cone tip representing an uncontrolled baseline was documented only through surface flow visualization. This was the only viable approach for a full-field survey without a defined roughness pattern that was fixed from one run to the next in the Ludwieg tube. This however did reveal a stationary pattern with azimuthal wave lengths (mode numbers) that were in the band predicted to be most amplified from linear theory by which our critical roughness was selected. The transition location with the smooth tip was also in good agreement with that for the critical roughness, suggesting that the disturbance amplitude of the critical roughness was comparable to that of random roughness on the smooth tip.

Transition front measurements using the Preston tube approach indicated that the transition Reynolds number had increased by 25% with the subcritical wavenumber roughness compared to the critical wavenumber roughness. This is less than the 40% increase in the transition Reynolds number in the lower Mach number, quiet environment documented by Schuele, Corke and Matlis [34]. Given that the roughness design was the same in both experiments, one can question if

1) The difference in the increase in transition Reynolds number was due to a Mach number effect; or

2) If the difference is due to the difference in acoustic disturbance levels between the experiments.

With regard to the latter, we can look to the results of the experiments presented in Section 12.3. For example, the thermal images in Figure 12-9 show more distinct streaks, attributed to stationary cross-flow vortices, in the lower disturbance condition. In this case, being in a conventional tunnel, the disturbances could be any combination of entropy, vorticity, and acoustic fluctuations that either reduce the strength of the stationary modes, or reduce their spatial coherence.

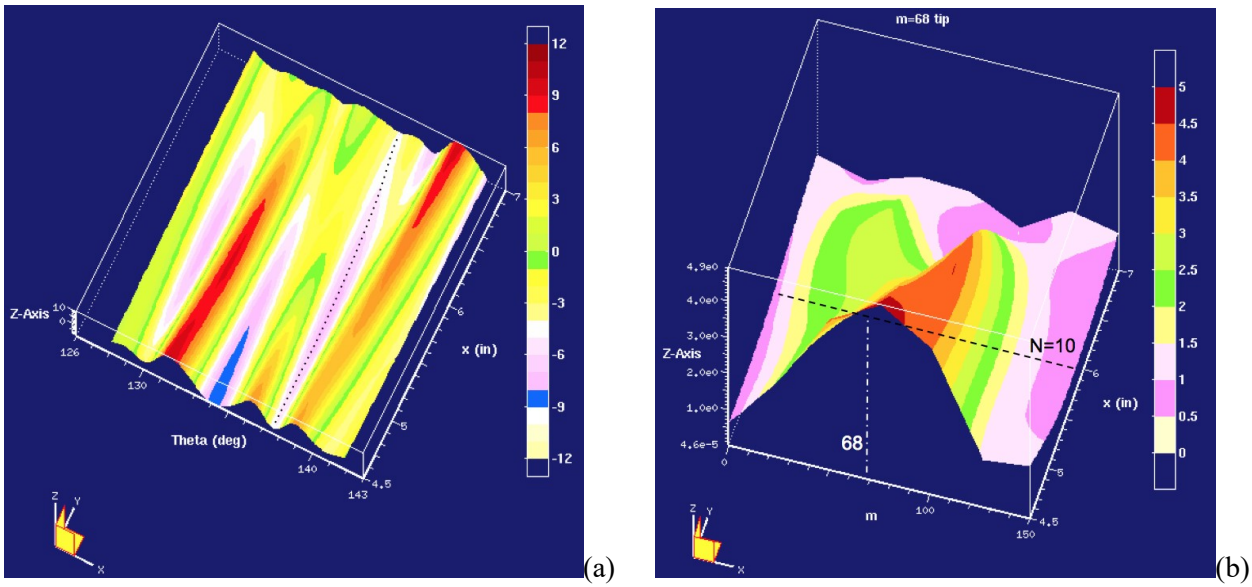

(a) (b)

Figure 12-22: Azimuthal Total Pressure Distributions at a Constant Height Above the Surface (a) and Corresponding Wave Number Spectra (b) for the Case with the Subcritical (m = 68) Roughness Cone Tip. From Matlis, Arndt and Corke [45].

With regard to stationary cross-flow modes, evidence at subsonic Mach numbers indicates a lack of sensitivity to acoustic disturbances [6]. On the other hand, vortical disturbances have been documented to enhance traveling cross-flow modes [5] to the point of dominating over the stationary modes as the mechanism of transition.

The thermal images taken with the model in the quiet tunnel that were shown in Figure 12-14 revealed extremely sharp hot streaks that suggested well defined stationary cross-flow vortices. Model surface pressure measurements in the quiet tunnel environment showed energy in a band of frequencies centered about 40 kHz. that is expected to be due to traveling cross-flow modes. A narrower peak near 40 kHz was also evident in the spectra in Figure 12-13 with higher free-stream disturbances.

The origin of the stationary cross-flow modes in these experiments is expected to be due to randomly distributed surface roughness. In contrast, the patterned discrete roughness used in the experiments by Schuele, Corke and Matlis [34] and Matlis, Arndt and Corke [45] is fixed. This controlled roughness initial condition offers an approach to explore possible interactions between the traveling and stationary cross-flow modes. This follows the approach used by Corke and Matlis [51] and Corke, Matlis and Othman [30] in the cross-flow dominated transition on a rotating disk.

The evidence of an interaction between the stationary and traveling cross-flow modes is embodied in the spatial amplitude distributions for the two roughness cases that was shown in Figures 12-26 and 12-27. Recalling that these were the result of hundreds of individual wind tunnel runs, with the only constant, besides Reynolds number, being the controlled discrete roughness on the model, the coherent pattern in the spatial fluctuation amplitude is remarkable.

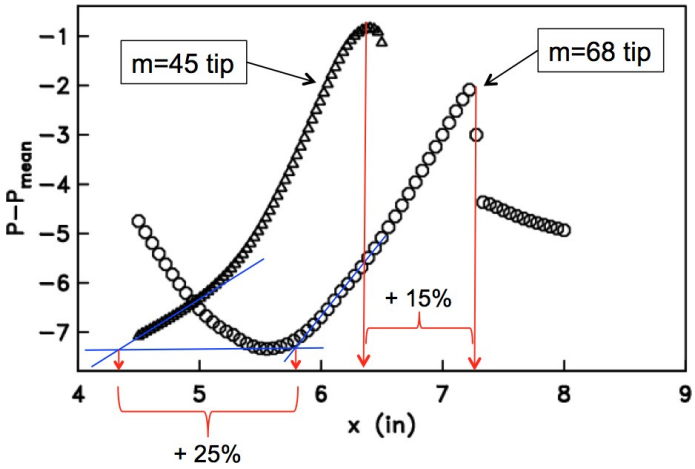

Figure 12-23: Axial Distributions Following Pressure Minima in the Total Pressure Distributions in Figures 12-21(a) and 12-22(a). From Matlis, Arndt and Corke [45].

The spatial amplitude distribution shows evidence of a quadratic interaction between the traveling and stationary cross-flow modes. For the critical roughness with frequency and mode number of (0, 45), this led to the generation of a pair of traveling modes (f_t, 85) and (f_t, 5) with the same frequency as the primary traveling mode, f_t. A sum and difference interaction between these would produce a harmonic traveling mode, ($2f_t$, 90), and a higher wave number stationary mode, (0, 80). In this process, the generation of higher wave number stationary modes would appear as more closely spaced hot streaks, such as in the images in Figure 12-9, as the flow approaches transition at the higher Reynolds number.

The process would continue to spread energy to an increasing number of modes leading to a broad spectrum associated with turbulence. Such a broadening spectrum was apparent in the wave number spectra based on the surface flow visualization and off-wall pressure measurements that were shown in Figures 12-19 and 12-20, and Figures 12-21(b) and 12-22(b) for the discrete roughness cases.

The strength of these interactions will depend on the initial amplitude of the traveling cross-flow modes. Evidence indicates that this depends on the free-stream disturbance level that particularly includes vortical disturbances, and possibly acoustic disturbances. If one excludes Mach number effects, the difference between the degree of transition suppression between the experiments of Schuele, Corke and Matlis [34] and Matlis, Arndt and Corke [45] is the level of acoustic disturbances. The potentially larger amplitude traveling cross-flow modes in the higher acoustic environment, and the nonlinear interaction with the stationary mode, could hasten transition, and reduce the effectiveness of the subcritical roughness. In a broader sense, this interaction between stationary and traveling cross-flow modes might account for the difference between the transition Reynolds number in conventional (noisy) and quiet hypersonic wind tunnels.

Collectively, the TAMU 2:1 elliptic cone experiments quantified the effects of freestream turbulence on the instability process for a range of Reynolds numbers at Mach 6. Under quiet conditions, the stationary, traveling (20 – 80 kHz) and secondary modes (100 – 400 kHz, 500 – 800 kHz) were observed. Also, the 2:1 cone did not

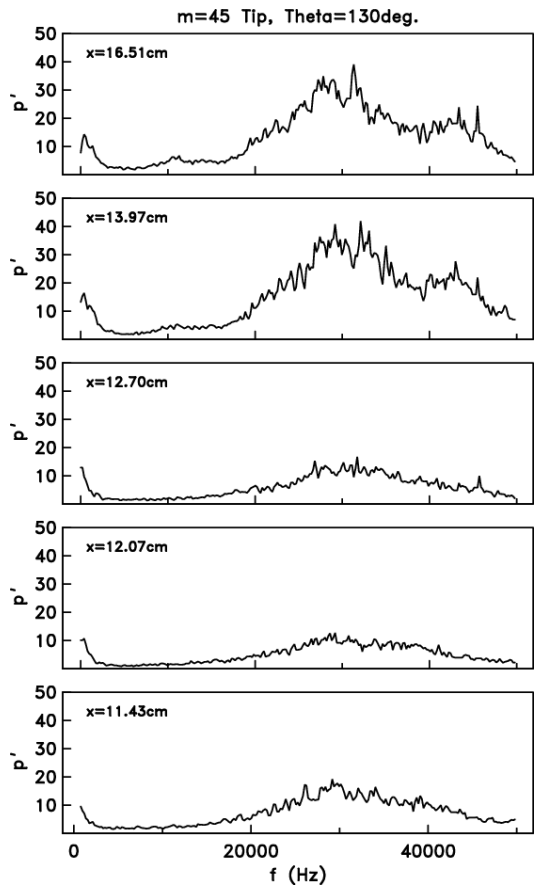

Figure 12-24: Spectra of Traveling Disturbances Measured at Different Axial Locations for a Constant Azimuthal Angle for the Critical (m = 45) Roughness. From Matlis, Arndt and Corke [45].

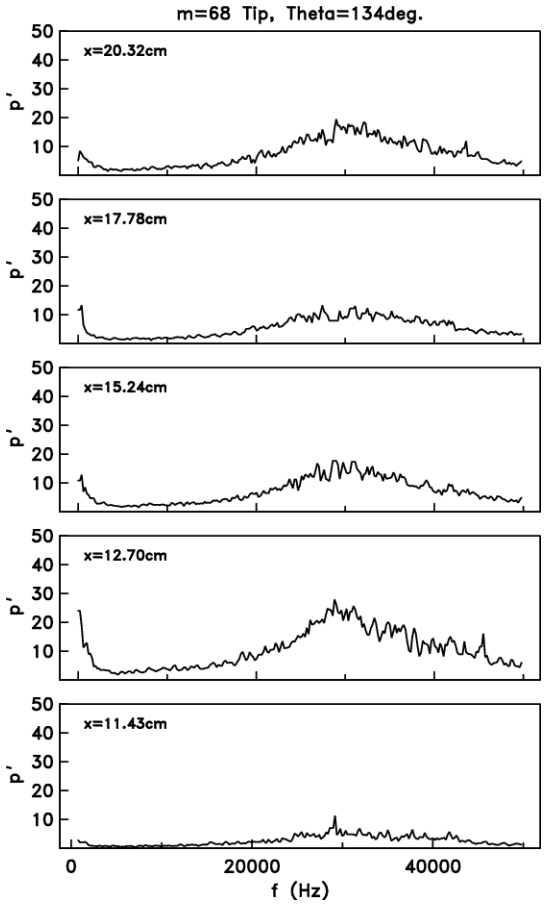

Figure 12-25: Spectra of Traveling Disturbances Measured at Different Axial Locations for a Constant Azimuthal Angle for the Subcritical (m = 68) Roughness. From Matlis, Arndt and Corke [45].

experience transition under quiet conditions. Under conventional tunnel conditions (Figures 12-2), stationary, 1st mode (10 – 20 kHz), traveling (20 – 80 kHz) and secondary modes (100 – 400 kHz) were observed. Transition was observed near a unit Reynolds number of 5 x 10^6 for both locations. The frequencies of the excited waves were independent of the freestream disturbance levels over the two test conditions presented. The resulting amplitudes of the excited waves varied as expected with freestream disturbance levels. Hence, the presence of freestream disturbances in the conventional tunnel fundamentally altered the transition process as compared to the results from the quiet tunnel. Specifically, under quiet conditions, the 1st mode frequency band was not observed, and under noisy conditions, the highest frequency band secondary disturbances were not observed.

12.5 SUMMARY AND FUTURE RESEARCH DIRECTIONS

The results in multiple facilities having different free-stream disturbance conditions, and test articles having random and controlled surface roughness provide a consistent picture of mechanisms for cross-flow dominated transition to turbulence. The results in conventional and quiet Mach 6 facilities each documented the presence of stationary cross-flow vortices.

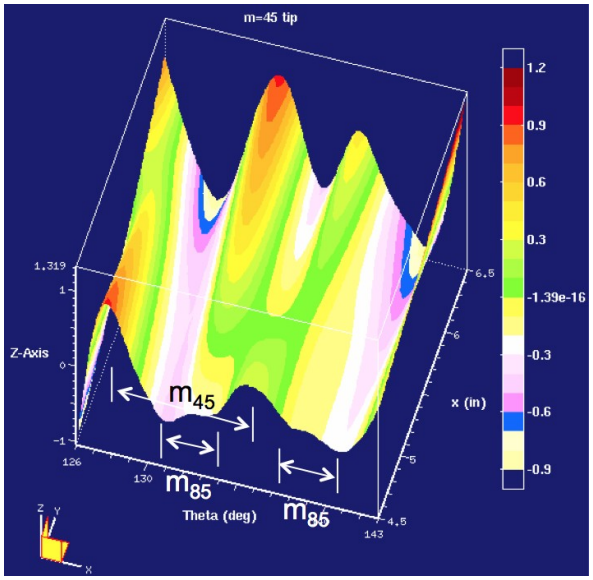

Figure 12-26: Spatial Amplitude Distribution of the Spectral Peak Amplitude of the Traveling Disturbances for the *m* = 45 Roughness Tip. From Matlis, Arndt and Corke [45].

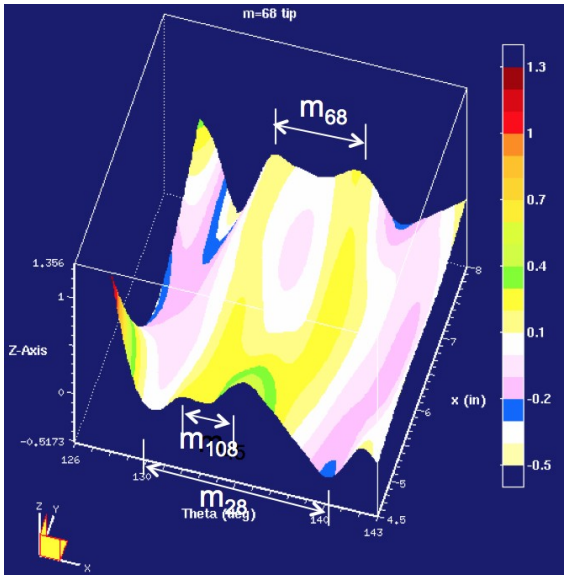

Figure 12-27: Spatial Amplitude Distribution of the Spectral Peak Amplitude of the Traveling Disturbances for the *m* = 68 Roughness Tip. From Matlis, Arndt and Corke [45].

Under quiet conditions, stationary, traveling (20 – 80 kHz), and a secondary mode (100 – 400 kHz) were observed. Under conventional tunnel conditions, stationary, low frequency disturbances (10 – 20 kHz and 20 – 80 kHz) and a single secondary instability (100 – 400 kHz) were observed. Transition was observed near a unit Reynolds number of 5 x 10^6 for all locations. Although not fully conclusive, the secondary wave growth was significant and appears to have led to transition. The frequencies of the excited waves were independent of the freestream disturbance levels over the test conditions studied. The resulting amplitudes of the excited waves varied as expected with freestream disturbance levels.

Based on evidence at subsonic Mach numbers, the difference in the level of acoustic disturbances found in these experiments is not expected to have a significant impact on the stationary cross-flow modes. The primary influence on stationary modes remains to be the surface roughness, both naturally (randomly) distributed or patterned to excite specific cross-flow instability wave numbers.

Experiments with prescribed roughness initial conditions revealed the potential for a nonlinear (quadratic) interaction between the stationary cross-flow mode and the more amplified, but usually less dominant traveling cross-flow mode. This initial interaction results in a pair of traveling modes with the same frequency as the primary traveling mode. These can then interact to produce a stationary mode with nearly half the spanwise wave length (twice spanwise mode number) of the primary stationary mode. Documentation of this in surface thermal images is evidence of this nonlinear interaction.

The impact that this nonlinear interaction has on transition will depend on the initial amplitude of the traveling modes. Again evidence at subsonic Mach numbers, suggests a dependence of the traveling cross-flow mode on the level of vortical disturbances. The effect of entropy disturbances on the traveling cross-flow modes at hypersonic Mach numbers is unknown.

The significance of this interaction is that it offers a mechanism to explain the variation in transition Reynolds numbers in different facilities. An approach to document this further, would involve experiments in different facilities that utilize the same test article that includes discrete roughness to fix the pattern of stationary cross-flow modes.

Another approach would be to control the initial amplitude of traveling cross-flow modes. This could be accomplished by introducing traveling disturbances on the surface of the test article. A possible method for this is an azimuthal array of plasma "roughness" such as used by Schuele, Corke and Matlis [34] to excite stationary cross-flow modes. A traveling disturbance could be produced by introducing a phase shift between the neighbor "roughness" elements. This would allow independent control of the traveling mode frequency and initial amplitude. It could be used in conjunction with passive stationary roughness to allow experiments to be performed in short run-time facilities like Ludwieg tubes.

ACKNOWLEDGMENTS

The authors wish to thank the members of the NATO AVT-240 Working Group on Hypersonic Boundary Layer Transition for the numerous discussions and feedback on the research that is highlighted in this manuscript.

The results presented were parts of research supported by Grants AFOSR FA9550-15-1-0278 and FA9550-14-1-0365 that are each monitored by Dr. Ivett Leyva.

REFERENCES

[1] Schneider, S. P., "Effects of High-Speed Tunnel Noise on Laminar-Turbulent Transition," *Journal of Spacecraft and Rockets*, Vol. 38, No. 3, May 2001, pp. 323-333.

[2] Kovasznay, L., "Turbulence in Supersonic Flow," *Journal of the Aeronautical Sciences*, Vol. 20, No. 10, Oct. 1953, pp. 657-674.

[3] Bushnell, D., "Notes on Initial Disturbance Fields for the Transition Problem," *Instability and transition*, Springer, 1990, pp. 217-232.

[4] Laufer, J., "Aerodynamic Noise in Supersonic Wind Tunnels," *Journal of the Aerospace Sciences*, Vol. 28, No. 9, Sept. 1961, pp. 685-692.

[5] Deyhle, H. and Bippes, H., "Disturbance Growth in an Unstable Three-dimensional Boundary Layer and Its Dependence on Environmental Conditions," *Journal of Fluid Mechanics*, Vol. 316, No. 1, June 1996, pp. 73.

[6] Radeztsky, R. H., Reibert, M. S., and Saric, W. S., "Effect of Isolated Micron-Sized Roughness on Transition in Swept-Wing Flows," *AIAA Journal*, Vol. 37, No. 11, Nov. 1999, pp. 1370-1377.

[7] Saric, W. S., Reed, H. L., and White, E. B., "Stability and Transition of Three-Dimensional Boundary Layers," *Annual Review of Fluid Mechanics*, Vol. 35, No. 1, Jan. 2003, pp. 413-440.

[8] Craig, S. A. and Saric, W. S., "Crossflow instability in a hypersonic boundary layer," *Journal of Fluid Mechanics*, Vol. 808, Oct. 2016, pp. 224-244.

[9] White, E. B. and Saric, W. S., "Secondary Instability of Crossflow Vortices," *Journal of Fluid Mechanics*, Vol. 525, Feb. 2005, pp. 275-308.

[10] Oliviero, N. B., Kocian, T. S., Moyes, A., and Reed, H. L., "EPIC: NPSE Analysis of Hypersonic Cross flow Instability on Yawed Straight Circular Cone," *45th AIAA Fluid Dynamics Conference*, Vol. 2772, American Institute of Aeronautics and Astronautics, June 2015, p. 2015.

[11] Moyes, A. J., Paredes, P., Kocian, T. S., and Reed, H. L., "Secondary Instability Analysis of Crossflow on a Hypersonic Yawed Straight Circular Cone," *Journal of Fluid Mechanics*, Vol. 812, 2017, pp. 370-397.

[12] Kimmel, R. L., Klein, M. A., and Schwoerke, S. N., "Three-Dimensional Hypersonic Laminar Boundary-Layer Computations for Transition Experiment Design," *Journal of Spacecraft and Rockets*, Vol. 34, No. 4, July 1997, pp. 409-415.

[13] Poggie, J., Kimmel, R. L., and Schwoerke, S. N., "Traveling Instability Waves in a Mach 8 Flow over an Elliptic Cone," *AIAA Journal*, Vol. 38, No. 2, Feb. 2000, pp. 251-258.

[14] Bowcutt, K., Paull, A., Dolvin, D., and Smart, M., "HIFiRE: An International Collaboration to Advance the Science and Technology of Hypersonic Fight," *Proceedings of the 28th International Congress of the Aeronautical Sciences*, ICAS Secretariat RA Leiden, The Netherlands, 2012, pp. 2012-998.

[15] Berger, K., Rufer, S., Kimmel, R., and Adamczak, D., "Aerothermodynamic Characteristics of Boundary Layer Transition and Trip Effectiveness of the HIFiRE Flight 5 Vehicle," *39th AIAA Fluid Dynamics Conference*, American Institute of Aeronautics and Astronautics, June 2009.

[16] Juliano, T. and Schneider, S., "Instability and Transition on the HIFiRE-5 in a Mach-6 Quiet Tunnel," *40th Fluid Dynamics Conference and Exhibit*, , No. July, 2010, pp. 1-34.

[17] Borg, M., Kimmel, R., and Stanfield, S., "Crossflow Instability for HIFiRE-5 in a Quiet Hypersonic Wind Tunnel," *42nd AIAA Fluid Dynamics Conference and Exhibit*, American Institute of Aeronautics and Astronautics, June 2012.

[18] Borg, M. P., Kimmel, R. L., and Stanfield, S., "Traveling Crossflow Instability for HIFiRE-5 in a Quiet Hypersonic Wind Tunnel," *43rd Fluid Dynamics Conference*, American Institute of Aeronautics and Astronautics, June 2013.

[19] Borg, M. P. and Kimmel, R. L., "Simultaneous Infrared and Pressure Measurements of Crossflow Instability Modes for HIFiRE-5," *54th AIAA Aerospace Sciences Meeting*, American Institute of Aeronautics and Astronautics, Jan. 2016.

[20] Choudhari, M., Chang, C.-L., Jentink, T., Li, F., Berger, K., Candler, G., and Kimmel, R., "Transition Analysis for the HIFiRE-5 Vehicle," *39th AIAA Fluid Dynamics Conference*, American Institute of Aeronautics and Astronautics, June 2009.

[21] Li, F., Choudhari, M., Chang, C.-L., White, J., Kimmel, R., Adamczak, D., Borg, M., Stanfield, S., and Smith, M., "Stability Analysis for HIFiRE Experiments," *42nd AIAA Fluid Dynamics Conference and Exhibit*, American Institute of Aeronautics and Astronautics, June 2012.

[22] Juliano, T. J., Borg, M. P., and Schneider, S. P., "Quiet Tunnel Measurements of HIFiRE-5 Boundary-Layer Transition," *AIAA Journal*, Vol. 53, No. 4, April 2015, pp. 832-846.

[23] Borg, M., Kimmel, R., and Stanfield, S., "HIFiRE-5 Attachment-Line and Crossflow Instability in a Quiet Hypersonic Wind Tunnel," June 2011.

[24] Borg, M. P., Kimmel, R. L., Hofferth, J. W., Bowersox, R. D., and Mai, C. L., "Freestream Effects on Boundary Layer Disturbances for HIFiRE-5," *53rd AIAA Aerospace Sciences Meeting*, American Institute of Aeronautics and Astronautics, Jan. 2015.

[25] Borg, M. P., Kimmel, R. L., and Stanfield, S., "Traveling Crossflow Instability for the HIFiRE-5 Elliptic Cone," *Journal of Spacecraft and Rockets*, Vol. 52, No. 3, May 2015, pp. 664-673.

[26] Juliano, T. J., Paquin, L., and Borg, M. P., "Measurement of HIFiRE-5 Boundary-Layer Transition in a Mach-6 Quiet Tunnel with Infrared Thermography," *54th AIAA Aerospace Sciences Meeting*, Vol. 595, American Institute of Aeronautics and Astronautics, Jan. 2016.

[27] Borg, M. P. and Kimmel, R. L., "Ground Test Measurements of Boundary-Layer Instabilities and Transition for HIFiRE-5 at Flight-Relevant Attitudes," *47th AIAA Fluid Dynamics Conference*, American Institute of Aeronautics and Astronautics, June 2017.

[28] Kocian, T. S., Moyes, A. J., Mullen, D., and Reed, H. L., "PSE and Spatial Biglobal Instability Analysis of Reduced Scale and Flight HIFiRE-5 Geometry," *55th AIAA Aerospace Sciences Meeting*, American Institute of Aeronautics and Astronautics, Jan. 2017, p. 0768.

[29] Corke, T. C. and Knasiak, K. F., "Stationary Travelling Cross-Flow Mode Interactions on a Rotating Disk," *Journal of Fluid Mechanics*, Vol. 355, 1998, pp. 285-315.

[30] Corke, T., Matlis, E., and Othman, H., "Transition toTurbulence in Rotating-disk Boundary Layers - Convective and Absolute Instabilities." *J. Engr. Math.*, Vol. 57, 2007, pp. 253-272.

[31] Saric, W. S. and Reed, H. L., "Supersonic Laminar Flow Control on Swept Wings Using Distributed Roughness," AIAA Paper AIAA 2002-0147, 2002.

[32] Saric, W. S., Ruben C, C., and Reibert, M. S., "Leading-Edge Roughness as a Transition Control Mechanism," AIAA Paper AIAA-98-0781, 1998.

[33] Radeztsky Jr., R., Reibert, M., and Saric, W., "Effect of Isolated Micron-Sized Roughness on Transition in Swept-Wing Flows," *AIAA Journal*, Vol. 37, No. 11, 1999, pp. 1370-1377.

[34] Schuele, C.-Y., Corke, T., and Matlis, E., "Control of Stationary Cross-flow Modes in a Mach 3.5 Boundary Layer Using Patterned Passive and Active Roughness," *J. Fluid Mech.*, Vol. 718, 2013, pp. 5-38.

[35] Saric, W., Reed, H., and Banks, D., "Flight Testing of Laminar Flow Control in High-Speed Boundary Layers," Paper presented at the RTO AVT Specialists' Meeting on 'Enhancement of NATO Military Flight Vehicle Performance by Management of Interacting Boundary Layer Transition and Separation', held in Prague, Czech Republic , 4-7 October 2004, Published in RTO-MP-AVT-111, 2004.

[36] Semionov, N. and Kosinov, A., "Method Laminar-Turbulent Transition Control of Supersonic Boundary Layer on a swept Wing," *Thermophysics and Aeromechanics*, Vol. 14, No. 3, 2007, pp. 337-341.

[37] Semionov, N., Kosinov, A., and Levchenko, V., "Experimental Study of Turbulence Beginning and Transition Control in a Supersonic Boundary Layer on Swept Wing," R. Govindarajan (ed.), Sixth IUTAM Symposium on Laminar Turbulent Transition, 2006.

[38] Semper, M., Pruski, B., and Bowersox, R., "Freestream Turbulence Measurements in a Continuously Variable Hypersonic Wind Tunnel," *AIAA Paper*, Vol. 732, 2012, pp. 2012.

[39] Hofferth, J. and Saric, W., "Boundary-Layer Transition on a Flared Cone in the Texas A&M Mach 6 Quiet Tunnel," *50th AIAA Aerospace Sciences Meeting including the New Horizons Forum and Aerospace Exposition*, American Institute of Aeronautics and Astronautics, Jan. 2012, pp. 1-14.

[40] Saric, W., Reed, H., and Kerschen, E., "Boundary-Layer Receptivity to Freestream Disturbances," *Annual Review of Fluid Mechanics*, Vol. 34, 2002, pp. 291-319.

[41] Duncan, G. T., Crawford, B., Tufts, M. W., Saric, W. S., and Reed, H. L., "Effects of Step Excrescences on Swept-Wing Transition," *31st AIAA Applied Aerodynamics Conference*, , No. August, June 2013, pp. 1 – 18.

[42] Neel, I. T., Leidy, A., and Bowersox, R. D., "Preliminary Study of the Effect of Environmental Disturbances on Hypersonic Crossflow Instability on the HIFiRE-5 Elliptic Cone," *55th AIAA Aerospace Sciences Meeting*, American Institute of Aeronautics and Astronautics, Jan. 2017.

[43] Neel, I. T., Leidy, A., Tichenor, N. R., and Bowersox, R. D., "Influence Of Environmental Disturbances on Hypersonic Crossflow Instability on the HIFiRE-5 Elliptic Cone," *Presnted at AIAA Scitech 2018, paper number to be assigned*, American Institute of Aeronautics and Astronautics, Jan. 2018.

[44] Beresh, S. J., Henfling, J. F., Spillers, R. W., and Pruett, B. O. M., "Fluctuating Wall Pressures Measured Beneath a Supersonic Turbulent Boundary Layer," *Physics of Fluids*, Vol. 23, No. 7, July 2011, pp. 075110.

[45] Matlis, E., Arndt, A., Corke, T., Semper, M., and McLaughlin, T., "Effect of Discrete Roughness on Cross-flow Transition at Mach 6." AIAA SciTech 2018, Denver CO., January 8-12, 2018.

[46] Swanson, E. and Schneider, S., "Boundary Layer Transition on Cones at Angles of Attack in a Mach 6 Quiet Tunnel." AIAA 48th Aerospace Sciences Meeting, Orlando, FL, January 4-7, 2010.

[47] Craig, S. and Saric, W., "Experimental Study of Crossflow Instability on a Mach 6 Yawed Cone." AIAA 45th Fluid Dynamics Conference, Dallas, TX, June 22-26, 2015.

[48] Li, F., Choudhari, M., Chang, C.-L., and White, J., "Analysis of Instabilities in Non-axisymmetric Hypersonic Boundary Layers Over Cones." 10th AIAA/ASME Joint Thermophysics and Heat Transfer Conference, Chicago, IL, 28 June – 1 July, 2010.

[49] Saric, W. S., "Private Communication," 2008.

[50] Bippes, H., "Basic Experiments on Transition in Three-dimensional Boundary Layers dominated by cross-flow instability," *Progress in Aerospace Sciences*, Vol. 35, 1999, pp. 363-412.

[51] Corke, T. and Matlis, E., "Transition to Turbulence in 3-D Boundary Layers on a Rotating Disk - Triad Resonance." Springer Publishers, Netherlands, 2006.

Chapter 13 – INFRARED THERMOGRAPHY DATA REDUCTION TECHNIQUE FOR HEAT FLUX MEASUREMENTS IN THE BOEING/AFOSR MACH-6 QUIET TUNNEL

Mirko Zaccara, Salvatore Cerasuolo, and Gennaro Cardone
University of Naples "Federico II"
ITALY

Joshua B. Edelman and Steven P. Schneider
Purdue University
UNITED STATES OF AMERICA

13.1 INTRODUCTION

Heat flux measurements in the hypersonic regime are extremely important in several science and engineering problems such as the investigation of hypersonic laminar-to-turbulent transition, which is crucial to lifting re-entry vehicles, airbreathing cruise vehicles, and high-speed missiles [1, 2]. In fact, boundary-layer state analysis is a key factor in the design of the thermal protection system and it deeply affects the skin friction, drag and moments [3, 4].

Conventional hypersonic wind tunnels have high levels of freestream fluctuations which are several orders of magnitude above flight levels. These freestream fluctuations are generally dominated by acoustic noise radiated from the turbulent boundary layers on the nozzle walls. The noise greatly affects the position and mechanism of laminar-turbulent transition on models [5]. This is why quiet flow wind tunnels, such as the Boeing/AFOSR Mach-6 Quiet Tunnel (BAM6QT), have been sought for more than 60 years. They provide uniform flow with noise levels less than 0.10% which is more representative of flight [6].

Measurement of the convective heat flux is traditionally performed using heat flux sensors such as heated thin-foil, thin film sensors, and wall calorimeters [7]. When their application is not feasible, the surface heat flux distribution is obtained by solving an inverse heat transfer problem (IHTP) [8] starting from temperature measurements by means of thermocouples, resistance temperature detectors (RTDs), Temperature Sensitive Paint (TSP) or infrared (IR) thermography. If the velocity and the temperature fields, and thus the heat flux distribution, exhibit very high spatial gradients, the heat flux evaluation, using zero dimensional sensors such as thermocouples or RTDs, can be troublesome [9, 10]. Instead, IR thermography is a non-contact technique which allows for accurate measurements of surface temperature maps. Compared to standard techniques, the use of the IR technique has several advantages: it is non-intrusive and IR cameras have high sensitivity (up to 20 mK), fast response time (down to 20μs), and relatively high spatial resolution [11].

In this work, a data reduction technique to solve IHTPs starting from IR measurements is presented to evaluate convective wall heat transfer on a sharp cone in hypersonic flow. In Section 13.2, the main features of the hypersonic quiet tunnel BAM6QT are described. The procedure to convert the raw IR data to 3D surface temperature map, considering lens distortions, model oscillations and model directional emissivity, is presented in Section 13.3. In Section 13.4, the IHTP is presented while the results are discussed in Section 13.5 and summarized in Section 13.6. In particular, this methodology has been applied to several tests of a 7° half-angle circular sharp cone tested in the BAM6QT at Mach 6. The 1D IHTP is solved and the results are validated against the

theoretical solution by performing runs with the cone at 0 deg angle of attack as described in Section 13.5.2. Schmidt-Boelter gauges and CFD simulations represented additional terms of comparison for the validation. A 2D IHTP has been implemented to take into account tangential conduction caused by the crossflow vortices on the cone at 6 deg angle of attack. In these cases, measurement accuracy calculations have been conducted to check the 1D IHTP application and confirmed by the 2D IHTP results.

13.2 THE BOEING/AFOSR MACH-6 QUIET TUNNEL

The Boeing/AFOSR Mach-6 Quiet Tunnel is a facility at Purdue University in West Lafayette, Indiana, USA. A schematic of the tunnel is provided in Figure 13-1.

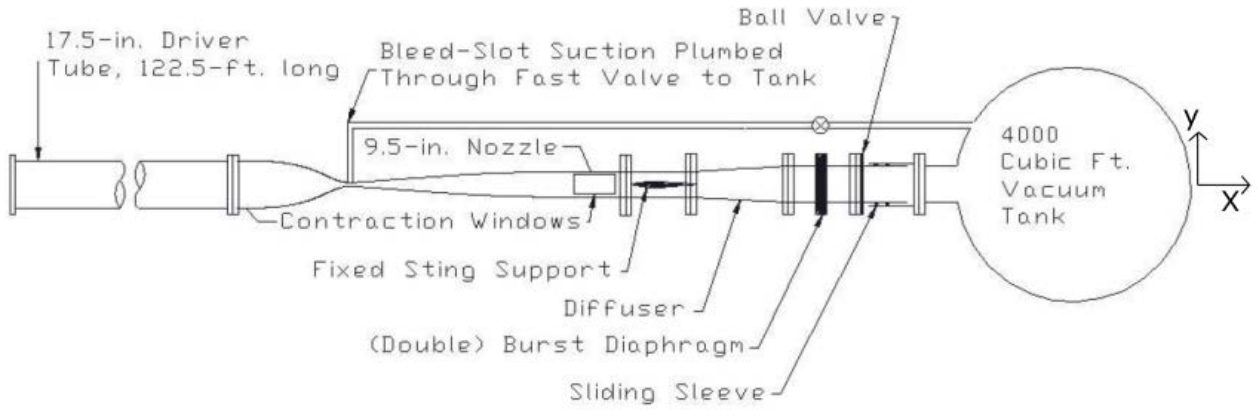

Figure 13-1: Schematic of the Boeing/AFOSR Mach-6 Quiet Tunnel [6].

The BAM6QT is a Ludwieg tube design incorporating a long driver tube (37.3 m) connected to a converging-diverging nozzle to accelerate flow to Mach 6. Two burst diaphragms divide the facility into high and low pressure regions and they are positioned after the diffuser. This guarantees a reduction of disturbances in the test-section flow by producing a naturally low-noise acceleration from stagnation to nominal conditions. The test section consists in the aft part of the nozzle, where the cross-sectional area increases slowly and is 241 mm in diameter. The BAM6QT viewing window is made of Calcium Fluoride CaF_2 covered with an anti-reflection layer to increase the transmissivity. It is transparent to radiations with a wavelength down to 7 μm. Further details on the design of the facility are discussed by Schneider [6].

The BAM6QT has some additional features to keep a laminar boundary layer on the nozzle wall to enable operation at low freestream noise levels less than 0.05%. The nozzle is very long to minimize the growth of the Görtler instability and it is highly polished to avoid roughness which could lead to early transition. To help protect the mirror finish of the nozzle, a series of filters eliminate particles larger than 0.01 μm from the air used to pressurize the driver tube. Just upstream of the throat, a bleed-slot connected to the vacuum tank through a fast-opening butterfly valve is used to remove the wall boundary layer allowing a new laminar boundary layer to develop on the nozzle wall. If this slot is closed, the tunnel can be run noisy and the Mach number is 5.8, since the turbulent boundary layer reduces the effective area ratio between the nozzle exit and the throat. When the desired pressure is reached in the driver tube, the air gap between the pair of diaphragms

is evacuated and they are burst in quick succession. A shock wave and an expansion fan propagate downstream and upstream respectively. Once the expansion fan has passed through the throat, the air behind the expansion fan is accelerated through the nozzle at Mach 6. At present, the maximum stagnation pressure to obtain quiet flow conditions is 931 kPa. Since the driver tube is kept at 433 K, the maximum unit Reynolds number at the quiet condition is $Re = 9.90 \cdot 10^6$ m^{-1}.

A Dantec hot-film sensor is installed on the nozzle wall to detect the turbulence level of the boundary layer and a typical output is shown in Figure 13-2a from which it is clear that the quiet flow conditions are reached about 1 s after the diaphragms burst (run starts in Figure 13-2) and last about 2.5 s. Data are collected with the presence of travelling expansion waves in the driver tube causing the stagnation pressure drop of 1% after each reflection. After a few reflections the fan spreads out and the thermodynamic quantities change nearly continuously dividing the run in different segments in which the mean thermodynamic conditions can be considered. As described later, the IHTP has been solved only in a time interval of 0.18 s when the flow is quasi-static. In fact, as shown in Figure 13-2b, the first part of the run is unsteady, the model experiences two sharp boosts of heat flux and therefore is not possible to define the IHTP because the convective heat transfer is time dependent.

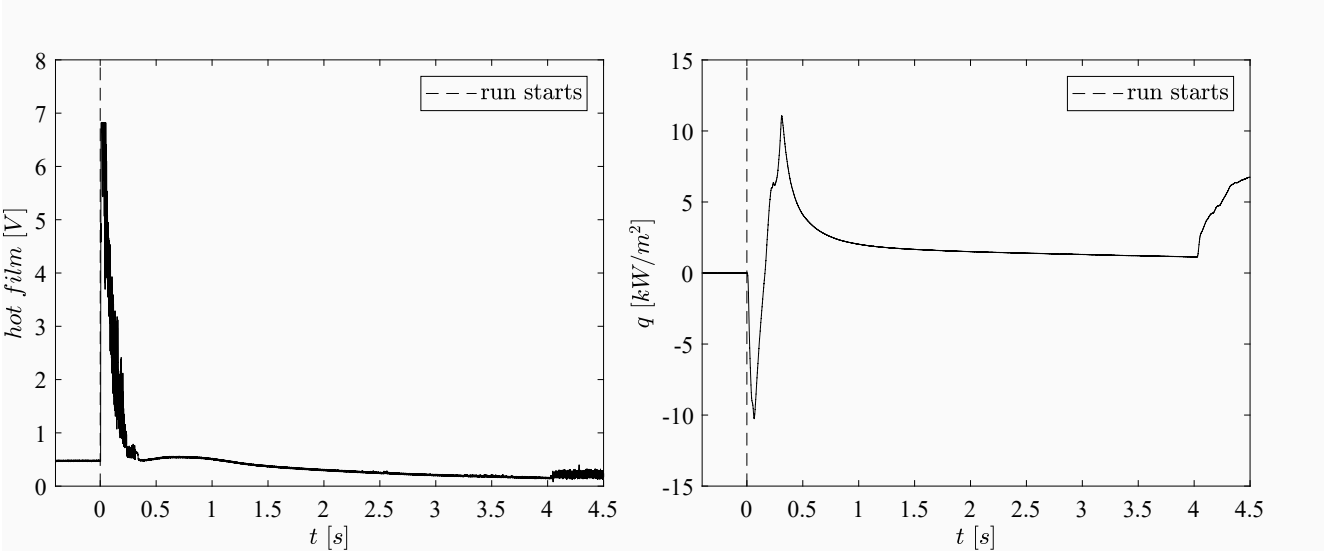

(a) Hot Film Output. **(b) Schmidt-Boelter Gauge Output.**

Figure 13-2: Typical Hot Film Output and Convective Heat Transfer on the Model for a BAM6QT Quiet Flow Run.

13.3 INFRARED IMAGE PROCESSING

In this paragraph, the steps involved in the approach to rebuild temperature maps onto a 3D surface grid from 2D IR images are described. Firstly, a radiometric camera calibration to convert IR raw data into temperature values is needed. Secondly, it is necessary to establish a correspondence between the points of the observed object and the pixels of the images by means of an optical camera calibration. Since the model oscillates, a correction is needed to reduce the data noise and assure to relate the temperature values always to the same pixel. Lastly, 3D temperature maps can be reconstructed by taking into account the directional emissivity of the model.

13.3.1 Radiometric Calibration

A radiometric camera calibration is necessary to convert the output signal of the IR camera to the object temperature. The IR camera used for the present work is the Infratec imageIR® 8300 hp provided by Dr. Juliano at the University of Notre Dame. Like the most modern cameras, it is already calibrated for a different number of integration times that give accurate output in an established temperature measurement range. However, the factory calibration is not accurate when a viewing window is present in the optical path since the window absorbs part of the radiation. As a result, it is expected that the factory calibration would underrate the temperature values.

The IR camera radiometric calibration has been conducted by using a black body [7]. It is advisable to calibrate the IR camera by using the actual optical path employed in the experimental tests, which means having the black body in the test section and the camera looking at it through the viewing window. Unfortunately, this configuration was considered not feasible in the BAM6QT because of a possible contamination of the nozzle polishing and size problems. As a consequence, the calibration has been conducted outside the wind tunnel by respecting the model - window - camera distances and therefore taking into account the viewing window transmissivity.
A total of 28 infrared images of the black body have been collected for a temperature range from 283 K to 324 K. An infrared image of the black body is shown in Figure 13-3a in which the square region of interest is also represented. In the latter, the digital values of each infrared image have been averaged in order to apply the optimization process, resulted in a temperature accuracy of ± 0.08 K. The experimental calibration curve is provided in Figure 13-3b.

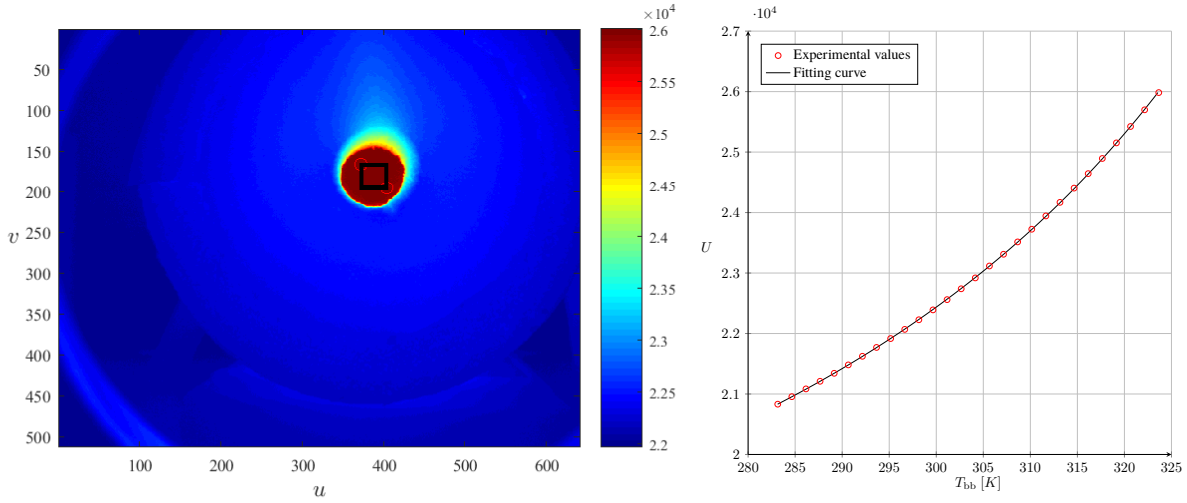

(a) Infrared Image of the Black Body.

(b) Calibration Fitting Curve.

Figure 13-3: Infratec ImageIR® 8300 hp Radiometric Calibration Results.

13.3.2 Optical Calibration

The two-dimensional temperature map detected by an infrared camera is the planar projection of the thermal field which is viewed in the physical three-dimensional space. Since the tested model is not planar, an optical calibration to define a correspondence between the image and the real world coordinate systems is needed. The approach proposed by Cardone et al. [11] is used. The method uses a camera model that is based on a

combination of linear and nonlinear techniques using a perspective projection model, called the pinhole model, augmented with a correction for lens distortions [12]. The employed calibration target is an aluminum plate with a grid of regularly spaced drilled holes shown in Figure 13-4a. Due to the symmetry of circular markers, a detection scheme is easy to implement as well as robust in off-axis or rotated viewing arrangements. The target was moved along the volume occupied by the tested model. In this way, more images of the target were taken and the whole observed volume was mapped. As it can be noted in Figure 13-4b, the markers appear as hot spots on a cold surface thanks to the low emissivity of the aluminum plate. The positions of the markers are found within the IR images as the barycenter of the hot regions and their position are used to determine the camera calibration constants.

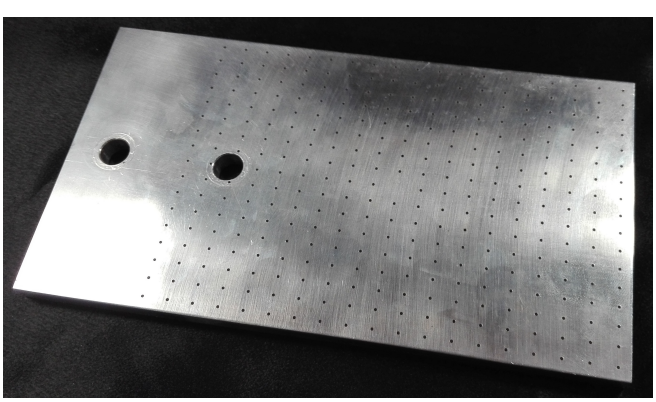

(a) Optical Calibration Target.

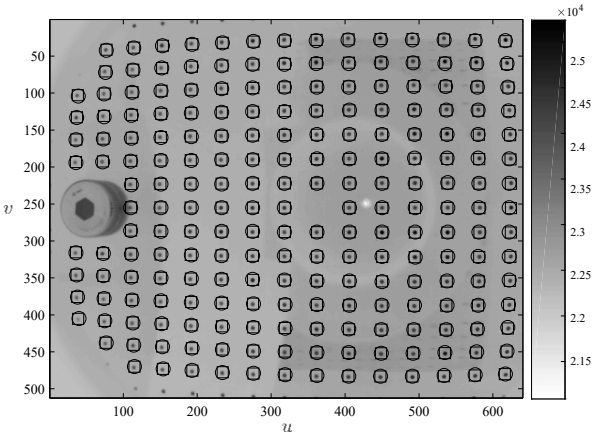

(b) Focusing Plane of the IR Camera with Optical Calibration Output.

Figure 13-4: Infratec ImageIR® 8300 hp Optical Calibration Target and Results.

As proposed by Heikkilä [12], a Direct Linear Transformation (DLT) is used to produce the first constants estimation by considering the optical center as the center of the square sensor and no lens distortions with the ideal focal length. The calibration constants are then found by minimizing the root mean square residual between the known image coordinates of the control points and their image coordinates computed in accordance with the camera model. The minimization process is performed with Levenberg-Marquardt method [13]. In the present work, only three planes have been used for the optical calibration to map the whole volume occupied by the model with a coefficient of determination $R^2 = 0.999$ and a standard residual of 0.51 pixels. The latter can be checked by looking at the Figure 13-4b. The circles represent the center of the control points while the squares are the marker positions computed in accordance with the aforementioned camera model and they should coincide. For the present work, these requirements seem to be clearly satisfied.

13.3.3 Model Oscillation

In order to complete the image registration procedure, model oscillations must be taken into account to ensure that they do not affect the time history used in the IHTP. For the BAM6QT, the main reason for model movements is the burst of the diaphragms at the beginning of the run, which makes the whole tunnel oscillate. Actually, the burst mainly causes oscillations of the model along the tunnel x-axis, while they are small along the y-axis and z-axis. As a consequence, the in-plane displacements are represented by 2D rigid translations and the out-of-plane displacements are not considered.

The image registration algorithm used in the present work is the single-step Discrete Fourier Transform (DFT) proposed by Manuel Guizar-Sicairos et al. [14]. The proposed method reduces computational load and memory requirements without sacrificing accuracy. The IR image at $t = 0.5$ s has been chosen as a reference image to compute the model displacements moving forward from $t = 0.5$ s. Moving backward from $t = 0.5$ s, the corrected previous image is used as a reference for the next one. In fact, as shown in Figure 13-2b, the model experiences two sharp boosts of heat flux which deeply change the measured digital values. As a consequence, each image is too different to the reference one at $t = 0.5$ s to give good results.

The image registration process is based on two steps. An initial estimate of the location of the cross-correlation peak between the investigated image and the reference one to compute the displacements is obtained by the FFT method with an upsampling factor of $r_i = 2$ [13]. The second step refines the location of the peak, to within a desired fraction of a pixel, by means of matrix multiplication of the 2D DFT [15]. In the single-step DFT algorithm, an upsampled cross-correlation (by a factor r_i) is computed in a 1.5×1.5 pixel neighborhood about the initial estimate. For the 512×640 pixels camera used in this work, the computational load with $r_i = 10$ is of order of magnitude $4.5 \cdot 10^8$ for the FFT approach and $3.3 \cdot 10^6$ with this more efficient method. Typical model displacements evaluated during the run are shown in Figure 13-5. While along the tunnel y-axis the displacements are only about 5 pixels, along the x-axis it is larger than 30. This is why it is extremely important to c

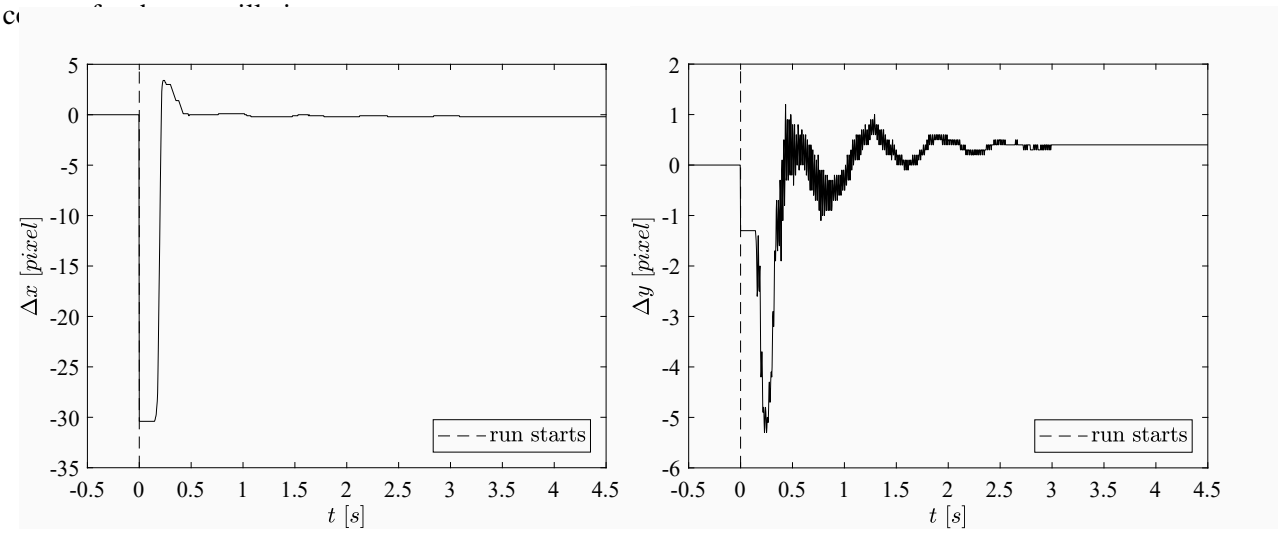

(a) Displacement Along Tunnel x-axis. **(b) Displacement Along Tunnel y-axis.**

Figure 13-5: Typical Model Displacements for a BAM6QT Quiet Flow Run.

13.3.4 3D Surface Temperature Maps

The first step of 3D temperature map reconstruction is the generation of the mesh on the model surface. The mesh spacing has to be chosen to be just slightly higher than the spatial resolution of the IR camera, to avoid both loss of information and useless extra points, which would only increase the computational load. The previously computed camera model constants are used to establish a correspondence between the points of the mesh and the pixels of the IR image. As a result, it is possible to project the mesh points on the IR images. Actually, the mesh points do not correspond with the centers of the pixels so the digital values acquired by the IR camera need to be interpolated.

At this point, the viewing angle on the object surface can be easily evaluated as the scalar product between the viewing ray direction and the known normal unit vector of the model surface [11]. Since the dependence between the emissivity ϵ and viewing angle was expected to be strong at high viewing angles, an experimental study has been conducted. The emissivity coefficient has been measured using a square reference element of PEEK whose radiation emitted was directly compared to a black body emission. This means that both a black body and the reference element were in the field of view of the camera and both the elements were connected to a thermostatic bath that kept them at the same temperature. The output of the camera has been averaged over the cavity of the black body and the PEEK surface in analogous way as it had been done for the radiometric camera calibration. In order to characterize the emissivity coefficient with the viewing angle, the PEEK reference element, positioned vertical, has been rotated using a precision rotary stage. It has been found that the directional emissivity coefficient $\epsilon(\ )$ is well described by the following semi-empirical formula [16, 17]

$$\epsilon(\ ) = [\epsilon_n cos(\ )]^{\frac{\breve{a}}{cos(\theta)^{\breve{b}}}} \tag{13-1}$$

where ϵ_n, $\breve{a}$ and $\breve{b}$ have been evaluated by means of an optimization process with a coefficient of determination of $R^2 = 0.968$. The best fitting curve is provided in Figure 13-6.

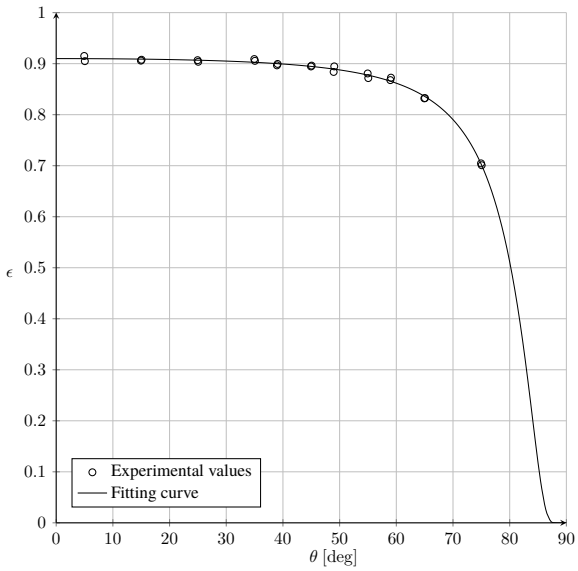

Figure 13-6: Directional Emissivity of the PEEK.

Then, the model emissivity can be corrected with a law that relates it to the viewing angle [16, 17]. Eventually, as described by Cardone et al. [11], the temperature for each grid point can be evaluated and an example of 3D surface temperature maps is shown in Figure 13-7.

13.4 INVERSE HEAT TRANSFER PROBLEM

Inverse Heat Transfer Problems are applied to estimate the convective wall heat flux in high-speed flows to better understand physical phenomena like boundary-layer transition, shock-boundary layer interaction, and flow separation. An overview of heat flux estimation methods is provided by Walker and Scott [8] who demonstrated the necessity of solving IHTPs instead of direct methods especially when dealing with high unsteady heat flux and strong temperature gradients.

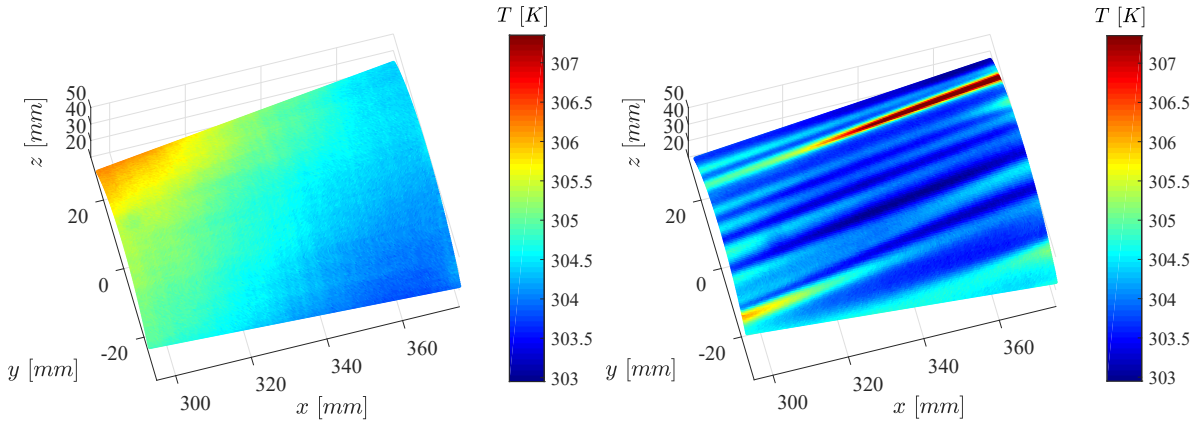

(a) 0 deg Angle of Attack. **(b) 6 deg Angle of Attack.**

Figure 13-7: Examples of 3D Temperature Maps Reconstruction of the Cone Surface Under Analysis.

The IHTP is classified as an ill-posed problem: the solution is not unique and it can considerably vary with small changes in input data caused by measurements and modelling errors [18]. An overview of the IHTP past applications and resolution methods is provided by Avallone et al. [19, 20].

In the presence of phenomena characterized by strong temperature gradients, it may be necessary to solve a multidimensional full inverse heat transfer problem. It is necessary to define the boundary conditions adopted for the heat equation as follows (see Figure 13-8 for the sketch of a generic 3D problem):

$$\begin{cases} k\nabla^2\left(T\right) = \rho c_p \frac{\partial T}{\partial t} & \\ T\left(x,y,z,0\right) = T_{w,i} & \text{at } t = 0 \\ T\left(x,y,z,t\right) = T_{w,i} & \text{at } z \in F,\ \forall t \in [0, t_f] \\ T\left(x,y,z,t\right) = T_w & \text{at } z \in S,\ \forall t \in [0, t_i] \\ k\frac{\partial T(x,y,z,t)}{\partial n}\Big|_S = q_w\left(x,y,t\right) & \text{at } z \in S,\ \forall t \in [t_i, t_f] \end{cases} \tag{13-2}$$

Here, k is the thermal conductivity, ρ is the model material density, and c_p is the specific heat of the material, all of which are assumed constant in Eq. (13-2). F and S refer to "Wall F" and "Wall S" in Figure 13-8 respectively. The time interval of interest is identified by t_i and t_f. The initial temperature distribution is assumed to be constant in the entire domain and equal to the initial surface temperature $T_{w,i}$ which is known from the infrared measurements. The first boundary condition is to consider the wall F to be isothermal. This assumption is valid if the thickness of the material is larger than the penetration depth [21]. The second boundary condition is chosen in relation to the time during the run. Since the decrease of the stagnation quantities in the tunnel is nearly continuous, it has been decided to calculate the heat flux after the quiet flow conditions are reached ($t > 1$ s). In particular, a small time interval of interest of Δt has been chosen which represent the time needed for an expansion wave to travel from the contraction inlet, reflect at the upstream end of the driver tube and reach the contraction inlet again. For the BAM6QT, the time needed is 0.18 s for $T_0 = 433$ K. Within the time interval of study, mean values of the thermodynamic quantities and Reynolds number are considered. In this case, the boundary condition is represented by the unknown heat flux $q_w\left(x,y,z,t\right)$ on the surface (S) exposed to the flow.

The heat flux can be expressed as a function of the convective and radiative heat transfer:

$$q_w(x,y,z,t) = k\frac{\partial T(x,y,z,t)}{\partial n}\bigg|_S = h(x,y,z)\left(T_{w_{num}}(x,y,z,t) - T_{aw}\right) + \\ +\sigma\epsilon_t\left(T^4_{w_{num}}(x,y,z,t) - T_r^4\right) \quad \text{at } z \in S \tag{13-3}$$

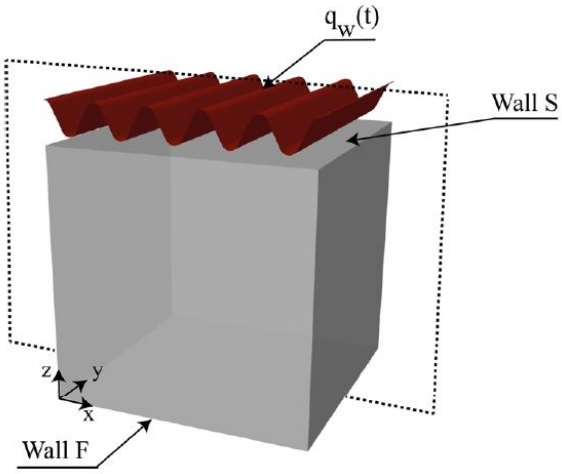

Figure 13-8: Sketch of a Generic 3D Model Adapted from [20].

The heat flux $q_w(x,y,z,t)$ at $z \in S$ depends on the convective heat transfer coefficient h which is the only unknown and needs to be estimated. When considering a short duration interval one can assume that the convective heat transfer coefficient remains constant and time-independent. This assumption can be made in the BAM6QT because the surface temperature rise is relatively small with respect to the adiabatic wall temperature T_{aw} and thus the boundary layer characteristics do not vary. In Eq. (13-3), $T_{w_{num}}$ is the transient wall temperature that, in the following, is obtained from the transient heat conduction equation Eq. (13-2); T_{aw} is the adiabatic wall temperature calculated either from the laminar boundary layer theory or chosen to be equal to the stagnation temperature T_0; ϵ_t is the total emissivity chosen to be equal to the normal surface emissivity in the infrared band studied; σ is the Stefan-Boltzmann constant, and T_r is the enclosure temperature towards which the model radiates. In practice, in cold wind tunnel applications like the BAM6QT, T_r is coincident with the ambient temperature [22].

The IHTP is solved by means of a recursive least-square approach in the time interval of interest. It works by varying the unknown parameter h in order to minimize the residual $f(\underline{h})$ between the measured temperature Tw_{exp} and $T_{w_{num}}$ generated by solving the heat equation Eq. (13-2):

$$f(\underline{h}) = \int_{t_i}^{t_f}\left[T_{w_{exp}}(\underline{x},t,\underline{h}) - T_{w_{num}}(\underline{x},t,\underline{h})\right]dt \tag{13-4}$$

Due to the long tunnel startup and the unsteady part of the run, before the time interval of study, the boundary condition $T(x,y,z,t) = T_w$ is applied to numerically solve the Direct Heat Transfer Problem (DHTP). This guarantees that the temperature state within the spatial mesh is approximately the correct initial condition for the time interval of interest $[t_i, t_f]$ in which the convective heat transfer coefficient h is evaluated. In the optimization procedure, the convergence is reached if, between two subsequent iterations, both the step sizes $\underline{\Delta h}$ and $f(\underline{h} + \underline{\Delta h}) - f(\underline{h})$ are lower than 10^{-6}.

13.5 EXPERIMENTAL DATA

13.5.1 Experimental Apparatus

The experimental tests have been carried out in the Boeing/AFOSR Mach-6 Quiet Tunnel described in Section 13.2. The IR thermography measurements are performed using the Infratec imageIR® 8300 hp. The camera has a Mercury Cadmium Telluride (MCT) quantum detector array of 640×512 pixels and a spectral range of 2.0 - 5.7 μm. The camera is operated at 300 Hz to have enough frames to better discretize the unsteady flow. The integration time was set to 1290 μs to increase the measurements accuracy. A wide-angle lens has been used with a focal length of 12 mm and a field of view of 43.6 deg $\times$ 35.5 deg. The camera was rotated with respect to the viewing window normal to prevent for self-reflection and it was shielded with black paper to prevent spurious reflections from the background and window.

The wind tunnel test model is a 7° half-angle sharp, circular cone 406 mm long [23] shown in Figure 13-9a. A polyether ether ketone (PEEK) sensor frustum (Figure 13-9b) has been used for infrared measurements. This element starts at $x = 247$ mm distance from the nosetip and ends at $x = 385$ mm, where x is along the cone axis. When performing runs at 0 deg angle of attack, three Schmidt-Boelter gauges have been fixed in the sensor frustum holes to provide local heat flux measurements for the validation.

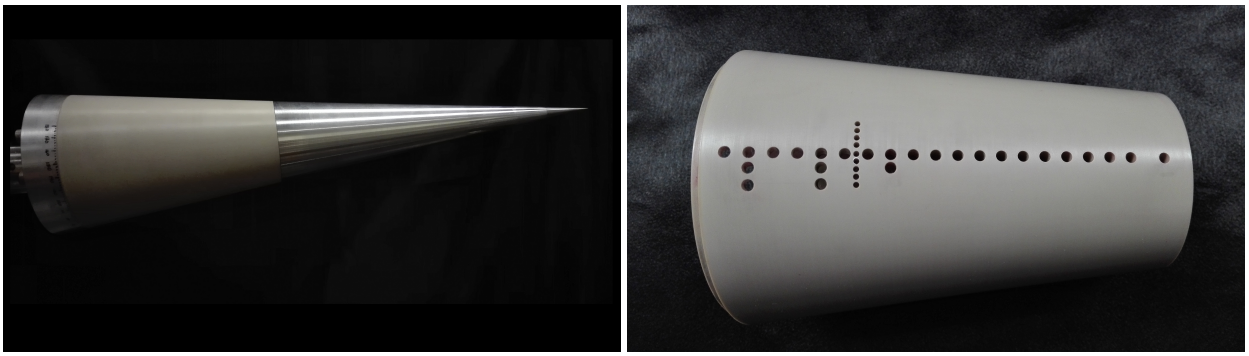

(a) The Model on the Wind Tunnel Sting. **(b) PEEK Sensor Frustum Overview.**

Figure 13-9: Wind Tunnel Test Model.

13.5.2 1D Data Reduction Results and Validation

In order to validate the infrared data reduction technique, some runs with the cone at 0 deg angle of attack have been conducted. The Reynolds number on the sensor frustum is sufficiently low to ensure a laminar boundary layer in a quiet environment ($Re < 10^7$). Since the flowfield is completely axisymmetric, a one-dimensional model of the problem Eq. (13-2) has been solved using a finite difference approach. In particular, a backward Euler implicit scheme has been implemented for the time integration because it is absolutely stable and second order accurate in space and time [24]. The domain depth was assumed equal to 5 mm to have margin of safety since the penetration depth was found to be 3.84 mm. The time step dt was forced to be equal to the time between two subsequent IR images. In the following, the Stanton number St is used as a non-dimensional parameter to discuss the experimental results related to the convective heat flux q_c and it is defined as

$$St = \frac{q_c}{c_{p_\infty} \rho_\infty U_\infty \left(T_{aw} - T_w\right)} \quad . \tag{13-5}$$

In Eq. (13-5) the parameters $T_w, c_{p_\infty}, \rho_\infty$ and U_∞ are respectively the wall temperature and the free-stream constant-pressure specific heat, flow density, and speed. The adiabatic wall temperature T_{aw} for a laminar boundary layer can be defined as

$$T_{aw} = T_e \left(1 + \frac{\gamma - 1}{2} r M_e^2\right) \tag{13-6}$$

where T_e and M_e are the static temperature and Mach number at the edge of the boundary layer respectively [25]. The recovery factor r was considered equal to $\sqrt{Pr}$ (flat plate), to a reasonable approximation.

The IHTP has been solved in a time interval of 0.18 s. Its time during the run is found by fixing a Reynolds number per unit arc length ξ ($Re/\xi = \rho_\infty U_\infty / \mu_\infty$) which decreases during the run because of the drop of both the stagnation pressure P_0 and temperature T_0. For each run, the experimental solution has been directly compared and validated against the theoretical laminar solution for the cone. The latter has been evaluated as proposed by Sullivan and Liu [26] using both a similarity solution and a reference temperature method. The conditions at the edge of the boundary layer are evaluated from the Taylor-Maccoll theory. In order to have additional terms of comparison, three Schmidt-Boelter gauges have been installed on the model to have local measurements of convective heat flux. Moreover, a Navier-Stokes analysis has been conducted for each run using the two-dimensional solver STABL2D [27].

A total of 19 runs have been performed with the cone at 0 deg angle of attack. Different free-stream conditions have been tested to have a wide range of data for the validation of the data reduction technique. The results are summarized in Figure 13-10. The experimental results from IR measurements show exceptional agreement with the theoretical solution. The relative error of the IR measurements $E_r = |St_{th} - St_{exp}|/St_{th}$ has been evaluated for five Reynolds numbers for a total of 67 values as a statistical population. The results are shown in Figure 13-11a. The average error is 3.6%, and it is an excellent result when compared with the Schmidt-Boelter gauges errors shown in Figure 13-11b with an average error of about 28%, 40% and 47% for the first, second, and third gauge (named SB1, SB2, and SB3) respectively. As can be noticed in Figure 13-10, the computational solution shows a constant error of 5% in respect with the theoretical solution. For $Re = 2.68 \cdot 10^6$ the Stanton number has been evaluated for each run and the normalized standard deviation has been found to be 4.35% which is promising for future work.

13.5.3 2D Data Reduction Results

Several runs with the cone at 6 deg angle of attack have been performed. Due to the spanwise temperature gradients caused by the crossflow vortices, a two-dimensional inverse heat transfer problem has been solved to take into account tangential conduction. In particular, a 2D heat equation in cylindrical coordinates (r, ψ, x) for a fixed x has been solved using a backward Euler implicit scheme with a finite difference approach. The domain has been discretized using a number of elements on the boundary surface with the same spatial resolution of the mesh grid used for the temperature map reconstruction, with a depth of 5 mm. A trust-region reflective algorithm is used for the residual optimization (Eq. (13-4)) and the computational costs are reduced by means of a Discrete Fourier Transform (DFT) iterative procedure proposed by Avallone et al. [20]. The relevance of the tangential conduction is quantified by means of the Modulation Transfer Function F [7] based on the modified Fourier number $Fo_{\overline{\omega}}$ evaluation. For the present work, a value of F = 0.958 is found which means a predicted modulation of 4.2% in terms of the peak to valley difference between the 1D and 2D solution.

In Figure 13-12, the results are shown in terms of Modified Stanton number Ch which is defined as Eq. (13-5) but with the stagnation temperature T_0 instead of the adiabatic wall temperature T_{aw}.

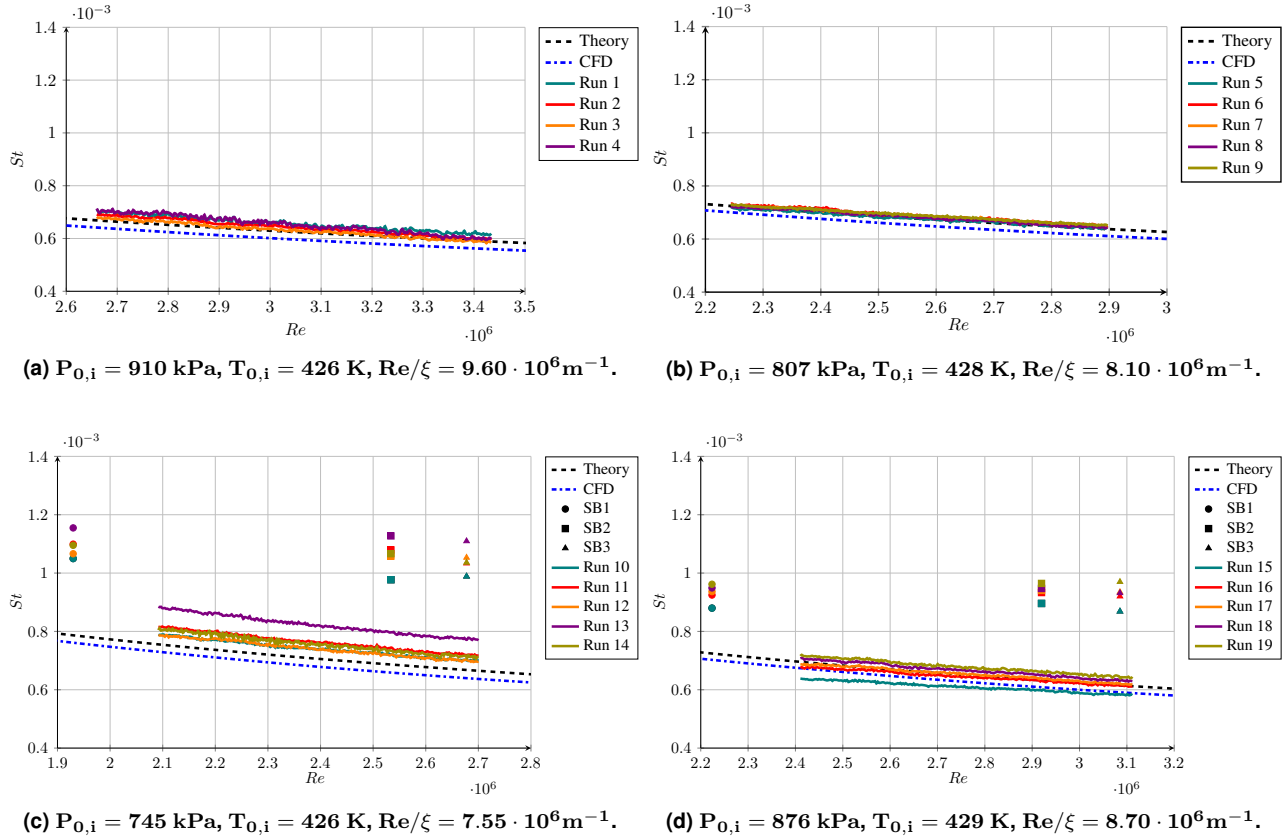

(a) $\mathbf{P_{0,i} = 910\ kPa,\ T_{0,i} = 426\ K,\ Re/\xi = 9.60 \cdot 10^6 m^{-1}}$.

(b) $\mathbf{P_{0,i} = 807\ kPa,\ T_{0,i} = 428\ K,\ Re/\xi = 8.10 \cdot 10^6 m^{-1}}$.

(c) $\mathbf{P_{0,i} = 745\ kPa,\ T_{0,i} = 426\ K,\ Re/\xi = 7.55 \cdot 10^6 m^{-1}}$.

(d) $\mathbf{P_{0,i} = 876\ kPa,\ T_{0,i} = 429\ K,\ Re/\xi = 8.70 \cdot 10^6 m^{-1}}$.

Figure 13-10: Experimental and Theoretical Results Comparison for the Cone at 0 deg Angle of Attack.

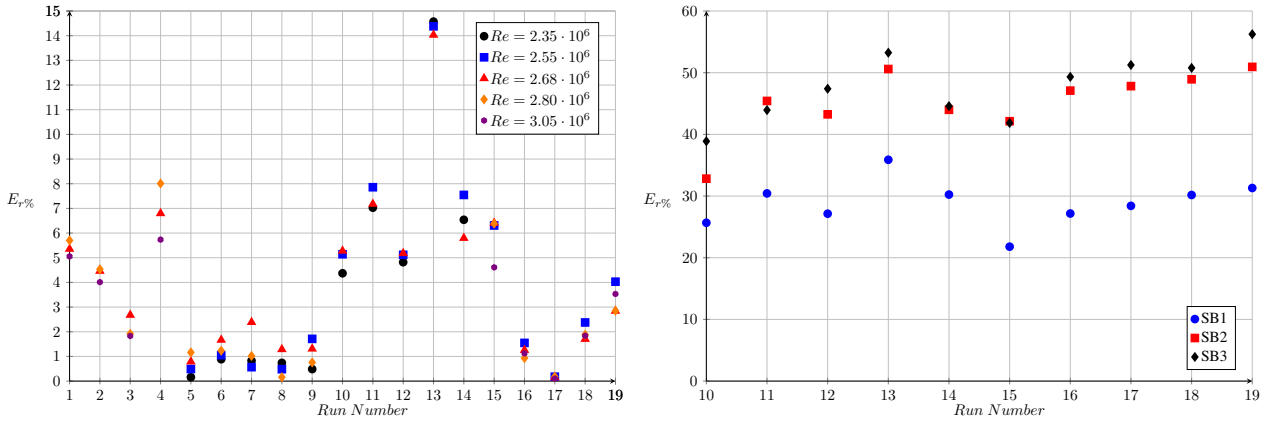

(a) IR Measurements Error.

(b) Schmidt-Boelter Gauges Measurements Error.

Figure 13-11: Measurement Errors of (a) IR Technique and (b) Schmidt-Boelter Gauges Against the Theoretical Solution for the Cone at 0 deg Angle of Attack.

The raw temperature data have been filtered by a second order polynomial space-time filter to reduce the random measurement noise. The 1D results are used as a first guess for the 2D optimization process to accelerate the convergence to the solution. The latter is obtained by optimizing only 70 coefficients of the DFT which represent the 27% of the total to reduce the computational load. In this way, the difference between the original signal and the one reconstructed by means of the Inverse Discrete Fourier Transform (IDFT) was lower than 1% when compared with the mean value in each point. The Modified Stanton number Ch evaluated with the 2D approach is compared against the 1D solution in Figure 13-12.

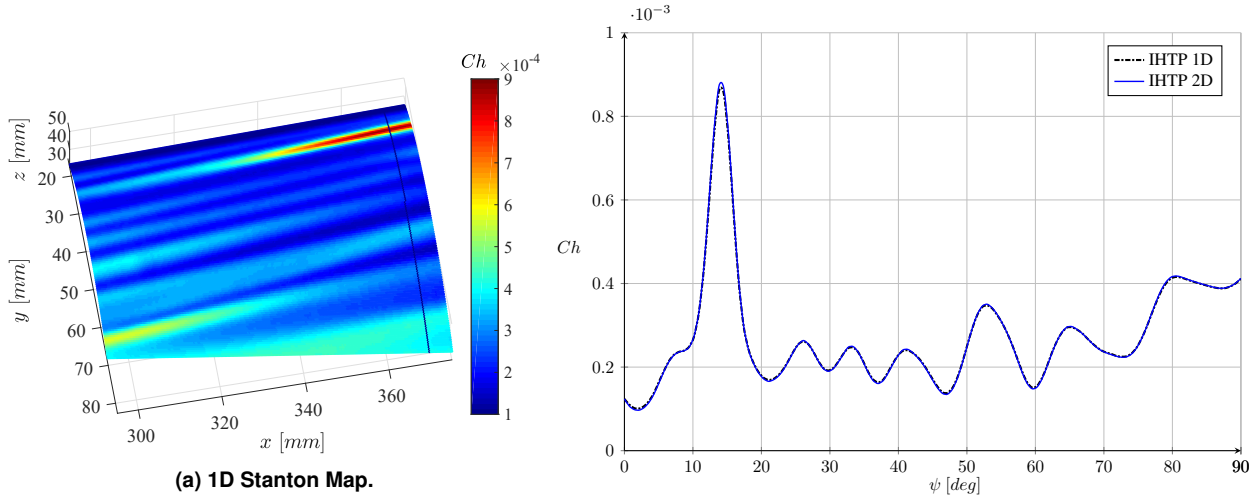

(a) 1D Stanton Map.

(b) 1D and 2D Solution Comparison.

Figure 13-12: Spanwise Modified Stanton Number Distribution Along the Black Line Shown in the 1D Map (a) from the 1D and 2D Technique. Cone at 6 deg Angle of Attack, $\mathbf{P_{0,i} = 762\ kPa}$, $\mathbf{T_{0,i} = 429\ K}$, $\mathbf{Re/\xi = 7.72 \cdot 10^6\ m^{-1}}$.

Due to the favorable thermal properties of the PEEK ($\alpha = 2.17 \cdot 10^{-7} \mathrm{m}^2/\mathrm{s}$ and $\epsilon = 0.91$), the experiment carried out is weakly affected by the tangential conduction. As a matter of fact, Figure 13-12b shows a modulation between the 1D and 2D estimation at most of about 3.8% on the higher peak around which the maximum temperature gradient is reached and this is in great agreement with the predicted value.

13.6 CONCLUSION

An infrared thermography data reduction technique to solve the 1D and 2D Inverse Heat Transfer Problem (IHTP) is presented. Firstly, the camera calibration has been conducted to incorporate the transmissivity of the wind tunnel viewing window. The infrared raw data were then converted to temperature values with a residual error of ± 0.08 K. The infrared directional emissivity of the model material has been taken into account to correct the temperature data and increase the results accuracy. IR images have been recorded using a camera model based on the perspective projection approach taking into account lens distortions. The optical calibration has been conducted with a coefficient of determination $R^2 = 0.999$. An image registration algorithm has been used to correct for model oscillations. The approach based on the single-step DFT seems to be very useful to reduce noise with subpixel accuracy. Eventually, three-dimensional maps of temperature have been presented. The 1D IHTP has been developed and validated by performing runs with the cone at 0 deg angle of attack. The results have been compared with the theoretical solution in terms of Stanton number showing exceptional agreement with an average error of 3.6% and a normalized standard deviation of 4.35%.

The experimental results are promising for future works especially when compared with the Schmidt-Boelter gauges whose error is higher than 22%. The 2D IHTP has been developed to take into account tangential conduction caused by the crossflow vortices on the cone tested at 6 deg angle of attack. The computational cost is reduced by optimizing only 70 coefficients (27% of the total) of the discrete Fourier decomposition of the convective heat flux coefficients vector. For the present work, the one-dimensional technique has been found to modulate the convective heat flux by 4.2% according the Modulation Transfer Function theory. The two-dimensional analysis showed a maximum Modified Stanton number modulation of 3.8% in respect to the 1D measurements which is in accordance with the predicted value. This error can be considered acceptable for future works and the application of the two-dimensional model should be checked in terms of computational cost feasibility.

13.7 REFERENCES

[1] Lin, T., Grabowsky, W., and Yelmgren, K., "The Search for Optimum Configurations for Re-entry Vehicles," *Journal of Spacecraft and Rockets*, Vol. 21, No. 2, mar 1984, pp. 142–149.

[2] Schneider, S., "Laminar-Turbulent Transition on Reentry Capsules and Planetary Probes," Vol. 43, No. 6, 11 2006, pp. 1153–1173.

[3] Anderson, J., *Hypersonic and High Temperature Gas Dynamics*, McGraw-Hill series in aeronautical and aerospace engineering, American Institute of Aeronautics and Astronautics, 2000.

[4] Legner, H., Gelb, A., Rosen, D., and Caledonia, G., "High Velocity Interceptor Investigations," 09 1998, pp. 103.

[5] Schneider, S., "Effects of High-Speed Tunnel Noise on Laminar-Turbulent Transition," Vol. 38, No. 3, 05 2001, pp. 323–333.

[6] Schneider, S., "The Development of Hypersonic Quiet Tunnels," Vol. 45, No. 4, 07 2008, pp. 641–664.

[7] Astarita, T. and Carlomagno, G., *Infrared Thermography for Thermo-Fluidynamics*, Berlin Heidelberg, New York (USA), 2013.

[8] Walker, G. and Scott, E., "Evaluation of Estimation Methods for High Unsteady Heat Fluxes from Surface Measurements," Vol. 12, No. 4, 07 1998, pp. 543–551.

[9] de Luca, L. and Cardone, G., "Modulation Transfer Function Cascade Model for a Sampled IR Imaging System," *Appl. Opt.*, Vol. 30, No. 13, May 1991, pp. 1659–1664.

[10] Schrijer, F., "Unsteady Data Reduction Techniques for QIRT: Considerations of Temporal and Spatial Resolution," *QIRT Conference*, 2012.

[11] Cardone, G., Ianiro, A., dello Ioio, G., and Passaro, A., "Temperature Maps Measurements on 3D Surfaces with Infrared Thermography," Vol. 52, 02 2011.

[12] Heikkila, J. and Silven, O., "A Four-Step Camera Calibration Procedure with Implicit Image Correction," *Proceedings of IEEE Computer Society Conference on Computer Vision and Pattern Recognition*, Jun 1997, pp. 1106–1112.

[13] Marquardt, D., "An Algorithm for Least Square Estimation of Non-Linear Parameters," Vol. 11, No. 2, 06 1963, pp. 431–441.

[14] Guizar-Sicairos, M., Thurman, S., and Fienup, J., "Efficient Subpixel Image Registration Algorithms," Vol. 33, No. 2, 02 2008, pp. 156–8.

[15] Barrett, H., *Foundations of Image Science*, Vol. 31, Wiley, 01 2004.

[16] Siegel, R. and Howell, J., *Thermal Radiation Heat Transfer*, Series in thermal and fluids engineering, Hemisphere Pub. Corp., 1981.

[17] Ianiro, A. and Cardone, G., "Measurement of Surface Temperature and Emissivity with Stereo Dual-Wavelength IR Thermography," *Journal of Modern Optics*, Vol. 57, No. 18, 2010, pp. 1708–1715.

[18] Beck, J., Blackwell, B., Clair, C., and Artûhin, E., *Inverse Heat Conduction: Ill-Posed Problems*, Wiley-Interscience publication, Wiley, 1985.

[19] Avallone, F., Greco, C., and Ekelschot, D., "Image Resection and Heat Transfer Measurements by IR Thermography in Hypersonic Flows," *Quantitative InfraRed Thermography Journal*, Vol. 10, No. 2, 2013, pp. 188–206.

[20] Avallone, F., Greco, C., and Ekelschot, D., "A Low-Computational-Cost Inverse Heat Transfer Technique for Convective Heat Transfer Measurements in Hypersonic Flows," *Experiments in Fluids*, Vol. 56, No. 4, 2015.

[21] Schultz, D. and Jones, T., "Heat-Transfer Measurements in Short-Duration Hypersonic Facilities," Vol. 165, 02 1973, pp. 155.

[22] Gülhan, A., Schütte, G., and Stahl, B., "An Experimental Study on Aerothermal Heating Caused by Jet-Hypersonic Cross Flow Interaction," *Journal of Spacecraft and Rockets*, Vol. 45, No. 5, September 2008.

[23] Chynoweth, B., Edelman, J., Gray, K., McKiernan, G., and Schneider, S., "Measurements in the Boeing/AFOSR Mach-6 Quiet Tunnel on Hypersonic Boundary-Layer Transition," *47th AIAA Fluid Dynamics Conference, AIAA AVIATION Forum*, 2017.

[24] LeVeque, R., *Finite Difference Methods for Ordinary and Partial Differential Equations: Steady-State and Time-Dependent Problems*, Other Titles in Applied Mathematics, Society for Industrial and Applied Mathematics, 2007.

[25] Shapiro, A., *The Dynamics and Thermodynamics of Compressible Fluid Flow*, Vol. 1 of *The Dynamics and Thermodynamics of Compressible Fluid Flow*, Wiley, 1953.

[26] Liu, T., Wang, B., Rubal, J., and Sullivan, J., "Correcting Lateral Heat Conduction Effect in Image-Based Heat Flux Measurements as an Inverse Problem," *International Journal of Heat and Mass Transfer*, Vol. 54, No. 5, 2011, pp. 1244–1258.

[27] Johnson, H., Candler, G., and Alba, C., "Three-Dimensional Hypersonic Boundary Layer Stability Analysis with STABL-3D," *40th Fluid Dynamics Conference and Exhibit Chicago, Illinois*, 06 2010.

Chapter 14 – RECEPTIVITY TO FREESTREAM ACOUSTIC NOISE IN HYPERSONIC FLOW OVER A GENERIC FOREBODY

Adriano Cerminara
University of Southampton
UNITED KINGDOM

Antoine Durant and Thierry André
MBDA-F
FRANCE

Neil D. Sandham
University of Southampton
UNITED KINGDOM

Nigel J. Taylor
MBDA UK Ltd
UNITED KINGDOM

14.1 INTRODUCTION

Transition to turbulence plays a crucial role in determining the heat-transfer rates on the surface of hypersonic vehicles, which makes it necessary to understand the physical mechanisms responsible for transition, in order to allow accurate prediction of the transition location. The main path to transition, in the case of linear disturbances, can be summarized in three fundamental steps: i) receptivity, ii) modal growth of the instabilities and c) nonlinear instability and final breakdown to turbulence.

Receptivity is the internalization process of the external disturbances into the boundary layer in the form of instability modes, and determines the initial conditions for the downstream linear growth of the unstable modes. In the case of high-amplitude disturbances, nonlinearities can become predominant in the receptivity process, which would lead directly to nonlinear growth and rapid transition to turbulence. In some particular conditions, an intermediate route to transition (between a linear modal and a fully nonlinear process) is possible, i.e. transient growth, consisting of a non-modal growth of linear instabilities, as in the case of lift-up-induced streamwise streaks in conjunction with secondary instabilities and consequent nonlinear breakdown [1, 2].

The body leading edge is a highly-receptive zone, due to the non-parallel effects and the related short-scale streamwise variations of the mean flow, which, in turn, cause a wavelength-conversion process from the scale of the external forcing to that of the induced boundary-layer disturbances [3]. At hypersonic Mach numbers, however, the small difference in phase speed between the forcing waves and the boundary-layer dominant modes can lead to a direct excitation of these modes via a resonance mechanism at the leading edge [4–7], without the need of a wavelength-conversion mechanism. By applying Fedorov's notation [5], the internal mode generated at the leading edge through the receptivity to fast acoustic waves is called the fast mode, or mode F, while the mode associated to the slow acoustic waves is known as the slow mode, or mode S, which is the mode pertaining to the class of the unstable boundary-layer modes. In hypersonic boundary layers, different unstable modes

can coexist, including the first mode, corresponding to the Tollmien-Schlichting (TS) waves, and the higher-frequency (second, third, etc.) 'Mack' modes [8]. Among the high-frequency modes, the second mode was found to play a crucial role in the transition process by the experiment of Stetson *et al.*[9] for a Mach 8 flow over a cone, and is, in general, known to be the dominant instability mode in two-dimensional (2D) hypersonic boundary layers [5, 10]. The receptivity to fast and slow acoustic waves has been numerically studied by several authors [6, 11–15], whose results agree, in general, in recognizing a major role played by the slow acoustic waves (in the linear case) in the maximum amplitude reached by the unstable second mode and, hence, in the transition process, compared to fast acoustic waves. However, recent numerical studies [16, 17] found that for high-amplitude freestream perturbations the strong resonance mechanism associated with fast acoustic waves at the leading edge can trigger a more rapid transition process, compared to the case of slow acoustic waves.

The focus of the present study is on the role of fast and slow acoustic waves in high-amplitude disturbance environments on the receptivity and transition over a 3D generic forebody model. This model was tested in transition experiments conducted by Durant *et al.*[18] in the Mach 6 Purdue wind tunnel (BAM6QT), both in noisy and quiet conditions. The tests (exploring the natural transition) made in quiet conditions showed the flow remaining laminar over the whole streamwise length, whereas in noisy conditions transition was observed to start just downstream of the nose region, with evidence of streamwise streaks developing off the centerline. Relevant computational studies on the same geometry can be found in the works of Orlik *et al.* [19] and Andre´ *et al.* [20, 21], which focused on the transition induced by wall injection.

Three-dimensional (3D) boundary layers in hypersonic flow can include crossflow and attachment-line instabilities. In particular crossflow instability, which is linked to the inflectional crossflow boundary-layer profile forming in regions of local sweep angles and high pressure gradients [22], can dominate in 3D configurations, e.g. on swept wings, axisymmetric cones at an angle of incidence and on rotating disks. Boundary layers in the presence of crossflow instabilities have been studied extensively in low-speed flows, e.g. in the works of Saric *et al.* [22], Reed and Saric [23], Bippes [24], and have been shown to be characterized, in cases of low freestream disturbances, by the formation of stationary vortices which grow and saturate nonlinearly, providing a pronounced distortion of the mean flow. The breakdown is then caused further downstream by the development of high-frequency secondary instabilities of the deformed mean flow [25, 26].

Crossflow instabilities include both stationary and traveling waves. The stationary modes are in general generated by surface roughness, whereas the traveling modes are linked to vortical freestream disturbances, hence they are expected to be dominant in noisy environments. Traveling crossflow waves are usually found in a relatively low frequency range. Borg *et al.* [27], for example, detected linearly growing traveling waves in quiet conditions with peak centered at 45 kHz, in their Mach 6 experiment over a scaled model of the Hypersonic International Research Experimentation Program's Five (HIFiRE-5) elliptic cone in the Mach 6 Purdue quiet tunnel. However, in contrast to their expectations, they did not observe the presence of traveling waves in noisy conditions. Craig and Saric [28] conducted an experimental investigation of the crossflow instability mechanism in hypersonic flow over a 7˚ right circular cone at 5.6˚ in the Mach 6 quiet tunnel at Texas A&M University. Consistent with the low-speed findings, they observed stationary vortices growing and significantly deforming the mean flow, and then attenuating after reaching nonlinear saturation. Moreover, they measured unsteady fluctuations in two different frequency bands, i.e. 15-60 kHz and 80-130 kHz. The disturbances in the lower frequency band were attributed to growing traveling crossflow waves, in agreement with the results of the nonlinear parabolized stability equations (NPSE) of Kuehl *et al.* [29] and Oliviero *et al.* [30], whereas those in the high-frequency band were identified as secondary instabilities. Similar results were obtained experimentally by Ward *et al.* [31] for a Mach 6 flow over a yawed circular cone.

The works of Choudhari *et al.* [32], based on linear/nonlinear parabolized stability equations, and of Li *et al.* [33], based on secondary instability theory, PSE and DNS results, have shed light on the important role played by the growth of the secondary instabilities of primary traveling crossflow waves, as a viable alternate transition scenario when the initial amplitudes of the traveling waves are comparable to those of the stationary modes. Li *et al.* [34] described, through results from quasiparallel stability theory and PSE, the role of primary traveling crossflow waves (below 100 kHz) and higher-frequency Mack modes as different sources of secondary instabilities, due to their strong modulation caused by the presence of the stationary modes.

Further stability calculations and direct numerical simulations of crossflow instabilities have been carried out for swept wings, circular cones at an angle of attack, and elliptic cones. Balakumar and Owens [35] and Balakumar and King [36] reported substantially higher N-factors for traveling crossflow waves compared to stationary waves in flows over a circular cone at 6° angle of attack, a swept cylinder and a swept wing with sharp and blunt leading edge. The DNS results of Bartkowicz *et al.* [37], for the Mach 8 flow over the HIFiRE-5 elliptic cone model, showed the evolution of a system of streamwise vortices forming next to the centerline bulge at different Reynolds numbers, and associated these vortices with stationary crossflow waves. The addition of acoustic noise caused unsteady waves to form on top of the vortices, causing their breakdown at the highest Reynolds numbers. More recent DNS simulations of Dinzl and Candler [38] have shown a difference between the centerline system of vortices, which is a baseflow property linked to the streamlines converging from the attachment line towards the centerline, and the crossflow vortices generated by surface roughness. When distributed roughness was added, a system of crossflow stationary vortices formed in the midspan region between the centerline and the attachment line, whose growth characteristics and wavelength were observed to be very sensitive to the roughness height and Reynolds number, respectively.

Recent studies based on BiGlobal linear stability analysis [39, 40] conducted on the HIFiRE-5 geometry confirmed the dominant role played by the crossflow instabilities in the off-centerline region, but showed also that different instability modes (denoted centerline modes) may occur along the centerline, which can significantly affect transition.

Experimental verification of the important role played by different boundary-layer modes in different flow regions of the HIFiRE-5 geometry, namely the centerline and the off-centerline region, can be found in the work of Juliano *et al.* [41]. Here, surface heat-flux measurements indicated the presence of both centerline and off-centerline transition in noisy conditions. The centerline transition was associated with second-mode waves.

The present work aims to explore through DNS the different transition scenarios associated with fast and slow acoustic waves in a three-dimensional boundary layer, and compare the obtained results with the experimental observations [18], which can provide significant further insight in the transition mechanism due to acoustic noise in hypersonic wind tunnels. Moreover, considering that the acoustic noise radiated from the turbulent boundary layer on the nozzle walls is, in general, known to be the dominant type of disturbances inside hypersonic wind tunnels [42–44], our study aims also to shed light, through direct comparison between DNS and experimental results, on the relative importance of fast and slow acoustic waves in the environmental noise of hypersonic wind tunnels. For such a purpose, the choice of the imposed disturbance amplitude is crucial to allow reliable comparison between experimental and numerical results. In our simulations, as will be shown later in this paper, the selected amplitude is based on the findings of recent experimental as well as numerical studies, e.g. Masutti *et al.* [45], Parziale *et al.* [46], Duan *et al.* [47] and Wagner *et al.* [48], aimed at investigating the noise characteristics in the environment of hypersonic wind tunnels.

After introducing the numerical method (Section 14.2), the computational mesh (Section 14.3) and the inflow conditions (Section 14.4), we review the experiments (Section 14.5) in order to size the computational domain (Section 14.6). The baseflow is presented in Section 14.7 and the main unsteady results in Section 14.8.

14.2 NUMERICAL METHOD

14.2.1 Governing Equations

We consider numerical solutions of the three-dimensional Navier-Stokes equations for compressible flows, written in conservation form, under the assumption of perfect gas. The set of non-dimensional conservation equations in Cartesian coordinates can be written as

$$\frac{\partial \mathbf{Q}}{\partial t} + \frac{\partial (\mathbf{F}_j)}{\partial x_j} = 0 \,, \tag{14-1}$$

In the equation above, **Q** is the vector of the conservative variables, while $\mathbf{F}_j$ is the vector of the fluxes in Cartesian coordinates. The components of the vectors of the system in conservative form are

$$\mathbf{Q} = \begin{bmatrix} \rho \\ \rho u \\ \rho v \\ \rho w \\ \rho E \end{bmatrix} , \; \mathbf{F}_j = \begin{bmatrix} \rho u_j \\ \rho u u_j + \delta_{1j} p - \frac{1}{Re} \tau_{1j} \\ \rho v u_j + \delta_{2j} p - \frac{1}{Re} \tau_{2j} \\ \rho w u_j + \delta_{3j} p - \frac{1}{Re} \tau_{3j} \\ \rho \left(E + \frac{p}{\rho} \right) u_j - \frac{1}{Re} \left(u_i \tau_{ij} + \frac{\mu}{(\gamma - 1) Pr M^2} \frac{\partial T}{\partial x_j} \right) \end{bmatrix} . \tag{14-2}$$

The terms ρ, ρu, ρv, ρw and ρE are the conservative variables of the system of equations, where ρ is the density, u, v and w are the velocity components respectively in the x, y and z directions, and E is the total energy per unit mass. The freestream reference values used for the normalization (denoted by the superscript *) are U_∞^*, ρ_∞^*, μ_∞^*, T_∞^*, U_∞^{*2}, $\rho_\infty^* U_\infty^{*2}$, for velocity, density, viscosity, temperature, energy and pressure respectively. The nose radius (R^*) is chosen as the characteristic length scale, while the characteristic time is given by R^*/ U_∞^* The Reynolds number is defined with respect to the nose radius, as $Re = (\rho_\infty^* U_\infty^* R^*)/\mu_\infty^*$; the Prandtl number is set to 0.72 for air, and γ is equal to 1.4, as we are considering a perfect gas model. The viscous stresses are defined in terms of the velocity derivatives, under the assumption of a Newtonian fluid, as

$$\tau_{ij} = \mu \left[\frac{\partial u_i}{\partial x_j} + \frac{\partial u_j}{\partial x_i} - \frac{2}{3} \delta_{ij} \frac{\partial u_k}{\partial x_k} \right] . \tag{14-3}$$

The dynamic viscosity is obtained through Sutherland's law, with Sutherland's constant equal to 110.4 K and reference temperature equal to the freestream temperature, T_∞. Finally, the system of equations is closed by the nondimensional equation of state for a perfect gas

$$p = \frac{1}{\gamma M^2} \rho T \,. \tag{14-4}$$

The system of equations in Cartesian coordinates is transformed into a system of equations in curvilinear coordinates (ξ, η, ζ) as

$$\frac{\partial \bar{\mathbf{Q}}}{\partial t} + \frac{\partial (\bar{\mathbf{F}}_j)}{\partial \xi_j} = 0, \tag{14-5}$$

where the relations between the vectors in curvilinear and Cartesian coordinates are expressed by

$$\bar{\mathbf{Q}} = J\mathbf{Q}, \qquad \bar{\mathbf{F}}_j = J\mathbf{F}_i \frac{\partial \xi_j}{\partial x_i},$$

with $J = \det ||\partial(x, y, z)/\partial(\xi, \eta, \zeta)||$ being the jacobian of the transformation matrix.

14.2.2 Modeling of Planar Oblique Acoustic Waves

A three-dimensional (3D) acoustic-wave system, consisting of a main two-dimensional (2D) wave and pairs of opposite-angle lower-amplitude oblique waves, is considered as freestream forcing in the unsteady simulations. The 2D wave has a wave-vector aligned in the streamwise (x) direction, whereas the oblique waves are considered as planar waves travelling with an angle θ in the xz-plane. The 3D wave model used for the present case is expressed by the following equation, which represents the freestream density fluctuation,

$$\rho'(x, y, t) = \sum_{m=0}^{M_z} \sum_{n=1}^{N} A_m \cos(\beta_m z) \cos(\alpha_n x - \omega_n t + \psi_n) \ , \tag{14-6}$$

where α_n and β_m are the wavenumbers respectively in the x and z directions, ω_n is the angular frequency, A_m is the amplitude of each wave mode, ψ_n is a random phase angle, whereas N and M_z represent the total number of frequencies and non-zero spanwise wavenumbers respectively. In the present study $N = 10$, indicating a spectrum of 10 different frequencies, and $M_z = 2$, thus giving two spanwise wavenumbers for the oblique waves, $\beta_m = 2\pi m/L_z$ (with L_z being the length of the domain in the z direction). Note that for $m = 0$ we have $\beta_0 = 0$, which is a 2D wave. The streamwise wavenumber, α_n, is linked to the angular frequency, $\omega_n = 2\pi f_n$, through the relation $\alpha_n = \omega_n/(1 \pm 1/M)$, in which the term $1 \pm 1/M$ represents the freestream phase speed in the x direction of the acoustic waves, with the plus sign indicating fast acoustic waves, and the minus sign standing for slow acoustic waves. For each frequency, and for each spanwise wavenumber $m = 1, 2$, two waves with the same amplitude A_m and opposite angle $\theta_{m,n} = \pm \arctan \frac{\beta_m}{\alpha_n}$ are inserted, such that the z-velocity perturbation relative to each wave ($w' = \pm (1/M)\rho' \sin\theta$) cancels. This gives $w' = 0$ identically in the freestream. Finally, the relation between the amplitude of each single oblique wave and that of the main 2D wave is $A_m = \frac{1}{4} A_0$ (for $m = 1, 2$) at each frequency, and the amplitude A_0 is independent of frequency.

14.3 GEOMETRY AND MESH

We consider now the three-dimensional geometry of a generic forebody model, proposed by MBDA-France, for which transition experiments were performed by Durant *et al.*[18] in the Mach 6 hypersonic wind tunnel of the Purdue University. Figure 14-1 shows different views of the geometry. It consists of a wedge with a rounded

leading-edge shape, nose radius of 1.25 mm (in the *xy*-plane), a length of 340 mm, maximum width along the *z*-axis of 120 mm, maximum height along the *y*-axis of 50 mm, and half-wedge angle (in the *xy*-plane, with reference to the side view in 14-1) of 4°. In our numerical simulations we consider a case with zero angle of attack and zero yaw angle, namely the flow direction is aligned with the *x*-axis of the body, and symmetry with respect to both the *xy* and *xz* planes (considering the origin of the reference system on the tip of the body) is assumed, including the upstream disturbances.

The grid is a body-fitted structured single-block grid. In each *xy* plane, the j-lines (the wall-tangential grid lines) are gradually adapted from the wall shape to the shock curve projected onto this plane, whereas the i-lines are normal to the wall. In an *xz* plane, the k-lines are initially aligned with the leading-edge shape, then they gradually become perpendicular to the centerline, as shown in Figure 14-2. A stretching is applied along the wall-normal direction, in order to increase the resolution towards the wall and at the shock. Stretching is also performed in the *x* direction in order to increase the resolution in the leading-edge region. A detailed description of the methodology used to generated the shock-adapted grid, as well as the stretching function applied, can be found in Cerminara [49]. Figure 14-2 shows the mesh details, in the *xz*-plane, of the surface in the leading-edge region. As can be seen, the point distribution is denser near the leading-edge, in order to resolve the high gradients characterising this zone of the flowfield, and gets coarser downstream. The internal grid lines are adjusted to follow the shape of the three-dimensional shock.

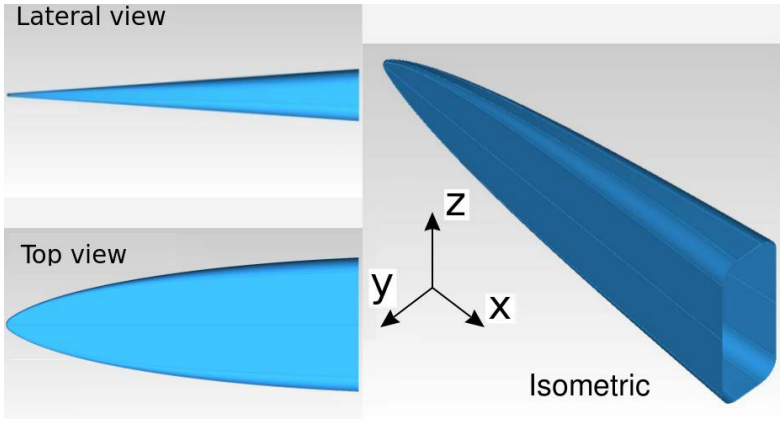

Figure 14-1: Lateral, Top (on the *xz*-Plane) and Isometric Views of the MBDA Forebody Geometry.

To simplify the mesh generation, the side boundary of the computational domain is obtained by cutting the geometry along the longitudinal direction at a particular spanwise distance from the symmetry axis. The side boundary condition consists of a zero-gradient condition, which sets the gradients of each quantity along the grid lines to zero, namely $\frac{\partial()}{\partial\tau} = 0$, with τ indicating the direction tangential to the *k*-grid lines. The use of the zero-gradient boundary condition is motivated by an observation that at sufficiently high distances from the centerline ($z = 0$) the gradients of the physical quantities in the tangential direction are small. Figure 14-3 shows the surface density field for a body with a width of 40 mm. As can be seen, the high gradients are confined in the near-centerline region, while the off-centerline region is characterised by much smaller gradients.

The above-described approach to obtain the computational domain presents the following advantages: i) it provides a uniform spanwise resolution, so that the breakdown region downstream is treated with the same spanwise resolution of the upstream receptivity region; and ii) it limits the number of points in the leading-edge region,

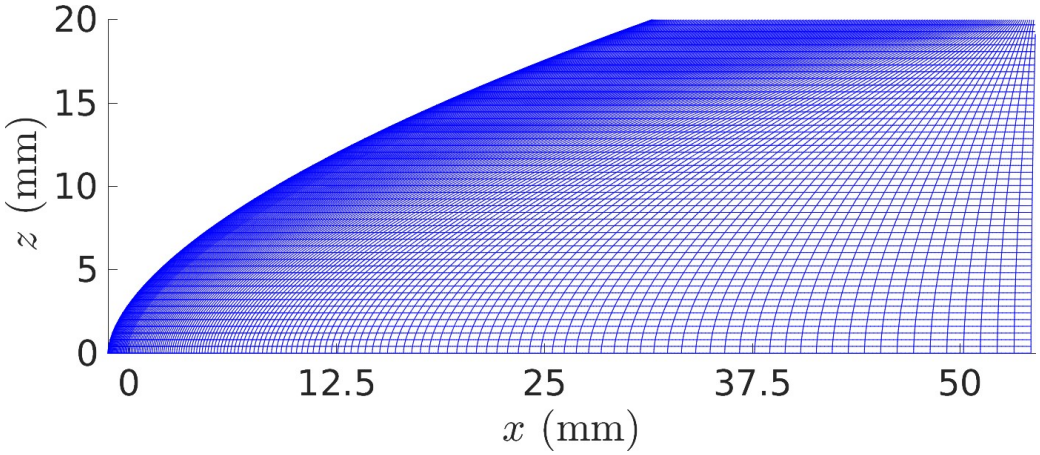

Figure 14-2: Example of a Coarse Mesh in the Leading-Edge Region of the Computational Domain (Top View).

avoiding a too-small z-spacing downstream, which would be a main issue for a grid built through grid lines in the radial (normal to the leading edge) direction.

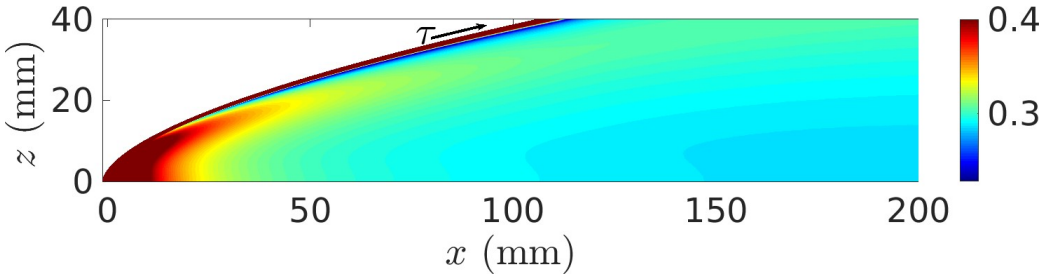

Figure 14-3: Density Field on the Wall Surface.

14.4 FLOW CONDITIONS AND SETTINGS OF THE NUMERICAL SIMULATIONS

The flow conditions of the present numerical case reproduce the freestream of the Mach 6 low-enthalpy wind tunnel at Purdue University. The experiments were carried out for different values of the unit Reynolds number (Re_m), ranging from 2.3 x 10^6 to 13 x 10^6/m. In our numerical study a unit Reynolds number of 4.6 x 10^6/m is considered, corresponding to one of the transitional cases in the experiments. The other flow conditions are $M = 6$, $T^*_\infty = 51.7$ K, $T^*_0 = 424$ K, $p^*_0 = 4.16$ x 10^5 Pa, $T^*_w/T^*_\infty = 5.8$. The latter condition for the wall temperature ratio corresponds to an isothermal wall with temperature assumed equal to 300 K.

On the xy and xz symmetric planes a symmetric boundary condition is adopted. A fixed uniform inflow boundary condition is set on the inlet boundary, and a zero-gradient boundary condition is used on both the side and the outlet boundaries. In the unsteady simulations the 3D acoustic-wave model described in Section 14.2.2 is used as inflow on the inlet boundary. The disturbance field is assumed to be symmetric with respect to both the

xy and *xz* symmetry planes of the body. The code used to carry out the numerical simulations is known as SBLI (Shock-Boundary-Layer-Interaction), developed over a number of years at the University of Southampton, consisting of a 4^{th}-order central differencing scheme, as base scheme, in conjunction with a 2^{nd}-order Harten-Yee TVD (Total-Variation-Diminishing) shock-capturing scheme [50], as a filter step. Validation of the code can be found in the works of Sandham *et al.* [51] and De Tullio *et al.*[52].

14.5 NATURAL TRANSITION EXPERIMENTS

Figure 14-4 shows the probe, made of aluminum, used in the transition experiments of Durant *et al.* [18]. Wall heat-flux measurements performed by Temperature-Sensitive Paint (TSP) were used to evaluate boundary-layer transition on the body surface, and two Schmidt-Boelter gauges were used to calibrate the TSP during post-processing. The luminophore used in the TSP was Ru(bpy). It was applied after a base coat of white primer and spray paint, which increases the signal-to-noise ratio. In addition, 15 flush-mounted pressure sensors were inserted (10 PCB132A31 and 5 Kulite XCQ-062-15A) for pressure measurements. Figure 14-5 shows the results for the wall heat flux (kW/m^2) at two Reynolds numbers for noisy wind-tunnel conditions. As can be seen, at the lowest unit Reynolds number (Re_m = 2.0 x 10^6/m) the low values of the heat flux indicate that the flow was laminar over the whole surface of the wedge, while at Re_m = 4.6 x 10^6/m transition is observed to take place at approximately a distance of 150 mm from the nose tip (note that the nose tip is not included in the figure, and its position in the figure reference system is about $x = -100$mm).

Figure 14-4: Lower Surface of the Probe, Cover Part Removed.

14.6 EXPERIMENTAL OBSERVATIONS AND DOMAIN SIZING

The observation of the experimental results [18], at the target unit Reynolds number considered in the numerical simulations (Re_m = 4.6 x 10^6/m), allows us to set the minimum required size of the computational domain to solve the most relevant flow regions for the receptivity-breakdown mechanism and to capture the main transition patterns obtained in the experiments. In Figure 14-6 the dimensional wall heat flux (kW/m^2) obtained in the experiment at Re_m = 4.6 x 10^6/m is shown. This experimental case was performed under noisy wind tunnel conditions. As can be seen, the highest heat-flux values are reached in the front leading-edge region, as expected from the high temperatures reached in the shock layer near the nose. In the downstream region, the wall heat flux assumes low values at the centerline, thus suggesting that the boundary layer near the symmetry plane is laminar; however, the off-centerline region is characterised by high heat flux values, starting from about x = 50 mm, which suggests, in contrast, that the boundary layer here undergoes transition toturbulence.

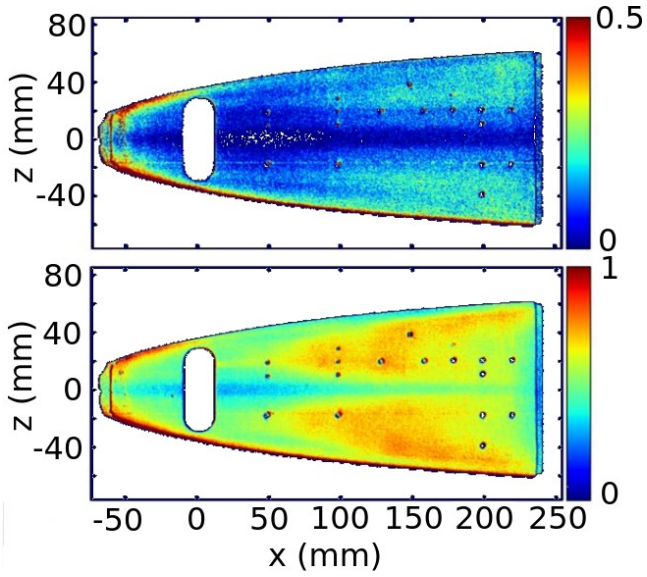

Figure 14-5: Wall Heat-Flux (kW/m^2) at Re_m = 2.0 x 10^6/m (Top) and Re_m = 4.6 x 10^6/m (Bottom).

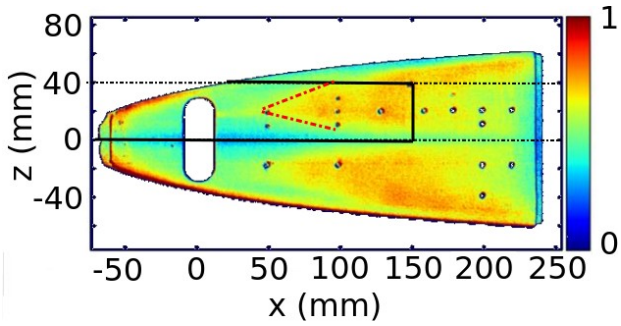

Figure 14-6: Edges of the Computational Domain Drawn on the Wall Heat-Flux Result (kW/m^2).

From the wall heat-flux experimental results the following observations can be made: i) transition appears to start at a streamwise distance from the tip between about 140 mm and 150 mm, and at a distance approximately of 20 mm from the centerline; ii) the transition front spreads downstream forming a wedge, as indicated by the red dashed lines drawn along the edges of the early transition front; iii) thus, transition might be induced by disturbances coming from the early leading-edge region and developing downstream at a distance from the centerline of approximately one-third of the maximum half-body width ($L_z^*/2 = 60$ mm).

These considerations allow us to shape the computational domain to investigate the main transition mechanism. The black solid lines drawn in Figure 14-6 represent the edges of the computational domain. The domain is 40 mm wide in the z direction (namely $L_z = 32$ in nondimensional coordinates) and 250 mm long in the x direction. The grid size used to carry out our numerical simulations is 2120 x 300 x 400 (N_x x N_y x N_z), which was observed to provide a grid-independent solution. A sensitivity analysis of the laminar baseflow solution to the domain size in the spanwise direction and to the side boundary condition can be found in the work of Cerminara *et al.* [53]. Results obtained for two different domain widths, namely

30 mm and 40 mm, with grid sizes of 2120 x 300 x 300 and 2120 x 300 x 400 respectively, indicated that the internal solution is not sensitive to the domain width. A slight effect from the side boundary was observed to be confined within a narrow region adjacent to the side boundary. Streamlines within the boundary layer were also presented in [53], which indicated flow converging from the attachment line towards the centerline, due to the crossflow effect. The influence of the streamlines coming from outside the side boundary (which are not considered in our simulations) was found to be confined in a limited region adjacent to the side boundary, downstream of the transition point observed in the experiment. Thus, it was concluded that our computational domain, with the considered size, is able to capture the main receptivity mechanism in the leading-edge region, as well as the streamwise evolution of the induced disturbances up to the observed transition location.

14.7 LAMINAR BASE FLOW RESULTS

The leading edge is a critical zone, determining the general flowfield characteristics. This is due to the crossflow that forms inside the boundary layer, due to the imposed pressure gradients. The wedge junction is defined as the interface point between the circle and the wedge profile of the wall in a *xy* plane, indicated by an arrow in Figure 14-8. As the flow coming from the leading edge approaches this point, a small region of strong crossflow (represented by a thin dark blue zone) forms inside the boundary layer. We refer to this region around the junction point as the wedge-junction region. The near-wall flow entering the wedge with an inwards (i.e., towards the centerline) orientation generates inflectional crossflow boundary-layer profiles in the zone of the wedge junction, as can be observed in Figure 14-7, which shows crossflow profiles at several x positions. Figure 14-8, for the contours of the crossflow velocity (w) on the xy-plane at z = 30 mm, shows that the wedge-junction region is characterized by highest negative peak (represented by the blue region) of the crossflow.

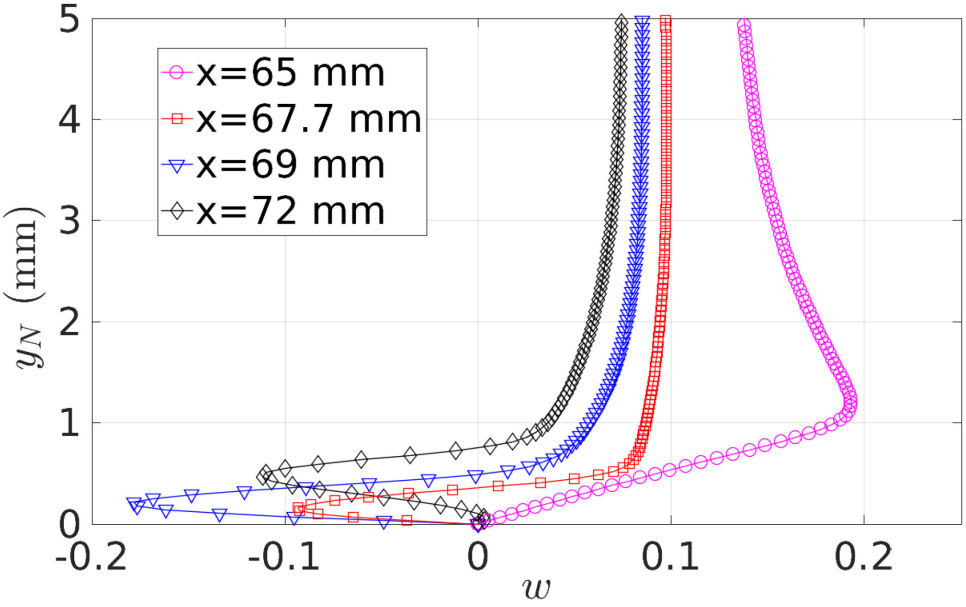

Figure 14-7: Crossflow Boundary-Layer Profiles at Different Streamwise Locations (z = 30 mm).

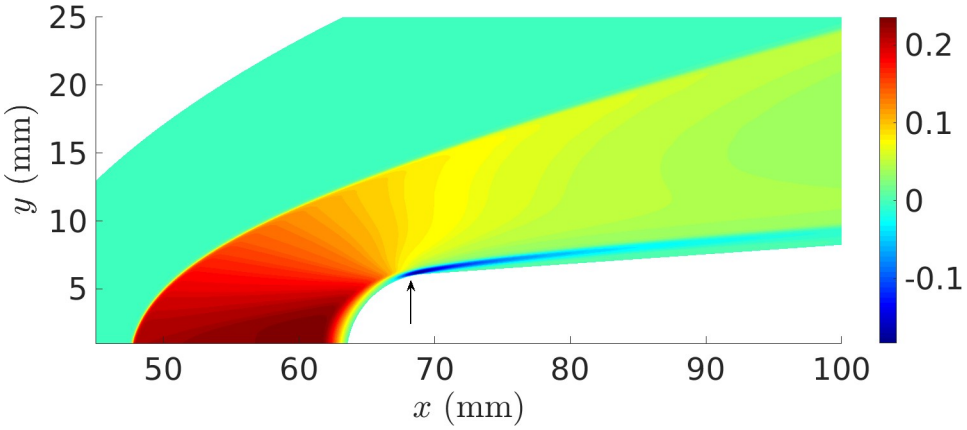

Figure 14-8: Crossflow (*w*) Contours in the *xy*-Plane at *z* = 30 mm.

The inflectional crossflow profiles have, as is known, an important impact on the boundary-layer stability. However, there is another important effect associated with the crossflow at the wedge junction, which has a direct impact on the local wall heat flux. Namely, the boundary layer becomes very thin at the wedge junction, due to the 3D effects related to the crossflow, hence, as a result, the outer cold fluid gets very close to the wall and produces a reverse of the wall heat flux, such that the fluid is heated by the wall in this region. This can be seen in Figure 14-9, showing the temperature boundary-layer profiles as a function of the wall-normal coordinate y_N at the same points of the crossflow profiles plotted in Figure 14-7. At $x = 65$ mm, which is ahead of the wedge junction, the maximum temperature is reached inside the boundary layer, but as soon as the wedge junction is reached and the negative crossflow develops, the boundary-layer thickness decreases dramatically and the temperature gradient at the wall becomes negative.

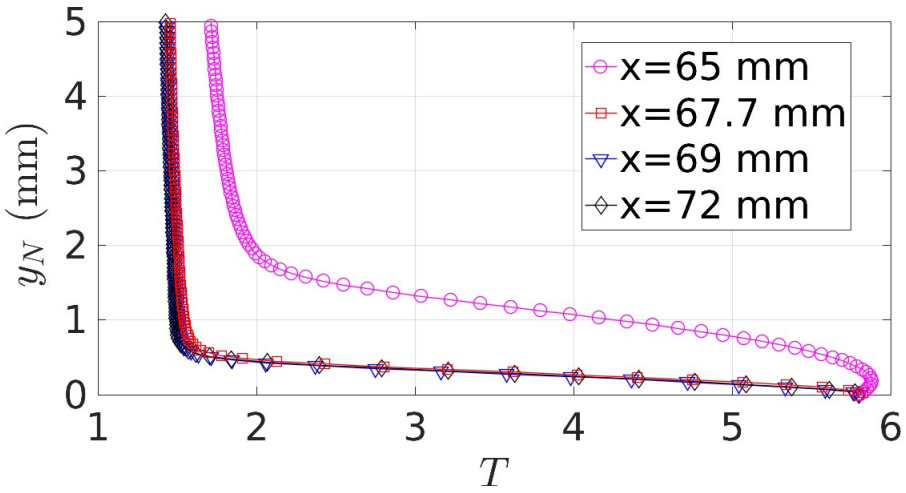

Figure 14-9: Temperature Boundary-Layer Profiles at Different Streamwise Locations (*z* = 30 mm).

In Figure 14-10, which shows a close-up of the wall heat flux at the leading edge, a narrow region of high negative (blue) heat-flux values, corresponding to the wedge-junction zone, is observed. The reversal of the

surface heat flux at the wedge junction can have important implications on the transition process and on the thermal-protection performance of a hypersonic vehicle. For example, in the presence of chemical surface reactions (e.g. oxidation), a high spatial gradient of the heat flux might produce localised gradients in the production/consumption rate of the reaction, resulting in gradients of the mass-loss rate and of the surface regression. Abrupt changes of the surface geometry might, in turn, induce transition through roughness.

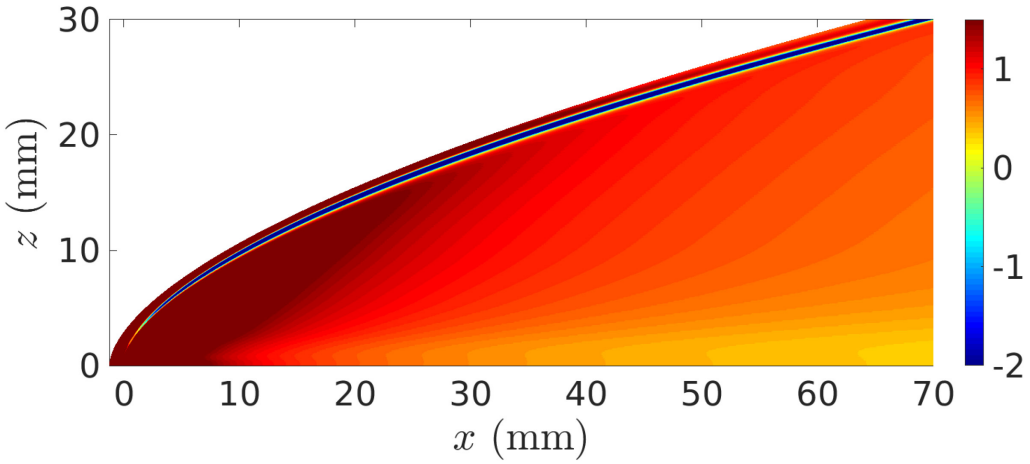

Figure 14-10: Wall Heat Flux (kW/m^2) in the Leading-Edge Region.

Figures 14-11 and 14-12 show temperature and crossflow velocity (w) cross sections (in the zy_N-plane) respectively, at the streamwise position x = 40 mm. The right edge of the plots corresponds to the spanwise position of the wedge junction. The figures highlight how the boundary layer gets rapidly thinner along the spanwise direction towards the wedge junction. The result in Figure 14-12 shows the high inwards crossflow velocity magnitudes reached at the wedge junction, compared to the other spanwise positions on the wedge. This indicates that a stream coming from the leading edge and flowing towards the centerline is released by the wedge junction into the flowfield over the wedge surface.

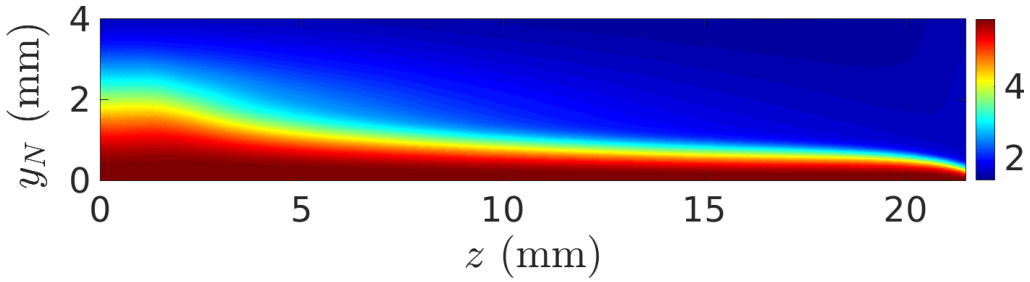

Figure 14-11: Temperature Contours in the zy_N-Plane at the Streamwise Position x = 40 mm.

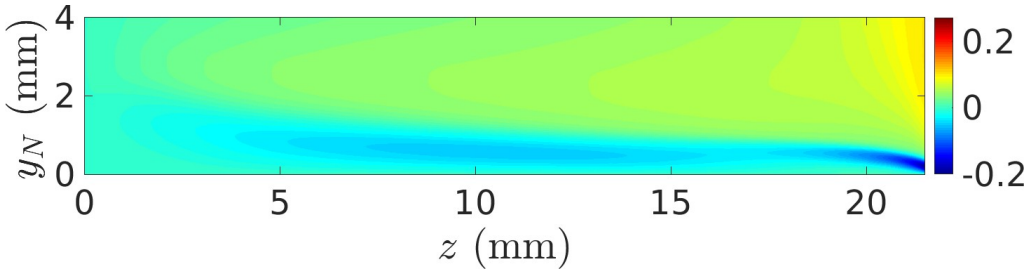

Figure 14-12: Crossflow Contours in the zy_N-Plane at the Streamwise Position x = 40 mm.

14.8 RESULTS FOR THE UNSTEADY SIMULATIONS

14.8.1 Transition Patterns with Fast and Slow Acoustic Waves

We now present numerical results for the unsteady simulations with three-dimensional freestream fast and slow acoustic waves (the wave model was described in Section 14.2.2), with the aim of understanding the transition mechanism associated with either type of waves. The numerical results will then be compared with the experimental results.

In order to reduce eventual effects associated to disturbance reflections from the side boundary into the internal flowfield, a z-dependent hyperbolic-tangent-based damping function, $h(z)$, was applied over the 3D wave model described in Section 14.2.2 which gradually damps out the amplitude of all the imposed freestream disturbance waves (both 2D and oblique) along the z-direction from a certain position (z_0) up to the side boundary. Hence, the modified 3D wave model can be expressed as,

$$\rho'(x,z,t) = \sum_{m=0}^{M_z} \sum_{n=1}^{N} A_m h(z) \cos\left(\beta_m z\right) \cos\left(\alpha_n x - \omega_n t + \psi_n\right), \tag{14-7}$$

$$h(z) = 1 - \frac{1}{2}\left(\tanh\left(\frac{S(z-z_0)}{L_z^* - z_0}\right) + 1\right), \tag{14-8}$$

in which S = 10, and z_0 = 26.5 mm. It should be noted that, while a random phase angle, ψ_n, is imposed in the streamwise direction, the phase angle in the spanwise direction is fixed to zero so that to guarantee the symmetry of the freestream disturbance field with respect to the $z = 0$ symmetry plane. For each single frequency, the freestream amplitude of the 2D wave (based on the density) is set to $A_0 = 2.5 \times 10^{-2}$, whereas each oblique wave is set with an amplitude of 1/4 that of the main 2D wave. The overall amplitude of the wave system (the sum between the 2D and the oblique waves) is $A_\infty = 5 \times 10^{-2}$. The level of 2.5 % for the 2D wave is of the same order as that measured by Masutti *et al.* [45] (4.9 %) for the density fluctuations in the Mach 6 blowdown facility at VKI, while the level relative to the overall wave system (5 %) reproduces this reference measured value very well. The 3D modes are set with an amplitude (0.625 %) similar to the levels reported by Parziale *et al.* [46], who measured density levels of 0.5 % for the Mach 5.5 flow in a T5 reflected-shock tunnel, Duan

et al. [47], who computed a value of 0.39 % for the pressure fluctuations radiated by a turbulent boundary layer in a Mach 2.5 flow, and Wagner *et al.* [48], who estimated a similar value of 0.48 % for the noise in a Mach 3 flow in the case of dominant slow acoustic waves, using a joint experimental-numerical approach. These disturbance levels were chosen in order to simulate noisy wind-tunnel conditions, thus allowing for nonlinear mechanisms to be triggered in the boundary layer. A set of 10 separate frequencies were introduced, ranging from $f_1 = 0.0105$ to $f_{10} = 0.105$, corresponding to the dimensional values of $f_1^* = 7.3$ kHz and $f_{10}^* = 73$ kHz. The considered frequency range captures the frequency band in which traveling crossflow waves were detected in several experimental and computational works [28, 31, 34], as described in Section I. Moreover, in the work of Wagner et al. [48] low frequencies (below 100 kHz) were found to have a significant effect on the response to slow acoustic waves, which was more amplified compared to the higher frequencies.

Figures 14-13 and 14-14 show the time-averaged surface heat flux (in kW/m^2) for fast and slow acoustic waves respectively. As can be seen, the surface heat-flux structure in the case of fast acoustic waves show the presence of wavefronts nearly perpendicular to the flow direction, which is consistent with the 2D fast mode being the dominant mode in the nose region, as shown in [16], due to the powerful resonance mechanism, and leading to a modulated response further downstream. The case of slow acoustic waves (Figure 14-14) shows a fundamentally different structure, that is characterised by the presence of elongated streamwise-oriented streaks generated in the early leading-edge region. In particular, three streaky structures can be distinguished (whose position and direction is indicated by arrows in Figure 14-14). One forms close to the centerline, near $z = 10$ mm, between $x = 50$ mm and $x = 100$ mm, and then decays rapidly downstream. Another, with higher spanwise size, is located near the side boundary at about $z = 35$ mm, forming just downstream of the leading edge and gradually decaying downstream. A third streak originates in the leading-edge zone at about $z = 20$ mm, which grows until it undergoes breakdown after $x = 200$ mm.

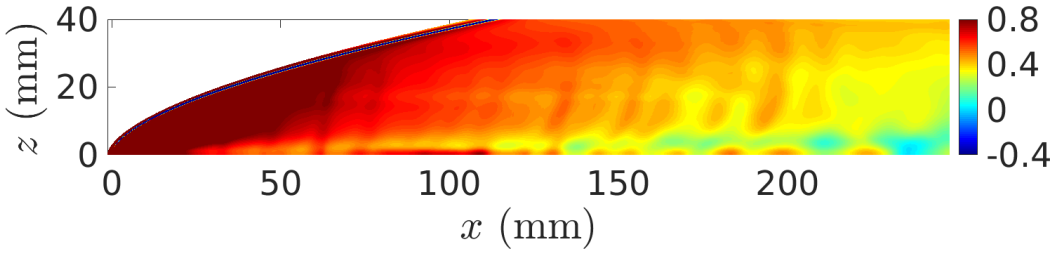

Figure 14-13: Time-Averaged Surface Heat Flux (kW/m^2) for Fast Acoustic Waves.

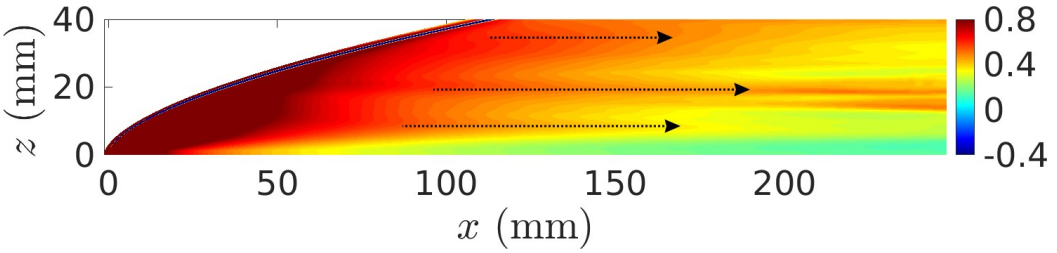

Figure 14-14: Time-Averaged Surface Heat Flux (kW/m^2) for Slow Acoustic Waves.

Another noticeable difference between the fast-wave and slow-wave results is observed for the solution in the near-centerline region, which suggests that in the slow-wave case the boundary layer along the symmetry plane is laminar through the whole domain length, whereas, in the fast-wave case, a highly perturbed boundary layer is obtained, with a nonlinear growth in the region x = 70 mm –150 mm. This is due to the amplification of the 2D fast mode in the upstream nose region in the fast-wave case. The centerline is indeed the region where the flow is most sensible to the 2D incident modes, as the baseflow here is quasi two-dimensional, due to the symmetry condition and the small local leading-edge sweep angles.

In Figure 14-15 a close-up of the heat flux for the slow-wave case in the downstream region is shown, providing more details of the nonlinear growth of the streamwise streak located at z = 20 mm. A secondary streak adjacent to the main one is formed at about x = 200 mm, which rapidly grows in amplitude and starts spreading downstream, deflecting its path towards the centerline.

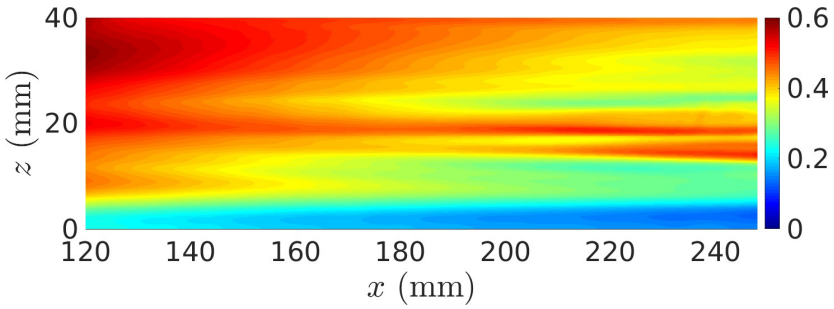

Figure 14-15: Close-up of the Heat Flux (kW/m^2) Solution for Slow Acoustic Waves in the Downstream Region.

The results for the surface heat flux indicate that the solution obtained with slow acoustic waves is closer to the experimental results observed in Figure 14-6, which showed an off-centerline transition core and a laminar boundary layer near the centerline. A direct comparison between numerical and experimental results for the slow-wave solution is shown in Figure 14-16, where the experimental figure has been adapted to match the scale of the numerical plot.

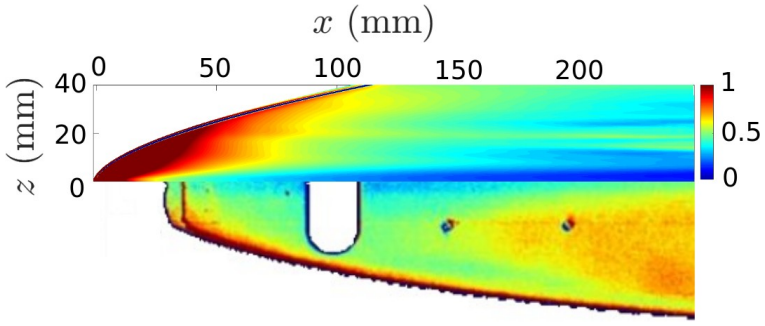

Figure 14-16: Comparison Between Numerical (Top) and Experimental (Bottom) Surface Heat Flux (kW/m^2).

The comparison shows similar heat-flux levels reached along the leading edge and in the upstream region of the wedge, which decrease towards the centerline, where the blue values indicate a laminar boundary layer. However, the high (red) heat-flux zone near the leading edge appears to cover a larger area in the numerical

result, which might be due to calibration effects of the experimental apparatus used to compute the heat flux, as well as to differences in amplitude between the applied 3D wave model and the real noise in the experiments. The main difference between the numerical prediction and the experimental results is observed downstream of x = 150 mm, where, in the experimental case, a wedge-shaped transition front is seen to develop and spread symmetrically downstream, affecting also the near-centerline region at longer distances. In contrast, in the numerical case, the heat flux near the symmetry plane keeps decreasing through all the domain length and no transition front is observed until the distance of about x = 230 mm is reached, where the streamwise streak located at z = 20 mm begins the nonlinear breakdown process.

Hence, the experimental results show a more rapid transition process, which may suggest the presence of a higher noise level in the wind tunnel, compared to the freestream disturbance amplitude used in the numerical simulations. In addition, the pressure transducer placed upstream of the position x = 150 mm, and at approximately z = 20 mm, as Figure 14-16 clearly shows, might have worked as a roughness element during the experimental tests, thus enhancing the transition process downstream. In order to see more details of the breakdown process taking place in the numerical solution, we show in Figure 14-17 the instantaneous contours of the streamwise wall-tangential velocity component (u_t) in the xy-plane along the j = 15 grid lines inside the boundary layer.

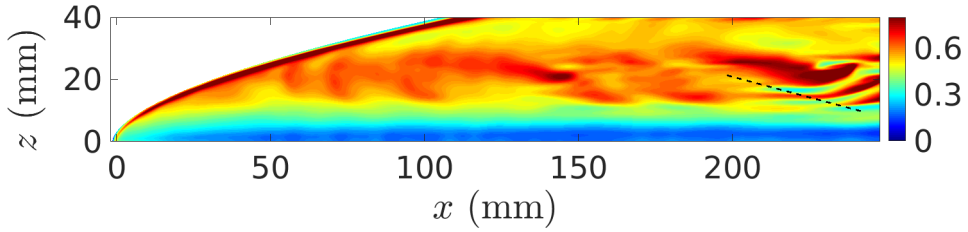

Figure 14-17: Wall-Tangential Velocity on the j = 15 Grid Lines Inside the Boundary Layer, for Slow Waves.

Here the main disturbances coming from the leading edge at about z = 20 mm, within the crossflow dominated region, are seen to undertake a nonlinear growth just upstream of x = 150 mm, which induces a transition process further downstream. This transition process, in turn, is observed to spread downstream forming a series of strong velocity spikes propagating towards the centerline with an inclination angle (indicated by the dashed line in the figure) close to the wedge-shaped transition front angle shown by the experimental results. Hence, the numerical solution inside the boundary layer shows transition patterns and location more similar to those observed in the experimental results at the wall. The numerical solution indicates that the transition process starts away from the wall, and that the perturbations related to the nonlinear breakdown process have not yet reached the wall.

14.8.2 Slow-Mode Receptivity and Streak Evolution

As shown in Section 14.8.1, the numerical solution with slow acoustic waves is closer to the experimental results in terms of transition patterns, so, in this Section, we focus on the results for the slow-wave case. The receptivity process is studied through contours of the Fourier transformed wall pressure fluctuations (real part) at different frequencies, f_3, f_4, f_6 and f_8, shown in Figure 14-18. Both lower and higher frequencies show high fluctuations near the leading edge, corresponding to waves travelling in the direction of the flow along the attachment line. Then, at about z = 20 mm, where sweep angles as high as $\Lambda = 70°$ are reached, the

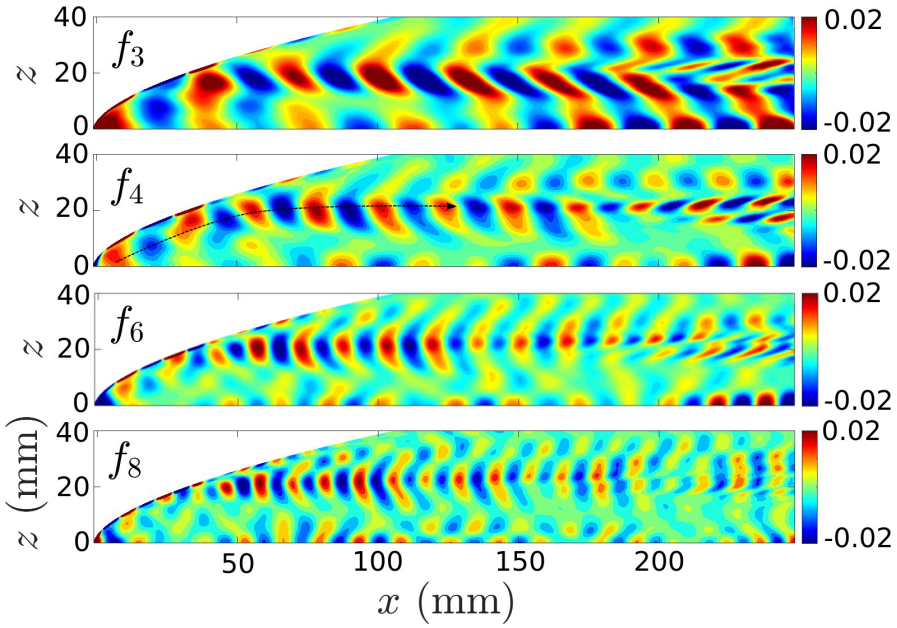

Figure 14-18: Real Part of Fourier-Transformed Wall-Pressure Fluctuations (p'_w) at Different Frequencies.

disturbances detach from the leading edge, and propagate downstream (this path is illustrated by the dashed black line in Figure 14-18 for the frequency f_4). The amplitude of the disturbances released from the leading edge onto the wedge surface reaches very high values near the wedge junction, namely between x = 40 mm and x = 100 mm, which is the zone characterised by high crossflow values (as seen in Figure 14.7). Then, dependent on the frequencies, the amplitude either decays downstream, or increases leading to the nonlinear growth of a streamwise streak downstream of x = 200 mm.

As shown in Figure 14-18, the lower frequencies are characterised by higher amplitude levels, and are responsible for the nonlinear growth and bifurcation of the streamwise streak downstream. Moreover, in the region downstream of x = 200 mm there is also a strong increase in amplitude of the disturbances along the symmetry plane, which is consistent, as seen in Section 14.8.1, with the spreading towards the centerline of the nonlinear breakdown process. Figures 14-19 and 14-20 show the downstream evolution and nonlinear growth of the streaks through cross-sections of the temperature and the streamwise vorticity at the positions x = 220 mm, x = 230 mm, x = 240 mm. The main streak is initially located at about z = 20 mm, as evident also in Figure 14-15. As it moves downstream, it increases rapidly in amplitude and spreads across the span, forming secondary vortices. At x = 230 mm two distinct co-rotating (negative vorticity) vortices appear with different amplitude. At the position x = 240 mm, both vortices show a higher amplitude, and appear shifted along the span. The main vortex is also shifted upwards, providing the pronounced deformation of the boundary-layer edge seen in Figure 14-19. The formation of a pair of counter-rotating secondary vortices is observed at about z = 13 mm, corresponding to the streak deflection towards the centerline shown in Figure 14-15. Another much weaker secondary vortex (with negative sign) is seen to start forming at the boundary layer edge alongside the main vortex, at about the position z = 27.5 mm. This fragmentation of the boundary-layer structure corresponds to a breakdown process, which actually started upstream ($x \approx$ 140 mm), as seen in Figure 14-17, where it involved only the upper region of the boundary layer.

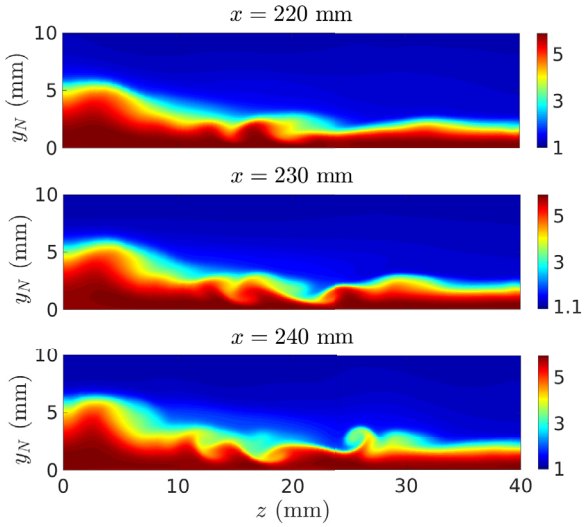

Figure 14-19: Temperature Cross-Sections on zy_N-Plane at Different x-Positions.

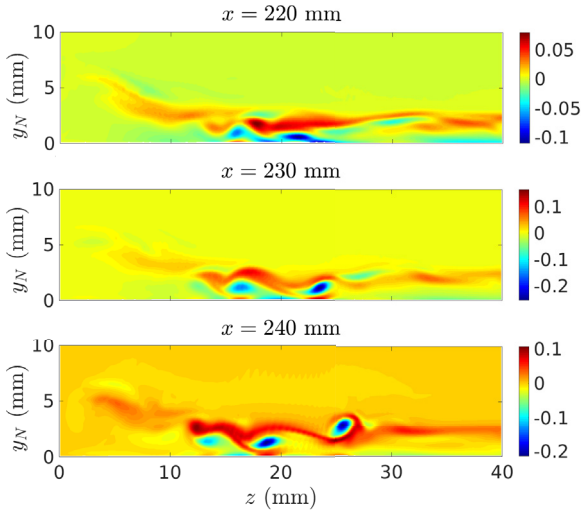

Figure 14-20: Streamwise Vorticity Cross-Sections on zy_N-Plane at Different x-Positions.

Finally, we present in Figure 14-21 the frequency spectra of the surface pressure fluctuations at the three PCB transducer locations considered in the experiment, namely x = 150 mm, x = 200 mm, x = 230 mm, with z = 18 mm for each position. These locations correspond respectively to the transducers PCB7, PCB8 and PCB1 used in the experiment [18]. It should be mentioned that PCB7 and PCB8 were actually placed at the spanwise position z = –18 mm in the experiment, but due to the symmetric flow assumption applied in the simulations, this position corresponds to z = 18 mm in the present numerical study. This spanwise position corresponds approximately to the position of the main streamwise streak.

As can be seen in Figure 14-21, the highest pressure levels are concentrated in the frequency band of the imposed freestream disturbances, i.e. 7.3 − 73 kHz. Within this frequency band three local peaks are evident

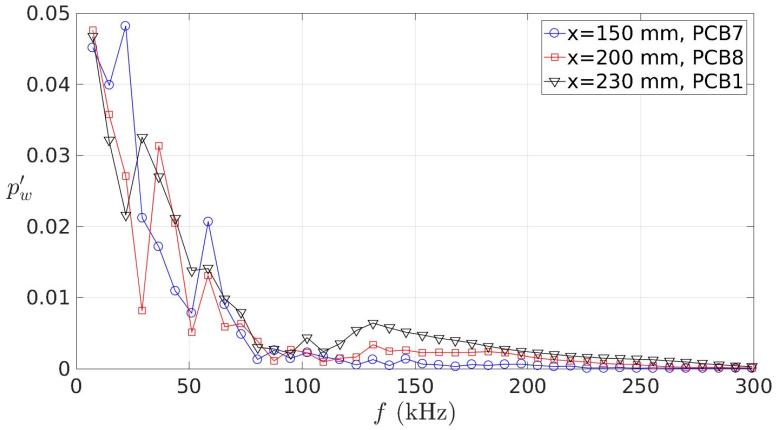

Figure 14-21: Frequency Spectra of the Wall-Pressure Fluctuation Amplitude at the PCB Transducer Locations.

at all the transducer locations: the first is at the lowest frequency, 7.3 kHz; the second one varies between the different positions, and is observed at 21.9 kHz at the foremost position (PCB7), 36.5 kHz at the second transducer (PCB8), and at 29.2 kHz at the most downstream position (PCB1); whereas the third (lower) peak is found at 58.4 kHz for all the positions. These frequencies are in a good agreement with the frequencies where traveling crossflow vortices were observed in different studies [28, 31, 34]. We also note the presence of a lower peak at a higher frequency, i.e. 131.4 kHz, which shows a pronounced growth downstream, reaching its maximum at the transducer located at 230 mm (PCB1). This is the location where the main streak is observed to split into two separate co-rotating vortices (with reference to Figure 14-20) that change their spanwise and vertical position and develop other secondary vortices. This higher frequency is outside the imposed frequency range, thus it has been generated by nonlinear effects, and could be evidence for the start of a secondary instability stage of the breakdown to turbulence.

14.9 CONCLUSION

Numerical simulations were run to study transition scenarios for 3D fast and slow freestream acoustic wave disturbances, for the MBDA 3D forebody model tested in the Purdue Mach 6 hypersonic wind tunnel. The base flow in the leading-edge zone is found to be characterised by a region of inflectional crossflow profiles, extending from the side up to a small distance from the symmetry plane. This was expected, consistent with the high values of the local leading-edge sweep angle. The 3D effects linked to the presence of the crossflow were found to lead to a reversal of the surface heat flux near the wedge junction, due to very small values of the boundary-layer thickness.

Unsteady numerical simulations with fast and slow acoustic waves were performed at a high freestream amplitude, in order to simulate the noisy wind tunnel conditions of the considered experimental case. Two important differences were observed between the transition patterns in the fast and the slow acoustic wave cases. First, in the fast-wave case the surface heat-flux structure shows signs of 2D oscillations which resemble a modulation process of the fast mode induced in the boundary layer and the fast acoustic waves, as seen in previous studies. In the slow-wave case, instead, the heat-flux structure is characterised by the formation and downstream growth

of streamwise streaks associated with traveling crossflow instabilities originating near the leading edge. The results with slow acoustic waves provide a better correlation with the experiments, which suggests that the wind tunnel noise was characterised mostly by slow acoustic disturbances during the experimental tests. Transition is induced by the nonlinear growth of streamwise streaks in the off-centerline region. The receptivity study shows that disturbances coming from the nose tip are released through the wedge junction onto the wedge surface 20 mm off the centerline, and then propagate downstream forming streaks. Frequency spectra of the wall pressure disturbances at different streamwise positions along the main streak show peaks for frequencies between 7.3 kHz and 58.4 kHz, consistent with the frequency range of traveling crossflow waves. Higher-frequency disturbances are seen to form downstream, where the main streak undergoes nonlinear growth, indicating that secondary instabilities of the primary crossflow waves may be developing and leading to the breakdown, with generation of secondary vortices spreading towards the centerline. The initial stage of the nonlinear growth is actually observed upstream ($x \approx 140$ mm) within the boundary layer. However, in contrast with the experiments, the numerical results show that at this streamwise location the nonlinear breakdown process is confined within the upper part of the boundary layer, thus not yet involving the flow near the wall and the surface heat flux.

The disagreement between the numerical and experimental results in terms of the exact location of the transition point is most probably related to differences between the real freestream noise in the wind tunnel and the disturbances used in the numerical simulations, in terms of both amplitude and frequency content, which would indicate, for example, that even higher noise levels were reached in the wind tunnel runs. This motivates future DNS studies aimed at improving the calibration of the numerical freestream disturbance model to reliably replicate the real experimental noise.

14.10 ACKNOWLEDGEMENTS

This work has been carried out in the scope of the NATO STO AVT-240 Hypersonic Boundary-Layer Transition Prediction task group. Computer time on the UK National Supercomputing Service (ARCHER) was provided by the UK Turbulence Consortium (UKTC) under EPSRC (Engineering and Physical Sciences Research Council) Grant No. EP/L000261/1. Finally, support is gratefully acknowledged from EPSRC under the Grant No. EP/J016381/2 ‘Thermal and Reactive Flow Simulation on High-End Computers’ for additional computer time.

The content of this chapter is taken from the manuscript: Cerminara, A., Durant, A., André, T., Sandham, N.D., and Taylor, N.J., “Receptivity to Freestream Acoustic Noise in Hypersonic Flow over a Generic Forebody”, *Journal of Spacecraft and Rockets*, 56(2), 2018, pp. 447-457.

14.11 REFERENCES

[1] Andersson, P., Brandt, L., Bottaro, A., and Henningson, D. S., “On the Breakdown of Boundary Layer Streaks”, *Journal of Fluid Mechanics*, 428, February 2001, pp. 29-60. doi:10.1017/S0022112000002421

[2] Brandt, L., and Henningson, D. S., “Transition of Streamwise Streaks in Zero-Pressure-Gradient Boundary Layers”, *Journal of Fluid Mechanics*, 472, December 2002, pp. 229-261. doi:10.1017/S0022112002002331

[3] Saric, W., Reed, H., and Kerschen, E., "Boundary-Layer Receptivity to Freestream Disturbances", *Annual Review of Fluid Mechanics*, 34(1), 2002, pp. 291-319. doi:10.1146/annurev.fluid.34.082701.161921

[4] Fedorov, A. V., and Khokhlov, A. P., "Prehistory of Instability in a Hypersonic Boundary Layer", *Theoretical and Computational Fluid Dynamics*, 14(6), 2001, pp. 359-375. doi:10.1007/s001620100038

[5] Fedorov, A. V., "Transition and Stability of High-Speed Boundary Layers", *Annual Review of Fluid Mechanics*, 43(1), 2011, pp. 79-95. doi:10.1146/annurev-fluid-122109-160750

[6] Zhong, X., and Ma, Y., "Boundary-Layer Receptivity of Mach 7.99 Flow over a Blunt Cone to Free-Stream Acoustic Waves", *Journal of Fluid Mechanics*, 556, June 2006, pp. 55-103. doi:10.1017/S0022112006009293

[7] Zhong, X., and Wang, X., "Direct Numerical Simulation on the Receptivity, Instability, and Transition of Hypersonic Boundary Layers", *Annual Review of Fluid Mechanics*, 44(1), 2012, pp. 527-561. doi:10.1146/annurev-fluid-120710-101208

[8] Mack, L. M., "Boundary-layer Linear Stability Theory", *Special Course on Stability and Transition of Lam- inar Flow*, California Inst. of Technology, JPL, AGARD Rept. 709, Pasadena, CA, 1984, pp. 3.1-81.

[9] Stetson, K. F., Thompson, E. R., Donaldson, J. C., and Siler, L. G., "Laminar Boundary Layer Stability Experiments on a Cone at Mach 8. II-Blunt Cone", *22nd Aerospace Sciences Meeting*, AIAA Paper 1984-0006, 1984.

[10] Fedorov, A. V., Malmuth, N. D., Rasheed, A., and Hornung, H. G., "Stabilization of Hypersonic Boundary Layers by Porous Coatings", *AIAA Journal*, 39(4), 2001, pp. 605-610. doi:10.2514/2.1382

[11] Ma, Y., and Zhong, X., "Receptivity of a Supersonic Boundary Layer over a Flat Plate, Part 3: Effects of Different Types of Free-Stream Disturbances", *Journal of Fluid Mechanics*, 532, June 2005, pp. 63-109. doi:10.1017/S0022112005003836

[12] Balakumar, P., "Receptivity of a Supersonic Boundary Layer to Acoustic Disturbances", *AIAA Journal*, 47(5), 2009, pp. 1069-1078. doi:10.2514/1.33395

[13] Malik, M. R., and Balakumar, P., "Acoustic Receptivity of Mach 4.5 Boundary Layer with Leading-Edge Bluntness", *Theoretical and Computational Fluid Dynamics*, 21(5), 2007, pp. 323-342. doi:10.1007/s00162-007-0050-5

[14] Kara, K., Balakumar, P., and Kandil, O. A., "Receptivity of Hypersonic Boundary Layers Due to Acoustic Disturbances over Blunt Cone", *45th AIAA Aerospace Sciences Meeting and Exhibit*, AIAA Paper 2007-945, January 2007.

[15] Egorov, I. V., Sudakov, V. G., and Fedorov, A. V., "Numerical Modeling of the Receptivity of a Supersonic Boundary Layer to Acoustic Disturbances", *Fluid Dynamics*, 41(1), 2006, pp. 37-48. doi:10.1007/s10697-006-0020-4

[16] Cerminara, A., and Sandham, N., "Boundary-Layer Receptivity and Breakdown in Hypersonic Flow over a Swept Blunt Wedge with Three-Dimensional Freestream Acoustic Disturbances", *8th AIAA Flow Control Conference, AIAA AVIATION Forum*, AIAA Paper 2016-4247, 2016.

[17] Cerminara, A., and Sandham, N. D., "Acoustic Leading-Edge Receptivity for Supersonic/Hypersonic Flows over a Blunt Wedge", *AIAA Journal*, 2017, pp. 4234-4244. doi:10.2514/1.J055749

[18] Durant, A., André, T., Edelman, J. B., Chynoweth, B. C., and Schneider, S. P., "Mach 6 Quiet Tunnel Laminar to Turbulent Investigation of a Generic Hypersonic Forebody", *20th AIAA International Space Planes and Hypersonic Systems and Technologies Conference*, AIAA Paper 2015-3575, 2015.

[19] Orlik, E., Fedioun, I., and Lardjane, N., "Hypersonic Boundary-Layer Transition Forced by Wall Injection: A Numerical Study", *Journal of Spacecraft and Rockets*, 51(4), 2014, pp. 1306-1318. doi:10.2514/1.A32645

[20] André, T., Orlik, E., Durant, A., and Fedioun, I., "Global Mode Analysis in the L/T Transition of a Hypersonic Boundary Layer Forced by Wall Injection", *Procedia IUTAM*, 14, 2015, pp. 58-67. doi:10.1016/j.piutam.2015.03.024

[21] André, T., Durant, A., and Fedioun, I., "Numerical Study of Supersonic Boundary-Layer Transition due to Sonic Wall Injection", *AIAA Journal*, 55(5), 2017, pp. 1530-1547. doi:10.2514/1.J055164

[22] Saric, William S., Helen L. Reed, and Edward B. White., "Stability and Transition of Three-Dimensional Boundary Layers", *Annual Review of Fluid Mechanics*, 35(1), 2003, pp. 413-440. doi:10.1146/annurev.fluid.35.101101.161045

[23] Reed, H. L., and Saric, W. S., "Stability of Three-Dimensional Boundary Layers", *Annual Review of Fluid Mechanics*, 21(1), 1989, pp. 235-284.

[24] Bippes, H., "Basic Experiments on Transition in Three-Dimensional Boundary Layers Dominated by Crossflow Instability", *Progress in Aerospace Sciences*, 35(4), 1999, pp. 363-412. doi:10.1016/S0376-0421(99)00002-0

[25] Kohama, Y., "Some Expectation on the Mechanism of Cross-Flow Instability in a Swept Wing Flow", *Acta Mechanica*, 66.1-4, 1987, pp. 21-38. doi:10.1007/BF01184283

[26] White, Edward B., and William S. Saric., "Secondary Instability of Crossflow Vortices", *Journal of Fluid Mechanics*, 525, February 2005, pp. 275-308. doi:10.1017/S002211200400268X

[27] Borg, M. P., Kimmel, R. L., and Stanfield, S., "Traveling Crossflow Instability for the HIFiRE-5 Elliptic Cone", *Journal of Spacecraft and Rockets*, 52(3), 2015, pp. 664-673. doi:10.2514/1.A33145

[28] Craig, S. A., and Saric, W. S., "Crossflow Instability in a Hypersonic Boundary Layer", *Journal of Fluid Mechanics*, 808, October 2016, pp. 224-244. doi:10.1017/jfm.2016.643

[29] Kuehl, J., Perez, E., and Reed, H., "JoKHeR: NPSE Simulations of Hypersonic Crossflow Instability", AIAA 2012-0921, *50th AIAA Aerospace Sciences Meeting Including the New Horizons Forum and Aerospace Exposition*, 2012, Nashville, TN.
doi:10.2514/6.2012-921

[30] Oliviero, N. B., Kocian, T. S., Moyes, A., and Reed, H. L., "EPIC: NPSE Analysis of Hypersonic Crossflow Instability on Yawed Straight Circular Cone", AIAA 2015-2772, *45th AIAA Fluid Dynamics Conference*, 2015, Dallas, TX.
doi:10.2514/6.2015-2772

[31] Ward, C., Henderson, R., and Schneider, S. P., "Secondary Instability of Stationary Crossflow Vortices on an Inclined Cone at Mach 6", AIAA 2015-2773, *45th AIAA Fluid Dynamics Conference*, 2015, Dallas, TX. doi:10.2514/6.2015-2773

[32] Choudhari, M. M., Li, F., Chang, C. L., Carpenter, M., Streett, C., Malik, M. R., and Duan, L., "Towards Bridging the Gaps in Holistic Transition Prediction via Numerical Simulations", AIAA 2013-2718, *21st AIAA Computational Fluid Dynamics Conference*, 2013, San Diego, CA.
doi:10.2514/6.2013-2718

[33] Li, F., Choudhari, M. M., Duan, L., and Chang, C. L., "Nonlinear Development and Secondary Instability of Traveling Crossflow Vortices", *Physics of Fluids*, 26(6), 2014, pp. 064104-1-19.
doi:10.1063/1.4883256

[34] Li, F., Choudhari, M., Paredes, P., and Duan, L., "High-Frequency Instabilities of Stationary Crossflow Vortices in a Hypersonic Boundary Layer", *Physical Review Fluids*, 1(5), 2016, pp. 053603-1-32.
doi:10.1103/PhysRevFluids.1.053603

[35] Balakumar, P., and Owens, L., "Stability of Hypersonic Boundary Layers on a Cone at an Angle of Attack", AIAA 2010-4718, *40th Fluid Dynamics Conference and Exhibit*, 2010, Chicago, IL.
doi:10.2514/6.2010-4718

[36] Balakumar, P., and King, R. A., "Receptivity and Stability of Supersonic Swept Flows", *AIAA Journal*, 50(7), 2012, pp. 1476-1489.
doi:10.2514/1.J051064

[37] Bartkowicz, M. D., Subbareddy, P. K., and Candler, G. V., "Simulation of Boundary Layer Transition on Elliptic Cones in Hypersonic Flow", AIAA 2010-1064, *48th AIAA Aerospace Sciences Meeting Including the New Horizons Forum and Aerospace Exposition*, 2010, Orlando, FL.
doi:10.2514/6.2010-1064

[38] Dinzl, D. J., and Candler, G. V., "Direct Simulation of Hypersonic Crossflow Instability on an Elliptic Cone", *AIAA Journal*, 55(6), 2017, pp. 1769-1782.
doi:10.2514/1.J055130

[39] Paredes, P., and Theofilis, V., "Centerline Instabilities on the Hypersonic International Flight Research Experimentation HIFiRE-5 Elliptic Cone Model", *Journal of Fluids and Structures*, 53, February 2015, pp. 36-49.
doi:10.1016/j.jfluidstructs.2014.11.002

[40] Paredes, P., Grosse R., Theofilis, V., Kimmel, R., "Linear Modal Instabilities of Hypersonic Flow over an Elliptic Cone", *Journal of Fluid Mechanics*, 804, October 2016, pp. 442-466. doi:10.1017/jfm.2016.536

[41] Juliano, T. J., Borg, M. P., and Schneider, S. P., "Quiet Tunnel Measurements of HIFiRE-5 Boundary-Layer Transition", *AIAA Journal*, 53(4), 2015, pp. 832-846. doi:10.2514/1.J053189

[42] Schneider, S. P., "Effects of High-Speed Tunnel Noise on Laminar-Turbulent Transition", *Journal of Spacecraft and Rockets*, 38(3), 2001, pp. 323-333. doi:10.2514/2.3705

[43] Schneider, S. P., "Development of Hypersonic Quiet Tunnels", *Journal of Spacecraft and Rockets*, 45(4), 2008, pp. 641-664. doi:10.2514/1.34489

[44] Schneider, S. P., "Developing Mechanism-Based Methods for Estimating Hypersonic Boundary-Layer Transition in Flight: The Role of Quiet Tunnels", *Progress in Aerospace Sciences*, 72, January 2015, pp. 17-29. doi:10.1016/j.paerosci.2014.09.008

[45] Masutti, D., Spinosa, E., Chazot, O., and Carbonaro, M., "Disturbance Level Characterization of a Hypersonic Blowdown Facility", *AIAA Journal*, 50(12), 2012, pp. 2720-2730. doi:10.2514/1.J051502

[46] Parziale, N. J., Shepherd, J. E., and Hornung, H. G., "Free-Stream Density Perturbations in a Reflected-Shock Tunnel", *Experiments in Fluids*, 55(2), 2014, pp. 1665-1-10.

[47] Duan, L., Choudhari, M. M., and Wu, M., "Numerical Study of Acoustic Radiation due to a Supersonic Turbulent Boundary Layer", *Journal of Fluid Mechanics*, 746, May 2014, pp. 165-192. doi:10.1017/jfm.2014.116

[48] Wagner, A., Schülein, E., Petervari, R., Hannemann, K., Ali, S. R., Cerminara, A., and Sandham, N. D., "Combined Free-Stream Disturbance Measurements and Receptivity Studies in Hypersonic Wind Tunnels by means of a Slender Wedge Probe and Direct Numerical Simulation", *Journal of Fluid Mechanics*, 842, 2018, pp. 495-531. doi:10.1017/jfm.2018.132

[49] Cerminara, A., "Boundary-Layer Receptivity and Breakdown Mechanisms for Hypersonic Flow over Blunt Leading-Edge Configurations", *Doctoral Thesis*, University of Southampton Repository, 2017.

[50] Yee, H. C., Sandham, N. D., and Djomehri, M. J., "Low-Dissipative High-Order Shock-Capturing Methods Using Characteristic-Based Filters", *Journal of Computational Physics*, 150(1), 1999, pp. 199-238. doi:10.1006/jcph.1998.6177

[51] Sandham, N. D., Li, Q., and Yee, H. C., "Entropy Splitting for High-Order Numerical Simulation of Compressible Turbulence", *Journal of Computational Physics*, 178(2), 2002, pp. 307-322. doi:10.1006/jcph.2002.7022

[52] De Tullio, N., Paredes, P., Sandham, N. D., and Theofilis, V., "Laminar-Turbulent Transition Induced by a Discrete Roughness Element in a Supersonic Boundary Layer", *Journal of Fluid Mechanics*, 735, November 2013, pp. 613-646.
doi:10.1017/jfm.2013.520

[53] Cerminara, A., Durant, A., André, T., Sandham, N., and Taylor, N.J., "DNS of Acoustic Receptivity and Breakdown in a Mach 6 Flow over a Generic Forebody", AIAA 2018-0348, *AIAA Aerospace Sciences Meeting*, 2018, Kissimmee, FL.
doi:10.2514/6.2018-0348

REPORT DOCUMENTATION PAGE

1. Recipient's Reference	2. Originator's References	3. Further Reference	4. Security Classification of Document
	STO-TR-AVT-240 AC/323(AVT-240)TP/902	ISBN 978-92-837-2227-4	PUBLIC RELEASE

5. Originator

Science and Technology Organization
North Atlantic Treaty Organization
BP 25, F-92201 Neuilly-sur-Seine Cedex, France

6. Title

Hypersonic Boundary-Layer Transition Prediction

7. Presented at/Sponsored by

Summary Report of the NATO STO AVT-240 Task Group.

8. Author(s)/Editor(s)	9. Date
Multiple	August 2020
10. Author's/Editor's Address	**11. Pages**
Multiple	400

12. Distribution Statement

There are no restrictions on the distribution of this document. Information about the availability of this and other STO unclassified publications is given on the back cover.

13. Keywords/Descriptors

Boundary layers; Computational fluid dynamics; Ground testing; Hypersonic laminar-turbulent transition

14. Abstract

Hypersonic boundary-layer transition can have dramatic effects on aeroheating and control authority, yet it remains very difficult to predict. Applications include missiles for time-critical strike, hypersonic cruise vehicles, reusable launch and re-entry vehicles, and missile-defence interceptors. Although researchers have been working toward mechanism-based prediction methods for several decades, designers are still using empirical methods, and there is a need to narrow the gap between the two groups. Transition is complex, as it can be caused by several different instability mechanisms, is affected by various freestream and surface perturbations, and can occur under a variety of flow conditions. Accordingly, the activities of the group were divided into multiple Subtasks. For each Subtask, several experts from various NATO nations embarked in cooperative research, each with their own financial support. These subtasks covered: (1) Second-mode transition on slender geometries in quiet and conventional ground based facilities, (2) Cross-flow transition on conical geometries at wind tunnel flow conditions, (3) Mechanism of windside forward transition on sharp and blunted cones at angle of attack, and (4) Mechanism of boundary layer transition on nonablating capsules and its sensitivities.

NORTH ATLANTIC TREATY ORGANIZATION

BP 25
F-92201 NEUILLY-SUR-SEINE CEDEX • FRANCE
Télécopie 0(1)55.61.22.99 • E-mail mailbox@cso.nato.int

SCIENCE AND TECHNOLOGY ORGANIZATION

DIFFUSION DES PUBLICATIONS
STO NON CLASSIFIEES

Les publications de l'AGARD, de la RTO et de la STO peuvent parfois être obtenues auprès des centres nationaux de distribution indiqués ci-dessous. Si vous souhaitez recevoir toutes les publications de la STO, ou simplement celles qui concernent certains Panels, vous pouvez demander d'être inclus soit à titre personnel, soit au nom de votre organisation, sur la liste d'envoi.

Les publications de la STO, de la RTO et de l'AGARD sont également en vente auprès des agences de vente indiquées ci-dessous.

Les demandes de documents STO, RTO ou AGARD doivent comporter la dénomination « STO », « RTO » ou « AGARD » selon le cas, suivi du numéro de série. Des informations analogues, telles que le titre est la date de publication sont souhaitables.

Si vous souhaitez recevoir une notification électronique de la disponibilité des rapports de la STO au fur et à mesure de leur publication, vous pouvez consulter notre site Web (http://www.sto.nato.int/) et vous abonner à ce service.

CENTRES DE DIFFUSION NATIONAUX

ALLEMAGNE
Streitkräfteamt / Abteilung III
Fachinformationszentrum der Bundeswehr (FIZBw)
Gorch-Fock-Straße 7, D-53229 Bonn

BELGIQUE
Royal High Institute for Defence – KHID/IRSD/RHID
Management of Scientific & Technological Research
for Defence, National STO Coordinator
Royal Military Academy – Campus Renaissance
Renaissancelaan 30, 1000 Bruxelles

BULGARIE
Ministry of Defence
Defence Institute "Prof. Tsvetan Lazarov"
"Tsvetan Lazarov" bul no.2
1592 Sofia

CANADA
DGSIST 2
Recherche et développement pour la défense Canada
60 Moodie Drive (7N-1-F20)
Ottawa, Ontario K1A 0K2

DANEMARK
Danish Acquisition and Logistics Organization
(DALO)
Lautrupbjerg 1-5
2750 Ballerup

ESPAGNE
Área de Cooperación Internacional en I+D
SDGPLATIN (DGAM)
C/ Arturo Soria 289
28033 Madrid

ESTONIE
Estonian National Defence College
Centre for Applied Research
Riia str 12
Tartu 51013

ETATS-UNIS
Defense Technical Information Center
8725 John J. Kingman Road
Fort Belvoir, VA 22060-6218

FRANCE
O.N.E.R.A. (ISP)
29, Avenue de la Division Leclerc
BP 72
92322 Châtillon Cedex

GRECE (Correspondant)
Defence Industry & Research General
Directorate, Research Directorate
Fakinos Base Camp, S.T.G. 1020
Holargos, Athens

HONGRIE
Hungarian Ministry of Defence
Development and Logistics Agency
P.O.B. 25
H-1885 Budapest

ITALIE
Ten Col Renato NARO
Capo servizio Gestione della Conoscenza
F. Baracca Military Airport "Comparto A"
Via di Centocelle, 301
00175, Rome

LUXEMBOURG
Voir Belgique

NORVEGE
Norwegian Defence Research
Establishment
Attn: Biblioteket
P.O. Box 25
NO-2007 Kjeller

PAYS-BAS
Royal Netherlands Military
Academy Library
P.O. Box 90.002
4800 PA Breda

POLOGNE
Centralna Biblioteka Wojskowa
ul. Ostrobramska 109
04-041 Warszawa

PORTUGAL
Estado Maior da Força Aérea
SDFA – Centro de Documentação
Alfragide
P-2720 Amadora

REPUBLIQUE TCHEQUE
Vojenský technický ústav s.p.
CZ Distribution Information Centre
Mladoboleslavská 944
PO Box 18
197 06 Praha 9

ROUMANIE
Romanian National Distribution
Centre
Armaments Department
9-11, Drumul Taberei Street
Sector 6
061353 Bucharest

ROYAUME-UNI
Dstl Records Centre
Rm G02, ISAT F, Building 5
Dstl Porton Down
Salisbury SP4 0JQ

SLOVAQUIE
Akadémia ozbrojených síl gen.
M.R. Štefánika, Distribučné a
informačné stredisko STO
Demänová 393
031 01 Liptovský Mikuláš 1

SLOVENIE
Ministry of Defence
Central Registry for EU & NATO
Vojkova 55
1000 Ljubljana

TURQUIE
Milli Savunma Bakanlığı (MSB)
ARGE ve Teknoloji Dairesi
Başkanlığı
06650 Bakanliklar – Ankara

AGENCES DE VENTE

The British Library Document Supply Centre
Boston Spa, Wetherby
West Yorkshire LS23 7BQ
ROYAUME-UNI

Canada Institute for Scientific and Technical Information (CISTI)
National Research Council Acquisitions
Montreal Road, Building M-55
Ottawa, Ontario K1A 0S2
CANADA

Les demandes de documents STO, RTO ou AGARD doivent comporter la dénomination « STO », « RTO » ou « AGARD » selon le cas, suivie du numéro de série (par exemple AGARD-AG-315). Des informations analogues, telles que le titre et la date de publication sont souhaitables. Des références bibliographiques complètes ainsi que des résumés des publications STO, RTO et AGARD figurent dans le « NTIS Publications Database » (http://www.ntis.gov).

NORTH ATLANTIC TREATY ORGANIZATION

BP 25
F-92201 NEUILLY-SUR-SEINE CEDEX • FRANCE
Télécopie 0(1)55.61.22.99 • E-mail mailbox@cso.nato.int

SCIENCE AND TECHNOLOGY ORGANIZATION

DISTRIBUTION OF UNCLASSIFIED STO PUBLICATIONS

AGARD, RTO & STO publications are sometimes available from the National Distribution Centres listed below. If you wish to receive all STO reports, or just those relating to one or more specific STO Panels, they may be willing to include you (or your Organisation) in their distribution.

STO, RTO and AGARD reports may also be purchased from the Sales Agencies listed below.

Requests for STO, RTO or AGARD documents should include the word 'STO', 'RTO' or 'AGARD', as appropriate, followed by the serial number. Collateral information such as title and publication date is desirable.

If you wish to receive electronic notification of STO reports as they are published, please visit our website (http://www.sto.nato.int/) from where you can register for this service.

NATIONAL DISTRIBUTION CENTRES

BELGIUM
Royal High Institute for Defence – KHID/IRSD/RHID
Management of Scientific & Technological Research for Defence, National STO Coordinator
Royal Military Academy – Campus Renaissance
Renaissancelaan 30
1000 Brussels

BULGARIA
Ministry of Defence
Defence Institute "Prof. Tsvetan Lazarov"
"Tsvetan Lazarov" bul no.2
1592 Sofia

CANADA
DSTKIM 2
Defence Research and Development Canada
60 Moodie Drive (7N-1-F20)
Ottawa, Ontario K1A 0K2

CZECH REPUBLIC
Vojenský technický ústav s.p.
CZ Distribution Information Centre
Mladoboleslavská 944
PO Box 18
197 06 Praha 9

DENMARK
Danish Acquisition and Logistics Organization (DALO)
Lautrupbjerg 1-5
2750 Ballerup

ESTONIA
Estonian National Defence College
Centre for Applied Research
Riia str 12
Tartu 51013

FRANCE
O.N.E.R.A. (ISP)
29, Avenue de la Division Leclerc – BP 72
92322 Châtillon Cedex

GERMANY
Streitkräfteamt / Abteilung III
Fachinformationszentrum der Bundeswehr (FIZBw)
Gorch-Fock-Straße 7
D-53229 Bonn

GREECE (Point of Contact)
Defence Industry & Research General Directorate, Research Directorate
Fakinos Base Camp, S.T.G. 1020
Holargos, Athens

HUNGARY
Hungarian Ministry of Defence
Development and Logistics Agency
P.O.B. 25
H-1885 Budapest

ITALY
Ten Col Renato NARO
Capo servizio Gestione della Conoscenza
F. Baracca Military Airport "Comparto A"
Via di Centocelle, 301
00175, Rome

LUXEMBOURG
See Belgium

NETHERLANDS
Royal Netherlands Military Academy Library
P.O. Box 90.002
4800 PA Breda

NORWAY
Norwegian Defence Research Establishment, Attn: Biblioteket
P.O. Box 25
NO-2007 Kjeller

POLAND
Centralna Biblioteka Wojskowa
ul. Ostrobramska 109
04-041 Warszawa

PORTUGAL
Estado Maior da Força Aérea
SDFA – Centro de Documentação
Alfragide
P-2720 Amadora

ROMANIA
Romanian National Distribution Centre
Armaments Department
9-11, Drumul Taberei Street
Sector 6
061353 Bucharest

SLOVAKIA
Akadémia ozbrojených síl gen M.R. Štefánika, Distribučné a informačné stredisko STO
Demänová 393
031 01 Liptovský Mikuláš 1

SLOVENIA
Ministry of Defence
Central Registry for EU & NATO
Vojkova 55
1000 Ljubljana

SPAIN
Área de Cooperación Internacional en I+D
SDGPLATIN (DGAM)
C/ Arturo Soria 289
28033 Madrid

TURKEY
Milli Savunma Bakanlığı (MSB)
ARGE ve Teknoloji Dairesi Başkanlığı
06650 Bakanliklar – Ankara

UNITED KINGDOM
Dstl Records Centre
Rm G02, ISAT F, Building 5
Dstl Porton Down, Salisbury SP4 0JQ

UNITED STATES
Defense Technical Information Center
8725 John J. Kingman Road
Fort Belvoir, VA 22060-6218

SALES AGENCIES

The British Library Document Supply Centre
Boston Spa, Wetherby
West Yorkshire LS23 7BQ
UNITED KINGDOM

Canada Institute for Scientific and Technical Information (CISTI)
National Research Council Acquisitions
Montreal Road, Building M-55
Ottawa, Ontario K1A 0S2
CANADA

Requests for STO, RTO or AGARD documents should include the word 'STO', 'RTO' or 'AGARD', as appropriate, followed by the serial number (for example AGARD-AG-315). Collateral information such as title and publication date is desirable. Full bibliographical references and abstracts of STO, RTO and AGARD publications are given in "NTIS Publications Database" (http://www.ntis.gov).

ISBN 978-92-837-2227-4